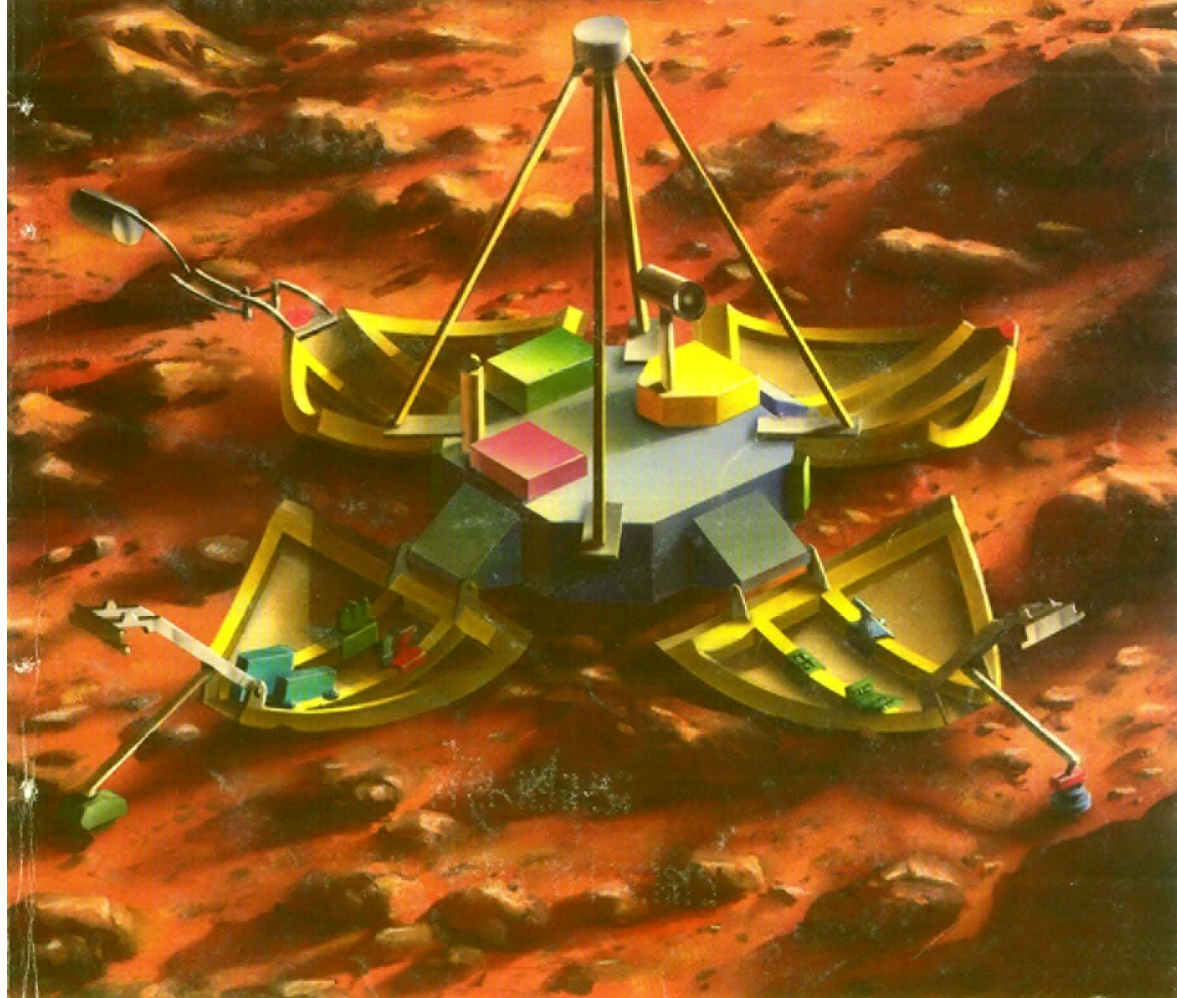


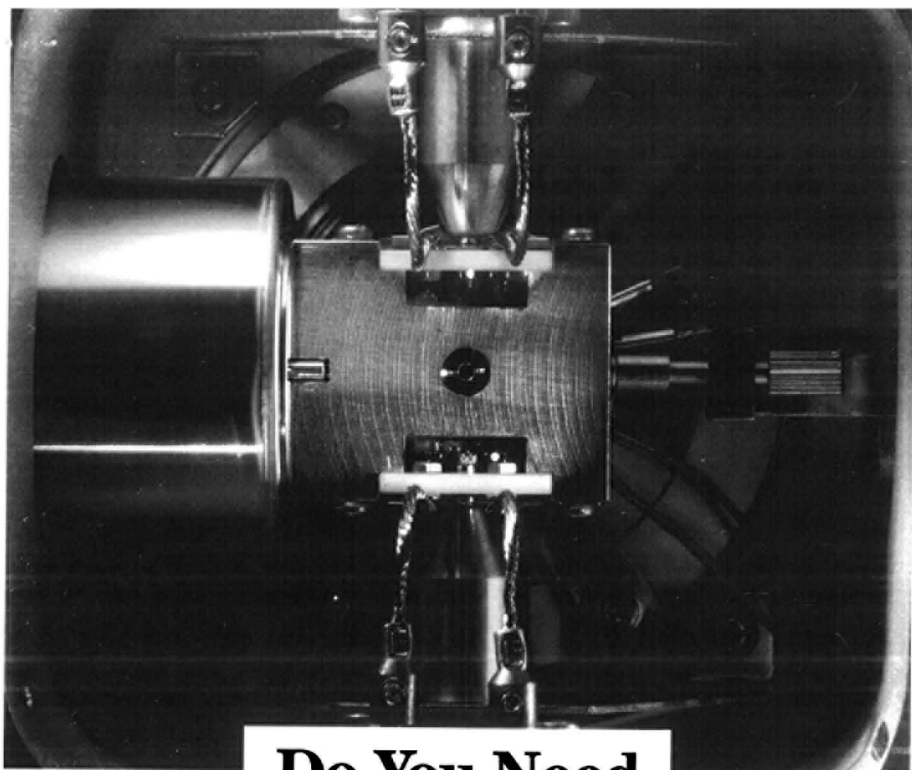
ANCHAM

ANALYTICAL CHEMISTRY

OCTOBER 1, 1995

Investigating the Surface Chemistry of Mars 605 A



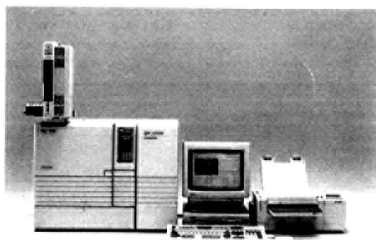


Do You Need A Comprehensive GC/MS Solution?

The Shimadzu GC/MS QP-5000. The new generation. Compact and complete.

Regardless of whether you work in water, air, or soil analysis, or whether you are looking for environmental analysis, additives in food, or forensics drug abuse, our new GC/MS QP-5000 is sure to exceed your expectations. Its mass spectrometer, covering the range 10 amu to 700 amu, is coupled to the proven performance of the GC-17A gas chromatograph, including AFC for setting carrier related flows and pressures. Our new GC/MS QP-5000 has been designed for the most stringent analytical methodology as well as routine analytical laboratory work. Its compactness and range

of features are truly impressive. The overall width of the GC and MS is just 72.5 cm (28.5"). All system operations are controlled by Microsoft® Windows™-based software. The GC/MS QP-5000 is a highly sensitive bench-top GC/MS with computer-simulation-optimized ion optics and fully automated vacuum control. Available options include a jet-separator interface, a high capacity turbomolecular pump, chemical-ionization, and a direct inlet system for low volatiles. Call your nearest Shimadzu Representative today for more details on the GC/MS QP-5000. You can count on a prompt response from us.



Microsoft® Windows™ is a registered trademark of Microsoft Corporation, Redmond, WA, USA.

SHIMADZU CORPORATION,
International Marketing Division
3, Kanda-Nishikicho 1-chome, Chiyoda-ku, Tokyo 101, Japan
Phone: 81(3)3219-5641 Fax: 81(3)3219-5710

SHIMADZU SCIENTIFIC INSTRUMENTS, INC.
7102 Riverwood Drive, Columbia, Maryland 21046, U.S.A.
Phone: 1(410)381-1227 Fax: 1(410)381-1222

SHIMADZU EUROPA GmbH
Phone: 49(203)7687-0 Fax: 49(203)766625 Germany.

SHIMADZU (ASIA PACIFIC) PTE LTD.
Phone: 65-778 6280 Fax: 65-779 2935 Singapore.

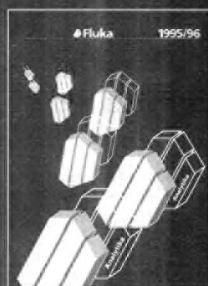
SHIMADZU OCEANIA PTY. LTD.
Phone: 61(2)684-4200 Fax: 61(2)684-4055 Australia.

For more information, please contact us.

 **SHIMADZU**
Solutions for Science
since 1875

CIRCLE 4 ON READER SERVICE CARD

Discover The World of Fluka...



...in the new catalogue 1995/96, listing
a broad range of chemicals,
biochemicals and analytical reagents.

Ask for your free copy.

Fluka

Fluka Chemie AG Industriestrasse 25
CH-9471 Buchs/Switzerland
(41-81-755 25 11 Fax 41-81-756 54 49

Australia Castle Hill (02-899 9977

Austria Wien (0222-740 40 644

Benelux Bornem (03-899 13 01

Brazil São Paulo (011-231 1866

Czech Republic Praha (02-2422 5285

France St. Quentin Fallavier (74 82 28 00

Germany Neu-Ulm (0731-973 03

Great Britain Gillingham (01747-82 30 97

Hungary Budapest (06-1-269 1288

India Hyderabad (040-244 739

Israel Holon (03-559 6610

Italy Milano (02-33417310

Japan Chuo-ku, Tokyo (03-5640 8865

Korea Seoul (02-783 5211

Mexico México, D.F. (05-631 3671

Poland Poznań (061-232 481

Spain Alcobendas (91-661 99 77

Sweden Stockholm (08-742 02 50

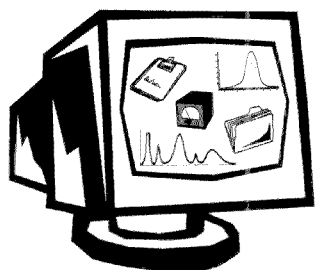
USA Ronkonkoma, New York

(516-467-0980

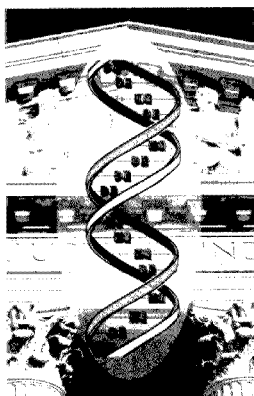
CIRCLE 1 ON READER SERVICE CARD

Analytika

Analytika



617 A



613 A



592 A



605 A

REPORT

592 A
Measuring colloidal and macro-molecular properties by FFF

Although FFF is commonly thought of as a separation technique, it can also be used for measurement. J. Calvin Giddings of the University of Utah enumerates the various properties of macromolecules and colloids that can be measured using FFF, and explains how these measurements are made and how measurement capabilities are enhanced by the separation process.

REPORT

605 A
ON THE COVER. Investigating the surface chemistry of Mars

The unusual conditions found on the Martian surface 20 years ago have prompted development of the Mars Oxidant Experiment to further investigate the chemical nature of the Martian surface material, with particular emphasis on its oxidative character. Anthony Ricco and the members of the Mars Oxidant Experiment Team describe the scientific rationale and basis for the MOx instrument, along with details of its design and construction.

COVER ART BY MARK MILLE

DEPARTMENTS

575 A In AC Research

583 A Editorial

What's in a title? Because the title is the first (and sometimes the only) part of a research article that is read, careful thought should always go into its construction.

585 A Analytical Currents

590 A News

Ten students to receive graduate fellowships. • NIST announces Advanced Technology Program awards. • Thermo to acquire ATI. • Life Sciences purchases Spectronic Instruments. • For Your Information.

600 A Software

A cyclic voltammetric simulator for Windows. *DigiSim 2.0*, an electrochemical digital simulation package, is reviewed by Dieter Britz of Aarhus University (Denmark). • Software released.

602 A Books

An affinity for biomolecules. *Molecular Interactions in Bioseparations* is reviewed by Michael R. Ladisch of Purdue University. • **CE for the novice.** *Capillary Electrophoresis* is reviewed by Michelle M. Bushey of Trinity University. • Books received.

611 A Meetings

EAS returns to New Jersey. The 34th Annual Eastern Analytical Symposium will be held at the Garden State Convention and Exhibit Center in Somerset, NJ, Nov. 12-17.

613 A Focus

Forensic PCR: Primed, amplified, and ready for court. Standardized protocols make this DNA typing method robust enough for criminal investigations.

617 A Product Review

Chromatography data systems. Computers are becoming more integral to chromatography, but there are trade-offs in flexibility. We review the basic theory involved and compare the features of representative systems.

622 A New Products

An immunoanalyzer, a TGA instrument for gas mixture interactions, and a confocal fluorescence correlation spectrometer are featured. • Instrumentation. • Literature.

626 A Information Express

1C AC Research Contents

3377-3611 AC Research

3612 Author Index

Analytical Chemistry (ISSN 0003-2700) is published semimonthly by the American Chemical Society, 1155 Sixteenth St., N.W., Washington, DC 20036. Second-class postage paid at Washington, DC, and additional mailing offices. Postmaster: Send address changes to *Analytical Chemistry*, Member & Subscriber Services, P.O. Box 3337, Columbus, OH 43210.

Canadian GST Reg. No. 127571347.

DISCOVER SOMETHING STUNNINGLY SMALL WITH OUR NEW LC/MS/MS...



...ITS PRICE.

You'll literally be amazed to discover that our new LCQTM delivers MS/MS capability for just the cost of an MS-only instrument.

Now you can use the LCQ to solve problems such as drug metabolism, pharmaceutical quantitation, structural elucidation, natural products analysis, combinatorial libraries, protein and peptide analysis and QA/QC.

This power-packed benchtop detector offers MSⁿ, an LCQ exclusive, and it's absolutely the most sensitive full scan MS/MS mass spectrometer ever. LCQ's Windows NT[®] data system also makes all this power easy to use. For a quote on this stunning value, just fax us at 408-433-4823.



THE MASS SPECTROMETRY COMPANY

9001
SERIES

Australia Tel. (02) 646 2211 • France Tel. (1) 69 41 98 00 • Germany Tel. (0421) 54 930 • Italy Tel. (02) 66011742 • Japan Tel. (03) 3372 3001 • Netherlands Tel. (08385) 27266 • People's Republic of China Tel. (01) 8362441 • Sweden Tel. (08) 6800101 • United Kingdom Tel. (01442) 233555 • U.S.A. Tel. (408) 433-4800

Copyright 1995 by Finnigan Corporation, a subsidiary of Thermo Instrument Systems, Inc., a Thermo Electron Company. All rights reserved.

[®]Windows NT is a registered trademark of Microsoft Corporation.

Brief introductions to the research articles appearing in the October 1 issue and tentatively scheduled to appear in the October 15 issue

Accelerated Articles

FT spectroscopic imaging

Combining IR or Raman spectroscopic methods with microscopic or macroscopic spatial imaging techniques is a new discipline that combines the analytical capabilities of spectroscopy with the ability to visualize the spatial distribution of a sample's components. E. Neil Lewis and colleagues at the National Institutes of Health, the University of Pittsburgh, and Procter & Gamble describe a technique for high-fidelity FT-IR imaging spectroscopy using an indium antimonide focal plane array detector coupled to an IR microscope and a step-scan FT-IR interferometer. They discuss step-scan imaging principles, instrument design, and IR chemical imaging results. ("Fourier Transform Spectroscopic Imaging Using an Infrared Focal-Plane Array Detector"; AC9505785; p. 3377)

Monitoring oxidative stress

When exposed to environmental hazards and foreign substances, living cells increase their levels of reactive oxygen species and free radicals. This can result in a condition called oxidative stress, which has implications for carcinogenesis. Monique Vuillaume, Christian Amatore, and their colleagues at the Ecole Normale Supérieure (France) and the Institute de Recherche sur le Cancer (France) measure the H_2O_2 concentration of individual cells in a virus-transformed fibroblast cell line using platinumized carbon-fiber microelectrodes for amperometry. The addition of H_2O_2 scavengers indicates that peroxide is the major oxidizing agent detected in the cells during oxidative stress. ("Monitoring an Oxidative Stress Mechanism at a Single Human Fibroblast"; AC950383X; p. 3382)

Near-IR fluorescence detection for CGE and DNA

Because of lower background in the near-IR, on-column detection can be performed without sacrificing sensitivity. Steven A. Soper and Daryl C. Williams of Louisiana State University demonstrate near-IR fluorescence in DNA sequencing in conjunction with capillary gel electrophoresis in a single-lane, single-dye base identification protocol with a tricyanine-labeled sequencing primer. The detection limit using the near-IR dye-labeled primer is 3.4×10^{-20} mol versus 1.5×10^{-18} mol for a visible fluorescein-labeled primer. ("Ultrasensitive Near-IR Fluorescence Detection for Capillary Gel Electrophoresis and DNA Sequencing Applications"; AC9504140; p. 3427)

Monitoring metals in the water

The ability to monitor metal concentrations in both fresh water and seawater is important as a pollution monitoring tool and as a surrogate for bioavailability. William Davison and Hao Zhang of Lancaster University (U.K.) use the diffusive gradient in thin film method to measure in situ concentrations of Cd, Fe, Mn, and Cu in coastal and open seawater. Deployment of the film for one day results in a concentration factor of ~ 300 , allowing metals to be measured at extremely low levels (4 pmol/L). ("Performance Characteristics of Diffusion Gradients in Thin Films for the in Situ Measurement of Trace Metals in Aqueous Solution"; AC9504676; p. 3391)

LC/NMR of glucuronide isomers

Glucuronides are used as nonsteroidal anti-inflammatory drugs, but their susceptibility to spontaneous acyl migration and mutarotation in aqueous solutions may be responsible for some side effects. In some cases, HPLC separation followed by off-line NMR allows the drugs too much isomerization time for accurate reactivity studies. Jeremy K. Nicholson and colleagues at the University of London (U.K.), Wellcome Research Laboratories (U.K.), and Zeneca Pharmaceuticals (U.K.) develop an on-line separation and characterization method for these drug isomers using directly coupled isocratic HPLC/NMR in stopped-flow mode. The method characterizes positional isomers with direct detection and allows the observation of mutarotation. ("Identification of the Positional Isomers of 2-Fluorobenzoic Acid 1-O-Acyl Glucuronide by Directly Coupled HPLC-NMR"; AC950379L; p. 3401)

Resolving peptide isomers

At room temperature, the cis and trans forms of most peptide bonds interconvert with rates on the order of seconds to minutes, and analysis of proline-containing peptides with CZE gives two peaks for dipeptides and multiple peaks for oligopeptides with more than one proline. James W. Jorgenson and Alvin W. Moore, Jr., of the University of North Carolina-Chapel Hill use fast CZE to resolve the cis and trans isomers of proline-containing dipeptides. They use a digital simulation model to extract kinetic information from the experimental data. ("Resolution of Cis and Trans Isomers of Peptides Containing Proline Using Capillary Zone Electrophoresis"; AC950678A; p. 3464)

Glycosyltransferases by MALDI

Chromatographic and immunological methods that measure the products of glycosyltransferase reactions, a class of en-

BIOANALYTICAL

zymes that control assembly of oligosaccharides in cells, can be time consuming and cumbersome. Liang Li and colleagues at the University of Alberta (Canada) use matrix-assisted laser desorption ionization to determine enzymatic reaction products of oligosaccharides in serum. The technique can detect labeled oligosaccharides at the fmol/ μ L level. ("Direct Analysis of Enzymatic Reactions of Oligosaccharides in Human Serum Using Matrix-Assisted Laser Desorption Ionization Mass Spectrometry"; AC950307U; p. 3509)

CIEF with ESMS

The traditional biochemical approach to protein characterization has been the use of two-dimensional gel electrophoresis. Cheng S. Lee and colleagues at Iowa State University demonstrate the on-line combination of capillary isoelectric focusing with electrospray MS as a two-dimensional separation system for protein characterization. The concentration detection limit for myoglobin for a full-scan CIEF-ESMS analysis is in the range of 10^{-7} M, an improvement of 2 orders of magnitude. ("Capillary Isoelectric Focusing-Electrospray Mass Spectrometry for Protein Analysis"; AC950348Q; p. 3515)

Enantiomeric protein binding

Protein binding of the optical isomers of a chiral drug can potentially differ because of the inherent chirality of proteins. Akimasa Shibukawa and colleagues at Kyoto University (Japan) develop a CE method for enantioselective determination of the unbound concentration of a basic drug under plasma protein binding equilibrium. Sample size is ~ 200 nL, one-thousandth that used in the reference method. Their results compare favorably with those determined by conventional ultrafiltration/chiral HPLC. ("Capillary Electrophoresis/Frontal Analysis for Microanalysis of Enantioselective Protein Binding of a Basic Drug"; AC950400I; p. 3520)

CE alternative to Scatchard analysis

For many biochemical interactions, such as protein-ligand binding, more than one covalent interaction is involved, and each site of attachment has its own kinetic dissociation constants. George M. Whitesides and colleagues at Harvard University use changes in electrophoretic mobility to monitor binding interactions between antibodies with two binding sites and charged ligands containing a *N*-dinitrophenyl group in affinity CE. They observe cooperativity effects and compare affinity CE with Scatchard analysis. ("Determination of the Binding of Ligands Containing the *N*-2,4-Dinitrophenyl Group to Bivalent Monoclonal Rat Anti-DNP Antibody Using Affinity Capillary Electrophoresis"; AC950368S; p. 3526)

Optimizing the detector

In microbore LC with electrochemical detection for determining peptides, the only control over selectivity is the separation—detection does not typically distinguish among various peptides. In a continuation of earlier work, Stephen G. Weber and Jian-Ge Chen of the University of Pittsburgh examine the parameters that control detection selectivity for mixtures of 23 peptides. They discuss the effects of postcolumn pH, buffer type, temperature, reaction time, and anode potential. ("Detection of Bioactive Oligopeptides after Microbore HPLC with Electrochemical Detection of Their Cu(II) Complexes: Effect of Operating Parameters on Sensitivity and Selectivity"; AC9504373; p. 3596)

A new way to immobilize antibodies

Over the past decade, there has been great interest in site-specific deposition of biological molecules and in constructing complex patterns of immobilized biological molecules on surfaces. Jonathan M. Cooper and colleagues at the University of Glasgow (U. K.) describe a new technique for site-specific immobilization of six different proteins within an area of $200 \mu\text{m} \times 50 \mu\text{m}$. The procedure involves coating the surface with deglycosylated avidin, which binds a photoactive biotin analogue, thus providing a light-addressable surface onto which proteins can be immobilized. ("Patterning and Regeneration of Surfaces with Antibodies"; AC950324J; p. 3605)

Hydrating proteins in reverse micelles

The degree of protein hydration and/or local solvent composition can affect a protein's structure and dynamics, and in turn its performance in a biosensor. Frank V. Bright and colleagues at the State University of New York—Buffalo investigate the effects of hydration on acrylodan-labeled bovine and human serum albumin in aerosol-OT reverse micelles solubilized in *n*-heptane. Time-resolved fluorescence intensity decay experiments reveal a dipolar relaxation process surrounding the acrylodan cybotactic region. ("Dynamics of Acrylodan-Labeled Bovine and Human Serum Albumin Sequestered within Aerosol-OT Reverse Micelles"; AC950404N)

Detecting increased blood silicon levels

The fate of silicone leaked from silicone gel breast implants has become the focus of intense scrutiny. Peter Macdonald and colleagues at the University of Toronto (Canada) compare results of ^{29}Si magic-angle spinning NMR and AA spectroscopy for determination of blood silicon levels in control patients and patients with silicone gel breast implants. Although AA spectroscopy yielded blood silicon levels in the ng/mL range for control patients and somewhat higher levels for patients with implants, the ^{29}Si NMR technique was unable to detect silicon in any of the samples. ("Failure of ^{29}Si NMR To Detect Increased Blood Silicon Levels in Silicone Gel Breast Implant Recipients"; AC950448W)

Studying the hydrolysis of a β -lactamase inhibitor

Although β -lactam antibiotics are commonly used for the treatment of bacterial infections, hydrolytic enzymes produced by many bacterial pathogens render many such antibiotics ineffective in the clinical environment. Patrick Camilleri and colleagues at SmithKline Beecham Pharmaceuticals study the hydrolysis of the four-membered lactam ring of a potent β -lactamase inhibitor mediated either by Tris buffer or by Tem2 β -lactamase. Free-zone CE is used to identify reaction products, interpret the mechanism of hydrolysis, and determine the kinetic parameters and stoichiometry. ("Capillary Electrophoresis Study of the Hydrolysis of a β -Lactamase Inhibitor"; AC950531J)

DNA sequencing on a chip

Miniaturization of electrophoretic instrumentation to increase the speed and throughput of separations is necessary to meet the needs of the Human Genome Project. Richard A. Mathies and Adam T. Woolley of the University of California—Berkeley demonstrate high-speed DNA sequencing on microfabricated CE chips. Using a four-color labeling and detection format, DNA sequenc-

ing with 97% accuracy and single-base resolution to ~ 150 bases is achieved in only 540 s. ("Ultra-High-Speed DNA Sequencing Using Capillary Electrophoresis Chips"; AC9505379)

Fiber-optic sensing for glucose and oxygen

Electrochemical biosensors for glucose based on glucose oxidase require tight control of the oxygen concentration to avoid interferences. For applications where measurement of both glucose and oxygen is desirable, spectroscopic methods might present fewer complications. David R. Walt and Lin Li of Tufts University fabricate a fiber-optic sensor with two polymer-coated sites for continuous and simultaneous determination of glucose, using glucose oxidase, and oxygen, using an oxygen-sensitive ruthenium dye. Response time varies from 9 to 28 s and the sensor maintains its sensitivity for two days. ("Dual-Analyte Fiber-Optic Sensor for the Simultaneous and Continuous Measurement of Glucose and Oxygen"; AC050344L)



Potential-modulated spectroelectrochemistry

The redox properties of compounds adsorbed at an electrode surface are often quite different from those of the bulk solution and can either enhance or inhibit electrode reactivity. Spectroelectrochemical techniques allow both the measure-

ment of these redox properties in situ and structural characterization of the adsorbates. Takamasa Sagara, Katsumi Niki, and Zhi Quiang Feng of Yokohama National University (Japan) explore the use of sinusoidal potential modulation at the electrode with UV-vis reflectance spectroscopy to determine reaction rate constants for Nile Blue A adsorbed onto a glassy carbon electrode. ("Application of Potential-Modulated UV-Visible Reflectance Spectroscopy to Electron Transfer Rate Measurements for Adsorbed Species on Electrode Surfaces"; AC940668U; p. 3564)

Determining trace mercury

Because mercury is one of the most toxic metals, its determination at trace levels is important in both environmental and biological analyses. Jyh-Myng Zen and Mu-Jye Chung of the National Chung-Hsing University (Republic of China) develop a poly(4-vinylpyridine)/gold film electrode to determine trace mercury in water samples by square-wave anodic stripping voltammetry. The modified electrode shows improved resistance to interferences from surface-active compounds and common ions compared with a conventional gold film electrode. ("Square-Wave Voltammetric Stripping Analysis of Mercury(II) at a Poly(4-vinylpyridine)/Gold Film Electrode"; AC950179+; p. 3571)

SECM of immobilized antibodies

Much attention has been paid to applying antibodies as selective agents for analytical purposes, but the optimization of assay or sensor surfaces is complicated by a lack of suitable methods for characterizing their properties. William R. Heineman and colleagues at the University of Cincinnati use scanning electrochemical microscopy to visualize immobilized antibodies by saturating antigen binding sites with an alkaline phosphatase-antigen conjugate, which catalyzes hydrolysis of redox-inactive 4-aminophenyl phosphate to redox-active 4-aminophenol. The

collection mode at an amperometric SECM tip is then used to detect the 4-aminophenol. ("Imaging of Immobilized Antibody Layers with Scanning Electrochemical Microscopy"; AC9500141; p. 3578)

Improved voltammetry of NADH

The analytical performance of carbon electrodes is highly dependent on the manner in which the carbon surface is prepared. Werner G. Kuhr and Wilbur B. Nowall of the University of California-Riverside show that a simple electrochemical treatment of a carbon-fiber electrode surface can dramatically improve the voltammetry of NADH and several other anionic molecules under steady-state and fast-scan conditions. Oxidation overpotentials are shifted by different magnitudes for each analyte tested, allowing discrimination among analytes of interest and their major interferences. ("Electrocatalytic Surface for the Oxidation of NADH and Other Anionic Molecules of Biological Significance"; AC950229A; p. 3583)

Photocurable polymers for ISE membranes

Interest in the development of ion sensors based on polymer membranes has recently been renewed because of advances in microelectronics. Carlos Domínguez and colleagues at the Centre Nacional de Microelectrónica (Spain) and the Universitat Autònoma de Barcelona (Spain) investigate the compatibility of photocurable oligomers based on urethane and bisphenol A (epoxy) diacrylates for ion-selective membranes. They demonstrate a potassium-sensitive electrode made with a photocured urethane membrane and valinomycin as the ionophore. ("Photocurable Polymer Matrices for Potassium-Sensitive Ion-Selective Electrode Membranes"; AC950249C; p. 3589)



Organophosphate pesticides by electron capture negative ion MS

Because of the widespread use of organophosphate pesticides in agriculture, there is concern about the level of residues in animal and plant tissues, food, air, and water samples. Max L. Deinzer and colleagues at Oregon State University use electron capture negative ion MS to study the resonant electron energies of organophosphate pesticides. Both resonance electron capture ions and dissociative electron capture ions are produced; electrons of energies 0.03–7 eV and ions may be formed from as many as three observable resonance states. ("Analysis of Organophosphate Pesticides by a Trochoidal Electron Monochromator Mass Spectrometer System"; AC950265+; p. 3476)

Nitrocellulose substrate for MALDI of DNA

The possibility of separating and characterizing mixtures of DNA fragments rapidly and directly by MS rather than by cumbersome electrophoretic methods is tantalizing. David M. Lubman and colleagues at The University of Michigan and Michigan State University use nitrocellulose film rather than a metal sample probe as the substrate for MALDI of DNA fragments up to 622 base pairs long from complex mixtures. Shot-to-shot reproducibility of the ion yield is improved because the matrix and sample are distributed more homogeneously on the film than on a metal surface. ("Use of a Nitrocellulose Film Substrate in Matrix-Assisted Laser Desorption/Ionization Mass Spectrometry for DNA Mapping and Screening"; AC9503318; p. 3482)

ESI metal-carbohydrate complexation

MS/MS structural characterization of carbohydrates is a growing field, but on-line derivatization methods that would allow LC/MS/MS are still lagging. In a continuation of work showing that metal coordination of oligosaccharides enhances sensitivity in FABMS and ESIMS, Julie A. Leary and Martin Kohler of the University of California-Berkeley design a triaxial electrospray probe that adds a sheath solution of metal chlorides to carbohydrate eluates from an LC column and forms metal-carbohydrate complexes directly in the ion source. ("LC/MS/MS of Carbohydrates with Postcolumn Addition of Metal Chlorides Using a Triaxial Electrospray Probe"; AC950315A; p. 3501)

MALDI-FTMS of high-mass biomolecules

A current limitation of MALDI-FTMS is the inherent difficulty in trapping high-mass species. Charles L. Wilkins and co-workers at the University of California-Riverside describe a new decelerating technique that places dc potentials on the orthogonal excitation and receiver plates as well as the rear trapping plate of the source cell of a dual cubic cell. When this five-plate trapping method is applied, high-mass ions with large translational kinetic energies can be trapped efficiently and detected. ("Analysis of High-Mass Biomolecules Using Electrostatic Fields and Matrix-Assisted Laser Desorption/Ionization in a Fourier Transform Mass Spectrometer"; AC950419L)

SIM in an ion trap

Selected ion monitoring is commonly used to increase the S/N of ions in MS. Greg Wells and Chuck Huston of Varian Chromatography Systems describe a new method of SIM that combines the sensitivity enhancement of selective ion accumulation and the specificity of unit mass isolation. The ionization time for each mass is individually adjusted to optimize the filling of the trap with selected ions, and the individual spectra for each mass are added together to form a mass spectrum containing all specified ions. ("High-Resolution Selected Ion Monitoring in a Quadrupole Ion Trap Mass Spectrometer"; AC950390L)

SEPARATIONS

Fluorescence detection in DNA slab gels

Although ultrathin slab gels used in automated DNA sequencers transfer heat efficiently and allow the use of higher electric fields for faster electrophoretic separations, their use complicates DNA detection by laser-induced fluorescence

excitation. Lloyd M. Smith and co-workers at the University of Wisconsin and the Lawrence Berkeley Laboratory design a laser configuration that allows illumination from the side edge of the ultrathin gels and reduces the background fluorescence and scattering. They also develop a model for describing beam throughput. ("Side Excitation of Fluorescence in Ultrathin Slab Gel Electrophoresis"; AC9504070; p. 3405)

Native fluorescence detection of peptides in CE

CE, with its minuscule sample volume requirements and high separation capabilities for complex mixtures, is well suited to the separation of contents from single cells, but detecting these contents is another matter. At the analyte concentrations expected from a single cell, derivatization with fluorescent tags for laser-induced fluorescence detection is impractical.

Jonathan V. Sweedler and colleagues at the University of Illinois design a system for low-attomole native fluorescence detection of peptides that incorporates a UV laser for excitation and both an imaging spectrograph and a CCD detector. ("Native Fluorescence Detection and Spectral Differentiation of Peptides Containing Tryptophan and Tyrosine in Capillary Electrophoresis"; AC950479R; p. 3421)

Investigating adsorption/desorption kinetics

Knowledge of the kinetics involved in reversed-phase LC separations is important for the design of effective column packing materials and for a fundamental understanding of the chemistry of bonded phases and the retention behavior of analytes. J. M. Harris and colleagues at the University of Utah use temperature-jump perturbation to investigate the adsorption/desorption kinetics of ionic and nonionic solute probes at a C_1 -silica surface in contact with a variety of methanol-water solutions. The adsorption rate of the ionic probe is slower than is a diffusion-controlled probe and the adsorption rate of the neutral probe is indistinguishable from the diffusion limit. ("Temperature-Jump Investigation of Adsorption/Desorption Kinetics at Methylated Silica/Solution Interfaces"; AC950358R; p. 3441)

Multidimensional separations

Because their operating buffers are compatible and their separating mechanisms are different, the orthogonality of reversed-phase LC and CZE should allow many of the advantages of these techniques to be realized in 2-D operation. James W. Jorgenson and Alvin W. Moore of the University of North Carolina-Chapel Hill demonstrate the coupled-column approach to linking reversed-phase LC with optically gated CZE for the analyses of peptides in < 10 min. They also demonstrate a 3-D approach by sending the effluent from SEC through the 2-D reversed-phase LC/CZE system. ("Rapid Comprehensive Two-Dimensional Separations of Peptides via RPLC/Optically Gated Capillary Zone Electrophoresis"; AC9506793; p. 3448; "Comprehensive Three-Dimensional Separation of Peptides Using Size Exclusion Chromatography/Reversed Phase Liquid Chromatography/Optically Gated Capillary Zone Electrophoresis"; AC9506802; p. 3456)

Determining BTEX in oils

The levels of benzene, toluene, ethylbenzene, and xylene isomers in petroleum can directly affect the physical and chemical properties of the oil. Zhendi Wang and colleagues at Environment Canada develop a GC/MS method for determining BTEX components in oil. Using this method, they identify 58 alkyl-substituted benzene components in a light crude oil, Alberta Sweet Mixed Blend, and determine the concentrations of the individual BTEX compounds and C_3 -benzene isomers in more than 200 crude and weathered oils. ("Identification of Alkylbenzenes and Direct Determination of BTEX and (BTEX + C_3 -Benzenes) in Oils by GC/MS"; AC950168G; p. 3491)

Pyrolysis GC for polymer structure determination

Styrene and *n*-butyl acrylate emulsion polymers are widely used in coating and adhesive applications in the paper, paint, and construction industries. Frank Cheng-Yu Wang and colleagues at the Dow Chemical Company use pyrolysis GC to investigate the microstructure of emulsion polymers. The composi-

tion elucidated from the number-average sequence length matches the preparation recipe and/or the results obtained by ^{13}C NMR. ("Structure Determination of Polymeric Materials by Pyrolysis Gas Chromatography"; AC950515M; p. 3536)

SFE/GC of organics in aerosols

Sample preparation techniques used for atmospheric organic aerosols typically require large volumes of solvents and long periods for extraction. Robert E. Sievers and colleagues at the University of Colorado describe an integrated sampling and SFE cell that can be coupled directly to a gas chromatograph. After on-line SFE and separation by GC, MS or flame ionization is used for detection. The authors present a comparison between SFE and thermal desorption and ambient and spiked aerosols. ("Supercritical Fluid Extraction-Gas Chromatographic Analysis of Organic Compounds in Atmospheric Aerosols"; AC950393Y; p. 3541)

Predicting drug-membrane interactions

The molecular recognition properties of immobilized artificial membrane surfaces toward drug binding/partitioning appear to be remarkably close to the molecular recognition properties of fluid membranes. Charles Pidgeon and colleagues at Purdue University and Regis Technologies synthesize an immobilized octanol surface and evaluate the ability of this surface to predict drug partitioning into *n*-octanol/water phases and into fluid membranes. Their results suggest that chromatographic surfaces containing interfacial polar groups model drug-membrane interactions, but that surfaces lacking these groups are poor models. ("Predicting Drug-Membrane Interactions by HPLC: Structural Requirements of Chromatographic Surfaces"; AC950267U; p. 3550)

Total and free metal ion concentration in solution

The amount of metal ion sorbed onto a resin under a given set of conditions can be predicted if the composition of the solution is known. Maria Pesavento and Raffaela Biesuz of the Università di Taramelli (Italy) demonstrate that it is possible to do the same with a solution of unknown composition by putting different aliquots of the sample in contact with the resin, keeping the acidity constant, and determining the concentration of the sorbed metal. The validity of the procedure is demonstrated on some synthetic systems. ("Simultaneous Determination of Total and Free Metal Ion Concentration in Solution by Sorption on Iminodiacetate Resin"; AC940897G; p. 3558)

Separating cisplatin with graphite

When the cancer drug cisplatin, its trans isomer, and its hydrated complexes are separated by LC, they react with constituents of the mobile phase, such as acetonitrile and phosphate buffers. Hans C. Ehrsson and colleagues at Karolinska Pharmacy (Sweden) and Pharmacia AB (Sweden) separate these compounds on porous graphitic carbon, demonstrating that it is possible to isolate the pure monohydrated complex of cisplatin, the most cytotoxic form of the drug, from an equilibrium mixture of cisplatin in distilled water for subsequent use *in vivo* and *in vitro* studies. Detection is accomplished by electrospray ionization MS. ("Cisplatin, Transplatin, and Their Hydrated Complexes: Separation and Identification Using Porous Graphitic Carbon and Electrospray Ionization Mass Spectrometry"; AC9500904; p. 3608)

MEKC of hypoglycemic drugs*

Sulfonylurea drugs used to treat hyperglycemia are also used as drugs of abuse and can cause symptoms that mimic tumor-associated overproduction of insulin. A screening method for these drugs could prevent erroneous pancreatic surgeries. J. P. Landers and co-workers at the Mayo Foundation/Mayo Clinic develop MEKC separations of sulfonylurea drugs that are spiked into urine or present in the urine of hyperglycemic patients. They evaluate various detergents and achieve baseline separation of seven analogues with 50-ng/mL detection limits. ("Detection of Hypoglycemic Drugs in Human Urine Using Micellar Electrokinetic Chromatography"; AC950016L)

Pyrolysis for polymer modifier extraction*

Many polymers contain small amounts of organic polar modifiers with very different LC or GC retention characteristics from the mostly nonpolar polymer. Frank Cheng-Yu Wang and colleagues at Dow Chemical Company combine pyrolysis with solvent trapping to extract acrylic acid and methacrylic acid modifiers from a solid-emulsion polymer prior to separation. The polymer is pyrolyzed and introduced into a GC system optimized for that polymer; the acid modifiers in the solvent can be separated by an HPLC or GC system with conditions that are more suitable for them. ("Pyrolysis with a Solvent Trapping Technique. Qualitative Identification of Acrylic Acid and Methacrylic Acid in Emulsion Polymers"; AC9505381)

Magnetic separation*

Because of the increasing use of magnetic separation techniques in biotechnology, magnetic analytical methods must be further developed to ensure optimization of the separation process. Maciej Zborowski and colleagues at the Cleveland Clinic Foundation and The Ohio State University use analytical magnetapheresis to determine the effective magnetic volumetric susceptibility of human lymphocyte cells labeled with ferritin. They achieve almost complete deposition of the lymphocytes at an average flow velocity of 0.28 mm/s. ("Analytical Magnetapheresis of Ferritin-Labeled Lymphocytes"; AC950248K)

Modeling electroosmotic flow*

Electroosmotic flow (EOF), which is affected by the chemical interactions at the inside surface of a capillary, is an important factor in CE because it influences retention times and can allow simultaneous determination of cations and anions. Victoria L. McGuffin and Marina F. M. Tavares of Michigan State University develop a mathematical model of EOF in CE using solutions of singly-charged strong electrolytes and find a linear correlation between the ζ potential and the logarithm of cation activity. They propose that the capillary surface behaves as an ion-selective electrode. ("Theoretical Model of Electroosmotic Flow for Capillary Zone Electrophoresis"; AC950051S)

FT meets its reflection

The Fourier transform (FT) is one of the most commonly used and most powerful tools for enhancing spectral data in near-IR, NMR, and ICPMS methods. Several new algorithms have been introduced in recent years to improve the resolution of FT spectra. Michael V. Gorshkov and Richard T. Kouzes of Pacific Northwest Laboratory develop a data reflection algorithm for enhancing FT results in



Separations as sharp as a razor with the ultrapure NUCLEOSIL®

Separation of natural porphyrins

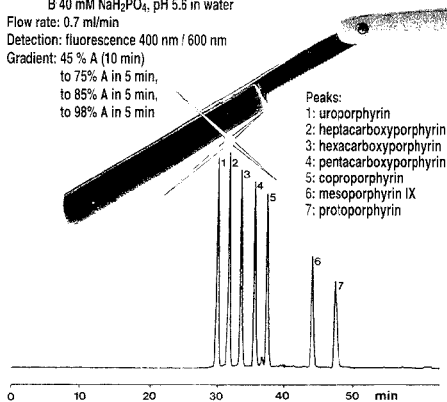
Column: ET 250/8/4 NUCLEOSIL® 120-5 C₁₈
Eluent: A methanol, 12.5 mM tetrabutylammonium dihydrogen phosphate, pH 6.6
B 40 mM NaH₂PO₄, pH 5.6 in water

Flow rate: 0.7 ml/min

Detection: fluorescence 400 nm / 600 nm

Gradient: 45 % A (10 min)

to 75% A in 5 min,
to 85% A in 5 min,
to 98% A in 5 min



Specialists in Chromatography

● NUCLEOSIL®
HPLC packings for
analytical and preparative separations

○ spherical particles

○ pore sizes from 50 to 4000 Å

○ outstanding separation performance and
very good reproducibility from lot to lot

○ high pressure stability even for wide pore materials

○ numerous chemically bonded phases

Please ask for further information!



MACHEREY-NAGEL GmbH & Co. KG · P.O. Box 10 13 52
D-52313 Düren · Germany · Tel. (02421) 969-0 · Fax (02421) 969 199
Switzerland: MACHEREY-NAGEL AG · P.O. Box 224 · CH-4702 Oensingen · Tel. (052) 76 20 66
France: MACHEREY-NAGEL S.à.r.l. · B.P. 135 · F-67222 Hoerdt · Tél. 88 51 76 89

CIRCLE 2 ON READER SERVICE CARD

In AC Research

FT-ICR and FT-NMR spectra. They replace the time-domain signal with a composite of the original time-domain signal and a reflected signal to generate a centerburst time-domain spectrum, and they compare this method with magnitude-mode derivative methods. The resulting FT spectra have improved resolution and S/N. ("Data Reflection Algorithm for Spectral Enhancement in Fourier Transform ICR and NMR Spectroscopies"; AC9502561; p. 3412)

Using ¹³C NMR to determine carbons in coal-derived liquids

The ratio of protonated to nonprotonated carbons provides an estimate of the average ring size in complex PAH mixtures such as heavy oils and coal-derived liquids. Ronald J. Pugmire, David M. Grant, and colleagues at Brigham Young University and the University of Utah use differential proton-induced dipolar relaxation rates to determine this ratio for liquid hydrocarbon mixtures. The method is applied to representative coal-derived oil samples and is useful for estimating the structure of liquids obtained at various stages of a coal liquefaction process. Their results indicate that the carbon relaxation rates for both protonated and nonprotonated carbons are consistent with the dipolar coupling of carbons to protons. (¹³C NMR Determination of Protonated and Nonprotonated Carbons in Model Compounds, Mixtures, and Coal-Derived Liquid Samples"; AC950384P; p. 3433)

Near-IR plastic sorting for recovery from mixed waste

Remote near-IR imaging methods have been introduced for sorting different types of plastics, but for identifying plastics among nonplastics in mixed municipal wastes, a great deal of image improvement is needed to make the technique feasible on a large scale. I. Buydens, D. Wienke, and co-workers at the Catholic University of Nijmegen (The Netherlands) apply singular value decomposition (SVD) to optimize the sample-to-background signal ratio for qualitative analysis and improvement of multivariate images taken with a near-IR camera. They develop a multivariate image rank analysis algorithm that produces a decision limit for plastic identification from three-dimensional stacks of SVD-improved images. ("Identification of Plastics among Nonplastics in Mixed Waste by Remote Sensing Near-Infrared Imaging Spectroscopy. 1. Image Improvement and Analysis by Singular Value Decomposition"; AC950116R; and "2. Multivariate Image Rank Analysis for Rapid Classification"; AC950117J)

Multivariate curve resolution for spectrophotometric titrations

Treating several sets of correlated matrices that have one or two orders in common with multivariate curve resolution yields information that is superior to that obtained by individual analysis of a single data matrix. S. Hernández-Cassou and colleagues at the Universitat de Barcelona (Spain) use multivariate curve resolution to analyze data from the continuous-flow spectrophotometric titration of amino acids with 1,2-naphthoquinone-4-sulfonate at pH 6.5-12.5. They obtained the pure spectra profiles of reagent and product species, the pH profiles of all species present, the percentage of reacted analyte, and the optimum pH for development of the reaction. ("Multivariate Curve Resolution Applied to Continuous-Flow Spectrophotometric Titrations. Reaction between Amino Acids and 1,2-Naphthoquinone-4-sulfonate"; AC950343T)

From the basics to the cutting edge...

JOHN WILEY & SONS

MODERN PRACTICE OF GAS CHROMATOGRAPHY, 3E
ROBERT L. GROB

This new edition of a best-selling reference/text features entirely new chapters on gas chromatography/mass spectrometry (GC/MS), optimizing separations using GC, forensic and environmental applications and injection systems. Includes expanded coverage of instrumentation, updated chapters on detectors, and qualitative and quantitative analysis by GC.
1-59700-7 1995 800 pp. \$89.95



ENVIRONMENTAL ANALYSIS
R. REEVE

This book provides a practical introduction to the techniques involved in environmental analysis. Introduces the reader to the basic concepts and principles, then goes on to cover the analysis of water, solid and gaseous samples. Written with a gradation in complexity, starting with routine techniques.

A volume in the ACOL Series
1-93833-5 1994 300 pp. \$34.95pb

PHOTOTHERMAL SPECTROSCOPY METHODS FOR CHEMICAL ANALYSIS
STEPHEN E. BIALKOWSKI

This book concentrates on the theoretical basis and practical considerations for applications of photothermal spectroscopy to the analysis of samples in homogenous media. Provides a complete description of the topic using a common mathematical language; the information gathered originates from analytical spectroscopy, measurement physics, physical optics, and chemical dynamics.

1-57467-8 11/95 528 pp. \$84.95

THERMAL ANALYSIS Fundamentals and Applications to Polymer Science

T. HATAKEYAMA & F. X. QUINN
This practical guide provides newcomers to TA with a comprehensive introduction to the basic principles of the technique. Includes instrument operation, sample preparation, optimization of operating conditions, and a guide to interpreting results.

1-95103-X 1995 168 pp. \$54.95

SELECTIVE DETECTORS
ROBERT E. SIEVERS

Provides an overview of the fundamentals and applications of analytical detectors that are selective for particular classes of chemical species. Leading applications of selective detection technologies, such as GC-atomic emission, plasma mass spectroscopy and flame ionization are covered in relation to real-world applications.
1-01343-9 1995 200 pp. \$64.95

HYDRIDE GENERATION ATOMIC ABSORPTION SPECTROMETRY

DIMITER L. TSALEV & JIRI DEDINA
Arranged in an easy to use element-by-element format, this book is the first comprehensive monograph available on HG-AAS. Divided into two parts - Part I covers the theoretical and experimental aspects of the topic, and Part II discusses the methodology and analytical applications.

1-95364-4 12/95 526 pp. \$84.95

HIGH SPEED COUNTERCURRENT CHROMATOGRAPHY

YOICHIRO ITO & WALTER D. CONWAY
This book presents comprehensive coverage of current theory, state-of-the-art instrumentation and applications. One of the first books on this new technique, it brings together information that was previously found only in journal articles. Includes numerous examples.

1-63749-1 1995 400 pp. \$79.95

PRACTICAL HIGH-PERFORMANCE LIQUID CHROMATOGRAPHY, 2E
V. MEYER

This book provides a systematic and easy-to-read text on the everyday running of an HPLC instrument. Features numerous footnotes, question and answer section, and a complete bibliography.

1-94132-8 1993 390pp. \$49.95 paper

PRACTICAL ORGANIC MASS SPECTROMETRY, 2E A Guide for Chemical and Biochemical Analysis

J. R. CHAPMAN
This new edition offers a complete handbook of current techniques for the use of mass spectrometry in organic and biochemical analysis.

1-95831-X 1995 338 pp. \$37.95 paper

PARTICLE-INDUCED X-RAY EMISSION SPECTROMETRY

SVEN A. E. JOHANSSON, KLAS G. MALMQVIST & JOHN L. CAMPBELL
This new book provides an assessment of the present state of development of Particle-Induced X-Ray Emission (PIXE), and includes a detailed overview of PIXE's impact in several major areas of application - atmospheric science, geology, art and archaeology.

1-58944-6 1995 408 pp. \$89.95

GAS CHROMATOGRAPHY, 2E
IAN FOWLIS

Provides an easy-to-understand introduction to gas chromatography and its applications. Featuring self-assessment questions, this book covers many recent developments in new detectors and equipment, and includes updated chapters on data handling, and quantitative and qualitative analysis.

A volume in the ACOL Series.
1-95468-3 1995 300 pp. \$39.95 pb

ANALYSIS OF MICROELECTRONIC MATERIALS AND DEVICES

M. GRASSERBAUER & H. W. WERNER
Provides a comprehensive overview of the techniques and methods used in the analysis of microelectronic materials and devices. Covers analysis, instrumentation, sample preparation and applications.

1-95013-0 12/95 704 pp. \$54.95 paper

CAPILLARY ELECTROPHORESIS
DALE R. BAKER

Presents a practical description of capillary electrophoresis covering development, principles, modes, instrumentation, method development and applications. Accessible to those just starting to use the technique, this book presents sufficient detail to be used as a reference for the more experienced reader. Features numerous figures and illustrations, and end-of-chapter references.

1-11763-3 1995 256 pp. \$49.95

EXAMINE ANY TITLE FREE FOR 15 DAYS!



TO ORDER BY PHONE:
CALL TOLL-FREE 800-US-WILEY
In Canada call: 800-263-1590
All other inquiries, call: 212-850-6418

Order through your bookseller or to order by mail, check off your selection & mail entire ad to:
JOHN WILEY & SONS, INC., Attn: E. Perzi, 605 Third Ave., New York, NY 10158-0012
 Send for a 15 day exam, with bill. *Valid in US only.* Payment enclosed.

Name _____
Affiliation _____
Address _____ City/State/Zip _____
Signature _____

Prices subject to change without notice

CIRCLE 5 ON READER SERVICE CARD

Analytical Chemistry, October 1, 1995 **581 A**

ANALYTICAL CHEMISTRY

EDITOR: ROYCE W. MURRAY
University of North Carolina

ASSOCIATE EDITORS: Catherine C. Fenselau, University of Maryland Baltimore County, William S. Hancock, Hewlett Packard, James W. Jorgenson, University of North Carolina, Robert A. Osteryoung, North Carolina State University, Edward S. Yeung, Iowa State University/Ames Laboratory

Editorial Headquarters, research section
Department of Chemistry
Venable and Kenan Laboratories
University of North Carolina
Chapel Hill, NC 27599-3290
Phone: 919-962-2541
Fax: 919-962-2542
E-mail: analyt_chem@unc.edu

Editorial Headquarters, A-page section
1155 Sixteenth St., N.W.
Washington, DC 20036
Phone: 202-872-4570
Fax: 202-872-4574
E-mail: analytical@acs.org

Managing Editor: Mary Warner

Associate Editors: Alan R. Newman, Felicia Wach

Editorial Assistant: Deborah Noble

Contributing Editor: Marcia Vogel

Head, Graphics and Production: Leroy L. Corcoran

Division Art Director: Alan Kahan

Art Director: Michele Telschow

Manager, Copy Editing: Elizabeth Wood

Production Editor: Eric Sorensen

Electronic Composition: Wanda R. Gordon

Journals Dept., Columbus, Ohio

Editorial Office Manager: Mary E. Scanlan

Journals Editing Manager: Kathleen E. Duffy

Associate Editor: Lorraine Gibb

Assistant Editor: Stephanie L. Mallon

Advisory Board: Phyllis Brown, Karl Cammann, Brian Chait, Bruce Chase, Joseph Glajch, Joseph G. Gordon, David M. Haaland, Kiyokatsu Jinno, Peter Kissinger, Gary E. Maciel, Linda B. McGown, Scott McLuckey, Milos V. Novotny, Jeanne Pemberton, J. Michael Ramsey, James A. Yergey *Ex Officio:* Henry Blount, III

A-page Advisory Panel: Frank V. Bright, Therese M. Cotton, Royce C. Engstrom, Curtis Marcott, Mary Ellen P. McNally, Jonathan V. Sweeder, Thomas Tiernan, Vicki Wysocki, Robert D. Voyksner

Publications Division

Director: Robert H. Marks

Director, Special Publishing Operations: Anthony Durniak

Director, Journal Publishing Operations: Charles R. Bertsch

Head, Publications Marketing: David Schulbaum

Copyright permission: Reprographic copying beyond that permitted by Section 107 or 108 of the U.S. Copyright Act is allowed, provided that the fee of \$9.00 per article copy is paid directly to the Copyright Clearance Center (CCC), 222 Rosewood Dr., Danvers, MA 01923, USA. A CCC code printed at the bottom of the first page of an article indicates that ACS owns copyright or has permission to collect the copying fee for that article. A record of that code should accompany payment. Direct reprint permission requests to ACS Copyright Office, Publications Division, 1155 Sixteenth St., N.W., Washington, DC 20036.

Registered names and trademarks, etc., used in this publication, even without specific indication thereof, are not to be considered unprotected by law.

1995 subscription rates include air delivery outside the U.S., Canada, and Mexico. Canadian subscriptions are subject to 7% GST.

	Members	Nonmembers (personal)	Nonmembers (institutional)
U.S.	\$ 40	\$ 85	\$ 570
Canada and Mexico	77	122	607
Europe	123	168	653
Other countries	148	193	678

Members may share/donate their personal subscriptions with/to libraries and the like but only after 5 years from publication.

Nonmember rates in Japan: Rates above do not apply to nonmember subscribers in Japan, who must enter subscription orders with Maruzen Company Ltd., 3-10, Nihonbashi 2-chome, Chuo-ku, Tokyo 103, Japan. Tel: (03) 272-7211.

For multi-year and other rates, call toll free 800-227-5558 in the U.S. and Canada; in the Washington, DC, metropolitan area and outside the U.S., call 202-872-4363, fax 202-872-4615.

Single issues, current year, \$24.00 except review issue, \$50.00, and LabGuide, \$50.00; **back issues and volumes and microform editions** available by single volume or back issue collection. For information or to order, call the number listed for subscription orders; or write the Microform & Back Issues Office at the Washington address.

Subscription orders by phone may be charged to VISA, MasterCard, or American Express. Call toll free 800-333-9511 in the continental U.S.; in the Washington, DC, metropolitan area and outside the continental U.S., call 202-872-8065. Mail orders for new and renewal subscriptions should be sent with payment to American Chemical Society, Department L-0011, Columbus, OH 43268-0011.

Changes of address must include both old and new addresses with ZIP code and a recent mailing label. Send all address changes to the ACS Columbus address. Please allow 6 weeks for change to become effective. **Claims for missing issues** will not be allowed if loss was due to failure of notice of change of address to be received in the time specified; if claim is dated (a) North America—more than 90 days beyond issue date, (b) all other foreign—more than 180 days beyond issue date. Hard copy claims are handled at the ACS Columbus address.

Instructions for authors of AC Research and guidelines for the Instrumentation, Report, Analytical Approach, and A/C Interface features are published in the Jan. 1 issue, p. 229, or can be obtained from our e-mail reflector "ainfo@acs.org" using the keyword phrases "ac research" or "ac apguide," respectively. Please consult these instructions prior to submitting a manuscript for consideration for publication.

Manuscripts for publication in AC Research (4 copies of text and illustrative material) should be submitted to the Editor at the University of North Carolina address. Please include a signed copyright status form: a copy of this document appears on p. 235 of the Jan. 1 issue. Manuscripts for publication in the A-page section should be submitted to the Washington editorial staff.

Supporting information is noted in the table of contents with a ■. It is available as photocopy (\$12.00 for up to 3 pages and \$1.50 per page for additional pages, plus \$2.00 for foreign postage) or as 24x microfiche (\$12.00, plus \$1.00 for foreign postage). Canadian residents should add 7% GST. See supporting information notice at the end of journal article for number of pages. Orders must give complete title of article, names of authors, journal, issue date, and page numbers. Prepayment is required and prices are subject to change. In 1995, electronic supporting information is available to current journal subscribers via the Internet using either gopher or World Wide Web protocols. Most often, the material is available as PDF files, which may be viewed using Adobe's Acrobat Reader, a program that is freely available on the Internet. However, some articles may include computer programs. PostScript files, word-processing files, experimental data in a standard format (e.g., crystallographic parameters in CIF format), etc. In order to download the supplementary material files, users will need to enter their journal subscriber number, which can be found on the mailing label. Detailed instructions for using this service can be found on the Internet. With gopher, connect to pubs.acs.org, go to the "ACS Publications" selection, then to the "Supporting Information" selection. Read the README file in this directory for detailed instructions. When using a WWW client (e.g., Mosaic, Netscape), connect to the URL, "<http://pubs.acs.org/>" and select the "Supporting Info. for Journals" link. For further information on electronic access, send electronic mail to gopher@acsinfo.acs.org, or phone (202) 872-4434. For information on microforms, contact Microforms & Back Issues at the ACS Washington address or phone (202) 872-4554. Supporting information, except structure factors, also appears in the microfiche edition.

The American Chemical Society and its editors assume no responsibility for the statements and opinions advanced by contributors. Views expressed in the editorials are those of the editors and do not necessarily represent the official position of the American Chemical Society.

Journals Department, American Chemical Society, 2540 Olentangy River Road, P.O. Box 3330, Columbus, OH 43210 (614-447-3600, Ext. 3171; TELEX 6842086; Fax 614-447-3745)

Member & Subscriber Services: American Chemical Society, P.O. Box 3337, Columbus, OH 43210 (614-447-3776; 800-333-9511)

Advertising Management: Centcom, Ltd., 1599 Post Rd. East, P.O. Box 231, Westport, CT 06881 (203-256-8211; fax 203-256-8175)

What's in a Title?

What does the title of a research report reveal? Authors often choose a title to convey a statement of accomplishment; just as often the title comes out flatly descriptive of the methodology or chemistry investigated. Because fast visual scanning of a journal's table of contents and the use of electronic keyword searches have become a regular part of our reading of the literature, it is important that authors think carefully about their choice of a title. Identifying the substance of the work in the title is just a part of ensuring that other scholars become immediately aware of the paper's contribution.

I attempt here a brief analysis of different styles of titles used for chemistry research papers and offer some opinions of their merits. Although there are differences in practice and style among chemical subdisciplines, analytical chemistry is not atypical of the whole.

Snappy titles. These attempt to invent a phrase or label descriptive of the subject. These can be successful when the subject is genuinely new; "self-assembled monolayers" and "electrospray ionization" are good examples. However, snappy phrases and new labels should be deployed infrequently and with discretion. They generate confusion in the literature, especially when they attempt to define a new but narrow segment of an older subject or redefine a known but dully named subject. They always require a careful definition in the text or abstract.

Titles that announce the method or the chemistry. Sometimes, when there is singular newness, the title announces only one thing, such as "Fourier Transform Raman Spectroscopy" or "Catalytic Antibodies." More often, particularly in analytical chemistry, we learn that a certain kind of method is applied to a particular chemical problem (such as "Laser-Induced Fluorescence of Native Proteins" or "Ion Chromatography of Complex Surfactants"). This kind of title generally provides a good topical description; its shortcoming is silence about results or conclusions.

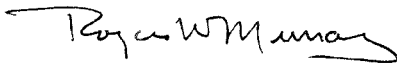
The assertion title. This title states a central conclusion of the paper and is one of the more aggressive, and newer, styles of titling. Consider, for example, the title "Chemically Modified Tips Enable Selective Atomic Force Nanoanalysis." These can have a healthy impact on the reader; at least for me it's interesting to learn before reading the article that a definite conclusion is made. Assertion titles also dangle a little challenge—to see if the author makes the case well enough for such a bold announcement.

The acronym title. These titles typically abbreviate hyphenated methods, such as "EC-LC" or "CZE-ES-MS-MS" or "FIA-AAS." They seem to be the analytical chemist's answer to the biochemist's use of acronyms for complex chemicals but, in both cases, they are not very useful to readers who are not members of that particular acronym club.

The buzzword title. These titles often exploit high levels of current interest in a topic or theme. Years ago, the prefix "micro" in the title of a paper in analytical chemistry announced a presence on the "microfrontier" (microcolumn, microelectrodes, etc.); now the "nanofrontier" is being delineated.

The series title. This title says the author has been in business for a while and this is Paper XXIV on the topic XYZ. Series titles seem to be going out of style.

Of course, many titles combine elements of several of these styles, and the style can be chosen to fit the particular research. No title will alone convey the full substance of the article, and I don't mean to imply that it ever can. But the title is the first (and sometimes the only) part of an article that is read. Careful thought should always go into its construction.



METROHM TITRATION SYSTEMS



GIVING YOU THE DATA YOU NEED
IN A FORMAT YOU CAN USE.

From stand-alone to LIMS-integrated, Metrohm lets you titrate your way with a broad choice of titrators and accessories.

The Metrohm family of titrators handles *all* your titrations, giving you quality data quickly over a large dynamic range. Let Brinkmann help you put it all together—from sample prep through data management—in an easy-to-use, economical titration system.

For more information, call 1-800-645-3050 (fax 1-516-334-7506).
In Canada call 800-263-8715 (fax 905-826-5424).

 Metrohm

BRINKMANN Quality products for research and control.

Brinkmann Instruments, Inc., One Cantiague Road, Westbury, NY 11590-0207
Outside U.S. and Canada; Metrohm Ltd., Switzerland • Phone: 071/53 85 85 • Fax: 071/53 89 01

CIRCLE 3 ON READER SERVICE CARD



0701-307 MET

Synopses of significant analytical articles from other publications

BIOANALYTICAL

Filtering out viruses

Blood-derived products such as clotting factors are indispensable in emergency medicine, but the risk of

viral infection in human-source blood or plasma remains a problem, particularly with human immunodeficiency virus, which can't be detected directly. In recent years, pharmaceutical companies have explored both chemical and chromatographic methods for inactivating or removing viral contaminants from blood-derived therapeutic products, but these approaches are hard to scale up without either damaging the product or reducing its effectiveness. Dj. Josic and colleagues at Octapharma Pharmazeutika (Austria) and Georg Speyer Haus (Germany) have evaluated a combination of chemical inactivation and removal by nanofiltration for removing viruses from a concentrate of coagulation Factor IX.

Coagulation factors were extracted from plasma by SPE, incubated with a solution of Tween detergent for several hours for viral inactivation, and concentrated by affinity chromatography. The product was subjected to tangential flow filtration on a commercially prepared PVDF membrane that had been made extremely hydrophilic for virus filtration. Radial immune diffusion, sodium dodecyl sulfate-polyacrylamide gel electrophoresis, and size exclusion chromatography showed viral reduction and slight protein concentration in the samples after filtration. Coagulation assays showed that Factor IX retained its function after detergent treatment and filtration. (*J. Chromatogr. B* 1995, 669, 187-96)

Pseudo-reagentless biosensor

Amperometric glucose biosensor design requires the immobilization of glucose oxidase in a stable active form and the addi-

tion of electron transfer mediators, in part to eliminate electroactive interference by compounds such as vitamin C that are likely to be present in the sample matrix. Third-generation biosensor fabrication usually involves co-immobilization of the mediator and the enzyme in a reagentless process in which the mediator is already part of the immobilizing polymer film. Unfortunately, substrate sensitivity for these glucose biosensors is generally low, with detection limits of ~ 1 mmol/L. John H. T. Luong and R. Stephen Brown of the National Research Council of Canada used the co-immobilization process of the reagentless biosensors in combination with cation-exchange uptake of a mobile mediator to fabricate a regenerable glucose biosensor with a mobile mediator.

Glucose oxidase and Nafion, an ion-exchange polymer, were codeposited onto a glassy carbon electrode from aqueous solution to form a film. Dimethylferricinium ion was exchanged into the polymer film as a mediator on Nafion electrodes that were either bare or covered with a dialysis membrane to aid retention. The ion's incorporation into the film was monitored by cyclic voltammetry at 25 mV/s. Electrodes with a dialysis membrane retained the mediator sufficiently to measure glucose in mediator-free solutions in the range of 0.1-1 mmol/L for up to 20 assays. (*Anal. Chim. Acta* 1995, 310, 419-27)

A twist on DNA dynamics

The twisting behavior of DNA coils is difficult to measure for longer than a few nanoseconds because most of the commonly used fluorophore compounds, such as ethidium bromide, that intercalate into the DNA helix and allow time-resolved fluorescence measurement have nanosecond decay times. Joseph R. Lakowicz and colleagues at the University of Maryland School of Medicine and Johns Hopkins University have used ruthenium complexes as fluorophores to extend the time scale to several hundred nanoseconds in time-resolved anisotropy studies.

The ruthenium complex $[\text{Ru}(2,2'\text{-bipyridine})_2(\text{dipyrido}[3,2\text{-}a':2',3'\text{-}c']\text{phenazine})]^{2+}$ displayed high anisotropy near 0.2 at -60°C in 100% glycerol when excited in its long-wavelength absorption bands. When bound to DNA, the complex's decay time was > 100 ns and allowed intensity to be measured for > 400 ns. Other Ru complexes had decay times up to 750 ns when bound to DNA, and the researchers concluded that these complexes could allow practical time-resolved fluorescence measurement of DNA torsional dynamics for > 1 μs . (*Biospectroscopy* 1995, 1, 163-68)

ELECTROANALYTICAL

Investigating co-porphyrin catalyzed oxygen reduction

Gas-permeable electrodes, in which the reacting

gas stream is introduced through the back of the electrode and penetrates through the porous material to the gas-liquid interface, are often used in fuel cells for oxidation or reduction of reacting gas streams. The mechanism of these reactions is often complex, however, and its elucidation requires sophisticated numerical and experimental means. Ovadia Lev and Michael Tsionsky of the Hebrew University of Jerusalem (Israel) have studied the electrochemical mechanism of pyrolyzed carbon-supported Co-tetramethoxymeso-porphyrin catalysis of oxygen reduction using a fuel-cell-type hydrophobic ceramic-carbon electrode (CCE) made of sol-gel-derived material.

Because only a thin layer at the outermost surface of the hydrophobic porous CCE is in contact with the electrolyte, effects of electrode structure on the current density are minimized. The researchers were able to show that the porous structure of the electrode and the inherent hydrophobicity of the modified silica matrix minimize liquid-side mass transport effects

and make CCEs good model electrodes for studies of gas electroconversion. (*J. Electrochem. Soc.* 1995, 142, 2132-38)

Using STM and IR to study electrooxidation

Progress toward understanding the behavior of small molecules on surfaces immersed in liquids has been greatly accelerated by the development of in situ microscopic techniques such as scanning tunneling microscopy (STM) and atomic force microscopy (AFM) that can provide real-space images of surfaces with atomic resolution. Andrew A. Gewirth and Katherine M. Richard of the University of Illinois have used STM to monitor the electrooxidation of phenoxide to oligophenol on Au(111) in alkaline solutions.

They found that prior to oxidation, phenol associates as phenoxide to Au(111) in a $(\sqrt{3} \times \sqrt{3})R30^\circ$ structure with the molecule oriented end-on through the oxygen atom. After oxidation, they found a disordered, close-packed array of oxidation products consisting of monomers, dimers, trimers, and a few higher lengths oriented with the ring roughly parallel to the electrode surface. They also conducted IR studies prior to oxidation, which confirmed the nonparallel orientation of the ring relative to the electrode surface and showed that the orientation of the molecule doesn't change with potential through the double-layer region of the voltammetry. (*J. Phys. Chem.* 1995, 99, 12288-93)

Surface plasmon imaging of potential waves

The two-dimensional potential wave patterns that form at electrode-electrolyte surfaces are difficult to map at high temporal resolution. Unless the process that produces them forms or erodes a coating, optical methods are not effective for detecting them, and mapping with arrays of microprobes produces low spatial resolution. However, optical excitation of surface plasmons at metal-electrolyte interfaces has been shown to depend on the applied potential. Katharina Krischer and co-workers at the Max-Planck Institut (Germany) took advantage of this dependence to develop a high-resolution optical method for characterizing and imaging these potential wave patterns in time.

They fabricated a working electrode for surface plasmon microscopy by evaporating an Ag film onto a glass prism. The prism was back-irradiated for excitation using a broadened laser beam, and the reflected beam was imaged onto a screen and re-

corded with a charge-coupled device camera. Local variations in potential drop across the electrode surface produced local variations in excitation and could be mapped at up to 800 frames/s with ~ 1 -ms resolution. Patterns were imaged for both ring and disk electrode films cast on the prism surface. (*Science* 1995, 269, 668-71)



Chiral recognition by FABMS

Many host-guest combination systems demonstrate a high degree of chiral recognition.

Although MS is highly sensitive, it cannot generally be used for detecting chiral recognition properties because of the absence of mass differences between diastereoisomeric isomers. Masami Sawada, Koichiro Naemura, and colleagues at Osaka University (Japan) and Osaka Institute of Technology (Japan) have described a FABMS method for determining chiral recognition of crown-ether hosts and amino acid ester ammonium-ion guests.

They used a 1/1 mixture of the guest with its enantiomer isotopically labeled with deuterium. Chiral recognition of a given host was measured with a given guest from the peak intensity ratio of the two diastereoisomeric host-guest complexes. Both the degree and direction of chiral recognition were characterized. Their results correlated with the thermodynamic relative stabilities for the corresponding host-guest complexation equilibria in solution. (*J. Am. Chem. Soc.* 1995, 117, 7726-36)

Electrostatic energy analysis for MALDI-TOFMS

Accurate ion energy profiling is an inherent problem for time-of-flight MS because converting the mass spectrum to an energy spectrum requires the assumption that the position or the time of ion formation is uniform. For matrix-assisted laser desorption/ionization, this assumption is approximate at best. Gary R. Kinsel of the University of Texas-Arlington and David H. Russell of Texas A&M University have designed and evaluated the performance of an electrostatic energy analyzer (ESA) that measures ion kinetic energies in conjunction with TOFMS much the way it would in conventional use with a sector mass spectrometer.

The ESA was designed to accommodate a laser for direct laser desorption/

ionization (LDI) of solids or for multiphoton ionization (MPI) of neutrals in the gas phase. Measurements of the most probable ion translational energies of Na⁺, K⁺, and *m*-xylene were used for calibration with low-energy LDI at 266 nm. The measured energies all had significant variability, contradicting the assumption of near-thermal translational energies for the alkali ions produced by simple LDI. A discrepancy between the observed energy bandpass of the ESA-TOF mass spectrometer and the bandpass calculated based on instrument geometry also flagged poor collimation of collected ion angular trajectories that was probably caused by distortion of accelerating electric fields. (*J. Am. Soc. Mass Spectrom.* 1995, 6, 619-26)

Screening for genetic polymorphisms

Detecting genetic variations is important for the mapping and screening of genes, especially those associated with genetic disorders. Electrophoresis is commonly used for detecting mutations, but it is too time consuming and laborious for large-scale testing. David M. Lubman and colleagues at The University of Michigan and Michigan State University have demonstrated a rapid and cost-effective approach for the detection of human genetic polymorphisms using MALDI MS with a nitrocellulose film substrate.

The method uses PCR amplification of DNA extracted from buccal cells as templates, followed by direct digestion with restriction enzymes and analysis by MALDI MS. This method of collecting DNA eliminates the inconvenience and hazards inherent in many traditional methods of PCR-based diagnostic analysis. Although less DNA is extracted, there is enough for both normal PCR amplification and amplification of mismatched and multiple primers. The researchers examined the disease-related genes carbonic anhydrase and cystic fibrosis transmembrane conductance regulator and found that their results were comparable to those obtained with gel electrophoresis but that the MALDI technique was much faster. (*Rapid Commun. Mass Spectrom.* 1995, 9, 735-43)

Determining VOCs in water

Although the GC and GC/MS methods currently used to determine VOCs in water provide reproducible and quantitative data, they tend to be time consuming and labor intensive. R. Graham Cooks and Philip S. H. Wong of Purdue University

have used an ion trap mass spectrometer equipped with a membrane/jet separator interface for the direct analysis of VOCs and semivolatile compounds in water.

Aqueous sample is passed through a capillary membrane, the outside surface of which is continuously purged with helium. The permeate is pneumatically transported to the mass spectrometer via a jet separator that acts as an additional enrichment device. Cooks and Wong evaluated the performance and response characteristics of both nonporous silicone and microporous polytetrafluoroethylene and found that both types of membranes provide detection limits in the part-per-trillion to part-per-billion range, with a linear dynamic range of 3 orders of magnitude for some VOCs. Their results indicate that there is no detectable matrix effect on response in the cases examined. (*Anal. Chim. Acta* **1995**, *316*, 387-98)

SEPARATIONS

Monitoring chemical weapons

Under the Chemical Weapons Convention, the treaty that bans chemical warfare, a network of international inspection teams monitors compliance by on-site challenge sampling and analysis of suspected production and storage facilities. On-site analyses require instrumentation that is portable and field operational, and current protocols are based on analysis by GC/MS. A significant portion of chemical warfare compounds, particularly degradation products, are polar and nonvolatile, and for these compounds, extensive sample preparation and derivatization procedures are required. Richard L. Cheicante and colleagues at EAI Corp. and the Army Materials Command Treaty Laboratory have investigated the separation and detection of 27 chemical weapons degradation products using CZE and MEKC.

Anionic, cationic, zwitterionic, and neutral components were determined with either direct UV absorbance or indirect UV displacement detection. Sodium dodecyl sulfate was used as the micelle-forming surfactant, and phenylphosphonic acid was used as the background electrolyte in borate buffer solutions. They found that the methods were fast and required very small sample volumes and little or no sample preparation. Linearity, detection limit, and precision were good. (*J. Cap. Elec.* **1995**, *2*, 157-63)

Measuring carbonyls by GC/MS and derivatization

Carbonyl compounds are important in atmospheric chemistry because they are the products of incomplete combustion, are intermediates in the atmospheric oxidation of organic compounds, and initiate and sustain the photochemical radical pool necessary for the production of tropospheric ozone. Harvey E. Jeffries and colleagues at the University of North Carolina-Chapel Hill have used chemical ionization of *O*-(2,3,4,5,6-pentafluorobenzyl) hydroxylamine hydrochloride (PFBHA) derivatives in an ion trap mass spectrometer to determine the molecular weight of unknown carbonyls.

Carbonyls are derivatized with PFBHA and the resulting derivatives are determined by methane chemical ionization in an ion trap mass spectrometer. The researchers first studied model carbonyls and then conducted experiments using carbonyl products formed from methyl vinyl ketone and methacrolein in an indoor irradiation chamber and using isoprene in a dual outdoor smog chamber. Their results indicate that the new method is superior to the frequently used DNPH method in that it is able to determine α -hydroxy carbonyls and α -dicarbonyls as well as the molecular weight of unknown carbonyls. (*Environ. Sci. Technol.* **1995**, *29*, 1923-32)

Comparing CD-MEKC and RPLC for separating PAHs

Although micellar electrokinetic capillary chromatography (MEKC) has been proven to be a highly efficient separation technique for a variety of applications, the addition of cyclodextrins to the buffer promises to improve the selectivity of MEKC separation systems. Kiyokatsu Jindo and Yoshie Sawada of the Toyohashi University of Technology (Japan) have studied the elution mechanism of polycyclic aromatic hydrocarbons in cyclodextrin-modified MEKC and compared it with that of reversed-phase LC.

They found that the use of a C_{18} -coated capillary in MEKC can produce a separation field similar to that found in RPLC with a C_{18} -alkyl bonded stationary phase. The researchers postulate that the main migration mechanism is facilitated by the hydrophobic interactions between the solutes and the cyclodextrins. They conclude that higher resolution and faster separation of PAHs can be achieved using a C_{18} -coated capillary as the medium in CD-MEKC than can be obtained using the usual RPLC methods. (*J. Cap. Elec.* **1995**, *2*, 151-55)

HPLC of carotenoid isomers

Carotenoids, some of which are metabolic precursors to vitamin A, are long-chain hydrocarbons with multiple double bonds and some unusual antioxidant properties that have brought them into the spotlight as possible agents for cancer prevention. However, although calcium hydroxide columns for normal phase LC can separate the *cis* and *trans* isomers well, preparation of these columns is not very reproducible, and they are not commercially available. The carotenoids are more difficult to separate by standard reverse-phase HPLC on a monomeric C_{18} column, but polymeric columns show some success. Steven J. Schwartz and colleagues at North Carolina State University and the National Institute of Standards and Technology have developed a polymeric C_{30} stationary phase for RPLC determination of *cis* and *trans* isomers of six carotenoids and compared its performance with that of commercially available C_{18} columns.

All-*trans* standards of the six carotenoids were exposed to light to isomerize them and separated by RPLC with photodiode array detection. Electronic absorption spectra and relative retention patterns were used for tentative peak assignments for the all-*trans* configurations and *cis*-bond positions in each of the six sets of geometric isomers. For all six, the C_{30} stationary phase had higher resolution than the commercial columns and produced unique separations. For asymmetrical carotenoids such as lutein, mono-*cis* isomers, in which the *cis* bonds were at the same carbon number but at opposite ends of the molecule, could be distinguished. Resolution was slightly higher for C_{30} alkane-bonded phases on 3- μ m silica particles than for phases made with 5- μ m particles. (*J. Chromatogr. A* **1995**, *707*, 205-16)

SPECTROSCOPY

Imaging electroosmotic flow

Electroosmosis, the movement of a liquid along a capillary under the influence of an externally applied electric field, is an important factor in capillary electrophoretic separations. Observation of electroosmosis requires a technique in which the solvent flow can be profiled in a noninvasive manner. P. T. Callaghan and colleagues at Massey University (New Zealand), the Royal Institute of Technology (Sweden), and Lund University (Sweden) have used NMR microimaging techniques to mea-

sure the velocity distributions in a capillary following application of pulsed electric fields in a weak ionic solution.

The researchers were able to measure the velocity/time profiles with a velocity resolution of $\sim 15 \mu\text{m/s}$. They discovered that the electroosmotic flow velocities are of the same magnitude as the ionic electrophoretic motion, but they typically reach a steady-state distribution in capillary geometry on a time scale of 100 ms rather than at the subnanosecond relaxation times pertinent to the ionic electrophoretic response. (*J. Phys. Chem.* **1995**, *99*, 11297–301)

Flow injection and microwave digestion of food samples

Acid digestion of samples is often necessary for trace analyses of metals, but is prone to contamination and loss of sample. Although using a microwave oven as a heat source is an effective alternative to conventional procedures, the manual transfer, addition, and dilution of reagents can still cause loss and contamination problems. Miguel Valcárcel and colleagues at the University of Córdoba (Spain) have devised a flow injection system that incorporates a microwave oven for the digestion of food samples and tested its efficacy by determining aluminum in an oyster tissue reference material by electrothermal AA spectrometry.

A 100- μL slurry sample was simultaneously injected with nitric acid and transferred to a PTFE reactor coiled around a flask filled with water located inside a microwave oven. The digested sample and flushing solution were then collected in an autosampler cup and diluted 20-fold within the manifold. The combined sample preparation and analysis time for one sample was ~ 20 min, and aluminum recovery was $\sim 90\%$. The researchers have used the method to determine the presence of aluminum in clams, oysters, and mussels. (*J. Anal. At. Spectrom.* **1995**, *10*, 501–504)

Analyzing underground storage tank waste

Underground storage tank waste sludge from nuclear fuel processes is difficult to analyze because of its extreme heterogeneity, chemical reactivity, and radioactivity. Conventional methods require extensive sample handling and increase the risk of exposing workers to radiation hazards. Stanley J. Bajic and colleagues at Iowa State University have developed a method that uses FT-IR photoacoustic

spectroscopy to analyze hazardous underground storage waste with a small amount of sample and minimum sample handling.

The researchers developed the method using waste tank simulants obtained from the Westinghouse Hanford Company, and focused their attention on determining disodium nickel ferrocyanide, sodium nitrate, and sodium nitrite because of the concern for the potential of exothermic reactions between oxidizers and ferrocyanide-containing compounds. They note that the method is rapid enough to be used for mapping sample cores taken from underground storage tanks, which will assist remediation efforts by quickly identifying the various layers within the tanks. (*Appl. Spectrosc.* **1995**, *49*, 1000–1005)

Using the stickiness of surfaces to map functional groups

In atomic force microscopy, the physical and electrostatic interactions between a scanning probe tip and the atoms of a sample surface produce small measurable deflections of the probe that can be used to image the sample. Charles M. Lieber and co-workers at Harvard University and the Massachusetts Institute of Technology hypothesized that intermolecular forces such as adhesion and friction should also be measurable this way and that these measurements could lead to chemical force microscopic mapping of functional groups on surfaces. They modified commercial AFM probes and sample surfaces with a series of functional groups to evaluate the specificity of the method.

The researchers first modified a series of probe tips by coating them with polycrystalline Au and immersing them in various thiol or silane solutions to create self-assembled thiol or silane monolayers containing $-\text{COOH}$, $-\text{CH}_3$, or $-\text{NH}_2$ functional endgroups that could interact chemically with sample surfaces prepared in a similar fashion. They then measured adhesion and friction forces between the different probe and surface combinations. Friction and adhesion forces were correlated and specific for different probe-surface functional group interactions, and observed adhesion agreed with theoretical predictions. (*J. Am. Chem. Soc.* **1995**, *117*, 7943–51)

Between FMN and an electrode

In most flavoproteins, the flavin is in the form of flavin mononucleotide (FMN), which contains an isoalloxazine ring that

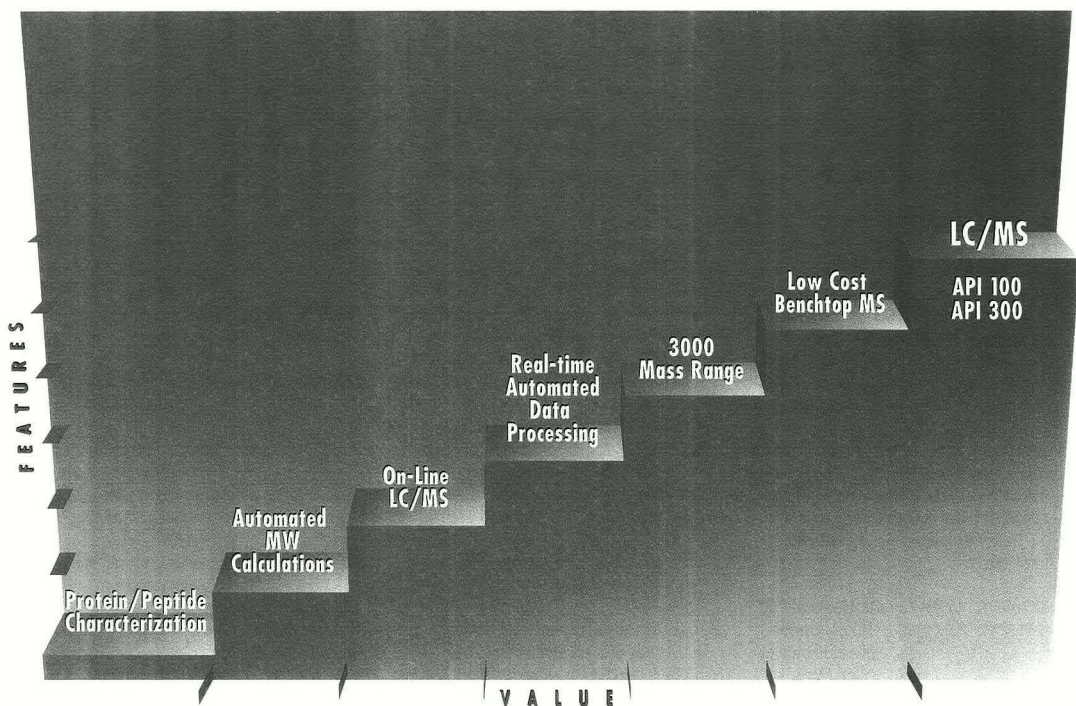
plays an important role in flavoprotein catalysis. Ronald L. Birke and colleagues at the City University of New York used time-resolved surface enhanced Raman spectroscopy (SERS) to observe the direct photoinduced charge transfer from adsorbed FMN to a silver electrode.

The researchers identified two short-lived ion intermediates as the enol and keto forms of a photo-oxidized flavin monocation radical in aqueous and deuterated solution. The resulting spectral shifts were analyzed by normal coordinate calculations that enabled localization of vibrational motions to well-defined parts of the molecule. They found that the enol configuration of the FMN cation forms by electron injection to the metal and intramolecular proton transfer from N3-H to the C2=O keto group on ring III in less than 75 ns upon excitation at 350 or 337 nm. By 775 ns, the proton transfers from the C2-OH enol group back to the N3 atom of ring III of the FMN cation. Photooxidation to the keto form of the radical cation occurs upon excitation with light in the 450–610 nm range. The radical cation decays back to FMN in 1.5 μs . (*J. Phys. Chem.* **1995**, *99*, 12846–57)

Selenium in soil by X-ray absorption spectroscopy

The valence and coordination of selenium radically affect its mobility, bioavailability, and toxicity. Although the occurrence of selenium in soil has been inferred from extraction techniques, chemical changes caused by soil treatment and the inability to distinguish adsorption from precipitation make the results from these analyses less than optimal. Ingrid J. Pickering and colleagues at the Stanford Synchrotron Radiation Laboratory, Stanford University, and Lawrence Berkeley Laboratory used synchrotron radiation-based X-ray absorption edge-fitting analysis for the quantitative speciation of selenium in contaminated soil samples.

The edge can be used as a fingerprint to identify the species, and quantitative analyses of mixtures of species can be obtained by fitting with a linear combination of reference spectra. The researchers obtained information on the oxidation state and molecular environment of selenium in all phases of the soil and determined that selenium kinetics in soil are relatively rapid (within a few days of contamination). They note that the method can be used for any element that has an absorption edge at an accessible energy. (*Environ. Sci. Technol.* **1995**, *29*, 2456–59)



PE SCIEX takes a step up with the new benchtop API 100 and API 300 LC/MS systems.



PE SCIEX is the world leader in API LC/MS technology for both single and triple quadrupole mass spectrometers. In over

100 of the world's largest pharmaceutical and bioresearch labs, API LC/MS technology from PE SCIEX is being used to analyze a wide variety of samples—from small pharmaceutical metabolites, through peptides, to large proteins and glycoproteins.

Outselling and outperforming all other dedicated LC/MS systems, the API I and API III have been accepted worldwide as the industry standard. Our innovative IonSpray™ and TurboIonSpray™ interfaces have made LC/MS a routine and reliable technique—even for complex biological samples.

Now we've taken API technology another step up: onto the lab bench. The new API 100 and API 300 are benchtop

quadrupole mass spectrometers offering a newly designed IonSpray interface with the option of μ IonSpray.™ With the new μ IonSpray, protein sequencing, peptide mapping, and molecular weight determinations with biomolecular characterization at femtomole levels is now possible.

Both systems offer a mass range of up to 3000, highly reliable turbomolecular pumps, and improved sensitivity. New software, fully compatible with the latest computer technology, enables the user to take advantage of the increased performance of the Apple Power Macintosh®.

Our BioToolBox™ application software is ideal for complete characterization of proteins and peptides from LC/MS, CID/MS and MS/MS data.

For more information about the new benchtop API 100 and API 300, call 1-800-345-5224 in the U.S. or contact your local Perkin-Elmer representative.

PE SCIEX

Australia Tel: 3 212 8500 Fax: 3 212 8501 Latin America Tel: 11 578 9800 Fax: 11 276 1864 Italy Tel: (039) 23831 Fax: (039) 2383490
 France Tel: 1 3085 6363 Fax: 1 3085 6300 Germany Tel: 6150 101 0 Fax: 6150 101 101 UK Tel: 01494 67 6161 Fax: 01494 67 9331
 Japan Tel: 45 314 8010 Fax: 45 314 5142 Singapore Tel: 336 9322 Fax: 338 3991
 All trademarks are the property of their respective owners.

CIRCLE 6 ON READER SERVICE CARD

Analytical Chemistry, October 1, 1995 589 A

Ten students to receive graduate fellowships

Ten analytical chemistry graduate students have been selected by the ACS Division of Analytical Chemistry to receive either full-year (\$14,000 paid over nine months) or summer (\$4650 paid over three months) fellowships. The program encourages basic research in analytical chemistry and recognizes its leaders.

Full-year fellowships have been awarded to:

David E. Cliffel of the University of



Texas. Under the guidance of Allen Bard, Cliffel plans to modify a scanning electrochemical microscope to be used simultaneously with a quartz crystal microbalance for probing metal, conductive polymer, fullerene, and other thin films. His fellowship is sponsored by Procter & Gamble.

Joseph Coury of the Georgia Institute of Technology.



Under the direction of Larry Bottomley, Coury plans to develop strategies for immobilizing DNA

for imaging by scanning tunneling and atomic force microscopies. His fellowship is sponsored by Eli Lilly.

Michael McDonald of Purdue University.



Under the guidance of Dale Margerum, McDonald plans to study the role of trivalent copper in metallo-protein-mediated cleavage of DNA. In addition, he is working on a pulsed ac-

celerated-flow spectrometer to study reactions with half lives of 50-5000 μ s. His fellowship is sponsored by Eastman Chemical Co.

Aliston Thomas of the University of



Illinois at Urbana-Champaign. Under the direction of Andrej Wiekowski, Thomas is using radio-

active labeling to study the adsorption and desorption processes of corrosion-active and inhibitive species on stainless steel. His fellowship is sponsored by DuPont.

James Ziegler of the University of



Cincinnati. Under the guidance of John Dorsey, Ziegler is investigating the behavior of supercritical fluids

to further enhance supercritical fluid chromatography. He has applied several equations of state to phase data for binary mixtures containing CO₂ and provided estimates of the mixtures' critical behavior. His fellowship is sponsored by Perkin Elmer.

Summer fellowships have been awarded to:

Jennifer Finnegan of the University of North



Carolina. Under the guidance of Mark Wightman, Finnegan has combined the electro-

chemical measurement of hormone release with fluorescence microscopic monitoring of intracellular Ca²⁺ at the single-cell level. Her fellowship is sponsored by

the Society for Analytical Chemists of Pittsburgh.

Marilyn Kanna of The Pennsylvania State University.



Under the direction of Paul Weiss, Kanna is working on understanding the role of surface steps, defects, and co-

adsorbates in the chemistry, interactions, and motions of adsorbed molecules and on developing spectroscopies for identifying and characterizing single molecules on surfaces. Her fellowship is sponsored by the Society for Analytical Chemists of Pittsburgh.

Pat Mahoney of Indiana University.



Under the direction of Gary Hieftje, Mahoney's goal is to improve the capabilities of a time-of-flight mass analyzer

for plasma-source MS. Isobaric interferences caused by oxygen and nitrogen have been resolved and ion throughput has been increased. His fellowship is sponsored by the Society for Analytical Chemists of Pittsburgh.

Maria Brak Smalley of Duke Uni-



versity. Under the guidance of Linda McGown, Smalley is using a frequency-domain lifetime detector that

uses multi-harmonic Fourier transform for simultaneous excitation and detection of multiple modulation frequencies. The technique is being used for wastewater samples. Her fellowship is sponsored by Dow.

Jan Sudor of Indiana University. Under the direction of Milos Novotny, Sudor is working to achieve a fundamental understanding of the electromigration mechanism of large flexible biopolymers in continuous and pulsed-field gel electrophoresis. His fellowship is sponsored by the Society for Analytical Chemists of Pittsburgh.



NIST announces ATP awards

The National Institute of Standards and Technology has announced 24 new R&D projects to receive funding under the Advanced Technology Program (ATP). The ATP provides cost-shared funding from the federal government and private industry for high-risk projects that industry would not undertake on its own and that have the potential for broad-based economic benefits for the United States. ATP awards are made on the basis of a rigorous review, considering the scientific, technical, and economic merits of each proposal.

Although the program does not fund product development, each application must include a business plan for bringing the technology to market once the technical problems have been resolved under the ATP. When carried through to completion, these projects will cost ~\$60.5 million in ATP funding, matched by ~\$52.4 million in funding from private industry.

Seventeen award winners were selected from 251 applicants in the general competition; projects include diamond-like nanocomposite thin films, nonchromatographic separations of enantiomers, protein methods to obtain molecular structural data, and ultrapure synthetic sand for semiconductor manufacturing. The other seven award winners were selected from 27 applicants in a competition on advanced tools for DNA diagnostics; projects include protein-based agents for binding

and cleaving DNA at predetermined sites for mutation detection and "bar code" diagnostics to simultaneously analyze up to 100 DNA samples in a miniaturized system.

Thermo to acquire ATI

Thermo Electron Corp. (Waltham, MA) has signed a letter of intent to acquire Analytical Technology Inc. (ATI, Boston, MA). Terms of the sale were not disclosed. ATI was one of the most acquisitive companies in the late 1980s and early 1990s with purchases of Mattson Instruments, Unicam Ltd., Cahn Instruments, and others.

It is expected that Thermecics will acquire ATI's laboratory products business, consisting primarily of Orion, Cahn, and Harvard, and that Thermo Instrument Systems will acquire the analytical instrumentation business, consisting of Mattson and Unicam. ATI's instrument lines, including AA, ICP, and FT-IR spectrometers as well as GC, HPLC, CE, and GC/MS systems, will complement Thermo's products from Thermo-Jarrell Ash, Nicolet, Finnigan/Tremetrics, and Thermo Separations.

Life Sciences purchases Spectronic Instruments

Life Sciences International PLC (U.K.), manufacturer and distributor of scientific equipment and supplies, has purchased Spectronic Instruments (Rochester, NY) for \$19 million. Spectronic Instruments, formerly part of Milton Roy Co., manufactures UV-vis spectrophotometers and refractometers, fluorescence instrumentation, cell disrupters, color spectrophotometers, and gratings.

Life Sciences considers the purchase in line with its strategy to build "the foundations for a strong international business focusing on research, clinical, and industrial markets and to take advantage of our growing strengths in Europe and the Far East on behalf of our U.S.-based businesses." Operating units of Life Sciences include IEC/Labsystems, Neslab, and Savant.

FOR YOUR INFORMATION

■ New WWW sites

Hewlett Packard—<http://www.dmo.hp.com/apg/main.html> or <http://www.hp.com/go/analytical>; includes general company information, phone numbers, a calendar of events, application notes, and product and service information.

Perkin Elmer—<http://www.perkin-elmer.com>; includes general company and financial information, phone numbers, applications notes, and product information.

Water Purge Systems—<http://www.waterweb.com>; includes information on water treatment services, equipment, chemicals, conservation, a calendar of events, and databases.

■ New methods

AOAC International has adopted six methods to be published in the second supplement to the 16th edition of *Official Methods of Analysis of AOAC International*: atrazine in water by immunoassay (995.08), tetracyclines in edible animal tissues by LC (995.09), patulin in apple juice by LC (995.10), total phosphorus in foods by colorimetry (995.11), *Staphylococcus aureus* by latex agglutination (995.12), and carbohydrates in coffee by LC-EC (995.13). For more information, contact AOAC International (703-522-3032).

■ Metric system guide

The 1995 edition of NIST's *Guide for the Use of the International System of Units* (Special Publication 811) offers advice on the proper use of the metric system and includes definitions, rules and style conventions, and conversion factors. Contact NIST Calibration Program, Rm. A104, Bldg. 411, NIST, Gaithersburg, MD 20899-0001 (301-975-2002; fax 301-926-2884).



FFF

Field-flow fractionation (FFF) is a family of chromatographic-like elution techniques in which an external field or gradient, rather than partitioning between phases, causes differential retention. FFF techniques are applicable to a broad range of polymers, biological macromolecules, colloids, polymer-colloid complexes, and larger cell-sized particles.

FFF has two broad functions: separation and measurement (1). The separation process is best known; this article, however, describes FFF measurement. It enumerates various properties of macromolecules and colloids that can be measured by FFF but are often difficult or impossible to measure using other techniques. This article further explains how FFF measurements are made and how these measurement capabilities are enhanced by the separation process.

FFF separation originates in the fact that different field-based forces acting on unlike macromolecules or particles in an FFF system induce differential migra-

FFF can be used to measure both primary and secondary properties of colloids and polymers

tion. The measurement capabilities of FFF have a related origin: Quantitative values of the forces responsible for separation can be obtained from measured retention times. Measurement of these forces can provide the analytical chemist with a host of fundamental physicochemical constants for the retained particles and macromolecules.

Different constants are acquired using different fields (1, 2). By using a variety of fields, a wealth of fundamental physicochemical data can be acquired, including particle and polymer mass and molecular weight, density, equivalent spherical diameter, hydrodynamic diameter, charge, diffusion coefficient, and thermal diffusion coefficient.

The acquisition of a primary property, such as mass or molecular weight, aids in the characterization of numerous secondary properties, such as the mass of an adsorbed film on a colloidal particle, the shell thickness of a core-shell latex, the surface area of a lipid bilayer in a liposome, the level of colloidal aggregation, or particle composition (Figure 1).

Measurement capability is enhanced by the fractionating power of FFF. Species can be isolated from complex matrices and simultaneously subjected to measurement. Thus the properties of a number of intermixed components can be measured in a single run (Figure 2). For populations having properties with a continuum of values, the property distribution can be measured, yielding mass distribution, size distribution, and so on.

The purified fractions in the eluting FFF stream can be diverted (often on line) to other instruments in which complementary measurements can be made fraction by fraction (1, 3-6), as shown in Figure 2. These measurements can be made using electron microscopy, light microscopy, photon correlation spectroscopy, classical light scattering, multiangle laser light scattering, ICPMS, or another FFF

J. Calvin Giddings
University of Utah

technique, and may yield either physical constants or chemical composition profiles (3). The property or properties measured by these downstream techniques, when combined with the property measured by FFF, enrich the information base that characterizes the sample and its components. Thus broad new capabilities have arisen for characterizing complex colloids of environmental, biological, and industrial origin.

Other separation techniques can be used for measuring macromolecular and particulate properties, but their scope is more limited, providing at most a single property. For example, size exclusion chromatography (SEC) yields the hydrodynamic diameter of polymers (7), but the measurement requires a calibration run with known standards, is based on the assumption that hydrodynamic diameter underlies retention rather than on theory, and cannot be readily extended to high molecular weight polymers or typical colloids.

In contrast to SEC, HPLC gives the distribution coefficient K , which yields information on relative hydrophobicity, polarity, and related properties. However, K values, which arise from the mutual interaction of a solute and a stationary phase, are difficult to translate into true physicochemical constants of the solute alone.

Capillary electrophoresis can yield electrophoretic mobilities if the electroosmotic flow is properly accounted for (8). Mobility, a useful parameter, is actually a composite of more fundamental parameters: effective charge and friction coefficient (9). Mobility values cannot be broken down into these fundamental constants without complementary measurements.

FFF, however, is capable of measuring a large array of properties, all based on simple theoretical principles. It is readily coupled to other instruments and can be used for the difficult but increasingly important range of large polymers, microgels, simple and complex colloids, various association complexes, and diverse particles with sizes from 1 nm to 100 μm .

The recognition of measurement as a capability of FFF occurred early in its development. For example, in a 1975 paper (10), we stated, "The elution pattern in SFFF [sedimentation FFF] hinges on properties such as molecular weight, density, diffusion coefficients, and related quantities; one can thus obtain various physical parameters from measured elution properties." Since then, numerous studies have been reported on measurements made by FFF (1, 11).

Basis of measurement

FFF is a differential elution process outwardly resembling chromatography but applicable across a much greater mass range. The retention of a component depends on one or more of the component's properties. A relevant property, p , of a macromolecule or colloidal particle can be calculated when a valid relationship exists between the property and the retention time t_r , or volume V_r . The simplicity of the FFF channel, with its open parallel-plate structure, leads to theoretical t_r - p relationships with only an occasional need to rely on calibration.

FFF takes place in a thin ribbonlike channel (Figure 2). A field or gradient applied perpendicular to the channel axis drives components toward one wall (the

accumulation wall) of the channel, where each forms a steady-state distribution. The compression of the distribution against the accumulation wall increases as the force applied by the field on the particles increases. Because of the different force levels, different components have steady-state distributions of different thicknesses. In most cases, particles are driven to within 1–10 μm of the accumulation wall.

A stream of carrier liquid transports the particles toward the channel exit and a detector. The flow is laminar and parabolic because of channel thinness (75–250 μm). Components with distributions compressed tightly against the accumulation wall are carried slowly by flow because they are immersed in streamlines of low velocity adjacent to the wall. More expanded distributions (subject to lesser forces) travel more rapidly and elute earlier. If the channel structure is uniform with known dimensions and the field is applied evenly, the displacement velocity and thus the retention time of a component can be related by theory to the force exerted on the component particles. Calculation of the forces yields knowledge of particle properties (1, 2, 12).

In principle, any field or gradient capable of differentially compressing sample components against the accumulation wall

Force equations

$$F(\text{sedimentation}) = m'G = mG(\Delta\rho/\rho_p) = \frac{V_p \Delta\rho G}{(\pi/6)d^3} = \frac{m'G}{d^3} \quad (2)$$

$$F(\text{flow}) = fU = 3\pi\eta d_p U = (kT/D)U \quad (3)$$

$$F(\text{thermal}) = D_T f(dT/dx) = \alpha k(dT/dx) = \frac{kT(dT/dx)}{D_T} \quad (4)$$

$$F(\text{electrical}) = qE = \mu fE \quad (5)$$

Properties derivable from known forces

m' = effective mass

m = particle mass

V_p = particle volume

$\Delta\rho$ = density difference

ρ_p = particle density

d = effective spherical diameter

d_h = hydrodynamic diameter

f = friction coefficient

D = ordinary diffusion coefficient

D_T = thermal diffusion coefficient

α = thermal diffusion factor

q = effective charge

μ = electrophoretic mobility

Other symbols: dT/dx = temperature gradient, E = electrical field strength, G = acceleration, k = Boltzmann's constant, T = absolute temperature, U = crossflow velocity, η = viscosity

can be used in FFF. Because this compression is opposed only by Brownian motion, weak forces suffice, and many types of fields can be used. Each field exerts a force with its own unique dependence on particle properties and its own selectivity.

Four fields have been widely studied. Most prominent is sedimentation, usually generated by a centrifuge but sometimes by gravity. The sedimentation force acts perpendicularly to the flow-separation axis, a configuration with little resemblance to conventional centrifugation.

Other important fields include a temperature gradient (thermal FFF), in which the perpendicular force is a result of thermal diffusion; a cross flowstream of carrier liquid (flow FFF), in which the force originates in the friction of the cross flowstream moving across the components; and electrical fields (electrical FFF), in which force depends on particle charge.

The starting point for measuring macromolecular and colloidal properties is the so-called standard equation relating retention time t_r to the force F exerted by the applied field on a single particle. When the particle is strongly retained, t_r becomes proportional to F , as shown in the approximate form of the standard equation

$$t_r = \frac{Fw^0}{6kT} \quad (1)$$

where T is absolute temperature, k is Boltzmann's constant, w is the channel thickness, and w^0 is the channel void time (the elution time of a nonretained species). The standard equation provides the mathematical link needed to convert an experimentally measured t_r into a value for force F .

Once the force on a component is obtained, the next step is to translate this force into the desired properties of the component. Here we step outside the arena of FFF theory and use the classical scientific laws that relate forces to the properties of bodies on which the forces are exerted. Four classical force equations, for the four major fields of FFF, are shown in the box on the previous page. These equations show how F depends on various particle properties; the properties in these equations can be measured by FFF.

This approach applies to macromolecules and colloidal particles but is not applicable to particles (such as biological cells) $> 1 \mu\text{m}$ in diameter. Larger particles are governed by a steric mechanism of separation, which alters the relationship between retention time and force; properties of larger particles (such as size, density, porosity, and hydrodynamic lift forces) can be measured by steric FFF (13, 14). These measurements will not be described here.

Primary measurements

Primary properties of a retained particle or polymer are those that can be measured directly from FFF retention data with little or no prior knowledge about the species. (Primary properties generally appear in the basic force equations; the properties shown in the box are examples.) Secondary properties, by contrast, generally require outside information, assumptions, or a model describing the retained components (e.g., they are needle shaped, aggregated, coated by a thin film, or their composition is known). Note that a primary property measured by one FFF technique may become a secondary property when measured by another FFF technique.

Flow FFF. Flow FFF is one of the most universal separation techniques. It can separate and measure virtually all classes of macromolecules and particles in both aqueous and nonaqueous environments.

As shown in the box, F in flow FFF is related to several physical parameters of the particles or polymers: the hydrodynamic diameter d_h , the diffusion coefficient D , and the friction coefficient f . We consider these primary properties because they are obtained directly from flow FFF retention measurements without any need to know the composition or conformation of the retained components. Whether the retained species are polymeric, particulate, aggregated, associated, coated, or platelike is irrelevant to the measurement.

Figure 3 shows the flow FFF of two circular DNA molecules (one single stranded and the other double stranded) that have approximately the same chain length (15). The single-stranded DNA elutes first because it is more flexible and folds into a more compact random-coil structure with a smaller d_h and a larger D than the double-stranded DNA. Although some noise is apparent in the peaks because of the small amount injected ($\sim 0.2 \mu\text{g}$ each), the retention time can be measured to within a few percent. Based on Equation 3 in the box, the ratio of retention times of the two peaks equals the ratio of the hydrodynamic diameters, 2.1:1. The two diffusion coefficients (reduced to 20 °C in water) are calculated to be $5.01 \times 10^{-8} \text{ cm}^2/\text{s}$ and $2.44 \times 10^{-8} \text{ cm}^2/\text{s}$. Diffusion co-

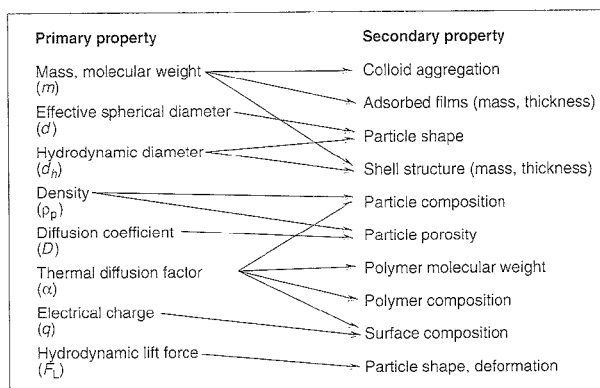


Figure 1. Primary and secondary properties of colloids and macromolecules measurable by FFF.

Arrows indicate routes (not comprehensive) from primary to secondary properties.

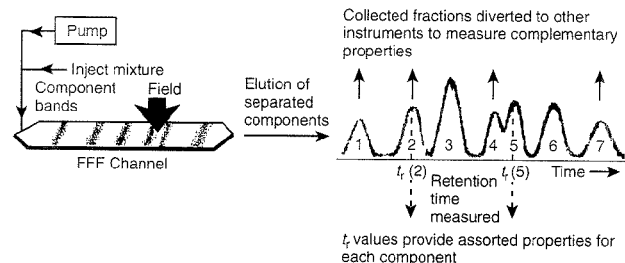


Figure 2. Approaches to measuring various properties of macromolecular and colloidal/particulate mixtures using FFF.

First, the measured retention time of any separated component can be converted to a fundamental component property (bottom) with different fields yielding different properties. Second, any desired component can be collected and subjected to measurement by some other instrument (top), leading to measurement of additional properties for that component.

efficients for other DNA molecules have been similarly obtained; the average standard deviation of the diffusion coefficients for all DNA molecules measured was 4.1% (15). We observe that although single- and double-stranded DNA was injected as a mixture, diffusion coefficients can be measured for both components as a result of the separation.

Many diffusion coefficients have been reported for proteins as well (16). Measurement precision is about 5%, comparable to that of other techniques. The flow FFF method for measuring protein diffusion coefficients is rapid (run times down to 1 min), can be automated, and can resolve important minor components such as protein dimers while simultaneously measuring their diffusion coefficients.

Because flow FFF yields a diffusion coefficient, hydrodynamic diameter, or friction coefficient for each retention time, continuous distributions yield a continuum of retention times and thus a continuum of diffusion coefficients, hydrodynamic diameters, or friction coefficients. As a result, size distributions can be calculated. Because of the technique's high resolving power, details of the size distribution are revealed with much greater fidelity than that provided by dynamic light scattering.

Some measurement uncertainty in flow FFF arises from the uneven surfaces and compressible membranes used as the accumulation wall of the FFF channel. Accuracy can be improved by using a calibra-

tion standard with a known diffusion coefficient or hydrodynamic diameter or by coupling the flow FFF system to an on-line detector, such as a multiangle laser light-scattering instrument, that can determine the size or molecular weight of each fraction. Measurements made by sedimentation FFF tend to be more accurate than those from flow FFF because of higher selectivity and more precisely machined channel walls.

Sedimentation FFF. Sedimentation FFF is a powerful method for the separation and characterization of colloidal particles. Particle mass governs sedimentation forces, and is thus measurable by FFF. However, sedimentation forces are

complicated by buoyancy; the mass actually measured is the true particle mass minus the mass of liquid displaced by the particle. This mass difference is known as the effective mass m' , and it is m' that emerges most directly from sedimentation FFF measurements.

Although buoyancy complicates sedimentation FFF measurements, it also enriches measurement opportunities. For example, controlled variations in the density of the carrier liquid (e.g., by adding sucrose) will alter buoyancy forces by a known percentage and thereby produce data yielding true particle mass m , density ρ_p , volume V_p , and effective spherical diameter d (1, 11).

Using this approach, with carrier densities adjusted close to the particle density of latex, the actual density of latex particles and other low-density colloids can be determined to four-figure accuracy. The measurement is so sensitive that small effects due to molecular restructuring at the interface can be detected (17).

A shortcut is usually taken to measure particle diameter. If particle density is known, a single measurement of the force, rather than a series of measurements at different carrier densities, yields the effective spherical diameter. Technically, if a particle's density is required to measure its diameter, the diameter is a secondary property. (Density is never needed to acquire diameter in flow FFF, thus diameter from flow FFF is unequivocally a primary property.) Because particle densities

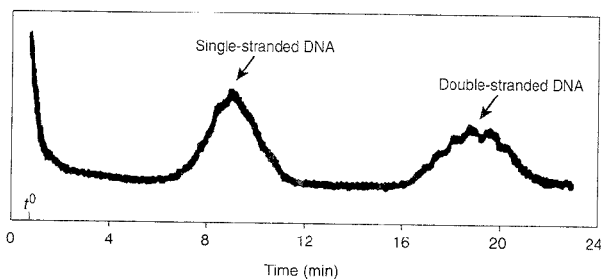


Figure 3. Separation of single-stranded from double-stranded circular DNA chains of the same approximate length by flow FFF.

Separation is based on differences in hydrodynamic diameter, or equivalently, diffusivities, both of which can be obtained in terms of measured retention times. The single-stranded DNA contains 7599 bases and has a molecular weight of 2,510,000; the double-stranded DNA contains 7250 base pairs and has a molecular weight of 4,785,000.

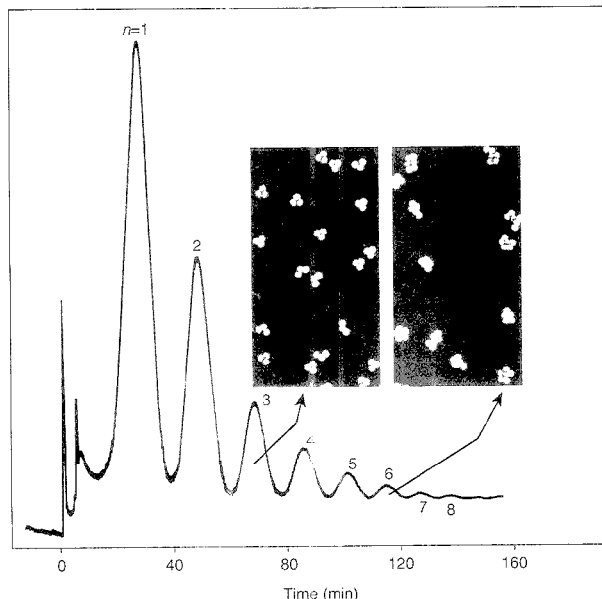


Figure 4. Separation of aggregates of different cluster size by sedimentation FFF.

The elementary particles forming clusters are monodisperse polymethylmethacrylate latex microspheres with 0.23 μm diameter. Each succeeding peak corresponds to the addition of one elementary microsphere to the previous cluster. The total number of microspheres per cluster (n) varies from 1 to 8. The fact that successive peaks are generated by pure populations of a fixed cluster size n is verified by electron microscopy of collected fractions. (Adapted with permission from Reference 24.)

are commonly known, we include for convenience particle diameters measured by sedimentation FFF in this section on measurement of primary properties.

For continuous particle distributions, sedimentation FFF, like flow FFF, yields high-resolution size distribution curves. However, size distributions, like single sizes, can be obtained from sedimentation FFF data only if particle density is known. For nonspherical particles, the diameters obtained by sedimentation FFF and flow FFF data are different, with sedimentation FFF providing equivalent spherical diameter and flow FFF providing hydrodynamic diameter (D).

Thermal FFF. Thermal FFF has been used primarily for fractionating polymers, especially those of high molecular weight. Recent studies have shown that thermal FFF is also applicable to particles, both in aqueous and nonaqueous media. For

both polymers and particles, retention depends on composition as well as size.

Thermal FFF, as shown by Equation 4 in the box, provides values for the thermal diffusion factor α and the ratio of the thermal diffusion coefficient to the ordinary diffusion coefficient D_T/D for both polymers and particles. These parameters describe the strength of thermal diffusion, a poorly understood transport process that is important for physicochemical studies. More importantly, D_T/D can be converted into polymer molecular weights (18), a secondary measurement that will be discussed in the next section.

Electrical FFF. In principle, electrical FFF is capable of measuring the charge residing on macromolecular and colloidal species. Although implementation of charge measurements has been slow, recent advances have been made by Caldwell and co-workers (19).

Secondary measurements

Secondary properties arise when primary properties measured for particles or polymers are extended to incorporate new features by virtue of some model, assumption, or body of prior knowledge. The possibilities for practical measurement are numerous.

Polymer molecular weight. Flow FFF yields the hydrodynamic diameter of polymers, particularly water-soluble polymers, as a primary property. If it is assumed, following random-coil models (20), that the hydrodynamic diameter is related to molecular weight by $d_h = kM^p$, molecular weight (and molecular weight distribution) can be obtained as a secondary property.

Similarly, thermal FFF yields the thermal diffusion factor or the ratio of the thermal diffusion coefficient to the ordinary diffusion coefficient as primary properties. Molecular weight is not a primary property. However, for linear polymers it has been established empirically that $(D/D_T) = \phi_0 M^{-n}$, where ϕ_0 and n are universal calibration constants (18). Once these constants are known for a given polymer-solvent system, the polymer molecular weight and molecular weight distribution can be determined.

If the diffusion coefficient for either polymers or particles can be independently determined, thermal FFF yields the physicochemical parameter D_T . Thermal FFF has thus become the simplest available tool for measuring D_T , and abundant data have been produced.

Association and multiphase colloids. Sedimentation FFF is the most powerful FFF technique for measuring the secondary properties of complex colloids, particularly of particles that consist of two or more parts or phases bonded together. For such particles, the mass (or effective mass) measured by sedimentation FFF is a simple sum of the mass of the individual parts. Several strategies are available for isolating constituent masses, thereby providing an analytical tool for unraveling the structure and composition of complex colloidal materials.

One strategy for two-phase particles is to adjust the carrier density so that one phase is neutrally buoyant; the other phase is then responsible for the measured force and its effective mass can be

calculated. For example, if the carrier density is adjusted to equal the density of a liposome's liquid interior, the interior mass effectively becomes invisible and the measured mass is reduced to that of the encircling lipid bilayer. Because the density and thickness of the bilayer can be estimated, the area of the bilayer can be obtained. For unilamellar vesicles, area can be translated into diameter. (An independent diameter can be measured by flow FFF.) For polydisperse populations, distributions in lipid bilayer mass, area, and vesicle size can be obtained (1, 21).

Colloidal aggregates. The formation of aggregates is one of the most important phenomena in colloid science (22, 23). The distribution of subunits in aggregated clusters is needed to understand aggregation dynamics. The measurement of cluster distributions is difficult, even by electron microscopy.

FFF techniques are highly sensitive to aggregation (5). Aggregated subpopulations elute later than do nonaggregated species because of the increased force. Sedimentation FFF is particularly informative about aggregation because the force is proportional to cluster mass and is additive for all subunits. When monodisperse particles aggregate, each size cluster generates its own peak, as shown in Figure 4 (24). The spacing of successive peaks is regular with peak area proportional to amount.

For polydisperse colloids, cluster peaks will overlap, yielding continuous mass distributions shifted to higher mass values than those of nonaggregated populations. A combination of sedimentation FFF and electron microscopy is required to unravel the aggregation. The equal-mass fractions collected from an FFF run can be further broken down into morphological classes by electron microscopy. The potential of these two complementary techniques is substantial (5).

Particles with adsorbed layers or shells. Particles with relatively homogeneous interiors but with an outer layer or shell of a distinctly different composition are major players in many fields, including industry, biology, pharmacy, and the environment. Such particles include liposomes, cells, core-shell latexes, immunodiagnostic latexes, waterborne colloids, and a myriad of other particles in different

environments that have adsorbed some chemically or biologically active substances on their surfaces. Many environmental particles adsorb toxic materials such as pesticides or heavy metals from air or water; the fate of these toxic burdens depends largely on the size and density of the core particle, which determines their rate of sedimentation, ingestion, lung penetration, and so forth.

These particles can generally be considered as two-phase particles, although the core itself is in some cases (as in cells) rather heterogeneous. Characterization of these particles is a daunting task: The composition of each phase must be known and the mass or volume of each phase must be obtained. In addition, for most real-world samples with broad distributions, information on the nature of the distributions must be obtained so that the role of the subpopulations can be determined. Most analytical techniques are ill equipped to unravel the physical and chemical complexities of two-phase par-

ticles and are particularly unable to provide valid distributions of properties. FFF, used alone or in combination with other techniques, has some unique abilities in this area.

Beckett and co-workers have obtained detailed size distributions of numerous environmental colloids by FFF (25). By feeding fractions into an ICP mass spectrometer, they observed systematic shifts in element ratios with increasing particle diameter, an observation with significant geochemical implications (3, 26). Among other findings, they have obtained evidence that the iron content of colloids in river water is concentrated at the surface of the suspended particles, thus providing clues to particle genesis.

Another important secondary measurement capability of sedimentation FFF is measurement of adsorbed mass, as illustrated in Figure 5, which shows the elution diagram of three different peaks acquired for 0.2- μm polystyrene microspheres (27). The retention shift between

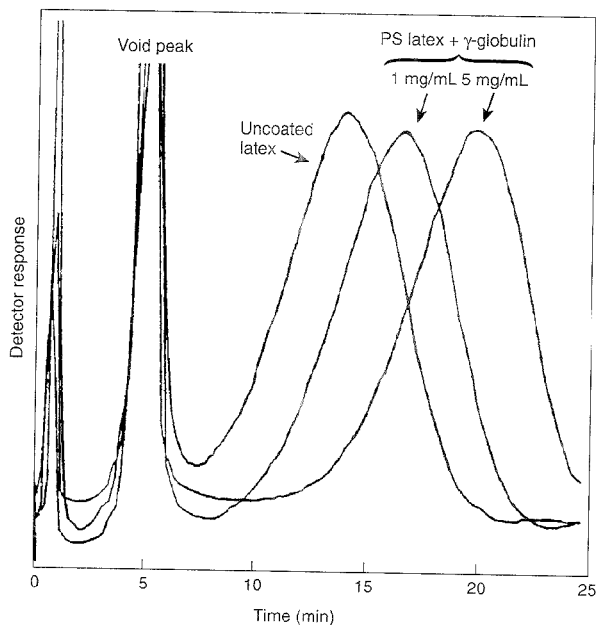


Figure 5. Sedimentation FFF of 0.2- μm latex beads.

The peak corresponding to beads without an adsorbed protein coat precedes those corresponding to protein-coated beads. (Adapted from Reference 26.)

peaks is due to the adsorption of minus-cule amounts ($\sim 10^{-16}$ g) of γ globulin on each latex particle shown in the two right-hand peaks. These small adsorbed masses are sufficient to significantly increase the retention time, and the increase in retention times gives a direct measure of adsorbed mass using the basic equations described earlier. (Our more recent studies of IgG adsorption show that only six IgG molecules yield a perceptible shift in retention time [28]). By making measurements at different solution concentrations, protein adsorption isotherms can be obtained (27, 28). The measurement of protein adsorption is important in the design of immunodiagnostic assays and the evaluation of biomedical implants. Such measurements are usually made by indirect means (the solution depletion method) that are both laborious and error-prone. Strategies for using sedimentation FFF to probe the structures and content of a variety of other colloids with outer layers or shells have been described (1, 21, 29).

Bulk and surface composition. FFF is generally considered to be a family of physical techniques that respond to physical rather than chemical properties. Nonetheless, some primary properties measurable by FFF are sensitive to chemical composition. In such cases, FFF can be used to probe compositional variations in subpopulations of macromolecules and colloids. However, such secondary compositional analysis by FFF has received little attention. (A more elaborate approach is to couple FFF to composition-sensitive instruments, such as an ICP mass spectrometer, to provide a matrix of physical and chemical properties.)

Even the primary particle property, density, is fixed by composition. Although density alone does not specify composition, it can be used to distinguish among suspected compositional variants or to fix the ratio of two known components. For example, the drug load in a liposome can in theory be determined by sedimentation FFF density measurements.

Thermal FFF is also a promising tool for compositional studies, although the fundamental basis of compositional effects is not understood. It has long been known that retention is sensitive to polymer composition, an observation that has

spurred efforts to determine the compositional distribution of copolymers by thermal FFF (30).

Thermal FFF is also sensitive to the composition of colloidal particles (31, 32). Surface composition appears to play a major role. For example, silanized silica colloids are retained $\sim 60\%$ longer in an aqueous suspension than are unmodified silica colloids. In a similar vein, surface charge, and thus electrical FFF retention, depends on surface composition and constitutes a sensitive probe of compositional shifts (33).

Still ahead

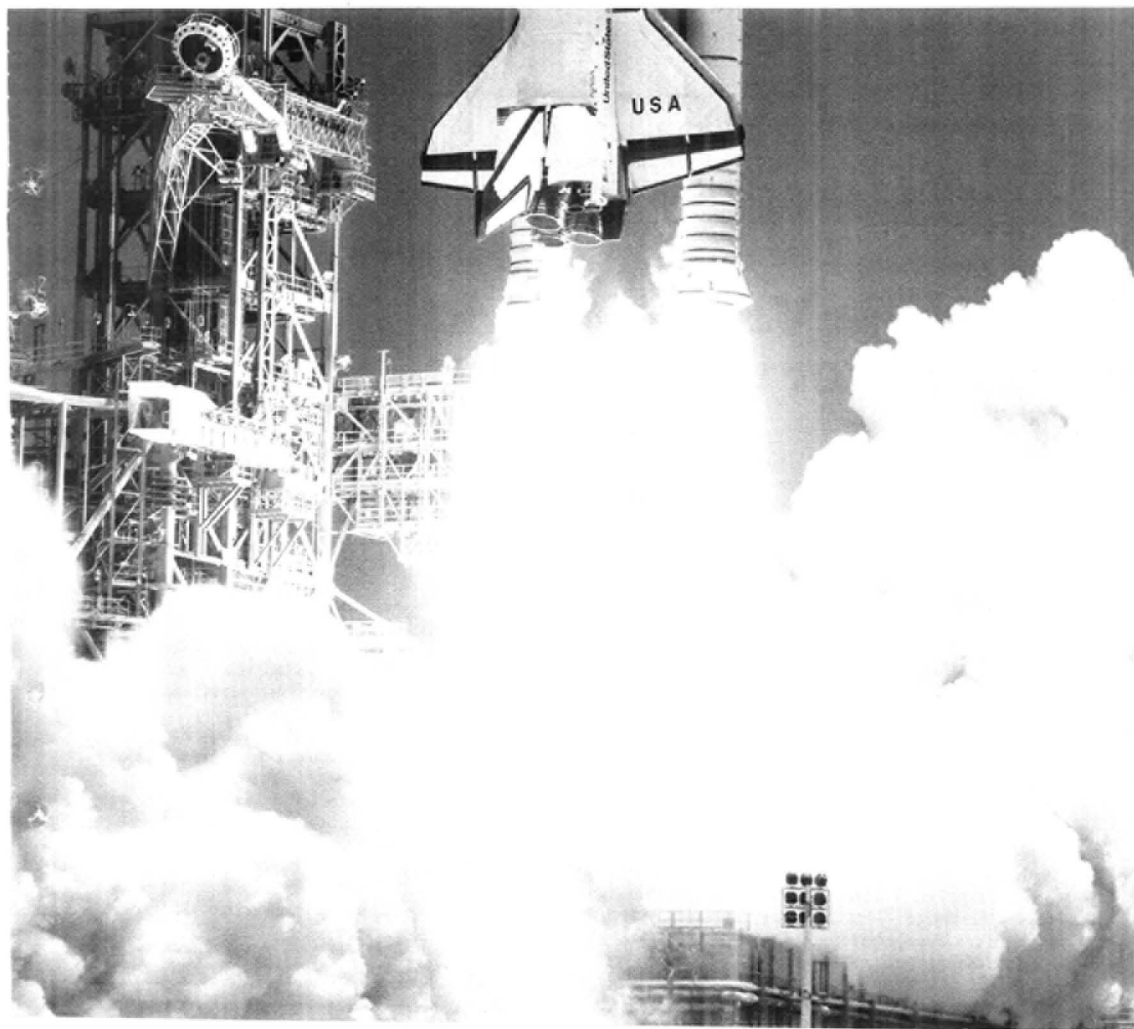
The future of FFF measurement is bright because so many primary and secondary properties of macromolecules and colloids can be obtained, some of which are inaccessible by other techniques. However, the field is still in its infancy, with most applications still ahead. We anticipate further development of measurement strategies and thus an expanded base of measurement capabilities in the next few years. Particularly vigorous development is expected in finding and exploiting new combinations of FFF and downstream measurement techniques with increasingly powerful capabilities for probing the structure and composition of complex real-world colloidal and macromolecular materials.

This work was funded by the National Science Foundation (grant CHE-9322472) and by a Public Health Service grant (GM10851-37) from the National Institutes of Health.

References

- Giddings, J. C. *Science* **1993**, *260*, 1456-65.
- Giddings, J. C.; Caldwell, K. D. In *Physical Methods of Chemistry*; Rossiter, B. W.; Hamilton, J. F., Eds.; John Wiley and Sons: New York, 1989; Vol. 3B, pp. 867-938.
- Taylor, H. E.; Garbarino, J. R.; Murphy, D. M.; Beckett, R. *Anal. Chem.* **1992**, *64*, 2036-41.
- Caldwell, K. D.; Li, J. *J. Colloid Interface Sci.* **1989**, *132*, 256-68.
- Barman, B. N.; Giddings, J. C. *Langmuir* **1992**, *8*, 51-58.
- Giddings, J. C.; Caldwell, K. D.; Jones, H. K. In *Particle Size Distribution: Assessment and Characterization*; Provder, T., Ed.; ACS Symposium Series 332, American Chemical Society: Washington, DC, 1987; Chapter 15.
- Yau, W. W.; Kirkland, J. J.; Bly, D. D. *Modern Size Exclusion Liquid Chromatography*; John Wiley and Sons: New York, 1979.
- Giddings, J. C. *Unified Separation Science*; John Wiley and Sons: New York, 1991.
- Lee, T. T.; Dadoo, R.; Zare, R. N. *Anal. Chem.* **1994**, *66*, 2594-2700.
- Giddings, J. C.; Yang, F. J. F.; Myers, M. N. *Sep. Sci.* **1975**, *10*, 133-49.
- Giddings, J. C.; Karaiskakis, G.; Caldwell, K. D.; Myers, M. N. *J. Colloid Interface Sci.* **1983**, *92*, 66-80.
- Giddings, J. C. *Chem. Eng. News* **1988**, *66*(41), 34-45.
- Giddings, J. C.; Moon, M. H. *Anal. Chem.* **1991**, *63*, 2869-77.
- Williams, P. S.; Lee, S.; Giddings, J. C. *Chem. Eng. Commun.* **1994**, *130*, 143-66.
- Liu, M.-K.; Giddings, J. C. *Macromolecules* **1993**, *26*, 3576-88.
- Liu, M.-K.; Li, P.; Giddings, J. C. *Protein Sci.* **1993**, *2*, 1520-31.
- Giddings, J. C.; Ho, J. *Langmuir* **1995**, *11*, 2399-2404.
- Giddings, J. C. *Anal. Chem.* **1994**, *66*, 2783-87.
- Caldwell, K. D.; Gao, Y.-S. *Anal. Chem.* **1993**, *65*, 1764-72.
- de Gennes, P.-G. *Scaling Concepts in Polymer Physics*; Cornell University Press: Ithaca, NY, 1979.
- Moon, M. H.; Giddings, J. C. *J. Pharm. Biomed. Anal.* **1993**, *11*, 911-20.
- Everett, D. H. *Basic Principles of Colloid Science*; The Royal Society of London: London, 1988.
- Hiemenz, P. C. *Principles of Colloid and Surface Chemistry*, 2nd ed.; Marcel Dekker: New York, 1986.
- Giddings, J. C.; Barman, B. N.; Li, H. *J. Colloid Interface Sci.* **1989**, *132*, 554-65.
- Beckett, R.; Hart, B. T. In *Environmental Particles*; Buffle, J.; van Leeuwen, H. P., Eds.; CRC Press: Boca Raton, FL, 1993; Vol. 2, pp. 165-205.
- Murphy, D. M.; Garbarino, J. R.; Taylor, H. W.; Hart, B. T.; Beckett, R. *J. Chromatogr.* **1993**, *642*, 459-67.
- Beckett, R.; Ho, J.; Jiang, Y.; Giddings, J. C. *Langmuir* **1991**, *7*, 2040-47.
- Yong, Y.; Giddings, J. C.; Beckett, R. In *Proteins at Interfaces 1994*; Horbett, T. A., Ed.; ACS Symposium Series, American Chemical Society: Washington, DC, in press.
- Langwoest, B.; Caldwell, K. D. *Chromatographia* **1992**, *34*, 317-24.
- Schimpl, M. E.; Giddings, J. C. *J. Polym. Sci. Part B: Polym. Phys.* **1990**, *28*, 2673-80.
- Shiundu, P. M.; Liu, G.; Giddings, J. C. *Anal. Chem.* **1995**, *67*, 2705-13.
- Shiundu, P. M.; Giddings, J. C. *J. Chromatogr.*, in press.
- Schimpl, M. E.; Caldwell, K. D. *Am. Lab.* **1995**, *30*, 1435-53.

J. Calvin Giddings, Distinguished Professor of Chemistry, conducts research in FFF, macromolecular separations, and the theory of chromatography. Address comments to him at the Field-Flow Fractionation Research Center, Dept. of Chemistry, University of Utah, Salt Lake City, UT 84112.



*When you're going from zero to 17,000 mph,
the last thing you want is dirty fuel.*

No wonder NASA scientists chose Scott to help them develop the standards for analyzing shuttle fuels.

After all, Scott has also established standards for automotive emissions, semi-volatile organic air pollutants, and the measurement of carbon dioxide in the atmosphere, to name a few. We've supplied the specialty gases and equipment needed to meet those standards, including parts-per-trillion mixtures and ultra-pure zero gases. And we have always supplied them quickly. Anywhere on earth. Overnight, if needed.

As to space shuttle launches, Scott gases have been "mission critical." Because NIST-traceable Scott gases are among those used to calibrate the spectrometer on the launch pad. The spectrometer checks the integrity of the shuttle's entire fuel system. And if it detects a fuel problem, the mission is cancelled.

When your mission is critical, depend on gases that set the standards for accuracy and performance: Scott specialty gases.

Call 1-800-21SCOTT for a complete catalog of our specialty gases and equipment.



Scott Specialty Gases

6141 Easton Road, P.O. Box 310, Plumsteadville, PA 18949-0310
Telephone: 215-766-8861 Fax: 215-766-0320

A Cyclic Voltammetric Simulator for Windows

DigiSim 2.0

Bioanalytical Systems Inc.
2701 Kent Ave.
West Lafayette, IN 47906
317-463-4527; 317-497-1102 (fax);
brad@bioanalytical.com (e-mail)
Version 2.0; \$1895

DigiSim 2.0 is one of about four commercially available packages for electrochemical digital simulation. It is limited to cyclic voltammetry (CV), but CV is by far the most commonly used technique for electrochemical mechanistic studies. *DigiSim 2.0* will simulate CV for any complex (but sensible) mechanism for a great variety of electrode geometries (including the rotating-disk electrode) and semi-infinite or confined diffusion space with either an open-ended or blocked outer boundary. Results can be printed out or plotted, and data files can be written to disk for later comparison. *DigiSim 2.0* can also fit parameters to actual experimental CV curves.

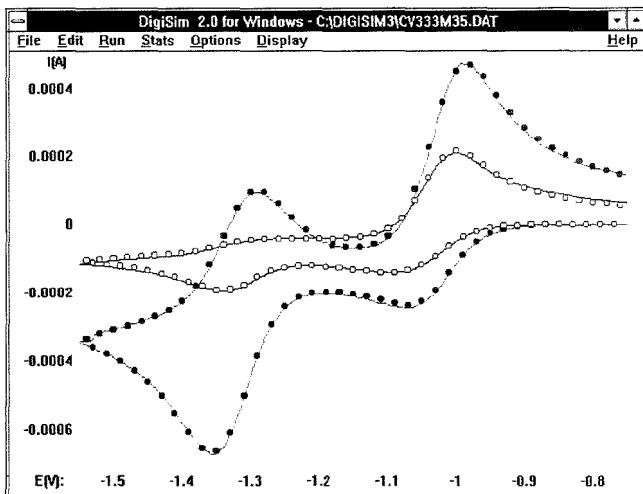
Installation instructions were simple, and I encountered no problems on our 486-based system. The program creates its own directory and icons on the Windows screen. Documentation consists of a manual thin enough for most users to want to read it, as well as hypertext help files. Most of the manual can probably be skipped, at least until you get stuck.

DigiSim 2.0 invites users to experiment with it, and once I understood its simple rules, it was easy to use. You type in a given mechanism, just as you would normally write it down. Next, you supply

the parameters for that mechanism (there are a lot of sensible defaults), click on Run, and the program generally produces results in just a few seconds. The reason for this efficiency is the FIFD algorithm used behind the scenes, combined (by default) with a nonlinear unequal-intervals sequence that results in a small number of boxes; in my case, typically, just 13. (This has all been described earlier in *Anal. Chem.* **1994**, *66*, 589 A). The "movie" Run option shows both the CV curve (now a minor feature on the screen) and the concentration profiles for all species, varying with time. Although the program is designed to do only CV simulations, with a little ingenuity you can bend *DigiSim 2.0* to some other tasks such as potential jump and slow rotating-disk scan. Naturally, mechanism specifications as well as parameter values can be stored on disk and retrieved.

The mechanism you provide must be sensible, and the authors devote a whole chapter in the manual to overspecified or contradictory reactions, which they term "thermodynamically superfluous," within a mechanism. The program refuses to run a simulation with such flaws. I tried a really nonsensical mechanism ($A + e = B$; $B + e = A$) and was promptly thrown out to the main Windows menu without comment. I did my best to trick *DigiSim 2.0* into accepting incorrect mechanisms but did not succeed.

Ivory-tower simulators will find that *DigiSim 2.0* forces them to think like chemists. Although it is possible to write differential equations with totally irreversible reactions, *DigiSim 2.0* does not allow them. Reactions are all reversible to some extent and are specified here by a forward rate and equilibrium constant. Unless specifically prevented from doing



DigiSim 2.0 shows the optimized least-squares fit of a square scheme ($A + e = B$; $AL + e = BL$; $A + L = AL$; $B + L = BL$; $BL + A = AL + B$) where A is a co-enzyme-related nickel complex and L is 2, 2'-dipyridyl.

so, *DigiSim 2.0* always makes sure that there is initial equilibrium, both at the interface and throughout the simulation space. This feature can be disabled, and it is quite instructive to experiment with the two modes.

The outstanding feature of *DigiSim 2.0* is the parameter-fitting option. Pick up a data file, specify a mechanism, suggest values for the parameters you want to optimize, and let it run. If a fit is possible, it is a pleasure to see the two curves (the data and the simulation) merge into one within just a few iterations. At the end, the fitted values can be read off the parameter table. The optimized simulation for a given data file may be saved.

How accurate are the simulations? In a case where I knew what the current should be, I found that it was correct to 3 decimals, a very impressive result given that only 13 boxes were used for that run. You can read current and potential off the CV curves by clicking on parts of the curve.

No program is perfect, and I encountered some problems. First, the manual states that the program will run on a 386-based system with a math coprocessor, but the Win 32 installation failed on our 386-based PC. Second, one would also like to see true batch-run capability in the program (i.e., a number of simulations or parameter fits running in sequence, without the necessity for user intervention). Third, although error checking is good, the messages are not always explicit. Presumably, there will soon be no more 386-based PCs, so the first problem will go away, and no doubt *DigiSim* will add features as it evolves.

The most serious drawback for me is the strict format required for imported data in parameter fitting. CV data files produced by the major manufacturers' instruments can be read, as well as general user files. *DigiSim 2.0* expects these files to have a header containing a set of specifications, but it ought to find out some of

the information for itself (e.g., minimum and maximum current, number of data points). With one data file from an actual experiment, I took great care to write a correct header (using a *DigiSim 2.0*-generated template) but never did manage to convince the program that the data file was acceptable. In the end, the program did grudgingly try to fit to it (with an error message at every iteration). Admittedly, in most cases, the data will be generated by some program that can be made to write the header correctly. Nevertheless, I suggest that a future version should allow the import of "foreign" data consisting only of CV data points. Users would then have to type in a lot of information for the suggested mechanism and parameters, but this might often take less time than writing an acceptable header.

This program is a wonderful tool (and toy!) that frees electrochemists from the need to learn how to program simulations. Long computing times, more or less taken for granted in CV simulations, are a thing of the past. If the price were not so high, no one would think twice about buying *DigiSim 2.0*. This program will no doubt set a standard for competitors to follow, and I look forward to future versions.

Reviewed by Dieter Britz, Aarhus University (Denmark)

SOFTWARE RELEASED

HPLC Column Manager

Phenomenex
2320 W. 205th St.
Torrance, CA 90501
310-212-0555; fax 310-328-7768
Version 3.0; \$650

HPLC Column Manager is a relational database program for managing HPLC column inventories and tracking column performance. Features include the ability to set validation and performance test criteria, troubleshoot column problems, and

build a complete audit trail for GLP/GMP compliance. Also integrated into the program is HPLC Reference Manager, a suite of more than a dozen reference utilities, libraries, and tools for chromatographers. Minimum system requirements include an IBM or compatible PC with a 386DX or faster processor, 8 MB of RAM, 10 MB of free disk space, MS-DOS 5.0 or later, Windows 3.1 or later, and a mouse. A network version is available.

DOE-101

Scientific Software
5 Birch St.
Mundelein, IL 60060
708-949-1764; fax 708-949-4478
Version 1.0; \$300

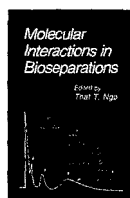
DOE-101, an experimental design package for non-statisticians, guides the user through each step of planning, designing, conducting, and analyzing the results of multifactor experiments. Features include randomization of runs, data transformations, presentation of results in a variety of graphic formats, and automatic report writing. Minimum system requirements include an Apple Macintosh computer with 2.5 MB free RAM and at least 8 MB free disk space. A demo disk is available.

Alarm!

Justice Innovations, Inc.
1240 L'Avenida Ave.
Mountain View, CA 94043
415-969-6122; fax 415-969-6140
Version 1.0; \$395

Alarm!, an enhancement to the Chrom-Perfect chromatography data system, enables fully automatic real-time monitoring of chromatographic analyses to initiate quality or process control actions. It can check up to 100 alarm events, such as out-of-range peak area or width, and can ensure GLP compliance by automatically checking system suitability values such as resolution, skew, and noise.

An affinity for biomolecules



Molecular Interactions in Bioseparations

That T. Ngo, Ed.
Plenum Press
233 Spring St.
New York, NY 10013
1993, 570 pp., \$95

This book succeeds where many other compiled volumes fail, in that the editor demonstrates that a compilation of 35 chapters written by 72 international experts can make a compelling and readable book. Ngo has managed to solicit an outstanding set of chapters with intriguing titles. Weak affinity chromatography, slalom chromatography, antisense-family peptides, biorecognition in molecularly imprinted polymers, and affinity electrophoresis are a few examples. The chapters appear to have been thoroughly reviewed and, with only a few exceptions, are well written. Most chapters are organized to give an overview of recent developments, followed by a brief and readable description of methods, and finally results. The book is a salute to the editor's outstanding knowledge of the field as well as his organizational skills.

The first chapter ties the book together. It gives a brief history (1 page) of the past 25 years of affinity chromatography and then quickly moves to applications in rDNA, proteins, hormones, and low molecular weight compounds. The reader finds, in retrospect, that this volume actually covers applications in all of these areas.

The second chapter defines weak affinity chromatography as systems for which $K_a < 10^4 M^{-1}$, or one that displays the chromatographic attribute of peak elution and

separation isocratic conditions. The chapter proceeds smoothly to a discussion of affinity chromatography on inorganic materials written by one of the experts in the field. Preparation of various types of inorganic supports is clearly and concisely described. The description that precedes this section and the applications that follow it give the reader an overview of which type of material might be preferred for a given molecule. The succeeding chapters on 2-fluoro-1-methylpyridinium salt-activated gels, and later parts of the book on biological ligands, immunofluorescence, and biometric ligands, are organized in a similar manner. Applications, with a clear explanation of principles, follow the descriptions of the biochemistry of many of the affinity materials.

The book is a salute to the editor's outstanding knowledge of the field.

Part I, although a general introduction, ends with a chapter on slalom chromatography. The name is derived from DNA that weaves through a column of closely packed, nonporous, spherical polymer beads, much like a skier racing down a slope around flags. The longer, higher molecular weight DNA makes more turns than shorter, lower molecular weight DNA. This causes the larger DNA to elute first. This derivative of hydrodynamic chromatography, although not affinity chromatography, gives a sufficiently novel result to justify its inclusion.

The section on affinity chromatography with biological ligands is complete enough to qualify as a monograph on recent developments in the field. It covers affinity chromatography with immobilized bacterial immunoglobulin-binding pro-

teins, glycoproteins (lectins), anhydrotypsin (trypsin in which the active site Ser-195 is a dehydroalanine residue), interleukin-2 receptor, phosphatidylcholine (otherwise known as immobilized artificial membranes), antisense peptides, and cellobiohydrolase and cyclodextrins (both are for chiral resolution). These chapters show the reader how far affinity chromatography has come in 25 years and, more importantly, where it could go.

The third part of the book builds on the second and shows how immobilized antibodies have applications in the purification of organelles and cells. Part III, although short, makes a good bridge between Part II and the practice of affinity chromatography (Part IV). A discussion of the use of small molecules (dyes, histidine, adenine, cytosine, benzeneboronates, and metals) as affinity ligands completes the applications section in Part IV. The last chapter in Part IV is on hydrophobic chromatography and seems out of place at first glance. Further reading shows it is useful, because hydrophobic interactions with affinity chromatography matrices can enhance or compromise the biospecificity of affinity supports, particularly silica materials. The background on hydrophobic interactions is clearly presented, and the comparison to reversed-phase chromatography states that the extent of surface coating on a reversed-phase material is 10–100 times greater than on a similar hydrophobic interaction support. Hence, adsorption is stronger. Although not all chromatographers would agree, the take-home message is that hydrophobic interaction chromatography occurs because of conditions selected by the chromatographer (i.e., support and eluting buffer composition).

The sections on novel concepts (Part V) and applications (Part VI) of affinity-related techniques round out the book. Part VI is a collection of case studies; Part V focuses on molecular-imprinted polymers. The principles, methodology, and possibility of using these materials for both affinity chromatography and catalysis are presented.

Overall, the book delivers a quick primer on the recent advances in affinity chromatography, together with a comprehensive set of references at the end of each chapter. Readers who seek an update on advances in affinity chromatography, as well as a reference for derivatization methods, will find this book to be worthwhile.

Reviewed by Michael R. Ladisch, Purdue University

CE for the novice



Capillary Electrophoresis

Dale Baker
John Wiley & Sons
605 Third Ave.
New York, NY 10158
1995, 272 pp., \$49.95

This book is designed primarily for those unfamiliar with capillary electrophoresis, HPLC, or slab gel electrophoresis. The author also intended this book to serve as a reference for those more familiar with the field as well as a reference or text for CE courses. As part of the *Techniques in Analytical Chemistry Series*, the book is intended to provide background information for novices, provide a sense of the capabilities and limitations of various techniques, and cover both mature and newer topics in the field.

This book is aimed primarily at the novice. It provides an overview of the technique, and the various CE modes are mentioned. Limitations are presented, and some of the newer and more exotic CE topics are discussed. Practical informa-

tion, such as tips on frequent buffer replenishment and finding the optimum operating voltage, is given, and the section on injection techniques is very thorough. The book points to the appropriate primary literature references that would lead a novice deeper into the field. The included list of journals publishing CE papers should be of particular interest, as should the limited applications table with references in Chapter 7.

The book has seven chapters, each with a separate reference list. The number of references varies from 16 to 156, and most are from the late 1980s or early 1990s, the most recent being 1993. Using a somewhat limited reference list is arguably a better approach than overwhelming the reader with an exhaustive list that includes some papers of little note. This is particularly true if this book is being used as an introduction to CE. A moderate subject index is also provided.

Overall, however, I am not pleased with this book. First, I found much of the presentation of the information to be uneven and poorly organized. For instance, the book has many sections that are not specific to CE, but rather address analysis techniques in general; a brief Beer's law discussion is presented in Chapter 4, and an extensive section in Chapter 6 addresses the use of internal and external standards. In addition, some information is overly simplified or wrong, such as the recommendation that optimizations can only be performed by changing one variable at a time. The low assumption of reader knowledge makes reading the book from cover to cover rather tedious.

Very little advanced information is discussed in any significant manner. For example, coupling to MS with CE is given only scant attention, although this can be forgiven as the book is not designed for the experienced CE user. The book does not provide enough details for the experienced researcher; other books on CE provide more extensive reference lists and fuller discussions of various techniques, applications, and theory.

Perhaps what bothered me the most was the author's repetition. For instance, the "typical dimensions of a capillary" are given at least three times in Chapter 1.

There are several examples of figures that are essentially the same as other figures in different chapters. Some sections on method development in Chapter 5 provide information that was presented in Chapter 3. In Chapter 4 it is mentioned twice within three pages that electrokinetic injections, as opposed to pressure injections, must be used with gel-filled capillaries. Such redundancy points to a poor editing job.

This book could be successfully used in a course if novice readers had an experienced teacher to lead them through it. In this way, the problem sections could be effectively passed over and the merits emphasized.

Reviewed by Michelle M. Bushey, Trinity University

BOOKS RECEIVED

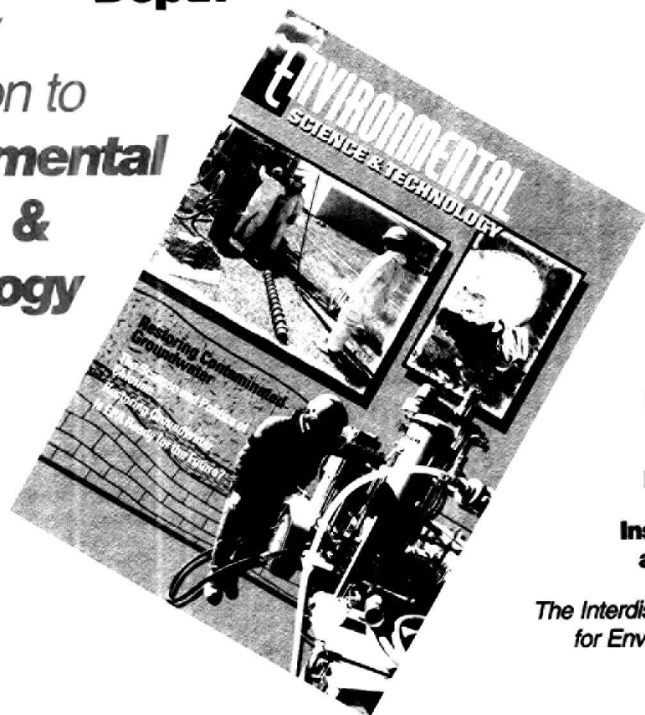
Principles and Practice of Modern Chromatographic Methods

Kevin Roberts, Paul R. Haddad, and Peter E. Jackson
Academic Press
1250 Sixth Ave.
San Diego, CA 92101
1995, 495 pp., \$35

This book is intended as a comprehensive and unified approach to chromatographic separations both for the novice and for the chromatographic specialist who needs to switch from one technique to another. Chapter topics include introduction and overview, theory of chromatography, GC, planar chromatography, HPLC instrumentation and techniques, HPLC separations, SFC, and sample handling in chromatography. Each chapter contains a list of references to the original literature and a bibliography of useful books and review articles arranged by topic. A subject index is included at the end of the book.

Focus
Insight
Depth

The New
 Dimension to
**Environmental
 Science &
 Technology**



New Editorial Mix
Expanded News
Research Articles
Insights into Trends
and Controversies

*The Interdisciplinary Publication
 for Environmental Scientists
 and Professionals*

Our expanded editorial coverage provides a balance of focus, insight, and depth in topics ranging from remediation and air quality to regulations and public policy. Two new departments, "Research Watch" and "EPA Watch," highlight current activities emerging at these two ends of the spectrum.

Critical analysis of policy, worldwide news, innovations in measurement, research articles by well-known authorities — all of these features offer you a broader base of knowledge than ever before. And, our new cover and interior design spotlight information so you'll know exactly where to look for new developments in areas that are beginning to affect your work.

In addition to the cutting-edge research for which this publication is highly acclaimed, the new editorial mix includes in-depth feature articles covering the areas that drive the environmental field: Science, technology, government, and society.

While many other environmental publications are devoted to one discipline or another, no other journal completely integrates all disciplines of the environmental field.

Experience the new *Environmental Science & Technology*.
 Subscribe today!

To order your one-year subscription right away call toll-free, 1-800-333-9511 (U.S. only). Outside the U.S. call 614-447-3776. Fax to 614-447-3671.

Editor

William H. Glaze
 University of North Carolina, Chapel Hill

Associate Editors

Walter Giger
 EAWAG, Switzerland
 Ronald A. Hites
 Indiana University at Bloomington
 Cass T. Miller
 University of North Carolina, Chapel Hill
 Jerald L. Schnoor
 University of Iowa
 John Seinfeld
 California Institute of Technology
 Joseph M. Sullita
 University of Oklahoma

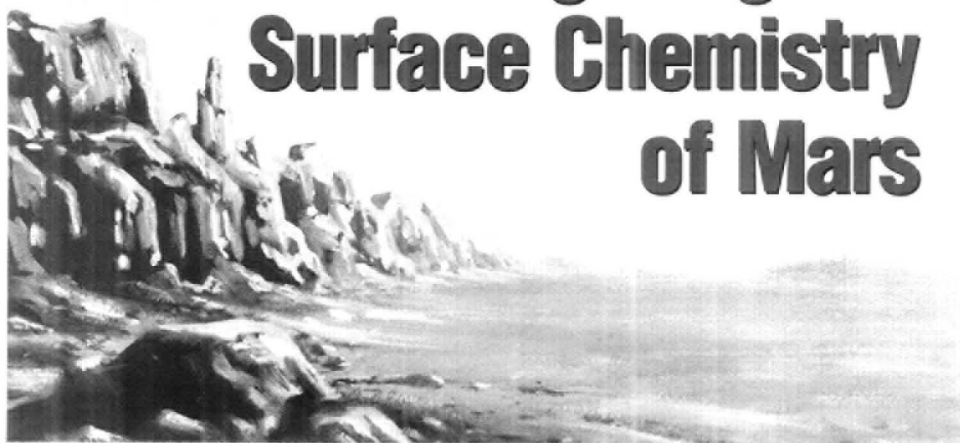
1995 Subscription Rates

	U.S.	Canada & Mexico	Europe*	All Other Countries*
Member	\$44	\$68	\$96	\$113
Nonmember Personal	\$90	\$114	\$142	\$159
Nonmember Institutional	\$585	\$609	\$637	\$654

*Includes air service.

ACS PUBLICATIONS
 Essential Research for the Chemical Sciences

Investigating the Surface Chemistry of Mars



One of the primary objectives of the Viking missions to Mars in the 1970s was to search for life. The landing crafts, or landers, detected extraordinary reactivity in the Martian soil, but no organic material (1). Numerous theories were put forth to explain the Viking data, most of which involved an oxidizing species in the Martian surface material. In December 1992, the Mars Oxidant Experiment (MOx) was selected as the U.S. contribution to the Russian Mars '96 mission. Two landers are scheduled for launch in November 1996 and should arrive at Mars in September 1997. This is the first mission in 20 years to conduct experiments on and near the surface of Mars.

The MOx instrument, shown on the Russian lander in Figure 1, is designed to

The Mars Oxidant Experiment Team

0003-2700/95/0367-605A/\$09.00/0
© 1995 American Chemical Society

The unusual conditions found on the Martian surface 20 years ago prompt the Mars Oxidant Experiment

investigate the chemical nature of the Martian surface material, with particular emphasis on its oxidative character. The instrument uses fiber-optic technology to monitor real-time physicochemical changes in a suite of chemically sensitive thin-film materials, some in contact with the Martian surface, others exposed only to the atmosphere.

Designing MOx was extremely challenging. The entire instrument had to fit

within a very small volume in the Russian lander, could not exceed 850 g, and could consume no more than 25–50 mW of the lander's power for very short periods of time. It had to survive landing shocks with a force 250 times that of Earth's gravity and diurnal temperature variations of $\sim 100^\circ\text{C}$, and it had to have its own central processor, command set, and memory. This report describes the scientific rationale and basis for the MOx instrument, along with details of its design and construction.

Background

The objective of MOx is to examine broad and important questions in Martian exobiology (nonterrestrial biology) and geochemistry. These include heterogeneous geochemical weathering of the surface and the hypothesis that one or more inorganic oxidants is responsible for the unexpected results obtained by the Viking biology experiments. The Martian

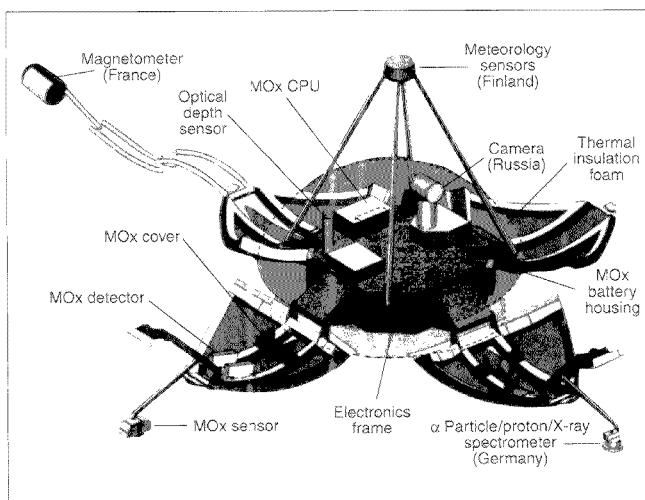


Figure 1. Russian lander showing the MOx sensor and its components.

surface material was found to be uniquely reactive, an observation that provoked a host of explanations (2, 3), but the mechanisms involved remain open to interpretation. Identification of reaction mechanisms in the soil could, however, explain why no organics were found in the Martian surface material and could assist in predicting the depth to which future missions must penetrate to possibly recover organic materials that may be "leftovers" from a period of organic and chemical evolution. The absence of organic material is surprising, because organics are believed to be almost ubiquitous throughout the solar system as a result of the accumulation of carbonaceous meteoritic material. If the Martian surface is an exception, an explanation is required.

If primitive organic materials exist in the Martian surface material, they will provide the best-preserved record of the chemical evolution of early Mars. On Earth, organics recovered from the stratigraphic column have yielded preserved cellular materials, morphological microstructures (4), and chemical discontinuities associated with the appearance of life (5-7). Finding geographic or stratigraphic domains on Mars from which primitive, unoxidized material might be recovered is a fundamental objective of the exobiology community.

Given the absence of liquid water, the interaction between the Martian atmosphere and the surface may be the most active and important geochemical process. The thin films that will be exposed to the Martian environment were selected to span a wide range of chemical activity. The cumulative response of the films will indicate whether oxidizing species are produced in the atmosphere and soil and will help identify the species by bracketing the strength of any oxidant(s). (The Martian atmosphere is 95.3% CO₂; a few percent nitrogen and argon; and trace amounts of oxygen, carbon monoxide, water, and ozone [8].) In addition, specific minerals in the Martian surface material may be identified if their pattern of reactivity is sufficiently distinct.

A final environmental consideration that could be a driving factor in the chemical state and reactivity of the Martian surface is the influence of solar radiation. The thin Martian atmosphere provides minimal shielding from solar UV radiation. Compared with the spectrum of the solar radiation found at the top of the Earth's atmosphere, the solar radiation reaching Mars' atmosphere has the same spectral distribution and about 43% of the intensity. The UV cutoff at the Martian surface is about 190 nm because of absorption by CO₂.

The chemical micromirror array approach

In its most general form, a chemical microsensor combines a physical transduction platform with a chemically sensitive layer or interface (9). Mechanical, electrical, electrochemical, thermal, and optical means of transduction have all been examined in detail, as have a wide range of chemically sensitive interface materials (10, 11). With the appropriate choice of physical platform, chemical microsensors can be small and compact. Optical sensors are particularly promising in this regard, because a single light source and one detector array can be combined with hundreds of optical fibers to create a suite of chemical microsensors.

In general, the key to devising an array of chemically sensitive interfaces that produces a unique response pattern for each analyte is the "chemical orthogonality" of the sensitive interfaces: If the responses of one of the interfaces can be expressed as a linear combination of the responses of the other members of the array, then it has little added value. This particular requirement means that chemically sensitive interfaces must have a degree of selectivity, although the selectivity need not be as perfect as in the one-film/one-analyte approach.

For chemical detection using nonbiological interfaces, the partial selectivity that works best with pattern recognition allows for the consideration of many more candidate chemically sensitive interface materials than would a requirement for perfect selectivity. For the MOx experiment the relatively unknown nature of the Martian surface means that a wide variety of sensitive coatings, some with very high reactivity, are needed.

The MOx instrument uses micromirror chemical sensor technology developed at Sandia National Laboratories (12). The end of an optical fiber is coated with a material that acts as a chemical transducer through changes in its optical properties that result from exposure to the chemical to be detected (13). These changes alter the reflectivity at the end of the fiber. This instrument takes advantage of components developed for optical communications using silica-clad-silica communications fibers, an LED as the source, and a conventional photodiode as the detector.

Sensitivity to different chemicals is achieved by selecting the appropriate coating material for the end of the fiber. The overall reflectivity of the coated optical fiber tip depends on both its Fresnel reflectivity (front-surface reflectivity) and its integrated optical thickness. Thus, for metal films, which have large indices of refraction, very small effective changes in the film thickness, as little as 0.01 nm, can be measured. Metal films must be thin enough to be optically semitransparent, and so are typically in the 5- to 15-nm thickness range. When the reflective element is a film with a predominantly real refractive index, such as a polymer or inorganic dielectric layer, thickness changes of a few tenths of a nanometer (equivalent to a fraction of a percent of the wavelength of light) are necessary for detection; these films must be several wavelengths thick, so they are typically a few micrometers thick.

The MOx instrument was designed to include as many as 256 integrated micromirror chemical sensors, one for each pixel of the linear diode array detector. Sets of 12 micromirrors are grouped in micromachined silicon structures called cells. A number of these 12-micromirror cells, along with a precision optical reflectometer that includes light source, distribution system, detector, and minimal analog conditioning electronics, are housed in the sensor head.

Several factors were taken into account in designing the optical measurement system, or reflectometer. Reflectivity measurements are made at 590 nm (amber) and 870 nm (near-IR) with two illumination intensities for each wavelength. The dual-wavelength feature is especially helpful for some organic coatings, such as pH indicators, that change absorbance (hence reflectivity) at only a single wavelength in response to a change in concentration of a particular chemical species; the unaffected wavelength is used as a reference. High-intensity illumination is used to provide a stronger signal to probe poorly reflective materials, and low-intensity illumination avoids the problem of detector saturation for highly reflective materials.

Bringing the micromirror coatings into contact with the Martian surface material is a primary concern, so each cell was designed using a passive pivoting system for

mounting. Optical fibers were chosen as a means of delivering and collecting light, as opposed to rigid, integrated-optics construction. The optical layout of the reflectometer is shown in Figure 2. The "light table" (upper left of Figure 2) provides multiple sources of light that can be conveniently coupled into a large number of fiber bundles. After passing a collimating lens, the light from both LEDs is folded into a single beam using a dichroic mirror. This illuminates the input of the optical fiber distribution system, which starts with a set of rigid light pipes or guides that dispense light into several fiber bundles. The function of the "harness" is to deliver light from the light table to the sampled films, to collect the reflected light, and deliver it to the detector, a 256-pixel linear diode array.

Each pixel is used to detect the light intensity from one fiber. Coupling the fibers

into the detector pixels was accomplished by mounting the fibers in "plugs" in groups of 12, with each plug butting the fibers against the detector surface. The spacing between the fibers, the depth of the fiber-retaining groove, and the thickness of the plug are chosen such that, by placing the plug at an angle of 8° from the vertical pixel dimension of the detector, each fiber is aligned with one detector pixel. Cross-talk between pixels is controlled by a metal mask deposited on the surface of the protective oxide covering the face of the detector.

The chemical sensor cell (Figure 3) consists of four parts. The silicon retaining sleeve assembly aligns the fiber guides with the set of micromirrors. The etched "egg crate" assembly, made from a 250- μm -thick silicon wafer fusion bonded to a 50- μm -thick fused-silica wafer, divides the

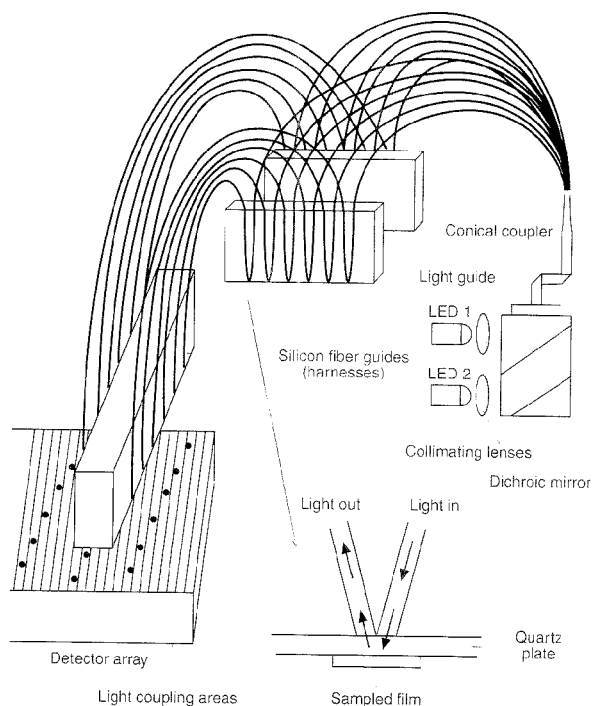


Figure 2. Optical layout of the reflectometer.

fused-silica surface into 12 distinct micromirrors. The chemically sensitive films are deposited on the front face of the fused silica through the egg crate assembly. A membrane-based silicon nitride hermetic seal is applied over the egg crate assembly to minimize contamination.

Thin films

Twenty-one chemically diverse coatings were chosen for use on the cells. These coatings had to be highly reactive because of the anticipated low temperatures (-80 to -20 °C) and short measurement period (40–100 days). Permanent hermetically sealed cells serve as controls, experiencing the same temperature fluctuations and mechanical perturbations but having no contact with chemical species. Three of every 12 micromirrors are reference films: optically thick Au/Pt/Ti to provide a constant-reflectivity film, unperturbed by chemical reaction, as a check on LED illumination levels; bare SiO₂ to monitor ambient light levels and scattering of light by dust; and a thick Au/Pt/Ti/Si composite to monitor ambient temperature by variations in the bandgap and refractive index of the Si film.

The seven metal films listed in Table 1 have a range of electrochemical potentials and oxidation chemistries. These metals are listed in the approximate order of increas-

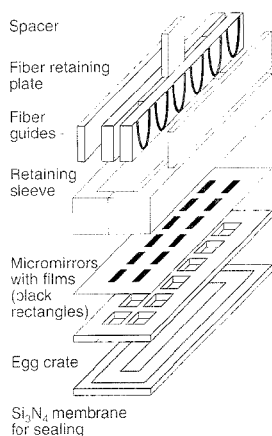


Figure 3. Exploded view of an optical sensor cell.

ing reactivity. Learning which metals do and do not oxidize will give a first-order estimate of the approximate "oxidizing power" of the Martian surface and atmosphere, and some specific reactions may be detected by particular metal films. (The Au/Pt/Ti film in Table 1 is not as thick as the film used for the reference.)

The other films were selected for their characteristic reactivities. Two kerogen-like films, with ratios of hydrogen to carbon of 0.5 and 1.2 that approximate some of the carbonaceous species thought to be deposited on Mars by meteorites, will be monitored for oxidation to CO₂. A polybutadiene film will be used to check for traces of ozone (14) present in the Martian atmosphere. L- and D-Cysteine are used to monitor the rate of degradation of simple amino acids and to ascertain whether any chiral species, such as a transition metal complex, are in the Martian dust and involved in the degradation of organics.

The pH indicators thymol blue, bromothymol blue, and 2,6-dichloroindophenol will be used to characterize proton activity of the surface material and of gaseous species, including water, that may adsorb from the atmosphere onto the surfaces of the films. We attempted to choose indicators with a pH-sensitive absorbance maximum overlapping the wavelength of one of the LEDs used to measure reflectivity but without significant absorbance at the second LED wavelength so that non-specific changes in the film, such as oxidative degradation, can be separated from proton activity effects.

Methylene blue is sensitive to reducing agents, and fluorescein could provide additional information regarding proton activity. In its long-lived excited electronic state, fluorescein is both a stronger reducing agent and a stronger oxidizer than the ground-state molecule, which means that solar UV light can be used to convert a fairly unreactive material into a high-reactivity coating. Like the pH indicators, hematin has an absorbance maximum near one of the two LED wavelengths and can change reflectivity depending on whether it binds O₂ or CO. Whether such binding can occur in the solid state under anticipated Martian conditions is unclear; during the Martian day, the atmospheric cells will be exposed to solar UV radiation, which could affect both the

Table 1. Metal micromirror coatings

Coating	Purpose
Au/Pt/Ti	Indicates frost and organic adsorption; reacts with sulfur compounds
Pd	Sensitive to H ₂ , H ₂ S, and unsaturated hydrocarbons
Ag	Extremely reactive to O ₂ and O ₃
V	Moderately to highly reactive to oxidants
Ti	Highly reactive to oxidants
Al	Highly reactive to oxidants
Mg	Very highly reactive to oxidants; reactive to CO ₂ if film is clean enough

kinetics and equilibrium concentration of bound O₂ and CO.

Cells are located in two places on the sensor head: Eight cells face downward to contact the surface material, and four face upward for exposure to the atmosphere and solar irradiation. To distinguish photo-assisted from unassisted chemical reactions, some atmosphere-probing cells will use dust filters that have a thin layer of metal deposited onto the surface, eliminating about 95% of light transmission without hindering gas permeation. Any photo-assisted deposition of organic materials will be indicated by a difference between the response of the solar-exposed and solar-unexposed bare SiO₂ micromirrors.

Preliminary results

From the reflectivity-versus-thickness curves for deposited metals and organics, and assuming reflectivity can be measured to within 0.3% accuracy over a 40-day experiment lifetime, it is possible to estimate minimum changes in material thickness, and thus minimum reaction rates, that can be detected by the instrument. (Laboratory measurements are significantly more stable and accurate, but 0.3% is consistent with the capabilities of the MOx instrument). For metal films the minimum detectable thickness change is 0.1 nm; therefore, the minimum detectable reaction rate is 3 × 10⁻⁶ nm/s. For organic films the corresponding values are 10 nm and 3 × 10⁻⁶ nm/s.

From these numbers and reaction rates for various chemical species, the minimum detectable average concentration of such species can be estimated. For example, to study possible degradation of organic compounds, a clean fiber end was monitored during plasma deposition of hydrogenated carbon films. Figure 4 shows deposition of a kerogen film $\sim 1 \mu\text{m}$ thick. As the thickness of the film grows to one, two, or more half-multiples of the wavelength of the illuminating light in the film material, reflections from the front and rear interfaces of the layer alternately add and cancel, producing the interference fringes. This film was subsequently exposed to atomic oxygen, a strong oxidant produced in an oxygen plasma, resulting in the removal of the film, as indicated by the second set of interference fringes. The oxygen concentration was estimated to be 10^{13} – 10^{14} atoms/cm³.

Assuming impact rate-limited kinetics and a chemical reaction that is first order in atomic oxygen, the measured rate of reaction of 1 nm/s for removal of the hydrocarbon film, together with the minimum detectable reaction rate of 10^{13} – 10^{14} atoms/cm³, yields a minimum average concentration of atomic oxygen of 3×10^7 to 10^8 atoms/cm³, which corresponds to 0.5 ppb by volume in the 5.6-Torr Martian atmosphere. The detection limit for oxidants that have a lower relative rate of removal of the film (i.e., weaker/less active oxidants) is higher. This estimate gives an idea of the sensitivity of the micromirror technique for detection of oxidants at room temperature. The lower Martian temperatures would result in slower reaction rates and therefore higher minimum detectable limits for equivalent reactive species for a given exposure period.

The micromirror approach (13, 15) has largely been applied to the measurement of reactions between gases and the micromirror. To study the Martian surface material, the micromirror must be brought into contact with a granular surface. However, chemical reactivity at a dry, solid–solid interface could be orders of magnitude slower than at a gas–solid interface. Scanning electron microscopic images of films placed in varying degrees of contact with 1.0- and 0.1- μm particle-size powders suggest a strong bonding of powder to film by an electrostatic mecha-

nism. This particle pickup also suggests that intimate contact with Martian surface material may not be necessary, although electrostatic pickup will undoubtedly oversample the fine-grained fraction of the surface material. Laboratory studies of micromirror materials indicate that a pure superoxidant material such as KO_2 can react at -30°C with several metallic films, providing about a 0.3% relative change in optical reflectivity in a 5- to 15-day period.

The lander and MOx components

Each craft lands on an airbag cushion after a parachute descent. Approximately 10 min after landing, the lander separates from the airbag, dropping 30–50 cm to the surface. The instrument begins its internal calibration and measurement sequence, which continues through petal opening. Some 3–5 min later, the petals of the lander open, providing an upright

*Each craft lands
on an airbag
after a parachute
descent.*

configuration for the station. About a minute later, a 150-g Russian designed and built boom, which holds the MOx sensor head on the inside of one petal, is activated and the sensor head descends to the surface in 3–5 s. As the sensor head extends away from the lander, the protective membranes over the reaction cells are pulled and shattered. The electronics are checked to determine whether they withstood landing and any subsequent bouncing. The estimated lifetime for the lander is ~ 1 Mars year or ~ 2 Earth years.

The basic long-duration measurements begin ~ 28 s after boom deployment and continue until the memory buffer is filled. For the first 40 days measurements are made at a logarithmically decreasing rate to maximize the range of chemical reaction rates that can be detected. After 40 days, additional measurements are made every third day, but only if there is any re-

maining memory into which data can be placed. The instrument should provide active measurements for at least 50 days.

Because the lander cannot provide power or accept data for transmission until 20–40 days after landing (and then only at data rates sufficient for slower-than-normal operation of the MOx instrument), the instrument requires batteries and memory to enable stand-alone operation during the active chemical measurement portion of the instrument's activity. The MOx data system will retain data in memory, sustained by a long-lived battery, and will provide several repeated transmissions of data acquired early and any subsequent data, assuming the lander-orbiter pair lifetime exceeds 70 days.

The design of the mechanical aspects of the instrument was driven by having to fit pieces wherever room could be found in the lander. To minimize mass and cost and to maintain instrument integrity, enclosures were made from aluminum or magnesium. The MOx sensor head had to be similar in mass and size to the German α particle/proton/X-ray (APX) sensor, for which the boom was originally designed. The analog and sequencer electronics box is located on the lander petal, close to the sensor head. A temperature sensor is located near the A/D converter to monitor that critical area's temperature swings for calibrating the data. The central processing unit is located between the APX instrument electronics and the top of the instrumentation frame within the lander.

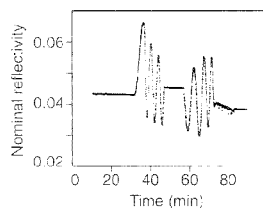


Figure 4. Response during the deposition and subsequent removal of a $\sim 1\text{-}\mu\text{m}$ kerogen film on the tip of an optical fiber.

The first three interference fringes correspond to film deposition from a hydrocarbon plasma that was extinguished at ~ 48 min. An oxygen plasma was ignited 10 min later, which removed the film as indicated by the final three interference fringes.

The battery box, containing sets of primary power cells that drive the experiment and a single memory backup power cell, is located external to the instrumentation frame, inside insulating foam that fills much of the empty space in the lander. Lithium/thionyl chloride batteries were selected because of their ability to deliver power at temperatures below $-30\text{ }^{\circ}\text{C}$ once properly conditioned. Three sets of these batteries should be sufficient to provide power to operate MOx for 50–70 days. Two internal radioactive heater units in the lander should provide enough heat to prevent the CPU and battery box from being exposed to the extremes of the Martian day. The late summer/early fall landing at latitudes $25\text{--}40^{\circ}\text{ N}$ means a peak day temperature around -20 to $-30\text{ }^{\circ}\text{C}$ and a dawn temperature of around -95 to $-105\text{ }^{\circ}\text{C}$. The electronics in the petal box and sensor head were designed and tested to operate in these temperature extremes.

Final words

Many exciting prospects exist for using fiber optic-based sensors in future planetary missions. The MOx experiment is a nearly unprecedented combination of translating advanced laboratory technology into a foreign spacecraft, doing retrofits and, of course, trying to follow a compressed schedule. Data from these experiments, conducted over a few tens of days, will give us insight into the chemistry that has defined the Martian surface over the course of eons.

We gratefully acknowledge contributions by B. C. Clark, Martin Marietta; T. Kenny, L. Miller, M. Hecht, J. Podosek, E. Vote (deceased), S. Fortier, A. Seminara, H. Price, E. Carrel, K. Manatt, S. Kuo, R. Anderson, and R. Wilson, JPL; C. Palermo, Optical Corporation of America; S. Rudaz, J. Fouquet, and A. Liao, Hewlett Packard; M. Klausmeier-Brown, Varian Research Center; C. A. Ray and E. Miller, Microflow Analytical; and J. Saunders and M. Watson, Biospherics Inc. Work at Sandia National Laboratories was supported by DOE (DE-AC04-94LA85000) under contract to NASA.

References

- (1) Biemann, K. et al. *J. Geophys. Res.* 1977, 82, 4641.
- (2) Klein, H. P. *Icarus* 1978, 34, 666.
- (3) Levin, G. V.; Straat, P. A. *Icarus* 1981, 45, 494.
- (4) Campbell, S. E. *Nature* 1982, 299, 429.
- (5) Schidlowski, M. A. *Nature* 1988, 333, 313.
- (6) Friedmann, E. I. *Adv. Space Res.* 1986, 6, 265.
- (7) McKay, C. P.; Stoker, C. R. *Rev. Geophys.* 1989, 27, 189.
- (8) Owen, T. In *Mars*; Kieffer, H. H.; Jakosky, B. M.; Snyder, C. W.; Matthews, M. S., Eds.; University of Arizona Press: Tucson, AZ, 1992; p. 818.
- (9) Hughes, R. C.; Ricco, A. J.; Butler, M. A.; Martin, S. J. *Science* 1991, 254, 74.
- (10) Madou, M. J.; Morrison, S. R. *Chemical Sensing with Solid-State Devices*; Academic: New York, 1989.
- (11) Janata, J. *Principles of Chemical Sensors*; Plenum: New York, 1989.
- (12) Butler, M. A.; Ricco, A. J. *Anal. Chem.* 1992, 64, 1881.
- (13) Butler, M. A.; Ricco, A. J. *Appl. Phys. Lett.* 1988, 53, 1471.
- (14) Fog, H. M.; Rietz, B. *Anal. Chem.* 1985, 57, 2634.
- (15) Butler, M. A.; Ricco, A. J.; Buss, R. J. *Electrochem. Soc.* 1990, 137, 1325.



We're revolutionizing the Art of Electrochemistry.

G&G Princeton Applied Research is pleased to announce the new Model 283 Potentiostat/Galvanostat. The M283 is compatible with all of our present software. You can combine the unit with our impedance systems and take your research to frequencies of up to 5 MHz. Or, add a wave form generator and take your CVs to unheard of speeds. The new Model 283 has an impressive low current range of 20 picoamps* for your microelectrode research! For more information please contact us at 1-800-366-2741.

* Under computer control; call for complete specifications.



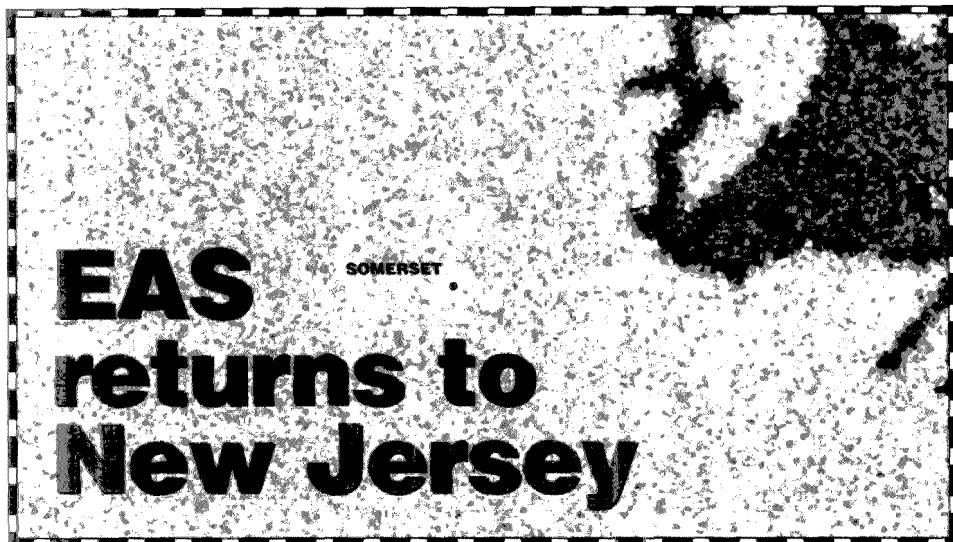
EG&G INSTRUMENTS

Princeton Applied Research

P.O. Box 2565 • Princeton, N.J. 08543 • (609) 530-1000 • FAX: (609) 883-7259 • TELEX: 843409
United Kingdom (44) 734-773003 • Canada 905-827-2400 • Netherlands (31) 034-0248777
Italy (39) 02-27003636 • Germany (49) 89-926920 • France (33) 01-69898920 • Japan (03) 638-1506

Circle 10 for Literature. Circle 11 for Sales Rep.

The Mars Oxidant Experiment Team members contributing to this article are Frank J. Grunthaner, senior research scientist in the Nanotechnology and Science Group at the Jet Propulsion Laboratory (JPL); Antonio J. Ricco and Michael A. Butler, senior members of the technical staff in the Microsensor R&D Dept. at Sandia National Laboratories (SNL); Arthur L. Lane, planetary scientist and senior science architect at JPL; Christopher P. McKay, research scientist at NASA Ames Research Center; Aaron P. Zeni, geologist and research scientist, and Richard C. Quinn, associate research scientist, at the Search for Extraterrestrial Intelligence (SETI) Institute and NASA Ames Research Center; Bruce Murray, professor of planetary science and geology at the California Institute of Technology; Harold P. Klein, scientist-in-residence at Santa Clara University and research scientist at SETI; Gilbert V. Levin, president of Biospherics; Robert W. Terhune (retired), member of the technical staff at JPL; Margie L. Homer, member of the technical staff in the Semiconductor Sensor Technology Group at JPL; Alexander Ksendzov, member of the technical staff at the Center for Space Microelectronics at JPL; and Phillip Niedermann, former postdoctoral associate at JPL, currently at the Swiss Federal Polytechnic Institute. Address correspondence to Ricco at SNL, Microsensor R&D Dept., Albuquerque, NM 87185-1425.



The 34th Annual Eastern Analytical Symposium (EAS) will be held at the Garden State Convention and Exhibit Center in Somerset, NJ, Nov. 12–17. The meeting is sponsored by the Division of Analytical Chemistry and the New York and North Jersey Sections of the American Chemical Society; the American Microchemical Society; the Chromatography Forum of Delaware Valley; the New York Microscopical Society; and the Delaware Valley, New York, and New England Sections of the Society for Applied Spectroscopy.

Fifty-seven oral and nine poster sessions are scheduled from Monday, Nov. 13, through Thursday, Nov. 16. An exposition of scientific instruments and supplies will be open from 9 A.M. to 5 P.M. Monday through Wednesday, and from 9 A.M. to 2 P.M. Thursday. Approximately 200 exhibit booths are anticipated.

The program will feature symposia honoring this year's award recipients. Royce W. Murray of the University of North Carolina at Chapel Hill, who will receive the EAS Award for Outstanding Achievements in

the Fields of Analytical Chemistry; William G. Fateley of Kansas State University, who will receive the EAS Award for Achievements in Near-Infrared Spectroscopy; James W. Jorgenson of the University of North Carolina at Chapel Hill, who will receive the EAS Award for Achievements in Separation Science; Ad Bax of the National Institutes of Health, who will receive the EAS Award for Achievements in Magnetic Resonance; Peter R. Griffiths of the University of Idaho, who will receive the New York Section, Society for Applied Spectroscopy's Gold Medal Award; and Les Ebdon of the University of Plymouth (U.K.), who will receive the American Microchemical Society's Benedetti-Pichler Award.

Twenty-three EAS-sponsored short courses, eight tutorials, and five seminars are scheduled. ACS will sponsor 17 short courses in conjunction with the meeting (see page 612A). For more information on these ACS short courses, contact ACS Short Courses, ACS, 1155 16th St., NW, Washington, DC 20036 (800-

227-5558 or 202-872-4508; fax 202-872-6336; e-mail hgw97@acs.org).

An employment service bureau will be available from 9 A.M. to 4 P.M. Monday through Wednesday and 9 A.M. to 2 P.M. Thursday.

EAS has reserved rooms for conferees at the Radisson Hotel Somerset (\$105 single/double), Somerset Marriott (\$117 single/double), Holiday Inn Somerset (\$99 single/double), Hampton Inn (\$90 single/double), and Hyatt Regency New Brunswick (\$120 single/double). Complimentary shuttle service will be available. To obtain special rates, rooms must be reserved through EAS.

For additional information about registration, EAS short courses, workshops, housing, and the employment service, contact EAS, P.O. Box 633, Montchanin, DE 19710-0633 (302-738-6218; fax 302-738-5275; Internet www.eas.org/~easweb). On-site registration hours are 3 P.M. to 5 P.M. Saturday, 8 A.M. to 5 P.M. Sunday through Wednesday, 8 A.M. to 2 P.M. Thursday, and 8 A.M. to 10 A.M. Friday.

Program

Monday morning

Chemometrics
 Process near-IR spectroscopy
 Solid-phase microextraction: A new technique for a broad range of applications
 Matrix effects in ICP atomic spectroscopy
 50 years of IR spectroscopy
 GC: Ramping up to new challenges
 Analytes in biological fluids—A multifaceted approach
 Improvements in LC techniques and hardware
 Hot topics in atomic spectroscopy
 Developments in environmental analysis

Monday afternoon

Noninvasive bioanalysis
 The Eastern Analytical Symposium Award for Achievements in Near-Infrared Spectroscopy—Honoring William G. Fateley
 Optimization of capillary GC methods
 Laboratory automation—Sample preparation to data management
 50 years of Raman spectroscopy
 Advances in atomic spectroscopy
 Solid-state NMR: New methods for studying catalysis

Tuesday morning

The Eastern Analytical Symposium Award for Achievements in Separation Science—Honoring James W. Jorgenson
 Near-IR in pharmaceuticals
 NMR in biomolecules

Process spectroscopy
 Imaging for conservation
 50 years of atomic absorption
 Alternatives to solvent extraction in the environmental lab
 GC techniques and equipment: Solutions to your problems
 Lighting the way: Spectroscopy in the mid-90s
 Innovation in the analytical sciences

Tuesday afternoon

CE: Affinity interactions and optimization
 On-line and process near-IR
 The Eastern Analytical Symposium Award for Achievements in Magnetic Resonance—Honoring Ad Bax
 New horizons in forensic DNA analysis
 Microanalysis for conservation
 Maximization of HPLC selectivity
 50 years of emission spectroscopy

Wednesday morning

HPLC of pharmaceuticals
 Near-IR spectroscopy: Sublime solutions to tricky problems
 Protein analysis and characterization
 The Eastern Analytical Symposium Award for Outstanding Achievements in the Fields of Analytical Chemistry—Honoring Royce W. Murray
 Analytical microscopy
 50 years of NMR spectroscopy
 IR spectroscopy: Solutions to intriguing problems
 Near-IR spectroscopy: Providing answers for diverse problems
 MS: Mighty answers from little fragments grow
 NMR: Providing a continuing supply of answers

Wednesday afternoon

Chiral separations
 Near-IR spectroscopy in natural products
 Qualitative characterization of drug metabolites and related compounds using LC/MS
 The USP and the emergence of ICH
 The New York Section of the Society for Applied Spectroscopy Gold Medal Award—Honoring Peter R. Griffiths
 Sensors that work
 NMR of synthetic and naturally occurring compounds

Thursday morning

Frontiers in DNA sequencing
 Chemometrics: Numerical models turn hills into mountains
 LC/MS in the pharmaceutical industry
 The American Microchemical Society Benedetti-Pichler Memorial Award—Honoring Les Ebdon
 Electrochemistry: Increasing the potential
 Capillary electrophoresis: Problems and answers
 Clever developments in environmental analysis
 The industry-academe interface

Thursday afternoon

LC: Novel answers and novel solutions
 Immunoassays
 Near-IR spectroscopy: Practical solutions for process applications
 Impurities in pharmaceuticals
 Analysis of flavors and fragrances
 Electrochemistry and the environment
 Sample preparation and pharmaceutical analysis

ACS Short Courses

Troubleshooting and Maintaining Gas Chromatographs with and without Spectrometers

Nov. 13. John Q. Walker and Bert Gordon

Basic GC

Nov. 13-14. Harold McNair

Environmental Data Validation

Nov. 13-14. William Purves

Practical Electroanalysis

Nov. 13-14. Larry Taylor

Winning at Chemometrics

Nov. 13-14. Steven Brown and Barry Lavine

Validation of Chromatography Data Systems

Nov. 14. Glenn I. Ouchi

Analytical Inductively Coupled Plasma Emission and MS

Nov. 14-15. Howard E. Taylor

Interpretation of IR Spectra

Nov. 14-16. Howard Sloane

Laboratory Data Management Using a Personal Computer

Nov. 15. Glenn I. Ouchi

Laboratory Information Management Systems: From Problem Definition to System Evaluation

Nov. 15. Gerst Gibbon and Joseph Golden

Chemical Engineering and Process

Fundamentals for Chemists

Nov. 15-17. Richard Griskey

Laboratory Safety and Health

Nov. 16. David Van Horn and Roger Conrad

Analytical Methods for Proteins

Nov. 16-17. Robert Copeland

Fundamentals of HPLC

Nov. 16-17. Lee Polite

Interpretation of Mass Spectra

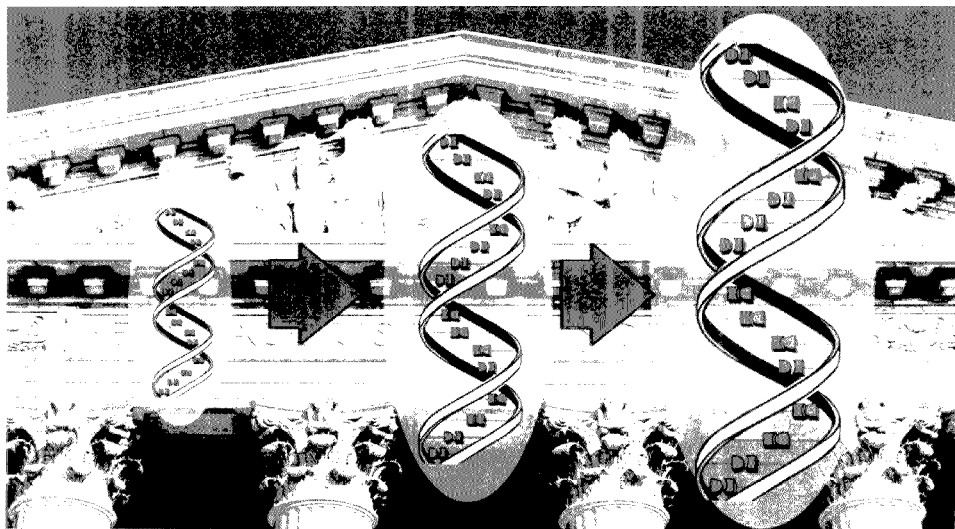
Nov. 16-17. J. Throck Watson and O. David Sparkman

Organic Chemistry of Drug Design and Drug Action

Nov. 16-17. Richard Silverman

Technical Writing Workshop

Nov. 16-17. Ann Eisenberg



FORENSIC PCR

Primed, Amplified, and Ready for Court

Since its introduction by Nobel laureate Kary Mullis in the early 1980s, the polymerase chain reaction (PCR) has gained a strong following in DNA analysis research as a rapid way to detect very small amounts of specific DNA sequences. Current applications include identification of cancer-associated genes, viral subtyping for AIDS and hepatitis, bacterial drug susceptibility research, and the determination of genetic disorders. In the past five years, PCR has become reliable enough to introduce into the precarious waters of the U.S. criminal justice system for forensic human identification and paternity testing.

DNA typing methods were first approved for inclusion in court evidence in 1988. They have since been featured in more than 150 trials and have given rise to several official and semiofficial guidelines for laboratory protocols and interpretation. These include a 1992 report by the National Research Council of the Na-

Standardized protocols make this DNA typing method robust enough for criminal investigations

tional Academy of Sciences that was being updated at press time and an ongoing practice standards development effort by the FBI-sponsored Technical Working Group for DNA Analysis Methods (TWGDAM). Currently, at least 13 contract laboratories perform DNA assays for criminal cases in the United States.

The PCR assays used for forensic work are for the most part simplified commercial tests that are complementary to the

more common restriction fragment-length polymorphism (RFLP) assay. But they have gained enough prominence in court cases such as the O. J. Simpson trial that the National Institute of Justice recently commissioned the National Institute of Standards and Technology (NIST) to develop a standard reference material (SRM) for forensic PCR proficiency testing. As new PCR techniques come into play, the 20-component SRM kit should be useful for validating them and determining whether they can be used for forensic work.

PCR primer

PCR uses sequence-specific oligonucleotide probes called "primers" that are designed to bind specifically with a single target gene or short DNA fragment in a sample and initiate enzyme-mediated replication (known as "amplification") of that fragment. Several cycles of amplification are performed in the same vial so that

enough copies of the desired sequence are reproduced for analysis. First, sample DNA is heated in a vial to $\sim 90^\circ\text{C}$ to separate the strands. The primers, free nucleotides, and a heat-stable DNA polymerase are present in the vial as the temperature is lowered to $\sim 70^\circ\text{C}$. At this temperature, the primers attach to the sample DNA sequences that match them. The primers contain a sequence that signals the polymerase to begin replicating DNA at that location.

If the primers don't match any of the DNA in the sample, nothing happens, but if they do match, the polymerase starts to copy the matching portion of the DNA strand. As the next temperature cycle begins, the DNA is heated and the newly synthesized strands separate from the original strands. The enzymes start the copying process all over again, doubling the number of DNA copies with each pass. After ~ 30 cycles, the desired DNA fragment may be multiplied more than 1 million-fold.

The method is especially useful for detecting very low concentrations of a DNA sequence. For instance, fewer than five original copies of a telltale bacterial DNA fragment for Lyme disease can be detected by PCR in the blood of patients, although the bacterium itself usually sequesters in the tissues and can be impossible to detect in blood by standard culture methods.

In the technique's early years, PCR's high sensitivity was actually a mixed blessing. The method was so sensitive that very low levels of contaminating DNA from other samples or from the user's hands could be amplified and produce a false signal. At the time, the standard laboratory precautions for DNA work weren't stringent enough to control contamination; some researchers recommended extreme isolation protocols, including dedicated clean rooms and separate air vents, to prevent these problems. By the late 1980s, though, robust commercial thermocyclers (programmable-temperature heating blocks for the samples) and variations on the basic PCR reagent protocol were introduced to eliminate some of the problems and make PCR a routine method for DNA analysis.

Once the sample DNA has been amplified (or not, if there are no matches to the

probes or if something went wrong with the assay), its molecular weight or sequence can be determined for DNA typing by standard gel electrophoresis or by capillary electrophoresis. A simpler way to type PCR-amplified DNA is the "reverse dot blot" method: A set of DNA probes for different sequence variants in the amplified region is immobilized in discrete dots on a membrane (commercial kits include prepared membranes dotted with a standard set of probes for the locus along with dots for control probes). The membrane is incubated with a solution of the amplified sample DNA and washed. Positive matches between the sample DNA and one or more of the immobilized probes are detected through an enzymatic color generation scheme similar to those used for immunoassays.

PCR, which is used to amplify short fragments, can be performed on degraded DNA.

Human variations

PCR can identify small base-sequence or length variations that may occur in specific regions or "loci" of human DNA. Some of these loci contain sequences that are "polymorphic," or highly variable among individuals. Because everyone inherits two copies of each gene from their parents, the varied combinations of two such sequences per locus increase the chances that a match will identify individuals in a population. PCR formats for forensic human identification, most of them commercial reverse dot blot kits, use one primer that binds to the generic portion of a polymorphic locus for amplification as well as sets of more sequence-specific probes for subtyping the polymorphic portion of the amplified DNA.

Dennis Reeder, NIST group leader for DNA technologies, and members of his laboratory developed the SRM kit for RFLP analysis in 1992. This summer, they

introduced the new SRM kit for PCR. (See *Anal. Chem.* **1994**, *66*, 3303-17 and **1995**, *67*, 1220-31.)

When PCR was first attempted for human identification, says Reeder, many forensic laboratories used a variety of loci that made population frequency studies and interlaboratory comparisons, the two keys for validation and test interpretation, almost impossible. Since that time, TWGDAM, the NRC, and other consensus groups have identified several loci with high variation in the population and provided guidelines for performing PCR for human identification. These groups continue to standardize protocols for forensic PCR as new loci are discovered.

Commercial standardization has been simplified by the fact that Roche Molecular Laboratories owns the patent for PCR and licenses it to other companies for limited clinical, forensic, and research product development. The three most common commercial kits are one for the D1S80 locus, one for the human leukocyte antigen (HLA) DQ α locus, and a polymerase kit that has amplification and identification probe sets for each of five different loci. Jenifer Lindsey, unit chief of the central FBI DNA laboratory in Washington, DC, says the FBI and most of the forensic contract laboratories use these kits for their standard methods.

The reverse dot blot is the method used most commonly in forensic PCR applications such as human identification and paternity testing, because with it DNA typing takes only a few hours. Lindsey explains that by comparison RFLP analysis, which measures the characteristic lengths of larger variable-length regions of DNA by gel electrophoretic fragment sizing, can take several weeks if autoradiography is used to visualize the separated DNA bands.

RFLP analysis requires large intact pieces of DNA, but PCR, which identifies sequence or length variations in short fragments, can be performed successfully on degraded samples. PCR also requires much less sample for identification, perhaps only 1-2 ng of DNA as opposed to the 25-50 ng of total DNA that must be extracted from a sample for RFLP analysis, says Reeder.

However, RFLP analysis can identify an individual more conclusively using fewer

loci than are needed for PCR typing. "Because PCR is a discrete system," Reeder says, "the numbers aren't quite as powerful." Forensic scientists start by trying to exclude suspects from the pool of likely matches with crime scene evidence. "Most courts require a four- or five-probe match for RFLP analysis as evidence of inclusion [i.e., that a suspect is one of the likely matches]. You need 9 or 10 matches for PCR-based systems to get the kind of specificity that you get with a five-probe match for RFLP," says Reeder. Although this sounds like a daunting number of analyses per sample, Lindsey notes that "with PCR, you only need one difference in the results to exclude a suspect. On the other hand, there's no test to date for perfect identity. The number of loci that have to match to identify someone positively is still under debate."

She adds that the choice of method isn't a simple issue of PCR versus RFLP. "I look at both methods as tools. Because we have both methods in our lab, I can let a [forensic sample] stain dictate which method I use." For large blood or semen stains containing DNA in good condition, RFLP analysis is preferable, but PCR is the method of choice for typing the minuscule amounts of DNA from cells present in the saliva residue left on cigarette butts and postage stamps. Some labs use all PCR, Lindsey says, because most standard RFLP analysis methods use ³²P-labeled probes for autoradiography, and not all labs are licensed to use radioactive materials. However, nonradioactive labels are being developed commercially. "We're hoping to bring chemiluminescence detection on line by the end of the year."

Although sophisticated PCR methods are fast developing in research applications, Lindsey says that the FBI methods are developed for simplicity and robustness so that results are reliable for a vast number of different samples and can be repeated without large errors in different laboratories.

Developing the standards kit

The NIST SRM kit for forensic PCR will likely be used to validate a laboratory's ability to participate in the proficiency testing required for it to receive federal funds from the FBI. Designed to troubleshoot

PCR for human identification and paternity testing, the kit is quite complex for a NIST SRM, but Reeder says it contains enough varied materials to determine whether there's a problem with a laboratory's PCR protocols for human identification and, if so, to identify which step is at fault. The kit is certified for D1S80 DNA typing and includes genomic DNA extracted from the white blood cells of eight people who were selected for the maximum amount of inter-individual genetic variation for that locus.

D1S80 polymorphisms vary by fragment length (similar to RFLPs, but much shorter) and are determined by gel electrophoresis rather than by reverse dot blot. The standardized allelic ladder for this locus contains a mix of fragments that are 14-41 repeat units long; the 8 human

NIST plans to examine "problem" DNA that contains stems, loops, and other hard-to-sequence structures.

reference materials in the kit contain alleles (inherited variants) for the D1S80 locus that range from 17 to 37 repeat units in length. Some of the 8 genotypes are homozygous (i.e., the alleles from both parents are the same length), giving rise to results such as "18, 18" and producing a single band on the gel. Others, which are heterozygous, produce a 2-band pattern (e.g., "18, 24"); some are common and some are rare, and the kit contains genomic DNA stocks of both male and female origin.

In addition, one male and one female human cell line, together with aliquots of extracted DNA and PCR-amplified DNA derived from them, are included in the kit for troubleshooting the different steps in the PCR protocol for D1S80. "For example," Reeder says, "if the extracted DNA SRM gives you results but you don't get

anything when you try to extract DNA from the cell line samples in your lab, you know that your amplification is okay but your extraction protocol isn't working." The PCR-amplified SRMs can be run on a gel for comparison with the laboratory's amplification of the extracted DNA from the kit or with laboratory-extracted and amplified DNA from the cell lines.

Future methods

The eight genomic DNA standards have enough variety to accommodate other DNA typing assays such as HLA DQ α typing, polymarker typing, or amylgenin gender determination, Reeder says, and should make it possible to adapt the kit to new PCR methods as they become available without having to find and add new genomic DNAs from the population.

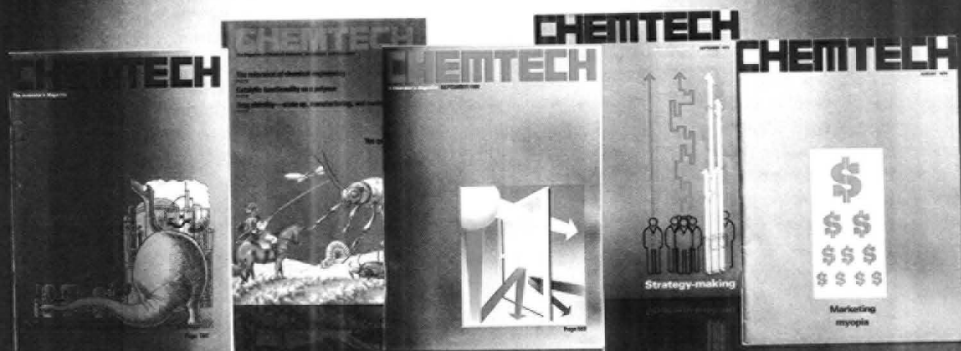
New methods under consideration for forensic use include short tandem repeat PCR, which identifies base-length variations as short as two to four repeat segments and may be useful for analyzing highly degraded DNA. Another possibility, says Reeder, is the identification of human remains through PCR amplification and DNA sequencing of mitochondrial DNA, which is inherited only through the maternal side. "In accidents where the remains aren't easily identifiable," he says, "the identity could be verified by comparing mitochondrial DNA with that of siblings or maternal relatives of the deceased." Other plans for the NIST laboratory include the examination of "problem" DNA that contains stems, loops, and other structural or sequence characteristics that make it difficult to perform PCR and DNA sequencing.

Lindsey says the FBI plans to bring CODIS (Combined DNA Index System), a national DNA typing database based on RFLP loci, on line at the national level this fall; the system also allows PCR typing results to be maintained. It consists of databases of typed DNA from unsolved crimes and from criminals convicted of rape or murder, the two crimes that most commonly require DNA typing. That system, together with a newly mandated DNA advisory committee that will set laboratory proficiency standards for the FBI, should expand the standardization and case-solving power of DNA typing in the U.S. forensic community. *Deborah Noble*

CHEMTECH

CELEBRATES ITS **25**TH YEAR!

SPECIAL SILVER ANNIVERSARY RATE FOR NEW SUBSCRIBERS ONLY!



For 25 years, CHEMTECH has reached into research labs and executive board rooms to pull out the ideas, insights, and briefings that have helped chemistry professionals manage the advances in their industry and careers. Now with new departments, a faster-reading format, and a timely new focus, CHEMTECH is the source that provides you with the new technology that fosters innovation.

And now in honor of our 25th year, CHEMTECH is offering new subscribers a 25% discount on their first year's subscription. It's like getting three issues FREE! Simply fill in and mail the coupon below, or call toll-free 1-800-333-9511. This is a limited time offer, so order your subscription today!

1995 CHEMTECH SUBSCRIPTION ORDER FORM

NEW SUBSCRIPTIONS ONLY!

YES! Please sign me up for a one-year CHEMTECH subscription at the special Silver Anniversary rate of (please check one):

	U.S.		Canada & Mexico		Europe*		All Other Countries*	
ACS Members	<input type="checkbox"/> \$ 42	\$ 31.50	<input type="checkbox"/> \$ 32	\$ 41.50	<input type="checkbox"/> \$ 59	\$ 48.50	<input type="checkbox"/> \$ 64	\$ 53.50
Nonmember Personal	<input type="checkbox"/> \$ 85	\$ 63.75	<input type="checkbox"/> \$ 95	\$ 73.75	<input type="checkbox"/> \$102	\$ 80.75	<input type="checkbox"/> \$107	\$ 85.75
Nonmember Institutional	<input type="checkbox"/> \$395	\$296.25	<input type="checkbox"/> \$495	\$306.25	<input type="checkbox"/> \$412	\$313.25	<input type="checkbox"/> \$417	\$318.25

*Includes Air Service

- Check enclosed (payable to American Chemical Society).
 Bill Me. Bill Company.
 Charge My:
 VISA MasterCard
 American Express

SHIP TO:

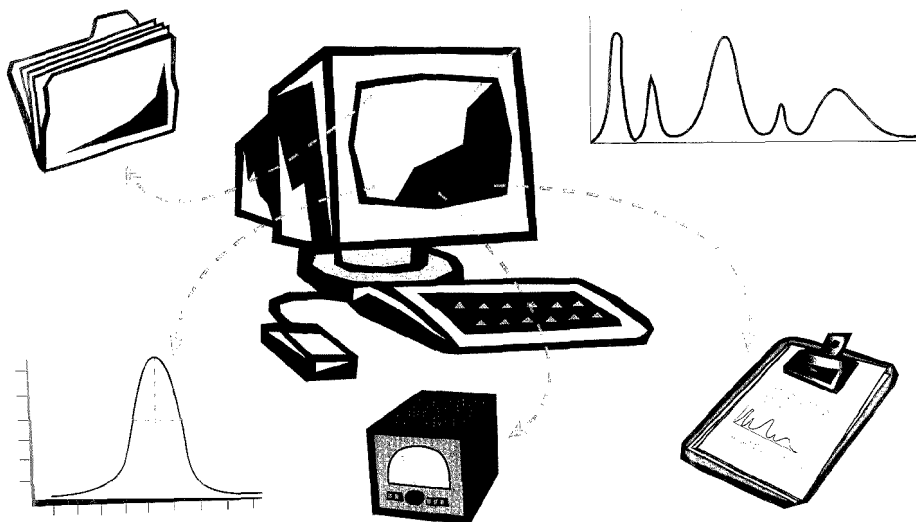
Name _____
 Title _____
 Address _____
 Home Work
 City _____ State _____ ZIP _____

Acct. No. _____
 Exp. Date _____
 Signature _____

For faster service call 1-800-333-9511 (U.S.) or 614-447-3776. Offer expires December 31, 1995. CHEMTECH is published monthly by the American Chemical Society. Subscription starts when order is received.
 6500/12/0770/95

0770J

OFFER EXPIRES 12/31/95



Chromatography Data Systems

For many instruments, it is now almost unthinkable to operate without computer-mediated control and data acquisition. This is particularly true for HPLC and GC, where "good laboratory practice" (GLP) documentation has become a commonplace requirement. Whether it's the vendor's dedicated station or your own PC, a data system for chromatography has five basic functions: instrument control, data acquisition, data analysis, method and data archiving, and reporting. According to some chromatographers, chromatography system hardware is now so modular and variable that the computer interface becomes the "real" instrument in the user's mind.

However, automation and computer power have not made LC and GC systems foolproof, say Andrew Papas of Polaroid and John Elling of Los Alamos National Laboratory. Both researchers say users can benefit from knowing how these systems interact with the chromatograph and what the problem areas are. We asked them for their comments on current trends in chromatography instrument control, data acquisition, and analysis, and

their advice for potential buyers. Table 1, though not intended to be comprehensive, lists characteristics of several major chromatography data stations manufactured in the United States. For more information on these products, fill out the reader service card or send e-mail to acprodrev@acs.org with a keyword from the table in the subject heading. Additional vendors are listed in the 1996 *Analytical Chemistry* LabGuide that was published August 15.

Instrument control

Although they still retain their on-board microprocessors and keypads, most chromatographs are now controlled through dedicated PC-based data stations or

a user's PC equipped with appropriate control and analysis software. "Manufacturers are realizing that most users prefer to control their instruments through software," says Elling. "We may see them pulling the onboard computer out of the next generation of chromatographs, which would bring down expenses." However, the keypad is still valuable as a manual control path (e.g., for override of software commands) and can be used to extend the instrument's compatibility with other systems.

To use your own PC, says Papas, you need to buy the appropriate software and an interface board that contains an analog-to-digital converter (ADC) chip. PCs can be loaded with third-party data analysis software for special applications or for collating data from several brands of instruments. Third-party GC and GC/MS data-processing software also is available on UNIX-based engineering workstations. These tend to be ~ 2 orders of magnitude faster than PCs, have better data storage, are generally easier to back up and archive, and are more powerful for data processing and instrument multitasking, says Elling.

Product Review

Many of the vendors' data stations are also designed to control several instruments simultaneously, with one window or channel for each instrument method and its data. Most are multitasking and can collect data in the background. In these cases, says Papas, "assuming the software is bug-free, if one instrument crashes, it shouldn't affect the other runs." Multi-instrument control allows a single point of communication with a laboratory information management system (LIMS). However, no vendor's data station will let you control another vendor's chromatograph completely, except perhaps for the HP 5890. It may be possible to control two ven-

dors' chromatographs from your own PC by putting both interface boards in your computer, says Elling, but the setup may not be very efficient, and the two may not operate simultaneously.

One area of control that has not been fully developed is that of feedback for warnings and errors. "You need a system that can identify errors smartly," says Papas. "A message that just says 'error' without telling you where or what it is doesn't do you much good." Elling agrees, noting that most chromatographs have very few diagnostic sensors and failsafe controls compared with other types of analytical instruments.

"GCs especially are very undersensored," he says. "If you load up an autosampler for an overnight run, there's no automatic [system] shutdown if the chromatograph fails. Sensors for the carrier gas flow or, in LC, for the solvent reservoir, could help prevent instrument damage." Some data systems do halt injection of the next sample if there's a problem and several smaller companies supply these kinds of sensors and diagnostic software for retrofitting.

In addition, Elling says, "it would be nice if you could get some kind of automated logic for method validation in the software so that if your parameter settings conflict

Table 1. Summary of representative products

Product	Chrom-Card	ChemStation	Turbochrom
Company	Fisons 55 Cherry Hill Drive Beverly, MA 01915 508-524-1000	Hewlett-Packard P. O. Box 9000 San Fernando, CA 91341 800-227-9770	PE Nelson 3833 N. 1st St. San Jose, CA 95134 408-577-2200
Price	\$4400 and up	\$4000 and up	\$4000-\$15,000
Methods	GC	LC, GC, GC/MS, CE	LC, GC, CE; optional GPC and simulated distillation
Hardware	ADC card with software; network version available	Data station; license available for running software on user's PC; network version available	DEC PC or user PC; network version available
Operating system	DOS, Windows	DOS, Windows, Windows for Workgroups	Windows, Windows for Workgroups, Windows 95
Control			
Max. no. of instruments	4	4	8
Max. channels/instrument	4	2	2
Cross-compatibility	Data acquisition with other analog GC systems	ADC interface option with event controls and remote start and stop for other analog GC systems	Digital chromatographs via digital controllers; HP 5890; other analog detectors through ADC interface
Data acquisition			
ADCs	20-bit solid-state with 0-1 V input	24-bit, 2-channel	20-bit, 2-channel; optional ADC validation module
Diode array module	N	Y	Y
MS module	N	Y	N
Heartout/2D	N	Y for LC and GC	Y for GC
Integration			
Peak calculation	Area, height	Area, height	Area, height; automated integration parameter sensing
Calibration	Averaged, linear, or nonlinear	Automatic recalibration: point-to-point, linear, quadratic, cubic, exponential, logarithmic, and average response	Point-to-point, linear, quadratic, cubic; weighting and scaling factors
Manual reintegration	Y; can save reintegrated peaks	Y; can save integrated peaks with method	Y; can save integrated peaks
AIA/netCDF data format	INA	Y	Y
Special features	Report; publisher; password access; chromatogram overlay; control of autosampler parameters	ChemStore results database for control charting; data analysis-only version optional	Externally buffered interface design; automatic data transfer to LIMS
RSN	401	402	403
E-mail reflector keyword	ac SEP622	ac SEP623	ac SEP624

Y = Available N = Not available INA = Information not available at press time

with the type of inlet or column you've specified, the software gives you a warning."

Data acquisition

Acquiring data from the instrument requires an interface that combines analog-to-digital conversion of the detector signal with some form of noise filtering. What type of ADC and filtering capabilities to look for depends on what separation method the instrument performs. For example, characteristic peak widths for GC are generally narrower and the baseline tends to be noisier than for HPLC; there's less latitude for filtering the noise out in GC without filtering out peaks as well. But

as laboratories move toward using narrowbore and microbore columns for LC, Papas says, the LC peaks, and therefore the requirements for data acquisition and noise filtering, are beginning to resemble those for capillary GC.

In general, the more bits for the ADC, the higher the voltage resolution. The minimum required for accurate results is 16 bits, Papas says. However, he adds, "At a certain point, you're wasting time distinguishing between 1.0000 and 1.00001 V. I haven't seen anything greater than a 24-bit ADC in regular use."

A rule of thumb for how many data points you need to collect overall is ~ 20

points per peak. "Above 200 points per peak," Papas says, "you end up with significant noise and need to filter the signal." For example, a 16-bit discrete ADC samples very frequently, 100-1000 data points in ~ 10 ms, and provides a lot of data per peak, but it also catches most of the voltage spikes and requires data smoothing algorithms such as boxcar or Savitzky-Golay filtering. "Now [with narrower columns] as the peaks become narrower in time, you can't filter as long as you want," Papas remarks. "A lot of LC manufacturers have gone to 18-20-bit integrating ADCs." These ADCs integrate a peak over ~ 10 ms, which allows the voltage spikes to average out and requires less data smoothing.

"For LC," he says, "it's more difficult to get a true specification for ADC performance. An integrating ADC may collect 2000 points/s, but using an on-board digital filter reduces that effectively to 200 points/s, and picking peak widths reduces it still further." Mass spectral detection further complicates the data acquisition picture, he says. "There's a lot of 'specmanship' between the manufacturers with regard to how many amu/s their systems achieve, which is related to the ADC sampling rate."

Special software may be needed to accommodate data from diode array detectors, hyphenated techniques, or multidimensional chromatography. LC/IR and GC/IR interfaces demand different types of data acquisition packages than standard LC and GC, as do GC/MS and LC/MS. These methods require more than one data channel for acquisition or, in the case of LC/IR, do not have real-time continuous interfaces. Heartcutting for multidimensional chromatography requires valve control between the two columns, and a data station may not handle the data from two detectors without the addition of a second ADC and/or interface. MS detection may require up to four additional data channels if, for example, you want to plot the UV chromatogram alongside the total ion chromatogram.

Peak interpretation

PCs and workstations have advanced enough that a separate integrator is often redundant, especially when statistical analysis, GLP documentation, or reintegration must be performed on a regular basis. Newer systems can also provide more sophisticated algorithms for peak interpretation when the data are nonideal, and some now have automatic routines to

PC1000	Star	Millenium
Thermo Separation Products 355 River Oaks Pkwy. San Jose, CA 95134 800-532-4752	Varian Chromatography Systems 2700 Mitchell Drive Walnut Creek, CA 94598 415-242-6880	Waters 34 Maple St. Milford, MA 01757 800-252-4752
\$2500-\$6500	\$2800 and up	\$5000 and up
LC, CE, tablet dissolution-LC, analog GC and IC	LC, GC	LC, GC, LC/MS, CE, IC, GPC/viscometry
User PC	Data station, ADC card with software for running on user PC	Data station, Client server network for Novell, VAX, Alpha
OS/2 Warp	Windows	Windows
4	4	4
3 (2 analog)	2	4
Analog interface for data acquisition, some method archiving for LC or GC	ADC interface available for analog instruments	HP 5890
20-bit, 2 channel interface	21-bit, 2-channel with 10-V voltage reference	24-bit, 2-channel per interface, -0.250 V to +2.25 V
Y	Y	Y
N	N	Y
N	N	N
Area, height	Area, height, or square root of height	Sensitive for smaller peaks; auto- optimized integration parameters
Linear, quadratic, exponential, power fits; weighting and scaling factors	Automated multilevel; linear, quadratic, or cubic curves	Automated, multilevel; exponential, linear, point-to-point
Y via graphical commands or timed events; saves inte- grated peaks	Y	Y; can save results and methods
Y	Y	Y
Interactive system suitability check; tablet dissolution LC	Database, AuroLink to external applications, system suitability, simulated distillation, hydrocarbon analysis	Built-in relational database; audit trail; report publisher; runs 3rd- party applications
404	405	406
ac SEP625	ac SEP626	ac SEP627

optimize the integration parameters for a chromatogram.

Accurate peak integration depends largely on how the software interprets the baseline. "If you have baseline-resolved peaks," Papas says, "any system will integrate them correctly. If you have baseline shifts or overlapped peaks, however, no system has full intuition. They all still rely on first- and second-derivative algorithms for baseline interpretation. The refinements to the standard algorithms affect how the data system reacts in contingency situations."

To test the performance of a peak integration program, he suggests applying the software to standard chromatographic methods and cross-checking samples you usually run in your lab. "Skewness and tailing peaks are a good test for differentiating some of these algorithms. You want to see what the system's automatic response to these peaks will be. A lot of systems will calculate skewness values as well as the k' and α values."

Automated baseline placement carries a degree of built-in error. "You can stand back and interpret the baseline by eye," Papas says. "The algorithms may not agree with you, but you can override the automatic baseline and peak-picking functions using timed event parameters."

Elling notes that the standard peak selection and integration algorithms used in some of the major data systems stem from early "cut-and-weigh" strip chart recorder methods that are still part of some Environmental Protection Agency (EPA) protocols. In many cases, the algorithms haven't been updated in the primary vendor software because environmental monitoring laboratories are still required to use these methods. "More accurate methods have been developed in the past few years," Elling says; several software packages from third-party vendors offer newer peak deconvolution algorithms for determining areas of peaks that aren't baseline resolved.

One of the new sticking points of data archiving, Papas says, is whether you can save your data as manually integrated peaks using a selected method or whether you must store your data raw and reintegrate them every time you open the file. "It used to be that you could save the chromatogram as raw data in the file and save the integrated data with the baseline markers you used as another part of the file," he says. "Now you can't always save the integrated data, so if you integrated the peaks manually, this reintegration won't

be stored. Then when you pull up the stored raw data, the program will incorrectly reintegrate it for you using the manufacturer's most current method."

Cross-compatibility

Cross-compatibility is a thorny issue, say Elling and Papas. None of the manufacturers make data stations that will readily talk to most other vendors' instruments, but a few third-party data systems are starting to offer multivendor compatibility for data acquisition and processing.

"Data station software is difficult to use in general," Elling adds. "It's based on the manufacturer's vision of how its instrument works, which may not be your idea of how the instrument works. For instance, where do you think detector attenuation information belongs—with the detector, with the data file, or somewhere else? Different vendors have different ways of dealing with these issues and that can make it very hard to switch from one vendor's software to another's."

The manufacturer's vision of how its chromatography system works may not be yours.

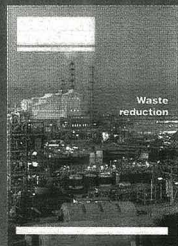
A little in-lab ingenuity makes it possible to use the more familiar data station to collect data from other vendors' instruments, Elling notes, but not always to control them or to archive method information with the data. "If you just want to get the data from a run, you can jury-rig the data system you like best to work with the hardware you like best, but it can be really dangerous to collect the data without the method parameters. You can't do this for regulatory work." Another way around this impasse is to do hyphenated techniques using commercial instrument "packages" designed for the task. According to Papas, an LC/MS system from one vendor may well have software that is licensed to control a liquid chromatograph from another vendor in a coordinated fashion with its own mass spectrometer and interface hardware. These systems store the MS data with the LC run conditions, thereby satisfying GLP requirements.

Few vendors show consistency between their own software packages for LC, GC, LC/MS, and GC/MS, Papas notes, although some vendors are moving toward creating a uniform interface for these four methods. "Some of the GC/MS software is still operating in a DOS platform only, so it can't be run simultaneously with other method software that operates under a graphical user interface." Rewriting these software packages, which were originally produced by separate groups within each company, will be difficult and expensive but necessary, Papas says.

Each vendor also has a proprietary data format that may be updated periodically with or without the company notifying its customers of every change; to use advanced statistical analysis packages from third-party vendors, the data files must be converted from the primary vendor's format to the new one. The Analytical Instrument Association (AIA) recently established a standard chromatography data file format (known as AIA or netCDF) that contains the chromatogram, time stamp, operator stamp, and the method file. It has been tested for interconversion between several major vendors' data systems, but in general the vendors have been slow to adopt it, Elling says. "At present, several manufacturers' systems allow you to convert your data to netCDF format, but none of them allow you to save directly to netCDF as a native file format."

Papas and Elling both see chromatography data systems, and the instrument systems themselves, moving away from formats that users can tailor to their own preferences and toward simplified and standardized integrated designs where more of the choices are preset. "Many of these vendors are developing their own LIMS packages, and we'll be seeing a closer connection between the workstations and their LIMS," says Elling. "That should benefit a lot of labs, because more than 50% of the cost of sample processing these days comes from processing the data. If I were setting up a routine lab now, I would go with only one brand of chromatograph—it's not so important which one, but I would want to be able to set up all my instruments and calibrate them as quickly and efficiently as possible. On the other hand, the manufacturers aren't really providing enough flexibility and cross-compatibility to satisfy many of the users, or there wouldn't be so many third-party products out there to help users mix and match instruments and software." *Deborah Noble*

Analyze worldwide chemical solutions with **Chemistry & Industry.**



Through a special arrangement with the Society of Chemical Industry in London, the American Chemical Society proudly presents in North America: **Chemistry & Industry**. From breaking news and research to key opinions worldwide, **Chemistry & Industry** brings you the science and business of chemistry from the all-important European perspective. Each twice-monthly issue delivers:

News Reports— Complete coverage of current international news in applied chemistry and the chemical industry.

Feature Articles— Authoritative, in-depth reviews on a wide range of subjects spanning the applied sciences.

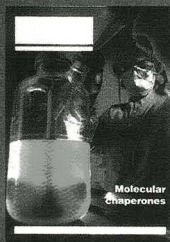
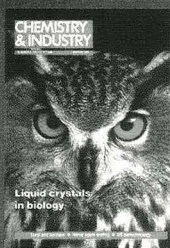
Comment— Thought-provoking opinions from internationally known figures in science and industry.

Legislation— Critical analyses of the public policy changes in the European Community and around the world.

Highlights— Single-source summaries of vital research from primary journals.

Plus, employment opportunities, book reviews, a calendar of upcoming events, and more!

Let **Chemistry & Industry** bring you Europe's wide world of applied chemistry. **Subscribe today!**



Chemistry & Industry Subscription Order Form **YES! I want the European connection. Please start my one-year subscription today.**

1995 One-Year Subscription Rate (please check one).

U.S./Canada/Mexico only ACS Member \$61 Nonmember \$356

Name _____ ACS Member# _____

Address Business Home _____

City _____ State _____ Zip _____

Telephone _____

Please select method of payment:

Check enclosed \$ _____ (payable to American Chemical Society) Bill me Charge my: VISA/MasterCard American Express

Name (please print) _____

Account Number _____ Expiration Date _____

Signature (required on all orders) _____

For subscribers in North America, mail this coupon to:
American Chemical Society, Publication Marketing Department, 1155 Sixteenth Street, NW, Washington, DC 20036

For subscribers in all other countries, contact *Chemistry & Industry*, 15 Belgrave Square, London SW1X 8PS, England.

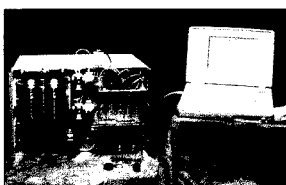
0816L

0900/12/0816L

Immunoanalyzer

KinExA is an automated fluorescence detection instrument designed to perform kinetic exclusion assays for ligand-binding experiments as well as competitive immunoassays, and sandwich-format immunoassays. Kinetic exclusion permits the direct determination of free ligand or antibody in a sample without derivatization and can be used for antibody or biomolecule determinations in serum, milk, and other complex biological matrices.

Polymer beads are used as the solid phase for the kinetic exclusion and other assays. The beads are coated with an antigen or ligand for the antibody or other biomolecule being determined, suspended in buffer, and then flowed into a capillary flow cell, where they are trapped on a screen. Sample is flowed through the cell at a high enough rate that any biomolecule-ligand or antibody-antigen complexes already formed in the sample will not dissociate. Under these conditions, only free biomolecule or antibody binds to the coated particles. Once the sample has passed over the particles, a fluorescence-labeled second antibody or other fluorescent reagent is in-



jected to allow the determination of free analyte in the original sample.

The flow cell is embedded in a lens and backed with a reflector to increase the efficiency of both fluorescence excitation and the collection of fluorescence emission. When used with a conventional epi-illumination filter fluorometer, slightly more than 50% of the fluorescence emitted in the active region of the flow cell reaches the detector. The fluorescence signal is monitored continuously in real time.

The system includes an in-line degasser, and all pumps and valves are electrically actuated and controlled through Windows-based software that allows the user to specify flow sequence, times, and rates. Multiple determinations per sample can be performed automatically. **Sapidyne**

■ 408

INSTRUMENTATION

Radio-HPLC

β -RAM Micro is an in-line radioisotope detector for microbore HPLC. The detector, which is available with a range of counting cells for β -, positron-, and low-energy γ -emitters, accommodates eluent flows of 50–300 μ L/min. Dead volume for a solid-scintillator system is 0.7 μ L and < 4 μ L for a liquid scintillator system. The detector can be connected in line with a mass spectrometer. **IN/US Systems** ■ 407

Laser spectroscopy

Dapromat hybrid apochromatic lenses are designed for applications involving broad-

band light sources, multiwavelength lasers, and tunable lasers. Operating from 480 to 780 nm without the need for refocusing, these lenses combine diffractive and refractive elements to reduce chromatic aberration by a factor of 10 and improve off-axis performance over that of standard achromatic doublet lenses. **Melles Griot** ■ 409

Protein purification

BioSys 500 Series workstations are dedicated chromatography systems for protein purification that operate in isocratic or gradient mode. The systems deliver buffer gradients at up to 30 mL/min and accommodate pressures to 2500 psi. Man-

ual and automatic injection modes are available, and the Model 510 selection valves offer four different buffers per pump. **Beckman** ■ 410

GC

FIDamat 5E is a flame ionization detector for GC designed to measure total hydrocarbon content in air as well as determine corrosive and condensing gases. Applications include monitoring the airborne hydrocarbons produced by smokestacks, waste incinerators, power stations, coating equipment, and automobile exhaust systems. The detector has a dynamic range from < 1 ppm to 99.999 ppm. **Siemens** ■ 411

Spectrophotometry

PELA-1016 0°/45° reflectance spectroscopy accessory is designed for use with the Perkin Elmer Lambda 900 spectrophotometer. It measures reflectance and color parameters in both 0° incident and 45° collection geometries and features a 50-mm Spectralon collection sphere, transfer optics, and both PbS and PMT detectors. The accessory mounts in the sample chassis of the spectrophotometer and is compatible with all system hardware and software. **Labsphere** ■ 412

LITERATURE

ICPMS

Literature describes the UV MicroProbe laser for laser ablation ICPMS. The brochure provides a system overview and application notes on direct analysis of transparent minerals and independence of mineral orientation. Features of the optics, sampling stages, and control software are described. **Fisons** ■ 413

**For more information,
please circle the appropriate
numbers on one of our
Reader Service Cards.**

Food analysis

"Food and Beverage Analysis Guide" contains information on 260 food reference standards, immunoassay kits, and GC and HPLC applications. Techniques for sample preparation such as SPME, SPE, and SFE are also described. The guide suggests appropriate products for use with a list of AOAC methods. **Supeico**

■ 414

TGA for gas mixture interactions

IGA-003 automated gravimetric analyzer is designed to measure the magnitude and kinetic parameters of sorption reactions between the sample and variable-composition mixed gases. Up to four gases can be mixed to specified compositions before introduction to the analyzer. Methods for this analyzer include measurement of multicomponent isotherms, temperature-programmed oxidation and reduction assays, and catalyst characterization.

An internal gas feed introduces the gas mixture into the sample reactor just below the sample, and a diffuser ring at the inlet homogenizes the gas. Flow rates range from 100 to 1000 mL/min, and automated thermal ramping can be performed at rates of 0.1–20 °C/min at temperatures to 1000 °C. A separate purge stream can be used to protect the microbalance from corrosive gases, and gas streams can be humidified to study water sorption in vacuum-labile materials.

High flow rates can be used to reduce the depleted zone at the sample surface so that the sample is exposed to a constant gas or vapor composition. For measurement of multicomponent isotherms (e.g. for gas separation processes), the pressure in the system is changed at constant flow rate and then regulated during mass relaxation to the new equilibrium conditions.

The analyzer controller can also be programmed to switch between single

Petroleum analysis

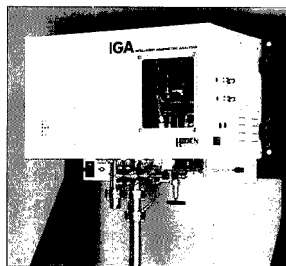
Brochure describes the Reformulyzer GC system, which is designed for the analysis of reformulated gasolines. The system determines paraffins, isoparaffins, olefins, naphthenes, and aromatic compounds in FCC gasoline, finished gasoline, naphthas, and other intermediates. It can also be used to determine oxygenates.

AC Analytical Controls ■ 415

or multicomponent gas streams either at predefined times or on completion of a particular reaction. This feature permits the study of catalytic reactions or cyclic behavior to characterize sample regenerability. The IGA-003 can also be interfaced with a mass spectrometer to perform TGA/MS of species generated by gas desorption or decomposition.

The controlling software operates in three interface modes. The interactive chart mode logs parameters such as weight, pressure, temperatures, flow rate, and gas composition and displays them as a function of time. The isothermal mapper determines multicomponent isotherms at specified gas compositions and flow rates and provides real-time analysis of the mass relaxation to derive adsorption rates of gas components. The automatic event sequencer is designed for protocol setup and recall. **Hidden Analytical**

■ 416

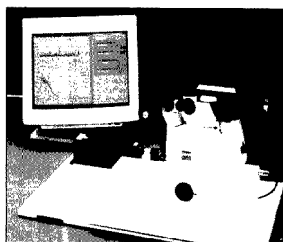


Confocal fluorescence correlation spectroscopy

ConfoCor fluorescence spectrometer uses confocal laser optics to observe molecular diffusion, concentration, and reaction or binding kinetics of analytes in very small volumes by fluorescence correlation spectroscopy. The sensitivity of the method permits rapid determination of these properties for molecules in a single cell or viral particle and increases with decreased analyte concentration. Complexation reactions such as antibody or ligand binding or nucleic acid hybridization can be observed in solution.

The spectrometer's confocal optics focus a laser into a volume of ~ 1 fL (about the volume of an *E. coli* cell). The laser excites fluorescence in the molecules present, and the fluorescence is conducted by confocal optics to a single-photon detector. If the sample concentration is < 1 µmol/L, only a few molecules will occupy the observation region at a time.

The fewer molecules in the region, the larger the signal fluctuation whenever individual molecules move in or out. Complexation of the analyte molecules with a ligand or antibody changes the diffusion parameters for the analyte. The system includes dedicated correlation software for calculating diffusion and kinetic parameters as well as analyte concentration. **Carl Zeiss** ■ 417



THERMAL ANALYSIS IN POLYMER CHARACTERIZATION

THE RENOWNED FACULTY: EDITH A. TURI, COURSE DIRECTOR,
RESEARCH PROFESSOR, POLYTECHNIC UNIVERSITY

HARVEY E. BAIR, TECHNICAL STAFF, AT&T BELL LABS

RICHARD P. CHARTOFF, PROFESSOR OF MATERIALS ENGINEERING,
UNIVERSITY OF DAYTON

Learn the basic principles of thermal techniques

Understand the characteristics of commercial instruments: learn their applicability to your needs

Learn the systematic application of thermal analysis to a broad range of polymers

Learn ways to enhance polymer performance

Learn how to optimize experimental conditions and interpret thermal data obtained by different techniques

Optimize processes and quality control methods

Learn how to increase your direct input in achieving marketing objectives

Eliminate expensive trial-and-error experiments by cost-efficient, speedy, small-scale thermal analysis

Enhance your capability to conduct experiments targeted to improving quality and increasing productivity

Discuss with leading experts your specific questions such as problem solving, troubleshooting, and operation safety

Please send me more information on the new ACS Short Course, *Thermal Analysis in Polymer Characterization*, to be held October 23-24, 1995, in Washington, DC.

NAME _____

TITLE _____

ORGANIZATION _____

ADDRESS _____

CITY, STATE, ZIP _____

BUSINESS PHONE _____ FAX _____



If this research succeeds, you'll be the next to know

But only if you subscribe to the *Journal of Medicinal Chemistry*! As the leading journal covering drug design and development, it's your best source for up-to-the-minute news about original research, early findings, and critical evaluations.

As a subscriber, you'll gain valuable access to landmark studies exploring the relationship between molecular structure and biological activity. And, cutting-edge information on drug design and allied activities will help you increase your research scope and efficiency. The *Journal of Medicinal Chemistry* spotlights the most significant primary research in the world today, and gives you new information with unprecedented speed!

Be the next in line for critical information.

Subscribe to the *Journal of Medicinal Chemistry* today!

Call Toll-Free 1-800-333-9511

ACS PUBLICATIONS
Essential Resources for the Chemical Sciences

American Chemical Society
1155 Sixteenth Street, N.W.
Washington, DC 20036

Laboratory Service Center

LABORATORY SERVICE CENTER

(Equipment, Materials, Services, Instruments for Leasing). Maximum space — 4 inches per advertisement. Column width, 2-3/16"; two column width, 4-9/16". Artwork accepted. No combination of directory rates with ROP advertising. Rates based on number of inches used within 12 months from first date of first insertion. Per inch: 1" — \$200; 12" — \$195; 24" — \$190; 36" — \$185; 48" — \$180.

ANALYTICAL CHEMISTRY

1599 Post Road East
P.O. Box 231
Westport, CT 06881
203-256-8211/FAX: 203-256-8175

Adenosine-5-Triphosphate, DiNa • 3-Aminophthalhydrazide • Benzanilide
Benzoic Anhydride • Bromosulfophthalein • 2,4-Diaminophenol DIHCl
Diphenylcarbazine • Fructose • Glutaric Acid • p-Hydroxybenzaldehyde
3-(p-Hydroxyphenyl)propionic Acid • Iminodiacetic Acid, Na Salt
Malonic Acid • 2-Mercaptobenzimidazole • 4-(p-Nitrobenzyl)pyridine
Orcinol • Phenylurea • Pimelic Acid • Sodium Diethyldithiocarbamate
Sodium Pyruvate • Sodium Tetraphenylboron • SPADNS • Succinic Acid
Succinimide • Sulfosalicylic Acid • Triphenyltetrazolium Chloride

Write for our Products List of over 3,000 chemicals

Tel: 516-273-0900 • TOLL FREE: 800-645-5566 Telefax: 516-273-0858 • Telex: 497-4275

EASTERN CHEMICAL

ADMIRAL SPECIALTY PRODUCTS, INC.

P.O. Box 18050

DEPT. AC

HAUPPAUGE, N.Y. 11788

FREE DATA, FAST

To quickly amass data on all of the products you need, consult the Lab Data Service Selection on our *Analytical Chemistry* reader reply card insert.

Index to Advertisers

CIRCLE INQUIRY NO.	ADVERTISERS	PAGE NO.
10, 11	* EG&G Princeton Applied Research	610A
9	Finnigan MAT, Inc. Communications West	574A
1	Fluka Chemie AG Tachezy, Klieger & Partner	571A
7	JEOL USA, Inc.	OBC
2	Macherey-Nagel GmbH & Co. KG MP Design Werbeagentur	580A
3	Metrom Ltd. Ecknauer + Schoch Werbeagentur ASW	584A
6	* Perkin-Elmer Corporation VBG	589A
8	Scott Specialty Gases, Inc. Becker/Jani, Inc.	599A
4	* Shimadzu Scientific Instruments, Inc. West & Brady, Inc.	IFC
5	John Wiley & Sons, Inc.	581A

Directory section, page 625A.
*See ad in 1996 LabGuide Edition.

Advertising Management for the American Chemical Society Publications

CENTCOM, LTD.

President

James A. Byrne

Executive Vice President

Benjamin W. Jones

Joseph P. Stenza, Production Director

Laurence J. Doyle, Director of Marketing

1599 Post Road East

P.O. Box 231

Westport, Connecticut 06881-0231

(Area Code 203) 256-8211

Fax No. 203-256-8175

DIRECTOR, ADVERTISING SALES, LABORATORY PRODUCTS
Bruce E. Poorman

ADVERTISING PRODUCTION MANAGER
Jane F. Gatenby

SALES REPRESENTATIVES

Philadelphia, PA . . . CENTCOM, LTD., The Meadows, 485 Devon Park Drive, Suite 106, Wayne, PA 19087. Telephone: 610-964-8061, FAX: 610-964-807

New York/New Jersey . . . Dean A. Baldwin, John F. Rafferty, CENTCOM, LTD., Schoolhouse Plaza, 720 King Georges Post Road, Fords, NJ 08863. Telephone: 908-738-8200, FAX: 908-738-6128

Westport, CT/Boston, MA . . . Dean A. Baldwin, Michael J. Pak, CENTCOM, LTD., 1599 Post Road East, P.O. Box 231, Westport, CT 06881-0231. Telephone: 203-256-8211, FAX: 203-256-8175

Cleveland, OH . . . Bruce E. Poorman, Dean A. Baldwin, CENTCOM, LTD., 19035 Old Detroit Road, Suite 203, Rocky River, OH 44116. Telephone: 216-331-5151, FAX: 216-331-3432

Chicago, IL . . . Michael J. Pak, CENTCOM, LTD., 540 Frontage Rd., Northfield, IL 60093. Telephone: 708-441-6383, FAX: 708-441-6382

Houston, TX/Atlanta, GA . . . Edward M. Black, CENTCOM, LTD., P.O. Box 820966, Houston, TX 77082-0966. Telephone: 713-493-1560, FAX: 713-493-6673

West Coast . . . Bob LaPointe, CENTCOM, LTD., Suite 808, 2672 Bayshore Parkway, Mountain View, CA 94043-1010. Telephone: 415-969-4604, FAX: 415-969-2104

Denver, CO . . . Bob LaPointe, CENTCOM, LTD., Suite 808, 2672 Bayshore Parkway, Mountain View, CA 94043-1010. Telephone: 415-969-4604, FAX: 415-969-2104

United Kingdom, Scandinavia and Europe (Except: Germany, Switzerland, Austria, France, Italy, Spain) . . . Malcolm Thiele, Technomedia Ltd., Wood Cottage, Shurlock Row, Reading RG10 0QE, Berkshire, England. Telephone: 1734-343-302, FAX: 1734-343-848

Germany, Switzerland, Austria . . . IMP InterMediaPartners, GmbH, Deutscher Ring 40, 42327 Wuppertal, Germany. Telephone: (0202) 711091, FAX: (0202) 712431

France . . . Gerard Lecoqeur, Aidmedia, 31-33 Grand rue de Saint-Rambert, 69009 Lyon, France. Telephone: 78-64-20-37, FAX: 78-83-56-67

Italy, Spain . . . Tess Serranti, Serranti Communications, 43 Van Sant Road, New Hope, PA 18938. Telephone: 610-598-0668, FAX: 610-598-0670

Hong Kong . . . SEAVEX, LIMITED, 503 Wilson House, 19 Wyndham Street, Central, Hong Kong. Telephone: 858-2010, FAX: 810-1283

Japan . . . Shigeyuki Yasui, Intercommunications (Japan), Inc. 2F Ginza EtwaBldg. 8-18-7 Ginza, Chuo-ku, Tokyo 104, Japan. Telephone: (03) 5565-0861, FAX: (03) 5565-0860.

Korea . . . DooBee International Limited, Center Building (Byulgwang), 1-11 Jeong-dong, Choong-ku C.P.O. Box 4557, Seoul, Korea. Telephone: 822-776-2096, FAX: 822-755-9860

Singapore . . . SEAVEX, LIMITED, 400 Orchard Road, #10-01 Orchard Towers, Singapore 0923. Telephone: 734-9790, FAX: 732-5129

Taiwan . . . Epoch Limited, 2F No. 3, Lane 52, Nanking East Road, Section 4, P.O. Box 1642, Taipei, Taiwan, R.O.C. Telephone: 577-5441, FAX: 578-4308

South America . . . Bruce E. Poorman, CENTCOM, LTD., 19035 Old Detroit Road, Suite 203, Rocky River, OH 44116. Telephone: 216-331-5151, FAX: 216-331-3432

ANALYTICAL CHEMISTRY Information Express

Get the product data you need fast...

By Phone: Use the reference list below, and contact the companies to fill an immediate need, or...

By Fax: Use the fax form on the opposite page to send a direct written request.

Company	Page	Issue	RSN	Data*	Phone	Fax	Contact
AC Analytical Controls	623 A	10/1/95	415		215-638-7078	215-638-7096	Jim McCormack
AccuStandard	503 A	8/1/95	416	●	800-442-5290	203-786-5287	Matt Bolgar
Analytical Innovations	467 A	8/1/95	6		800-901-8576	513-298-4807	John H. Garratt
J. T. Baker	451 A	8/1/95	7	●	800-582-2537	908-859-9318	William Broad
Bear Instruments	503 A	8/1/95	417		408-773-0462	408-773-0463	Urs Steiner
Beckman Instruments	622 A	10/1/95	410	●	800-742-2345	714-773-8186	Amy Bratcher
Bioanalytical Systems	564 A	9/1/95	408	●	317-403-4572	317-497-1102	Ruth Reanck
Bruker Instruments	498 A, 502 A	8/1/95	401, 411	●	508-667-9580	508-663-9177	Mark Chaykovsky
Bruker Instruments	560 A	9/1/95	401	●	508-667-9580	508-66-3954	Mark Chaykovsky
Carl Zeiss	565 A	9/1/95	415	●	800-356-1090	914-681-7443	Irv Toplin
Carl Zeiss Jena GmbH	623 A	10/1/95	417	●	49-3641-64-2500	49-3641-64-3311	Zeiss Gruppe
Cetac Technologies	502 A	8/1/95	413	●	800-369-2822	402-733-5292	John J. Uhr
Chem Service	538 A	9/1/95	1	●	800-452-9994	610-692-8729	Ron Gray
Comstock	498 A	8/1/95	402	●	615-483-7690	615-481-3884	Susan Zell
EG&G Instruments (Princeton)	475 A	8/1/95	8	●	609-530-1000	609-883-7259	Ruth Reanck
EG&G Instruments (Princeton)	610 A	10/1/95	10, 11	●	609-530-1000	609-883-7259	Ruth Reanck
Finnigan MAT	459 A, 502 A	8/1/95	5, 408	●	408-433-4800	408-433-4823	Gary Spear
Finnigan MAT	498 A	8/1/95	403	●	44-1442-233555	44-1442-233666	Stan Evans
Finnigan MAT	529 A	9/1/95	9	●	408-433-4800	408-433-4823	Gary Spear
Finnigan MAT	574 A	10/1/95	9	●	408-433-4800	408-433-4823	Gary Spear
Finnigan/Tremetrics	565 A	9/1/95	411	●	512-251-1555	512-251-1597	Elaine Moody
Fisons Instruments	499 A	8/1/95	404	●	508-524-1000	508-524-1100	Cathy Schaub
Fisons Instruments	622 A	10/1/95	413	●	508-524-1000	508-524-1100	Cathy Schaub
Fisons Instruments	618 A	10/1/95	401	●	508-524-1000	508-524-1100	Cathy Schaub
Fluka Chemie	509 A	9/1/95	5	●	41-81-7562511	41-81-7565449	
Fluka Chemie	571 A	10/1/95	1	●	41-81-7562511	41-81-7565449	
Galileo Electro-Optics	503 A	8/1/95	418	●	508-347-9191	508-347-3849	Laune Placolla
Hammatsu	487 A	8/1/95	none	●	800-524-0504	508-231-1216	Robert Wisner
Hamilton	IFC	8/1/95	9	●	800-648-5950	702-856-7259	B. Milne/R. Beavers
Hamilton	OBC	9/1/95	8	●	800-648-5950	702-856-7259	B. Milne/R. Beavers
Hewlett-Packard	499 A	8/1/95	415	●	415-857-5603	415-857-8228	Doug Forsyth
Hewlett-Packard	618 A	10/1/95	402	●	415-857-5603	415-857-8228	Doug Forsyth
Hidden Analytical	623 A	10/1/95	416	●	44-1925-445225	44-1925-416518	Ian D. Neale
Hinds Instruments	564 A	9/1/95	410	●	503-690-2000	503-690-3000	Teri Oakberg
Hi-Tech Scientific	564 A	9/1/95	409	●	44-722-323643	44-722-412153	David Mitchell
INUS Systems	622 A	10/1/95	407	●	800-875-4687	813-620-3708	John Hinzil
Isoo	502 A	8/1/95	412	●	402-464-0231	402-464-0318	Gary Barken
Jeol USA	OBC	8/1/95	10	●	508-535-5900	508-536-2205	Brian Musselman
Jeol USA	561 A	9/1/95	402	●	508-535-5900	508-536-2205	Robert D.Pasquale
Jeol USA Inc.	OBC	10/1/95	7	●	508-535-5900	508-536-2205	Brian Musselman
John Wiley & Sons	561 A	10/1/95	5	●	212-850-6137	212-850-6264	S. Nelson
K&M Electronics	475 A	8/1/95	2	●	413-781-1350	413-737-0608	Rick Brightini
Labsphere	622 A	10/1/95	412	●	603-927-4266	603-927-4694	John A. Beaulieu
Macherey-Nagel	580 A	10/1/95	2	●	(02421) 969-0	(02421) 969-199	
McPherson	502 A	8/1/95	411	●	800-255-1055	508-263-1458	Christi Schoeffel
Melles Griot	622 A	10/1/95	409	●	800-835-2626	714-261-7589	Lynn Strickland
Metrohm	454 A	8/1/95	1	●	41-071-538-585	41-071-538-9041	R. Steiner
Metrohm	512 A	9/1/95	2	●	41-071-538-585	41-071-538-9041	R. Steiner
Metrohm	584 A	10/1/95	3	●	41-071-538-5	41-071538-90	R. Steiner
Mettler-Toledo	565 A	9/1/95	412	●	800-638-8537	609-426-0121	Al Beronio
Molecular Dynamics	564 A	9/1/95	407	●	800-333-5703	408-773-1493	Jim Bull
PE Nelson	618 A	10/1/95	403	●	408-577-2200	408-894-9307	Alycia Cornez-Frank
Perkin-Elmer	OBC	9/15/95	none	●	203-761-2574	203-762-6000	Mary Cooke-Kager
Perkin-Elmer	IBC	9/15/95	none	●	415-570-6667	415-638-6199	Valerie Tucker
Perkin-Elmer	502 A	8/1/95	410	●	203-761-2574	203-762-6000	Carol Blaszczynski
Perkin-Elmer	589 A	10/1/95	6	●	415-570-6667	415-638-6199	Valerie Tucker
PerSeptive Biosystems	499 A	8/1/95	406	●	800-899-5858	808-383-7885	Charles Cuneo
Photometrics	564 A	9/1/95	405	●	602-889-9933	602-573-1944	Michelle Downs
Quadrex Corporation	503 A	8/1/95	414	●	800-275-7033	203-993-0391	John Lipsky
Spigdyne Instruments	622 A	10/1/95	408	●	208-345-7677	208-392-4985	Steve Lackie
Scott Specialty Gases	IFC	9/1/95	7	●	215-766-8861	215-766-0320	Donna M. Vito
Scott Specialty Gases	599 A	10/1/95	8	●	215-766-8861	215-766-0320	Donna M. Vito
Shandon Lipshaw	565 A	9/1/95	413	●	800-547-7429	412-768-1138	Beverly Miller
Shimadzu Scientific Instruments	499 A	8/1/95	407	●	800-477-1227	410-381-1222	Roger Greathead
Shimadzu Scientific Instruments	IFC	9/15/95	none	●	800-477-1227	410-381-1222	Roger Greathead
Shimadzu Scientific Instruments	IFC	10/1/95	4	●	81-3-3219-5641	81-3-3219-5710	Y. Kawabe
Siemens Industrial Automation	622 A	10/1/95	411	●	404-740-3931	404-740-3998	Herbert Stuhler
Supelco	623 A	10/1/95	414	●	800-247-6628	800-447-3044	Michael Gray
Teledyne Electronic Technologies	521 A	9/1/95	3	●	415-962-6526	415-967-4353	Sharon Gomez
Thermo Separation Products	619 A	10/1/95	404	●	800-532-4752	408-526-9810	Brent Davis
Topac Scientific Instruments	565 A	9/1/95	414	●	617-740-8778	617-740-8778	Antoni Dryobanski
Upchurch Scientific	503 A	6/1/95	415	●	800-426-0191	800-359-3460	Amy King
Varian Associates	561 A	9/1/95	403, 404	●	415-424-6786	415-858-0480	Carl Hadjis
Varian Associates	619 A	10/1/95	405	●	415-242-6880	510-945-2335	Deborah Kohnstamm
Varian Instruments	564 A	9/1/95	406	●	800-729-4447	815-729-3700	Steve Klingler
Waters	619 A	10/1/95	406	●	800-252-4752	508-482-2674	Tony Lewtas

Data+ Column: A bullet indicates that additional product and company information is available in the 1995 Analytical Chemistry LabGuide Edition.

RSN: Reader Service Number

PRODUCT DATA SERVICE

ANALYTICAL CHEMISTRY

VALID THROUGH FEBRUARY 1996

OCTOBER 1, 1995

Please circle the appropriate Reader Service Numbers to receive additional information.

Please help us determine your future laboratory buying trends. Which of the following products do you use, buy, specify, recommend or purchase? Circle all appropriate numbers on the attached reply card.

- 327 AA Spectroscopy
- 328 Analytical Services
- 329 Baths/Circulators
- 330 Biotechnology
- 331 Books/Periodicals
- 332 Centrifugation
- 333 Chemicals/Gases/Solvents
- 334 Computers/Software
- 335 Cooling/Freezing/Refrig.
- 336 Databases, Online
- 337 Densitometry
- 338 Detectors
- 339 Dryers/Evaporators
- 340 Electrochemistry
- 341 Elemental Analysis
- 342 Filtration
- 343 Flow Meters/Regulators
- 344 FT-IR Spectroscopy
- 345 Furnaces/Ovens
- 346 Gas Chromatography
- 347 General Lab Equipment
- 348 Heating/Temperature
- 349 Ion Chromatography
- 350 Lab Furniture/Hoods
- 351 Labware/Apparatus
- 352 Lasers/Fiber Optics
- 353 Liquid Chrom./HPLC
- 354 Mass Spectrometry
- 355 Microscopy
- 356 Capillary Electrophoresis
- 357 Mix/Stir/Blend/Grind
- 358 NMR Spectroscopy
- 359 Particle Size Analysis
- 360 Plasma Spectroscopy
- 361 pH/Ion Meters/Titrators
- 362 Pumping Monitoring
- 363 Recording/Integrating
- 364 Robotics/Automation
- 365 Sampling/Dispensing
- 366 Supercritical Fluid Chrom.
- 367 Spectrofluorometry
- 368 Still/Purification
- 369 Surface Analysis
- 370 Thermal Analysis
- 371 Thin Layer Chrom.
- 372 UV-Vis Spectroscopy
- 373 Valves/Tubes/Fittings
- 374 Viscometry
- 375 Water/Moisture Analysis
- 376 Weighing/Balances
- 377 X-Ray Diffraction
- 378 X-Ray Spectroscopy

1	2	3	4	5	6	7	8	9	10	11	12	13	14	15	16	17	
18	19	20	21	22	23	24	25	26	27	28	29	30	31	32	33	34	
35	36	37	38	39	40	41	42	43	44	45	46	47	48	49	50	51	
52	53	54	55	56	57	58	59	60	61	62	63	64	65	66	67	68	
69	70	71	72	73	74	75	76	77	78	79	80	81	82	83	84	85	
86	87	88	89	90	91	92	93	94	95	96	97	98	99	100	101	102	
103	104	105	106	107	108	109	110	111	112	113	114	115	116	117	118	119	
120	121	122	123	124	125	126	127	128	129	130	131	132	133	134	135	136	
137	138	139	140	141	142	143	144	145	146	147	148	149	150	151	152	153	
154	155	156	157	158	159	160	161	162	163	164	165	166	167	168	169	170	
171	172	173	174	175	176	177	178	179	180	181	182	183	184	185	186	187	
188	189	190	191	192	193	194	195	196	197	198	199	200	201	202	203	204	
PRODUCT DATA SERVICE				327	328	329	330	331	332	333	334	335	336	337	338	339	340
341	342	343	344	345	346	347	348	349	350	351	352	353	354	355	356	357	
358	359	360	361	362	363	364	365	366	367	368	369	370	371	372	373	374	
375	376	377	378														
NEW PRODUCTS				401	402	403	405	406	407	408	409	410	411	412	413	414	415
416	417	418	419	420	421	422	423	424	425	426	427	428	429	430	431	432	
433	434	435	436	437	438	439	440	441	442	443	444	445	446	447	448	449	
450	451	452	453	454	455	456	457	458	459	460	461	462	463	464	465	466	
467	468	469	470	471	472	473	474	475	476								

NAME (PLEASE PRINT) _____
 TITLE _____
 COMPANY _____
 ADDRESS _____ MAIL STOP _____
 CITY _____ STATE ZIP _____
 TELEPHONE _____ FAX _____

A. PRIMARY FIELD OF WORK

- 01 Energy
- 02 Environmental
- 03 Medical/Clinical
- 04 Drug/Toiletries
- 05 Forensic/Narcotic
- 06 Biotechnology
- 07 Metals
- 08 Pulp/Paper/Wood
- 09 Soaps/Cleaners
- 10 Paint/Coating/Inks
- 11 Electrical/Electronic
- 12 Instrument Dev./Design
- 13 Plastic/Polymer/Rubber
- 14 Agriculture/Food/Bev.
- 15 Inorganic Chemicals
- 16 Organic Chemicals

B. MY PRIMARY AREA OF EMPLOYMENT IS:

- | | |
|---|--|
| INDUSTRIAL | COLLEGE/UNIVERSITY |
| 17 <input type="checkbox"/> Research & Development | 22 <input type="checkbox"/> Research & Development |
| 18 <input type="checkbox"/> Quality/Process Control | 23 <input type="checkbox"/> Teaching |
| MEDICAL/HOSPITAL | INDEPENDENT/CONSULTING |
| 19 <input type="checkbox"/> Research & Development | 24 <input type="checkbox"/> Research & Development |
| 20 <input type="checkbox"/> Clinical/Diagnostic | 25 <input type="checkbox"/> Analysis/Testing |
| GOVERNMENT | |
| 21 <input type="checkbox"/> Research & Development | |

C. INTENSITY OF PRODUCT NEED

- 26 Purchasing Immediately 27 Within 3-6 months 28 Within 6-12 months 29 Future project

D. Is this your personal copy of Analytical Chemistry?

- Yes No



FOR FASTEST SERVICE, USE THIS CARD TO FAX YOUR REQUEST DIRECTLY TO THE ADVERTISER.
 PLEASE PHOTOCOPY THIS CARD FOR MULTIPLE USE.

TO: _____
 FROM: _____
 FAX: () _____ DATE: _____

MY NEED IS:

- Immediate
- 6 - 12 Mos.
- 12 + Mos.

I WANT TO KNOW MORE, PLEASE...

- Send Literature
- Have a Salesman Call
- Send Name of Nearest Dealer
- Send Me a Price Quote

Description: _____

Quantity: _____

I saw your... Advertisement Editorial Listing Regarding...
 on page _____ of the (date) _____ issue of AC

NAME: _____
TITLE: _____
COMPANY: _____
MAILSTOP: _____
STREET: _____
CITY: _____ **STATE:** _____ **ZIP:** _____
PHONE: _____ **FAX:** _____

NO POSTAGE
NECESSARY
IF MAILED
IN THE
UNITED STATES



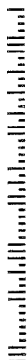
BUSINESS REPLY MAIL

FIRST CLASS MAIL PERMIT NO. 307 PITTSFIELD MA

POSTAGE WILL BE PAID BY ADDRESSEE

**ANALYTICAL
CHEMISTRY**

PO BOX 5511
PITTSFIELD MA 01203-9384



PRODUCT DATA SERVICE

Please help us determine your future laboratory buying trends. Which of the following products do you use, buy, specify, recommend or purchase? Circle all appropriate numbers on the attached reply card.

- 327 AA Spectroscopy
- 328 Analytical Services
- 329 Baths/Circulators
- 330 Biotechnology
- 331 Books/Periodicals
- 332 Centrifugation
- 333 Chemicals/Gases/Solvents
- 334 Computers/Software
- 335 Cooling/Freezing/Refrig.
- 336 Databases, Online
- 337 Densitometry
- 338 Detectors
- 339 Dryers/Evaporators
- 340 Electrochemistry
- 341 Elemental Analysis
- 342 Filtration
- 343 Flow Meters/Regulators
- 344 FT-IR Spectroscopy
- 345 Furnaces/Ovens
- 346 Gas Chromatography
- 347 General Lab Equipment
- 348 Heating/Temperature
- 349 Ion Chromatography
- 350 Lab Furniture/Hoods
- 351 Labware/Apparatus
- 352 Lasers/Fiber Optics
- 353 Liquid Chrom./HPLC
- 354 Mass Spectrometry
- 355 Microscopy
- 356 Capillary Electrophoresis
- 357 Mix/Stir/Blend/Grind
- 358 NMR Spectroscopy
- 359 Particle Size Analysis
- 360 Plasma Spectroscopy
- 361 pH/Ion Meters/Titrators
- 362 Pumping Monitoring
- 363 Recording/Integrating
- 364 Robotics/Automation
- 365 Sampling/Dispensing
- 366 Supercritical Fluid Chrom.
- 367 Spectrofluorometry
- 368 Stills/Purification
- 369 Surface Analysis
- 370 Thermal Analysis
- 371 Thin Layer Chrom.
- 372 UV-Vis Spectroscopy
- 373 Valves/Tubes/Fittings
- 374 Viscometry
- 375 Water/Moisture Analysis
- 376 Weighing/Balances
- 377 X-Ray Diffraction
- 378 X-Ray Spectroscopy



FOR FASTEST SERVICE, USE THIS CARD TO FAX YOUR REQUEST DIRECTLY TO THE ADVERTISER.
PLEASE PHOTOCOPY THIS CARD FOR MULTIPLE USE.

TO: _____
FROM: _____
FAX: (_____) _____ DATE: _____

MY NEED IS:

- Immediate
- 6 - 12 Mos.
- 12 + Mos.

WANT TO KNOW MORE, PLEASE...

- Send Literature
- Have a Salesman Call
- Send Name of Nearest Dealer
- Send Me a Price Quote

Description: _____

Quantity: _____

I saw your... Advertisement Editorial Listing Regarding...
on page _____ of the (date) _____ issue of AC

NAME: _____
 TITLE: _____
 COMPANY: _____
 MAILS' OP: _____
 STREET: _____
 CITY: _____ STATE: _____ ZIP: _____
 PHONE: _____ FAX: _____

ACCELERATED ARTICLES

- E. Neil Lewis,* Patrick J. Treado,
Robert C. Reeder, Gloria M. Story,
Anthony E. Dowrey,
Curtis Marcott, and Ira W. Levin*
- 3377** Fourier Transform Spectroscopic Imaging Using an Infrared Focal-Plane Array Detector
- Stéphane Arbault, Paul Pantano,
Jeffrey A. Jankowski,
Monique Vuillaume,* and
Christian Amatore**
- 3382** Monitoring an Oxidative Stress Mechanism at a Single Human Fibroblast
- Hao Zhang and William Davison**
- 3391** Performance Characteristics of Diffusion Gradients in Thin Films for the in Situ Measurement of Trace Metals in Aqueous Solution
- Ulla G. Sidelmann, Claire Gavaghan,
Howard A. J. Carless,
R. Duncan Farrant, John C. Lindon,
Ian D. Wilson, and
Jeremy K. Nicholson**
- 3401** Identification of the Positional Isomers of 2-Fluorobenzoic Acid 1-O-Acyl Glucuronide by Directly Coupled HPLC-NMR

ARTICLES

- Danhua Chen, Marie D. Peterson,
Robert L. Brumley, Jr.,
Michael C. Giddings, Eric C. Buxton,
Michael Westphall, Lloyd Smith, and
Lloyd M. Smith**
- 3405** Side Excitation of Fluorescence in Ultrathin Slab Gel Electrophoresis
- Michael V. Gorshkov* and
Richard T. Kouzes*
- 3412** Data Reflection Algorithm for Spectral Enhancement in Fourier Transform ICR and NMR Spectroscopies
- Aaron T. Timperman,
Kurt E. Oldenburg, and
Jonathan V. Sweedler**
- 3421** Native Fluorescence Detection and Spectral Differentiation of Peptides Containing Tryptophan and Tyrosine in Capillary Electrophoresis
- Daryl C. Williams and
Steven A. Soper**
- 3427** Ultrasensitive Near-IR Fluorescence Detection for Capillary Gel Electrophoresis and DNA Sequencing Applications
- Shi Bai, Ronald J. Pugmire,*
Charles L. Mayne, and
David M. Grant**
- 3433** ¹³C NMR Determination of Protonated and Nonprotonated Carbons in Model Compounds, Mixtures, and Coal-Derived Liquid Samples

- F. Y. Ren, S. W. Waite, and J. M. Harris** **3441** Temperature-Jump Investigation of Adsorption/Desorption Kinetics at Methylated Silica/Solution Interfaces
- Alvin W. Moore, Jr. and James W. Jorgenson** **3448** Rapid Comprehensive Two-Dimensional Separations of Peptides via RPLC—Optically Gated Capillary Zone Electrophoresis
- Alvin W. Moore, Jr. and James W. Jorgenson** **3456** Comprehensive Three-Dimensional Separation of Peptides Using Size Exclusion Chromatography/Reversed Phase Liquid Chromatography/Optically Gated Capillary Zone Electrophoresis
- Alvin W. Moore, Jr. and James W. Jorgenson** **3464** Resolution of Cis and Trans Isomers of Peptides Containing Proline Using Capillary Zone Electrophoresis
- James A. Laramée, Peter C. H. Eichinger, Paul Mazurkiewicz, and Max L. Deinzer** **3476** Analysis of Organophosphate Pesticides by a Trochoidal Electron Monochromator Mass Spectrometer System
- Yan-Hui Liu, Jian Bai, Xiaoli Liang, David M. Lubman,* and Patrick J. Venta* **3482** Use of a Nitrocellulose Film Substrate in Matrix-Assisted Laser Desorption/Ionization Mass Spectrometry for DNA Mapping and Screening
- Zhendong Wang,* Merv Fingas, Michael Landriault, Lise Sigouin, and Nanni Xu* **3491** Identification of Alkylbenzenes and Direct Determination of BTEX and (BTEX + C₃-Benzenes) in Oils by GC/MS
- Martin Kohler and Julie A. Leary** **3501** LC/MS/MS of Carbohydrates with Postcolumn Addition of Metal Chlorides Using a Triaxial Electrospray Probe
- Randy M. Whittall, Monica M. Palcic, Ole Hindsgaul, and Liang Li** **3509** Direct Analysis of Enzymatic Reactions of Oligosaccharides in Human Serum Using Matrix-Assisted Laser Desorption Ionization Mass Spectrometry
- Qing Tang, A. Kamel Harraia, and Cheng S. Lee** **3515** Capillary Isoelectric Focusing-Electrospray Mass Spectrometry for Protein Analysis
- Toshio Ohara, Akimasa Shibukawa,* and Terumichi Nakagawa* **3520** Capillary Electrophoresis/Frontal Analysis for Microanalysis of Enantioselective Protein Binding of a Basic Drug
- Mathai Mammen, Frank A. Gomez, and George M. Whitesides** **3526** ■ Determination of the Binding of Ligands Containing the N-2,4-Dinitrophenyl Group to Bivalent Monoclonal Rat Anti-DNP Antibody Using Affinity Capillary Electrophoresis
- Frank Cheng-Yu Wang,* Bruce B. Gerhart, and Patrick B. Smith* **3536** Structure Determination of Polymeric Materials by Pyrolysis Gas Chromatography
- Kristen J. Hansen, Brian N. Hansen, Eric Cravens, and Robert E. Sievers** **3541** Supercritical Fluid Extraction-Gas Chromatographic Analysis of Organic Compounds in Atmospheric Aerosols
- Hanlan Liu, Shaowei Ong, Louis Glunz, and Charles Pidgeon** **3550** Predicting Drug–Membrane Interactions by HPLC: Structural Requirements of Chromatographic Surfaces
- Maria Pesavento* and Raffaella Biesuz* **3558** Simultaneous Determination of Total and Free Metal Ion Concentration in Solution by Sorption on Iminodiacetate Resin

- Zhi Qiang Feng, Takamasa Sagara,* and Katsumi Niki** **3564** Application of Potential-Modulated UV-Visible Reflectance Spectroscopy to Electron Transfer Rate Measurements for Adsorbed Species on Electrode Surfaces
- Iyh-Myng Zen* and Mu-Iye Chung* **3571** Square-Wave Voltammetric Stripping Analysis of Mercury(II) at a Poly(4-vinylpyridine)/Gold Film Electrode
- Gunther Wittstock, Kejia Yu, H. Brian Halsall, T. H. Ridgway, and William R. Heineman** **3578** Imaging of Immobilized Antibody Layers with Scanning Electrochemical Microscopy
- Wilbur B. Nowall and Werner G. Kuhr** **3583** Electrocatalytic Surface for the Oxidation of NADH and Other Anionic Molecules of Biological Significance
- Andrey Bratov, Nataliya Abramova, Javier Muñoz, Carlos Dominguez,* Salvador Alegret, and Jordi Bartroli* **3589** Photocurable Polymer Matrices for Potassium-Sensitive Ion-Selective Electrode Membranes
- Jian-Ge Chen and Stephen G. Weber** **3596** Detection of Bioactive Oligopeptides after Microbore HPLC with Electrochemical Detection of Their Cu(II) Complexes: Effect of Operating Parameters on Sensitivity and Selectivity

TECHNICAL NOTES

- David J. Prichard, Hywel Morgan, and Jonathan M. Cooper** **3605** Patterning and Regeneration of Surfaces with Antibodies
- Hans C. Ehrsson,* Inger B. Wallin, Anita S. Andersson, and Per Olof Edlund* **3608** Cisplatin, Transplatin, and Their Hydrated Complexes: Separation and Identification Using Porous Graphitic Carbon and Electrospray Ionization Mass Spectrometry

■ Supporting information for this paper is available separately (consult a current masthead page for ordering information). Supporting information is available to subscribers electronically via the Internet at <http://pubs.acs.org> (WWW) and pubs.acs.org (Gopher). All supporting information except for structure factor tables will also appear following the paper in the microfilm edition of the journal.

* In papers with more than one author, the asterisk indicates the name of the author to whom inquiries about the paper should be addressed.

*Accelerated Articles**Anal. Chem.* 1995, 67, 3377–3381**Fourier Transform Spectroscopic Imaging Using an Infrared Focal-Plane Array Detector****E. Neil Lewis,^{*†} Patrick J. Treado,[‡] Robert C. Reeder,[§] Gloria M. Story,[§] Anthony E. Dowrey,[§] Curtis Marcott,[§] and Ira W. Levin[†]***Laboratory of Chemical Physics, National Institute of Diabetes and Digestive and Kidney Diseases, National Institutes of Health, Bethesda, Maryland 20892, Department of Chemistry, University of Pittsburgh, Pittsburgh, Pennsylvania 15260, and The Procter and Gamble Company, Miami Valley Laboratories, Cincinnati, Ohio 45253-8707*

A powerful new mid-infrared spectroscopic chemical imaging technique combining step-scan Fourier transform Michelson interferometry with indium antimonide focal-plane array (FPA) image detection is described. The coupling of an infrared focal-plane array detector to an interferometer provides an instrumental multiplex/multichannel advantage. Specifically, the multiple detector elements enable spectra at all pixels to be collected simultaneously, while the interferometer portion of the system allows all the spectral frequencies to be measured concurrently. With this method of mid-infrared spectroscopic imaging, the fidelity of the generated spectral images is limited only by the number of pixels on the FPA detector, and only several seconds of staring time is required for spectral image acquisition. This novel, high-definition technique represents the future of infrared chemical imaging analysis, a new discipline within the chemical and material sciences, which combines the capability of spectroscopy for molecular analysis with the power of visualization. In particular, chemical imaging is broadly applicable for noninvasive, molecular characterization of heterogeneous materials, since all solid-state materials exhibit chemical nonuniformity that exists either by design or by development during the course of material preparation or fabrication. Imaging, employing Raman and infrared spectroscopy, allows the precise characterization of the chemical composition, domain structure, and chemical architecture of a variety of substances. This information is often crucial to a wide range of activities, extending from the fabrication of new materials to a basic understanding of biological samples. In this study, step-scan imaging principles, instrument design details, and infrared chemical imaging results are presented. Since

the prospect of performing high-resolution and high-definition mid-infrared chemical imaging very rapidly has been achieved with the step-scan approach, the implications for the chemical analysis of materials are many and varied.

The utility of vibrational spectroscopy originates in the wealth of compositional and quantitative information contained in infrared (IR) and Raman spectra. These details are obtained by carefully monitoring the spectral frequency, intensity, and line-width parameters which sensitively reflect a sample's molecular structure and provide specific fingerprints for a given molecular component. In addition, infrared spectroscopy directly provides quantitative information from the application of Beer's law.

A significant extension of conventional vibrational spectroscopy involves the development of imaging approaches that integrate either infrared or Raman spectroscopic methods with microscopic or macroscopic spatial imaging techniques. In this context, chemical imaging represents a new discipline that combines the analytical capabilities of spectroscopy with the ability to visualize the spatial distribution of a sample's constituents. Several fundamental motivations exist for employing vibrational spectroscopy to image materials. First, vibrational spectroscopy generates image contrast that is chemically specific. For example, functional groups can be visualized in complex substances through their intrinsic vibrational spectral signatures.¹ Second, vibrational spectroscopic imaging is almost universally applicable because

^{*} National Institutes of Health.[†] University of Pittsburgh.[§] The Procter and Gamble Co.(1) Harthcock, M. A.; Altin, S. C. *Appl. Spectrosc.* 1988, 42, 449–455.

image contrast is generated without the use of potentially invasive contrast-enhancing agents.²

Vibrational spectroscopic imaging methodologies may employ three general approaches to obtain spatial/spectral information. These techniques rely on (1) scanning, (2) spatial encoding/decoding, and (3) the use of imaging spectrometers in combination with staring optics and multichannel detectors. In particular, Raman imaging methods have been based upon scanning,^{3,4} spatial encoding/decoding,⁵ or tunable filter approaches.⁶⁻¹⁰ Despite the relative inefficiency of the Raman scattering process relative to IR absorption, Raman imaging approaches have found a greater utility primarily due to the availability and moderate cost of high-quality silicon charge-coupled device (CCD) detectors. In general, high-fidelity imaging can most efficiently be performed with multichannel detectors. In contrast, infrared imaging methods for chemical analysis have relied in the past on relatively inefficient scanning methods because sensitive, multichannel infrared cameras have not been available or have been cost prohibitive. Traditionally, infrared imaging has been performed with a conventional transmissive/reflective, raster-scanned infrared microprobe coupled to a rapid-scan Fourier transform infrared spectrometer.¹¹ Since images are constructed by mapping the substance of interest a single pixel at a time, the technique is time consuming and only images of limited fidelity are typically recorded.

Recently, multichannel IR imaging detectors originally developed for military and surveillance applications¹²⁻¹⁴ have become commercially accessible. These infrared focal-plane array (FPA) detectors, or *staring arrays*, can be fabricated from materials that are sensitive from 1 μm to over 20 μm (10 000–500 cm^{-1}) with as many as 1 million (1024 \times 1024) detector elements and readout rates in excess of 16 000 000 pixels/s.

Infrared chemical imaging methods have been devised that employ indium antimonide (InSb) focal-plane array multichannel detection in combination with electronically tunable filters¹⁵ and mechanically tuned spectral filters.¹⁶ While powerful approaches, these specific methods employ imaging spectrometers that function as notch filters in which spectroscopic image information is selected by rejecting the majority of light available. Although chemical image contrast is enhanced by these means, the light levels detected may be low.

Infrared spectroscopy and Raman spectroscopy performed on Fourier transform (FT) Michelson-type interferometers are widely used in chemical analysis.^{17,18} Fourier transform methods benefit significantly by exploiting the Connes, Jacquinot and Fellgett's advantages inherent in interferometer design.¹⁹⁻²³ The Fellgett's multiplex advantage is particularly important in that it contributes a signal-to-noise ratio (S/N) enhancement relative to single spectral channel instruments of $N^{1/2}$, where N is the number of multiplexed resolution elements being monitored across the spectrum. A $N^{1/2}$ S/N enhancement is also realized in dispersive spectrometers that employ multichannel detection where N is the number of detector elements. Experimentally, the multiplex advantage is only achieved with detection systems that are detector-noise limited rather than shot-noise limited.

While original FT spectrometers were constructed as step-scan devices, continuous-scan interferometers are currently the dominant mode of FT technology for routine vibrational spectroscopic analysis. More recently, however, step-scan devices have found a variety of uses in time-resolved, photoacoustic, and two-dimensional FT-IR applications.²⁴⁻³⁰

In this study, we describe an efficient technique for rapidly performing high-fidelity FT-IR imaging spectroscopy using an InSb FPA detector coupled to an IR microscope and a step-scan FT-IR interferometer. The strategy of combining an infrared detector array with an interferometer provides a *multiplex/multichannel* advantage. The multiple detector elements enable spectra from all pixels to be collected simultaneously, while the modulation of infrared radiation by the interferometer allows all the spectral frequencies across the wavelength range to be measured concurrently.³¹ The step-scan imaging approach provides chemically distinct, mid-infrared images and spectra with unprecedented speed and quality. The image fidelity is limited only by the number of pixels contained on the array. For example, we have recorded infrared chemical image data sets containing 16 384 spatially resolved FT-IR spectra at 16- cm^{-1} resolution with data acquisition times of only 12 s. While the spectral resolution was limited to 16 cm^{-1} , in these experiments, due to the complexity of handling large data sets (40 megabytes per experiment), the spectral resolution for each data set is dependent upon the interferometer's mirror displacement, which may be readily extended for the acquisition of higher spectral resolution images.

- (2) Treado, P. J.; Morris, M. D. In *Microscopic and Spectroscopic Imaging of the Chemical State*; Morris, M. D., Ed.; Marcel Dekker: New York, 1993; pp 71-108.
- (3) Delhaye, M.; Dhamelincourt, P. *J. Raman Spectrosc.* **1974**, *3*, 33-43.
- (4) Bowden, M.; Gardner, D. J.; Rice, G.; Gerrard, D. L. *J. Raman Spectrosc.* **1990**, *21*, 37-41.
- (5) Treado, P. J.; Govil, A.; Morris, M. D.; Sternitzke, K. D.; McCreery, R. L. *Appl. Spectrosc.* **1990**, *44*, 1270-1275.
- (6) Batchelder, D. N.; Cheng, C.; Smith, B. J. E. *Makromol. Chem., Makromol. Symp.* **1991**, *46*, 171-173.
- (7) Puppels, G. J.; Grond, M.; Greve, J. *Appl. Spectrosc.* **1993**, *47*, 1256-1267.
- (8) Treado, P. J.; Levin, I. W.; Lewis, E. N. *Appl. Spectrosc.* **1994**, *48*, 607-615.
- (9) Morris, H. R.; Hoyt, C. C.; Treado, P. J. *Appl. Spectrosc.* **1994**, *48*, 857-866.
- (10) Lewis, E. N.; Levin, I. W. *J. Microsc. Soc. Am.* **1995**, *1*, 35-46.
- (11) *Infrared MicroSpectroscopy*; Messerschmidt, R. G.; Harthcock, M. A., Eds.; Marcel Dekker: New York, 1988.
- (12) Bailey, G. C. *Proc. SPIE* **1979**, *197*, 83-88.
- (13) Parrish, W. J.; Blackwell, J.; Paulson, R.; Arnold, H. *Proc. SPIE* **1991**, *1512*, 68-72.
- (14) Forrest, W. J.; Pipher, J. L. *NASA Tech. Memo.* **1986**, 88213, 11-15.
- (15) Treado, P. J.; Levin, I. W.; Lewis, E. N. *Appl. Spectrosc.* **1994**, *48*, 607-615.
- (16) Lewis, E. N.; Levin, I. W. *Appl. Spectrosc.* **1995**, *49*, 672-678.

- (17) Griffiths, P. R.; de Haseth, J. A. *Fourier Transform Infrared Spectrometry*; Wiley-Interscience: New York, 1986.
- (18) *Fourier Transform Raman Spectroscopy*; Chase, D. B.; Rabolt, J. F., Eds.; Academic Press: San Diego, CA, 1994.
- (19) Michelson, A. A. *Philos. Mag.* **1891**, *31* (Ser. 5), 256-259.
- (20) Michelson, A. A. *Philos. Mag.* **1892**, *34* (Ser. 5), 280-299.
- (21) Fellgett, P. *J. Phys. Radium* **1958**, *19*, 187-191.
- (22) Jacquinot, P.; Dufour, J. C. *J. Rech. C.N.R.S.* **1948**, *6*, 91.
- (23) Connes, J.; Connes, P. *J. Opt. Soc. Am.* **1966**, *56*, 896-910.
- (24) Noda, I.; Dowrey, A. E.; Marcott, C. *Appl. Spectrosc.* **1993**, *47*, 1317-1323.
- (25) Gregoriou, V. G.; Chao, J. L.; Toriumi, H.; Marcott, C.; Noda, I.; Palmer, R. A. *SPIE J.* **1991**, *1575*, 209-210.
- (26) Nakano, T.; Yokoyama, T.; Toriumi, H. *Appl. Spectrosc.* **1993**, *47*, 1354-1366.
- (27) Marcott, C.; Dowrey, A. E.; Noda, I. *Anal. Chem.* **1994**, *66*, 1065A-1075A.
- (28) Budevskas, B. O.; Griffiths, P. R. *Anal. Chem.* **1993**, *65*, 2963-2971.
- (29) Dittmar, R. M.; Chao, J. L.; Palmer, R. A. In *Photoacoustic and Photothermal Phenomena*; Bicanic, O., Ed.; Springer: Berlin, 1992; Vol. III, pp 492-496.
- (30) Story, G. M.; Marcott, C.; Noda, I. *SPIE J.* **1993**, *2089*, 242-243.
- (31) Lewis, E. N.; Levin, I. W.; Treado, P. J. U.S. Patent 5,377,003, December 1994.

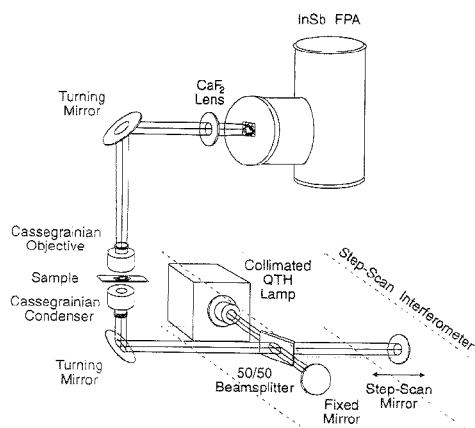


Figure 1. Step-scan infrared imaging system. A commercial FT-IR step-scan interferometer (shown in box) is coupled to an IR microscope. Samples mounted on quartz microscope slides are analyzed in transmission mode. The IR image is collected with a Cassegrainian (reflective) objective. The image is projected to a liquid nitrogen-cooled InSb FPA detector (128×128 pixels) with a CaF_2 image lens. The interferometer timing and image acquisition is controlled externally via a computer (not shown).

EXPERIMENTAL SECTION

Figure 1 is a diagram of the high-definition step-scan FT-IR microscope. The instrument is comprised of a commercially available mid-infrared Michelson-type step-scan interferometer (Bio-Rad FTS-60A) coupled to an IR microscope (Bio-Rad UMA 300A) and incand antimonide focal-plane array detector (ImagIR, Santa Barbara Focalplane). The microscope optics and interferometer electronics were modified to couple efficiently with the InSb camera. Optical modifications included the addition of a CaF_2 50-mm image formation lens placed between the microscope objective and infrared camera. Synchronizing the movement, or stepping, of the interferometer with the camera was performed by the addition of a counter/timer board, which, in conjunction with the computer, controlled the camera frame acquisitions.

The experiment was performed so that each time the interferometer mirror was retarded a TTL pulse was generated by the spectrometer and recorded by the counter/timer board; this in turn triggered the collection of a series of image frames by the infrared camera. Each 12-bit image frame in the series was summed, averaged, and written as a 32-bit floating point file. The final data set therefore consisted of 128×128 floating point images collected at several hundred different interferometer retardations.

InSb detectors are sensitive from 1 to $5.5 \mu\text{m}$ ($5000\text{--}2500 \text{ cm}^{-1}$) using an optical filter placed inside the detector cold shield. Bandpass filtering was performed for two reasons. First, it minimizes the longer wavelength black-body radiation emitted from all the optical surfaces in the instrument, reducing the total signal integrated by the detector not related to source brightness and therefore sample absorption. Second, reduction of the spectral bandwidth of the instrument enables a larger interferometer step size (undersampling) to be chosen between image frames. Undersampling without optical filtering can cause spectral artifacts as a consequence of frequency aliasing. The larger step

size for the experiment provides higher spectral resolution with fewer data points, therefore minimizing the number of images to be collected. This, in turn, reduces the storage and processing requirements for the resulting data set.

The total data acquisition or "staring" time for the camera for each complete data set of 16 384 spectra was 12 s. To collect each image, a frame was integrated for 4 ms with 10 frames being averaged for each interferometer mirror position. A total of 300 mirror positions were recorded for each complete spectral image data set. After apodization, a single-sided interferogram containing 300 data points yielded a nominal spectral resolution for each image of 16 cm^{-1} .

Data collection and processing is similar to that performed for conventional FT-IR studies with the exception that much larger data sets are handled. Analysis involves first collecting a step-scan image sequence data set of background, typically air. Then, using identical sampling parameters, a step-scan sequence is collected with a sample placed under the microscope. The spatial/spectral interferometric data are organized in a 32-bit/pixel spectral image file format (SPIFF).³² The interferograms at each pixel in the data sets are apodized and Fourier transformed with commercial software (Spiff 1.0, ChemIcon) to yield a total of 16 384 FT-IR spectra for both the background and sample data sets. The ratio of the two data sets is taken to yield infrared transmittance images of the sample over the spectral range of $3950\text{--}1975 \text{ cm}^{-1}$. Finally, the infrared image data set spectra are converted to absorbance.

SPIFF files are visualized with commercial spectral image visualization software (ChemImage 1.0, ChemIcon) and image processing software (Optimas 4.02, Optimas). For publication, digital images are printed on a dye sublimation printer (Tektronix, Phaser SDX).

A standard USAF 1951 optical resolution target (Rolyon Optics) was employed to characterize the imaging quality of the step-scan imaging system. A commercially available aqueous surfactant dispersion consisting of sodium and potassium hexa- and octadecanoate was analyzed with the instrument. The surfactant thin-film sample was cast on a quartz microscope slide. After partial drying overnight, the dispersion was covered with a second quartz microscope slide to prevent further evaporation of water. A $36\times$ Cassegrainian microscope objective was used to image the optical resolution target, while a $15\times$ Cassegrainian objective was used for the surfactant dispersion.

RESULTS AND DISCUSSION

Figure 2 describes the imaging quality of the step-scan imaging system. Figure 2A shows an infrared transmission image of a resolution target collected with the step-scan imaging system. Modulated infrared radiation from the interferometer is coupled into the microscope and transmitted through the sample, and the target image is presented to the focal-plane array detector. The infrared image in Figure 2A is recorded at the zero path difference (ZPD) point of the step-scan interferometer mirror arms. At ZPD, the maximum radiant power is incident on the InSb camera and represents the image frame exhibiting the highest image brightness. Figure 2A is one image frame extracted from the single-beam SPIFF file in which a complete interferogram was recorded for each pixel in the target image, yielding 16 384 interferograms.

⁽³²⁾ *ChemImage Technical Reference Manual*; ChemIcon: Pittsburgh, 1995.

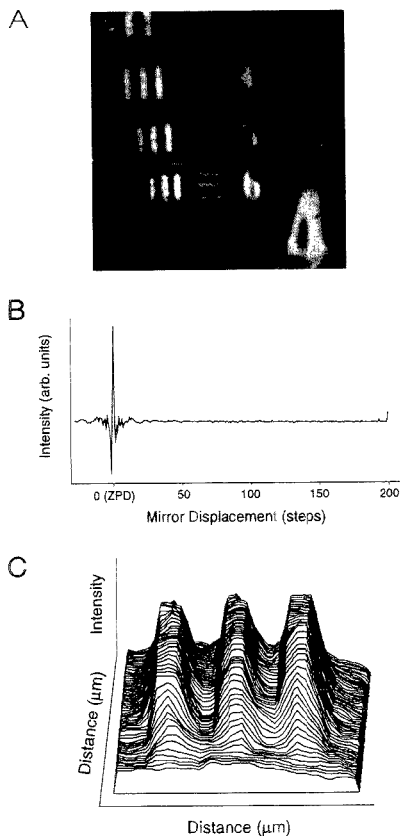


Figure 2. Step-scan interferometer imaging of a USAF 1951 resolution target. (A) InSb infrared image collected at interferometer zero path difference (ZPD); (B) single-beam interferogram extracted from SPIFF compound data set; (C) high-contrast (78%) axonometric view of resolution target (17.5- μm target spacing). Axonometric plot is taken from region outlined in (A).

A representative interferogram of one pixel is shown in Figure 2B.

Analysis of the resolution target image shown in Figure 2A reveals that each pixel in the magnified digital image collected under the microscope has an effective size of 2.9 $\mu\text{m}/\text{pixel}$. The image pixel does not define the spatial resolution of the step-scan imaging system. The theoretical spatial resolution (R) determined by the 35 \times microscope objective (0.65 NA) and limited by diffraction is 7.6 μm , according to the Rayleigh criterion,³³ where $R = 2\lambda/1.22 \text{ NA}$ and $\lambda = 3 \mu\text{m}$.

Figure 2C shows a portion (outlined in the white box) of the resolution target image in axonometric view. The vertical and horizontal bar targets having 17.5- μm center-to-center spacing are clearly resolved. The practical spatial resolution and image quality can be quantified by the modulation transfer function (MTF). The MTF describes the ability of the imaging system to generate image contrast as a function of bar target spatial frequency (line

(33) Inoue, S. *Video Microscopy*; Plenum Press: New York, 1986.

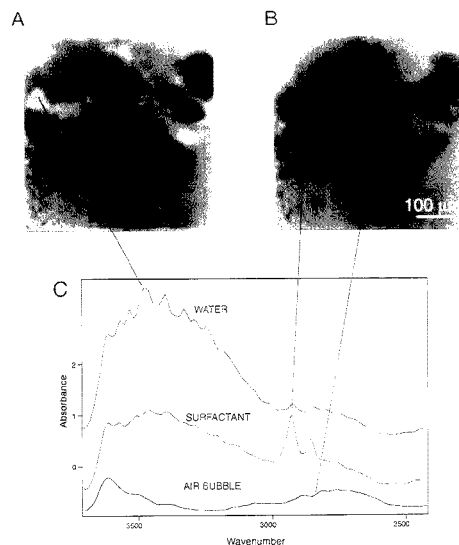


Figure 3. Infrared chemical absorbance imaging of surfactant dispersion in water. Air bubbles appear consistently as nonabsorbing black features in all images. (A) IR image showing water distribution at 3450 cm^{-1} ; (B) IR image showing surfactant domain distribution at 2920 cm^{-1} ; (C) IR absorption spectra from the water, surfactant, and air bubble regions of the images. The high-frequency "ripple" apparent in the spectra in (C) is attributed to the presence of water vapor in the instrument. Each spectrum corresponds to $\sim 3 \mu\text{m}^2$ of the sample surface.

pairs/mm). Image contrast is measured by plotting a cross section through the axonometric image. The percent contrast for the smallest target shown in Figure 2A, having a center-to-center spacing of 17.5 μm , is $78 \pm 3.0\%$. According to the Rayleigh criterion, features are just resolved at the 26.5% image contrast level. Based on the MTF, it is anticipated that the practical resolution of the step-scan imaging system using the current optics will approach the diffraction limit.

Figure 3 displays IR absorbance images of an aqueous surfactant dispersion consisting of sodium and potassium hexa- and octadecanoate. The wavenumber-resolved IR image data set is calculated from the sample and background interferometric data sets after Fourier transformation and conversion to absorbance. Figure 3A corresponds to an image at 3450 cm^{-1} (OH-stretching mode region), while Figure 3B represents an image at 2920 cm^{-1} (CH-stretching mode region). The very dark regions in the center of the images correspond to air bubbles in the sample and therefore contribute no infrared absorbance intensity to the image.

As anticipated, the images are complementary. Many of the regions that are light in Figure 3A are dark in Figure 3B and vice versa. Since this sample is a heterogeneous two-component system (excluding air) of surfactant and water, regions that are light (high absorbance at 3450 cm^{-1}) in Figure 3A correspond to domains that have a higher local water content, while light regions (high absorbance at 2920 cm^{-1}) in Figure 3B correspond to domains rich in surfactant and lower in water.

In order to verify these conclusions, the data set can also be displayed as spectral vectors corresponding to individual pixels. In Figure 3C, three spectra extracted from distinct regions of the

sample are displayed. Two of the pixels/spectra chosen correspond to ones that are bright in the CH-stretching mode image at 2920 cm^{-1} and bright in the OH-stretching mode region at 3450 cm^{-1} . From these spectra, it is clear that they are representative of the two very distinct and spatially separated components of the sample, namely, water and surfactant. In fact, for the pixel that is high in water, little or no trace of the CH-stretching vibrations corresponding to the surfactant component can be seen. It is also seen from the quality of these individual spectra from a single pixel of the total 16 384, that not only can the analysis give qualitative determination of sample composition but it can provide quantitative results as well. A spectrum from a pixel corresponding to a region through one of the air bubbles displays no features in either the CH- or OH-stretching mode region. We emphasize that the specific images shown in Figure 3 are only two selected from the entire data set and were chosen for the greatest difference in chemical image contrast. It should be understood that this hybrid data set (images and spectra) is amenable to many different types of digital spectral and digital image processing methods which then yield new images highlighting many more subtle characteristics of the sample.

CONCLUSIONS AND FUTURE DIRECTIONS

We have demonstrated a powerful, new approach to high-definition infrared chemical imaging that combines the multiplexing power of interferometry performed in a step-scan mode with the multichannel characteristics of an indium antimonide focal-plane array detector. Thus with step-scan interferometry, high-definition infrared chemical imaging now becomes practical. With the current state-of-the-art instrumentation, infrared chemical image analyses can be performed under almost real-time conditions. It is anticipated that as detector readout and image storage hardware improve, infrared spectroscopic imaging can be performed with a continuous or rapid-scanning interferometer.

FT-IR spectroscopic imaging is an important technique since it can be broadly applied to materials analysis. The method can potentially be used to study any heterogeneous condensed phase system amenable to study by conventional FT-IR spectroscopy. Most materials, manufactured or naturally occurring, either by design or by accident, are spatially and chemically heterogeneous. Chemical imaging provides the means to simultaneously explore both these properties, thus advancing our ability to better understand the molecular composition and architecture of complex materials.

It is anticipated that step-scan infrared imaging will be widely applicable, perhaps more so than Raman imaging, though the two methods are complementary. Also, it is likely that *macroscale infrared* imaging will be feasible by employing a modulated, infrared incandescent source to illuminate large fields of view. In contrast, macroscale analysis by Raman chemical imaging techniques requires the use of high power lasers whose power density must be distributed over large sampling areas, conditions which are often impractical for routine analysis.

The wide applicability of infrared chemical imaging is due, in part, to the high degree of flexibility available in performing the infrared imaging experiment. Specifically, the interferometer can be employed to modulate the infrared source radiation before it interacts with the sample (source modulation), or the interferometer can be positioned between the image collection optic and the imaging detector (image modulation). Image modulation is the most broadly applicable method, since it can be utilized in both absorption and emission spectroscopies. Source modulation, however, is simpler to implement.

Source modulation has the added bonus that any achromatic optic can be employed to deliver source radiation to the sample, as for example, fiber optics, while still maintaining maximum image resolution and contrast. The only requirement is that the source radiation be uniformly modulated across the image field of view by the interferometer. Image quality is, therefore, determined by the collection optics (the microscope) and the imaging detector and not the imaging performance of the interferometer itself. In the image modulation configuration, however, the interferometer is anticipated to be the optical element that determines the ultimate imaging quality, and as such will most likely provide the major source of image degradation.

Chemical imaging problems currently under investigation in the authors' respective laboratories are many and varied. All can be impacted by the use of high-definition infrared chemical imaging. Studies include, for example, the chemical imaging of cholesterol gradients within retinal rod outer segments and neurotoxicity problems involving brain slices derived from animals treated with various drugs (E.N.L., I.W.L.). In these studies, interferometric imaging methods afford determinations at the micrometer spatial level of the subtle structural and environmental changes induced in both the cellular lipid and protein components within these tissue sections. Material studies currently underway include rapid, noninvasive visualization of polymer blend architecture (P.J.T.) and chemical imaging histopathology of disease states (P.J.T., E.N.L., I.W.L.). Details of these studies will be described in forthcoming papers.

ACKNOWLEDGMENT

We thank Dr. A. Adams of Santa Barbara Focalplane and Dr. Richard Crocombe and Dr. Raul Curbelo of Bio-Rad for technical assistance in interfacing the detector with the interferometer. We also thank Mr. Michael Schaeberle of the University of Pittsburgh for assistance in generating the hard copies of the gray-scale images reproduced in the manuscript.

Received for review June 13, 1995. Accepted July 28, 1995.*

AC9505785

* Abstract published in *Advance ACS Abstracts*, September 1, 1995.

Monitoring an Oxidative Stress Mechanism at a Single Human Fibroblast

Stéphane Arbault,[†] Paul Pantano,^{†,‡} Jeffrey A. Jankowski,^{†,§} Monique Vuillaume,^{*,||} and Christian Amatore^{*,†}

Département de Chimie, Ecole Normale Supérieure, URA CNRS 1679, 24 rue Lhomond, 75231 Paris Cedex 05, France, Institut de Recherche sur le Cancer, UPR CNRS 42, BP 8, 94801 Villejuif Cedex, France, and Département de Biologie, Ecole Normale Supérieure, 46 rue d'Ulm, 75230 Paris Cedex 05, France

Easily oxidizable substances inside human diploid fibroblast cell strains were monitored amperometrically with a platinumized carbon-fiber microelectrode. The experiment involved positioning a microelectrode over a single biological cell, forcing the electrode tip into the cell via micromanipulator control, and measuring the transient current corresponding to the complete electrolysis of electroactive species released by the cell. A second series of experiments involved puncturing a hole into the cell with a micropipet and measuring the transient current corresponding to the complete electrolysis of electroactive species emitted by the cell with an electrode positioned above the cell. The selectivity of both amperometric measurements was demonstrated through the use of known hydrogen peroxide scavengers (added catalase or intracellular peroxidase + added *o*-dianisidine) to the media bathing the cells. The abolition of the amperometric signal under these conditions suggested that hydrogen peroxide was the primary substance detected. The magnitude and the time course of the transient current measured implied that the hydrogen peroxide detected was not only that initially present in the cell before its membrane was pierced but represented mostly an oxidative stress response of the cell to its injury.

Reactive oxygen species, such as the superoxide anion, the hydroxyl radical, and hydrogen peroxide, are generated as side products during normal oxygen metabolism in all aerobic cells. In addition, these and other related compounds are produced to a larger extent in living cells that have been exposed to environmental hazards and miscellaneous xenobiotics (e.g., cigarette smoke, air pollution, herbicides, various forms of radiation, etc.). When the levels of these oxygen species and free radicals rise, a situation known as oxidative stress is created which can lead to a variety of biochemical and physiological lesions (often resulting in metabolic impairment and cellular transformation or carcinogenesis).¹⁻¹⁰ Many antioxidant defense mechanisms limit

the levels of (and the damage from) these reactive oxidants. Among these physiological defenses are the enzymes (superoxide dismutases, catalase, glutathione peroxidase) and the dietary antioxidants (β -carotene, α -tocopherol, ascorbic acid, other vitamins).¹¹

While hydrogen peroxide might be one of the least reactive of the oxygen metabolites, it is one of the most interesting since it appears to be the central oxygen metabolite from which other oxygen species are generated in situ. Many assays and detection methods have been developed to measure hydrogen peroxide and the other reactive oxygen species.^{12,13} Unfortunately, the indirect/direct quantitative determination of the in vitro production and release of these reactive oxygen species is often limited by the sensitivity and selectivity of the traditional detection schemes. In addition, the inability to directly measure the steady state concentration of hydrogen peroxide in biological systems is a result of the low physiological levels of hydrogen peroxide maintained by the enzymatic systems that actively metabolize it. However, while the presence of catalase, superoxide dismutases, glutathione peroxidase, and other enzymes prevents the direct chemical analysis of hydrogen peroxide, these enzymes can be used to produce some indirect analytical approaches.¹⁴ Unfortunately, most of these methods require large populations of ruptured cells and therefore are not suitable for single-cell analyses; in addition, they are not able to make a *real-time* measurement with any spatial or temporal resolution.

The use of microelectrodes (electrodes of micrometer dimensions) permits electrochemical measurements to be performed in *real time* in discrete locations (e.g., inside¹⁵ or near the surface¹⁶

[†] URA CNRS 1679.
[‡] Present address: Department of Chemistry, Tufts University, Medford, MA 02155.

[§] Present address: Nalco Chemical Co., 1 Nalco Center, Naperville, IL 60563.
^{||} UPR CNRS 42.

^{*} Département de Biologie, Ecole Normale Supérieure.
(1) Chance, B.; William, G. R. *J. Biol. Chem.* **1955**, *217*, 409-427.
(2) Chance, B. *Annual Review of Biophysics and Biophysical Chemistry*; Engleman, D. M., Ed.; Annual Reviews: Palo Alto, CA, 1991; Vol. 20, pp 1-28.

(3) Sies, H. *Metabolic Compartmentation*; Academic Press: New York, 1982.
(4) Denk, W.; Strickler, J. H.; Webb, W. W. *Science* **1990**, *248*, 73-76.
(5) Zimmerman, R.; Cerutti, P. *Proc. Natl. Acad. Sci. U.S.A.* **1984**, *81*, 2085-2087.
(6) Cerutti, P. A. *Science* **1985**, *227*, 375-381.
(7) Vuillaume, M. *Mutat. Res.* **1987**, *189*, 43-72.
(8) Ames, B. N. *Free Radical Res. Commun.* **1989**, *7*, 121-128.
(9) Stadman, E. R. *Science* **1992**, *257*, 1220-1224.
(10) Scandalios, J. S., Ed. *Molecular Biology of Free Radical Scavenging Systems*; Cold Spring Harbor Press: Cold Spring Harbor, NY, 1992.
(11) Ames, B. N. S.; Shigenaga, M. K. In *Molecular Biology of Free Radical Scavenging Systems*; Scandalios, J. S., Ed.; Cold Spring Harbor Press: Cold Spring Harbor, NY, 1992; pp 1-22.
(12) Packer, L., Ed. *Oxygen Radicals in Biological Systems*; Academic Press: Orlando, FL, 1984; Vol. 105.
(13) Panus, P. C.; Radi, R.; Chumley, P. H.; Lillard, R. H.; Freeman, B. A. *Free Radicals Biol. Med.* **1993**, *14*, 217-223.
(14) Chance, B.; Sies, H.; Boveris, A. *Physiol. Rev.* **1979**, *59*, 527-605.
(15) Ewing, A. G.; Strein, T. G.; Lau, Y. Y. *Acc. Chem. Res.* **1992**, *25*, 440-447.
(16) Schroeder, T. J.; Jankowski, J. A.; Kawagoe, K. T.; Wightman, R. M.; Lefrou, C.; Amatore, C. *Anal. Chem.* **1992**, *64*, 3077-3083.

of single biological cells). The majority of these investigations have involved the detection of neurochemicals, but recently other molecules of biological interest such as insulin¹⁷ and the superoxide anion^{18,19} have been studied. Nonetheless, in all these applications, the biological cell has been chemically or electrically stimulated to release the electroactive analyte(s) of interest. We believe the following work to be the first example whereby a microelectrode was used to probe the response of a biological cell without electrical or chemical stimulations. Instead, the microelectrode itself is used to enter into and then detect electroactive species emitted by the cell and even stimulate an oxidative stress response, mimicking a defensive response to a cellular intrusion by a virus, a particle, a bacterium, etc.

Carbon fibers are the most common material for the construction of microelectrodes since they display a very stable background current in biological media and can be subjected to various electrode modification procedures.²⁰ Unfortunately, hydrogen peroxide oxidation is not easily detected at carbon electrodes.²¹ While platinum is an extremely good catalytic surface for hydrogen peroxide oxidation, the use of disposable noble metal electrodes in biological media is inconvenient and expensive. In this work, platinumized carbon-fiber microelectrodes were used to monitor the dynamics of electroactive species contained inside cultured human fibroblasts. Carbon-fiber surfaces were platinumized by reducing hydrogen hexachloroplatinate in the presence of lead acetate.²² By platinumizing a carbon-fiber microelectrode, a stable and a catalytic surface for hydrogen peroxide oxidation was created. In addition to increasing the number of electroactive sites, the platinumized carbon-fiber surface permitted a lower applied potential to be used for the electrochemical hydrogen peroxide oxidation (relative to that at a bare carbon-fiber surface). This was advantageous since there is less susceptibility to interferences from other electroactive species when the electrode is operated at a lower applied potential.

Simian virus 40 (SV₄₀)-transformed human fibroblast cell lines were chosen as a model system for this work since they were characterized previously with respect to their catalase activity.^{23–25} Specifically, their catalase activities were shown to become markedly deficient following transformation by SV₄₀. A decrease in catalase activity, the enzyme that catalyzes the dismutation of hydrogen peroxide into water and molecular oxygen, is expected to result in larger intracellular steady state concentrations of hydrogen peroxide than in cells with normal catalase activity. However, amounts of hydrogen peroxide released naturally by cells were undetectable with our electrodes. The intracellular H₂O₂ measurements thus required that the cytoplasmic membrane

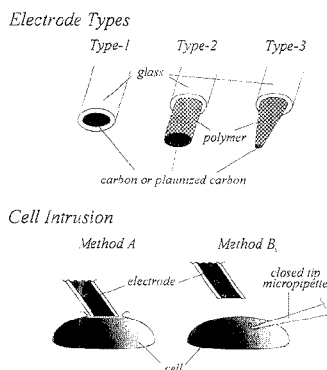


Figure 1. Schematic representation of the various electrode shapes used in this study and of the different methods of penetration into SV₄₀-transformed fibroblasts (see text and Experimental Section for details).

be perforated by an intruding object. Two series of experiments were performed using living fibroblast cells maintained under normal aerobic conditions in physiological buffer (Figure 1). One involved positioning a microelectrode (set at an appropriate potential) over the living cell, rupturing the cell membrane by forcing the electrode tip into the cell via micromanipulator control, and measuring the transient current corresponding to the complete electrolysis of electroactive species inside the cell. The second series involved puncturing the cell membrane with a closed-tip pulled glass capillary tube analogous to those used in patch-clamp techniques. A fused closed tip was used to avoid intracellular fluid leaking into the capillary. In this arrangement, the hydrogen peroxide flux leaking outside the cell through the hole punctured into its membrane was measured with an electrode positioned above the cell. The selectivity of the amperometric measurements was demonstrated through the addition of known hydrogen peroxide scavengers (catalase or peroxidase + *o*-dianisidine) to the media that bathed the cells, prior to puncturing the cell membrane. The abolition or great reduction of the amperometric signal when either of these specific scavengers was added to the media and other data suggested that hydrogen peroxide was the primary substance detected.

EXPERIMENTAL SECTION

Chemicals. Catalase (from bovine liver), horseradish peroxidase, *o*-dianisidine, ascorbic acid, and ascorbate oxidase (Sigma Chemical Co., St. Louis, MO); allylamine, 2-allylphenol, 2-butoxyethanol and *p*-phenylenediamine (Aldrich Chemical Co., Milwaukee, WI); lead acetate and hydrogen hexachloroplatinate (Janssen Chimica), and Shell Epon-828 resin (Miller-Stephenson, Danbury, CT) were used as received. Phosphate-buffered saline (PBS) pH 7.4 (Catalog No. 79332, Fluka Chemika) was prepared with water purified by a Milli-Q purification system (Millipore, Bedford, MA). Hydrogen peroxide solutions were prepared by making the appropriate dilutions in PBS from a 30% hydrogen peroxide solution (Labosi) whose concentration was assayed spectrophotometrically ($\lambda_{\text{max}} = 230 \text{ nm}$, $\epsilon = 81 \text{ M}^{-1} \text{ cm}^{-1}$).

Microelectrodes Fabrication. Three different carbon-fiber microelectrode tip geometries were utilized throughout the course of this work. The first type (type-1, Figure 1) was a glass-encased

- (17) Kennedy, R. T.; Huang, L.; Atkinson, M. A.; Dush, P. *Anal. Chem.* **1993**, *65*, 1882–1887.
- (18) Hill, H. A. O.; Tew, D. G.; Walton, N. J. *FEBS Lett.* **1985**, *191*, 257–263.
- (19) Tanaka, K.; Kobayashi, F.; Isogai, Y.; Iizuka, T. *Bioelectrochem. Bioenerg.* **1991**, *26*, 413–421.
- (20) Stamford, J. A. *J. Neurosci. Methods* **1986**, *17*, 1–29.
- (21) Heider, G. H.; Sasso, S. V.; Huang, K. M.; Yacynych, A. M.; Wieck, H. J. *Anal. Chem.* **1990**, *62*, 1106–1110.
- (22) Ikarizawa, Y.; Yamauchi, S.; Yukiashi, T.; Ushioda, H. *J. Electroanal. Chem.* **1988**, *251*, 267–274.
- (23) Vuillaume, M.; Calvayrac, R.; Bes-Belpomme, M.; Tarroux, P.; Hubert, M.; Decroix, Y.; Sarasin, A. *Cancer Res.* **1986**, *46*, 538–544.
- (24) Vuillaume, M.; Daya-Grosjean, L.; Vincens, P.; Pennerier, J. L.; Tarroux, P.; Barci, A.; Calvayrac, R.; Taieb, A.; Sarasin, A. *Carcinogenesis* **1992**, *13*, 321–328.
- (25) Hoffschic, P.; Vuillaume, M.; Sabatier, L.; Ricoul, R.; Daya-Grosjean, L.; Estrade, S.; Cassingena, R.; Calvayrac, R.; Sarasin, A.; Dutrillaux, B. *Carcinogenesis* **1993**, *14*, 1569–1572.

carbon-fiber microelectrode.²⁶ Briefly, individual carbon fibers (10- μm diameter, Thornel P-55S, Amoco Performance Products, Greenville, SC) were aspirated into glass capillary tubing (GC120F-10, Clark Electromedical Instruments), and a tapered end was produced after the capillary was pulled with a microelectrode puller (Model PB-7, Narishige). Epon-828 epoxy was used with 14% by weight *p*-phenylenediamine as hardener to seal the carbon fiber inside the glass capillary tube (where the epoxy was cured at ~ 150 °C for a minimum of 3 h). Initial activation of these microelectrodes was achieved by polishing the tip of a freshly exposed carbon-fiber surface on a diamond particle whetstone microgrinder (Narishige Model EG-4) at an angle of 45° for 2 min. The polished beveled microelectrodes were sonicated in refluxing toluene for 10 s and then in deionized water for 30 s. Type-1 microelectrodes had 15–20- μm tip diameters as a result of the glass insulation and beveling. In addition, a glass-encased, solid platinum wire microelectrode (10- μm diameter, Goodfellow) was constructed and activated in the same fashion as described above.

Smaller carbon-fiber microelectrodes could be made through the use of a thin insulating polymeric layer. After individual carbon fibers were aspirated into glass capillary tubing and pulled, a short length of the carbon fiber was allowed to protrude from the pulled glass capillary tube's tapered end. The protruding carbon fiber was insulated by the electrochemical deposition of poly(oxyphenylene) according to a previously described method.²⁷ This electrodeposition was carried out in a solution comprising 0.4 M allylamine, 0.23 M 2-allylphenol, and 0.23 M 2-butoxyethanol in 1:1 (v/v) water–methanol at +4 V for 3 min with a platinum counterelectrode. Following the polymer deposition, the electrodes were washed thoroughly in distilled water, and the polymer was cured for 3 h at 150 °C. Finally, the polymer insulation was removed from the carbon-fiber's tip by polishing the microelectrode for 1 min on a diamond particle whetstone. These polymer-insulated carbon-fiber microelectrodes (type 2, Figure 1) had 10- μm tip diameters. In some cases, the protruding carbon fiber was flame-etched in a Bunsen burner flame before it was insulated with the polymer.²⁸ These flame-etched, polymer-insulated carbon-fiber microelectrodes (type-3, Figure 1) had 2–5- μm tip diameters. In all cases, glass capillary tubes were back-filled with a drop of mercury and an electrical contact was made using a nichrome wire.

All polished carbon-fiber surfaces were platinized by reducing hydrogen hexachloroplatinate (45 mg) in the presence of lead acetate (0.9 mg) in 1.5 mL of PBS at -0.10 V (where a platinum wire was used as the auxiliary electrode and a freshly anodized (in 1 M NaCl) Ag/AgCl electrode was used as the reference electrode).²² The extent of the platinization reaction was controlled by monitoring the electrodeposition current. Platinized carbon-fiber microelectrodes were soaked in PBS for a minimum of 1 h before use and were stored at 4 °C in filtered PBS when not in use. All platinized carbon-fiber microelectrodes were precalibrated in amperometric mode (Table 1, $E_{\text{app}} = +600$ mV vs Ag/AgCl) with 10^{-5} M H_2O_2 in PBS.

Instrumentation. Constant potential amperometry (Tacussel Electroniques Model PRG-DEL amperometric detector) and fast-scan cyclic voltammetry (EI400 potentiostat, Ensman Instruments,

Table 1. Responses (Current in nA) of Microelectrodes toward Various Concentrations of Hydrogen Peroxide or Ascorbate in a Flow Injection Cell^a

electroactive species	carbon fiber	
	bare	platinized
H_2O_2 , 10^{-3} M	0.005 ± 0.0015 ($n = 3$)	85 ± 7 ($n = 3$)
H_2O_2 , 10^{-5} M	not detectable	0.80 ± 0.15 ($n = 3$)
ascorbate, 10^{-3} M	2.5 ± 0.5 ($n = 3$)	35 ± 4 ($n = 3$)
ascorbate, 10^{-5} M	0.025 ± 0.008 ($n = 3$)	0.40 ± 0.02 ($n = 3$)

^a Average plateau currents in dc amperometric detection (+600 mV vs Ag/AgCl) in PBS solutions. Platinized electrodes were produced using a maximum electrodeposition current of ~ 500 nA. Results are given as mean \pm standard deviation (number of electrodes tested).

Bloomington, IN) were performed in an aluminum Faraday cage. A 1-MHz digital oscilloscope (Model 310, Nicolet, Madison, WI) was used to observe and store all transients. The flow injection analysis (FIA) system, which consisted of a pneumatic actuator (Model 5701, Rheodyne, Coati, CA) coupled to a solenoid valve kit (Rheodyne Model 7163), was identical to the one described previously with the exception that the buffer flow (5 mL/min) was controlled by a syringe pump (Model 22, Harvard Apparatus, South Natick, MA).²⁶

Cell Cultures. SV₄₀-transformed human fibroblasts (MRC5 V1) were grown at a density of 10^5 cells/cm² in MEM medium (Gibco BRL) supplemented with 15% fetal calf serum in a 5% CO₂ incubator at 37 °C. The origin of the cells was described previously.^{23–25} All cells adhered to the base of the 35-mm-diameter polystyrene crystal Petri dishes during the culture. Experiments were performed at room temperature from confluent monolayer fibroblasts when the growth medium was replaced with sterile PBS solution.^{23–25}

Single-Cell Experiments. All measurements were made on the stage of an inverted microscope (Axiocvert 135, Carl Zeiss) equipped with a charge-coupled device video camera (Model SSC-M350CE, Sony) and video monitor (Sony Model PVM-122CE). Microelectrodes were mounted with their exposed surfaces parallel to the cell plate and were positioned above the pole of a single cell with a three-dimensional manipulator (Narishige Model MN-2) as described previously.¹⁶ Two methods were employed to monitor the diffusion of intracellular electroactive species to the microelectrode surface. The first method involved crushing the cytoplasmic region of an isolated, nondividing cell via micromanipulator control with the microelectrode itself (method A, Figure 1). The smaller polymer-insulated (type 2 or type 3) microelectrodes allowed a closed-tip, pulled glass capillary tube (1–3- μm tip diameter), via a second micromanipulator, to be positioned between the microelectrode and the cell for the purpose of puncturing a hole in the cell (method B, Figure 1). All amperometric transients were characterized (Table 2) with respect to their peak height (i_{max} in picoamperes), their half-width ($t_{1/2}$ in seconds), and their area (Q in picocoulombs). Integration of the current for the charge determination was performed over a time period extending over $10t_{1/2}$ after the current maximum using a program developed previously.¹⁶ In some experiments, the PBS in the Petri dish was replaced with a PBS solution containing a hydrogen peroxide scavenger or with a degassed PBS solution (see Results). In other experiments, a dioxygen-sensitive electrode was used to monitor the cellular dioxygen metabolism during the experiments.

(26) Kuhr, W. G.; Barrett, V. L.; Gagnon, M. R.; Hopper, P.; Pantano, P. *Anal. Chem.* **1993**, *65*, 617–622.

(27) Kawagoe, K. T.; Jankowski, J. A.; Wightman, R. M. *Anal. Chem.* **1991**, *63*, 1589–1594.

(28) Srein, T. G.; Ewing, A. G. *Anal. Chem.* **1992**, *64*, 1368–1373.

Table 2. Current Spike Characteristics Measured in PBS at SV₄₀-Transformed Human Fibroblasts as a Function of the Method and of the Platinized Carbon-Fiber Microelectrode Type (See Figure 1)^a

	microelectrode type		
	1	2	3
Method A			
i_{\max} (pA)	30 ± 7 ($n = 8$)	25 ± 20 ($n = 8$)	8 ± 6 ($n = 20$)
$t_{1/2}$ (s)	4 ± 2 ($n = 8$)	2.5 ± 1 ($n = 8$)	5.5 ± 3.5 ($n = 20$)
Q (pC)	300 ± 200 ($n = 8$)	130 ± 110 ($n = 8$)	70 ± 50 ($n = 20$)
Method B			
i_{\max} (pA)	4 ± 2 ($n = 8$)		3 ± 2 ($n = 6$)
$t_{1/2}$ (s)	10 ± 5 ($n = 8$)		9 ± 3 ($n = 6$)
Q (pC)	55 ± 15 ($n = 8$)		30 ± 15 ($n = 6$)

^a dc amperometric detection (+600 mV vs Ag/AgCl). Platinized microelectrodes of each type were produced with a maximum electrodeposition current of -300 nA. Results are given as mean ± standard deviation (number of data).

Control Experiments. To determine the activity of the chemical hydrogen peroxide, hydroperoxides, or ascorbate scavengers, control experiments were performed in Petri dishes without cells. The Petri dish was filled with a 4-mL PBS solution containing the enzyme (catalase, horseradish peroxidase, or ascorbate oxidase) or the enzyme and its cosubstrate (horseradish peroxidase and *o*-dianisidine). A 100- μ L aliquot of 10^{-4} M H₂O₂ or 10^{-4} M ascorbate was then injected into the Petri dish, and the electrode's amperometric response was recorded at +600 mV vs Ag/AgCl.

RESULTS

Characterization of Platinized Carbon-Fiber Microelectrodes. All polished carbon-fiber electrode surfaces were platinized by reducing hydrogen hexachloroplatinate in the presence of lead acetate.²² The extent of the platinization reaction was controlled by monitoring the increasing electrodeposition current during the reduction of hydrogen hexachloroplatinate onto the carbon-fiber surface. Extremely sensitive electrodes, capable of detecting 10 nM H₂O₂ with S/N = 5 (dc amperometry, +0.6 V vs Ag/AgCl), could be made by depositing a thick Pt layer (i.e., using a maximum electrodeposition current of -5 μ A). Unfortunately these thick Pt layers were very fragile and would frequently detach upon piercing a biological cell. Robust platinized carbon-fiber microelectrodes were constructed when the electrodeposition current was interrupted at minor current maxima (i.e., a maximum electrodeposition current of -300 nA). These thinner Pt layers were very stable and rarely became detached. Unless otherwise noted, all data were obtained with these latter electrodes.

All microelectrodes were characterized in PBS using a flow injection analysis electrochemical system.²⁶ This permitted the microelectrode to be exposed to a rapid and brief pulse of concentration in a consistent and reproducible manner and, thus, allowed calibration and examination of the stability and reproducibility of the electrode response. The overall response time of the FIA - microelectrode system was evaluated by monitoring the time course of the chronoamperometric current following injection of samples, since this afforded an upper limit of the electrode's response time (Figure 2). The overall response times of these FIA + microelectrode systems were on the order of 0.5

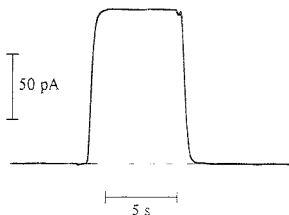


Figure 2. Amperometric response of a type-2 platinized microelectrode (-300-nA maximum electrodeposition current) polarized at +0.6 V vs Ag/AgCl in a flow injection cell following a loop injection of 10^{-5} M H₂O₂. PBS solution.

s (0.475 ± 0.125 s, $n = 14$ electrodes tested) based on the time required to reach 63% of the steady state current. Unless noted otherwise, all amperometric measurements for H₂O₂ oxidation were made at +0.6 V vs Ag/AgCl. The response of platinized carbon-fiber microelectrodes made with a -500-nA electrodeposition current was linear between 10^{-3} and 10^{-6} M H₂O₂ ($r^2 = 0.975$, $n = 4$; slope, 70 nA/mM) with a detection limit of 5×10^{-7} M H₂O₂. The amperometric response of platinized carbon-fiber microelectrodes towards the oxidation of 10^{-5} M H₂O₂ was linear ($r^2 = 0.99$, $n = 20$; slope, 1.5 pA/nA) with respect to the maximum electrodeposition current used in their fabrication between values of -200 to -500 nA. In addition, the behavior (response time and maximum current response) of platinized carbon-fiber microelectrodes obtained with low electrodeposition currents (i.e., -300 nA) toward H₂O₂ oxidation was nearly identical to that of a 10- μ m-diameter solid platinum wire microelectrode.

Bare (polished but not platinized) and platinized carbon-fiber microelectrodes were also characterized with respect to their response toward ascorbic acid oxidation (Table 1). They were both sensitive toward ascorbic acid oxidation in the concentration range of 10^{-3} - 10^{-5} M with the platinized surfaces being 15 times more sensitive than the bare carbon-fiber microelectrodes (dc amperometry at +0.6 V vs Ag/AgCl, $n = 6$ electrodes tested). On the other hand, platinized carbon-fiber microelectrodes were 17 000 times more sensitive toward 10^{-3} M H₂O₂ than the bare carbon-fiber microelectrodes. Moreover, the oxidation of 10^{-5} M H₂O₂ was not detectable at bare carbon (dc amperometry, +0.6 V vs Ag/AgCl, $n = 6$ electrodes tested). No changes in any of these responses were observed when oxygen was removed from the PBS by degassing with argon (data not shown).

Amperometric Measurements from Isolated Biological Cells. Amperometric measurements with a type-2, platinized carbon-fiber microelectrode were obtained from isolated SV₄₀-transformed cells using methods A and B (as defined in Figure 1). In both cases, the oxidative current monitored at +600 mV vs Ag/AgCl increased immediately following the insertion of the microelectrode tip (or that of the glass capillary tube) into the biological cell (Figure 3). The signals obtained with method A were substantially larger than those obtained with method B (Table 2). Positioning a type-2 platinized carbon-fiber microelectrode at various distances from the cell (method B) showed that when the microelectrode was placed farther away from the cell, less current is observed (Figure 4).^{16,27,29,30}

(29) Engstrom, R. C.; Wightman, R. M.; Kristensen, E. W. *Anal. Chem.* **1988**, *60*, 652-656.

(30) Fosset, B.; Amatore, C. A.; Bartelt, J. E.; Michael, A. C.; Wightman, R. M. *Anal. Chem.* **1991**, *63*, 306-314.

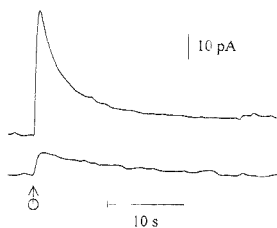


Figure 3. Current response of the same platinized microelectrode (type 2, -300 -nA maximum electrodeposition current) polarized at $+0.6$ V vs Ag/AgCl during cell intrusion using either method A (top: $i_{\max} = 21$ pA, $t_{1/2} = 3$ s, $Q = 130$ pC) or method B (bottom: $i_{\max} = 3.8$ pA, $t_{1/2} = 7$ s, $Q = 45$ pC). The vertical arrow indicates the moment of intrusion. Two different SV₄₀-transformed fibroblasts were used sequentially in the order, top, bottom.

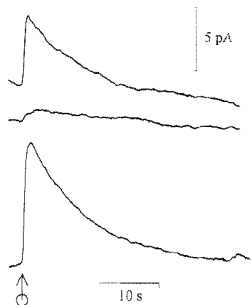
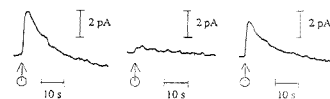


Figure 4. Current response of the same platinized microelectrode (type 2, -300 -nA maximum electrodeposition current) polarized at $+0.6$ V vs Ag/AgCl during cell intrusion using method B with different cell-electrode distances (d). Top: $d \approx 1$ μm , $i_{\max} = 5.5$ pA, $t_{1/2} = 5$ s, $Q = 40$ pC. Middle: $d \approx 3$ μm , $i_{\max} \approx 1$ pA, $t_{1/2} \approx 8$ s, $Q \approx 10$ pC. Bottom: $d \approx 1$ μm ; $i_{\max} = 9$ pA, $t_{1/2} = 7.5$ s, $Q = 95$ pC. The vertical arrow indicates the moment of intrusion. Three different SV₄₀-transformed fibroblasts were used sequentially in the order, top, middle, bottom. Bottom trace was used as a postcontrol to establish that the middle response was not the result of electrode fouling.

In order to examine the effect of the mechanical movements involved when the micromanipulator set a microelectrode in motion to enter into a cell in method A, several microelectrodes (all types) were used on noncellular entities or the bottom of the cell culture dish. In all cases, no signal was observed. In addition, when a platinized carbon-fiber microelectrode was positioned directly next to a cell, no signals were ever detected before the cell membrane was punctured (method A or B).

When electrodes were used to puncture different cells in succession (method A), platinized carbon-fiber microelectrodes (all types) retained approximately 70–75% of their activity compared to their first insertion into a biological cell. More precisely, the current maxima were $\sim 65\%$ and the charges $\sim 80\%$ of those monitored for first runs. These measurements were averaged over 30 experiments (30 electrodes; two different cells per electrode) to avoid differences due to cell metabolism variability. With method B more than 90% of the activity was retained. When the electrodes were left in PBS for 15 min in between two consecutive runs, the responses (current maximum and charge) were restored to their initial values (method A or B). When the consecutive responses of several cells needed to be compared (vide infra), all experiments were performed with method B,

A. Control of Release by Catalase



B. Control of Release by *o*-dianisidine

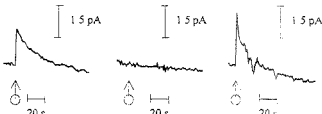


Figure 5. Effect of 2.5 mg/mL catalase in PBS (A, middle) and of 0.1 mM *o*-dianisidine in PBS (B, middle) on the current response of a platinized microelectrode (type 2, -300 -nA maximum electrodeposition current) polarized at $+0.6$ V vs Ag/AgCl during cell intrusion using method B. In (A) and (B), the left and right curves are pre (left) or post (right) control experiments performed in PBS alone with the same electrode. The vertical arrows indicates the moment of intrusion in each case. In (A) and (B), three different SV₄₀-transformed fibroblasts were used sequentially in the order, left, middle, right.

where the electrode was left in PBS for at least 15 min in between two successive measurements, except when otherwise stated.

Selectivity of the Biological Measurements. Fast-scan cyclic voltammetry (100 V s⁻¹) at a platinized carbon-fiber microelectrode was used in an attempt to identify the electroactive species diffusing out of the cells.²⁶ However, the S/N ratios after background subtraction were insufficient to detect electroactive material with method B. In method A, changes (15–20%, data not shown) in the electrode capacitive currents were observed during and following the intrusion process which made background subtraction impossible.

The selectivity of the amperometric measurement was analyzed through a series of experiments (method B) where the cells were bathed with a known hydrogen peroxide or hydroperoxide (i.e., ROOH with R = alkyl) scavenger immediately before the cell membrane was punctured. The first scavenger employed was catalase.³¹ These data are shown in Figure 5A where the left-hand trace represents the oxidation of electroactive species released from the cell without catalase present in the surrounding medium, and the middle trace shows the response at another cell using the same platinized microelectrode when catalase (2.5 mg/mL) was present. The right-hand trace (control) is the response of a third cell with the same electrode after catalase has been removed. Since three different cells must be used (two without, one with catalase), these series of consecutive experiments were repeated with each electrode on five triplets of cells chosen randomly. Each series gave similar results.

After a platinized carbon-fiber microelectrode (-1 μA maximum electrodeposition current) was placed in a Petri dish without cells containing 4 mL of PBS, a 100- μL aliquot of 10^{-4} M H₂O₂ was injected into the dish and a steady state oxidative current (1.4 nA) was recorded at $+0.6$ V vs Ag/AgCl. When the same experiment was performed within a Petri dish containing in addition 10 mg/mL catalase, there was absolutely no signal recorded. When a 100- μL aliquot of 10^{-4} M ascorbate was injected into the dish containing catalase, the signal at the same electrode

(31) Chance, B. *J. Biol. Chem.* 1949, 179, 1331–1349.

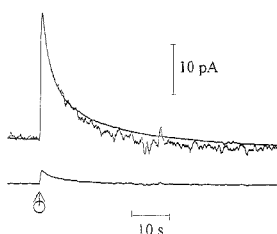


Figure 6. Current response of a type-2 microelectrode polarized at +0.6 V vs Ag/AgCl after cell intrusion using method A. Top: smooth curve; platinized microelectrode (−300-nA maximum electrodeposition current); $i_{\max} = 26 \text{ pA}$, $t_{1/2} = 3.5 \text{ s}$, $Q = 180 \text{ pC}$. Bottom: bare carbon microelectrode; $i_{\max} = 2.6 \text{ pA}$, $t_{1/2} = 3.5 \text{ s}$, $Q = 15 \text{ pC}$. In the top, the noisy curve is an enlargement ($\times 9.9$) of the bottom curve. The vertical arrow indicates the moment of intrusion in all cases. Two different SV₄₀-transformed fibroblasts were used.

for ascorbate oxidation was identical to that measured (*pre*control) at this electrode in the absence of catalase (data not shown).

An identical series of experiments was performed using 10^{-4} M *o*-dianisidine³² to bathe the cellular surroundings before the cell membrane was punctured. This series of experiments led to the same observations as described with catalase (Figure 5B). Control experiments were conducted. The microelectrode response was recorded with 10^{-3} M H₂O₂ in a Petri dish without cells and containing horseradish peroxidase³³ (2.5 mg/mL) with or without *o*-dianisidine. In the absence of *o*-dianisidine, the electrode response over a time scale of 40 s was identical to that obtained in the absence of peroxidase. When 10^{-4} M *o*-dianisidine and peroxidase were present together, no faradaic signal was detected. When 10^{-1} M ascorbate was added to the same Petri dish containing peroxidase and *o*-dianisidine, the current response at the same electrode for ascorbate oxidation was identical to that measured for 10^{-4} M ascorbate without peroxidase or *o*-dianisidine.

A series of experiments was performed in which the cell-electrode interspace was bathed with ascorbate oxidase (250 units/mL) immediately before the cell membrane was punctured (method B). No change in amplitude and time course of the current responses were observed (data not shown). When a 100- μ L aliquot of 10^{-4} M ascorbate was introduced in a Petri dish containing ascorbate oxidase (250 units/mL) without cells, no faradaic signal was detected. When 10^{-4} M H₂O₂ was added to the same Petri dish containing ascorbate oxidase, the same electrode gave a response identical to that obtained for 10^{-4} M H₂O₂ alone.

Bare (polished but not platinized) and platinized carbon-fiber microelectrodes were compared using method A (Figure 6). Peak height values obtained from the bare carbon-fiber microelectrodes ranged from 2 to 3 pA with an integrated area of $\sim 20 \text{ pC}$, while typical peak height values obtained with the type-2 platinized carbon-fiber microelectrodes (−300 nA electrodeposition currents) were $\sim 50 \text{ pA}$ with integrated areas over 200 pC (Table 2). Bare carbon-fiber microelectrodes could not be precalibrated with low concentrations of hydrogen peroxide ($\leq 10^{-3}$ M, Table 1). Their pre- and postcalibration in the FIA cell with ascorbate gave identical results.

(32) Fridovich, I. *J. Biol. Chem.* **1963**, *238*, 3921–3940.

(33) Chance, B.; Herbert, D. *Biochem. J.* **1950**, *46*, 402–414.

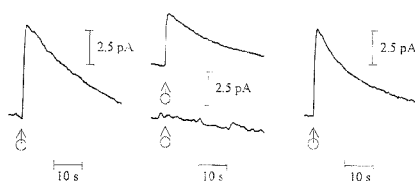


Figure 7. Effect of dioxygen availability on the current response of the same platinized microelectrode (type 2, −300-nA maximum electrodeposition current) polarized at +0.6 V vs Ag/AgCl during cell intrusion using method B. Left and right: pre (left) or post (right) control experiments in PBS saturated with dioxygen. Middle, responses in dioxxygenated PBS; top, immediately after replacing the air saturated PBS by a degassed PBS solution; bottom, when the initial air saturated PBS solution was progressively degassed by argon bubbling over 10 min. Four different SV₄₀-transformed fibroblasts were used. Left: $i_{\max} = 7 \text{ pA}$, $t_{1/2} = 15.5 \text{ s}$, $Q = 105 \text{ pC}$. Middle, top: $i_{\max} = 4 \text{ pA}$, $t_{1/2} = 16 \text{ s}$, $Q = 55 \text{ pC}$. Right: $i_{\max} = 6.5 \text{ pA}$, $t_{1/2} = 13 \text{ s}$, $Q = 90 \text{ pC}$.

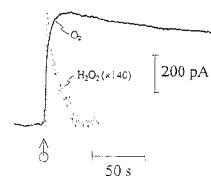


Figure 8. Solid curve: current response of a platinized microelectrode (type 2, −300-nA maximum electrodeposition current) polarized at −0.2 V vs Ag/AgCl during cell intrusion using method B. The vertical arrow indicates the moment of intrusion. The dashed curve is the superimposed current response (enlargement $\times 140$) obtained with a different SV₄₀-transformed fibroblast when the electrode was positioned similarly (method B) but was polarized at +0.6 V vs Ag/AgCl (see text for details).

The response of isolated biological cells was investigated with platinized carbon-fiber microelectrodes (method B) in the presence and absence of dioxygen. The first control experiment (Figure 7, left) consisted of puncturing a cell placed in PBS in equilibrium with the atmosphere. In a second experiment, the dioxygen-saturated PBS solution in the cell-containing Petri dish was exchanged rapidly by a degassed PBS solution and the oxidation current at the same microelectrode was recorded immediately. The current detected was approximately half of that in the control experiment (Figure 7, middle top). Several pairs of experiments gave similar results. When the same series of experiments was performed by degassing the cell containing PBS solution with argon for 10 min, the current responses obtained were less than a few percent of those in the control experiments (Figure 7, middle bottom). In both series of experiments, the degassed PBS solutions were allowed to reequilibrate with the atmosphere for 10 min and the same cell population was examined. The currents detected were identical to those in the control experiments (Figure 7, right).

The dioxygen reduction near the cell surface was monitored at −0.2 V vs Ag/AgCl with a platinized carbon-fiber microelectrode, while the cell membrane was punctured (method B). FIA experiments indicated that dioxygen reduction was detected at −0.2 V vs Ag/AgCl with these microelectrodes. Figure 8 (solid curve) shows the variations of the current detected while the cell membrane was punctured.

DISCUSSION

SV₁₀-transformed diploid human fibroblast cell lines were chosen as a model system for this work since they had been characterized previously with respect to their catalase activity.^{23–25} Two methods were evaluated for their ability to allow the microelectrode to probe the intracellular domain of these fibroblast cells (Figure 1). The main difference between the two was that while method A led to measurements with higher sensitivity, it caused extensive cell damage. The localized cell damage obtained with method B mimicked more closely a cellular intrusion by a particle, a virus, or a bacterium but led to smaller currents (Figures 3 and 4). Besides these differences, the time course and nature of the electrode responses were comparable with the two methods (Figure 3). In addition, in method B less fouling of the electrode surfaces was observed.²⁴

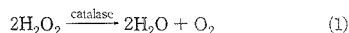
There are several reasons why the oxidative current obtained with method A was larger than with method B. A smaller hole (~1–3- μ m diameter) was created in the cell membrane by the micropipet in method B compared with that produced when the ~20- μ m-diameter type-1 microelectrode was used in method A. Also, in method B the micropipet may have partially blocked diffusion of electroactive species out of the cell by acting partially as a seal. Finally, in method A, the active surface of the electrode was right into the cell being placed at the source of the electroactive material. In this latter case, the collection efficiency should be very close to unity.^{16,30} In method B, the electroactive substance had to diffuse spherically from the hole to reach the microelectrode surface. This led to smaller collection efficiencies than in method A (Figure 3), which decreased further on increasing the electrode–cell distance (Figure 4).^{16,30}

Selectivity of the Biological Measurement. Since transient cyclic voltammetry was not suited here, other avenues were explored to identify the electroactive species released by these biological cells. The first involved amperometric measurements at platinized and nonplatinized carbon-fiber microelectrodes. The response of a platinized and a bare carbon microelectrode (both type 2, method A) are shown in Figure 6. Comparison of the two traces established that they displayed the same time dependence. Thus, the two electrodes were detecting a common species or a combination of different species whose production fluxes were identical. Since we know from the FIA experiments that H₂O₂ resulted in currents that were ~17 000 times larger at the platinized electrode than at the bare carbon one (Table 1), the ratio (~10) between the two signals in Figure 6 showed that the bare carbon electrode was monitoring the flux of a species that was not H₂O₂. The current for ascorbate at the platinized electrode was ~15 times that observed at the bare carbon electrode (Table 1). This was close to the ratio of 10 observed in Figure 6, suggesting that ascorbate may have been the main common species detected at both electrodes.

The following experiment ruled out any significant involvement of ascorbate oxidation. The assembly of a cell and a microelectrode in method B was formally equivalent to a generator–collector electrode assembly.³⁰ We showed in previous studies that the collection efficiency at such assemblies depended strongly on the chemical stability of the species generated at the generator, viz. by the cell here.³⁰ This could be used to identify the species generated at the collector by its chemical reactivity. Thus, a decreased collection efficiency when the collector–generator

interspace contained a specific chemical reagent would indicate that the species produced at the generator reacted significantly with this reagent. The converse would also be true. If ascorbate were a major component of the species emitted by the cell, the electrode current should have decreased drastically when the cell–electrode interspace contained ascorbate oxidase since virtually no ascorbate could have “survived” its trip to the electrode surface through the enzyme solution. The efficiency of the enzyme was demonstrated in the control experiments using bulk ascorbate solutions in the absence of cells. Since the current detected did not depend on the presence of ascorbate oxidase, ascorbate could not be a significant component of the cell release.

Similar experiments were performed to establish that hydrogen peroxide was actually the main species diffusing out of the cell. These were performed with method B, with catalase bathing the cell–electrode interspace. This enzyme catalyzes H₂O₂ disproportionation and is totally selective to hydrogen peroxide, which is the only species identified both as a substrate and as a hydrogen donor:^{31,35,36}



The nearly complete abolition of the microelectrode current under these conditions (Figure 5A, middle) demonstrated that the main species detected at the platinized electrode was H₂O₂. The absence of any artifact due to possible fouling of the electrode by catalase was established as follows. First, the electrode response was restored when the same electrode was used to investigate another cell in the same Petri dish in the absence of catalase (Figure 5A, right). Second, the electrode response for ascorbate was maintained while that for H₂O₂ was suppressed when a bulk solution of catalase was used (without cells). However, it was observed that the current response was not abolished completely in the presence of catalase; a small oxidation current was detected with a time course akin to that observed in the absence of catalase (Figure 5A, middle). This observation is to be paralleled with that made above when the current responses of the bare carbon and platinized electrodes are compared (compare Figure 5A, left and middle, to Figure 6, top and bottom, respectively). This suggested that at least two species were detected at the platinized electrode. The main one (~90%) was H₂O₂, and it was annihilated by catalase.^{31,35,36} The minor one(s) (~10%) was (were) not annihilated by catalase under our conditions and was (were) also electroactive at the bare carbon surface.

Still using the generator–collector analogy, one could devise another means of assessing the nature of the species detected at the collector. This was a transposition of the classical electrochemical method where the flux of the species to be detected at the collector was controlled by varying the potential of the generator.^{30,37} A correlation between the two electrode currents indicated the nature of the species detected. Here, the generator equivalent was the hole formed in the cell membrane. Based on biological data, within this membrane, a natural enzyme, peroxidase, is present and uses hydroperoxides, viz. H₂O₂ and ROOH,

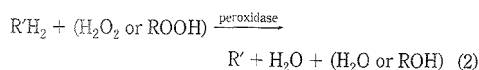
(35) Schonbaum, G. R.; Chance, B. In *The Enzymes*; Boyer, P. D., Ed.; Academic Press: New York, 1976.

(36) Schumb, W. C.; Satterfield, C. N.; Wentworth, R. L. *Hydrogen Peroxide*; Reinhold Publishing Corp.: New York, 1955.

(37) Bartelt, J. E.; Deakin, M. R.; Amatore, C.; Wightman, R. M. *Anal. Chem.* **1988**, *60*, 2167–2169.

(34) Lau, Y. Y.; Wong, D. K. Y.; Ewing, A. G. *Microchem. J.* **1993**, *47*, 308–316.

R = alkyl, to oxidize (-2e, -2H⁺ overall process) organic substrates noted R'H₂ in eq 2.³³ Its efficiency vis a vis H₂O₂ or



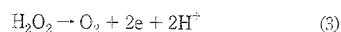
hydroperoxides has been reported to depend severely on the presence of the cosubstrate R'H₂.³³ We confirmed this point, since the electrode response remained unaffected for over 40 s upon using bulk H₂O₂ with horseradish peroxidase alone. In the presence of *o*-dianisidine,³³ the peroxidase activity was considerably enhanced, as evidenced by using bulk H₂O₂ and mixtures of horseradish peroxidase and *o*-dianisidine. Thus, if H₂O₂ or ROOH were released by the cell and a cosubstrate was not present (or present in insufficient amounts), a large fraction of these species would have been allowed to diffuse out of the cell and eventually be oxidized at the electrode surface. Providing a local excess of an enzyme substrate R'H₂ was a means to reduce significantly the flux of hydroperoxide or hydrogen peroxide. When the cell/microelectrode region was bathed with *o*-dianisidine, absolutely no current was detected at the microelectrode (Figure 5B, middle). These experiments, together with those using catalase (Figure 5A), demonstrated that the major (~90%) species detected under our conditions was hydrogen peroxide (annihilated by catalase or cell peroxidase + *o*-dianisidine), while the minor one(s) was (were) alkyl hydroperoxide(s) (~10%, annihilated by cell peroxidase + *o*-dianisidine, but not by catalase). Since hydroperoxides are followup products of hydrogen peroxide,¹² and were only minor components of the cellular release, we wish not to emphasize this distinction hereafter.

Analysis of Current-Time Profiles. Individual measurements were expected to be different because of biological variability (e.g., health and metabolism of the cells, the fact that some cells may have retained an activity over longer time periods than others after intrusion, the size and nature of the hole created in the membrane, the cellular location that was invaded, etc.). They also may have differed because the variability of mechanical movements leading to intrusion into the cell may have affected the local hydrodynamics near the cell. Because of such expected variations, hundred of biological cells were analyzed with different micromanipulator operations (i.e., slow or fast displacement of the electrode or of the micropipet) and three different operators. Interestingly, all current-time profiles were very similar in shape, amplitude, and charge. The figures reported here and the data in Table 2 are representative of this moderate overall variability.

All current responses were spike shaped with half-widths in the range of 3–10 s (Table 2), extending over 30–50 s (method A) or even longer with method B (50–70 s). Using a diffusion coefficient of $0.8 \times 10^{-5} \text{ cm}^2 \text{ s}^{-1}$,³⁶ a 10-s time course corresponded to diffusion over ~100 μm. Such a number was unrealistic by comparison to the cell dimensions ($h \times l \times L = 1 \times 10 \times 20$ in micrometers) even for the maximum cell-electrode distance (5 μm with method B). Therefore, these long time courses must have reflected a slow kinetics of release rather than diffusion. The small size of the membrane hole could have limited the kinetics of release in method B. This hypothesis could, however, be rejected since both methods produced signals with similar half-widths (note that in method A, the electrode surface is directly positioned into the cell). This established that the signals

observed corresponded to the kinetics of production by H₂O₂ by the cell following its injury.

This conclusion was further supported by the large charge detected in each spike. Most of the spikes had a charge area ranging from 0.5 (method A, type 1, Table 2) to 0.1 nC (method A, types 2 and 3, Table 2). Considering that H₂O₂ was the primary species detected, the stoichiometry in eq 3 indicated that this



charge corresponded to the electrolysis of at least 5×10^8 molecules. Considering the cell's dimensions, its inner volume was at most 200 fL. If all the material detected were present initially in the cell, the charge detected would represent an intracellular H₂O₂ concentration of at least 5 mM. This is more than 10 000 times larger than the physiological levels of hydrogen peroxide admissible in a living organism.¹⁴

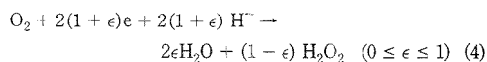
These two observations above implied that H₂O₂ detected represented, for the most part, a *biological response of the cell following its aggression and injury*. Our results appear to be the first *in-time* and *local* (viz., at a single cell) observation of the cellular defense mechanism called *oxidative stress*.

Oxidative Stress Response at a Single Cell. The above rationalization implied that the cells were able to generate considerable quantities of H₂O₂. Dioxygen (whose concentration in the PBS surrounding the cell is 0.25 mM at 25 °C)^{10–14} appeared to be the most natural source of this hydrogen peroxide. To test this hypothesis, we examined the response of cells placed under anaerobic conditions.

When the PBS solution was quickly replaced by a degassed PBS solution, the responses were approximately half of those obtained under aerobic conditions (Figure 7, middle top). This result was compatible with the fact that cells can maintain an aerobic activity for a period of several minutes after a sudden change of the dioxygen concentration.³⁸ However, when the solution surrounding the cell was progressively degassed by argon bubbling (over 10 min), the current detected (Figure 7, middle bottom) was considerably reduced and the charge detected was at least 10–50 times smaller than under aerobic conditions. The cells were observed to be alive after this long anaerobic period and, as soon as aerobic conditions were restored, were capable of responses comparable to those observed before their exposure to anaerobic conditions (compare Figures 7, right and left). The considerable reduction of the response intensity under complete and prolonged anaerobic conditions indicated a dependence between dioxygen availability and the magnitude of the oxidative stress response. The nature of this connection was investigated in the following series of experiments.

The dioxygen concentration near the cell was monitored with a microelectrode held near its surface while its membrane was pierced with a micropipet. In these experiments, the cell and the electrode competed for dioxygen. The microelectrode consumed dioxygen by

(38) Boveris, A. In *Tissue Hypoxia and Ischemia*; Reivich, M., Coburn, R., Lahir, S., Chance, B., Eds.; Plenum: New York, 1977; pp 67–82.



The cell consumed it according to its metabolism and shielded the diffusion of dioxygen to the microelectrode, similar to the situation where two microelectrodes positioned at micrometric distances compete for the same chemical substrate.³⁷ The microelectrode current reflected the importance of the diffusional shielding by the cell, i.e., the rate of dioxygen consumption by the cell. Quantitative analysis³⁰ of the shielding was almost impossible here owing to the geometrical complexity of the system. Qualitatively, an increase of the dioxygen consumption by the cell was expected to result in a decrease of the cathodic current at the microelectrode (as observed in Figure 8). This initial current drop was concomitant with the rise of H₂O₂ as shown by comparison of the solid (O₂ consumption) and dashed (H₂O₂ production, current \times 140) curves in Figure 8. This established that the release of H₂O₂ by the cell corresponded to a sudden rise of its dioxygen consumption, demonstrating again the strong correlation between oxidative stress and dioxygen metabolism. Thus it was puzzling to observe that such a correlation was not maintained at longer times. Dioxygen consumption remained high over a period of several minutes after the H₂O₂ flux had become undetectable (Figure 8). This suggested that the decay of the hydrogen peroxide flux did not reflect at all a suppression of the oxidative stress mechanism.

The following view then emerges: (i) a cell "defends" itself by producing an intense "blast" of H₂O₂; (ii) as a side effect, this provokes a large rise in the intracellular H₂O₂ concentration which (iii) triggers independent cellular systems designed to protect the cell against H₂O₂;³⁹ (iv) scavenging of H₂O₂ by these systems results in an apparent decay of the H₂O₂ flux. Although very speculative, this view seems the only simple one to reconcile our

two data sets. Besides supplying a source for H₂O₂ production, dioxygen would power these simultaneous phenomena that have already been identified by biologists and that require an accelerated metabolism: (i) strong secretion of defense enzymes by peroxisomes;³⁹ (ii) generation of energetic molecules (e.g., ATP) to aid the repair of damages to the cytoplasmic membrane and cytosol;⁴⁰ (iii) progressive cellular death by apoptosis⁴¹ and necrosis.^{38,42}

CONCLUDING REMARKS

Having considered the most obvious possibilities, our combined evidence suggests that the major substance observed in this work is hydrogen peroxide, which is used by these cells to defend themselves. We believe that the use of platinumized carbon-fiber microelectrodes to detect hydrogen peroxide is a major step forward in investigating the biological role of reactive oxygen species at the level of single cells. Using this technique, we have been able to demonstrate for the first time, a defense mechanism (oxidative stress) at the level of a single cell and have been able to investigate its time course. Since oxidative stress is thought to be an important causative agent in several pathologies (e.g., in aging, in some carcinogenesis, in Parkinson or Alzheimer's diseases and possibly in AIDS and several other viral dysregulations, in autoimmune disorders, etc.), we believe that this technique may find an increasing utility in the future.

ACKNOWLEDGMENT

This work was supported in part by MESR, ENS, CNRS (URA 1679, UPR 42, Ultimatch), and the HAS Foundation. P.P. was recipient of a CNRS postdoctoral position. J.A.J. acknowledges the support by UICC during his one-month stay in Paris. Dr. L. Becucci is thanked for her participation with some of the reported experiments during her research stay at ENS in Paris. The authors also thank Prof. W. G. Kuhr for the loan of a FIA-electrochemical cell, and T. J. Schroeder for providing a copy of his data analysis program. We are also indebted to Mrs. A. Benoit and A. Margot for cell culturing. Prof. E. Guyon is acknowledged for his interest in this project and for financial support. We finally thank Prof. R. M. Wightman for stimulating discussions during the earliest stages of this project and for having made available some of his laboratory facilities to M.V. before our own equipment was available.

Received for review April 19, 1995. Accepted July 20, 1995.*

AC950383X

* Abstract published in *Advance ACS Abstracts*, August 15, 1995.

- (39) (a) Christman, M. F.; Morgan, R. W.; Jacobson, F. S.; Ames, B. N. *Cell* **1985**, *41*, 735-762. (b) Darr, D.; Fridovich, I. *Free Radicals Med.* **1995**, *18*, 195-203. (c) Lönitz, W.; Sirsjö, A.; Liu, W.; Lindberg, M.; Rollman, O.; Törnå, H. *Free Radicals Biol. Med.* **1995**, *18*, 349-357.
- (40) (a) Chance, B.; Williams, R. *Adv. Enzymol.* **1956**, *17*, 65-134. (b) Kinkle, P. C.; McCarty, R. E. *Pour Science* **1978**, *7*, 35-53. (French edition of *Sci. Am.*)
- (41) (a) Arends, M. J.; Morris, R. G.; Wyllie, A. H. *Am. J. Pathol.* **1990**, *136*, 593-603. (b) Cohen, J. J. *Hosp. Part.* **1993**, *28*, 35-43. (c) Schwartz, L. M.; Osborne, B. A. *Immunol. Today* **1993**, *14*, 582-590.
- (42) (a) Zimmerman, R.; Chan, A.; Leadon, S. A. *Cancer Res.* **1989**, *49*, 1644-1648. (b) Bast, A.; Haenen, G. R. M.; Doleman, C. J. A. *Am. J. Med.* **1989**, *91*, 2S-13S. (c) Sacks, T.; Moldow, C. F.; Craddock, P. R. *J. Clin. Invest.* **1978**, *50*, 327-337.

Performance Characteristics of Diffusion Gradients in Thin Films for the in Situ Measurement of Trace Metals in Aqueous Solution

Hao Zhang and William Davison*

Environmental Sciences, IEBS, Lancaster University, Lancaster LA1 4YQ, UK

The technique of diffusive gradients in thin films (DGT) provides an in situ means of quantitatively measuring labile species in aqueous systems. By ensuring that transport of metal ions to an exchange resin is solely by free diffusion through a membrane, of known thickness, Δg , the concentration in the bulk solution, C_b , can be calculated from the measured mass in the resin, M , after time, t , by $C_b = M\Delta g/DA t$, where D is the molecular diffusion coefficient and A is the exposure surface area of the membrane. If a sufficiently thick (~ 1 mm) diffusion layer is selected, the flux of metal to the resin is independent of the hydrodynamics in solution above a threshold level of convection. Deployment for 1 day results in a concentration factor of ~ 300 , allowing metals to be measured at extremely low levels (4 pmol L^{-1}). Only labile metal species are measured, the effective time window of typically 2 min being determined by the thickness of the diffusion layer. Because metals are quantified by their kinetics of uptake rather than the attainment of equilibrium, any deployment time can be selected from 1 h to typically 3 months when the resin becomes saturated. The measurement is independent of ionic strength (10 nM – 1 M). For Chelex-100 as the resin, the measurement is independent of pH in the range of 5–8.3, but a subtheoretical response is obtained at pH < 5 where binding to Chelex is diminished. The effect of temperature can be predicted from the known temperature dependence of the diffusion coefficient and viscosity. The application of DGT to the in situ measurement of Cd, Fe, Mn, and Cu in coastal and open seawater is demonstrated, and its more general applicability as a pollution monitoring tool and for measuring an in situ flux, as a surrogate for bioavailability, is discussed.

The technique of diffusive gradients in thin films (DGT) has been recently developed¹ and used to measure labile species quantitatively in situ in freshwater^{2,3} and marine¹ systems. During deployment metal ions are continuously accumulated, in proportion to their bulk concentration, in the chemically and physically well-defined DGT unit. The total amount of metal ions accumulated in a given time is measured after retrieval of the device

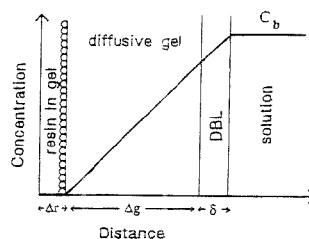


Figure 1. Schematic representation of the free concentration of ionic species in a hydrogel assembly in contact with aqueous solution, where the concentration is C_b (DBL is diffusive boundary layer). The rate of diffusion is assumed to be the same in the gel and solution.

and used to calculate the concentration of labile species present in bulk solution during its in situ deployment. In its applications to trace metals, a layer of polyacrylamide hydrogel of known thickness is backed by a layer of ion-exchange resin (Chelex). The gel and resin layers are so arranged that transport of metal ions to the resin is solely by molecular diffusion (Figure 1). DGT's major advance over previous in situ accumulation techniques, such as ion-exchange resins in dialysis bags,⁴ is that it constrains mass transport. By selection of an appropriated gel layer thickness (~ 1 mm), the mass of accumulated metal ions is independent of the hydrodynamics in solution above a threshold level of convection. Consequently, when DGT devices are deployed in uncontrolled convective regimes, such as rivers, effluents, and the well-mixed surface waters of lakes and seas, the measurements should be fully quantitative and independent of variations in flow. Moreover, because mass transport is so well-defined, there is a precise effective measurement time that can be calculated and used to define the measured species in terms of their lability.⁵ Other virtues of DGT include its simplicity, its automatic facility for providing in situ preconcentration, its multielement capability, and its ability to provide time-averaged mean concentrations when used for long deployment times (days and weeks) in solutions of varying concentration.

These attractive features of DGT have led to its rapid application prior to its complete development. It has been used to provide direct in situ measurements of labile metal species in seawater¹ and to provide the first ever concentration profiles of trace metals in pore waters at a spatial resolution of 1 mm.^{2,3} In its application to sediments it has also been used to measure, for the first time,

(1) Davison, W.; Zhang, H. *Nature* 1994, 367, 545.

(2) Zhang, H.; Davison, W.; Grime, G. W. Proc. of ASTM Symp. on Dredging, Remediation and Containment of Contaminated Sediments, June 1994, Montreal, Canada, in press.

(3) Zhang, H.; Davison, W.; Miller, S.; Tych, W. *Geochim. Cosmochim. Acta.* in press.

(4) Morrison, G. M. P. *Environ. Technol. Lett.* 1987, 8, 393.

(5) Buffle, J. *Complexation: Reactions in Aquatic Systems*; Ellis-Horwood: Chichester, UK, 1988.

in situ fluxes from solid phases to pore waters. There will undoubtedly be numerous other applications, including its extension to other elements by varying the binding agent and its use to provide an integrated record of trace metal concentrations in rivers and effluents. It is essential, however, that these developments are firmly based on a technique that has a well-developed theory validated by experiment. This paper reports the initial characterization of the DGT technique by systematically investigating the effect of varying solution conditions and the parameters of the gel assembly.

PRINCIPLE

Concentration Measurement. The DGT technique is based on Fick's first law of diffusion. An ion-exchange resin (Chelex-100) layer, of thickness, Δr , is separated from the bulk solution by an ion-permeable gel membrane of thickness Δg as shown in Figure 1. Between the gel layer and the bulk solution there is a diffusive boundary layer (DBL) of thickness δ , where transport of ions is solely by molecular diffusion. If δ is negligibly small compared to Δg , the flux (F) of metal ions diffusing through the gel layer to the resin can be expressed by

$$F = D(C_b - C')/\Delta g \quad (1)$$

where D is the diffusion coefficient in the gel, C_b the free concentration of a metal ion in bulk solution, and C' the free concentration of the metal ion in the resin gel layer. If the free metal ions are in rapid equilibrium with the resin, with a large binding constant, C' is effectively zero providing the resin is not saturated. Therefore eq 1 can be simplified to

$$F = DC_b/\Delta g \quad (2)$$

According to the definition of flux ($F = M/At$), the mass (M) diffused through an area (A), after given time (t) should be

$$M = DC_b t A / \Delta g \quad (3)$$

As the mass of ions that have diffused into the resin layer, M , can be analytically determined, the concentration in the bulk solution can be quantified by

$$C_b = M \Delta g / D t A \quad (4)$$

The mass of the diffused ion, M , can be obtained by direct measurement of the ion concentration, C_r , in the resin layer with total volume V_r .

$$M = C_r V_r \quad (5)$$

Direct measurement of the concentration in the resin layer is possible with techniques capable of analyzing solids, such as XRF or PIXE.^{6,7} Alternatively, metal ions in the resin layer can be eluted using a known volume of HNO₃ solution (V_e). The concentration of ions in the acid eluent, C_e , can then be measured by atomic absorption spectroscopy (AAS). In practice (see later),

Table 1. Examples of Theoretically Calculated Preconcentration Factors for DGT^a

deployment period	direct meas (C_r/C_b)	elution meas (C_e/C_b)
1 day	850	270
1 week	5950	1890
1 month	25500	8100

^a Typical values were used for the diffusion coefficient ($D = 1 \times 10^{-6} \text{ cm}^2 \text{ s}^{-1}$), the diffusion layer thickness ($\Delta g = 1 \text{ mm}$), exposure surface area ($A = 19.6 \text{ cm}^2$), resin layer volume ($V_r = 0.2 \text{ mL}$), and gel volume in the resin layer ($V_g = 0.1 \text{ mL}$). The minimum practical eluent acid volume ($V_e = 0.4 \text{ mL}$) was used for a resin layer volume of 0.2 mL.

only a fraction of the bound metal is eluted. The ratio of the eluted to bound metal is known as the elution factor, f_e . Taking the elution factor into account, the mass of diffused ions in the resin layer is

$$M = C_e(V_g + V_e)/f_e \quad (6)$$

where V_g is the volume of gel in the resin gel layer. In practice V_g is often negligible.

In the developmental use of DGT for this work, eq 4 was always used to calculate the bulk concentration. M was obtained as described above, Δg , A , and t were measured, and D was taken to be the value of the molecular diffusion coefficient in water at a given temperature (see later). In routine application at a given temperature, Δg , A , and t may be maintained constant and a calibration plot of M versus concentration, C_b , can be used, as for any analytical method.

One of the attractive features of the DGT technique is its ability to preconcentrate in situ. The metal ions are progressively accumulated in the resin layer as the deployment time is increased. The preconcentration factors, C_r/C_b for direct measurement and C_e/C_b for measurement after elution, were calculated for various deploying times using the above equations (Table 1). If Zeeman furnace AAS, with a typical detection limit of 1 nmol L⁻¹, is used to measure the concentration in the eluent, the detection limit for DGT after 1 day of deployment will be lower than 4 pmol L⁻¹.

Speciation Measurement. The polyacrylamide hydrogel used for the diffusion layer in DGT is commonly used in the electrophoretic separation of proteins where its sievelike structure modifies the extent of migration. The diffusion of large molecules is likely to be affected by the hydrogel in the DGT assembly, but simple metal ions have been shown to diffuse freely with an effective diffusion coefficient indistinguishable from that for the ion in water.⁸ Therefore the DGT technique will measure dissolved species with molecular sizes sufficiently smaller than the pore size of the hydrogel to allow them to diffuse freely through it, as well as a fraction of larger molecules which will be partly impeded.

In common with other analytical techniques such as voltammetry, DGT directly measures a flux, that is, the rate of supply of material in a given time. This rate of supply from solution depends on the kinetics of solution exchange so that DGT measures a labile fraction of species in solution. To appreciate more precisely the

(6) Davison, W.; Grime, G. W.; Morgan, J. A. W. *Nature* **1991**, *352*, 323.

(7) Johanson, S. A. E.; Campbell, J. L. *PIXE—A Novel Technique for Elemental Analysis*; Wiley: New York, 1988.

(8) Davison, W.; Zhang, H.; Grime, G. W. *Environ. Sci. Technol.* **1994**, *28*, 1623.

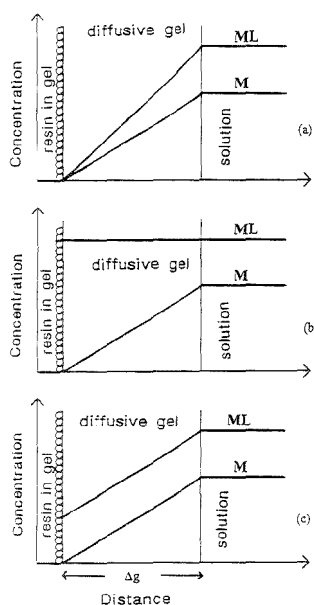


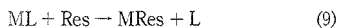
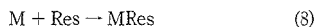
Figure 2. Schematic representation of concentration profiles at the resin layer surface for uptake of M in the presence of complexes ML which are (a) labile, (b) totally inert, and (c) partially labile.

measured species, particular cases will be considered in a scheme analogous to that used for considering complexation measurements by voltammetry.⁵ Speciation in solution can be represented by a simple equilibrium (eq 7) between free metal, M, and ligand,



L, with stability constant, K , where the ligand L is in excess.

In case 1 (labile complex), ligand exchange is very rapid so that effectively both M and ML react rapidly with the receiving resin (Res) (eqs 8 and 9), reducing their concentration at the resin



surface to virtually zero and generating a steady-state linear diffusion gradient in the gel layer (Figure 2a). If the ligand is in great excess, its additional concentration in the vicinity of the resin will not affect further transport of M and L and the DGT device will effectively measure the combined concentration of M and ML.

In case 2 (inert complex), only M reacts with the resin and there is no transfer between ML and M. Only the directly reacting metal, M, is then measured (Figure 2b).

In case 3 (partially labile), M reacts rapidly with the resin (eq 8), but the exchange between ML and M (eq 7) is slow. If ML does not react directly with the resin, the kinetics of ligand exchange determines whether ML will be measured. Providing some dissociation of ML takes place, the concentration of ML will be lowered in the resin layer and some diffusion of ML through the gel will occur (Figure 2c). The extent of the

dissociation and hence the amount of ML measured will depend on the time taken to diffuse through the gel layer. A characteristic reaction time, t , is determined by the mass transport and is given by eq 10.^{5,9} DGT will therefore measure those species that are

$$t = \Delta g^2 / \pi D \quad (10)$$

in labile equilibrium within this time which is determined by the gel layer thickness. For a 0.5 mm gel layer thickness and $D = 7 \times 10^{-10} \text{ cm}^2 \text{ s}^{-1}$, $t = 2 \text{ min}$. Clearly the species measured depends on the gel layer thickness and the rate of diffusion through the gel. For this particular partially labile case, varying the gel layer thickness should provide information about the measured species. If ML reacts directly with the resin within the characteristic reaction time, case 1 is approached and both ML and M are measured. The extreme of no reaction between ML and the resin therefore represents the most distinct example of the partially labile case. When a strong binding agent such as Chelex-100 is used, it can "induce" lability because the functional group, iminodiacetic acid, competes effectively with natural ligands for metal ions.¹⁰ For DGT, where speciation is partly determined by the pore structure of the gel, this competition is an advantage.

EXPERIMENTAL PROCEDURES

Gel Preparation and Mounting. A polyacrylamide hydrogel comprising 15% by volume acrylamide (Boehringer) and 0.3% by volume AcryLAide agarose cross-linker (Flow Gen Instruments Ltd.) was used throughout this work as the diffusive gel layer. For 10 mL of gel solution, 70 μL of freshly prepared ammonium persulfate initiator (10%) and 20 μL of TEMED catalyst were added. The solution was immediately cast between two glass plates separated by plastic spacers and allowed to set at a temperature of $40 \pm 5^\circ \text{C}$. The setting time of typically 45 min is controlled by the temperature and the concentration of initiator and catalyst. Although the reproducibility of pore size production is not easily controlled in polyacrylamide,¹¹ it did not appear to affect the reproducibility of DGT measurements, presumably because the pores are much bigger than the diffusing ions (see Results and Discussion).

The resin gel consisted of 2 g of ion-exchange resin Chelex-100 (Na form, 100–200 wet mesh) in 10 mL of gel solution. Less ammonium persulfate and TEMED were used to prolong the setting process and allow the resin to settle by gravity to one side of the gel as a plane of approximately close-packed beads.

Two types of gel holder were used. They were designed to support the gels and to ensure that a single surface of the diffusive gel was in contact with the solution. Gel holder I (Figure 3a) was constructed from two Perspex plates of 10 cm diameter. The base plate had a 6 cm diameter recess to accommodate the layers of gel. A window of 5 cm diameter in the top plate exposed the gel to solution. A lip around the window fitted with the recess in the bottom plate to provide compression and form a good seal on the gel surface. An O ring between the two plates prevented any lateral leakage of solution when the assembly was held together by six nylon bolts.

Gel holder II (Figure 3b) was based on a simple tight-fitting piston design. It consisted of a backing cylinder and a front cap

(9) Davison, W. J. *Electroanal. Chem.* 1978, 87, 395.

(10) Florence, T. M.; Stauber, J. L. *Agriat. Toxicol.* 1986, 8, 11.

(11) Chramback, A. *The Practice of Quantitative Gel Electrophoresis*; VCH: Weinheim, Germany, 1985.

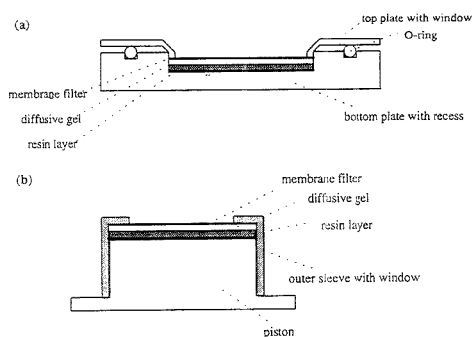


Figure 3. Schematic representation of a section through (a) holder I comprising two Perspex cylindrical plates bolted together and (b) holder II based on a piston design.

with 1.7 cm diameter window. Gels were placed on top of the cylinder, and the front cap was pressed down tightly until a good seal was formed on the gel surface.

All gels were hydrated in MQ water for at least 24 h before use. During this hydration step, the gel expanded to a new stable dimension. The volume of gel increased by a factor of 3.2, and the water content of the gel became $\sim 95\%$. By changing the water several times during hydration, any impurities such as unreacted reagents were removed by diffusion and the pH was lowered, eliminating the possibility of charge buildup within the gel. A layer of resin gel was placed in the recess of holder I or on top of the piston of holder II. The side which contains a plane of close-packed resin beads was arranged to face upward, and a layer of diffusive gel was directly placed on top of it. For most experiments, a 0.4 mm thick resin gel disk was used along with a 0.4 mm thick disk of pure gel. In those experiments where the gel layer thickness was deliberately varied, the thicknesses used are explicitly stated. The hydrated gel layer thickness was measured using a microscope and found to be entirely reproducible within the accuracy of the measuring procedure. For field applications, a 100 μm thick, 0.45 μm pore size Millipore cellulose nitrate membrane was placed on top of the diffusive gel. The filter has been shown to behave like an extension of the gel layer.¹ There was no discernible effect on the overall diffusion coefficient through gel and filter together, but as the filter is relatively thin, small changes in a composite value of D are not easily detectable. The filter was used because in natural waters fine particles have been found to adhere to an exposed gel surface, but not to a membrane filter.

Efficiency of Batch Elution. Chelex-100 (Bio-Rad Laboratories, 100–200 wet mesh, spherical 75–150 μm , capacity 0.4 mequiv mL^{-1} , density 0.65 g mL^{-1} , Na form) was chosen for accumulating trace metals, as it is capable of efficiently concentrating many metals simultaneously.^{12–15} Metal ions had to be eluted from the Chelex embedded in the gel using a batch technique. The efficiency of batch elution was tested for different metal ions (Zn, Cd, Cu, Ni, Fe, Mn) at various concentrations. Stock solutions of 0.5 M $\text{Zn}(\text{NO}_3)_2$, CdCl_2 , CuCl_2 , and NiCl_2 were

prepared by dissolving the appropriate amount of salt in MQ water. For each metal, five different concentrations, from 5×10^{-8} to 2.5×10^{-7} M, were obtained by diluting the stock solutions. The Fe and Mn solutions were prepared freshly, covering the concentration range of 2–10 mg L^{-1} for Fe and 0.3–1.5 mg L^{-1} for Mn. Washed and tissue-dried Chelex resin (0.5 g) was added to 5 mL of each solution in clean screw-top plastic tubes and shaken overnight. After removing the solution, 1 mL of 2 M HNO_3 was added to the residual Chelex-100. The acid–Chelex mixture was capped and left overnight or alternatively shaken for a few hours before analysing by Zeeman furnace atomic absorption spectroscopy (ZFAAS, Perkin Elmer Zeeman 4100 ZL). The concentrations of metal in each solution before and after reaction with Chelex were also analyzed by ZFAAS.

Time Dependence. Gels in holder II were exposed to a solution of 1 $\mu\text{g L}^{-1}$ Cd (CdCl_2 in MQ water) for different time periods up to 10 h. The holders were floating in the solution, which was stirred by bubbling vigorously with N_2 . All the holders were rinsed with MQ water thoroughly before disassembly. The diffusive gel layer was peeled off, and the resin gel layer was placed in a clean plastic tube. A 1 mL aliquot of 2 M HNO_3 was added to the tube to extract metal ions from the resin gel and the concentration of Cd was analyzed by ZFAAS.

Diffusion Layer Thickness. Diffusive gels of six different thicknesses from 0.4 to 2.4 mm were used for this experiment. Gel holder I was used and the gel assemblies with different thickness of diffusive gel were exposed to a solution of 1 $\mu\text{g L}^{-1}$ Cd (CdCl_2 in MQ water) for 10 h. The holders were fixed to the bottom of the container, and the solution was stirred using a magnetic follower.

Temperature, pH, and Ionic Strength. The gel assemblies (holder II) were exposed to CdCl_2 solutions (8 $\mu\text{g L}^{-1}$ Cd) at different temperature ranging from 5 to 35 $^\circ\text{C}$ for known times between 2 and 3 h. The effect of pH was investigated by immersing assemblies (holder II) in CdCl_2 solutions (3 $\mu\text{g L}^{-1}$ Cd) of various acidities (pH 2.3–8.3 in seven increments) for 2 h. The pH was adjusted using dilute HCl and NaOH. To test the effect of ionic strength (10 nM–1 M), gel assemblies (holder II) were exposed for 2 h to CdCl_2 solutions (3 $\mu\text{g L}^{-1}$ Cd) with appropriate additions of NaNO_3 . The gel assemblies (holder II) were exposed for 2 h.

Convection. Gel holder I with 0.4 mm thick diffusive gel layers was used to test the effect of flow velocity. The gel assemblies were immersed in filtered coastal seawater (salinity $\sim 30\%$) containing 2 $\mu\text{g L}^{-1}$ Zn, stirred using a magnetic follower. Four different stirring rates were used, and immersion times were varied from 1 to 10 h. Concentrations of Zn obtained by DGT were compared with concentrations directly measured in the untreated seawater by ASV. A computer controlled electrochemical system Autolab (PSTAT10, DAC124, Ecochimie) was used with a Metrohm electrode (663 VA stand).

Capacity. Gel holder II with a window area of 2.3 cm^2 was used for demonstrating the capacity of DGT for a single ion. The diffusive gel layer thickness was 0.4 mm, and the gel assemblies were immersed in CdCl_2 solution for 10 h at room temperature (20 ± 1 $^\circ\text{C}$). The concentration of CdCl_2 in the immersion solutions was varied logarithmically between 10 nM and 0.01 M.

Field Applications. DGT assemblies were deployed in situ in seawater in the Menai Straits (UK) and in the North Atlantic Ocean (N 49 $^\circ$ 12.57', W 12 $^\circ$ 37.26'). For the Menai Straits (32%

(12) Riley, J. P.; Taylor, D. *Anal. Chim. Acta* **1968**, *40*, 479.

(13) Florence, T. M.; Batley, G. E. *Talanta* **1976**, *23*, 179.

(14) Hart, B. T.; Davies, S. H. R. *Aust. J. Mar. Freshwater Res.* **1977**, *28*, 397.

(15) Figura, P.; McDuffie, B. *Anal. Chem.* **1977**, *49*, 13.

salinity, 14 °C), assemblies were suspended in May 1993 on 0.5 m nylon cords from a floating wooden board a few meters away from the boat. Gel assemblies with a fixed gel layer thickness of 0.4 mm were immersed for different periods from 1 to 6 h while assemblies with different gel layer thicknesses ranging from 0.4 to 2.4 mm were all immersed for 5 h 20 min. The diffusive gel surface was covered by a 100 μm thick, 0.45 μm pore size, cellulose nitrate membrane filter in order to prevent the particles in natural water from adhering to the gel surface. A seawater sample (100 mL) was collected and filtered (0.45 μm membrane) each time a gel assembly was deployed. Samples were acidified to pH 2 using HNO_3 immediately and analyzed in the laboratory by ASV after exposure to ultraviolet irradiation. The gel assemblies were copiously rinsed with MQ water immediately after retrieval from seawater. The resin gel layer was transferred into a clean plastic tube and immersed in 1 mL of 2 M HNO_3 . The concentrations of Zn, Mn, and Fe in the extractant were analyzed by ZFAAS.

For the North Atlantic Ocean, four gel assemblies with different diffusive gel layer thicknesses of 0.4, 0.8, 1.2, and 1.6 mm were fixed in a Perspex plate which was attached to a steel cable. A vane ensured that the assemblies were always upcurrent of the cable. They were deployed in January 1994 at 40 m water depth in the mixed layer (water temperature 11.3 °C) for 1 h 30 min. The gel assemblies were rinsed with MQ water after retrieval and kept in clean polyethylene bags prior to extraction and analysis in the laboratory.

RESULTS AND DISCUSSION

Recovery by Batch Elution. Reproducible elution of trace metal ions from the resin gel layer after deployment of the gel assemblies is crucial to the precision and accuracy of DGT. Metal ions are leached from an ion-exchange resin either by column elution, where a leaching solution passes through a column packed with resin, or by batch elution, where the resin is exposed to an excess of leaching solution. Column elution is the most commonly used method as it is more efficient and gives nearly 100% recovery. Unfortunately, it cannot be used when the resin is incorporated in a gel. Trace metal ions in the resin gel layer were extracted by soaking the gel in a 2 M HNO_3 solution, which is analogous to batch elution.

The recovery efficiency of batch elution using 2 M HNO_3 was investigated for Zn, Cd, Cu, Ni, Mn, and Fe at various concentrations. The experiments were so contrived that all the metal initially added in solution was taken up by the resin. The plots of metal concentration added in the initial solution versus metal concentration found in the eluent are shown in Figure 4. The recovery of trace metal ions from the resin, defined as the ratio of the concentration found to the concentration added times 100, was as follows: Zn, $80.3 \pm 5.5\%$; Cd, $83.9 \pm 2.7\%$; Cu, $79.3 \pm 6.4\%$; Ni, $81.6 \pm 6.9\%$; Mn, $81.4 \pm 2.2\%$; and Fe $69.7 \pm 5.0\%$. Within the error limits, all metal ions investigated except Fe^{2+} had a recovery of 80% irrespective of the amount of metal bound. The lower recovery for Fe^{2+} of 70% may be due to partial oxidation of Fe^{2+} to Fe^{3+} occurring during the ion-exchange process. An elution factor of 0.8 was adopted for the calculation of trace metal concentrations in bulk solution (eqs 4 and 6). The recovery was independent of elution time (1 h–1 week) and did not vary when the acid concentration was increased to 3 M.

Verification of Principles. Values of the diffusion coefficient, D , of metal ions in the gel are required for the calculation of their

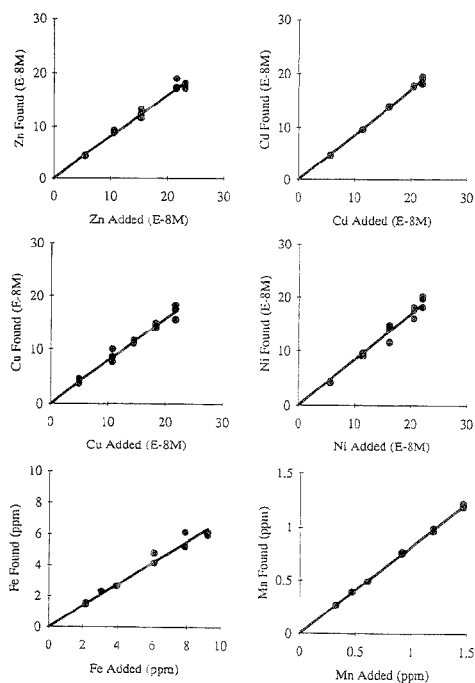


Figure 4. Recovery of trace metals from Chelex-100 in batch experiments.

concentrations in bulk solution using eq 4. Previous work has shown that the diffusion coefficient for Mn^{2+} within gels of the composition used here is effectively the same as in water.⁸ These results are in keeping with those of White and Dorion¹⁶ who found that, in gels of similar composition, the diffusion coefficient for KCl was within 5% of the value measured in water. This virtually unimpeded diffusion is not surprising as polyacrylamide gels are cross-linked, spongelike structures largely comprised of water. The hydrogels used in this work were 95% water when fully hydrated. All of the water is effectively available for diffusion, there being no bound water.¹⁶

Polyacrylamide gel has been commonly used in protein electrophoresis. It acts as a size-selective sieve to separate most proteins, ranging from approximately 2000 to 200 000 Da,¹⁷ which correspond to a molecule size range of about 2–9 nm diameter. The average pore size of gel is determined by the amount of acrylamide and cross-linker used. Throughout this work, a single gel composition was adopted and its pore size was estimated from data based on the mobility of known molecules^{11,17} to be not less than 2–5 nm. Hydrated cations with radii of 0.2–0.3 nm can be expected to move freely through the gels, as has been found to be the case for Mn^{2+} . Therefore, the assumption used in calculations of concentration, that the diffusion coefficient of ions in the gel is equal to their diffusion coefficient in the bulk solution, is reasonable.

(16) White, M. L.; Dorion, G. H. *J. Polym. Sci.* 1961, 55, 731.

(17) Dunn, M. J. *Gel Electrophoresis: Proteins*; Bios Scientific: Oxford, UK, 1993.

Several workers have investigated the diffusion of ions in seawater.^{18–21} The results showed that the diffusion coefficient in seawater is at most only ~8% smaller than that in water at the same temperature. The temperature dependence of diffusion coefficients is linked to the viscosity of water, η , and the absolute temperature, T , by the Stoke–Einstein equation:²⁵

$$(D\eta/T)_{T_1} = (D\eta/T)_{T_2} \quad (11)$$

As the temperature dependence of the viscosity of water is well established,²⁶ the diffusion coefficient of ions in water at different temperature can be calculated. Practically, the viscosity of water over its entire liquid range is represented with less than 1% error by eq 12,²⁷ where t is temperature (in °C). Combining eqs 11

$$\log \frac{\eta_{25}}{\eta_t} = \frac{1.37023(t - 25) + 8.36 \times 10^{-4}(t - 25)^2}{109 + t} \quad (12)$$

and 12, the diffusion coefficient at any temperature, D_t , can be calculated by eq 13, where D_{25} , the diffusion coefficient of ions in

$$\log D_t = \frac{1.37023(t - 25) + 8.36 \times 10^{-4}(t - 25)^2}{109 + t} + \log \frac{D_{25}(273 + t)}{298} \quad (13)$$

water at 25 °C, is well documented.²³

A series of experiments using gel assemblies were performed to test the simple theoretical eqs 1–4 describing DGT. When gel assemblies with fixed exposure surface area and diffusive gel layer thickness were exposed to a stirred solution for different times, the measured mass increased linearly with time (Figure 5a). Gel assemblies with different diffusive gel thicknesses were also exposed to a stirred 1 $\mu\text{g L}^{-1}$ Cd solution for a fixed immersion time. The measured mass of Cd diffused through the gel layer was inversely proportional to the diffusion layer thickness (Figure 5b). In both cases, the experimental data agree well with the theoretical prediction using eq 3. The results confirm the principle and mechanism of the DGT technique and allow eq 4 to be used for calculating bulk concentrations. The good fit of the experimental data to the theoretical line confirms the use of the value of the diffusion coefficient in water.

Effect of Temperature, pH, and Ionic Strength. Diffusion is a process of mass transport across a concentration gradient. The rate of such mass transport depends not only on the concentration gradient but also on the temperature through the variation of the diffusion coefficient, D , with temperature. Although the temperature dependence of D in water is well

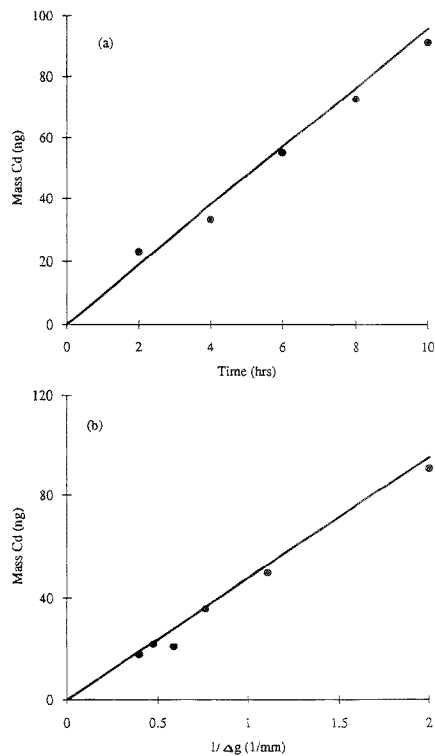


Figure 5. Measured mass of Cd in the resin layer (a) for gel assemblies immersed in a stirred CdCl₂ solution (1 $\mu\text{g L}^{-1}$ Cd) for different times and (b) for gel assemblies with different gel layer thicknesses exposed to CdCl₂ solution (1 $\mu\text{g L}^{-1}$ Cd) for 10 h. The solid lines are predicted by eq 3.

established,^{23,24} it is necessary to investigate the effect of temperature on the diffusion of ions in the gel, as gel properties such as structure and dimension may be altered by temperature and consequently affect the diffusion process. DGT assemblies were deployed in CdCl₂ solution (8 $\mu\text{g L}^{-1}$ Cd) at six different temperature ranging from 5 to 35 °C. The results are shown as a plot of the measured diffusive flux (F) of Cd versus the temperature of the bulk solution (Figure 6). The theoretical line in Figure 6 was obtained by combining eq 2 and eq 11 to give eq 14, where $k = 0.215C_b/\Delta g$, which is constant for a given bulk

$$F = k(T/\eta) \quad (14)$$

concentration and diffusion layer thickness. T is the absolute temperature, and η is the viscosity of water which can be obtained using eq 12. Good agreement between experimental data and the theoretical line (eq 14) in Figure 6 suggests that the structure and dimension of the gel are stable within the tested temperature range. It implies that DGT measurements made in aqueous environments with a temperature within the range of 5–35 °C may be theoretically interpreted using molecular diffusion coefficients measured in water.

(18) Cuddeback, R. B.; Koeller, R. C.; Drickamer, H. G. *J. Chem. Phys.* **1953**, *21*, 589.

(19) Cuddeback, R. B.; Drickamer, H. G. *J. Chem. Phys.* **1953**, *21*, 597.

(20) Benedek, G. B.; Purcell, E. M. *J. Chem. Phys.* **1954**, *22*, 2003.

(21) Horne, R. A.; Frysinger, G. R. *J. Geophys. Res.* **1963**, *68*, 1967.

(22) Wollast, R.; Garrels, R. M. *Nature (London) Phys. Sci.* **1971**, *229*, 94.

(23) Li, Y. H.; Gregory, S. *Geochim. Cosmochim. Acta* **1974**, *38*, 703.

(24) Poisson, A.; Papaud, A. *Mar. Chim.* **1983**, *13*, 265.

(25) Simpson, J. H.; Carr, H. Y. *Phys. Rev. 2nd Ser.* **1958**, *1201*.

(26) Dorsey, N. E. *Properties of Ordinary Water-Substance*; Reinhold: New York, 1940; p 673.

(27) Atkins, P. W. *Physical Chemistry*, 2nd ed.; Oxford University Press: Oxford, UK, 1982.

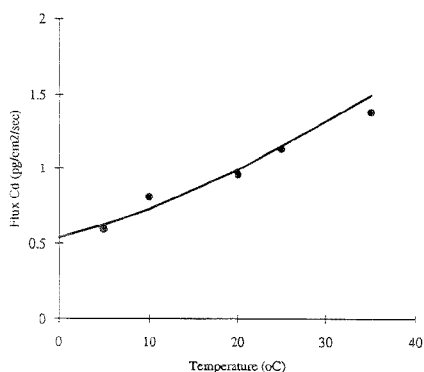


Figure 6. Temperature dependence of the diffusive flux of Cd in CdCl₂ (8 μg L⁻¹ Cd). The solid line represents the theoretical line (eq 14).

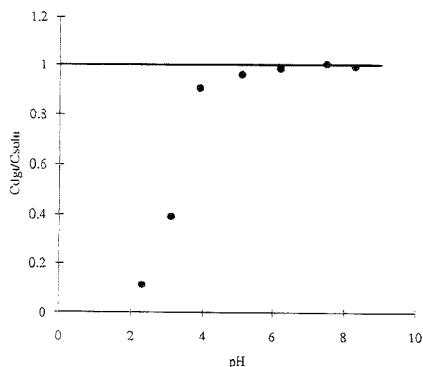


Figure 7. Effect of pH on DGT measurements assessed by the ratio of Cd concentrations measured by DGT (C_{dgt}) to the concentrations obtained by direct ZFAAS measurement in solution (C_{soln}).

The pH of natural waters is usually in the range of 4–9 while industrial effluents may have more extreme values. To assess the pH dependence of the DGT technique, gel assemblies were immersed in CdCl₂ solutions (3 μg L⁻¹ Cd) spanning the pH range of 2.3–8.3. The ratios of Cd concentrations measured by DGT to the concentration obtained by direct ZFAAS measurement were plotted against pH (Figure 7). The ratio of 1 within the pH range 5–8.3 confirms the accuracy of DGT. Most natural waters are within this pH range. Recoveries decrease when the pH of the solution is below 5. Much lower recoveries (less than 15%) were found at pH 2–3. These results are consistent with the properties of Chelex-100 resin, which binds metals less efficiently at low pH.²⁸ A similar pH effect was observed for Zn.¹ The working pH range of DGT could be extended by choosing an ion-exchange resin more suitable for lower or higher pH than Chelex-100.

The effect of ionic strength was investigated by adjusting the ionic strength of a CdCl₂ solution (3 μg L⁻¹ Cd) with NaNO₃ in the range of 10 nM–1 M. The Cd concentrations measured by DGT and directly by ZFAAS were in good agreement for all ionic

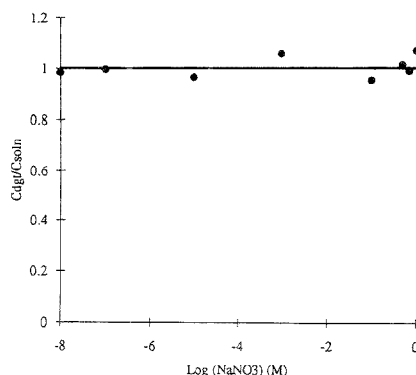


Figure 8. Effect of ionic strength (presented as concentration of NaNO₃) on DGT measurements assessed by the ratio of Cd concentrations measured by DGT (C_{dgt}) to the concentrations obtained by direct ZFAAS measurement in solution (C_{soln}).

strengths. It appears that the concentration measured by DGT is independent of ionic strength (Figure 8). The net diffusion flux (F) of an ion depends on the gradient of chemical potential.²⁹

$$F = -\frac{U C}{Q L} \left(\frac{\partial \mu}{\partial x} \right) \quad (15)$$

where U is mobility of the ion, Q is the charge, C is the molar concentration, and L is Avogadro's number. The chemical potential (μ) of an ion in a real solution is related to its activity (a) by

$$\mu = \mu^{\circ} + RT \ln a \quad (16)$$

where μ° is the standard-state chemical potential. At first sight, diffusion would consequently be expected to be driven by an activity gradient. However, differentiation of eq 16 and combination with eq 15 yields

$$F = -\frac{U C R T}{Q L a} \left(\frac{\partial a}{\partial x} \right) \quad (17)$$

Because the activity coefficient, γ , is constant in $a = \gamma C$, even for nonideal solutions this reduces to the well-known

$$F = -D \frac{\partial C}{\partial x} \quad (18)$$

where the diffusion coefficient, $D = (UL/Q)(RT/L)$. The negative sign indicates that the direction of diffusion is toward decreasing concentration. Therefore, the diffusional flux is proportional to the concentration gradient and independent of the activity coefficient and hence ionic strength. Other investigations have confirmed the virtual independence of the diffusion coefficient on ionic strength (I): the diffusion coefficient in seawater ($I \approx 0.7$) is at most only ~8% smaller than that in water ($I \approx 0$).²⁵

(28) Yates, J. Technical Report TR 181, Water Research Centre, Medmenham, Bucks, UK, 1982.

(29) Moore, W. J. *Physical Chemistry*, 4th ed.; Longmans: Harlow, UK, 1963.

Effect of the DBL. At the surface of any solid body in a flowing solution, such as the gel surface in the DGT assembly, there is a thin zone known as a diffusive boundary layer, where the tangential velocity component undergoes a very abrupt change from a high value at the outer border of the zone to zero at the solid surface.^{30,31} Within the boundary layer, mass transport is solely controlled by molecular diffusion. In practice, diffusion to the resin layer of a DGT assembly will depend on the total thickness of the diffusive gel layer and the DBL (Figure 1).

The factors affecting the thickness of the DBL are known from fluid mechanics for idealized situations. For nonturbulent flow (Reynolds number, $Re < 2 \times 10^{-3}$) parallel to the surface of a flat plate, the average DBL thickness, δ , is approximated by eq 19,

$$\delta = 5\sqrt{(x\eta/\rho\nu)}/2Sc \quad (19)$$

where x is the distance from the leading edge of the plate, η is the dynamic viscosity, ρ is the fluid density, ν is the free-stream velocity, and Sc is Schmidt number which can be obtained by $Sc = \eta/\rho D$. Equation 19 shows that the thickness of the DBL increases as distance x (i.e., size of the gel assembly) increases and it decreases with increasing fluid velocity, ν .

The DBL thickness, δ , between the gel and the bulk solution was neglected in calculations of bulk concentration using DGT (eqs 1–4). The implicit assumption was that it was negligibly small compared to the thickness of the diffusive gel layer. Although definitive data are not available, various estimates suggest the DBL thickness in fast flowing waters, such as rivers, streams, and the well-mixed surface water of lakes and sea, is in the range of 10–100 μm .³² If the diffusive gel layer is 1 mm thick, variation in δ between 10 and 100 μm would at most cause a variation in the measured flux to the resin gel layer of 10% and, hence, a similar uncertainty in any estimate of bulk concentration. By ensuring that the diffusive gel layer is sufficiently thick, the DGT device rather than the solution properties controls the mass transport of metal ions. In flowing solutions, the measurement should be effectively independent of the velocity of water in the bulk solution.

The effect of the DBL on DGT measurements was tested by immersing gel assemblies in stirred seawater containing $2 \mu\text{g L}^{-1}$ labile Zn^{2+} (measured directly by ASV). Gel holder I was used with a total diffusion layer thickness of 0.5 mm. Solutions were stirred at different rates from 0 to 1000 rpm with a 4 cm stirrer bar. At higher stirring rates, concentrations of Zn measured by DGT agreed well with independent ASV measurements (Figure 9), but at lower stirring rates, concentrations of labile Zn were underestimated by DGT, indicating a significant DBL thickness relative to the diffusive gel layer thickness. Rough calculations of the DBL thickness, δ , can be made using eq 19 if it is assumed that the screening effect of the top plate is negligible (Figure 3). The solution velocity is assumed to be that at the tip of the stirrer bar. At 1000 rpm, δ was estimated to be $\sim 45 \mu\text{m}$, $< 10\%$ of the total diffusion layer thickness, while at 110 rpm it was 170 μm ($> 25\%$). These estimates are broadly in line with the observations (Figure 9).

(30) Levich, V. G. *Physicochemical Hydrodynamics*; Prentice-Hall, Inc.: Englewood Cliffs, NJ, 1962.

(31) Welty, J. R.; Wicks, C. E.; Wilson, R. E. *Fundamentals of Momentum, Heat, and Mass Transfer*, 3rd ed.; John Wiley and Sons, Inc.: New York, 1984.

(32) Snodgrass, W. J. In *Sediments and Water Interactions*; Sly, P. G., Ed.; Springer: New York, 1986.

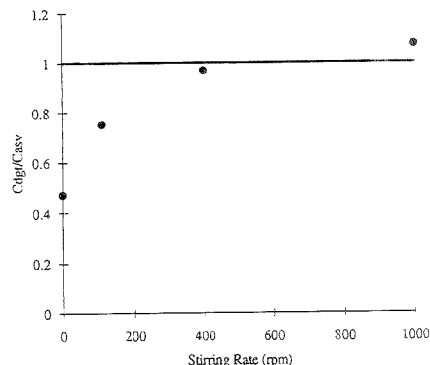


Figure 9. Effect of flow convection (presented as stirring rate) on DGT measurements assessed by the ratio of Cd concentrations measured by DGT (C_{DGT}) to the concentrations obtained by direct ASV measurement in seawater (C_{ASV}).

If the DBL thickness is negligibly small, the mass measured in a given time by DGT should be inversely proportional to the thickness of the diffusive gel layer (eq 20). When holder II was

$$M = DC_b t A / (\Delta g + \delta) \quad (20)$$

used with a stirring rate of 1000 rpm, this was indeed the case (Figure 5). Moreover, the measured mass was theoretically predicted from the known concentration in solution, further indicating that the DBL was negligibly small. Similar results were obtained when holder I was deployed directly in seawater,¹ indicating that in this natural aquatic environment there is sufficient natural convection to allow the use of eq (4) for calculating the bulk concentration. If δ is significant compared to Δg , a plot of M versus $1/\Delta g$ will be nonlinear. In this case, $1/M$ can be plotted against Δg providing the flow velocity is constant. The intercept of this line can be used to calculate δ according to eq 21.

$$\frac{1}{M} = \frac{\Delta g}{DC_b t A} + \frac{\delta}{DC_b t A} \quad (21)$$

The Capacity of DGT. The DGT technique has the potential to be used for long-term (weeks or months) deployment to obtain an integrated record of trace metal concentrations. For such application, the capacity of the resin layer may be a limiting factor. It is controlled by the capacity of the Chelex-100 resin and the amount of Chelex-100 used in the resin layer. In practice, the amount of Chelex-100 is limited to the quantity necessary to form a monolayer adjacent to the diffusive gel layer. The capacity of Gel holder II was measured by immersing gel assemblies with a 0.4 mm diffusive gel layer for 10 h in CdCl_2 solutions at various concentrations of Cd up to 0.01 M. The mass of Cd measured in the resin layer increased linearly with increasing Cd concentration in the bulk solution up to 5×10^{-4} M (Figure 10). At higher concentrations, the measured mass of Cd plateaued at a maximum value of 0.63 mg of Cd. This must represent the maximum capacity of this gel holder, which had a surface area of 2.3 cm^2 . Using the manufacturer's stated capacity, in terms of equivalents

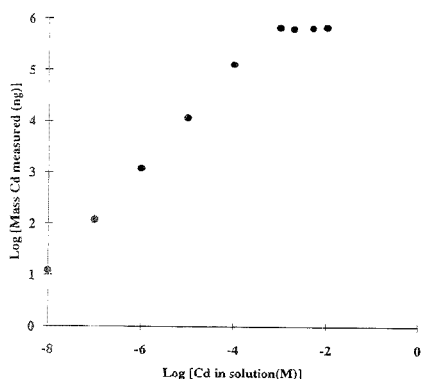


Figure 10. Capacity of DGT presented as a log-log plot of the mass of Cd measured by DGT versus the solution concentration.

per milliliter of Chelex, it was possible to predict the total capacity of the holder. The resulting value of 0.56 mg of Cd was in excellent agreement with the measurement. The linear relationship between mass of Cd measured and concentration in solution (Figure 10) shows that the principles of DGT, which allow calculation of bulk concentrations, are independent of the loading of metal on the resin providing saturation is not reached.

From a practical point of view, it is important to know the maximum immersion time of a DGT device before its capacity is exceeded. The effective DGT maximum accumulation time is independent of surface area but dependent on the other conditions contributing to the flux (eq 3). For a 1 mm thick diffusion layer and an average diffusion coefficient of metal ions of $1 \times 10^{-5} \text{ cm}^2 \text{ s}^{-1}$, its maximum accumulation time can be estimated using eq 3. In a simple solution of metal ions with a total concentration of $1 \times 10^{-3} \text{ M}$, the maximum accumulation time of DGT would be 15 months. Using the typical concentration of Chelex-exchangeable metals in ocean water,²³ the maximum accumulation time of a DGT device in the ocean was estimated to be ~2.5 years. Assuming the average concentration of metal ions in coastal seawater is 10 times higher than those in ocean water, DGT can be expected to provide a 3 month integrated record of trace metal concentrations in coastal environments. Similar maximum accumulation times are likely to apply to unpolluted freshwaters. These calculations do not consider binding of high concentrations of Ca and Mg ions, which trace metals are expected to replace. In practice, the maximum deployment time in natural waters is likely to be limited by microbial attack and biofouling. Trials in synthetic and natural waters will be required to test these effects.

The minimum deployment time where eqs 3 and 4 can be used to interpret the results is 1 h.³ Shorter times could be used if allowance is made for the non-steady-state conditions that apply during the first few minutes of deployment.

Field Measurements. The DGT technique has been used to measure trace metal concentrations in situ in the seawater of the Menai Straits (UK) and the North Atlantic Ocean. In the Menai Straits coastal water, six gel assemblies with a diffusion layer thickness of 0.5 mm were deployed for different time periods (1–6 h) and six gel assemblies with various diffusion layer thicknesses (0.5–2.5 mm) were deployed for 5.33 h. A linear relationship between the mass of diffused ions and the deployment

Table 2. In Situ Mean Concentrations and Standard Deviations ($n = 6$) of Zn, Mn, and Fe (in $\mu\text{g L}^{-1}$) Measured by DGT in the Menai Straits (UK) (Salinity 32‰, Temperature 14 °C)^a

	time series	thickness series
Zn	0.77 ± 0.04	0.73 ± 0.03
Mn	6.76 ± 0.50	6.27 ± 0.42
Fe	3.74 ± 0.21	3.60 ± 0.23

^a Data are presented for a series of measurements using different deployment times (time series) and a series using different gel layer thickness (thickness series).

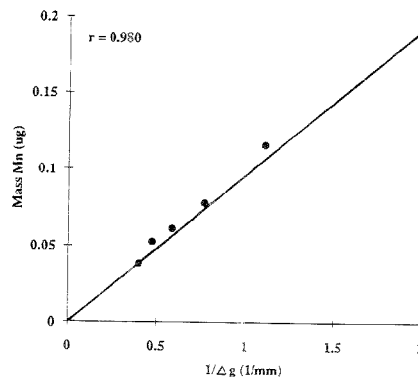


Figure 11. Measured mass of Mn in the resin layer as an inverse function of the diffusion layer thickness (combined gel and filter layer) for gel assemblies exposed to seawater (Menai Straits, UK, salinity 32‰, 14 °C) for 5.33 h.

time was found for the measured Zn, Mn, and Fe. The mean concentrations from these time-dependent measurements were very reproducible (Table 2). The mass of ions measured in the resin layer was inversely proportional to the diffusion layer thickness for Mn (Figure 11). As the tidal current varied from 0 to ~4 knots during the deployment, the thickness of the DBL is expected to vary as well. Consequently good linearity in Figure 11 indicates that the gel thickness is dominating the control of mass transport and that the DBL thickness is negligibly small. In other words, there is sufficient natural convection in this natural water to support the use of DGT. Mean concentrations obtained from the diffusion layer-dependent measurements were in excellent agreement with those from the time-dependent measurements (Table 2).

The total dissolved concentration of Zn was also measured by ASV after acidification and UV irradiation of filtered samples collected at hourly intervals during the DGT deployment. Its value of $1.72 \pm 0.18 \mu\text{g L}^{-1}$ was higher than the DGT measured concentration of $0.77 \pm 0.04 \mu\text{g L}^{-1}$. The difference is to be expected as DGT only measures labile species and therefore excludes kinetically inert organic species and large colloids.

The concentration of Cu in the North Atlantic water at 40 m depth was measured by DGT by deploying four assemblies with different gel thicknesses. Again plots of measured mass against $1/\Delta g$ are linear, showing that there was adequate natural convection for the use of DGT. The mean value of $0.15 \pm 0.01 \mu\text{g L}^{-1}$

Cu is comparable with typical concentrations in ocean water.³²

CONCLUSIONS

DGT has been shown to be a robust technique for in situ measurements. By simply controlling the mass transport to a binding agent, such as Chelex resin, it is possible to quantify the accumulated metal in terms of a measured flux or concentration. The equations which predict that the mass of accumulated metal ions per unit area is proportional to deployment time and inversely proportional to the thickness of the diffusion layer have been verified. The well-defined diffusion layer is a major factor in determining the measured species. Only those species are measured which react directly with the binding agent or, within an effective measurement time determined by the diffusion layer thickness, are in labile equilibrium with the reacting species. Above a threshold level of flow, the rate of accumulation of ions is independent of flow. The measurement of Cd by DGT using Chelex as a resin binding agent is independent of ionic strength (10 nM–1 M). Within the limits of the Chelex resin, which binds less effectively below pH 5, it is also independent of pH. The temperature dependence can be predicted from the known temperature dependence of diffusion coefficients and viscosity. Because metal ions are preconcentrated in situ in the resin layer, contamination problems associated with trace metal sampling and handling are greatly reduced, the final analysis is less demanding, and very low detection limits (pM) are possible. Metals are quantified according to their kinetics of uptake, so deployment times can vary from as little as 1 h to several months. The capacity of the resin is such that the device should still provide quantitative results when it is deployed for 3 months in coastal seawater.

This work briefly demonstrates the ability of DGT to make in situ speciation measurements of trace metals in coastal and open

seawater. It has also been applied to the measurement of trace metals in fresh waters and the pore waters of sediments.^{2,3} The measurements in pore waters can in some cases be interpreted as concentrations and in others they provide a direct in situ measurement of the flux of metal from solid phase to solution.³ Further applications can easily be envisaged. So far it has only been applied to the measurement of trace metals, but in principle it could be applied to any solution species that can be rapidly bound. Work in progress has shown phosphate can be quantitatively measured by DGT when an iron oxide binding agent is used. When concentrations vary during deployment, DGT provides a time-averaged mean concentration. It could therefore be used in streams and effluents to provide an integrated measurement of mean element concentrations over selected periods from days to months. Fully quantitative interpretation is only possible, however, if temperature is relatively constant (± 2 °C), the pH remains within the working range of the resin, and there is always adequate solution flow. DGT always measures a flux which is then interpreted as a concentration. In some cases, it is the flux which is required. The example of solid phase to solution fluxes in pore waters has already been mentioned. When the bioavailability of a nutrient or trace element is being assessed, the local or in situ flux is important. Therefore, DGT may be a useful tool for assessing bioavailability in situ in soils and sediments where the resupply from solid to solution phase must be considered.

ACKNOWLEDGMENT

We are grateful to Dr. Peter Statham for deploying the assemblies in the Atlantic water and to the NERC for providing financial support.

Received for review May 15, 1995. Accepted August 14, 1995.*

AC9504676

(33) Bruland, K. W. In *Chemical Oceanography*; Riley, J. P., Chester, R., Eds.; Academic Press: London, 1983; Vol. 8, p 157.

* Abstract published in *Advance ACS Abstracts*, September 1, 1995.

Identification of the Positional Isomers of 2-Fluorobenzoic Acid 1-O-Acyl Glucuronide by Directly Coupled HPLC–NMR

Ulla G. Sidelmann,^{1,†} Claire Gavaghan,[†] Howard A. J. Carless,[†] R. Duncan Farrant,[§] John C. Lindon,[§] Ian D. Wilson,^{||} and Jeremy K. Nicholson^{*†}

Department of Chemistry, Birkbeck College, University of London, Gordon House, 29 Gordon Square, London, WC1H 0PP, U.K., Department of Physical Sciences, Wellcome Research Laboratories, Langley Court, Beckenham, Kent, BR3 3BS, U.K., and Department of Safety of Medicines, Zeneca Pharmaceuticals, Alderley Park, Macclesfield, Cheshire, SK10 4TG, U.K.

Directly coupled HPLC–¹H NMR was used in the “stop-flow” mode to separate and rapidly identify an equilibrated mixture of ester glucuronide isomers formed spontaneously by intramolecular rearrangement reactions (internal acyl migration and mutarotation) of 2-fluorobenzoic acid β -1-glucuronide (1-O-(2-fluorobenzoyl)-D-glucopyranuronic acid). The equilibrated mixture of isomers was obtained by incubation of the synthetic 2-fluorobenzoic acid glucuronide in buffer solution (pH 7.4) at 25 °C for 24 h. The β -anomer of the 1-O-acyl glucuronide, and the 2-, 3-, and 4-positional glucuronide isomers (all three as both α - and β -anomers) present in the equilibrium mixture, were all characterized after separation in an isocratic chromatographic system containing phosphate buffer at pH 7.4 and 1% acetonitrile in the mobile phase. The HPLC–NMR investigations also elucidated the mutarotation of the positional glucuronide isomers as well as showing the benefits of the HPLC–NMR technique as a primary analytical tool. This HPLC–NMR method will be of particular value in studies on the acyl migration reactions of nonsteroidal antiinflammatory drug glucuronides which may be related to their toxicological properties.

It has been shown that NMR spectroscopy of biofluids can serve as an effective approach for the detection and identification of endogenous and xenobiotic metabolites.^{1,2} However, for such complex mixtures the direct hyphenation of NMR with liquid chromatography can offer clear benefits as metabolites can be separated and characterized directly.^{3–8} Recent advances in NMR

probe technology, improved dynamic range of receiver systems, and solvent suppression methods have resulted in major practical improvements in the HPLC–NMR technique,^{3,4} resulting in increased sensitivity and decreasing the need for deuterated organic modifiers in the eluent. In the present study, we show that HPLC–NMR in the “stop-flow” mode can be used to study a complex mixture of isomers that interconvert spontaneously in aqueous solution, i.e., acyl glucuronides that undergo reversible acyl migration and mutarotation reactions.

Many carboxylate-containing drugs form β -1-O-acyl glucuronic acid conjugates in vivo. The acyl glucuronides formed are potentially reactive metabolites due to the susceptibility of the acyl group to nucleophilic reactions. They have been shown to undergo hydrolysis (regeneration of parent compound),^{9,10} intramolecular rearrangement (isomerization by acyl migration),^{11,12} and covalent adduct formation with both low molecular weight nucleophiles (such as methanol) and proteins.^{11,13–15} In the rearrangement reactions of acyl glucuronides, the susceptibility of the ester linkage to nucleophilic reactions allows the drug moiety to move from one hydroxyl group to an adjacent hydroxyl group on the glucuronic acid ring (Scheme 1). The mechanism of transacylation via a tetrahedral cyclic ortho ester intermediate is well established.^{16,16–21} The acyl groups migrate from C-1

[†] University of London.

[§] Current address: Department of Analytical and Pharmaceutical Chemistry, The Royal Danish School of Pharmacy, Universitetsparken 2, DK-2100 Copenhagen, Denmark.

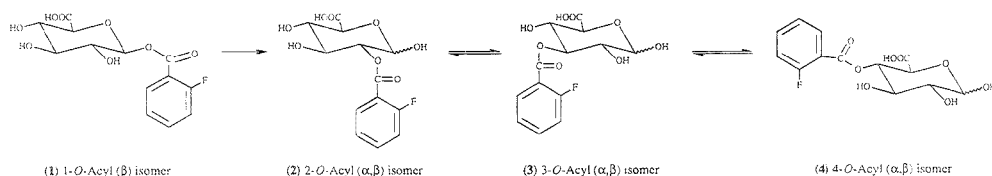
^{||} Wellcome Research Laboratories.

^{*} Zeneca Pharmaceuticals.

- (1) Nicholson, J.; Wilson, I. *Prog. NMR Spectrosc.* **1989**, *21*, 449–501.
- (2) Farrant, R. D.; Salman, S. R.; Lindon, J. C.; Cupid, B. C.; Nicholson, J. J. *Pharm. Biomed. Anal.* **1993**, *11*, 687–692.
- (3) Spraul, M.; Hofmann, M.; Dvorsak, P.; Nicholson, J. K.; Wilson, I. *J. Pharm. Biomed. Anal.* **1992**, *8*, 601–605.
- (4) Spraul, M.; Hofmann, M.; Dvorsak, P.; Nicholson, J. K.; Wilson, I. *Anal. Chem.* **1993**, *65*, 327–330.
- (5) Lindon, J. C.; Nicholson, J. K.; Spraul, M.; Hofmann, M.; Nicholson, J. K.; Lindon, J. C. *J. Chromatogr.* **1993**, *617*, 324–328.

- (6) Spraul, M.; Hofmann, M.; Wilson, I.; Lenz, E.; Nicholson, J. K.; Lindon, J. C. *J. Pharm. Biomed. Anal.* **1993**, *11*, 1009–1016.
- (7) Seddon, M. J.; Spraul, M.; Wilson, I.; Nicholson, J. K.; Lindon, J. C. *J. Pharm. Biomed. Anal.* **1994**, *12*, 419–424.
- (8) Spraul, M.; Hofmann, M.; Lindon, J. C.; Farrant, R. D.; Seddon, M. J.; Nicholson, J. K.; Wilson, I. *NMR Biomed.* **1994**, *7*, 295–303.
- (9) Spahn-Languih, H.; Benet, L. Z. *Drug Metab. Rev.* **1992**, *24*, 5–48.
- (10) Smith, P. C.; Song, W. Q.; Rodriguez, R. J. *Drug Metab. Dispos.* **1992**, *20*, 962–965.
- (11) Bradow, G.; Kan, L. S.; Fenselau, C. *Chem. Res. Toxicol.* **1989**, *2*, 316–324.
- (12) King, A. R.; Dickinson, R. G. *Biochem. Pharmacol.* **1991**, *42*, 2289–2299.
- (13) Smith, P. C.; McDonagh, A. F.; Benet, L. Z. *J. Clin. Invest.* **1986**, *77*, 934–939.
- (14) Smith, P. C.; Benet, L. Z.; McDonagh, A. F. *Drug Metab. Dispos.* **1990**, *18*, 639–644.
- (15) Weiss, J. S.; Guatam, A.; Lauff, J. J.; Sundberg, M. W.; Jatlow, P.; Boyer, J. L.; Saligson, D. N. *Engl. J. Med.* **1983**, *309*, 147–150.
- (16) Bradow, G.; Kan, L. S.; Fenselau, C. *Chem. Res. Toxicol.* **1989**, *2*, 316–324.
- (17) Blanckaert, N.; Compennolle, F.; Leroy, P.; Van Houtte, R.; Fevery, J.; Heirwegh, K. P. M. *Biochem. J.* **1978**, *171*, 203–214.
- (18) Haines, A. H. *Adv. Carbohydr. Chem. Biochem.* **1976**, *33*, 11–109.
- (19) Goebel, W. F. *J. Biol. Chem.* **1938**, *122*, 649–653.
- (20) Doerschuk, A. P. *J. Am. Chem. Soc.* **1952**, *74*, 4202–4203.
- (21) Fischer, E. *Chem. Ber.* **1920**, *53*, 1621–1633.

Scheme 1. General Scheme for the Acyl Migration of 1-*O*-(2-Fluorobenzoyl)- β -D-glucopyranuronic Acid (1)



toward C-4 on the glucuronic acid ring forming both the α - and β -anomers of the 2-, 3-, and 4-*O*-acyl positional isomers as shown in Scheme 1. All the reactions are reversible except for the reformation of the 1-*O*-acyl glucuronide, presumably because of the higher energy barrier to formation of the anomeric C–O bond. Mutarotation ($\alpha \leftrightarrow \beta$) of the isomers occurs via the open-chain aldehyde structure of the sugar ring. The acyl migration reactions occur spontaneously in aqueous solution, the isomerization rates being highly dependent upon the structure of the aglycon, pH, and temperature.¹² Acyl migration is inhibited under acidic conditions, but the migration rates increase dramatically with increasing pH; however, mutarotation occurs at all pH values studied (pH 3–8.5).¹²

Previously in studies on drug glucuronide reactivity, it would have been necessary to separate compounds and later analyze them off-line, during which time complete mutarotation and possibly further acyl migration rearrangements would have occurred. The analytical challenge presented here is to develop a system that would allow direct detection and, hence, signal assignment of each glucuronide isomer in an isocratic HPLC–NMR system at pH 7.4. We present here a novel HPLC–NMR approach for the separation and identification of the positional isomers (2–4) of the acyl glucuronide of 2-fluorobenzoic acid (1-*O*-(2-fluorobenzoyl)- β -D-glucopyranuronic acid, 1) and their corresponding α - and β -anomers as an example of a glucuronide isomer mixture.

EXPERIMENTAL SECTION

Chemicals. All chemicals were of analytical chemical grade and purchased from Aldrich Chemical Co. Ltd. (U.K.).

Synthesis of 2-Fluorobenzoic Acid β -1-Glucuronide (1). Benzyl 2,3,4-tri-*O*-benzyl glucopyranuronate (5) was synthesized according to the literature.^{22–24} 5 (200 mg, 0.37 mmol) and trichloroacetonitrile (0.37 mL, 3.7 mmol) were dissolved in dry dichloromethane (5 mL) under N_2 at room temperature. Sodium hydride (8 mg, 0.259 mmol, 80% in oil) was added under reflux, and the reaction was stirred for 15 min. Solvent was removed to yield a brown oil residue (0.376 g), which was purified by silica gel chromatography [petrol–ether (1:1)] to yield benzyl [1-*O*-trichloroethanimodoyl]-2,3,4-tri-*O*-benzyl-D-glucopyranuronate (6), a semicrystalline yellow residue (0.118 g, 46%). 6 (0.2 mmol) and 0.4 mmol of 2-fluorobenzoic acid were dissolved in dry dichloromethane (4 mL) under $Ar(g)$ at $-20^\circ C$. Boron trifluoride etherate (2 drops) was added, and the reaction was left at $-20^\circ C$ for 48 h. The reaction mixture was washed with $NaHCO_3$ (20

mL, 10% w/v) and distilled water (20 mL). The organic extract was dried ($MgSO_4$) and filtered, and the solvent was removed to yield a residue that after purification by silica gel chromatography [petrol–ether (1:1)] gave the 2,3,4-tri-*O*-benzyl-1-*O*-(2-fluorobenzoyl)- β -D-glucopyranuronate (7). 7 was deprotected by hydrogenation to give 1-*O*-(2-fluorobenzoyl)- β -D-glucopyranuronic acid (1; yield 34%). The structure of the compound synthesized was confirmed to be 1 by 1H NMR: 1H NMR (D_2O) δ 7.29 (t, H5, aromatic), 7.24 (m, H3, aromatic), 8.00 (m, H6, aromatic), 7.66 (m, H4, aromatic), 5.77 (d, H1', β -glucuronide), 3.63 (t, H2', β -glucuronide), 3.52 (m, H3', β -glucuronide), 3.60 (m, H4', β -glucuronide), 3.86 (d, H5', β -glucuronide).

Establishment of the Equilibrium Mixture of the 2-Fluorobenzoic Acid Glucuronide Isomers. A 1.5 mg sample of 1 was incubated in 1 mL of potassium phosphate buffer (100 mM) at pH 7.4, $25^\circ C$, for up to 24 h. The equilibration was followed by HPLC: when the relative amounts of the positional isomers had stabilized, the sample was stored at $-20^\circ C$ until further analysis.

Analytical Chromatography. The HPLC system consisted of a Bruker LC22C pump (Rheinstetten, Germany) and a Bischoff 1000 Lambda variable-wavelength UV detector (operated at 200 nm). The outlet of the UV detector was connected to the HPLC–NMR flow probe via an inert poly(ether ketone) capillary (0.25 mm i.d.). A column oven was used for thermostating the column at $25^\circ C$. Data were collected using the Bruker Chromstar HPLC data system. Analysis was performed on a Knauer column (120 \times 4.6 mm, i.d.) packed with Spherisorb ODS-2 (Phase Separations Ltd.), $5\ \mu m$. The final mobile phase developed for the separation of 2-fluorobenzoic acid glucuronides and their positional glucuronide isomers was acetonitrile–0.2 M potassium phosphate (pH 7.4)–deuterium oxide (1:10:89, v/v/v), with a flow rate of 1 mL/min.

NMR Spectroscopy. The HPLC–NMR data were acquired using a Bruker AMX-600 spectrometer equipped with a 1H flow probe (cell of 3 mm i.d., with a volume of 100 μL). 1H NMR spectra were obtained in the stop-flow mode²⁵ at 600.14 MHz. In order to suppress the solvent signals, the 1D 1H NMR spectra were acquired using a pulse sequence based on a one-dimensional version of the nuclear Overhauser effect spectroscopy experiment (NOESYPRESAT),²⁶ with double presaturation for suppression of the water and the acetonitrile signals. Free induction decays (FIDs) were collected into 32K computer data points with a spectral width of 7246 Hz, 90° pulses were used with an acquisition time of 2.26 s, and the spectra were acquired by accumulation of 128 scans. Prior to Fourier transformation, an exponential

(22) Schmidt, R. R.; Grundler, G. *Synthesis* 1981, 835–837.

(23) Van Boeckel, C. A.; Delbressine, L. P. C.; Kaspersen, F. M. *Recl. Trav. Chim. Pays-Bas* 1985, 104, 259–265.

(24) Gavaghan, C.; Carless, H. A. J.; Nicholson, J. K. unpublished work, 1995.

(25) Nicholson, J. K.; Foxall, P. J. D.; Spraul, M.; Farrant, R. D.; Lindon, J. C. *Anal. Chem.* 1995, 34, 793–811.

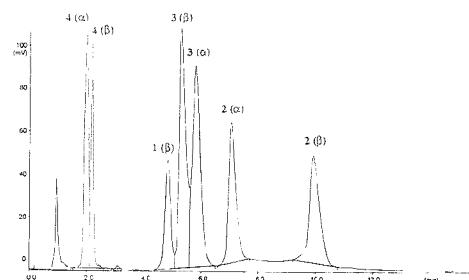


Figure 1. Resulting chromatogram of 1-*O*-(2-fluorobenzoyl)-*D*-glucopyranuronic acid (1), its 2-, 3-, and 4-positional isomers (2–4), and their α - and β -anomers. The isomers eluted with the following retention times (in minutes): $t_{R, 1-O-acyl(\alpha)}$ isomer = 1.99, $t_{R, 4-O-acyl(\beta)}$ isomer = 2.19, $t_{R, 1-O-acyl(\beta)}$ isomer = 4.84, $t_{R, 3-O-acyl(\beta)}$ isomer = 5.31, $t_{R, 3-O-acyl(\alpha)}$ isomer = 5.80, $t_{R, 2-O-acyl(\alpha)}$ isomer = 7.05, $t_{R, 2-O-acyl(\beta)}$ isomer = 9.91. Chromatographic system: Spherisorb ODS2 column, 5 μ m (120 \times 4.6 mm i.d.), mobile phase, CH₃CN–D₂O–KH₂PO₄ (0.2 M, pH 7.4) 1:89:10 by volume; flow rate, 1 mL/min; UV detection (200 nm); column temperature, 25 $^{\circ}$ C.

apodization function was applied to the FID corresponding to a line broadening of 1.1 Hz.

RESULTS AND DISCUSSION

Chromatography. An HPLC method was developed in order to separate the equilibrium mixture of 2-fluorobenzoic acid 1-*O*-acyl glucuronide and the 2–4 positional glucuronide isomers as well as the α - and β -anomer of each isomer. As the method is intended to be used to investigate the individual acyl migration rates of the 1-*O*-acyl glucuronide and its 2–4 positional glucuronide isomers, the pH of the buffer in the mobile phase was titrated to pH 7.4. The HPLC method was designed to keep the solvent systems as simple as possible to reduce problems with solvent suppression in the HPLC–NMR experiment.

A reversed phase ODS-2 column was chosen, as the glucuronides are very polar compounds and are ionized at pH 7.4; only small amounts of organic modifier are needed to elute the analytes from the column. Acetonitrile was chosen as organic modifier, as methanol can obscure the acyl migration rates by methanolysis.²⁶ A flow rate of 1 mL/min is most optimal with respect to filling the NMR flow cell.

The resulting optimized mobile phase contained 1% acetonitrile, and this enabled optimal resolution of the 2-fluorobenzoic acid 1-*O*-acyl glucuronide and its 2–4 positional glucuronide isomers as well as the α - and β -anomers. The chromatogram, obtained by UV detection, resulting from injection of 75 μ g of 2-fluorobenzoic acid glucuronides in total, can be seen in Figure 1.

¹H HPLC–NMR Identification of the Chromatographic Peaks. Identification of the different peaks in the HPLC chromatograms was achieved by one-dimensional ¹H proton HPLC–NMR in the stop-flow mode. Assignment of the NMR resonances for the various structures from the seven HPLC peaks of the equilibrium mixture (seen in Figure 1) is summarized in Table 1. The numbering system of the protons used for assignment of the ¹H signals resulting from the glucuronide isomers and anomers of 2-fluorobenzoic acid glucuronide is indicated in Figure

Table 1. ¹H NMR Chemical Shifts of the Positional Isomers of 2-Fluorobenzoic Acid 1-*O*-Acyl Glucuronide Obtained by Stop-Flow HPLC–NMR Analysis^a

isomer	t_R	aromatic protons (δ , pattern)				glucuronic acid protons (δ , pattern)				
		3	4	5	6	1'	2'	3'	4'	5'
4- <i>O</i> -acyl (α)	1.99	7.21	7.62	7.27	7.94	5.25	3.68	3.99	5.07	4.27
		dd	m	t	m	d	dd	t	t	d
4- <i>O</i> -acyl (β)	2.19	7.21	7.62	7.27	7.94	<i>b</i>	3.39	3.81	5.09	3.93
		dd	m	t	td		t	t	t	d
1- <i>O</i> -acyl (β)	4.84	7.24	7.66	7.29	8.00	5.77	3.63	3.52	3.60	3.86
		m	m	t	m	d	t	m	m	d
3- <i>O</i> -acyl (β)	5.31	7.23	7.63	7.28	7.98	<i>b</i>	3.80	5.20	3.55	3.83
		t	m	t	t		t	t	t	d
3- <i>O</i> -acyl (α)	5.80	7.23	7.63	7.28	7.98	5.27	3.85	5.38	3.78	4.17
		t	m	t	t	d	dd	t	t	d
2- <i>O</i> -acyl (α)	7.05	7.24	7.64	7.29	7.96	5.45	4.93	4.00	3.60	4.10
		dd	m	t	t	d	dd	t	t	d
2- <i>O</i> -acyl (β)	9.91	7.24	7.64	7.29	7.96	4.89	4.92	3.80	3.61	3.75
		dd	m	t	m	d	t	t	t	d

^a t_R refers to the retention time (min) in the chromatographic run. An HPLC–NMR experiment was performed in the stop-flow mode. All δ -values are in ppm. The splitting patterns of the ¹H NMR signals are indicated as follows: m, multiplet; d, doublet; dd, doublet of doublets; t, apparent triplet; td, triplet of doublets; ^b Not observed (obscured by H₂O resonant, δ 4.75).

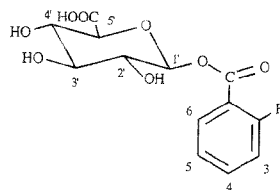


Figure 2. Numbering scheme for the protons of the 1-*O*-(2-fluorobenzoyl)-*D*-glucopyranuronic acid (1).

2. The 4-*O*-acyl isomers eluted first from the chromatographic column, the α -anomer eluting before the β -anomer. The β -anomer of the 1-*O*-acyl isomer eluted next, followed by the 3-*O*-acyl isomers, this time the β -anomer before the α -anomer. Finally, the 2-*O*-acyl isomers were eluted, the α -anomer before the β -anomer as seen with the 4-*O*-acyl isomers. In Figure 3, the ¹H NMR spectra obtained from peaks corresponding to 4 α , 3 α , and 2 α in Figure 1 are shown and compared with the ¹H NMR spectrum obtained from the equilibrium mixture.

The mutarotation rates were fast in comparison to the acyl migration rates. In the situation where all peaks were to be measured by NMR in a single chromatographic run, the later eluting peaks underwent mutarotation while they were stopped on the analytical column (in the stop-flow mode) and the two peaks corresponding to the α - and β -anomer of the 2-*O*-acyl isomer turn into four peaks, as can be seen in the chromatogram in Figure 4. The α - and β -anomers separate into two peaks on the first major part of the analytical column. When the flow is stopped, the α - and β -anomers are still on the column and they mutarotate into their respective equilibrium mixtures α/β , which then, as the flow is started again, separate into two new peaks. As there is only a minor part of the column left, this results in four peaks. The chromatographic peak shape corresponding to the β -anomer of the 3-*O*-acyl isomer is also obscured as it is converting into its α -anomer when the flow is stopped. Even in the second peak of the 4-*O*-acyl isomer (its β -anomer), traces of the α -anomer can

(26) Salmon, M.; Fenslau, C.; Cukier, J. O.; Odeil, G. B. *Life Sci.* **1973**, *14*, 2069–2073.

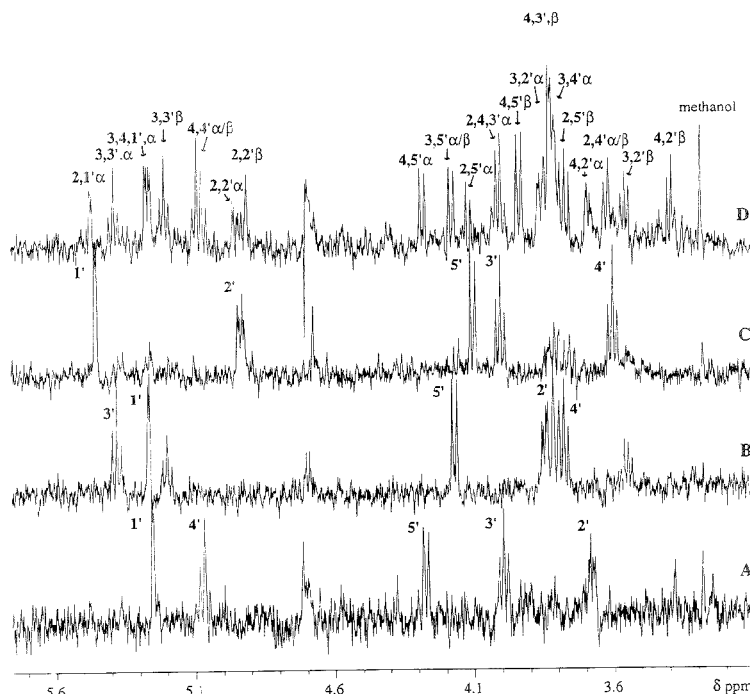


Figure 3. ^1H NMR spectra obtained from the chromatographic peaks: (A) peak corresponding to the α -4-*O*-acyl isomer, (B) peak corresponding to the α -3-*O*-acyl isomer, and (C) peak corresponding to the α -2-*O*-acyl isomer shown and compared with (D) the ^1H NMR spectrum obtained from the equilibrium mixture.

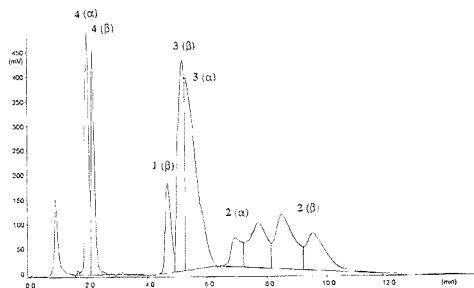


Figure 4. Resulting chromatogram of the 1-*O*-(2-fluorobenzoyl)-*D*-glucopyranuronic acid (1), its 2-4 positional isomers (2-4), and their α - and β - anomers resulting from the HPLC-NMR experiment in the stop-flow mode. Time on the column for the 2-*O*-acyl isomers (last eluting peaks) was approximately 90 min. For identification of peaks, see Figure 1. Chromatographic system: Spherisorb ODS2 column, 5 μm (120 \times 4.6 mm i.d.); mobile phase, $\text{CH}_3\text{CN}-\text{D}_2\text{O}-\text{KD}_2\text{PO}_4$ (0.2 M, pH 7.4) 1:89:10 by volume; flow rate, 1 mL/min; UV-detection (200 nm) and column temperature, 25 $^\circ\text{C}$.

be seen in the ^1H NMR spectrum in amounts that cannot be accounted for by chromatographic peak overlap.

In order to identify the last three peaks eluting from the HPLC column, a further chromatographic injection was made (skipping NMR acquisition of the first four peaks). Because of their longer retention times, there was still a significant amount of on-column mutarotation of the α - and β -anomers of the 2-*O*-acyl isomers.

Furthermore, as their chromatographic peaks were broader compared to the other isomers, the concentration of the isomer in the NMR flow probe was low. This had a detrimental effect on the signal-to-noise ratios of the NMR spectra, thus demanding longer NMR scanning times. In order to determine the elution order of the α - and β -anomers of the 2-*O*-acyl isomer, the amount of organic modifier in the mobile phase was increased (5% acetonitrile instead of 1%). Under these conditions, the 2-*O*-acyl isomers eluted with retention times of 3.5 and 4 min for the α - and β -anomers, respectively, and thereby allowing their structure assignment by HPLC-NMR.

We have demonstrated that directly coupled HPLC-NMR can be a highly effective analytical tool in situations that would otherwise require the extremely time-consuming purification of seven compounds that are in dynamic equilibrium and are constantly interconverting. HPLC-MS would be unrevealing in this situation as it is insensitive to the detection of positional isomerism. The HPLC-NMR approach to studying acyl migration should therefore be of considerable value in the investigations of drug glucuronide reactivity and related protein binding and toxicological problems.

Received for review April 18, 1995. Accepted July 26, 1995.*

AC950379L

* Abstract published in *Advance ACS Abstracts*, August 15, 1995.

Side Excitation of Fluorescence in Ultrathin Slab Gel Electrophoresis

Danhua Chen,[†] Mark D. Peterson,[†] Robert L. Brumley, Jr.,[†] Michael C. Giddings,[†] Eric C. Buxton,[†] Michael Westphall,[†] Lloyd Smith,[‡] and Lloyd M. Smith*[†]

Department of Chemistry, University of Wisconsin, Madison, Madison, Wisconsin 53706, and Lawrence Berkeley Laboratory, Berkeley, California 94720

Recent work has demonstrated the advantages of ultrathin slab gel electrophoresis for fluorescence-based automated DNA sequence analysis. The increased heat transfer efficiency of the thin (typically 50–100 μm) gels permits higher electric fields to be employed with concomitant increases in separation speed. Issues arise, however, in introducing the laser beam used for fluorescence excitation into the thin gels. This paper presents methods for bringing the excitation beam into the thin gels from the side. This permits a low-power air-cooled argon ion laser source to be utilized and produces much lower fluorescence and scattering background than alternative approaches. The beam is effectively trapped between the plates due to the high efficiency of reflection at the low-angle grazing incidence of the beam. A theoretical model describing beam throughput was developed which agrees well with experimental observations. In this model, attenuation of the beam intensity is attributed to four factors: aperturing at the entrance of the gel; reflective losses upon entrance into the gel; scattering during transmission through the gel; and reflective losses occurring upon successive "bounces" of the beam from the glass interface during propagation of the beam.

Electrophoresis in thin gels provides increased heat transfer efficiency, permitting larger electric fields to be employed with correspondingly more rapid separations.^{1,2} This is of particular interest in the area of fluorescence-based automated DNA sequence analysis, where there is a tremendous need for increased throughput from sequencing instruments.³ Kostichka et al. demonstrated an order-of-magnitude increase in separation speed for fluorescence-based DNA sequencing in ultrathin slab gels.⁴ In their work, 18 samples were loaded across an 18 mm width of a 75 μm ultrathin gel, which was cooled from the bottom with a

water jacket. The horizontal sequencing gel was illuminated from above with a beam from an argon ion laser. The beam was expanded into a line across the gel perpendicular to the direction of DNA migration using a cylindrical lens system, and directed into the gel at Brewster's angle, $\sim 34^\circ$ from the horizontal, to minimize reflections from the glass surface and to maximize light entering the gel.

Although this means of exciting the fluorescence was adequate for proof of principle, the approach has two major problems. First, ~ 2.5 W of 514 nm laser power was employed to excite fluorescence across the 18 mm region imaged. To excite fluorescence over the 75 mm width available in the electrophoresis cell with a comparable excitation power density, a much larger and more expensive laser would be needed. The size and expense of the laser source would compromise substantially the utility of the technology for routine sequence analysis. Second, the passage of the excitation beam through the glass plates and coolant excites considerable fluorescence and scattering leading to a high background signal. This high background signal increases noise and thereby decreases the detection sensitivity of the system.

An alternative approach to fluorescence excitation in DNA sequence analysis is to bring the excitation laser beam into the gel from the side^{5,6} (Figure 1). This permits a comparable excitation power density to be obtained from a much lower power laser, as the excitation beam cross section is much smaller. It also greatly decreases background light, as the beam does not pass through the glass or coolant exciting background. This approach has been used successfully for conventional sequencing gels about 400 μm in thickness and is employed in commercial sequencing instruments from Hitachi and Pharmacia. However, the fundamental properties of Gaussian laser beams introduce problems when one tries to pass the beam through an ultrathin gel. The tighter the focus of the beam, the shorter the distance over which the focus can be maintained. For example, beam profiles calculated as described in ref 7 show that in free space the beam diameter can only be maintained below 71 μm over a region 2×7.6 mm = 15.2 mm long (see Table 1). Also, a good

[†] University of Wisconsin.

[‡] Lawrence Berkeley Laboratory.

(1) Drossman, H.; Luckey, J. A.; Kostichka, A. J.; D'Cunha, J.; Smith, L. M. *Anal. Chem.* **1990**, *62*, 900–903.

(2) Brumley, R. L.; Smith, L. M. *Nucleic Acids Res.* **1991**, *19*, 412–4126.

(3) Hankapiller, T.; Kaiser, R. J.; Koop, B. F.; Hood, L. *Science* **1991**, *254*, 59–67.

(4) Kostichka, A. J.; Marchbanks, M. L.; Brumley, R. L.; Drossman, H.; Smith, L. M. *Bio/Technology* **1992**, *10*, 78–81.

(5) Ansorge, W.; Sproat, B.; Stegmann, J.; Schwager, C.; Zenke, M. *Nucleic Acids Res.* **1987**, *15*, 4593–4602.

(6) Kambara, H.; Nishikawa, T.; Katayama, Y.; Yamaguchi, T. *Bio/Technology* **1988**, *6*, 816–821.

(7) Self, S. A. *Appl. Opt.* **1983**, *22*, 658–661.

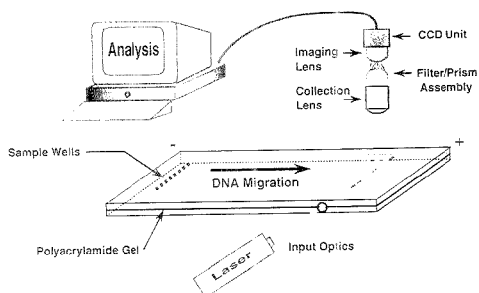


Figure 1. Overview diagram of fluorescence-based ultrathin slab gel electrophoresis system. The electrophoresis plates are 10 cm wide by 30 cm long, and the distance from the sample well to the detection region is 20 cm (see refs 1 and 2 for a more complete description).

Table 1. Depth of Focus (DOF) Calculations

beam width at focus ^a (μm)	F (calcd) ^b (mm)	DOF ^c (mm)	beam width at edge of DOF (μm)
1	2.0	3.1	1.4
10	20	310	14
25	50	1.9	35
50	99	7.6	71
75	150	17	110
100	200	31	140
150	300	69	210
200	400	120	280

^a The beam width at focus is taken as $2w_0$, where w_0 is the beam half-width at the waist; in the case of a round beam, w_0 is the beam radius (eq 5). ^b F is the focal length of the lens, which is dependent upon the spot size required. ^c Depth of focus is defined here as the distance to where the beam diameter is the square root of 2 times larger than it is at the beam waist.

quality optical interface has to be incorporated into the electrophoresis cell to permit the excitation light to be directed into the gel without distortion or loss. We describe here input optics and an optical interface that permit the laser excitation beam to be introduced into an ultrathin slab gel with high efficiency and reproducibility and little distortion. The high efficiency of grazing incidence reflection is shown to effectively trap the beam between the glass plates, resulting in a high throughput of the laser energy. The beam properties are characterized experimentally and theoretically with good agreement.

EXPERIMENTAL SECTION

Optics. Figure 1 shows an overview diagram of the fluorescence-based horizontal ultrathin slab gel electrophoresis sequencing system employed for these experiments. The system consists of a laser excitation source, input optics for the laser excitation beam, a gel electrophoresis assembly, collection-imaging optics, and a CCD detector and associated computer system. The present system differs from that previously described¹ in that it employs a larger area CCD chip (1024×1024 pixels, Tektronix 1024 TKS, Princeton Instruments Inc., NJ) and the prism-wedge assembly (Broomer, Islip, NY) was assembled into a single unit rather than as two separate pieces. The fluorescence collection lens is a Hasselblad (150 mm, $f/2.8$) and is used in conjunction with a secondary Nikkor lens (50 mm, $f/1.2$) to provide a demagnification of 3; thus an objective area 3 in. across is imaged onto the 1 in. CCD detector. In addition, the input optics have been redesigned

to permit the excitation beam to enter the gel from the side, as described in detail below. Critical factors include (a) cleanly introducing the beam into the gel with minimum loss or scattering, (b) minimizing the width of the beam across the gel, in order to maximize resolution of the DNA fragments,^{8,9} and (c) minimizing power loss as the beam propagates through the gel.

Parts A-C of Figure 2 show diagrams of the input optics and electrophoresis cell. An Omnicrome multiline argon ion laser (American Laser Corp., Salt Lake City, UT) operating primarily at 514 and 488 nm with a waist (Gaussian beam radius at $1/e^2$ intensity) of 0.298 mm was used for these experiments. The beam is directed into a spherical lens (No. BK7 PCX, $\phi = 25.4$ mm, $f = 200$ mm, Newport Corp., Fountain Valley, CA) positioned to focus at the center of the gel (Figure 2B). A second cylindrical lens (No. BK7 CKX 100, $\phi = 50.8$ mm, $f = 100$ mm, Newport) focuses the beam further only in the vertical direction to a spot coinciding with the side of the glass plates holding the gel. Thus, the focused beam has two waists: a vertical waist at the entrance to the glass plates and a horizontal waist centered in the gel. The location of the vertical waist minimizes aperturing losses at the entrance to the gel, whereas the location of the horizontal waist minimizes the beam width across the gel to the extent permitted by the Gaussian beam properties.

The small acrylamide chamber shown in Figure 2 provides an optical interface for entry of the laser beam into the gel. The chamber consists of a piece of plexiglass 3.4 cm wide \times 0.6 cm thick \times 1.5 cm high into which a rectangular notch 0.9 cm wide \times 1.2 cm high has been milled to yield a U-shaped piece. A fused-silica microscope slide 0.96 mm thick (the entrance window) glued to one side closes that side of the chamber, and a 0.85 mm thick silicon rubber gasket cut to the same shape as the plexiglass is glued to the other to provide a seal. The chamber (gasket side toward the gel) is placed against the side of the gel and secured by means of two thumbscrews affixed to the electrophoresis cell assembly. The electrophoresis cell glass plates thus form the back wall of the entrance chamber. In this region, the spacer material that separates the two plates (defining the gel thickness) has been removed (for further detail on the process of gel preparation see ref 10). During the gel-pouring process, the freshly prepared and as yet unpolymerized polyacrylamide solution seeps from between the glass plates into the chamber. Additional gel solution is added to the chamber to fill it after the seepage has slowed. Polymerization of the gel material in the chamber occurs in parallel with that between the plates, thus forming a continuum of gel material between the chamber and the electrophoresis cell. The edges of the upper and lower electrophoresis cell plates are beveled to a 45° angle at the position of beam entry and derivatized by a 2 min treatment with a solution of 0.5% [γ -(methacryloxy)propyl]-trimethoxysilane (Sigma Chemical Co., St. Louis, MO) in 20:1 ethanol-acetic acid to increase adhesion of the gel to the glass. This treatment stabilizes the gel-glass interface, which must be intact for proper entry of the laser beam between the glass plates. The laser beam enters the chamber perpendicular to the entrance window with the waist of the laser beam in the vertical dimension positioned at the back wall formed by the upper and lower gel

(8) Luckey, J. A.; Smith, L. M. *Anal. Chem.* 1993, 65, 2841-2850.

(9) Luckey, J. A.; Norris, T. B.; Smith, L. M. *J. Phys. Chem.* 1993, 97, 3067-3075.

(10) Smith, L. M.; Brumley, R. L.; Buxton, E.; Giddings, M.; Marchbanks, M.; Tong, X. High Speed Automated DNA Sequencing in Ultrathin Slab Gels. In *Methods in Enzymology*, in press.

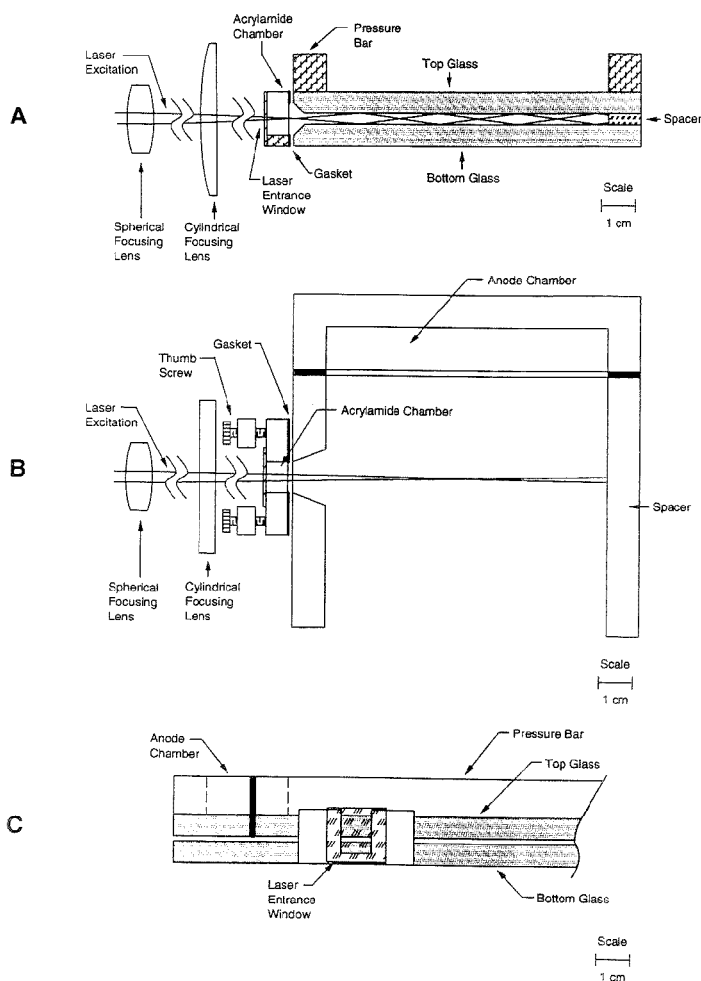


Figure 2. Diagram of input optics and optical interface.

plates. Gels employed in these studies were 4% total acrylamide with 5% bisacrylamide cross-linker and 7.5 M urea, unless otherwise specified.

Beam Attenuation Measurements. To measure the fraction of excitation light that passes through the gel, in some experiments, a second optical interface on the opposite side of the gel was employed to permit exit of the excitation beam. The power was measured with a Newport Model 820 laser power meter before entering and after exiting the gel. In the latter case, to exclude light propagating through the glass plates from being measured as well, a pinhole aperture adjusted to the beam size was placed directly in front of the power meter photosensor. The gel is usually bubble free. In rare cases, bubbles appear in the area where the laser beam passes through. In this case, either the laser beam is moved to an adjacent position to avoid scattering caused by the bubbles or a new gel is prepared. Relative standard

deviations for the beam throughput measurement are generally ~1–2%.

Gel Scattering Measurements. The amount of beam attenuation due to scattering of the excitation light in the gel was measured as follows: five 13 mm i.d. glass tubes, 1, 2, 5, 10, and 20 cm in length, were used to measure the scattering loss. A microscope cover glass (No. 12-540A, Fisher Scientific Corp., Pittsburgh, PA) was glued at one end of each tube with silicone sealant (Dow Corning Corp., Midland, MI). The polyacrylamide gel mixture was prepared and poured into each tube. A second microscope cover glass was affixed to the other end of the tubes using petroleum jelly (Anderson Laboratories, Inc., Fort Worth, TX). Gel polymerization was allowed to proceed for 2 h or more. The collimated (unfocused) beam of the argon ion laser was passed through each gel tube along the long axis, and the beam intensity before and after passage through the gel was measured

with the power meter for several different tube lengths. Control experiments using pure water instead of acrylamide gel were also performed. The decrease in beam intensity results from reflective losses at the two windows as well as scattering losses during propagation through the gel. Both gel and water showed the expected logarithmic relationship between tube length and the amount of light lost by scattering. The logarithmic relationship is consistent with Beer's law, $A = -\log(I/I_0) = \epsilon bC$, and the data yield values for ϵC of 0.00478 cm^{-1} for gel ($r^2 = 0.996$) and 0.000434 cm^{-1} for water ($r^2 = 0.972$). With this information, the loss due to scattering of the laser beam as it passes through the slab gel is readily calculated.

Refractive Index Measurements. An ABBE-3L refractometer (Milton Roy Co., Rochester, NY) was used to measure refractive indexes (RIs) of both polymerized and unpolymerized acrylamide gels containing varying amounts of urea and acrylamide. Gel solutions were prepared without added TEMED catalyst and the RIs of the unpolymerized solution were measured. Subsequently, TEMED was added and the gel was allowed to polymerize overnight. Since polyacrylamide gels polymerize poorly when in contact with air, the tubes were cut in half and slices were taken from the middle of the gel to minimize the effects of contamination by unpolymerized gel. For RI measurements, each slice was pushed between the two glass plates of the refractometer, breaking the slice up into fragments. In three sets of measurements, each of 10 gels, the relative standard deviation of the measured RI was less than 0.03%, similar to that obtained from pure liquids. This high degree of reproducibility confirms the absence of a problem due to air bubbles or other artifacts resulting from the disruption of the gel when placed into the refractometer cell. Calibration of the refractometer with distilled water yielded an RI of 1.3325, reasonably close to the literature value of 1.3330 for room-temperature water.¹¹ The results of duplicate measurements in which urea and acrylamide concentration are varied were obtained. The RI was found to be linearly dependent upon the concentrations of both polyacrylamide and urea, with observed values of 1.404, 1.405, 1.406, 1.409, and 1.413 at 3.5, 4, 5, 6, and 8% total polyacrylamide (of which 5% is bisacrylamide cross-linker; urea held fixed at 7.5 M) and 1.377, 1.385, 1.392, 1.401, and 1.405 at 4, 5, 6, 7, and 7.5 M urea (total polyacrylamide held fixed at 4%), respectively. A value of 1.405, corresponding to a 4% acrylamide gel containing 7.5 M urea, was used for the refractive index of the gels employed in the experiments described here.

THEORY

To be able to employ from-the-side fluorescence detection effectively for these ultrathin gel systems, it is essential that the laser excitation beam be introduced into and propagated through the gel with minimal loss of power. The electrophoresis cell employed is 10 cm wide, and desirable gel thicknesses are in the range of 50–100 μm .¹ The values in Table 1 show the problem that arises in trying to maintain such a tightly focused Gaussian beam over an extended region. For example, as mentioned above, a Gaussian beam focused to a 50 μm diameter diverges to 71 μm only 7.6 mm away in free space; thus, maintaining the beam diameter below 71 μm can only be accomplished for a region 1.5 cm long, much less than the desired 10 cm. This observation

suggests that it is not feasible to utilize from-the-side excitation in such thin gels without an unacceptable attenuation in power due to the spreading and subsequent decreased power density in the beam.

This result is in contrast, however, to visual observations made on the system. Using the input optics and optical interface described above, the laser beam does enter the gel cleanly and to the eye appears to propagate across the gel without excessive loss. Total internal reflection is not the explanation for this, as the gel RI of 1.4045 is less than 1.517 RI of the BK7 glass plates.

An alternative possibility considered was that the laser beam is reflecting off of the gel–glass interface with high efficiency due to the low angle of incidence. Reflection efficiency calculations using the Fresnel equations (see, for example, ref 12) were consistent with this idea. For example, at an angle of incidence of 0.7 mrad, 99.32% of the incident radiation will reflect from the gel–glass interface, using the refractive indexes above. To explore this hypothesis further, it was of interest to calculate the predicted transmission of the excitation beam through the gel, which would involve a number of successive reflections, with a certain loss from each reflection. These calculations are as follows:

Beam Throughput Calculations. A ray entering the gel at a given angle will be attenuated at each gel–glass interface reflection by an amount which may be calculated using the Fresnel equations: The number of bounces N is given by

$$N = l\theta/\alpha \quad (1)$$

where l is the width of the gel, θ is the ray input angle, and α is the gel thickness. The reflection efficiency of this ray is given by the Fresnel equations, which to first order in small grazing angle yield

$$E_r^2 = E_0^2(1 - 4\epsilon\theta)$$

$$\epsilon_{\perp} = \frac{n_1}{(n_2^2 - n_1^2)^{1/2}} \quad (\perp \text{ polarization})$$

$$\epsilon_{\parallel} = \left(\frac{n_2^2}{n_1^2}\right) \left[\frac{n_1}{(n_2^2 - n_1^2)^{1/2}}\right] \quad (\parallel \text{ polarization}) \quad (2)$$

where E_r is the reflected electric field amplitude, E_0 is the incident electric field amplitude, n_1 is the gel refractive index, and n_2 is the glass refractive index. The total transmission efficiency for this ray after N bounces is then given by

$$\begin{aligned} \left[\frac{E_r^2}{E_0^2}\right]^N &= \left[1 - \frac{4\epsilon\alpha N}{l}\right]^N \\ &= \left[\left(1 - \frac{4\epsilon\alpha N}{l}\right)^{1/4\epsilon\alpha N}\right]^{(4\epsilon\alpha N)^2} \\ &\approx e^{-(4\epsilon\alpha N)^2} \quad \text{for } \left[\frac{4\epsilon\alpha N}{l}\right] \ll 1 \\ &= e^{-(\theta^2/2\alpha^2)} \quad \text{where } \sigma = \left[\frac{\alpha}{8\epsilon l}\right]^{1/2} \end{aligned}$$

(11) *CRC Handbook of Chemistry and Physics*, 68th ed.; Weast, R. C., Ed.: CRC Press, Inc.: Boca Raton, FL, 1987–88; p E-372.

(12) Schwartz, M. *Principles of Electrodynamics*; McGraw-Hill Book Co.: New York, 1972; p 268.

$$\sigma_{\parallel} = (n_1/n_2)\sigma_{\perp}$$

$$\sigma_{\perp} = \left[\frac{\alpha(n_2^2 - n_1^2)^{1/2}}{8n_1^2} \right]^{-1/2} \quad (3)$$

The focused Gaussian laser beam may be thought of as a collection of such rays (plane waves) moving in directions given by \vec{k} with amplitudes $f(k_x, k_y, k_z)$. Thus

$$E = \int d\vec{k} e^{i(\omega t - \vec{k} \cdot \vec{r})} f(k_x, k_y, k_z) \quad (4)$$

If z is the direction of propagation of the Gaussian beam and y is the direction perpendicular to the gel-glass interface, the angle of interest is $\theta = k_y/k$ (small angles). The problem is to determine the density of waves as a function of θ . It is possible to find f in the general elliptical case, but, as discussed by Yariv,¹³ the x and y behavior can be considered separately. Without loss of generality, we will treat the case of a round beam with waist at $z = 0$. A convenient starting point is obtained from eq 6.8-7 of Yariv, with the parameter q_0 set equal to iz_0 .

$$E = e^{-ikz} e^{-\ln(1+z/iz_0)} e^{(-ik/2)(x^2+y^2)/(z+iz_0)}$$

$$= \frac{iz_0}{z+iz_0} e^{-izx} e^{(-ik/2)(x^2+y^2)/(z+iz_0)} \quad \text{where } z_0 = \pi w_0^2 n/\lambda \quad (5)$$

Here w_0 is the beam radius at the waist, n is the index of refraction, and λ is the wavelength. The Fourier transform of this expression is

$$f(k_x, k_y, k_z) = \frac{iz_0}{(2\pi)^3} \int dz \frac{e^{i(k_z - k)z}}{z + iz_0} \iint dx dy e^{i(k_x x + k_y y)} e^{(-ik/2)(x^2+y^2)/(z+iz_0)}$$

$$(6)$$

yielding upon integration

$$f(k_x, k_y, k_z) = \frac{1}{2\pi} \frac{z_0}{k} e^{-iz_0(k_x^2 + k_y^2)/2k} \delta \left[k_z - \left(k - \frac{k_x^2 + k_y^2}{2k} \right) \right] \quad (7)$$

In this integration the beam is treated as if it were propagating through free space; that is, the confining effect of the glass plates was neglected. Equation 7 may be further integrated over k_x and k_y to yield an expression for $f(k_z)$,

$$f(k_z) = \left(\frac{z_0}{2\pi k} \right)^{1/2} e^{-k_y^2 z_0/2k} \quad (8)$$

The ray density $d\rho$ as a function of angle θ is given by

$$d\rho = f(k_z) dk_y \quad (9)$$

Substituting $k_y = k\theta$ yields

$$d\rho = \left(\frac{kz_0}{2\pi} \right)^{1/2} e^{-kz_0\theta^2/2} d\theta \quad (10)$$

To get the total decrease in laser beam intensity after multiple bounces, square the electric field and multiply the number per unit angle (eq 10) by the loss at that angle (eq 3).

$$\frac{I}{I_0} = \left(\frac{kz_0}{2\pi} \right)^{1/2} \int_{-\infty}^{\infty} d\theta e^{-(1/2)kz_0\theta^2} e^{-(\theta^2/2\sigma^2)} \quad (11)$$

Here I_0 is the incident beam intensity and I is the attenuated beam intensity after passage between the plates. Solving the integral yields a final expression for the decrease in beam intensity

$$\frac{I}{I_0} = \left[1 + \frac{2}{k^2 w_0^2 \sigma^2} \right]^{-1/2} \quad (12)$$

Angular Alignment Error. Equation 12 gives an expression for the throughput of excitation light when the axis of propagation of the Gaussian beam lies in the horizontal gel plane. In a real optical system there may be, however, some misalignment of the beam. It is therefore of interest to evaluate the effect of alignment error upon beam throughput. In this case eq 11 becomes eq 13, with θ replaced by $\theta - \theta_0$, where θ_0 is the error in direction.

$$\frac{I}{I_0} = \left(\frac{kz_0}{2\pi} \right)^{1/2} \int_{-\infty}^{\infty} d\theta e^{-(1/2)kz_0(\theta - \theta_0)^2} e^{-(\theta^2/2\sigma^2)} \quad (13)$$

This yields upon integration

$$\frac{I}{I_0} = \left[1 + \frac{2}{k^2 w_0^2 \sigma^2} \right]^{-1/2} e^{-(1/2)(k^2 z_0^2 \theta_0^2 / (2 + k^2 w_0^2 \sigma^2))} \quad (14)$$

The additional attenuation of the beam caused by misalignment is contained in the exponential factor, the preexponential factor being identical to eq 12.

It should be noted that the approximation of $4\epsilon\alpha N/l$ made in the derivation of eq 3 is valid; taking $\epsilon = 2.60$, $\alpha = 63.5 \mu\text{m}$, $N = 3.494$, and $l = 10 \text{ cm}$ yields a value of $4\epsilon\alpha N/l = 0.02307$. This approximation will continue to hold true for laser incidence angles below $\sim 5 \text{ mrad}$.

RESULTS AND DISCUSSION

Three factors potentially affecting beam throughput were considered: (a) losses upon entering and/or exiting the gel; (b) losses due to scattering in the gel; (c) losses due to reflective inefficiencies as the beam propagates by reflection through the gel.

The first factor, losses upon entering and/or exiting the gel, has two parts: the first part is reflective losses at the air-glass (4.26%) and glass-gel (0.155%) interfaces on the entrance side (see Figure 2) and at their counterparts on the exit side when an exit window is also employed for the purpose of beam power measurements. The total reflective loss upon beam entrance is thus 4.41%, and the same loss is encountered upon beam exit. It may be noted that the reflection upon exit actually increases the power within the gel, although it decreases the measured power at a detector outside the gel. The second part is aperture losses

(13) Yariv, A. *Quantum Electronics*, 2nd ed.; John Wiley and Sons, Inc.: New York, 1975; pp 110-113.

Table 2. Calculated and Measured Beam Throughput

spacer thickness (μm)	reflective loss 1 X_1 (%)	blocking loss X_2 (%)	bouncing loss X_3 (%)	scattering loss X_4 (%)	reflective loss 2 X_5 (%)	calcd throughput I^a (%)	measd throughput (%)
Water							
63.5	4.67	13.47	11.52	0.995	4.67	68.89	65.6
89	4.67	3.62	8.63	0.995	4.67	79.23	74.5
127	4.67	0.30	6.29	0.995	4.67	84.06	77.6
152	4.67	0.034	5.33	0.995	4.67	85.15	80.1
177	4.67	0.028	4.63	0.995	4.67	85.78	82.0
354	4.67	0	2.40	0.995	4.67	87.81	83.9
531	4.67	0	1.62	0.995	4.67	88.52	83.9
708	4.67	0	1.22	0.995	4.67	88.88	85.1
885	4.67	0	0.98	0.995	4.67	89.09	86.4
Gel							
63.5	4.41	13.47	15.10	10.42	4.41	60.13	56.3
127	4.41	0.30	8.47	10.42	4.41	74.70	68.8
152	4.41	0.034	7.23	10.42	4.41	75.91	71.9
177	4.41	0.028	6.30	10.42	4.41	76.68	75.0
531	4.41	0	2.24	10.42	4.41	80.02	78.1
885	4.41	0	1.36	10.42	4.41	80.74	80.3

^a Calculated throughput: I (%) = $100(1 - X_1)(1 - X_2)(1 - X_3)(1 - X_4)(1 - X_5)$.

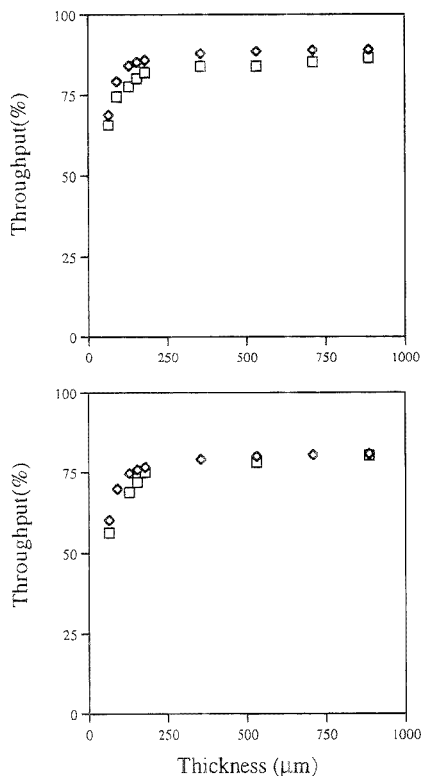


Figure 3. Calculated (\diamond) and measured (\square) beam throughput as a function of thickness for (A, top) water and (B, bottom) gel.

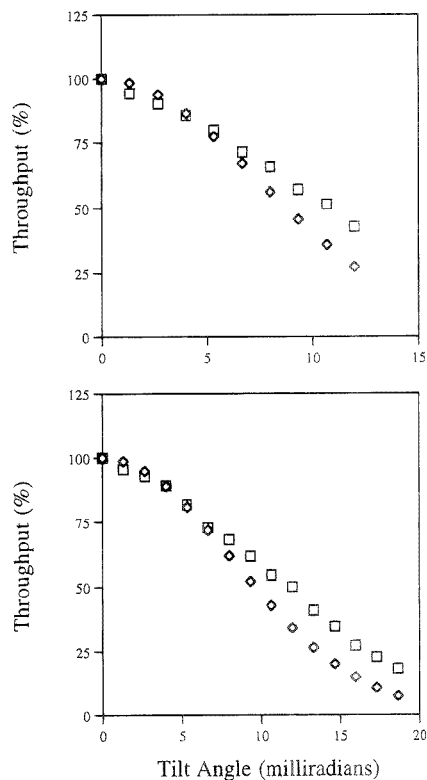


Figure 4. Calculated (\diamond) and measured (\square) beam throughput as a function of angle for (A, top) water and (B, bottom) gel.

upon entering the gel, due to beam power falling outside of the gel cross section. This may be minimized by (i) placing the beam focal waist at the entrance to the gel as diagrammed in Figure 2 and (ii) choosing the beam diameter at the focal waist to be

smaller than the entrance aperture. Use of the two lens input optics described above yields an elliptical spot with a $42.3 \mu\text{m}$ waist in the vertical direction. The electrophoresis cell was positioned so this waist coincided with the entrance to the gel

plates. In these experiments, the gel spacers employed in the electrophoresis cell were $63.5\ \mu\text{m}$ thick; for this elliptical Gaussian beam focused to a vertical waist of $42.3\ \mu\text{m}$, beam power blocked by the glass plates is calculated to be 13.47%.

Quantification of the second factor, scattering losses in the gel, was accomplished by measurement of the beam attenuation when a collimated laser beam was passed through an optical cell containing polymerized gel (see Experimental Section). Scattering losses determined in this way correspond to a gel absorbance of 0.00478 absorbance unit (AU) for a 1 cm path length; the absorbance for the 10 cm path length of the electrophoresis cell employed is thus 0.0478 AU, corresponding to a scattering loss of 10.42%. The scattering loss for water is similarly calculated to be 0.995% with the same 10 cm path length.

Finally, losses due to reflective inefficiencies during beam propagation may be calculated according to eq 12 above.

Table 2 and Figure 3 show the beam transmission efficiency calculated on the basis of these three factors, for several gel thicknesses, along with the measured values. Results are shown for both gel and pure water in the electrophoresis cell. The agreement is fairly good (compare last two columns of Table 2), suggesting that no significant beam attenuation mechanisms have been overlooked and that the proposed mechanism for propagation of the beam is valid. This latter point is substantiated in particular by the observed dependence of beam throughput upon gel thickness, which agrees well with experiment.

As neither the reflective nor the scattering components depend upon the gel thickness or the beam waist, most of the interesting

behavior is in the transmissive component described by eq 12. This equation shows that as gel thickness or beam focal radius is decreased, the transmission efficiency also decreases. Importantly, only $\sim 40\%$ attenuation of beam intensity is encountered in beam passage through even the thinnest gel studied ($63.5\ \mu\text{m}$). This relatively modest attenuation has only a minor effect upon the fluorescence data quality. It may thus be concluded that the side excitation method is well suited for even these ultrathin gel systems. Beam throughput may be calculated for still thinner gels by the methods described here, permitting the feasibility of side excitation in such systems to be readily assessed.

As sensitivity to alignment errors is an important aspect of the instrument design, it is of interest to determine this experimentally and compare the results with those predicted by eq 14. Figure 4 shows calculated and measured throughput for a $63.5\ \mu\text{m}$ thickness of gel or water when the tilt angle is varied from 0 to 12 mrad. Again, the agreement between calculated and measured results is quite good, although some deviation occurs at larger angles; this deviation reflects the small-angle approximation made in eq 3 by the assumption of $4\epsilon\alpha N/l \ll 1$.

Received for review April 27, 1995. Accepted July 16, 1995.*

AC9504070

* Abstract published in *Advance ACS Abstracts*, September 1, 1995.

Data Reflection Algorithm for Spectral Enhancement in Fourier Transform ICR and NMR Spectroscopies

Michael V. Gorshkov* and Richard T. Kouzes

Environmental Molecular Sciences Laboratory, Pacific Northwest Laboratory, Battelle Boulevard, P.O. Box 999, Richland, Washington 99352

The use of a data reflection algorithm in which the signal acquired in real time is juxtaposed with the same signal reflected relatively to zero time axis through exact phase matching is considered. Because of the additional information provided by a knowledge of the exact initial phase of the signal, the resulting Fourier transform (FT) spectra have a higher resolution and signal-to-noise ratio. This algorithm was applied to ion cyclotron resonance and nuclear magnetic resonance time-domain signals. In both cases, the method improved the FT spectra compared with the original ones. It was found that artifacts may result from the time delay between the end of the excitation event and the beginning of the acquisition period, as well as from time-dependent excitation wave forms such as chirp excitation. Possible ways to decrease or eliminate the artifacts are considered. Comparison to other spectral enhancement techniques is made.

The most widely used numerical method for spectral enhancement is the Fourier transform (FT), which gives a frequency analysis of the time-domain response of a physical system.¹ The Fourier transform is the main technique for extracting spectral information in infrared (FT-IR) spectroscopy,² nuclear magnetic resonance (FT-NMR) spectroscopy,³ and ion cyclotron resonance (FT-ICR) mass spectroscopy.^{4,5} There are several new methods and algorithms that have been developed recently to improve the frequency spectra obtained via FT. These methods are based upon a pretransform, time-domain signal processing technique known as the magnitude-mode derivative method,^{6,7} which leads to a resolution enhancement of FT spectra. In order to avoid a decrease in resolving power in a magnitude-mode FT spectrum, a FT convolution procedure has been proposed in which it was shown that the spectral line shape can be improved when the excitation frequency spectrum is known.^{8,9} Other methods based upon the deconvolution of partially resolved spectra include a Fourier self-deconvolution method (FSD),^{10,11} which was applied

to photoelectron and NMR spectroscopies, and a peak sharpening procedure,¹² implemented recently for resolution enhancement of translational energy spectra (TES). The non-FT methods of obtaining spectral information from time-domain data are linear prediction, such as the autoregression (AR) method, and probabilistic methods, such as the maximum entropy method (MEM), widely used in different physical applications.^{1,13} The AR and MEM methods have some drawbacks in that they provide incorrect information when the noise level is high, and they require considerable computational time in comparison to fast Fourier transform (FFT) analysis. Another approach to obtaining the information captured in the imaginary part of the FT has recently been demonstrated by implementing the Hartley/Hilbert transform (HHT), which gives the resolving power of an absorption-mode FT and the signal-to-noise ratio (SNR) of a magnitude-mode FT by using Hilbert relations between absorption and dispersion spectra.¹⁴

We suggest here the use of a data reflection algorithm (DRA) for enhancing the results of FT analysis in FT-ICR and FT-NMR. The time-domain signal is replaced by a new one consisting of two juxtaposed parts: the original time-domain signal and the reflected time-domain signal. An analogy can be found in Michelson interferometry with its centerburst interferograms, which are the signals detected as a function of path length difference between different light beam components.¹ With this DRA method, we generate a centerburst time-domain spectrum which contains the phase information of the original time-domain signal, higher resolving power compared with the original magnitude-mode FT spectrum (equivalent to the resolving power of the original absorption-mode spectrum), and higher SNR and precision for the spectrum due to effective "data-fill".

THEORY

Data Reflection Algorithm for Real Time-Domain Signals.

Most physical time-domain signals $f(t)$, as in the case of ICR or NMR spectroscopies, are causal functions in time, where we can write

$$f(t) = 0 \quad \text{for } t < 0 \quad (1)$$

because normally we have no information about the system

(1) Marshall, A. G.; Verdun, F. R. *Fourier Transforms in NMR, Optical, and Mass Spectrometry: A User's Handbook*; Elsevier: Amsterdam, 1990; 460 pp.

(2) Bell, R. J. *Introductory Fourier Transform Spectrometry*; Academic Press: New York, 1972; 382 pp.

(3) Ernst, R. R.; Anderson, W. A. *Rev. Sci. Instrum.* **1966**, *37*, 93–102.

(4) Comisarow, M. V.; Marshall, A. G. *Chem. Phys. Lett.* **1974**, *25*, 282–283.

(5) Comisarow, M. V.; Marshall, A. G. *Chem. Phys. Lett.* **1974**, *26*, 489–490.

(6) Balcou, Y. *Rapida Commun. Mass Spectrom.* **1994**, *8*, 942–944.

(7) Kim, H. S.; Marshall, A. G. *Private Commun. ICR/Ion Trap Newsl.* **1995**, *37*, 4–6.

(8) Marshall, A. G. *Chem. Phys. Lett.* **1979**, *63*, 515–518.

(9) Marshall, A. G.; Roe, D. C. *J. Chem. Phys.* **1980**, *73*, 1581–1590.

(10) McClure, W. F. *Spectrosc. World* **1991**, *3*, 28–34.

(11) Dromey, R. G.; Morrison, J. D.; Peel, J. B. *Chem. Phys. Lett.* **1973**, *23*, 30.

(12) Brenton, A. G.; Lock, C. M. *Rapida Commun. Mass Spectrom.* **1995**, *9*, 143–149.

(13) Ferrige, A. G.; Seddon, M. J.; Jarvis, S. *Rapida Commun. Mass Spectrom.* **1991**, *5*, 374–379.

(14) Williams, C. P.; Marshall, A. G. *Anal. Chem.* **1992**, *64*, 916–923.

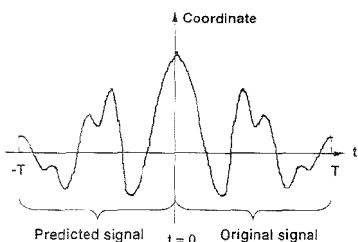


Figure 1. Schematic representation of the DRA algorithm. The resulting time domain signal has an acquisition period of $2T$, where T is the acquisition period for the originally recorded time-domain signal.

response before the detection period. The corresponding FT spectrum from such a function will reflect only the information acquired during the detection period. For example, the typical response signal in FT-ICR or FT-NMR will be an exponentially decaying sinusoid, or the sum of sinusoids if several different oscillators are subjected to the pulse action (excitation event):

$$f(t) = \sum_{i=1}^N A_i e^{-t/T_i} \cos(\omega_i t + \phi_i), \quad t \geq 0 \quad (2)$$

in which T_i is the time-decay constant determined by the rate of ion-neutral collisions in ICR spectrometry or by the spin relaxation processes in NMR spectroscopy, A_i is the corresponding ion or spin abundance, and ω_i and ϕ_i are the resonant frequencies and initial phases, respectively. In the case of ICR, the coherent spatial motion of the ions in the magnetic field is created by applying a resonant phase-coherent electric excitation field. If the energy absorbed by ions from the resonant excitation field is considerably higher than the ion initial energy (mostly thermal), the postexcitation phases ϕ_i of different ions subjected to the excitation will be the same and equal to the phase of the excitation field. Thus, for ICR or NMR spectroscopies, we can assume that we have $\phi_i = 0$ for all i in eq 2. Because $\phi_i = 0$ at $t = 0$, we may then data-fill the real time-domain signal $f(t)$ by reflection of the recorded data relative to time zero to obtain

$$f_{\text{inv}}(t) = f(t) \quad \text{when } t \geq 0 \quad (3)$$

$$f_{\text{inv}}(t) = f(-t) \quad \text{when } t < 0 \quad (4)$$

where $f_{\text{inv}}(t)$ defines a new time-domain signal consisting of the original and reflected time-domain signals, as seen in Figure 1. In terms of a computational problem, this signal prediction is trivial and does not require time-consuming computations as in the AR or MEM algorithms. Note that the reflected discrete signal $f_{\text{inv}}(t)$ contains $2n - 1$ data points, where n is the total number of data points in the original signal, since the data point corresponding to $t = 0$ is common for both the direct and reflected parts of the inverse array. Thus, the DRA procedure leads to the definition of the new time-domain signal $f_{\text{inv}}(t)$ that has the acquisition period T_{inv} elongated by a factor of 2 compared with that for the original time-domain signal. Since an improvement in resolution and SNR is not obvious for this new signal (for example, the time-decay constant remained the same), we now consider its frequency spectrum analytically.

FT Spectrum of Reflected Time-Domain Signal. The original time-domain signal $f(t)$ may be represented as the product

of three well-known functions:

a sinusoid $s(t) = A \cos(\omega_0 t)$ (5)

a boxcar $\Pi(t/T - 1/2) = 1$ for $0 < t < T$
 $\Pi(t/T - 1/2) = 0$ for $T < t < 0$ (6)

an exponential $e(t) = \exp(-\alpha t)$ for $t > 0$
 $e(t) = 0$ for $t < 0$ (7)

in which T is the acquisition period of the original signal, α is the decay constant, and ω_0 and A are the frequency and the amplitude of the signal, respectively.

The reflected time-domain signal $f_{\text{inv}}(t)$ may be represented in the same way by the following functions:

a sinusoid $s_{\text{inv}}(t) = A \cos(\omega_0 t)$ (8)

a boxcar $\Pi_{\text{inv}}(t/T_{\text{inv}} - 1/2) = 1$ for $0 < t < T_{\text{inv}}$
 $\Pi_{\text{inv}}(t/T_{\text{inv}} - 1/2) = 0$ for $T_{\text{inv}} < t < 0$ (9)

an exponential $e_{\text{inv}}(t) = \exp(-\alpha(t - T_{\text{inv}}/2))$ for $t \geq T_{\text{inv}}/2$
 $e_{\text{inv}}(t) = \exp(\alpha(t - T_{\text{inv}}/2))$ for $t < T_{\text{inv}}/2$ (10)

in which T_{inv} is the acquisition period of the new function, $T_{\text{inv}} = 2T$.

In accordance with the convolution theorem, we may represent the FT spectra $F(\omega)$ and $F_{\text{inv}}(\omega)$ for the functions $f(t)$ and $f_{\text{inv}}(t)$, respectively, as the convolution of the corresponding frequency spectra: $S(\omega)$ and $S_{\text{inv}}(\omega)$ for sinusoids, $\Pi(\omega)$ and $\Pi_{\text{inv}}(\omega)$ for boxcar functions, and $E(\omega)$ and $E_{\text{inv}}(\omega)$ for exponential functions:

$$F(\omega) = S(\omega) * \Pi(\omega) * E(\omega) \quad (11)$$

$$F_{\text{inv}}(\omega) = S_{\text{inv}}(\omega) * \Pi_{\text{inv}}(\omega) * E_{\text{inv}}(\omega) \quad (12)$$

From eqs 5–10, $S(\omega)$ and $S_{\text{inv}}(\omega)$ give δ functions reflecting the resonant frequency, $S(\omega) = S_{\text{inv}}(\omega) = 1/2 A \delta(\omega - \omega_0)$; $\Pi(\omega)$ and $\Pi_{\text{inv}}(\omega)$ lead to the well known sinc functions; and finally, $E(\omega)$ and $E_{\text{inv}}(\omega)$ are responsible for the spectral peak shape. $E(\omega)$ and $E_{\text{inv}}(\omega)$ are complex functions that can be found from the Fourier integral:

$$E(\omega) = \int_{-\infty}^{\infty} e(t) e^{-i\omega t} dt = \frac{1}{\alpha(1 + \omega^2/\alpha^2)} + i \frac{\omega}{\alpha^2(1 + \omega^2/\alpha^2)} \quad (13)$$

$$E_{\text{inv}}(\omega) = \int_{-\infty}^{\infty} e_{\text{inv}}(t) e^{-i\omega t} dt = \frac{2 \cos(\omega T)}{\alpha(1 + \omega^2/\alpha^2)} + i \frac{2 \sin(\omega T)}{\alpha(1 + \omega^2/\alpha^2)} \quad (14)$$

Figure 2 shows the functions $E(\omega)$ and $E_{\text{inv}}(\omega)$ in magnitude mode. We see that the peak width of the $E_{\text{inv}}(\omega)$ function is

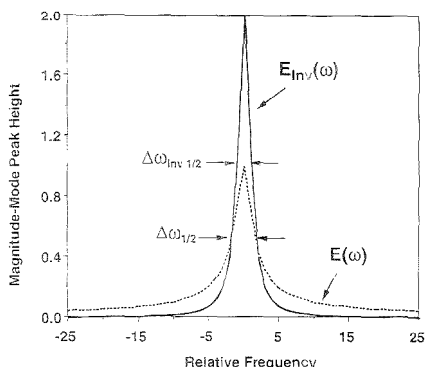


Figure 2. Comparison of the peak shape in the FT spectrum obtained for the original time-domain signal, $E(\omega)$, with that in the FT spectrum of the time-domain signal obtained via the DRA method, $E_{inv}(\omega)$. The $E_{inv}(\omega)$ spectrum has a higher magnitude-mode amplitude, narrower peak width, and faster peak height decay as the frequency increases.

narrower. Indeed, from eqs 13 and 14, we may find analytically

$$\Delta\omega_{1/2} = 2\sqrt{3}\alpha$$

for the magnitude-mode $E(\omega)$ function (15)

$$\Delta\omega_{inv1/2} = 2\alpha$$

for the magnitude-mode $E_{inv}(\omega)$ function (16)

Signal-to-Noise Ratio. By considering the magnitude-mode spectrum for the exponential functions in both cases of the original and the reflected time-domain signals, we can find from eqs 13 and 14

$$E_{\text{magnitude}}(\omega) = 1/\sqrt{\alpha^2 + \omega^2} \quad (17)$$

$$E_{\text{inv,magnitude}}(\omega) = 2\alpha/(\alpha^2 + \omega^2) \quad (18)$$

The peak height in both cases corresponds to $\omega = 0$ and is doubled for the function $E_{\text{inv,magnitude}}(\omega)$. This leads to the conclusion that the spectral amplitude of the reflected time-domain signal will be doubled since $S(\omega)$ and $\Pi(\omega)$ have the same magnitude-mode amplitude as $S_{\text{inv}}(\omega)$ and $\Pi_{\text{inv}}(\omega)$, respectively.

It is more difficult to evaluate the noise level. Since the data reflection procedure is equivalent in the DRA method to acquiring the reflected signal for twice as many counts as the original time-domain signal, the noise level will be a factor $2^{1/2}$ higher in both cases of detector-limited and source-limited noise. Thus, the resulting SNR will be increased by a factor $2^{1/2}$ in the DRA method. A separate consideration is the case of periodic noise in the original signal. The level of such noise will be increased by a factor of 2 only if its phase correlates with the phase of the signal.

Note in Figure 2 that the peak shapes are also different for the original spectrum and the spectrum obtained by the DRA method. The function $E_{inv}(\omega)$ is not a magnitude-mode Lorentzian

increased by a factor of 2, and it decays faster for frequencies far away from the resonance. Indeed, from eqs 17 and 18, we have

$$E_{\text{inv}}(\omega)/E(\omega) = 2/\sqrt{1 + (\omega/\alpha)^2} \rightarrow 0 \quad \text{when } \omega \rightarrow \infty \quad (19)$$

This fact is important since this gives an additional improvement in the peak separation of spectra obtained via the DRA method.

RESULTS AND DISCUSSION

FT-ICR Applications. Figure 3a shows a simulated time-domain signal and FT spectrum for a mass doublet of equal ion abundance. The DRA signal and the corresponding FT spectrum are shown in Figure 3b. In this calculation, we simulated Gaussian random noise at the level of 20% of the level of the acquired signal. The use of the DRA method improves considerably not only the resolution and SNR but also the accuracy in determining the relative peak intensities as a result of better peak separation. In Figure 4a, we show a doublet with frequencies so close to each other that the peaks in the FT spectrum cannot be resolved. By applying the data reflection algorithm, peak separation becomes possible (Figure 4b). This example directly shows that the proposed DRA procedure leads to additional information in FT spectra as well as better looking spectra.

The data reflection algorithm has been applied to actual experimental FT-ICR data. In Figure 5a, the mass spectrum from bovine insulin is shown. The ions were formed in the electrospray source (ESI) of a 7-T FT-ICR spectrometer at Pacific Northwest Laboratory.¹⁶ The spectrum corresponds to the $[M + 4H]^+$ -protonated multiply-charged molecular ion with a characteristic isotopic peak pattern. The acquired time-domain signal was 2 MB in size. The DRA mass spectrum is shown in Figure 5b.

Use of the Data Reflection Algorithm for Quadrature Detection. The method of data reflection for acquired time-domain signals may be used for real and complex data, such as for the case of quadrature detection that is typically used in NMR spectroscopy and can also be applied to ICR.¹ In quadrature detection, the signal from the excited spins (or ions) is acquired from two detection channels applied to the system's degrees of freedom, which are 90° out of phase with each other.¹⁵ The resulting time-domain signal is the complex array with both nonzero real and imaginary parts. Both parts make a contribution to the FT spectrum.

Figure 6a shows the simulated time-domain data and the corresponding FT spectrum typical in NMR spectroscopy with quadrature detection. In Figure 6b, the same data were transformed by applying the DRA procedure. Note that for the imaginary part of the time domain, the time reversed part is also 180° phase inverted to provide correct juxtaposition between the original data and the predicted data. The resulting reflected time domain, which has real and imaginary parts, was subjected to the complex FT in the same way as the original data. We see that the applied algorithm improved the resolution and SNR in accordance with eqs 15 and 16.

The data reflection processing of a quadrature detected signal has been applied to an experimental ^{113}Cd solid sample in NMR.

(15) Fukushima, E.; Roeder, S. B. W. *Experimental Pulse NMR: A Nuts and Bolts Approach*; Addison-Wesley Publishing Co., Inc., Advances Book Program: Reading, PA, 1981; 539 pp.

(16) Winger, B. E.; Hoisstadler, S. A.; Bruce, J. E.; Udseth, H. R.; Smith, R. D. *J. Am. Soc. Mass Spectrom.* 1993, 4, 566-577.

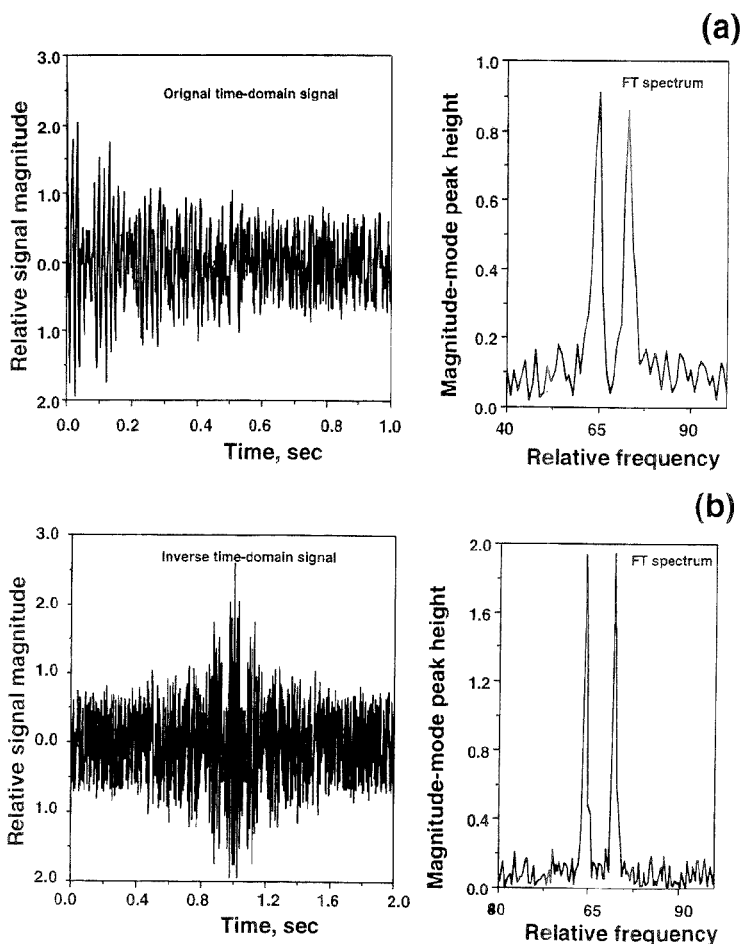


Figure 3. (a) Simulated time-domain signal (left) and the corresponding FT spectrum (right) for a mass doublet with equal peak abundance. (b) Time-domain signal obtained via the DRA method and the corresponding FT spectrum for the same mass doublet.

Data were obtained in the quadrature detection mode on a 300-MHz NMR spectrometer. The real and imaginary parts of the time-domain signal had 512 data points. The ^{111}Cd NMR spectrum contains more than 10 characteristic peaks, which can be recognized in Figure 7a. The reflected time-domain signal and the corresponding FT spectrum are shown in Figure 7b. The improvement in resolution and SNR is obvious, although artifacts appear in the spectrum. The main reason for artifacts in this particular case was associated with the presence of postexcitation relaxation of the receiver when the signal was acquired. To eliminate this postexcitation relaxation, two data points have been dropped from the beginning of the original time-domain signal. This procedure thus perturbed the phase matching between the direct time and the predicted parts. Additionally, the quadrature detection method is sensitive to the phase difference between the real and imaginary parts of the time domain signal.

Below, we consider in more details the artifacts associated with the proposed DRA method and the ways to eliminate them.

Artifacts. There will be no artifacts when all oscillators in the system under study are excited simultaneously, as in the case of single frequency excitation. This is also true when the harmonics in the excitation wave form, which correspond to the oscillators of different eigenfrequencies, have the same phases. In these cases, all excited oscillators (ions or spins) will have the same phases at the end of the excitation event, and phase matching in the DRA procedure may be done correctly. In practice, there is a time delay between excitation and detection. Thus, if there are several oscillators of different frequencies but the same phases when the excitation event is ended, the delay before detection leads to different phases at the moment the detection is started. This is not crucial for magnitude-mode FT spectra, which are not sensitive to the initial phase (Figure 8). But for the data reflection procedure, the initial phase is crucial to the correct juxtaposition of the original and predicted time-domain signals. Any delay leads to incorrect phase matching between the original and predicted parts, as is shown in Figure

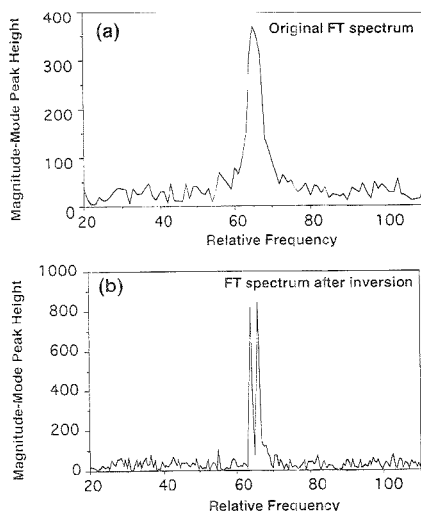


Figure 4. (a) FT spectrum of an unresolved mass doublet with equal peak abundance. (b) FT spectrum for the same doublet after the DRA method was applied to the original time-domain signal.

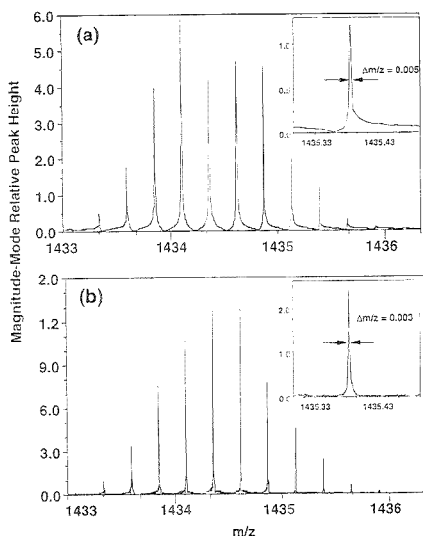


Figure 5. (a) $[M + 4H]^{4+}$ molecular ion mass spectrum of bovine insulin obtained in magnitude-mode FT by using an electrospray ion source interfaced with a 7-T FT-ICR mass spectrometer.¹⁶ The average mass resolution for the peaks was 250 000 defined as $m/\Delta m_{50\%}$, where $\Delta m_{50\%}$ is the full peak width at half-maximum peak height (fwhm). (b) FT magnitude-mode mass spectrum for the same ions after the DRA method was applied to the original time-domain signal. The average mass resolution (fwhm) for the peaks was 450 000.

9a for the same data as in Figure 8. The expanded view of the time-domain signal shows the phase mismatch at the central data point. This results in loss of information about the system. One of the possible ways to avoid this problem is to find the nearest

maximum in the original time-domain signal. This maximum corresponds to the point of phase synchronization for all oscillators in accordance with the principle of superposition for harmonic oscillations and with the assumption of synchronized oscillations at the moment the excitation ended (in practice, this becomes complex for multiple ion situations, as discussed later). For instance, for a doublet with two eigenfrequencies, ω_1 and ω_2 , the maxima in the time-domain signal correspond to the following times τ_{\max} after the excitation:

$$\tau_{\max} = 2\pi n / (\omega_1 - \omega_2), \quad n = 0, 1, 2, \dots \quad (20)$$

In most practical cases, the time interval between nearest maxima is small, and this suggested method of time shifting is equivalent to a slight elongation of the delay. Figure 9b shows the data reflected signal and corresponding FT spectrum for the same doublet as Figures 8 and 9a, for which the phase matching was corrected in the above-described way.

This method for eliminating artifacts by time shifting is not effective if (1) the number of oscillators is too large or (2) the oscillators have been excited by broadband chirp excitation. In these cases, a more general method of artifact elimination can be suggested: phase correction in the complex FT spectrum of the original time-domain data. Since all of the experimental parameters for the excitation and the delays before detection are known, a phase correction procedure can be performed in all practical cases. Consider the original time-domain signal consisting of N harmonic oscillators:

$$f(t) = \sum_{i=0}^{N-1} A_i \cos(\omega_i t - \phi_i) \quad (21)$$

where ϕ_i represents the individual phases that have to be corrected. This means that the phase of the i th peak has to be rotated by ϕ_i . The corresponding FT spectrum will be defined by the following expression:

$$F(\omega) = \sum_{t=-\infty}^{+\infty} f(t) e^{-i\omega t} dt = \sum_{i=0}^{N-1} F_i(\omega) \quad (22)$$

in which $F_i(\omega)$ is the complex frequency spectrum corresponding to the individual oscillator,

$$F_i(\omega) = \int_{-\infty}^{+\infty} A_i \cos(\omega_i t - \phi_i) e^{-i\omega t} dt = \text{Re}_i(\omega) + i\text{Im}_i(\omega) \quad (23)$$

where $\text{Re}_i(\omega)$ and $\text{Im}_i(\omega)$ are the real and imaginary parts of the Fourier spectrum, respectively. Each phase may then be corrected by obtaining the pure absorption $\text{Ab}_i(\omega)$ and dispersion $\text{De}_i(\omega)$ spectra that correspond to $\phi_i = 0$. This may be done by the procedure of phase rotation described elsewhere:¹

$$\text{Ab}_i(\omega) = \text{Re}_i(\omega) \cos \phi_i - \text{Im}_i(\omega) \sin \phi_i, \quad (24)$$

$$\text{De}_i(\omega) = \text{Re}_i(\omega) \sin \phi_i + \text{Im}_i(\omega) \cos \phi_i$$

The resulting corrected FT spectrum $F_c(\omega)$ will be

$$F_c(\omega) = \sum_{i=0}^{N-1} \text{Ab}_i(\omega) + i\text{De}_i(\omega) \quad (25)$$

and the following inverse Fourier transform will give time-domain data that will correspond to the original data but synchronized in phase for all oscillators. Thus, we have

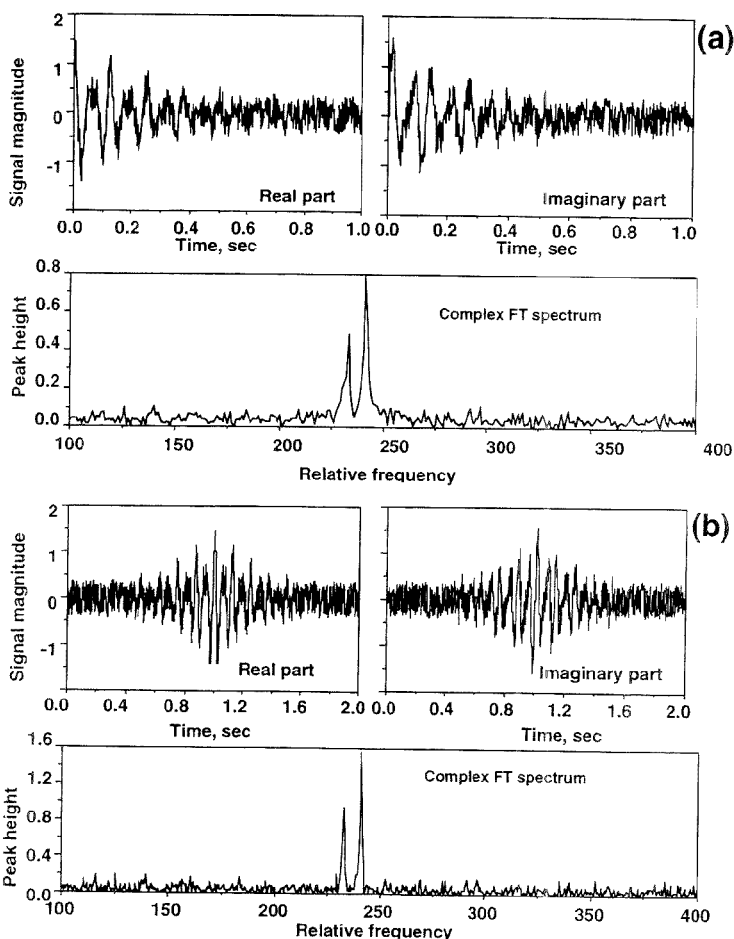


Figure 6. Use of the DRA method for time-domain data obtained by the method of quadrature detection followed by a complex Fourier transform. (a) Simulated real and imaginary parts of the original signal (top) and corresponding frequency spectrum. (b) Real and imaginary parts of the signal obtained via the DRA method from the same original data. The DRA imaginary part was created by both time and phase inversion.

$$\begin{aligned}
 f_c(t) &= F^{-1}[F_c(\omega)] = \int_{-\infty}^{\infty} F_c(\omega) e^{i\omega t} d\omega \\
 &= \sum_{i=0}^{N-1} \int [Ab_i(\omega) + iDe_i(\omega)] e^{i\omega t} d\omega \\
 &= \sum_{i=0}^{N-1} \int_{-\infty}^{\infty} [Re_i(\omega) + iIm_i(\omega)] e^{i(\omega t + \phi_i)} d\omega \\
 &= \sum_{i=0}^{N-1} f_i(t) e^{i\phi_i} \quad (26)
 \end{aligned}$$

That is, the phase of each oscillator will be corrected to be the same and equal to zero.

Figure 10 shows the result of applying the phase correction procedure to a spectrum in which the oscillators were excited by

chirp excitation. Each oscillator had an individual phase before correction (Figure 10a), resulting in a poor result from the data reflection procedure (Figure 10d). The phases of each oscillator were then corrected in accordance with eqs 24–26 to give a pure absorption spectrum (Figure 10b). The following inverse FT gave the time-domain signal in which the phases of all oscillators were the same and equal to zero in accordance with eq 26. The DRA procedure was then applied for spectral enhancement (Figure 10e).

Comparison of the DRA Method with Prior Work and Its Limitations. The DRA method can be compared to the method of data-filing suggested by Watson and Eyler.¹⁸ Their method

(17) Bartholdi, E.; Ernst, R. R. *J. Magn. Reson.* 1973, 11, 9–19.

(18) Watson, C. H.; Eyler, J. R. Proceedings of the 38th ASMS Conference on Mass Spectrometry and Allied Topics; San Francisco, CA, June 5–10, 1988; pp 600–601.

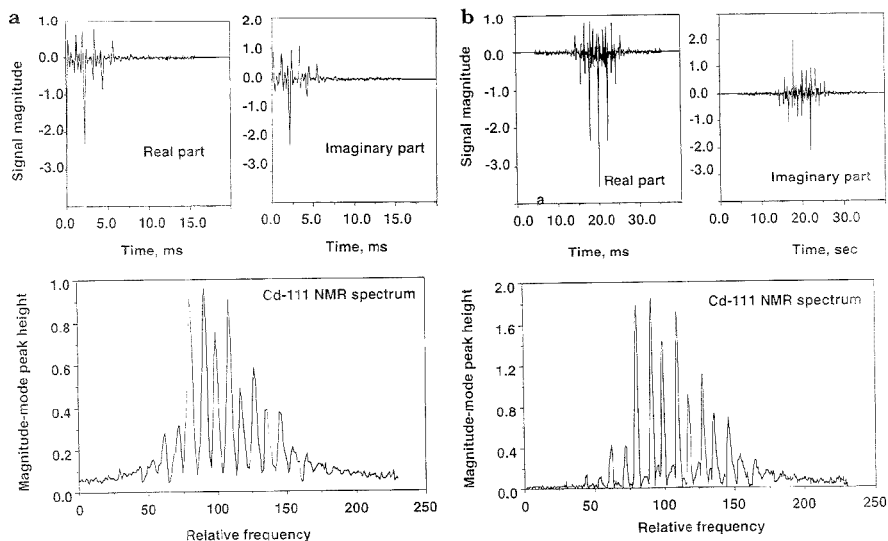


Figure 7. (a) Experimental time-domain signal and the corresponding NMR frequency spectrum of ^{111}Cd obtained by quadrature detection with a 300-MHz NMR spectrometer. (b) Time-domain signal and the corresponding NMR frequency spectrum obtained after application of the DRA method.

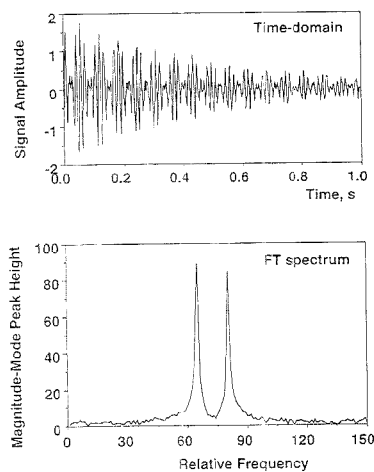


Figure 8. Simulated time-domain signal (top) and the corresponding FT spectrum (bottom) of the mass doublet for equal ion abundance. A 10-ms delay between the end of excitation and the beginning of detection was applied, which does not effect the frequency spectrum in magnitude mode.

was based upon time-domain signal elongation by juxtaposing the original data set with the same data set starting at the end of the acquisition period. This method has the major limitation of losing the phase information when the SNR is decreasing at the end of acquisition period. In the work described herein, we use data-filling through an algorithm of data reflection about zero time where the phase information is fixed by the predetection history and the SNR is high.

Another approach to the problem of recovering the information stored in the imaginary part of an FFT is to use time-domain zero-

filling as proposed by Bartholdi and Ernst and widely used in practice to transfer some of the information residing in the dispersion-mode FT into the absorption mode.¹⁷ Because the time domain is elongated by zeroes, not all the information is taken back into the magnitude-mode FT. The resolution improvement is not as great as in the DRA method, and the SNR does not change. Figure 11 shows a comparison between the magnitude-mode FT from a simulated FT-ICR signal obtained by a regular FFT without zero-filling, a regular FT with a single pretransform zero-fill, and the DRA method without zero-filling. Obviously, the zero-fill procedure improves the peak shape and the precision of peak measurements because of a larger number of data points. The DRA method adds spectral enhancement because it contains both phase restoration and data-filling. Moreover, the DRA method gives a better resolving power for a magnitude-mode FT spectrum compared with that of an absorption-mode FT.

An alternative method for spectral enhancement is the Hartley/Hilbert transform algorithm proposed by Williams and Marshall recently, in which the information residing in the dispersion-mode FT spectrum is recovered by using Hilbert relations between absorption and dispersion FT.¹⁴ This method gives an enhanced absorption spectrum which has the resolution of the absorption mode FT, which is better than that of the magnitude-mode FT by a factor of $3^{1/2}$, and the SNR of the magnitude-mode FT, which is better than that of the absorption-mode FT by a factor of $2^{1/2}$. In the DRA method, the same improvement in resolving power is achieved, together with a SNR increased by a factor of $2^{1/2}$ compared with the magnitude-mode FT and hence by a factor of 2 compared with the absorption-mode FT. Note that the DRA algorithm requires twice the number of data points to be processed as in the HHT method, but this is compensated by the trivial programming procedure for data reflection.

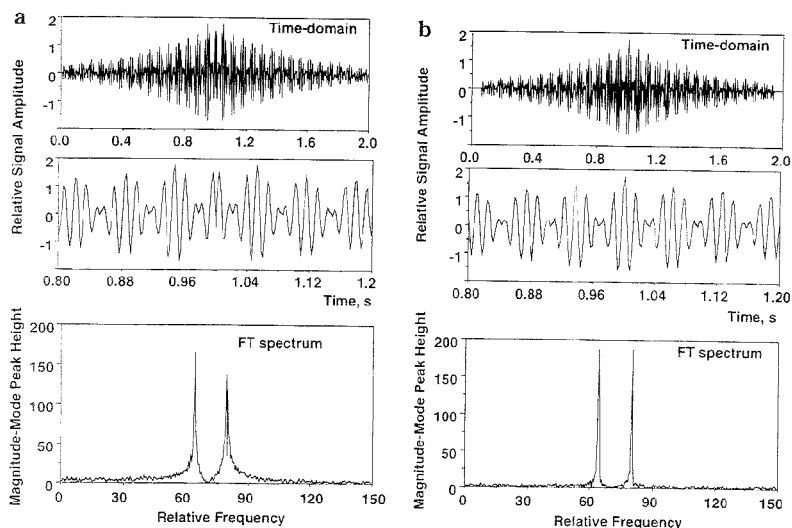


Figure 9. (a) Time-domain signal (top) and the corresponding FT spectrum (bottom) obtained via the DRA method for the same doublet as in Figure 8. The phase mismatch is shown in the extended figure (middle). The resulting FT spectrum is distorted and shows no improvement in resolution or signal-to-noise ratio. (b) The same signal after phase correction for both oscillators by choosing the first maximum in the beat pattern of the original time-domain signal shown in Figure 8. The DRA procedure leads to spectral enhancement compared with the original data.

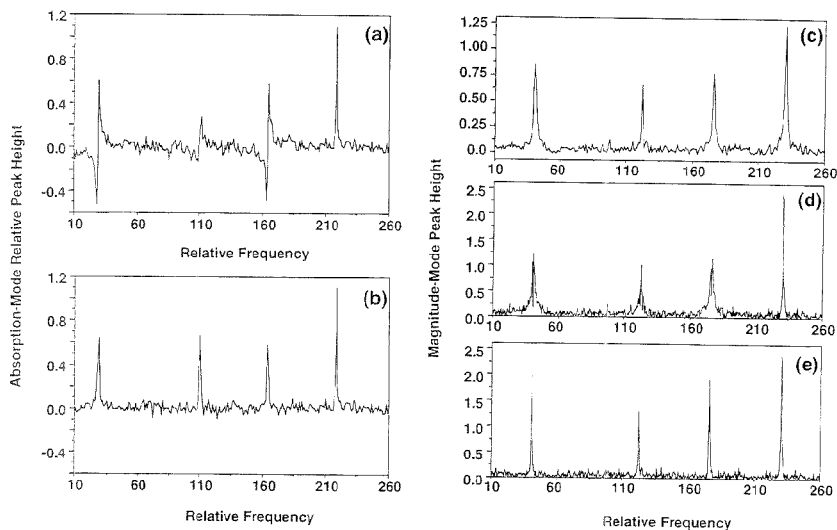


Figure 10. (a) Real part of a simulated FT spectrum for a multioscillator system. The oscillators were excited by chirp excitation, in which the excitation frequency was scanned over the frequency range of these oscillators. As a result, when detection is started, each of the oscillators has an individual phase. (b) Real part of the FT spectrum for the same system of oscillators after phase correction. The phases of all oscillators were corrected to be zero at the moment the detection is started. (c) FT magnitude-mode spectrum obtained for the original time-domain signal. (d) FT magnitude-mode spectrum obtained for the DRA transformed time domain signal corresponding to the data in (a) before the phase correction is applied. (e) FT magnitude-mode spectrum obtained for the DRA transformed time domain signal corresponding to the data in (b) after the phase correction is applied.

Both the DRA and HHT algorithms are limited in the case of frequency sweep excitation proposed by Comisarow and Marshall in FT-ICR⁸ by the necessity of having the phases of all oscillators the same at time zero. The phase of the system response depends

nonlinearly on the frequency. One of the possible solutions is a deconvolution technique proposed by Marshall for use in FT-ICR-MS.^{8,9} In this method, the response of each oscillator $h(t)$ to a δ function excitation is recovered from the frequency spectrum of

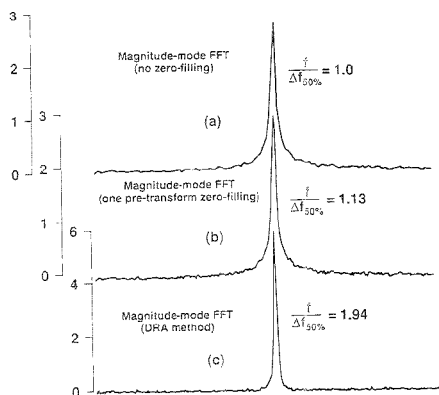


Figure 11. Comparison of the magnitude-mode FT spectrum (a) with those obtained by using a single zero-filling procedure (b) and by using a data reflection algorithm (c). The frequency resolution (fwhm) obtained by using the DRA method is higher by a factor of $3^{1/2}$ compared with that of a single zero-filled spectrum for the same number of data points in both spectra.

the excitation wave form $\text{Exc}(\omega)$ and the frequency spectrum of the detected signal $F(\omega)$,

$$F(\omega) = \text{Exc}(\omega) \cdot H(\omega) \quad (27)$$

followed by the inverse FT. This technique is limited to the case of a short delay between excitation and detection. In particular, the deconvolution technique is simple when detection occurs simultaneously with excitation or when there is no delay between excitation and detection.⁹

CONCLUSIONS

The results presented have shown that the simple procedure of juxtaposing the original time-domain signals obtained in FT-ICR spectrometry and FT-NMR spectroscopy with the same data set reversed in time improves the resolution of the corresponding FT spectra by a factor of $3^{1/2}$ and the SNR by a factor of $2^{1/2}$ compared with the magnitude-mode FFT and by a factor 2

compared with absorption-mode FFT. The procedure is equivalent to predicting the signal that the system of harmonic oscillators had when time was negative. The phase matching between the original and predicted parts of the signal obtained after inversion is the key aspect of getting additional information from the spectrum. The advantage of the proposed DRA procedure, compared with other existing methods of signal prediction or improving the spectral data, is the simplicity of the algorithm, which does not require time-consuming computational operations. Another advantage of the DRA method is the improvement of both the resolution and the SNR.

It was found that in some practical cases, when the oscillators under study are not excited simultaneously, as in the case of broadband chirp excitation, artifacts in the FT spectrum appeared. These artifacts may be eliminated by appropriate correction of the phases of each individual oscillator in the frequency spectrum of the original time-domain signal in combination with the inverse Fourier transform.

The data reflection algorithm may be especially helpful in quick analysis of poorly resolved or unresolved spectra in FT-ICR-MS and FT-NMR spectroscopy, as well as for the identification of unknown low-intensity peaks in noisy spectra because of the higher resolving power and SNR in DRA spectra.

ACKNOWLEDGMENT

This research was supported by Associated Western Universities under Grant DE-FG06-89ER-75522 with the U.S. Department of Energy and by The Laboratory Directed Research and Development Program at Pacific Northwest Laboratory (PNL). PNL is a multiprogram national laboratory operated by Battelle Memorial Institute for the U.S. Department of Energy under Contract DE-AC06-76RLO 1830. We thank Gordon A. Anderson, Herman M. Cho, and Andy S. Lipton for providing experimental FT-ICR and FT-NMR data. We also thank Alan G. Marshall, Shenheng Guan, and Michael W. Senko from The National High Magnetic Field Laboratory for useful discussions on the subject of this paper.

Received for review March 13, 1995. Accepted June 20, 1995.*

AC9502561

* Abstract published in *Advance ACS Abstracts*, August 1, 1995.

Native Fluorescence Detection and Spectral Differentiation of Peptides Containing Tryptophan and Tyrosine in Capillary Electrophoresis

Aaron T. Timperman, Kurt E. Oldenburg, and Jonathan V. Sweedler*

Department of Chemistry, University of Illinois, Urbana, Illinois 61801

A native fluorescence detection system for capillary electrophoresis is described that achieves low attomole detection limits and simultaneous acquisition of complete fluorescence emission spectra. The system is designed for detection of peptides through the intrinsic fluorescence of tryptophan and tyrosine residues. The detection system employs a frequency doubled krypton laser operating at 284 nm for excitation, a sheath flow cell, a reflective $f/1.2$ microscope objective, an imaging spectrograph, and a CCD detector. The detection capabilities are characterized with tryptophan and tyrosine, which have limits of detection (3σ) of 2×10^{-10} and 2×10^{-8} M, respectively. Acquisition of the fluorescence emission spectrum provides the ability to distinguish three classes of peptides: those that contain tryptophan, those that contain tyrosine, and those that contain both tryptophan and tyrosine.

Bioanalytical applications for capillary electrophoresis (CE) have grown rapidly since the demonstration of its ability to perform high-efficiency separations.¹ The characteristics that make capillary electrophoresis the method of choice for such applications include unparalleled separation efficiencies, small injection volumes, and low mass detection limits.²⁻⁴ With typical detection path lengths and volumes on the order of micrometers and femtoliters, respectively, development of detection schemes capable of low concentration detection limits is challenging.

An application of capillary electrophoresis which has drawn much interest is the analysis of single cells.⁵⁻¹⁰ The small volume, small mass, and complex chemical composition of samples available for single cell analysis are well suited to the small injection volumes, low mass detection limits, and high separation efficiency of CE. Mass detection limits below 100 molecules of sulforhodamine 101 have been obtained with fluorescence detec-

tion.^{11,12} However, detection capabilities are often still the limiting factor for analysis of biological samples. The major problem in using fluorescence detection for the analysis of biological samples is the difficulty of labeling the analyte with highly fluorescent probe molecules, such as fluorescein or sulforhodamine 101 derivatives. At low analyte concentrations (nanomolar range), the slow reaction rates and fluorescent byproducts of the labeling reactions lead to low yields of labeled analytes and large fluorescent backgrounds. Another difficulty with derivatization of biopolymers, such as proteins and peptides, is the formation of analytes labeled with multiple fluorophores, which makes quantitation difficult and causes multiple peaks.¹³⁻¹⁵ Thus, it has been difficult to obtain the most sensitive CE detection for low concentrations of peptides.

As a means to avoid the problematic derivatization reactions, a detection system utilizing native fluorescence has been developed. Native fluorescence detection takes advantage of the intrinsic fluorescence of tryptophan and tyrosine to eliminate the need for derivatization. Although the use of native fluorescence avoids derivatization, its major disadvantage for analysis of peptides is that tryptophan and tyrosine are much poorer fluorophores than probes like rhodamine and fluorescein.

Native fluorescence detection of tryptophan and tyrosine requires UV excitation in the 210-290 nm range, where few lasers are capable of operating. Recently, advancements in lasers operating within this range have made improvements in native fluorescence detection possible. Native fluorescence detection in capillary electrophoresis was first reported by Swalle and Sepaniak, with detection limits of 1.4×10^{-8} M for conalbumin using a frequency doubled Ar laser operating at 257 nm.¹⁴ The detection limits ($S/N = 2$) were improved to 1×10^{-10} M for conalbumin and 3×10^{-9} M for tryptophan (without stacking) with the use of the 275.4 nm line of an argon ion laser by Lee and Yeung.¹⁶ Issaq et al. have described a simple and rugged native fluorescence detection system utilizing a pulsed laser at 248 nm.¹⁵ They achieved detection limits of 3.3×10^{-8} ($S/N = 2$) for tryptophan but reported a decrease in the S/N at this wavelength for bovine serum albumin and conalbumin, which contain 2 and 15 tryptophan residues, respectively. Recently, Chang and Yeung reported further improvements with the same laser used in the system described here, a frequency doubled Kr laser operating

- (1) Jorgenson, J. W.; Lukacs, K. D. *Science* **1983**, *222*, 266-272.
- (2) Monnig, C. A.; Kennedy, R. T. *Anal. Chem.* **1994**, *66*, 280R-314R.
- (3) Jandik, P.; Bohm, G. *Capillary Electrophoresis of Small Molecules and Ions*; VCH Publishers: New York, 1993.
- (4) Landers, J. P., Ed. *Handbook of Capillary Electrophoresis*; CRC Press: Boca Raton, FL, 1994.
- (5) Jankowski, J. A.; Tracht, S.; Sweedler, J. V. *Trends Anal. Chem.* **1995**, *14*, 170-176.
- (6) Shippy, S. A.; Jankowski, J. A.; Sweedler, J. V. *Anal. Chim. Acta*, **1995**, *307*, 163-172.
- (7) Kristensen, H. K.; Lau, Y. Y.; Ewing, A. G. *Neurosci. Methods* **1994**, *51*, 183.
- (8) Kennedy, R. T.; Oates, M. D.; Cooper, B. R.; Nickerson, B.; Jorgenson, J. W. *Science* **1989**, *246*, 57.
- (9) Hogan, B. L.; Yeung, E. S. *Anal. Chem.* **1992**, *64*, 2841-2845.
- (10) Chang, H. T.; Yeung, E. S. *Anal. Chem.* **1995**, *67*, 1078-1083.
- (11) Chen, D. Y.; Adelhelm, K.; Cheng, X. L.; Dovichi, N. J. *Analyst* **1994**, *119*, 349-352.

- (12) Timperman, A. T.; Khatib, K.; Sweedler, J. V. *Anal. Chem.* **1995**, *67*, 139-144.
- (13) Chan, K. C.; Janini, G. M.; Muschik, G. M.; Issaq, H. I. *J. Liquid Chromatogr.* **1993**, *16*, 1877-1890.
- (14) Swalle, D. F.; Sepaniak, M. J. *J. Liquid Chromatogr.* **1991**, *14*, 869-893.
- (15) Nickerson, B.; Jorgenson, J. W. *J. Chromatogr.* **1989**, *480*, 157-168.
- (16) Lee, T. T.; Yeung, E. S. *J. Chromatogr.* **1992**, *595*, 319-325.

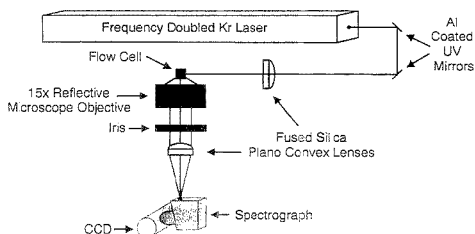


Figure 1. Schematic of the wavelength-resolved native fluorescence detection system showing the excitation and emission optics.

at 284 nm.¹⁰ They improved the limit of detection (LOD) for tryptophan to 7×10^{-13} M ($S/N = 2$) at a pH of 5.7. With this system, they were able to detect norepinephrine and epinephrine in single bovine adrenal medullary cells.

Sample stacking and other preconcentration techniques can be used to improve concentration LODs. For example, improvements in the concentration detection limits of 30 and 20 times for conalbumin and bovine serum albumin, respectively, have been reported by Lee and Yeung.¹⁶ As we are interested in mass-limited cellular samples, we have not employed stacking to improve the concentration LODs.

To increase the utility of native fluorescence for peptide detection in CE, we have sought to decrease the LODs and to achieve wavelength resolution of the fluorescence signal. To improve the lower limits of detection, a sheath flow cell is employed to reduce Rayleigh scattering and capillary background fluorescence. Both of these effects are greater in the UV than in the visible region. A reflective microscope objective is used for collection to eliminate fluorescence from the collection optics and to allow alignment of the system using visible light with minimal adjustment upon changing to UV light. The combination of a CCD and grating spectrograph is used to achieve wavelength resolution, allowing for the collection of complete emission spectra with each read of the detector. The emission spectra are used to determine if the analyte contains tryptophan or tyrosine or a combination of both. Thus, limited structural information is provided by the emission spectra aiding in identification of the analyte. The 2×10^{-10} M LOD is the lowest reported for tryptophan using fluorescence detection in capillary electrophoresis without derivatization.

EXPERIMENTAL SECTION

Fluorescence Spectra. Emission spectra of tryptophan, tyrosine, and phenylalanine are acquired with excitation at 229, 244, 257, and 284 nm. The acquisitions are performed using a Hitachi F-4010 fluorescence spectrophotometer with a Xe lamp and a Hamamatsu R928 photomultiplier tube. The excitation and emission bandpasses are both set to 3 nm, the PMT response time is 2 s, and the spectra are scanned at a rate of 120 nm/min.

Detection System. Figure 1 shows the arrangement of the optics, laser, spectrograph, and CCD used in the detector system. The 568 nm line of a krypton ion laser is doubled to 284 nm (Innova 300 FReD; Coherent, Palo Alto, CA) to achieve excitation in the ultraviolet region. The excitation is focused using an 80 mm focal length fused silica plano convex lens (Spindler and Hoyer, Milford, MA) ~ 0.5 mm below the capillary end in the

sheath flow cell. The sheath flow cell is used for end-column detection because it removes the capillary from the detection region, eliminating capillary fluorescence, and allows very efficient spatial filtering of Rayleigh scattering. To create the highest number of photons from a given number of fluorophore molecules, a low excitation irradiance and a long analyte residence time should be used with a typical on-column detection system.¹⁷ However, with a sheath flow cell detector, the process of diffusion limits the maximum observation time because the analyte continually diffuses into a larger volume after it exits the capillary. To provide an optimum combination of detection length and residence time, the detection length is kept short, and the linear velocity of the sheath fluid and the electroosmotic flow are matched. A four-sided quartz cuvette with 2 mm thick walls and a 3 mm \times 3 mm cross section (NSG Precision Cells, Farmingdale, NY) is used for the flow cell. The construction and interfacing of a sheath flow cell detection system to CE have been described in detail elsewhere.^{18–20} Gravimetric flow is used to provide a constant sheath flow rate, and a syringe pump is used to maintain the sheath fluid reservoir at a constant level. The sheath flow outlet is held at the same level as the capillary inlet and outlet.

The fluorescence emission is collected at 90° to the excitation with a 15 \times reflective microscope objective (Opticon, Billerica, MA). This objective collects light at $f/1.2$, with a center obscuration of 20%, and avoids fluorescence background caused by fused silica optics at this wavelength. The objective has an infinite conjugation ratio and is positioned so that the collimated emission is focused on the 100 μ m spectrograph slit with another 80 mm focal length fused silica plano convex lens (Spindler and Hoyer). The $f/2.2$ CP140 imaging spectrograph (Instruments SA, Edison, NJ), with a 285 grooves/mm holographic grating blazed at 350 nm, is used. The spectrograph has a high throughput and efficiency. In contrast to previous work,¹² neither a Rayleigh filter nor a pre-excitation laser-line filter is used because the sheath flow cell and spectrograph eliminate and separate most of the Rayleigh scattering.

The EEV15-11CCD (EEV, Essex, England) is mounted in a liquid nitrogen-cooled CH270 camera head and is operated at -125 °C. The CCD is controlled by a CE200A camera electronics unit and an AT200 controller card (Photometrics Ltd., Tucson, AZ). The CCD system has excellent figures of merit: a negligible dark current, an RMS read noise of $5 e^-$, and a quantum efficiency of 17–25% from 280 to 500 nm with the Metachrome II coating downconverter. The combination of the CCD and the grating yields a spectral dispersion of 0.7 nm/pixel.

With the use of a CCD, many readout parameters influence performance and need to be optimized to maximize S/N. We used a CCD readout rate of 5 Hz, a serial bin factor of 5, and a parallel bin factor of 256.^{21,22} For the tyrosine detection limit work, the signal is collected from 294 to 311 nm, and for tryptophan, the signal is collected from 323 to 396 nm. A slower CCD readout rate of 1 Hz is used when acquiring the wavelength-resolved electrochromograms to decrease the data file size. Signal is

(17) Mathies, R. A.; Peck, K. *Anal. Chem.* **1990**, *62*, 1786–1791.

(18) Zhang, J. Z.; Chen, D. Y.; Wu, S.; Harke, H. R.; Dovichi, N. J. *Clin. Chem.* **1991**, *37*, 1492–1496.

(19) Cheng, Y. F.; Dovichi, N. J. *ASTM Spec. Tech. Publ.* **1990**, 1066, 151.

(20) Cheng, Y. F.; Wu, S.; Chen, D. Y.; Dovichi, N. J. *Anal. Chem.* **1990**, *62*, 496–503.

(21) Sweedler, J. V. *Crit. Rev. Anal. Chem.* **1993**, *24*, 59–98.

(22) Sweedler, J. V.; Ratzlaff, K.; Denton, M. B., Eds. *CTDs in Spectroscopy*; VCH Publishers: New York, 1994.

collected from 290 to 396 nm using a serial bin factor of 1 and a parallel bin factor of 256. The data acquisition system and the method of determining the S/N of the analyte peaks are described in more detail elsewhere.¹²

Electrophoresis System. The separation potential is applied with a 30 kV high-voltage power supply (Glassman, Whitehouse Station, NJ). Due to the sheath flow cell design, the detection end is held at ground, while the injection end is connected to the positive potential. The contact to high voltage is made through a Pt electrode and running buffer at the capillary inlet, and the connection to ground is made through the aluminum body of the sheath flow cell mount and sheath fluid at the capillary outlet. The injection end is enclosed in a plexiglass box with high-voltage safety interlocks, and the capillary is insulated with Teflon and Tygon tubing between the injection box and the sheath flow cell mount. All separations are performed at 30 kV in a fused silica, polyimide-coated capillary (Polymicro Technologies, Phoenix, AZ), 375 μm o.d., 50 μm i.d., and 82 cm long.

Reagents. All solutions are prepared using ultrapure Milli-Q water (Millipore, Bedford, MA), and all buffer solutions are filtered using 0.2 μm syringe filters to minimize fluorescent impurities and remove particles. To determine the emission spectra of phenylalanine, tryptophan, and tyrosine, 0.1 mM solutions of each amino acid (Sigma, St. Louis) in Millipore water are used.

The sheath fluid is filtered with an in-line filter degasser (Whatman International Ltd., Maidstone, England) to remove fluorescent particles and air bubbles. These steps are particularly important in the present work because as the excitation moves further into the UV, fluorescent background resulting from contamination increases rapidly and becomes much more problematic than with visible excitation. The running buffer and sheath fluid, 50 mM borate buffer at pH 8.9, are prepared by dissolving 3.09 g of boric acid (J. T. Baker, Phillipsburg, NJ) and 7.29 g of sodium tetraborate decahydrate (Fischer, Fairlawn, NJ) in water to a final volume of 1.00 L.

For the tyrosine detection limit studies, Sigma cell culture grade L-tyrosine (Sigma Chemical Co., St. Louis, MO) is used. For the tryptophan study, contamination is more problematic, as impurity peaks often appear in the electropherogram. The peptide and tryptophan mixture is prepared using neuromedin U-8, Tyr-Gly-Gly, leucine-enkephalin, and cell culture grade L-tryptophan from Sigma Chemical Co. and cholecystokinin N-acetyl hexapeptide nonsulfated (26–31), α -mating factor (yeast), and α -1-mating factor 1–6 from American Peptide Co. (Sunnyvale, CA). The concentrations of the individual analytes in the mixture are $\sim 3 \times 10^{-5}$ M for neuromedin, Tyr-Gly-Gly, and leucine-enkephalin and $\sim 1 \times 10^{-6}$ M in Trp, cholecystokinin (26–31), α -mating factor (yeast), and α -1-mating factor 1–6. All sample stock solutions are prepared in 50 mM borate buffer, and all sample injection solutions are prepared in running buffer.

Injections. All injections are 20 cm, 10 s hydrodynamic injections with a calculated injection volume of 4.1 nL. The sheath flow is turned off with a valve during injection so it does not alter the injection volume²⁰ and is turned on ~ 15 s after the beginning of the separation. Immediately after an injection, the capillary inlet is quickly dipped in a vial of clean running buffer (at the same height as the injection vial) to minimize the effects of extraneous injection.²³

Background Subtraction. The wavelength-resolved electropherograms are background subtracted to remove the Raman band. To perform the subtraction, the spectra obtained from 100 to 200 s, where no peaks appear, are used to calculate an average background spectrum. This average spectrum is then subtracted from each of the spectra composing the wavelength-resolved electropherogram.

RESULTS AND DISCUSSION

Fluorescence Measurements of Tyr, Phe, and Trp. Of the naturally occurring amino acids, only three have appreciable native fluorescence: phenylalanine, tyrosine, and tryptophan. Figure 2 shows the fluorescence emission spectra for each of these amino acids at 100 μM concentration with excitation at several available UV laser wavelengths. The three shortest excitation wavelengths (229, 244, and 257 nm) correspond to the emission lines available for a doubled Ar laser, and the last line at 284 nm is from the doubled Kr laser. For other laser sources (i.e., the 248 nm excimer and the 275 nm full-frame Ar laser), similar emission profiles are observed. Even at the optimum wavelength for phenylalanine, the emission intensity is nearly 2 orders of magnitude lower than the emission intensity for tyrosine and tryptophan. Other factors are important in selecting the optimum excitation wavelength for a particular amino acid: for example, at 284 nm excitation, the major tyrosine emission is at a wavelength partially overlapping the major Raman band of water, and thus tyrosine sensitivity at 284 nm is expected to be much less than that at 229 nm. Based on the emission data in Figure 2, phenylalanine should have the highest and tryptophan the lowest LOD.

Limits of Detection. The limits of detection have been evaluated for both tyrosine and tryptophan to assess the useful concentration range of the system. The 284 nm laser line matches the longer wavelength end of the excitation spectra of both tryptophan and tyrosine. This line is not optimum for excitation, because absorbance is low at 284 nm, especially for tyrosine. The laser is capable of providing 30 mW of power at 284 nm, while 9 and 8 mW of excitation power are found empirically to yield the highest S/N for tryptophan and tyrosine, respectively.

An electropherogram of a 4 nL injection of 1×10^{-9} M tryptophan near the LOD yields a peak with S/N = 9. As shown in Figure 3A, filtering of the high-frequency noise with a 9 point cubic/quartic smoothing routine increases the S/N to 14, giving a detection limit (3σ)^{24,25} of 2×10^{-10} M, or 0.8 amol. These results are the lowest reported detection limits for tryptophan obtained with use of native fluorescence in CE.

The LOD for tyrosine is 2 orders of magnitude higher than that for tryptophan. An electropherogram of a 4 nL injection of 5×10^{-8} M tyrosine gives a concentration detection limit of 3×10^{-8} M before smoothing, and 2×10^{-8} M (80 amol) after smoothing (Figure 3B). The tyrosine detection limits are higher than those for tryptophan due to tyrosine's lower ϵ (1600 at $\lambda_{\text{max}} = 280$ nm vs 4500 at $\lambda_{\text{max}} = 274$ nm)^{26,27} similar fluorescence yield, and much higher baseline noise due to a shorter Stokes shift. At

(23) Fishman, H. A.; Anundi, N. M.; Lee, T. T.; Scheller, R. H.; Zare, R. N. *Anal. Chem.* 1994, 66, 2318–2329.

(24) Strobel, H. A.; Heineman, W. R. *Chemical Instrumentation: A Systematic Approach*, 3rd ed.; John Wiley & Sons, Inc.: New York, 1989.

(25) Skoog, D. A.; Leary, J. J. *Principles of Instrumental Analysis*, 4th ed.; Harcourt, Brace Jovanovich Publishers: Orlando, FL, 1992.

(26) Chen, R. F.; Guillaud, G. G., Eds. *Practical Fluorescence: Theory, Methods and Techniques*; Marcel Dekker: New York, 1993.

(27) Chen, R. F. *Anal. Lett.* 1967, 1, 35–42.

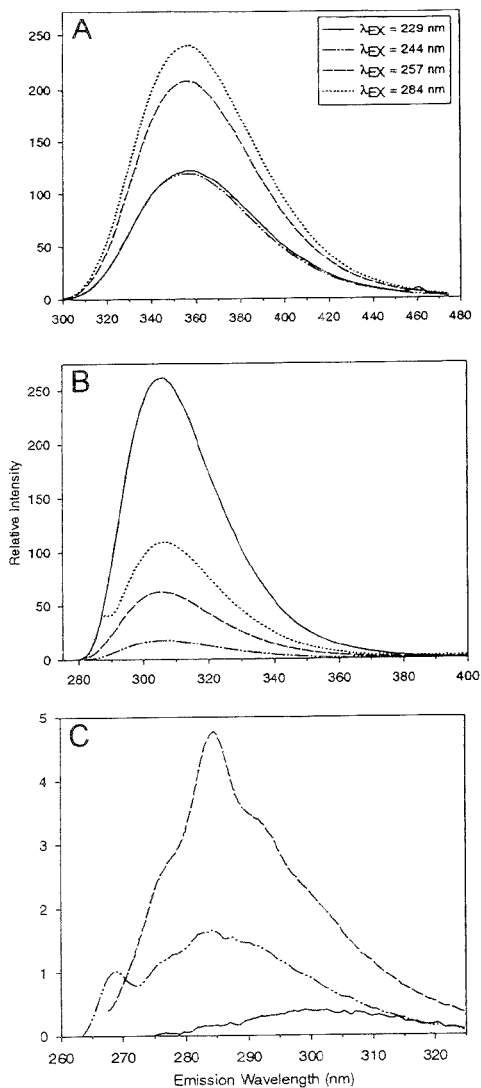


Figure 2. Emission spectra of 0.1 mM solutions of (A) tryptophan, (B) tyrosine, and (C) phenylalanine at several available UV laser excitation wavelengths.

this excitation wavelength, a significant portion of the tyrosine emission overlaps the major solvent Raman bands, while tryptophan has a longer Stokes shift, with most of the fluorescence signal appearing to the red of the Raman band. Thus, the baseline noise in the tyrosine channel is >5 -fold higher than that in the tryptophan channel.

The utility of CE is partly due to its high separation efficiency. The detection system can lead to band broadening, decreasing the separation efficiency if it is not designed and operated properly. We obtain a separation efficiency of $\sim 500\,000$ for a 10 s, 20 cm hydrodynamic tryptophan injection in a 50 mm capillary with a

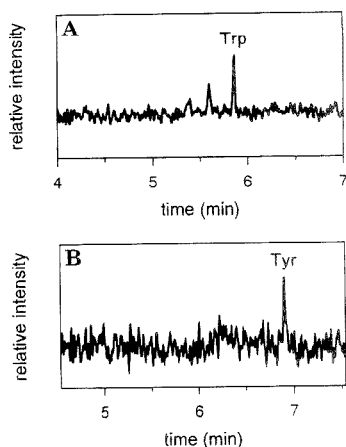


Figure 3. (A) Electropherogram of a 4 nL injection of 1×10^{-9} M tryptophan after smoothing, with $S/N = 14$, yielding a detection limit of 2×10^{-10} M. (B) Electropherogram of a 4 nL injection of 5×10^{-8} M tyrosine after smoothing, with $S/N = 8.5$, yielding a detection limit of 2×10^{-8} M.

Table 1. Analyte Sequences in Order of Elution

peak no.	peptide name	amino acid sequence
1	neuromedin	Tyr-Phe-Leu-Phe-Arg-Pro-Arg-Asn-NH ₂
2	α -mating factor (yeast)	Trp-His-Trp-Leu-Gln-Leu-Lys-Pro-Gly-Gln-Pro-Met-Tyr
3	tryptophan	Trp
4	α -1-mating factor	Trp-His-Trp-Leu-Gln-Leu
5	cholecystokinin (26-31)	Ac-Asp-Tyr-Met-Gly-Trp-Met-NH ₂
6	leucine-enkephalin	Tyr-Gly-Gly-Phe-Leu
7	Tyr-Gly-Gly	Tyr-Gly-Gly

30 kV separation potential. This value is twice the value obtained with a previous CCD system and is comparable to those obtained with use of other sheath flow detection systems in capillary electrophoresis.^{12,19-20}

Wavelength-Resolved Detection. The separation of a model mixture, composed of tryptophan and six peptides, demonstrates the differentiation of multiple analytes on the basis of their emission spectra. The mixture is composed of one peptide containing tryptophan, three peptides containing tyrosine, and two peptides containing both tryptophan and tyrosine. Table 1 shows the amino acid structures of the peptides, and Figure 4A shows the resulting wavelength-resolved electropherogram. The major Raman band of water is the dominant feature in this electropherogram. Figure 4B shows the results of subtracting out the spectral background from each emission spectrum.

Figure 5 shows the fluorescence emission spectra extracted and normalized from Figure 4B. As can be seen, the peptides that contain tryptophan are easily differentiated from those that contain tyrosine and no tryptophan, having peak maxima at about 358 and 304 nm, respectively. Teale reports similar results for proteins and categorizes them into those containing tyrosine but no tryptophan with a maximum at 305 nm and those containing tryptophan with a maximum at >330 nm.²⁸ Although the tryp-

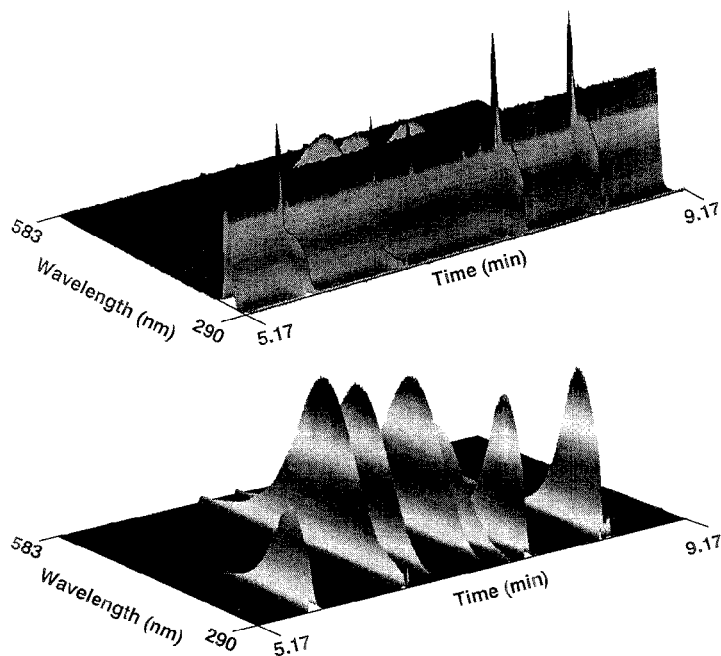


Figure 4. Wavelength-resolved electropherogram (A, top) before and (B, bottom) after background subtraction. A mixture of peptides containing tryptophan and tyrosine is separated, and the elution order of the analytes is shown in Table 1.

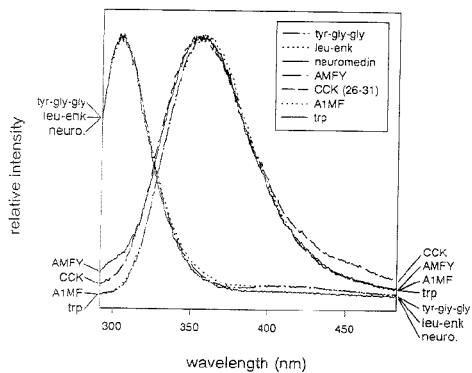


Figure 5. Extracted analyte spectra from the wavelength-resolved electropherogram, normalized with respect to peak intensity. The large differences in spectral emission of the analytes which contain only tyrosine and those which contain tryptophan are emphasized.

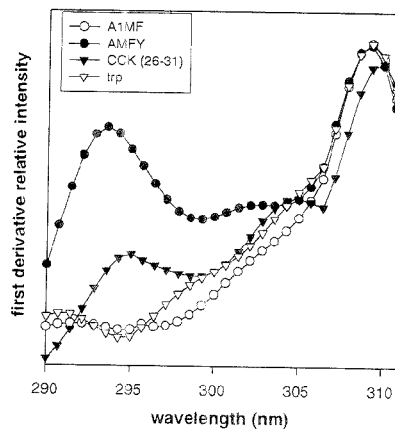


Figure 6. First derivative of the data in Figure 5. A local maximum can be seen at 294 nm for peptides that contain both tyrosine and tryptophan.

tophan maximum varies from protein to protein, the tyrosine position and lineshape do not significantly change.^{29,30}

Although the differences are more subtle, the peptides that contain both tryptophan and tyrosine can be differentiated from those which contain only tryptophan by the presence of a small

shoulder to the blue of the main feature at 304 nm³¹ and by a ~4 nm shift in the peak maximum from 358 to 354 nm. Figure 6 shows the first derivative spectra of the peptide emission spectra shown in Figure 5. The first derivative emphasizes the shoulder, as a local maximum appears at ~294 nm for species which contain both tryptophan and tyrosine.

(28) Teale, F. W. J. *Biochem. J.* **1960**, *76*, 381–388.

(29) Cowgill, R. W. In *Biochemical Fluorescence Concepts*; Chan, R. F., Edenhoef, H., Eds.; Marcel Dekker, Inc.: New York, 1976; Vol. 2, Chapter 2.

(30) Kronman, M. J.; Holmes, L. G. *Photochem. Photobiol.* **1971**, *14*, 113–134.

(31) R. F. Chan, H. Edenhoef, Eds. *Biochemical Fluorescence Concepts*; Marcel Dekker, Inc.: New York, 1976; Vol. 2.

These results show that it is possible to distinguish the three classes of peptides on the basis of their emission spectra. Peak identification and confirmation of known peptides is greatly aided by the information contained in the spectral emission profile. However, it is much more difficult to determine quantitatively how much tryptophan or tyrosine is present in peptides of unknown structure. The contribution of each fluorescent residue in different peptides and proteins to the overall fluorescence signal depends on its local environment. The differences in local environments change the intensity of fluorescence emission and shift the wavelength of emission maximum. Specifically, the fluorescence intensity significantly decreases (in some cases by 10–20-fold) for tyrosine contained within a peptide, as opposed to free tyrosine. The fluorescence intensity can increase or decrease by a factor of 2 for tryptophan contained within a peptide.³⁰ This greatly complicates quantitation of the numbers of these residues in the peptide or protein. For peptides that contain both tryptophan and tyrosine, quantitation is further complicated by energy transfer from tyrosine to tryptophan, which has a $1/r^6$ dependence on distance between the fluorophores, and so changes on the basis of the particular conformation of the protein.³² Thus, large differences in fluorescence intensity can be observed for peptides which contain the same number of tryptophan and/or tyrosine residues. Therefore, the optimum use of the fluorescence information is not to extract the total number of fluorescent residues but to place the peptide into one of the three categories described above. In addition, the emission spectrum can aid in identification by matching the emission profile to known standards on the basis of subtle changes in band shape.

A limitation of obtaining structural information from wavelength-resolved electropherograms is the need for analyte concentrations much higher than the detection limits shown in Figure 3. As lower concentrations are used, less information is obtained as noise degrades the spectral line shape. For example, the ability to detect the presence of tyrosine in a peptide that also contains tryptophan requires a high S/N to observe the small tyrosine

signal in the presence of a large tryptophan signal. Instead of using the entire wavelength-resolved electropherograms, two one-dimensional electropherograms can be obtained—a tyrosine channel and a tryptophan channel—simultaneously from different wavelength regions. These two channels of information can be used to discriminate between tyrosine and tryptophan while maintaining the low detection limits shown in Figure 3.

At 284 nm excitation, the tryptophan emission is much stronger than that of tyrosine; a better choice of excitation wavelengths may reduce the difference in sensitivities of the two residues. For example, exciting at 229 nm (the doubled 457 nm Ar line) is expected to improve the LOD of tyrosine by an order of magnitude due to better fluorescence characteristics (see Figure 2) and the reduction in the overlap of the emission and Raman scattering; this wavelength is expected to degrade tryptophan LODs by less than a factor of 2. In the future, more sophisticated algorithms will aid analyte identification using the wavelength-resolved electropherograms, confirm the identity of peptides on the basis of the emission profile, and extend the use of wavelength-resolved electropherograms to lower concentrations.

ACKNOWLEDGMENT

Insightful discussions with Tony Gilby (Waters) are acknowledged. The authors thank IBM for an RS6000 workstation through their SURS program and Coherent for the loan of the Innova 300 FreD Kr laser. Support from an NSF NYI Award, NIH (NS31609), the David and Lucille Packard Foundation, and the Searle Scholars Foundation is gratefully acknowledged. K.E.O. acknowledges the support of a Phillips Petroleum graduate fellowship.

Received for review May 17, 1995. Accepted July 16, 1995.*

AC950479R

(32) Steinberg, I. Z. *Annu. Rev. Biochem.* 1971, 40, 83–114.

* Abstract published in *Advance ACS Abstracts*, September 1, 1995.

Ultrasensitive Near-IR Fluorescence Detection for Capillary Gel Electrophoresis and DNA Sequencing Applications

Daryl C. Williams and Steven A. Soper*

Department of Chemistry, Louisiana State University, Baton Rouge, Louisiana 70803-1804

Electropherograms of oligonucleotides labeled with near-IR fluorescent dyes, separated by capillary gel electrophoresis and detected using an ultrasensitive near-IR fluorescence detection system, are presented. A universal M13 sequencing primer was labeled on the 5' end with a near-IR dye containing an isothiocyanate functional group. Comparison of the on-column detection limits in capillary gel electrophoresis for the near-IR dye-labeled sequencing primer to those obtained for a visible fluorescein-labeled primer indicated improved sensitivity for the near-IR case. The detection limit was found to be 3.4×10^{-20} mol (SNR = 3) for the near-IR dye-labeled primer, while the on-column detection limit for the fluorescein analog was 1.5×10^{-18} mol (SNR = 3). The sequence of nucleotide bases in an M13mp18 template was determined using a single lane, single dye technique. The molar concentrations of the ddNTPs used during chain extension reactions were varied to achieve a ratio of 4:2:1:0 (A:C:G:T), which allowed the identification of each terminal base via fluorescence intensity measurements. Sequencing ladders were prepared from the M13mp18 template using standard Sanger dideoxy chain-terminating techniques, the modified T7 DNA polymerase, and the near-IR dye-labeled M13 universal primer. The data indicated reliable sequence determination by the 4:2:1:0 (A:C:G:T) peak height identification method up to 250 bases from the annealing site. Comparison of the known sequence of the M13mp18 plasmid to that obtained using this protocol yielded a base-calling accuracy of 84% for the 4:2:1:0 ratio.

Fluorescence was first demonstrated by Smith et al.^{1,2} and Prober et al.³ to be a viable detection strategy in DNA sequencing applications using conventional slab gel electrophoresis (SGE) due to its ease of automation, its sensitivities comparable to those of autoradiography, and most importantly, its ability to provide real-time detection during the development of the electropherogram, which significantly increases the speed of the analysis. These advantages are extremely important in large-scale sequencing projects, such as the Human Genome Initiative. In their work,

fluorescent dyes were conjugated either to the 5' end of a sequencing primer or to a chain-terminating dideoxynucleotide at a non-hydrogen-bonding site. In all cases, labeling of the oligonucleotide with a fluorescent tag was required due to the poor intrinsic fluorescence quantum yields of the nucleotide bases and the need for deep UV excitation. The probes typically used for these DNA sequencing applications were fluorescein, NBD-Cl, or rhodamine derivatives, since they possess absorption maxima which matched the 488 and 514 nm lasing lines of the argon ion laser and have favorable fluorescence quantum yields.

Laser-induced fluorescence (LIF) detection coupled to capillary gel electrophoresis (CGE) has recently been shown to be an effective approach to DNA sequencing due to its speed and ultrahigh sensitivity.⁴⁻⁷ Since the volume of material that is loaded onto the column can be on the order of 1 nL in CGE, ultrasensitive detection is required. Investigators using LIF coupled with gel electrophoresis have reported detection limits which range from 6000 to 60 000 molecules with on-line visible fluorescence detection.⁹⁻¹² Dovichi and co-workers have reported detection limits as low as 1200 molecules obtained with use of an off-column sheath-flow cuvette in the detection scheme in order to reduce the level of the background produced from scattered and fluorescence photons originating from the gel matrix.¹⁰

Various strategies have been implemented in DNA sequencing applications to determine the identity of the terminal nucleotide in CGE using standard Sanger dideoxy chain-terminating methods and fluorescence detection. One strategy has been to employ a single chromophore attached to the 5' end of the sequencing primer and four sequential separations. The four runs can then be combined to yield the entire sequence of the template in question. However, gel breakdown during a typical CGE run can result in mobility shifts, which makes overlaying the single electrophoretic runs problematic. In addition, the time required

(1) Smith, L. M.; Sanders, J. Z.; Kaiser, R. J.; Hughes, P.; Dodd, C.; Connell, C. R.; Heimer, C.; Kent, S. B. H.; Hood, L. E. *Nature* 1986, 321, 674.
(2) Smith, L. M.; Kaiser, R. J.; Sanders, J. Z.; Hood, L. E. *Methods Enzymol.* 1987, 155, 260.
(3) Prober, G. M.; Trainor, G. L.; Dam, R. J.; Hobbs, F. W.; Robertson, C. W.; Zagursky, R. J.; Cocuzza, A. J.; Jensen, M. A.; Baumeister, K. *Science* 1987, 238, 336-341.

(4) Luckey, J. A.; Drossman, H.; Kostichka, A. J.; Mead, D. A.; D'Cunha, Swerdlow, H.; Gesteland, R. *Nucleic Acids Res.* 1990, 18, 1415-1419.
(5) Drossman, H.; Luckey, J. A.; Kostichka, A.; D'Cunha, J.; Smith, L. M. *Anal. Chem.* 1990, 62, 900-903.
(6) Luckey, J. A.; Drossman, H.; Kostichka, A.; Mead, D. A.; D'Cunha, J.; Norris, T. B.; Smith, L. M. *Nucleic Acids Res.* 1990, 18, 4417-4421.
(7) Smith, L. M. *Nature* 1991, 349, 812-813.
(8) Chen, D.; Swerdlow, H. P.; Härke, H. R.; Zhang, J. Z.; Dovichi, N. J. *J. Chromatogr.* 1991, 559, 237-246.
(9) Swerdlow, H.; Wu, S.; Härke, H. R.; Dovichi, N. J. *J. Chromatogr.* 1990, 516, 61-67.
(10) Swerdlow, H.; Zhang, J. Z.; Chen, D. Y.; Härke, H. R.; Grey, R.; Wu, S.; Dovichi, N. J. *Anal. Chem.* 1991, 63, 2835-2841.
(11) Swerdlow, H.; Gesteland, R. *Nucleic Acids Res.* 1990, 18, 1415-1419.
(12) Carson, S.; Cohen, A. S.; Belenki, A.; Ruiz-Martinez, M. C.; Berka, J.; Karger, B. L. *Anal. Chem.* 1993, 65, 3219-3226.

to perform the individual separations reduces the throughput of raw sequencing data.

Capillary gel sequencing has also been performed utilizing multiple dyes with distinct emission properties, allowing identification of the four terminal nucleotide bases by monitoring the fluorescence signal on separate detection channels.^{7,10,13} The difficulty with this approach results from the requirement of multiple detection channels and, in some cases, multiline laser excitation, which increases the complexity of the sequencing instrument. Recently, a single detection channel in the four-dye sequencing strategy has been developed by placing a rotating filter wheel in the optical train, which reduces the number of detection channels required in the four-dye base identification approach.¹⁰

The single chromophore method has also been adapted to a single electrophoretic run format using the modified T7 DNA polymerase enzyme and visible dye-labeled primers. Since this enzyme uniformly incorporates the four dideoxynucleotides (ddNTPs),^{14,15} identification of the terminal base can be accomplished by adjusting the molar ratio of the ddNTPs and calling the base from the fluorescence intensity of each electrophoretic band.^{10,16,17} Using a ddNTP ratio of 8.4:2:1 (A:C:G:T) and a primer labeled with the visible fluorescent dye TAMRA, the sequence of the M13mp18 template was determined.^{10,17} The accuracy rate was found to be 90% up to 250 bases from the primer, with significant reductions in the accuracy after this point. To increase the sequencing accuracy in this type of approach, a two-dye level system and fluorescence intensity ratios have been successfully used.^{10,18,19}

Near-IR fluorescence has recently been shown to be a viable alternative to visible fluorescence detection in many bioanalytical applications, such as fluorimmunoassays,^{20–22} high-performance liquid chromatography,^{23–26} analysis of intact proteins,²⁷ and free solution capillary electrophoresis.^{28–30} As a demonstration of the

impressive detection sensitivity that can be achieved in this region, several groups have reported the efficient detection of single molecules in the near-IR.^{31,32} The motivation for using fluorescence monitoring in the near-IR includes the smaller backgrounds observed during signal collection and the simpler instrumentation required to carry out detection. The lower background is a consequence of the fact that few species fluoresce in the near-IR, thereby reducing these interferences. The $1/\lambda^4$ dependence of the Raman cross section also provides a lower scatter contribution at these longer excitation wavelengths. The instrumentation required for near-IR fluorescence detection can consist of simple and inexpensive diode lasers and avalanche photodiodes. Since both of these components are solid state, the detector can be run for extended periods of time and require little maintenance or operator expertise. The use of a visible red-diode laser as an excitation source for detection of a cyanine dye-labeled oligonucleotide in CGE has recently been demonstrated.³³

Near-IR fluorescence can be a very attractive detection strategy in gel sequencing because of the highly scattering medium in which the separation is performed. Due to the intrinsically lower backgrounds that are expected in the near-IR when compared to the visible, on-column detection can be performed without sacrificing sensitivity. Near-IR has been demonstrated in DNA sequencing applications using SGE.^{34,35} The authors were able to obtain detection sensitivity of 2000 molecules in a monomeric (unpolymerized) acrylamide gel solution. We herein present our results demonstrating the first use of near-IR fluorescence in DNA sequencing applications in conjunction with CGE in a single lane, single dye base identification protocol with a tricarboyanine-labeled sequencing primer. Finally, a critical comparison of on-column detection limits for a visible and near-IR dye-labeled sequencing primers will be made in CGE.

EXPERIMENTAL SECTION

LIF-CGE Detector. Electrophoresis and detection were performed using a self-designed CE system, which is shown in Figure 1. The 10 mW excitation beam (795 nm) was supplied by a Ti:sapphire laser (Coherent Lasers Mira 900-F, Palo Alto, CA), pumped by the all-lines output of a small frame Ar ion laser (Coherent Lasers, Innova 310) and focused to a 10 μm diameter spot inside the capillary ($1/e^2$). For visible excitation, the 488 nm line of the Ar ion laser was used. The fluorescence was collected at right angles with a 40 \times high numerical aperture microscope objective (Nikon, Natick, MA; NA = 0.85) and spatially filtered through a slit with a width set at 2 mm, giving a viewing distance of 50 μm within the capillary. For near-IR fluorescence, a filter stack consisting of a Corning long-pass filter (50% T at 820 nm) and a bandpass interference filter (CWL = 830 nm, HBW = 15 nm; Omega Optical, Brattleboro, VT) were used. In the visible case, a Corning long-pass filter (50% T at 510 nm) and a bandpass interference filter (Omega Optical; CWL = 530 nm, HBW = 10 nm) served as the spectral filters. The light was then focused

- (13) Takahashi, S.; Katsuhiko, M.; Anazawa, T.; Kambara, H. *Anal. Chem.* **1994**, *66*, 1021–1026.
- (14) Tabor, S.; Richardson, C. C. *Proc. Natl. Acad. Sci. U.S.A.* **1987**, *84*, 4767–4771.
- (15) Tabor, S.; Richardson, C. C. *J. Biol. Chem.* **1990**, *265*, 8322–8328.
- (16) Ansoorge, W.; Simmermann, J.; Stegemann, J.; Erfle, H.; Voss, H. *Nucleic Acids Res.* **1990**, *18*, 3419.
- (17) Chen, D.; Swerlow, H. P.; Harke, H. R.; Zhang, J. Z.; Dovichi, N. J. *Proc. SPIE-Int. Soc. Opt. Eng.* **1991**, *1435*, 161–167.
- (18) Chen, D.; Harke, H. R.; Dovichi, N. J. *Nucleic Acids Res.* **1992**, *20*, 4873–4880.
- (19) Huang, X. C.; Quesada, M. A.; Mathies, R. A. *Anal. Chem.* **1992**, *64*, 2149–2154.
- (20) Imasaka, T.; Nakagawa, H.; Okazaki, T.; Ishibashi, N. *Anal. Chem.* **1990**, *62*, 2404–2405.
- (21) Boyer, A. E.; Lipowska, M.; Zen, J.; Patonay, G. *Anal. Lett.* **1992**, *25*, 415–428.
- (22) Williams, R. J.; Narayanan, N.; Casey, G. A.; Lipowska, M.; Strekowski, L.; Peralta, J. M.; Tsang, V. C. W.; Patonay, G. *Anal. Chem.* **1994**, *66*, 3102–3107.
- (23) Sauda, K.; Imasaka, T.; Ishibashi, N. *Anal. Chem.* **1986**, *58*, 2649–2653.
- (24) Sauda, K.; Imasaka, T.; Ishibashi, N. *Anal. Chim. Acta* **1986**, *187*, 353–356.
- (25) Mank, A. J. G.; Lingeman, H.; Gooijer, C. *Trends Anal. Chem.* **1992**, *11*, 210.
- (26) Williams, R. J.; Lipowska, M.; Patonay, G.; Strekowski, L. *Anal. Chem.* **1993**, *65*, 601–605.
- (27) Andrews-Wilberforce, A.; Patonay, G. *Spectrochim. Acta* **1990**, *46A*, 1153–1162.
- (28) Fuchigami, T.; Imasaka, T.; Shiga, M. *Anal. Chim. Acta* **1993**, *282*, 209–213.
- (29) Higashijima, T.; Fuchigami, T.; Imasaka, T.; Ishibashi, N. *Anal. Chem.* **1992**, *64*, 711–714.
- (30) Flanagan, J. H., Jr.; Legendre, B. L., Jr.; Hamner, R. P.; Soper, S. A. *Anal. Chem.* **1995**, *67*, 341–347.

- (31) Soper, S. A.; Matingly, Q. L.; Vegunta, P. *Anal. Chem.* **1993**, *65*, 746–747.
- (32) Lee, Y.; Maus, R. G.; Smith, B. W.; Winefordner, J. D. *Anal. Chem.* **1994**, *66*, 4142–4149.
- (33) Chen, F. A.; Tusk, A.; Pentoney, S., Jr.; Konrad, K.; Lew, C.; Koh, E.; Sternberg, J. *J. Chromatogr. A* **1993**, *652*, 355–360.
- (34) Middendorf, L. R.; Bruce, J. C.; Bruce, R. C.; Eckles, R. D.; Grone, D. L.; Roemer, S. C.; Sloniker, G. D.; Steffens, D. L.; Sutter, S. L.; Brumbaugh, J. A.; Patonay, G. *Electrophoresis* **1992**, *13*, 487–494.
- (35) Shealy, D. B.; Lipowska, M.; Lipowski, J.; Narayanan, N.; Sutter, S.; Strekowski, L.; Patonay, G. *Anal. Chem.* **1995**, *67*, 247–251.

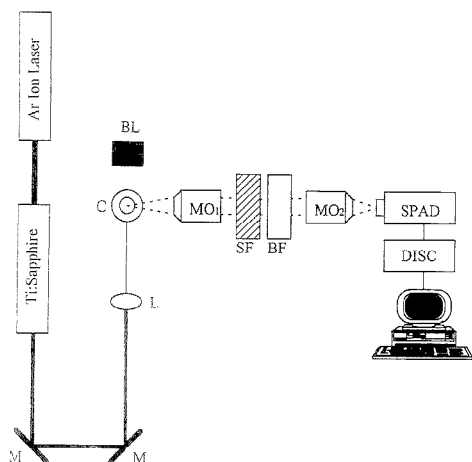


Figure 1. Block diagram of the capillary electrophoresis system. M, mirrors; L, focusing lens; C, capillary; BL, beam block; MO₁ and MO₂, microscope objectives; SF, spatial filter; BF, bandpass filter; SPAD, single photon avalanche diode; DISC, discriminator.

onto the photodetector by a 10× microscope objective. The detector was a single photon avalanche diode (SPAD; EG&G Electrooptics Canada, Vaudreuil, Canada) mounted on a thermoelectric cooler with a photoactive area of $1.77 \times 10^{-4} \text{ cm}^2$ (150 μm i.d.). The collected signal from the photodetector was conditioned using a discriminator (Tennelec Nucleus, TC 754) and sent to a multichannel scalar resident in a 486 PC for displaying the electropherograms (Tennelec PCA II, Oak Ridge, TN). Photocounts were typically integrated for 1 s during electrophoresis. The displayed data were not subjected to a filtering algorithm and are presented as raw data.

Capillary Gel Column Preparation. The column used for the separations was a 75 μm i.d., 375 μm o.d. fused-silica capillary (Polymicro, Phoenix, AZ). Before the column was filled with the polyacrylamide gel solution, a small portion of the polyimide coating was removed to provide an optical window by use of a low-temperature flame. The interior wall of the capillary was pretreated with 1 M NaOH (10 min), doubly distilled water (10 min), 1 M HCl (10 min), and finally, doubly distilled water (10 min). A mixture of [3-(methacryloxy)propyl]trimethoxysilane (Aldrich Chemical Co.) with methanol (50/50) was placed into the column and allowed to react overnight.³⁶ The column was then evacuated using low pressure, and the gel-forming solution was injected into the capillary. The gel-forming solution (3% T, 3% C or 6% T, 5% C) consisted of 0.1 M EDTA, 8 M urea, and riboflavin (Sigma Chemicals, St. Louis, MO), which was used as the polymerization initiator. Preparation of the polyacrylamide gel column was accomplished by vacuum injection of the gel-forming solution into the pretreated capillary, followed by photo-initiated polymerization.³⁷ The ends of the capillary were capped, and the column was submerged in an ice bath exposed to a high-energy UV light source overnight. After polymerization, the column was trimmed to a total length of 60 cm, with an effective

(36) Hjerten, S. *J. Chromatogr.* **1985**, *347*, 191–198.

(37) Wang, T.; Bruin, G. J.; Kraak, J. C.; Poppe, H. *Anal. Chem.* **1991**, *63*, 2207–2208.

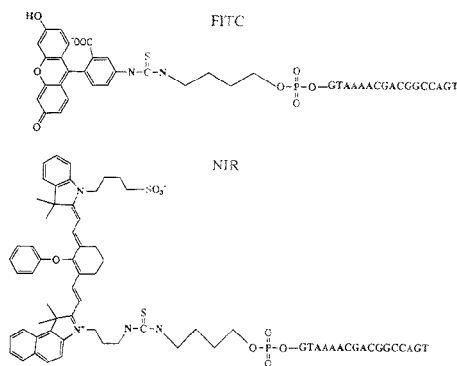


Figure 2. Structures of the near-IR and fluorescein dye-labeled primers.

length of 50 cm (injection to detection). The column was prerun for ~30 min at 6 kV prior to sample injection.

Polymerase Reactions. Extension of the primer was accomplished using a Sequenase Version 2 DNA sequencing kit (United States Biochemical, Cleveland, OH). Two picomoles of template DNA was annealed to 1 pmol of near-IR dye-labeled M13mp18 primer (LiCor, Lincoln, NE) at 65 °C for 2 min. Figure 2 shows the structures of the near-IR dye-labeled and the fluorescein-labeled primers. This mixture was allowed to cool slowly to room temperature over a period of 30 min. After the mixture cooled, 0.2 μmol of DIT, 0.1 μmol of MnCl_2 , 2 μL of 1:5 diluted dNTP solution, 0.004 unit of pyrophosphatase, and 0.4 unit of Sequenase enzyme were added. The mixture was allowed to sit at room temperature for 5 min. A 3.5 μL aliquot of this mixture was placed in a tube containing 3.2 pmol of ddATP, 1.6 pmol of ddCTP, 0.8 pmol of ddGTP, and no ddTTP, to achieve a ratio of 4:2:1:0 for A, C, G, and T terminators. Additional volumes of dNTPs were added to achieve an overall dNTP:ddNTP ratio of 1200:1. This mixture was incubated at 37 °C. The reaction was allowed to continue for 30 min before 4 μL of stop solution (95% formamide) was added to the reaction vessel.

RESULTS AND DISCUSSION

The fluorescence emission of many tricyanobenzene dyes intimately depends on the solvent and has been shown to increase when the dyes are placed in less H-bonding or more nonpolar solvents.³⁸ Recently, it has been shown that several red-emitting rhodamine dyes display enhanced fluorescence when dissolved in 7 M urea as compared to the same dyes dissolved in pure aqueous solutions.³⁷ In Figure 3 are shown the emission spectra of the near-IR dye-labeled primer in methanol, water, and unpolymerized denaturing gel solutions containing urea or formamide. In methanol, a quantum yield of 0.17 was determined for the near-IR dye-primer construct, and in pure water, the quantum yield was reduced to <0.01. When the dye-primer was placed in the denaturing gel solutions, the quantum yield was found to be ~0.09, significantly better than that observed in the pure aqueous solvent. The presence of the high organic content resulting from the formamide or urea helps in reducing fluorescence quenching that was observed in the pure aqueous solvent. Since many tricyar-

(38) Soper, S. A.; Mattingly, Q. L. *J. Am. Chem. Soc.* **1994**, *116*, 3744–3752.

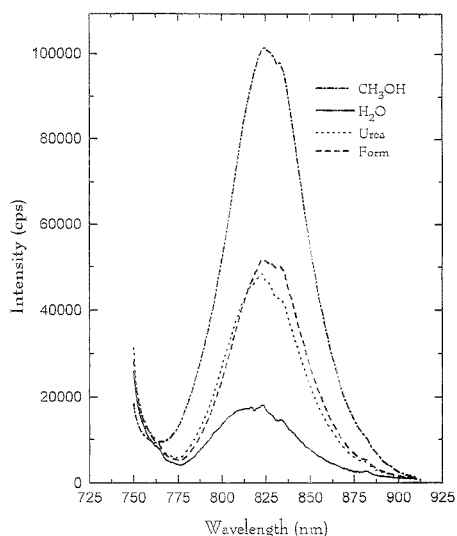


Figure 3. Fluorescence spectra of near-IR dye-labeled primer in methanol, 30% formamide, 8 M urea, and water. Dye-primer concentration was 1×10^{-6} M, and the excitation wavelength was set at 725 nm in all cases. The emission spectra were acquired on a conventional spectrofluorometer (SPEX Fluorolog) using a Xe lamp for excitation.

bocyanine dyes display quenching effects resulting from photoisomerization, the increased viscosity of the unpolymerized gel solution may result in the increased quantum yield. However, our previous research has demonstrated that the bridged tricarbo-cyanine dyes show negligible solvent viscosity-dependent photophysics.³⁸ These results indicate that increased viscosity associated with the gel solution does not result in the observed fluorescence enhancement.

To compare the limits of detection for our near-IR dye-labeled primer to those of a visible dye-labeled primer (fluorescein tag was fluorescein), the near-IR and visible dye primers were electrophoresed in a capillary column containing a 6% T, 5% C polyacrylamide gel. The resulting electropherograms are shown in Figure 4, and in Table 1, a summary of the data is presented. In order to achieve comparable backgrounds levels, the spatial filter slit width was reduced to 0.2 mm, and the laser power was dropped to ~ 3 mW in the visible case (488 nm). When the laser powers and slit widths were set to approximately the same values, the background level generated from the capillary gel matrix was found to be $> 200\,000$ counts/s for visible excitation, while in the near-IR case, the background was only 10 000 counts/s. The significantly smaller background for the near-IR results from a smaller Raman contribution and also fewer fluorescent impurities. The observed difference in the background counting rate did not result from differences in the efficiency of the photodetector at the monitored wavelengths, since the silicon avalanche diode has a larger single-photon detection efficiency at 800 nm than it does at 550 nm. The lower background level in the near-IR was observed in spite of the larger spectral window that was associated with the fluorescence bandpass filters (30 nm for near-IR and 10 nm for visible). In addition, there was a 42 nm shift between the

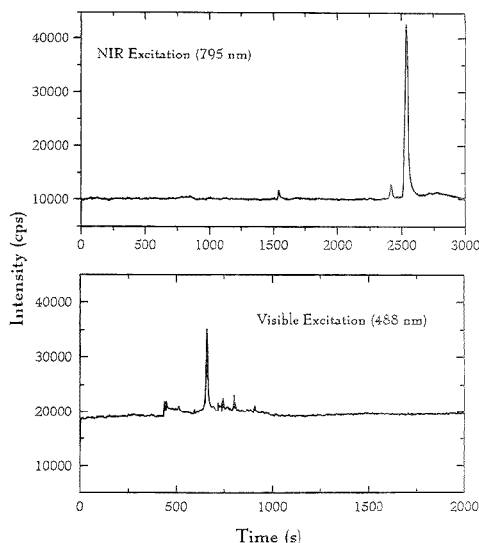


Figure 4. CGE separation and on-column detection of a 5.0×10^{-9} M solution of FITC-labeled M13mp18 universal primer and a 1.3×10^{-9} M solution of near-IR dye-labeled M13mp18 universal primer. The laser power was set at 10 mW for the near-IR case and 3 mW for visible excitation. The field strength in both cases was 250 V/cm. The samples were electrokinetically injected onto the gel column for 10 s at 5 kV. The gel column consisted of a 6% T, 5% C polyacrylamide matrix.

Table 1. Signal-to-Noise Ratios of Near-IR Dye- and FITC-Labeled M13 Universal Primers with On-Column Laser-Induced Fluorescence Detection^a

	near-IR dye primer	FITC primer
concn (M)	1.3×10^{-9}	5.0×10^{-9}
migrn time (s)	2555	660
mobility ($\text{cm}^2/\text{V s}$)	5.6×10^{-5}	2.1×10^{-1}
injectn vol (L)	2.9×10^{-9}	1.1×10^{-8}
no. of moles injected	3.8×10^{-19}	5.8×10^{-17}
net signal (counts/s) ^{b,c}	33 500	15 920
background (counts/s)	10 000	19 490
SNR	335	114
detectn limit (moles; SNR = 3)	3.4×10^{-20}	1.5×10^{-18}
quantum yield of dye	0.07	0.90

^a FITC primer was excited at 488 nm (argon ion laser) and the near-IR dye primer at 795 nm (Ti:sapphire laser); gel column (6% T, 5% C). Samples were injected onto the gel column for 10 s at 5 kV and separated at a field strength of 250 V/cm.^b The slit width on the LIF detector used in these experiments was set at 2.0 (near-IR) and 0.2 mm (visible) with a laser power of 10 (near-IR) and 3 mW (visible) in order to give comparable backgrounds.^c Net signal was calculated as peak height (counts/s) minus the average background (counts/s).

center wavelength of the interference filter and the excitation wavelength in the visible case, while for the near-IR, only 34 nm separated the excitation wavelength and the center wavelength of the interference filter.

As can be seen in Figure 4, a significant change in the apparent mobility of the near-IR dye-labeled primer was observed when compared to the fluorescein primer. Both electropherograms were run using the same capillary gel column and a field strength of 250 V/cm. The apparent mobilities were found to be 4.8×10^{-5} cm^2/Vs for the near-IR dye primer and 2.2×10^{-4} cm^2/Vs

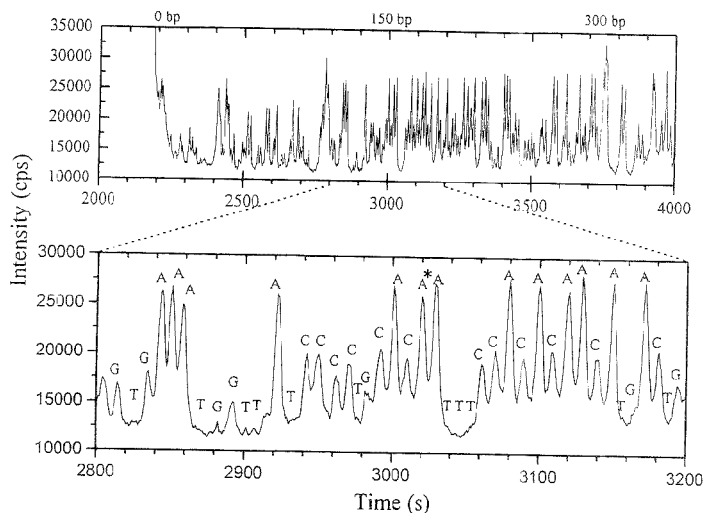


Figure 5. OGE sequencing run using a 4:2:1:0 peak height base identification system. Sample was electrokinetically injected for 120 s at 250 V/cm. The separation was performed at a field strength of 250 V/cm. Gel column consisted of a 3% T, 3% C polyacrylamide gel matrix. Laser excitation was achieved using 10 mW at 795 nm. The efficiency and resolution were calculated using the peak pair labeled in this electropherogram.

for the visible primer. A reduction in the mobility of the near-IR dye-labeled primer may result from the extended length of the near-IR dye label. Molecular modeling of this dye has indicated an overall length of ~ 17 Å.

Comparison of the on-column detection limits (SNR = 3, see Table 1) indicated a significant improvement for the near-IR dye primer, with a mass detection limit of 3.4×10^{-20} mol (34 zmol) for the near-IR case and 1.5×10^{-18} mol (1.5 amol) for the visible primer. While the laser power used in the near-IR case is near the saturation point of the electronic transition producing an optimal signal-to-noise ratio,³⁹ it is not in the visible case due to the smaller absorption cross section associated with fluorescein and the lower irradiance used. Improvement in the detection limit would be expected with higher laser powers. In spite of the lower quantum yield exhibited by the near-IR dye, we were able to realize an ~ 40 -fold improvement in detection sensitivity, primarily resulting from the significantly smaller background observed in the near-IR region. Based on the size of the effective sampling zone used in these experiments ($10 \mu\text{m} \times 50 \mu\text{m}$) and the cross sectional area of the capillary tube ($4418 \mu\text{m}^2$), the detection limit for only those near-IR dye-labeled molecules entering the sampling zone is 3.7 zmol (2250 molecules), comparable to state-of-the-art detection limits using off-column detection with a sheath-flow cuvette system.¹⁰ These detection limits are comparable to our previously reported results for several near-IR tricarboyanine dye separated by free-solution CE in methanol/water buffer systems.³⁰ The present results indicate minimal degradation of SNR arising from the complex gel matrix when near-IR monitoring is used.

In order to demonstrate the efficacy of using near-IR fluorescence in actual CGE DNA sequencing applications, we performed sequencing experiments with the M13mp18 plasmid and the single lane, single fluor peak height identification protocol using ddNTP concentration ratios of 4:2:1:0 (A:C:G:T). The result of a typical

sequencing run is shown in Figure 5. The gel concentration was reduced to 3% T, 3% C in order to increase the apparent mobility of the dye-labeled sequencing fragments and shorten the analysis time. The efficiency for the A-terminated peak (see Figure 5), calculated using the fwhm, was determined to be 2.0×10^6 plates, with a resolution of 0.8 between the adjacent A-terminated oligonucleotides. The sequence of the bases determined from the unconditioned electropherograms were compared to the known sequence of the M13mp18 template using the Genetics Computer Group (GCG, Madison, WI) program Pileup, which yielded an overlap rate of 84% (gap creation penalty, 0.10; gap extension penalty, 1) reading up to 250 bases from the primer annealing site. The sequencing data could be read to 400 bases per run, but the accuracy deteriorated significantly (60%). One source of error in the 4:2:1:0 ratio base-calling scheme arises from the necessity to use null signals to identify bases. Ambiguity is present when multiple null signals are encountered, which can lead to insertions or deletions. An additional problem occurs when a null signal appears between two large peaks. Another source of error results from the variance in the activity of the T7 DNA polymerase enzyme used to incorporate the ddNTPs at the desired 4:2:1:0 ratios. It has been reported that the incorporation efficiency of the various ddNTPs using this enzyme can vary by as much as 25%.¹⁰

CONCLUSION

The use of near-IR fluorescence in DNA sequencing applications using CGE can result in significant advancements in detection and instrumentation. The background resulting from scattering and fluorescence interferences is much smaller in the near-IR region, which results in impressive sensitivity without the need for off-column detection, which can add to the complexity of the instrument. Since many near-IR dyes have absorption maxima which match fundamental lasing lines of inexpensive semiconductor diode lasers, sensitive fluorescence detectors can be constructed in multiplexing devices appropriate for handling

(39) Mathies, R. A.; Peck, K.; Stryer, L. *Anal. Chem.* **1990**, *62*, 1786–1791.

large-scale sequencing projects, such as those encountered in the Human Genome Project, at a fraction of the cost associated with argon laser systems. In addition, these diode lasers can be constructed to deliver milliwatts to several watts of laser power and run continuously for long periods of time without the need for replacement of ion tubes. We have also shown that near-IR dye-labeled primers can be effectively used in the single lane, single fluor peak height identification protocol in CGE applications. Effective reads could be obtained up to 400 bases from the primer annealing site in a single run. However, the error rates arising from misidentifications of the terminal nucleotide bases were significant at these read lengths. Accuracy rates of 84% using a 4:2:1:0 intensity ratio were achieved up to 250 bases. Significant advances must still be made to improve the base-calling accuracy in a single lane, single fluor format.

ACKNOWLEDGMENT

The authors would like to thank the National Institutes of Health, Louisiana Educational Quality Support Fund, and Center for Energy Studies (Louisiana State University) for financial support of this research. The authors would also like to thank Prof. Simon Chang (Louisiana State University) for his helpful discussions during the course of this work.

Received for review May 1, 1995. Accepted July 11, 1995.*

AC950414O

* Abstract published in *Advance ACS Abstracts*, August 15, 1995.

¹³C NMR Determination of Protonated and Nonprotonated Carbons in Model Compounds, Mixtures, and Coal-Derived Liquid Samples

Shi Bai, Ronald J. Pugmire,* Charles L. Mayne, and David M. Grant*

Department of Chemistry, Brigham Young University, Provo, Utah 84602, and Departments of Chemistry and Chemical and Fuels Engineering, University of Utah, Salt Lake City, Utah 84112

The ratio of protonated to nonprotonated carbons provides an estimate of the average ring size in complex polycyclic aromatic hydrocarbon mixtures such as heavy oils and coal-derived liquids. Two model compounds, six mixtures of known composition, and nine heavy oil samples have been studied by ¹³C spin lattice relaxation inversion-recovery methods. Spin-lattice relaxation data differentiate protonated and nonprotonated carbons on the basis of relaxation differences arising from direct CH dipolar interactions. The integrated aromatic carbon intensities for a number of partially relaxed spectra were fit to a proposed spin relaxation rate expression. Results indicate that the carbon relaxation rates for both protonated and nonprotonated carbons are consistent, as expected, with the dipolar coupling of carbons to protons. The spin-lattice relaxation rates from nonlinear curve fitting of the composite resonance lines are consistent with experimental data for individual resonance lines in the model compounds and in the mixtures of model compounds involved in this study. The distribution of relaxation times for both carbon types is also estimated from the nonlinear fit of the experimental magnetization data. Simulations of composite magnetization under different conditions and an associated error analysis have been carried out to verify the validity of the composite relaxation expression. Low-temperature experiments were performed to simulate the heterogeneous lines observed in heavy oils and coal-derived liquids and to test the fitting method under heterogeneous line conditions.

NMR spectroscopy is a powerful tool for the structural analysis of complex organic substances, such as heavy oils, coals, and related geochemical samples. Solid state methods, developed to examine coal and other solid materials, provide useful information on average or composite structural features. Such an approach utilizes NMR data to estimate the average molecular size of an aromatic cluster in coal and also serves as the basis for defining a variety of other structural parameters.^{1,2} These data have been especially useful for modeling coal devolatilization behavior.^{3–5}

The experimental ratio of protonated to nonprotonated aromatic carbons, X_p/X_q , is used to estimate average cluster size parameters. Dipolar dephasing data and integrated intensities in selected chemical shift regions also may be used to measure the mole fraction of carbons that are found at bridgehead positions from which cluster sizes may be estimated. These aromatic clusters sizes have been determined in coals ranging in rank from lignite to anthracite, in an inertinite maceral, and in coal chars.^{6–9}

In this paper, differential proton-induced dipolar relaxation rates are used to determine the X_p/X_q ratio for liquid hydrocarbon mixtures, even when the complexity of the mixtures prevents resolution of individual resonance lines. Differential relaxation rates, acquired on two model compounds, six mixtures of model compounds, and nine heavy oil samples, are used in these substances to determine X_p/X_q for aromatic carbons. A composite relaxation rate expression is fit to the integrated aromatic spectral intensities for a variety of partially relaxed spectra. Results confirm that carbon relaxation processes depend, as expected, upon the nature of the dipolar couplings to either directly bonded or remote protons in protonated or nonprotonated carbons, respectively. The spin-lattice relaxation times obtained from nonlinear curve fitting of composite relaxation data in model compounds are found to agree well with the known structural features in these model systems. These composite relaxation times for protonated and nonprotonated carbons clearly differentiate the two types of carbon environments. This extension of related work on solids is helpful in estimating the average aromatic structural parameters of coal-derived liquid products and heavy oils.

The assumption that the relaxation times of individual carbons in the overall relaxation rate expression may be replaced by composite relaxation times for protonated and nonprotonated carbons has been verified by model calculations and error analysis using various hypothetical distributions of spin-lattice relaxation times. The calculations indicate that the approximation is valid when the average relaxation times of protonated and nonproton-

(1) Orendt, A. M.; Solum, M. S.; Sethi, N. K.; Pugmire, R. J.; Grant, D. M. In *Advances in Coal Spectroscopy*; Meuzelaar, H. L. C., Ed.; Plenum Press: New York, 1992; Chapter 10.

(2) Fletcher, T. H.; Kerstein, A. R.; Pugmire, R. J.; Grant, D. M. *Energy Fuels* 1992, 6, 414–438.

(3) Grant, D. M.; Pugmire, R. J.; Fletcher, T. H.; Kerstein, A. R. *Energy Fuels* 1989, 3, 175–186.

(4) Fletcher, T. H.; Kerstein, A. R.; Pugmire, R. J.; Grant, D. M. *Energy Fuels* 1990, 4, 54–60.

(5) Fletcher, T. H.; Solum, M. S.; Grant, D. M.; Pugmire, R. J. *Energy Fuels* 1992, 6, 643–650.

(6) Sethi, N. K.; Pugmire, R. J.; Facelli, J. C.; Grant, D. M. *Anal. Chem.* 1988, 60, 1574–1579.

(7) Solum, M. S.; Pugmire, R. J.; Grant, D. M. *Energy Fuels* 1989, 3, 187–193.

(8) Pugmire, R. J.; Solum, M. S.; Grant, D. M.; Critchfield, S.; Fletcher, T. H. *Fuel* 1991, 70, 414–422.

(9) Fletcher, T. H.; Solum, M. S.; Grant, D. M.; Critchfield, S.; Pugmire, R. J. *Twenty-Third International Symposium on Combustion*; The Combustion Institute: Pittsburgh, PA, 1990; p 1231.

Table 1. Model Compounds and Mixtures

C1	2-ethylnaphthalene (2.33) ^a
C2	pyrene (1.67)
M1	phenol (5.00), toluene (5.00), and <i>m</i> -xylene (2.00)
M2	naphthalene (4.00), 2-methylnaphthalene (2.33), 2-ethylnaphthalene (2.33)
M3	quinoline (3.50), 6-methylquinoline (2.00), 2,6-dimethylnaphthalene (1.50)
M4	naphthalene (4.00), tetralin (2.00), 1-naphthol (2.33)
M5	toluene (5.00), 2-ethylnaphthalene (2.33), phenanthrene (2.50), pyrene (1.67)
M6	toluene (5.00), <i>m</i> -xylene (2.00), <i>m</i> -cresol (2.00), naphthalene (4.00), 2-methylnaphthalene (2.33), 2-ethylnaphthalene (2.33), phenanthrene (2.50), pyrene (1.67), quinoline (3.50), 6-methylquinoline (2.00), 8-methylquinoline (2.00), 3-methyl-2-quinoxalinol (1.00)

^a The number in parentheses is the X_p/X_Q value for the corresponding compound.

ated carbons are clearly different and when the distributions of relaxation times about their average values are relatively narrow compared to the separation in the two average values. These numerical simulations of the relaxing magnetization also provide a means for estimating relative errors in X_p/X_Q . Results indicate that the typical X_p/X_Q values fall in a region where the systematic errors introduced by the above assumptions are relatively small.

EXPERIMENTAL SECTION

Samples. Model compounds were obtained from standard commercial sources and used without further purification. Mixtures were prepared by weighing samples into an NMR tube. Sufficient solvent (CD_2Cl_2) was added to dissolve solid samples and to obtain a strong lock signal. The components of model compounds (C1, C2) and mixtures (M1–M6) are listed in Table 1. The X_p/X_Q values for each individual compound, which range from 1.25 to 5.00, are also given in parentheses in the table. For single rings and some polycyclic aromatic hydrocarbons, the ^{13}C NMR spectra contain separated chemical shift regions for protonated and nonprotonated aromatic carbons. In many condensed aromatic systems, however, these regions overlap significantly. Because of this feature, both heterocyclic and homocyclic aromatic compounds were chosen as components in the model mixtures.

The coal-derived samples were provided by Consol, Inc. The liquids were process stream products from run CC-15 using the HRI, Inc., bench-scale liquefaction unit. The coal used was taken from the Wyodak and Anderson seam in the Black Thunder mine. The samples utilized in this study were three process filter liquids (PFL), three interstage samples (INT), and three combined samples of separator overhead and atmospheric still overhead (SOH). A detailed description how these samples were produced is given elsewhere.¹⁰

NMR Data. All ^{13}C spectra were obtained on a Varian VXR-500 spectrometer. The accuracy of the relaxation measurements was improved by calibrating the 90° pulse width before each relaxation time determination on all compounds. The inversion–recovery technique¹¹ was adapted to measure the magnetization variations with changing delay times. For each compound and

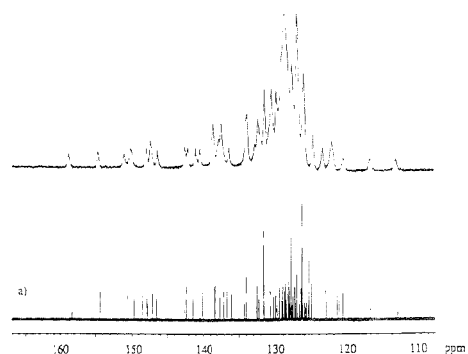


Figure 1. ^{13}C NMR spectrum of mixture M6: (a) at room temperature and (b) at -95 °C. Lower temperatures give heterogeneous line shapes seen in real coal liquid samples.

mixture, the total aromatic magnetization, i.e., the sum of the intensities of all resonances in the sp^2 chemical shift region, was measured as a function of delay time following the inversion pulse. The delay times consist of an array of 15–18 values ranging from 0.05 to 250 s for the experiments carried out at 26 °C, and from 0.1 and 40 s for the low-temperature experiments. The total aromatic magnetization of each spectrum was normalized to the magnetization value at the longest delay time used for the experiment. In order to obtain good signal-to-noise values, typical times for the inversion–recovery experiments were 60 h for the single compounds and 72 h for the mixtures. For the coal-derived liquid samples, 17 delay times ranging from 0.025 to 40 s were used. A total of 160 scans were accumulated for each delay time, and a 50 s delay was used to allow full recovery of all carbons between successive scans. The total acquisition time for each sample was approximately 48 h.

The room-temperature ^{13}C NMR experiment yields a spectrum with individually resolved resonances for the model mixture M6, as shown in Figure 1a. The resolution of this spectrum is quite different from the representative spectrum obtained for the coal-derived liquid sample INT 10 (see Figure 2). The remaining coal-derived liquid samples have spectral patterns similar to those of INT 10. Low-temperature experiments at -95 °C were performed for mixtures M1, M5, and M6 in order to simulate the relaxation regimes encountered in the spectra of coal-derived liquid samples. The low-temperature ^{13}C NMR spectrum of M6 shown in Figure 1b exhibits the broadened heterogeneous line shape noted in coal-derived liquids. Minor differences exist between (a) and (b). The shifting peaks presumably are due to thermal effects on the chemical shifts. It is possible at low temperatures that some of the components have precipitated or become suspended in the viscous liquids as colloids. However, the gross features of both (a) and (b) can be primarily accounted for with the differences in line broadening. Similar heterogeneous lines were also observed in samples M1 and M5 at low temperatures.

RESULTS AND DISCUSSION

Relaxation Model and Numerical Simulations. In an inversion–recovery experiment on a complex mixture, the total magnetization, $M(t)$, of all sp^2 carbons at any time, t , after a 180° pulse, can be expressed as follows:¹¹

(10) Pigmore, R. J.; Solum, M. S. Analysis of Black Thunder Coal and Liquefaction Products from HRI Bench Unit Ran CC-15. Report to CONSOL Inc., DOE Contract DE-AC22-89PC89883, 24 January 1994.

(11) Vold, R. L.; Waugh, J. S.; Klein, M. P.; Phelps, D. E. *J. Chem. Phys.* **1968**, *48*, 3831–3832.

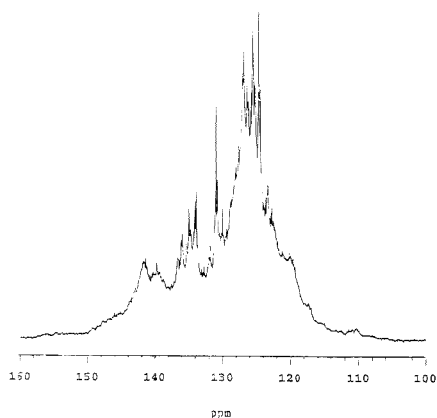


Figure 2. Quantitative ^{13}C NMR spectra of the aromatic region of the coal-derived liquid sample INT 10.

$$M(t) = \frac{M_0}{N} \sum_{i=1}^N (1 - (1 + \beta) \exp(-t/T_i)) \quad (1)$$

where β is a scaling parameter, close to unity, used to compensate for incomplete inversion arising from pulse imperfections and other experimental inefficiencies. T_i is the spin-lattice relaxation time for each individual carbon nucleus, and M_0 is the total equilibrium magnetization for all sp^2 carbons. The summation index, i , ranges over all sp^2 ^{13}C nuclei in the sample studied. If the sp^2 carbons are divided into two categories, protonated and nonprotonated carbons, eq 1 can be expressed as

$$\begin{aligned} M(t) &= \frac{N_P m_0}{N} \sum_{i=1}^{N_P} (1 - (1 + \beta) \exp(-t/T_{Pi})) + \\ &\quad \frac{N_Q m_0}{N} \sum_{j=1}^{N_Q} (1 - (1 + \beta) \exp(-t/T_{Qj})) \\ &= X_P \sum_{i=1}^{N_P} (1 - (1 + \beta) \exp(-t/T_{Pi})) + \\ &\quad X_Q \sum_{j=1}^{N_Q} (1 - (1 + \beta) \exp(-t/T_{Qj})) \quad (2) \end{aligned}$$

where i and j are, respectively, the summation indexes for the total number of protonated, N_P , and nonprotonated, N_Q , carbons in the sample. m_0 is the equilibrium magnetization for each individual carbon nucleus and is presumed to be unity for the sake of convenience. T_{Pi} and T_{Qj} are the corresponding spin-lattice relaxation times of each individual aromatic protonated or nonprotonated carbon, and X_P and X_Q are the mole fractions for protonated and nonprotonated carbons, respectively.

In solid state coal samples, the dephasing times for carbons strongly coupled to directly bonded protons are much shorter than those that are weakly coupled to remote protons. Solum et al.⁷ measured the Lorentzian (weakly coupled) and Gaussian (strongly coupled) decay time constants, T_L and T_G , for the Argonne premium coals and observed that the ratio of T_G/T_L is always less

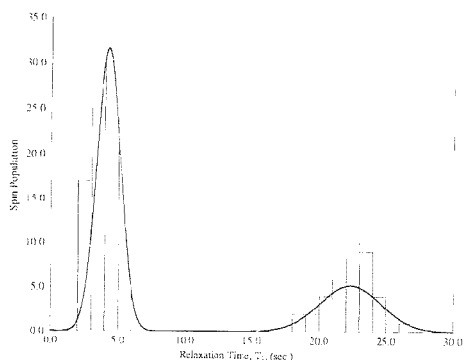


Figure 3. Spin population distribution of relaxation time for sample M6. The bar graph represents the experimental spin-lattice relaxation time distributions of molecules in M6, and the solid line is the simulation from eq 4 using the parameters found in Table 2.

than 0.1. On the basis of this information and other observations,¹²⁻¹⁴ the composite relaxation times, T_P and T_Q , for protonated and nonprotonated carbons, respectively, are used to replace the individual relaxation times, T_{Pi} and T_{Qj} found in eq 2. The summations in eq 2 are also dropped by the replacement of the individual relaxation times with the two average relaxation times. This approach, which we designate as the *average relaxation time* (ART) approximation, allows eq 2 to be simplified as follows:

$$M(t) = X_P (1 - (1 + \beta) \exp(-t/T_P)) + X_Q (1 - (1 + \beta) \exp(-t/T_Q)) \quad (3)$$

In a complex liquid sample, such as a coal-derived liquid or a heavy oil, there are so many different types of carbon nuclei that it is reasonable to assume that statistical relaxation time distributions exist for both T_P and T_Q . In the model mixture M6, which has more than 100 different types of carbons, the T_i spin-lattice relaxation times conform to a Gaussian distribution (see Figure 3). Therefore, Gaussian distribution functions with broadening measures, σ_P and σ_Q , are used to estimate the number of carbons with relaxation time T . This combined distribution function for protonated and nonprotonated carbons is expressed as

$$F(T) = \frac{X_P}{\sqrt{2\pi\sigma_P}} \exp\left(-\frac{1}{2}\left(\frac{T - T_P}{\sigma_P}\right)^2\right) + \frac{X_Q}{\sqrt{2\pi\sigma_Q}} \exp\left(-\frac{1}{2}\left(\frac{T - T_Q}{\sigma_Q}\right)^2\right) \quad (4)$$

where T_P and T_Q are average relaxation times, σ_P and σ_Q are standard deviations of these average relaxation times, and X_P and X_Q are the mole fractions for protonated and nonprotonated carbons, respectively. The composite distribution function, $F(T)$,

(12) Murphy P. D.; Cassidy T. J.; Gerstein, B. C. *Fuel* 1982, 61, 1233-1240.

(13) Murphy P. D.; Gerstein B. C.; Weinberg V. L.; Yen T. F. *Anal. Chem.* 1982, 54, 522-525.

(14) Alenany, L. B.; Grant, D. M.; Alger, T. D.; Pugmire, R. J.; Zilm, K. W. *J. Am. Chem. Soc.* 1983, 105, 6697-6704.

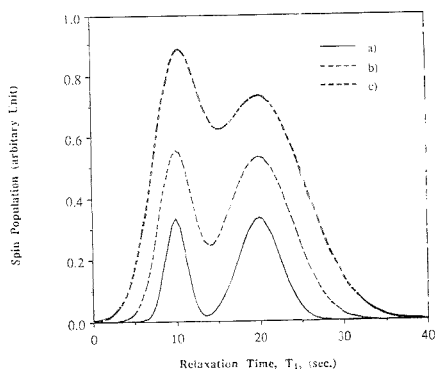


Figure 4. Gaussian spin population distributions at constant ratio of T_P/T_Q : (a) $r_P = r_Q = 0.125$. (b) $r_P = r_Q = 0.200$, and (c) $r_P = r_Q = 0.275$.

determines the relative number of spins corresponding to each relaxation time T_i in terms of the given statistical parameters. Using $F(T_i)$, eqs 1 and 2 may be modified to the following:

$$M(t) = \sum_i F(T_i) (1 - (1 + \beta) \exp(-t/T_i)) \quad (5)$$

In eq 5, i is a summation index over the different spin-lattice relaxation times. These times are assumed to be uniformly incremented between 0 and the maximum relaxation time measured in the systems studied. The parameters in eq 5 may be obtained by fitting the composite experimental magnetization data against the delay time t in an inversion-recovery experiment. These parameters are then used to identify the protonated and nonprotonated carbon magnetizations in the total sp^2 carbon magnetization. If the total magnetization is normalized (i.e., $X_P + X_Q = 1$), the six adjustable fitting parameters in this model are X_P (or X_Q), T_P , σ_P , T_Q , σ_Q , and β . The parameter X_P/X_Q may be calculated readily as follows:

$$X_P/X_Q = X_P/(1 - X_P) \quad (6)$$

The relaxation model described by eq 5 will be well behaved only if the ART approximation obtains. Further, the constants T_P and T_Q must be significantly different from each other relative to their respective σ_P and σ_Q distributed values. This is recognized graphically (see Figures 6 and 7) whenever the spin-lattice relaxation times have a narrow distribution around their average values. Designating the ratio σ_i/T_i as the parameter τ_i , it is observed that when r_P , r_Q , and T_P/T_Q comply with the ART approximation, reliable results will be achieved using equation 5. A cursory examination of equation 5 also suggests that a smaller value for T_P/T_Q can compensate for relatively larger values of r_P and r_Q and vice versa. Therefore, the distribution of relaxation times for the various ^{13}C nuclei in the sample becomes a critical factor in the ART approximation.

It is informative to consider several limits of eq 4, and various $F(t)$ distributions are shown in Figures 4 and 5. In Figure 4, we have used $T_P = 10$ s, $T_Q = 20$ s, $T_P/T_Q = 1/2$, and, for the sake of convenience, r_P and r_Q are taken to equal each other. Cases

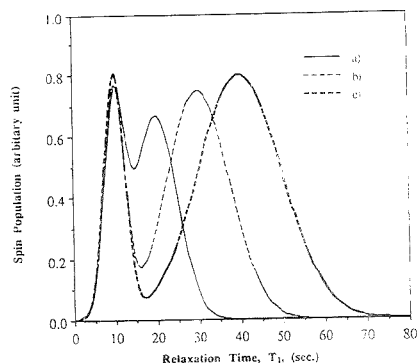


Figure 5. Gaussian spin population distributions at constant r_P and r_Q : (a) $T_P = 10$ s, $T_Q = 20$ s, and $T_P/T_Q = 1/2$; (b) $T_P = 10$ s, $T_Q = 30$ s, and $T_P/T_Q = 1/3$; and (c) $T_P = 10$ s, $T_Q = 40$ s, and $T_P/T_Q = 1/4$.

a-c in Figure 4 correspond to values of r_P and r_Q that are 0.125, 0.200, and 0.275, respectively. Case a represents a near ideal situation where the distribution of T_i values for protonated and nonprotonated carbons do not overlap appreciably. The simulation based on the assumptions of case a indicates that the error introduced by the ART approximation is less than 1% (see Figure 6). In case b, where the distribution of T_i values for protonated and nonprotonated carbons begins to overlap significantly, the separation of the two relaxation regimes is still adequate to satisfy the ART approximation and an error of only 2.5% is noted. This type of distribution is frequently encountered in coal-derived liquids. In case c, the protonated and nonprotonated relaxation time distributions overlap seriously and the ART approximation starts to fail. In this case, an approximately 10% error is introduced by the ART approximation. Another aspect of the same issue is demonstrated in Figure 5, where the values of r_P and r_Q are locked at 0.25, and ratios for T_P/T_Q of 1/2, 1/3, and 1/4 correspond to cases a-c, respectively. Case a demonstrates the maximum overlap of the distribution of T_i values for protonated and nonprotonated carbons, and the ART approximation introduces an error of approximately 7% into the estimation of X_P/X_Q . Case b is similar to the results observed in case b of Figure 4, but an error of only 1.5% is observed for this case in Figure 5. The T_i distribution described in case b approximates data observed in heavy oil liquids. Case c of Figure 5 represents an ideal distribution of T_i where the error introduced into the estimation of X_P/X_Q is less than 1%, similar to case a of Figure 4.

In order to examine the distribution of relaxation time constants in the model mixtures, the individual relaxation times for all carbon nuclei were measured for the set of model compounds used in these mixtures. The values of $T_P(\max)$, $T_P(\min)$, and $T_P(\text{av})$ listed in Table 2 were obtained for each compound from inversion-recovery experiments on individual lines. The respective values represent the maximum, minimum, and average values of relaxation times of the individual protonated carbon resonances in each sample. Corresponding notations, $T_Q(\max)$, $T_Q(\min)$, and $T_Q(\text{av})$ are used for the nonprotonated carbons. The ratio of $T_P/T_Q(\text{av})$ listed in Table 2 for all samples ranges from 0.19 to 0.33. These ratios are larger than the corresponding value (0.1) typically observed in the solid state data

Table 2. Comparison of Fitting Results with Experimental Measurements

	sample							
	C1	C2	M1	M2	M3	M4	M5	M6
Relaxation Parameters								
$T_p(\text{max})^c$	4.6	4.1	4.4	7.0	5.1	5.8	4.8	6.2
$T_p(\text{min})^c$	3.3	3.8	2.2	3.7	2.5	3.5	3.4	3.2
$T_p(\text{av})^c$	4.1 (5) ^f	3.9 (2)	3.5 (7)	5.7 (9)	3.5 (8)	4.5 (7)	4.0 (4)	4.8 (8)
$T_Q(\text{max})^c$	14.5	11.9	14.8	24.6	23.3	21.8	24.3	24.5
$T_Q(\text{min})^c$	13.8	11.6	6.3	16.1	8.4	12.7	12.6	16.2
$T_Q(\text{av})^c$	14.1 (3)	11.8 (2)	10.6 (2.5)	20.3 (3.1)	13.8 (4.6)	17.1 (3.3)	20.9 (3.3)	19.8 (2.3)
$T_p/T_Q(\text{av})^c$	0.291	0.331	0.330	0.281	0.254	0.263	0.191	0.242
r_p^b	4.18 (2)	4.09 (8)	3.50 (3)	5.99 (7)	3.61 (4)	4.56 (4)	3.94 (4)	4.25 (2)
σ_p^b	0.52 (2)	0.21 (2)	0.83 (2)	0.88 (3)	0.77 (2)	0.83 (2)	0.23 (1)	0.88 (7)
r_Q^b	15.04 (14)	11.63 (17)	11.23 (24)	20.73 (34)	14.40 (13)	18.23 (19)	18.03 (31)	22.33 (9)
σ_Q^b	0.48 (4)	0.51 (5)	1.39 (8)	3.22 (14)	3.57 (8)	2.73 (6)	3.22 (6)	2.29 (3)
$T_p/T_Q(\text{fit})^c$	0.277	0.350	0.312	0.289	0.251	0.250	0.219	0.190
Mole Fraction Data								
β^c	0.704 (3)	0.895 (4)	0.832 (3)	0.818 (2)	0.712 (2)	0.848 (2)	0.819 (2)	0.825 (1)
X_p^c	0.669 (14)	0.619 (15)	0.781 (6)	0.719 (31)	0.686 (6)	0.739 (5)	0.700 (7)	0.701 (2)
X_Q^c	0.331	0.381	0.219	0.281	0.314	0.261	0.300	0.299
$X_p/X_Q(\text{fit})^c$	2.11 (2)	1.82 (2)	3.57 (1)	2.56 (4)	2.18 (2)	2.83 (2)	2.33 (2)	2.34 (3)
$X_p/X_Q(\text{real})^c$	2.33	1.67	3.50	2.75	2.11	2.71	2.29	2.23

^a See text for the details. ^b Obtained by fitting the composite relaxation data on sp^2 carbon magnetization data with eq 5. ^c Calculated by dividing average protonated relaxation time from fitting to average nonprotonated relaxation time. ^d $X_Q = 1 - X_p$. ^e From sample preparations, i.e., the molar ratio of protonated and nonprotonated carbons. ^f Errors recorded in parentheses indicate uncertainty in the least significant digit(s).

for the Argonne coals. The standard deviations of relaxation time constants, σ_p and σ_Q , were found to be in the range of 0.2–0.9 and 0.2–4.6 for protonated and nonprotonated carbons, respectively. However, the reduced parameters, r_p and r_Q , which are the ratios of the standard deviations to the average relaxation times, range from 0.1 to 0.3 for all mixtures. From the individual T_1 measurements, the distribution of relaxation time constants for sample M6 is given in Figure 3. The column graphs in Figure 3 represent the measured relaxation time distribution for M6. It is noted that the distribution of relaxation times exhibits a slightly skewed shape for both protonated and nonprotonated carbons. The moments associated with this skewing were not calculated because of the limited data set and a simple Gaussian distribution was applied to these data. The sample M6 is the most "complex" model mixture and contains about 100 different carbon nuclei. As the number of different carbon nuclei in the sample increases along with the increase in the complexity of the mixtures, it is presumed that such deviations between the relaxation time distribution and a Gaussian distribution will be reduced.

To evaluate the validity of eq 5, numerical simulations of different transient magnetization have been carried out using a model calculation. Equation 5 was used to target spectral intensities as a function of delay time, t , for a variety of initial conditions (i.e., T_p/T_Q and r). The calculated magnetization data sets are then fit independently by eq 5 to determine the validity of the ART approximation. By comparing fitting results for X_p/X_Q with the true average input value of X_p/X_Q , the validity of various cases can be explored to determine the accumulation of errors in the ART approximation. The experimental observations of relaxation time constants of model compounds and mixtures also provide valuable information on the propagation of errors. The numerical simulation results are presented by plotting the relative errors $(X_p - X_p(\text{input}))/X_p(\text{input})$ vs the reduced parameter r ($r = r_p = r_Q$) at different values of T_p/T_Q . For an assumed T_p value of 5.0 s and a range of T_Q values between 15.0 and 60.0 s, the ratio of T_p/T_Q falls between 0.33 and 0.10. The resulting simulation with $X_p = 0.50$ is shown in Figure 6 and those with X_p

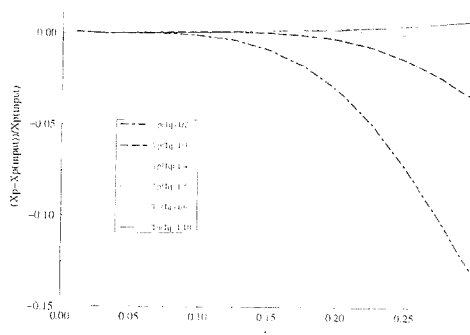


Figure 6. Plot of the simulated relative error as a function of r as $X_p(\text{input}) = 0.5$. Relative error is defined as $(X_p/X_Q - X_p(\text{input})/X_Q(\text{input})) / (X_p(\text{input})/X_Q(\text{input}))$. In this calculation, $r = r_p = r_Q$.

equal to 0.33 and to 0.67 are given in Figure 7. For all cases, the relative errors produced by the ART approximation will be less than 10% as long as the r value is less than 0.25. This relaxation model overestimates the values of X_p/X_Q when $X_p > 0.50$ and underestimates the X_p/X_Q when $X_p \leq 0.50$. As expected, when T_p/T_Q increases at a given value of r , the average relaxation time approximation introduces a larger relative error into the estimation of X_p/X_Q . Simulation results also indicate that the errors generated by the ART approximation are negligible in the solid state NMR studies of Argonne premium coals⁷ because of the small values of T_p/T_Q .

Model Compounds and Mixtures. The normalized total magnetizations, obtained from the summation of all resonance intensities in the sp^2 chemical shift region, were then used in eq 5 to obtain the composite relaxation parameters for samples C1, C2, and M1–M6. These results, presented in Table 2, for protonated, T_p , and nonprotonated, T_Q , carbons were obtained using a nonlinear least-squares fit of eq 5. Inspection of the parameters for all compounds and mixtures obtained

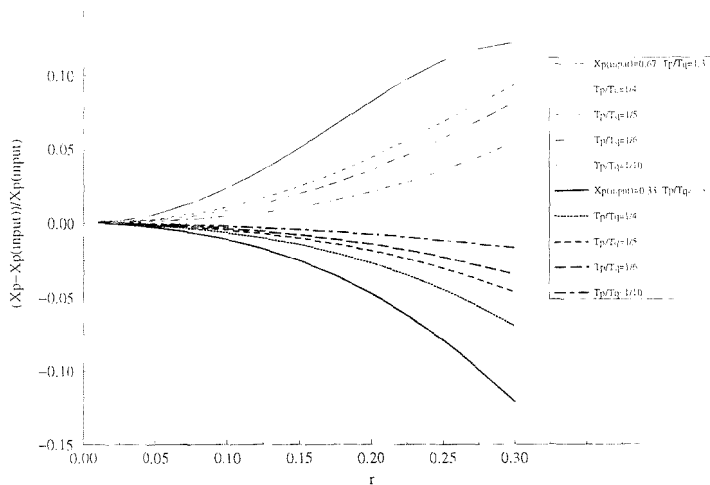


Figure 7. Plot of simulation relative error as a function of r when $X_p(\text{input}) = 0.33$ and $X_p(\text{input}) = 0.67$.

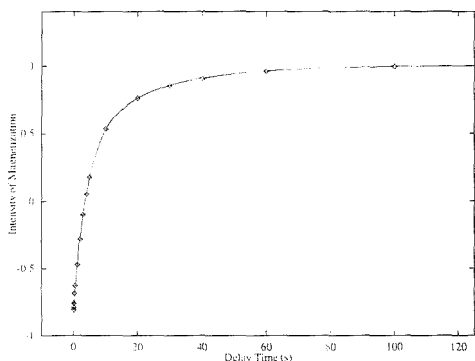


Figure 8. Plot of magnetization recovery vs delay time of M6. The solid line is calculated by the relaxation model of eq 5, and the diamond symbols represent the experimental data.

at room temperature shows that spin-lattice relaxation times for protonated carbons are smaller than those for nonprotonated carbons by a factor of 3–4-fold. These ratios of T_p/T_Q are comparable for both the experimental and the fitted values for all compounds and mixtures. The σ_p and σ_Q values listed in Table 2 represent the spin-lattice relaxation time distributions for protonated and nonprotonated carbons, respectively. The correspondence between experimental and theoretical distributions (from eq 4) was illustrated previously for mixture M6 in Figure 3. The solid line gives the fitted distribution, and it faithfully simulates the experimental relaxation time distribution represented by the bar plot. The remaining systems also exhibit similar distribution patterns to the representative data shown for M6 in Figure 3. By comparing all of the fitted values for σ_p and σ_Q with their corresponding experimental values, it is concluded that the relaxation model produces adequate relaxation time distributions for the model compounds and mixtures, giving confidence in the method which is used below for the complex coal-derived liquids.

The bottom part of Table 2 lists the equilibrium population data for protonated and nonprotonated carbons (i.e., the mole

Table 3. Fitting Parameters for M1, M5, and M6 at Low Temperatures

	sample		
	M1 (-65 °C)	M5 (-95 °C)	M6 (-95 °C)
β	0.534 (1) ^a	0.551 (1)	0.554 (2)
T_p (s)	1.31 (1)	3.49 (2)	3.37 (2)
σ_p (s)	0.21 (1)	0.60 (1)	0.76 (1)
T_Q (s)	8.52 (8)	8.06 (4)	10.45 (7)
σ_Q (s)	0.45 (1)	0.80 (2)	1.03 (1)
X_p	0.779 (4)	0.720 (4)	0.698 (3)
X_Q	0.221	0.280	0.302
$X_p/X_Q(\text{fit})$	3.52 (3)	2.57 (4)	2.31 (4)
$X_p/X_Q(\text{stoichiometric})$	3.50	2.29	2.23
relative error ^a (%)	0.57	12.2	3.58

^a Relative error, $(X_p/X_Q(\text{fit}) - X_p/X_Q(\text{stoichiometric}))/X_p/X_Q(\text{stoichiometric})$. ^b Errors recorded in parentheses indicate uncertainty in the least significant digit.

fractions X_p and X_Q), also obtained from nonlinear fitting, along with the ratio of X_p/X_Q . The stoichiometric X_p/X_Q values listed in Table 2 is determined during the sample preparation. For a single compound, it is simply the ratio of the number of protonated and nonprotonated carbons in the compound. For the mixtures, it is the molar ratio of protonated to nonprotonated carbons for all compounds in the mixture properly weighted by the molar compositions. The general agreement between $X_p/X_Q(\text{fit})$ and $X_p/X_Q(\text{stoichiometric})$ is encouraging. A correlation coefficient of 0.953 is obtained from a linear regression analysis between these two sets of data. An example of the agreement between the experimental magnetization data and magnetization predicted by the fitting parameters is shown in Figure 8 for the representative M6 sample. Similar correlations were observed for the other samples. As expected, all values of β , the pulse efficiency parameters, are less than 1, ranging from 0.7 to 0.9 in the room-temperature experiments.

The relaxation fitting parameters for M1, M5, and M6 are given in Table 3 for the low-temperature experiments. Compared with the results for M1, M5, and M6 at room temperature (26 °C), these relaxation times for both protonated and nonprotonated

Table 4. Fitting Parameters for Heavy Oil Samples^a

	sample								
	PFL2 ^b	PFL6	PFL10	INT4 ^c	INT8	INT12	SOH5 ^d	SOH9	SOH13
T_p (s)	0.62 (3)	0.38 (3)	0.84 (5)	0.34 (12)	0.92 (6)	0.82 (6)	2.06 (7)	3.03 (21)	2.63 (17)
σ_p (s)	0.159 (5)	0.092 (6)	0.271 (5)	0.070 (3)	0.112 (34)	0.176 (46)	0.112 (3)	0.563 (77)	0.156 (5)
T_Q (s)	4.42 (9)	1.41 (5)	4.85 (9)	2.06 (3)	7.37 (11)	4.97 (13)	8.25 (4)	9.23 (26)	11.47 (43)
σ_Q (s)	0.461 (9)	0.268 (9)	0.363 (7)	0.394 (5)	0.808 (58)	0.339 (34)	0.480 (6)	0.685 (67)	1.058 (16)
β	0.666 (7)	0.583 (3)	0.652 (4)	0.694 (1)	0.662 (7)	0.645 (1)	0.675 (11)	0.671 (1)	0.692 (2)
X_p	0.530 (17)	0.419 (29)	0.652 (12)	0.429 (75)	0.539 (12)	0.606 (18)	0.241 (23)	0.379 (52)	0.456 (24)
X_p/X_Q	1.127 (32)	0.721 (69)	1.874 (18)	0.751 (17)	1.169 (22)	1.765 (30)	0.318 (55)	0.610 (14)	0.838 (52)
T_p/T_Q	0.185	0.266	0.173	0.165	0.124	0.165	0.249	0.328	0.228
$r_p(=\sigma_p/T_p)$	0.19	0.24	0.32	0.21	0.12	0.21	0.05	0.18	0.05
$r_Q(=\sigma_Q/T_Q)$	0.10	0.19	0.08	0.19	0.11	0.07	0.06	0.07	0.09

^a The samples were provided by Consol, Inc. The samples are process products obtained from a single subbituminous coal (Wyodak and Anderson seam, Black Thunder mine). The samples were collected at different stages of process, HRI Bench Unit; Run CC-13. A detailed description of the samples, the liquefaction conditions that produced the samples, and the sampling point for each set of samples (PFL, INT, and SOH) is given in ref 10. ^b Pressure filter liquid sample. ^c Interstage liquid sample. ^d Separator overhead still sample. ^e Errors recorded in parentheses indicate uncertainty in the least significant digit.

carbons are significantly reduced at lower temperatures. The pulse efficiency parameters, β , ranged from 0.53 to 0.56 for samples M1, M5, and M6, indicating a deterioration in the instrumental response at lower temperatures. The average of the individual protonated and nonprotonated carbons in these samples as well as the maximum and minimum individual relaxation time constants are unavailable at low temperatures because of overlapping lines. However, the estimated ratio of X_p/X_Q continues to agree quite well with the stoichiometric X_p/X_Q ratios for samples M1 and M6. The relative error for M5 between estimated and stoichiometric X_p/X_Q ratio increases to 12.2%. The spectra obtained from these low-temperature experiments on model samples are quite similar to those observed in the coal-derived liquids. These comparisons support the utility of the method for analyzing data obtained from broader overlapping lines such as encountered in heavy oils and coal-derived liquids.

Coal-Derived Liquid Samples. The relaxation model has been used to estimate X_p/X_Q in nine coal-derived liquid samples, and the fitting parameters for these samples are given in Table 4. In general, average relaxation times for both protonated and nonprotonated carbons are decreased significantly compared with those of the model compounds and mixtures. The shorter T_1 values reflect the effects of increasing viscosity and may also indicate the presence of some free radicals which decrease the spin-lattice relaxation times. Higher viscosity in these oils, compared with the model systems, undoubtedly reduces the relaxation times. For the PFL and INT (pressure filter liquids and interstage liquids; see ref 10 for detailed description) samples, the average relaxation times of protonated carbons are less than 1 s and those for nonprotonated carbons range from 1 to 5 s, except in sample INT 8 where T_Q is 7.4 s. However, the average relaxation times of the SOH (separator overhead) samples for both protonated (2–3 s) and nonprotonated carbons (8–11 s) are longer than those of the PFL and INT samples. In general, the protonated carbon mole fraction, X_p , of SOH samples is reduced (0.2–0.5) from those estimated for the PFL and INT samples (0.4–0.6). The values of T_p/T_Q , r_p , and r_Q are also listed in Table 4. T_p/T_Q ranges from 0.12 to 0.33 and the reduced parameters r_p and r_Q range from 0.05 to 0.32 in these coal-derived liquids. These values assure that the ART approximation is reliable and that the relaxation time distributions for protonated and nonprotonated carbons are favorable for determining X_p/X_Q . Using T_p/T_Q

Table 5. Cluster Parameters for the Oil Samples^a

sample	C_{aro} ^b	$\sigma + 1$ ^c	bridges and loops ^d	MW ^e	side chains ^f	δ_{MW} ^g
PFL2	10	5.1 (1.1) ¹	3.3	346	1.8	37
PFL6	12	3.6 (1.0)	2.3	282	1.3	38
PFL10	8	2.2 (8)	1.4	192	0.8	44
INT4	12	3.9 (1.0)	2.7	275	1.2	34
INT8	10	2.7 (4)	1.7	216	1.0	36
INT12	9	2.5 (0.8)	1.8	195	0.7	35
SOH5	<i>h</i>	4.3 (1.0)				
SOH9	<i>h</i>	4.6 (1.1)				
SOH13	<i>h</i>	3.5 (1.1)				

^a See refs 1 and 7 for the details of the average cluster model and the corresponding parameters. ^b The average number of carbons per cluster. ^c Coordination number, or number of attachments per cluster. ^d Number of bridges and loops per cluster. ^e Average molecular weight per cluster. ^f Average number of side chains per cluster. ^g Average molecular weight per side chain. ^h These samples did not appear to contain a significant number of bridgehead carbons. (see text for details). Hence, they have assumed to be composed principally of single aromatic ring compounds. ⁱ Errors recorded in parentheses indicate uncertainty in the least significant digit(s).

T_Q , r_p , and r_Q values together with the plots in Figures 6 and 7, the errors produced by the ART approximation can be estimated from the model calculation results. It is found that the relative errors are +8%, +5%, and -5% in the X_p fitted parameters for sample PFL10, INT12, and SOH9, respectively. The relative error is negligible (<1%) for the remaining samples. The equilibrium magnetization data or mole fractions of protonated carbons listed in Table 4 can be used to estimate the average aromatic ring sizes in these coal-derived liquids using the procedures described by Solum⁷ and Orendt.¹ The values are given in Table 5. Both the aromatic and aliphatic regions of ¹³C NMR spectra of the separator overhead still (SOH) samples exhibited narrow, well-defined resonance lines similar to those observed in Figure 1a. These samples, of light brown optically transparent texture, were visibly much less viscous than the PFL and INT samples, and the NMR spectra were characteristic of light hydrocarbon mixtures. The relaxation times in these samples are significantly longer than those of the PFL and INT sets of samples, which probably reflects the effects of lower sample viscosity and, perhaps, a reduction of free radicals in these samples. The chemical shift region where aromatic bridgehead carbons generally cluster (130–135 ppm) exhibits very small integrated intensities in the SOH spectra, and hence, we have assumed that these samples contain only small

amounts of polycondensed aromatic species and only single aromatic rings dominate the average structural parameters in these samples. The estimated number of attachments per aromatic cluster ($\sigma + 1$) given in Table 5 indicates that the SOH samples have, on average, approximately twice as many substituents per aromatic carbon as are found in the PFL and INT samples. Hence, the values of X_0 is largest for SOH-5, -9, and -13. The "heavier oil" samples (PFL and INT) appear to be composed of two to three-ring aromatic compounds. These aromatic clusters consist of bridging groups or loops (naphthalenic structures) and side chains. The average length of the latter appear to be three to four carbons, but it should be remembered that these numbers are weighted averages between methyl groups and larger side chains.

CONCLUSIONS

The proposed composite double-exponential relaxation model works well on model compounds and analytical mixtures. The errors in this model have been assessed using model calculations of the magnetization for a range of relaxation times. With the results from numerical simulation of the magnetization, the relative error of the estimation by this proposed model may be readily calculated. The inversion-recovery experiment provides experimental relaxation times that may be used to approximate features

of the molecular structures in heavy oils and coal-derived liquids. This is done by separating protonated and nonprotonated aromatic carbons by their relaxation parameters even though their resonance lines are highly overlapped. From these data it is possible to estimate an average aromatic cluster size and other cluster parameters of the liquids under investigation. This technique has been applied to representative coal-derived oil samples and has been useful in estimating the structure of coal-derived liquids obtained at various stages of a coal liquefaction process.

ACKNOWLEDGMENT

This work was supported through the Advanced Combustion Engineering Research Center at Brigham Young University/University of Utah. Funds for the Center are provided by the National Science Foundation (Cooperative Agreement CDR 8522618), the State of Utah, and 28 industrial and government participants. The work on the coal-derived oil samples was supported by CONSOL, Inc.

Received for review April 19, 1995. Accepted June 20, 1995.*

AC950384P

* Abstract published in *Advance ACS Abstracts*, August 1, 1995.

Temperature-Jump Investigation of Adsorption/Desorption Kinetics at Methylated Silica/Solution Interfaces

F. Y. Ren, S. W. Waite, and J. M. Harris*

Department of Chemistry, University of Utah, Salt Lake City, Utah 84112

A temperature-jump relaxation technique is used to monitor reversible adsorption/desorption kinetics at the reversed-phase C1-silica/solution interface. A Joule discharge is used to heat a packed bed of trimethylchlorosilane-derivatized silica gel on a microsecond time scale. Single-exponential relaxation kinetics are observed for adsorption of an ionic fluorescent probe, 1-anilino-8-naphthalenesulfonate, to a C1-silica surface from methanol/water solution. The relaxation rate increases with concentration of solute in solution, which shows that adsorption kinetics are detectable in the relaxation. The adsorption rate of the ionic probe is slower than diffusion-controlled, exhibiting significant influence over the adsorption equilibrium constant. The adsorption rate of *N*-phenyl-1-naphthylamine is indistinguishable from the diffusion limit, indicating a negligible barrier to adsorption for this neutral species.

Separations in reversed-phase liquid chromatography result from complex thermodynamic and kinetic processes involving the transfer of solutes between the mobile and stationary phases. Knowledge of kinetics in this process is important for the design of effective column materials and for fundamental understanding of the chemistry of bonded phases and the retention behavior of analytes. The kinetics of chromatographic retention on bonded hydrocarbon stationary phases are not well-understood. Two approaches to gaining information about adsorption/desorption kinetics in chromatographic systems have been developed. Chromatographic techniques have been used to investigate these kinetics by measuring plate heights versus flow velocity and correcting for the estimated contributions from dispersion and diffusion.¹ Despite questions raised about the assumptions underlying this method² and errors associated with the fitting of peak shapes to determine kinetic parameters,³ two general conclusions can be made from band-broadening studies of adsorption/desorption kinetics: that slow rates of desorption dominate kinetic contributions to band broadening and that barriers to adsorption are much smaller and difficult to detect in the shape of eluted peaks.

A more direct approach to measuring adsorption/desorption rates is the use of relaxation kinetic methods. In relaxation kinetics, the equilibrium of a reversible process is shifted by a rapid change of conditions, such as temperature, pressure, or

electric field.⁴ Pressure-jump techniques are particularly useful for studying adsorption or binding kinetics of charged species due to the large molar volume change associated with ionic solvation; these methods have been successfully adapted to study proton transfer rates at oxide surfaces⁵⁻⁷ and more recently to investigate ion-pair adsorption/desorption kinetics at alkylated silica surfaces.^{8,9}

A temperature-jump perturbation can be used for studying adsorption kinetics of nonionic species, since most adsorption equilibria exhibit a nonzero enthalpy and are thus temperature-dependent. A Joule discharge was recently adapted to rapid heating of packed-bed samples of porous silica gel;¹⁰ it was demonstrated that the interior surfaces of chromatographic silica gel could be heated in a few microseconds. Heating rates were measured to study the effects of surface modification and pore size on the connectivity of the pore network.¹¹ More recently, the rates of solute sorption/desorption kinetics at alkylated-silica/solution interfaces have been measured by both Joule discharge heating and laser temperature-jump methods.^{12,13} In the Joule heating study, relaxation kinetics for an ionic fluorescent probe, 1-anilino-8-naphthalenesulfonate (ANS), and an uncharged probe of otherwise similar structure, 1-phenyl-1-naphthylamine (1-NPN), were measured at a C18-modified silica surface.¹² For ANS, a two-component relaxation was observed, where one relaxation exceeded the rate of heating ($k \geq 5 \times 10^5 \text{ s}^{-1}$) and where the rate of the slower relaxation increased with increases in retention of the solute due to changes in solvent composition. A two-step adsorption/partition model was developed to explain these results, where the faster relaxation was assigned to partitioning of adsorbed probe into the C18 layer while the slower rate was assigned to initial adsorption of solute from solution. The rate of the slow relaxation varied linearly with the concentration of the

(4) Bernasconi, C. F. *Relaxation Kinetics*; Academic Press: New York, 1976.

(5) Ashida, M.; Sasaki, M.; Kan, H.; Yasunaga, T.; Hachiya, K.; Inoue, T. *J. Colloid Interface Sci.* 1978, 67, 219.

(6) Astumian, R. D.; Sasaki, M.; Yasunaga, T.; Schelly, Z. A. *J. Phys. Chem.* 1981, 85, 3832-3835.

(7) Ikeda, T.; Sasaki, M.; Hachiya, K.; Astumian, R. D.; Yasunaga, T.; Schelly, Z. A. *J. Phys. Chem.* 1982, 86, 3861.

(8) Marshall, D. B.; Burns, J. W.; Conolly, D. E. *J. Chromatogr.* 1986, 360, 13-24.

(9) Marshall, D. B.; Burns, J. W.; Conolly, D. E. *J. Am. Chem. Soc.* 1986, 108, 1087-1088.

(10) Waite, S. W.; Harris, J. M.; Ellison, F. H.; Marshall, D. B. *Anal. Chem.* 1991, 63, 2365-2370.

(11) Ellison, F. H.; Waite, S. W.; Marshall, D. B.; Harris, J. M. *Anal. Chem.* 1993, 65, 3622-3633.

(12) Waite, S. W.; Marshall, D. B.; Harris, J. M. *Anal. Chem.* 1994, 66, 2052-2061.

(13) Waite, S. W.; Holzwarth, J. F.; Harris, J. M. *Anal. Chem.* 1995, 67, 1390-1399.

(1) Horvath, Cs.; Lin, H. J. *J. Chromatogr.* 1978, 149, 43-70.

(2) Arnold, F. W.; Bianchi, H. W.; Wilke, C. W. *J. Chromatogr.* 1985, 330, 159-166.

(3) Leshoff, A. M. *J. Chromatogr.* 1987, 384, 285-299.

solute in solution as expected for an adsorption step, and the rate constant was less than diffusion-limited. The adsorption rate of a neutral probe, however, was indistinguishable from the diffusion limit, indicating a negligible barrier to adsorption for the nonionic solute. To establish whether this two-step adsorption/partition mechanism is a reasonable kinetic model for sorption of ionic species at reversed-phase chromatographic interfaces, the present work considers adsorption/desorption kinetics at a methylated silica/solution interface. Using a C1-derivatized silica surface, the kinetics of adsorption can be investigated free of any intercalation or partition into the surface ligands. In addition, attaching shorter ligands to the surface would eliminate any slow heating effects on the kinetic response that arise from pores blocked by longer chain ligands.¹¹ An initial study of ANS adsorption kinetics in a suspension of methylated fumed silica was carried out using an iodine laser temperature-jump technique.¹³ The temperature-jump relaxation study was used to determine the effect of electrolyte on adsorption of a charged solute onto a C1-silica surface since Joule heating requires the addition of electrolyte while laser heating does not. Without electrolyte, the relaxation signal was biexponential, which was also reflected in a broad chromatographic peak shape and a two-site adsorption isotherm; when electrolyte was added, the relaxation signal became a nearly pure single exponential and the adsorption rate increased beyond the capabilities of the measurement. The effect of added electrolyte on the relaxation could be explained by compression of the electrical double layer at the silica surface, which reduces the charge repulsion between negatively charged ANS and deprotonated surface silanols, leading to a more homogeneous surface environment.

Despite the utility of the laser temperature-jump technique for investigating the effect of electrolyte on adsorption/desorption kinetics, the method could not generate excursions in temperature of more than a few degrees, and the stability and scattering of colloidal dispersions limited the concentration of surface sites present in the sample. These restrictions combined to lower the sensitivity for detecting relaxation transients so that adsorption kinetics at C1-silica surfaces could only be collected for a single-solvent condition corresponding to very high solute retention. Since the adsorption kinetics were homogeneous with electrolyte in the solvent, a more thorough investigation of these kinetics is possible by Joule discharge heating, which requires electrolyte to carry the current. In this work, therefore, a Joule heating temperature-jump perturbation is used to investigate adsorption/desorption kinetics of ionic and nonionic solute probes at a C1-silica surface in contact with a variety of methanol/water solutions. The adsorption rate of the ionic ANS probe is indistinguishable from the rate of the initial adsorption step observed at C18-silica/solution interfaces;¹² lack of a kinetic barrier to adsorption of neutral solutes to both C1 and C18 surfaces indicates that the nature of the adsorption barrier for the charged solute, ANS, is likely due to ionic solvation, which must be displaced to accommodate adsorption to the hydrophobic surface. The results show that similar adsorption equilibria can arise from quite different underlying kinetic mechanisms.

EXPERIMENTAL SECTION

Materials. The substrate silica gel used in this study was Licrosorb Si-60, 5- μm particle size, having a mean pore diameter of 60 \AA and a surface area of 550 m^2/g (by N_2 BET). Trimethylchlorosilane (TMCS) was purchased from Petrarch. Methanol,

toluene, chloroform, tetrahydrofuran, and acetonitrile solvents were all spectral grade (OmniSolve). The hydrophobic ionic probe, 1-anilino-8-naphthalenesulfonate ammonium salt (ANS; Aldrich) and nonionic probe, *N*-phenyl-1-naphthylamine (1-NPN; Aldrich) were used as fluorescence probes for sorption/desorption studies. The fluorescence of both ANS and 1-NPN exhibits a negligible sensitivity to changing temperature; both produce greater fluorescence intensity in nonpolar environments.^{12,13} Since the excitation and emission wavelengths of the two probes fall in the region where silica is transparent, the fluorescence signals report the adsorption/desorption kinetics in the interior of the silica particles where the vast majority of the surface area is located. Solutions of the probes were prepared of methanol (OmniSolve), and glass distilled, 18-M Ω water with sodium chloride (Mallinckrodt) was added electrolyte for both temperature-jump and chromatographic experiments.

Synthesis of Bonded Phase. The silica gel was surface-modified by TMCS according to the following procedure. An amount (3 g) of silica gel was placed in a dry round-bottom flask; the flask was evacuated to submillitorr pressures, heated to 110 $^\circ\text{C}$, and kept under vacuum for 24 h. Dry toluene (30 mL, stored over molecular sieves) and 3 mL of triethylamine (Fisher Scientific) were added to the reaction vessel. A 5-fold molar equivalent excess of TMCS (based on a silanol density of 8 $\mu\text{mol}/\text{m}^2$ ¹⁴) was dissolved in 10 mL of toluene and transferred to the vessel. The reaction mixture was heated to reflux for 2 h. After cooling, the derivatized silica was washed with 6 \times 150 mL of toluene, chloroform, tetrahydrofuran, acetonitrile, and methanol. The derivatized silica was then air-dried, placed in a clean round-bottom flask, evacuated to submillitorr pressure, and heated to 50 $^\circ\text{C}$ under vacuum for 24 h to remove all traces of the solvent. Elemental carbon and hydrogen analysis was performed by M-H-W Laboratories (Phoenix, AZ). The silica was found to have a specific fraction of 4.6% carbon and 1.4% hydrogen, corresponding to 2.5 $\mu\text{mol}/\text{m}^2$ based on the elemental analysis and the N_2 BET surface area.

Chromatographic Measurements. All chromatographic data were obtained with a high-performance liquid chromatography system consisting of a Beckman Model 210 injector, an Isco Model 2350 isocratic pump, a 150 mm \times 4.6 mm i.d. Licrosorb 5- μm Si-60 C1 column packed in-house (see below), and an Isco Model 229 UV/visible absorbance detector operated at 253 nm. An Eppendorf CH-30 column heater coupled with an Eppendorf TC-50 temperature controller was employed to measure temperature-dependent retention. Mobile-phase flow rate for all retention measurements was 1.0 mL/min. In addition, adsorption isotherm experiments were performed via the frontal elution method¹⁵ using a dual-pump system¹² with detection by a Beckman Model 153 UV/visible detector operated at 365 nm. Deuterium oxide was used as a dead-volume marker.

The column used in the chromatographic measurements was packed from a 2-propanol/C1-silica gel slurry using a Shandon column packer equipped with a Keystone Scientific slurry reservoir; the column was then conditioned with 50/50 methanol/water solvent.

Spectral grade methanol (OmniSolve) was used without further purification. The mobile phase used for these studies was

(14) Unger, K. K. *Porous Silica*; Elsevier: Amsterdam, 1979.

(15) Kati, A. M.; Guiochon, G. A. In *Advances in Chromatography*; Giddings, J. C., Ed.; Marcel Dekker: New York, 1991; Vol. 31, Chapter 1.

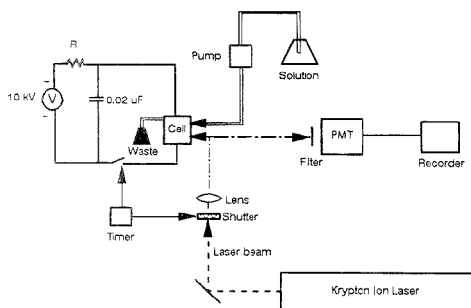


Figure 1. Schematic diagram of the Joule discharge temperature-jump experiment.

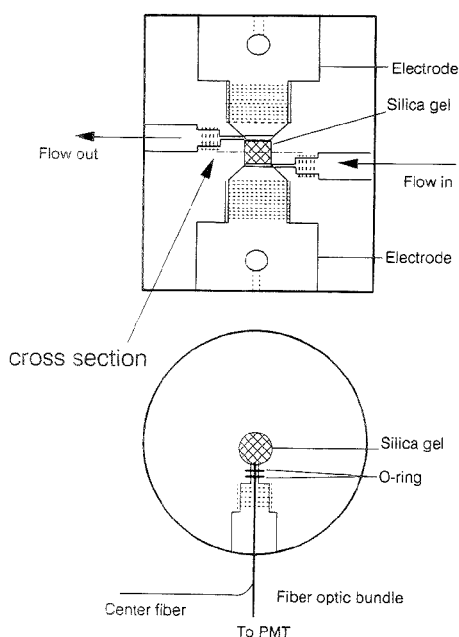


Figure 2. Structure of the temperature-jump cell.

methanol/water ranging from 70/30 to 30/70 (v/v); all methanol/water mobile phases were premixed in the appropriate proportions and degassed by sonicating for 15 min and then helium bubbling for 10 min prior to use. Capacity factors, k' , for chromatographic retention were determined over the temperature range of 25–55 °C. The chromatographic system was allowed to equilibrate at each temperature for at least 1 h prior to each experiment.

Temperature-Jump Measurements. A block diagram of the Joule discharge temperature-jump experiment is shown in Figure 1. The sample cell (Figure 2) was designed and constructed to contain a packed bed of silica with a sample volume of 38 μ L, an electrode gap of 4.8 mm, and an electrode area of 7.9 mm². A stainless steel frit (3.2 mm diameter and 2- μ m pore size) from Mott Metallurgical (Farmington, CT) was fitted into the outlet of the cell to retain the silica packing. Loading of silica samples into the cell was accomplished by slurry packing. Aqueous

Table 1. Adsorption Enthalpies for Fluorescent Surface Probes on C1-Silica versus Solvent Composition

MeOH/H ₂ O ^a (v/v)	r^2 ^b	ΔH (kJ/mol)
	ANS	
50/50	0.9976	-16.3 \pm 0.8
40/60	0.9981	-17.9 \pm 0.5
30/70	0.9969	-19.5 \pm 0.5
	NPN	
70/30	0.9973	-14.2 \pm 0.5
50/50	0.9945	-16.8 \pm 0.9

^a Solutions contain 0.4 M NaCl. ^b Correlation coefficient for a linear fit of the van't Hoff plot.

methanol solutions, containing electrolyte and probe molecules, were pumped through the sample cell at 0.1 mL/min by a Beckman Model 110A HPLC pump. Temperature jumps were carried out every 90 s, which allowed the solution in the cell to be exchanged \sim 10 times; this assured that the cell was cooled to the same initial temperature and that any electrolysis products were removed. Excitation radiation for fluorescence detection was provided by a Coherent 90-K krypton ion laser producing 200 mW in two lines at 350.7 and 356.4 nm; the radiation was coupled to the temperature-jump cell via a 200- μ m silica fiber optic (General Fiber Optics). Fluorescence was collected at 180° by six collection fibers surrounding the excitation fibers. Signal transients were acquired using a LeCroy Model 9400 digital oscilloscope and averaged until a reasonable signal-to-noise ratio was achieved (usually 20 shots). Transients were fit to single-exponential relaxation by nonlinear least squares using a modified Gauss-Newton method in ASYSTANT. Weighted linear least-squares fitting of the relaxation rate versus probe concentration was performed using the linear algebra facilities of QuatroPro.

RESULTS AND DISCUSSION

Adsorption of Solute Probes onto C1-Silica. In order to generate a significant perturbation to an adsorption equilibrium by a temperature jump, the enthalpy of adsorption of the equilibrium must be large, since the temperature dependence of the equilibrium constant at constant pressure depends on the enthalpy according to the van't Hoff equation: $\partial(\ln K)/\partial T = \Delta H/RT^2$. One can measure the enthalpy of adsorption from the temperature dependence of chromatographic retention:

$$\ln k' = -(\Delta H/RT) + \Delta S/R + \ln \phi \quad (1)$$

where k' is the capacity factor or mole ratio of solutes on the surface to solute in solution, $k' = (t_r - t_0)/t_0$, and ϕ is the phase ratio. A plot of the log of the capacity factor versus $1/T$ should yield a straight line with a slope equal to $-\Delta H/R$.

A series of van't Hoff plots were prepared for both ANS and 1-NPN retention onto C1-silica from several mobile-phase solvent compositions, and the results are summarized in Table 1. In all cases $\ln k'$ is linear with $1/T$ over a 30° range ($r^2 \geq 0.997$); despite the small temperature range, the enthalpies of adsorption are sufficiently large to determine their magnitude with less than 10% uncertainty. The smallest enthalpy change, $\Delta H = -14$ kJ/mol, corresponds to a temperature sensitivity of the equilibrium constant $\Delta K/K = -2\%$ per degree of temperature rise at room temperature. Since Joule heating can raise the temperature of a

packed bed of porous silica by more than 10 °C in a few microseconds,¹⁰ the adsorption enthalpies are sufficient to generate a significant perturbation to the adsorption equilibrium. It was found that ΔH of adsorption is more negative as the water content of the mobile phase is increased, which is consistent with the retention being primarily driven by the enthalpy change and not a hydrophobic interaction.¹⁶⁻¹⁸

In order to interpret adsorption/desorption kinetics at a C1-silica/solution interface, it is necessary to determine whether a single retention mechanism is responsible for the adsorption of solutes onto the surface. To test if the C1-silica behaves as homogeneous surface for adsorption, isotherms for both probes, ANS and 1-NPN, were measured by frontal elution chromatography. In these measurements, a "breakthrough" curve was obtained by pumping a series of mobile phases with increasing solute concentration through the column. The amount of solute adsorbed to the surface is calculated by¹⁵

$$Q_{i+1} = Q_i + \frac{(C_{i+1} - C_i)(V_{i+1} + V_0)}{A_s} \quad (2)$$

where Q is the surface concentration of the solute, C is the mobile-phase concentration of the solute, V_{i+1} is the breakthrough volume, V_0 is the system void volume, and A_s is the surface area of the adsorbent. The isotherms for ANS and NPN over the concentration range of 10 μM to 0.5 mM are linear ($r^2 = 0.9998$), with no site heterogeneity or detectable rollover due to surface site saturation. For ANS adsorption to C1-silica in the absence of electrolyte, evidence of site heterogeneity was observed previously as a nonlinear isotherm in this concentration region, which was attributed to charge repulsion between negatively charged ANS and deprotonated surface silanols.¹³ Addition of electrolyte to the solution leads to a more homogeneous surface environment by compression of the electrical double layer, which reduces the electrostatic repulsion between the solute and negatively charged sites on the surface. Nonlinearity due to coverage of the surface was not expected for this range of solution concentrations since the maximum surface concentration produced is $\sim 20 \text{ nm}^2$ or $\sim 1\%$ of a monolayer. This result also assures that surface sites are in large excess for the relaxation measurements; to observe pseudo-first-order kinetics in bimolecular reactions, the concentration of one of the reactants must be in excess. The linearity of the adsorption isotherms assures an excess, constant concentration of adsorption sites; this condition allows linearization of the rate equations and produces single-exponential relaxation kinetics even with large perturbations of the equilibrium constant.⁴

A final requirement for a successful temperature-jump relaxation experiment is to poise the equilibrium so that there are nearly equal populations of adsorbed and solution-phase molecules. This provides the largest relaxation amplitude in response to a change in the equilibrium constant.⁴ Capacity factors, k' , for retention of ANS and 1-NPN on a C1-silica column at room temperature are listed in Table 2 for a series of solvent compositions. The fraction of solute on the surface, $k'/(1+k')$, is also tabulated. For both probes, the fraction of molecules on the surface can be manipulated by solvent composition within the

Table 2. Capacity Factors for ANS and 1-NPN Retention on a C1-Silica Column^a

MeOH/H ₂ O ^b (v/v)	ANS		1-NPN	
	k'	$k'/(1+k')$	k'	$k'/(1+k')$
70/30	0.28	0.22	1.08	0.52
60/40	0.95	0.49	2.95	0.75
50/50	2.47	0.72	8.10	0.89
40/60	6.82	0.87		
30/70	14.6	0.94		

^a The fraction of molecules on the surface, $k'/(1+k')$ is also tabulated. ^b Solutions contain 0.4 M NaCl.

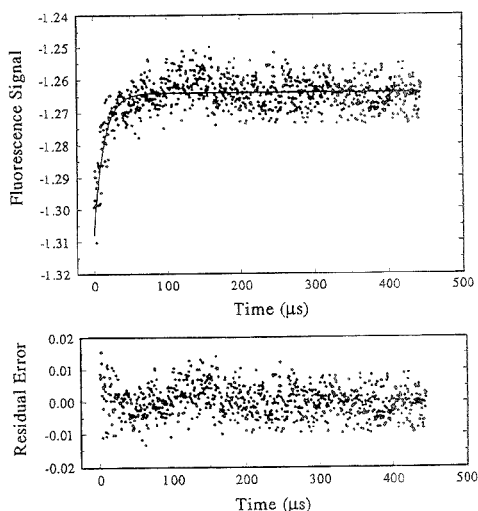


Figure 3. Temperature-jump relaxation for ANS adsorption/desorption kinetics at C1-silica/solution interface. The relaxation trace, a single-exponential best fit, and the residual error are shown. The conditions are 60/40 methanol/water (v/v), 0.4 M NaCl, 75 μM ANS, with packed bed of 5- μm C1-derivatized silica.

range where nearly half of the solute molecules reside on the surface. Comparing the retention of the two fluorescent probes, capacity factors for 1-NPN are significantly greater than those for ANS for the same mobile-phase conditions. The only structural difference between the two probes is the additional ionic sulfonate group in ANS.

Adsorption Kinetics at C1-Silica Interfaces. Temperature-jump relaxation kinetics were measured for ANS adsorption to C1-silica surfaces from 60/40, 50/50, 40/60, and 30/70 (v/v) methanol/water solutions containing 0.4 M NaCl electrolyte, which carries the discharge current and improves the homogeneity of adsorption. In all cases, fluorescence intensity from the probe decreased with increasing temperature of the sample, which is consistent with the lower fluorescence quantum yield of the probe in a polar solution and the negative enthalpy of adsorption (fewer molecules on the surface at higher temperature). An example relaxation transient is shown in Figure 3 for 75 μM ANS in 60/40 (v/v) methanol/water containing 0.4 M NaCl as electrolyte. The relaxation response is well fit by single-exponential decay as revealed by the random structure of the residuals; no significant improvement in the quality of fit is observed with a

(16) Cole, L. A.; Dorsey, J. G. *Anal. Chem.* **1992**, *64*, 1317-1323.

(17) Cole, L. A.; Dorsey, J. G.; Dill, K. A. *Anal. Chem.* **1992**, *64*, 1324-1327.

(18) Dorsey, J. G.; Cooper, W. T. *Anal. Chem.* **1994**, *66*, 857A-867A.

biexponential decay model. For a single-step, homogeneous adsorption process, a single-exponential relaxation is expected from the pseudo-first-order conditions imposed by the high concentration of adsorption sites in the packed bed of C1-silica. This expectation derives from a simple reaction model for the adsorption process:



where k_{ads} is the bimolecular rate constant for adsorption of the solute to a surface site, S and k_{des} is a unimolecular rate constant for desorption. Under conditions of a large excess of surface sites typical of a packed bed of silica gel, the relaxation of the adsorption equilibrium to a change in the equilibrium constant is a first-order decay with a relaxation rate given by^{4,13}

$$k_{\text{obs}} = 1/\tau = k_{\text{ads}}([M_{\text{soln}}] + [S]) + k_{\text{des}} \quad (4)$$

This first-order relaxation behavior requires a large excess of surface sites, which is consistent with the adsorption isotherm results discussed above. In addition, a maximum relaxation amplitude was observed with ANS for a 60/40 (v/v) methanol/water solution composition, which is the closest to an optimum equilibrium condition with an equal fraction of solute in each phase, $k/(1+k) = 0.5$. The minimum relaxation signal was observed for a 30/70 (v/v) methanol/water solvent due to the equilibrium being poised too far toward the adsorbed state for this probe (see Table 2).

The single-exponential temperature-jump relaxation of ANS at a C1-silica interface is different from what is observed at a C18 surface. Biexponential relaxations were observed in the adsorption/desorption kinetics of ANS on a C18-derivatized surface prepared on the same base silica.¹² Since the slower relaxation rate on the C18 interface increased with the concentration of ANS in solution, it was postulated that this slow step was associated with initial adsorption of the solute from solution to the interface; the faster relaxation was proposed to derive from a second step, namely the partitioning of the adsorbed solute into the C18 ligands. This faster relaxation was *not* observed in the temperature-jump data for ANS adsorption to a C1-silica; this is a reasonable since this surface avoids the possibility of a partition step, where one would expect a single-step adsorption to a C1 surface at a rate similar to the initial adsorption of ANS to a C18/solution interface.

To test this hypothesis, the adsorption rate of ANS to a C1 surface was determined by measuring the relaxation rate versus the concentration of the probe in solution; according to eq 4, one would predict a linear dependence of the observed rate on the probe concentration in solution where the slope is equal to the adsorption rate constant, k_{ads} . The results of this study are listed in Table 3 and plotted in Figure 4 for a series of methanol/water solvent compositions. As predicted by eq 4, the relaxation rates increase linearly with [ANS] in solution; the slopes of the lines in Figure 4, equal to the adsorption rate constants, are also listed in Table 3.

The values of k_{obs} indicate adsorption rates that are slower than diffusion-controlled, indicating a significant kinetic barrier for adsorption of the ANS probe to a C1 surface from solution. The rate of adsorption of ANS to a C18-silica surface was previously

Table 3. Kinetic Results for Adsorption of ANS onto C1-Silica^a

MeOH/H ₂ O ^b (v/v)	[ANS] × 10 ⁵ (M)	$k_{\text{obs}} \times 10^{-4}$ (s ⁻¹)	$k_{\text{ads}} \times 10^{-8}$ (M ⁻¹ s ⁻¹)	$k_{\text{des}} \times 10^{-4}$ (s ⁻¹)
60/40	1	3.5 ± 0.3	5.9 ± 0.1	1.14 ± 0.09
	2.5	4.8 ± 0.4		
	5.0	5.9 ± 0.8		
	7.5	7.4 ± 0.6		
50/50	1	3.9 ± 0.5	10.5 ± 1	0.55 ± 0.1
	2.5	6.3 ± 1.2		
	5.0	7.9 ± 0.8		
	7.5	10.8 ± 0.5		
40/60	1	4.7 ± 0.5	12 ± 2	0.27 ± 0.04
	2.5	6.1 ± 0.7		
	5	9.0 ± 1.4		
	9	14.3 ± 1.8		
30/70	1	5.5 ± 0.8	32 = 8	0.09 ± 0.05
	2.5	11.1 ± 1.3		
	5	16 ± 4		

^a Uncertainties are ±1σ. ^b Solutions contain 0.4 M NaCl.

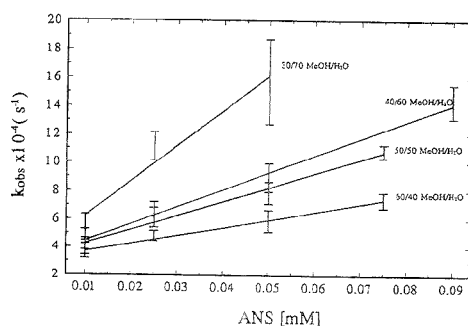


Figure 4. Relaxation rate ($1/\tau$) versus ANS concentration. Weighted linear least squares is used to determine the best fits to eq 4, which are also plotted.

measured for a single solution condition (60/40 methanol/water (0.4 M NaCl)) to be $4.9 (\pm 0.9) \times 10^8 \text{ M}^{-1} \text{ s}^{-1}$;¹² this result is indistinguishable from the rate of ANS adsorption to a C1-silica surface from 60/40 methanol/water solution listed in Table 3. Thus, a common barrier appears to exist for adsorption of the ionic solute from aqueous solution to a hydrophobic surface that is independent of the alkyl chain length. This barrier could be due to a requirement that the molecular ion shed part of its solvation sphere of water and counterions in order to adsorb; this hypothesis is supported by the lack of any barrier to adsorption for a comparable neutral probe (1-NPN) as discussed below.

The increase in k_{ads} values with increasing water in the solution phase follows the increase in the adsorption equilibrium constant (proportional to k). Thus, a portion of the response of the equilibrium to solvent composition arises from changes in the height of the barrier to adsorption. To determine what fraction of the equilibrium response is due to changes in k_{ads} , desorption rates are also estimated from the data in Figure 4. From eq 4, the intercept of a plot of k_{obs} versus $[M_{\text{soln}}]$ is defined to be $k_{\text{des}, [M=0]} = k_{\text{ads}}[S] + k_{\text{des}}$; while the intercept would appear to be sufficient to determine k_{des} , the concentration of surface sites, $[S]$, as they impact the collision rate with the surface, is not well defined for porous silica due to the inhomogeneous geometry of the pore network. Nevertheless, the desorption rate can be determined

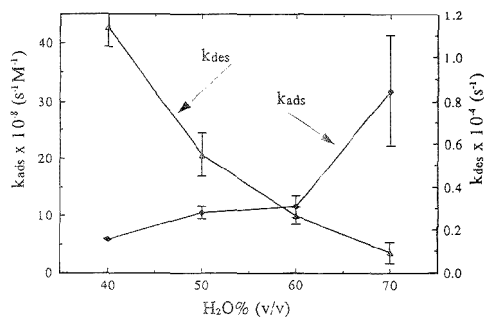


Figure 5. Adsorption and desorption rate constants for ANS at a C1-silica surface versus percent water in the methanol/water solution. Note: the solution also contains 0.4 M NaCl.

without knowledge of $[S]$ from the intercept and the equilibrium ratio of adsorbed solute to solution-phase solute. At equilibrium, the concentration ratio of adsorbed to solution-phase solute (both relative to the intraparticle solution volume) is given by the ratio of the adsorption to desorption rates: $[M_{ads}]/[M_{soln}] = n_{ads}/n_{soln} = k_{ads}[S]/k_{des}$, and therefore

$$k_{des} = k_{obs,[M]=j} / (1 + n_{ads}/n_{soln}) \quad (5)$$

The equilibrium mole ratio, n_{ads}/n_{soln} , needed to analyze the intercept rate is not identical to the measured chromatographic capacity factor, k' , since the latter includes molecules in the interparticle solution volume which do not participate in relaxation kinetics on a microsecond time scale (diffusion over distances comparable to the silica particle diameter requires ~ 10 ms). To determine n_{ads}/n_{soln} for the particle interior, one can correct k' to include only the intraparticle solvent volume: $n_{ads}/n_{soln} = k' V_0 / V_p m_p$, where V_0 (1.854 mL) is the total solvent volume in the column, V_p (0.7 mL/g) is the specific pore volume of the silica, and m_p (1.517 g) is the mass of the silica packing in the column.

Correcting the k' data from Table 2 to obtain n_{ads}/n_{soln} for the particle interior and substituting the results into eq 5 along with the intercept rates from the data in Figure 4, the desorption rates for ANS at each solvent composition are estimated and the results are included in Table 3. To assess the relative contributions of k_{ads} and k_{des} to changes in the adsorption equilibrium constant, these rates are plotted together as a function of solvent composition in Figure 5. As the water concentration in the solution phase increases, the desorption rate for ANS decreases by a factor of ~ 10 over the range of the experiment. This is an expected response as the equilibrium shifts toward the stronger adsorption, so that a molecule on the surface in a more stable (lower energy) state must overcome a larger potential energy barrier to leave the surface. Over this same range of conditions, the adsorption rate of ANS increases by a factor of 5, which indicates that changes in the adsorption rate are significantly influencing the adsorption equilibrium. In other words, the barrier to adsorption of ANS from solution to the C1 surface (which prevents the solute from adsorbing to the surface at a diffusion-limited rate) is being affected by changes in solvent composition. This is not surprising since solvation and counterions near the ion must be perturbed to allow adsorption and since organization of solvent around the

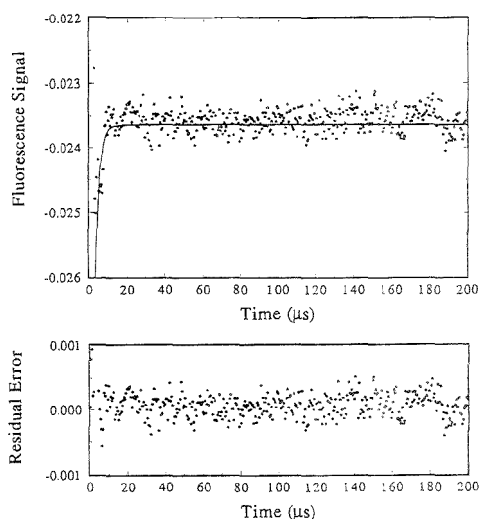


Figure 6. Temperature-jump relaxation for NPN adsorption on C1-silica 70/30 (M/W); 0.4 M NaCl; $[1\text{-NPN}] = 25 \mu\text{M}$. A least squares fit to a single-exponential relaxation is plotted for $\tau_{obs} = 2 \mu\text{s}$.

molecular ion depends on solvent composition: according to the results, at higher water concentrations and correspondingly lower methanol concentrations, solvation of the ion is more easily perturbed, thereby lowering the barrier to adsorption. This result is consistent with solvent exchange rates for transition metal ions, where rate constants for water exchange are 2 orders of magnitude faster than the rate constants for exchange of methanol.¹⁹

The detectable barrier to adsorption of ANS to a C1-silica surface can be contrasted with the behavior of an uncharged probe solute, *N*-phenyl-1-naphthylamine, whose structure is similar to ANS except that it lacks the ionic sulfonate group. Table 2 lists the chromatographic retention data for 1-NPN in methanol/water mobile phases containing 0.4 M NaCl; the adsorption of 1-NPN is ~ 3 times greater than ANS at the same solvent composition. The enthalpy of adsorption of 1-NPN to a C1-silica surface from a 50/50 methanol/water 0.4 M NaCl solution is indistinguishable from the adsorption enthalpy of ANS from the same solvent (see Table 1). It is interesting that the sulfonate group of ANS does not produce a detectable difference in the enthalpy of adsorption from solution compared to 1-NPN. Since the enthalpies of adsorption for the two probe molecules are indistinguishable, the greater adsorption equilibrium constant for 1-NPN must derive from differences in the entropy of adsorption, which would be consistent with greater hydrophobic interactions for the neutral probe in aqueous solutions.

Figure 6 shows the much faster temperature-jump relaxation of the neutral probe, where $k_{obs} = 5 \times 10^5 \text{ s}^{-1}$. The relaxation signals for this probe were single exponential within the uncertainty of the data and similar to the rate of energy deposition from the Joule discharge. With such a fast relaxation, the observed rate is convoluted with the finite rate of heating; one can estimate the underlying rate of the chemical relaxation by deconvolution.

(19) Wilkins, R. G. *Kinetics and Mechanisms of Reactions of Transition Metal Complexes*; VCH: Weinheim, Germany, 1991; Section 4.2.1.

This accomplished by the root-mean-square method, derived from the convolution of an exponential source function with an exponential decay: $\tau_{\text{chem}} = (\tau_{\text{obs}}^2 - \tau_{\text{flow}}^2)^{1/2}$,²⁰ where for our experiment $\tau_{\text{flow}} = 1.67 \mu\text{s}$; this approach to deconvolution has been recommended when fitting noisy relaxation kinetic data.²⁰ Using this formula, $\tau_{\text{chem}} = 1.1 (\pm 0.5) \mu\text{s}$, or $k = 9 \times 10^9 \text{ s}^{-1}$ for $[1\text{-NPN}] = 25 \mu\text{M}$; the corresponding adsorption rate (neglecting the contribution from the intercept term in eq 9) is $k_{\text{ads}} = 3 (\pm 2) \times 10^{10} \text{ M}^{-1} \text{ s}^{-1}$, which is at the limit of diffusion control. Therefore, no barrier to adsorption is detected for this neutral solute at a hydrophobic silica/solution interface.

The diffusion-controlled adsorption rate of the nonionic probe indicates that the barrier to adsorption observed for the charged solute is not common to both probes; displacement of a strongly adsorbed solvent component from the C1 surface is, therefore, ruled out as a significant kinetic barrier to adsorption since this barrier would be common to adsorption of either solute. The uncharged probe should not carry a strongly organized solvation sphere typical of an ionic species in aqueous solution; rearrange-

(20) Turner, D. H. In *Investigation of Rates and Mechanisms of Reactions*, 4th ed.; Bernasconi, C. F., Ed.; Wiley: New York, 1986; Part II, p 159.

ment or partial shedding of the solvation around the ionic probe to accommodate adsorption onto the hydrophobic surface could represent a unique kinetic barrier to adsorption of the ionic species. Further studies of solvation of organic ions near interfaces could help reveal the nature of the adsorption barrier to ionic solutes. Regardless of its origins, the resulting adsorption kinetics of ionic species onto a reversed-phase surface are demonstrated to significantly impact the adsorption equilibrium, and these kinetics differ from those of a comparable neutral species. These results show that similar chromatographic retention equilibria may arise from quite different underlying kinetic mechanisms.

ACKNOWLEDGMENT

This research was supported in part by a grant from the U.S. Department of Energy.

Received for review April 11, 1995. Accepted July 20, 1995.[®]

AC950358R

[®] Abstract published in *Advance ACS Abstracts*, September 1, 1995

Rapid Comprehensive Two-Dimensional Separations of Peptides via RPLC–Optically Gated Capillary Zone Electrophoresis

Alvin W. Moore, Jr., and James W. Jorgenson*

CB 3290, Department of Chemistry, University of North Carolina—Chapel Hill, Chapel Hill, North Carolina 27599

Coupled-column two dimensional (2D) separation systems offer potentially high peak capacity and are amenable to automation. Reversed phase liquid chromatography (RPLC) and capillary zone electrophoresis (CZE) are complementary techniques well suited for use in a 2D system. Optically gated CZE is a means of performing rapid CZE analyses. In a 2D system, these rapid CZE analyses enable more frequent sampling of the RPLC separation and thus more freedom in control of the RPLC analysis conditions. Complete 2D separations can be done in the time usually required to do the RPLC analysis alone. With the present system, a complete 2D analysis can be done in under 10 min. Because the peak capacity of a 2D method is inherently high, some of the available peak capacity can be exchanged for speed of analysis. Acceleration of the RPLC elution gradient will decrease analysis time, but RPLC resolution will suffer. However, because it is a 2D system, some of the resolution lost in the RPLC can be regained in the second dimension CZE analysis. Here, the RPLC gradient was done over only 2 min, but CZE analyses done every 2.5 s restore some of the resolution lost in the rapid RPLC gradient.

Two-dimensional (2D) separation methods are of interest because of the potentially high peak capacity possible with such methods. In particular, a coupled-column approach is appealing because of the possibilities of automation and on-line detection. Giddings has shown that the peak capacity of a 2D method is the product of the peak capacities of its component one-dimensional (1D) methods.¹ This is true if the component separation methods are orthogonal. Two methods are considered orthogonal if their selectivities are based on different and uncorrelated chemical or physical characteristics of the molecules of interest.

Reversed phase HPLC and capillary zone electrophoresis (CZE) are well suited for use in a 2D system. Their operating buffers are compatible, while their separating mechanisms are very different. In the case of reversed phase LC (RPLC) and CZE, separations depend on component hydrophobicity in the former and electrophoretic mobility (mass-to-charge ratio) in the latter. The orthogonality of these mechanisms enables many of the potential gains from 2D operation to be realized in practice.

A common example of multidimensional coupled-column separation is "heart-cutting",² in which particular regions of interest

from a separation done in one column are automatically reinjected onto a second column of different chemistry. Another method of 2D separation involves manually collecting fractions of effluent from one separation method and reinjecting them into a second separation system. Heart-cutting methods are of limited use if we desire to separate all of the components of the sample in both dimensions (a comprehensive 2D separation). Also, for a comprehensive method of this type, the manual fraction collection method is too labor-intensive and slow. We would like a continuous on-line system in which the entire effluent of the first dimension method is sampled into the second. In such a system, detection is usually done only after the second method. Detecting sample zones between the two 1D methods is of little practical utility and might contribute additional band broadening.

If detection is done only after the second separation method, then the sampling of the separation in the first dimension is limited by the analysis time of the second dimension separation. Each entire analysis in the second dimension represents only a single "point" in the first. To make full use of the resolution provided in the first dimension separation, the second dimension must have a significantly faster analysis time. This places a limitation on most 2D systems and generally results in very long 2D analysis times.

In CZE, unlike LC, separation efficiency is not a direct function of capillary length.³ In LC, with all other factors held constant, a column 20 cm long will give twice as many theoretical plates as a column 10 cm long. In contrast, in CZE, if the applied voltage remains constant, the separation efficiency will remain constant, independent of capillary length. The CZE efficiency is related to capillary length only indirectly, in that sufficient capillary surface area must be maintained to eliminate any Joule heat generated by the passage of current through the buffer-filled capillary. However, the migration time of solutes in CZE is a function of the capillary length squared. Assuming voltage is held constant, if capillary length is reduced by half, then the migration times of the analytes will be reduced by a factor of 4.

It has previously been shown that the combination of short capillaries with high applied voltages will give very fast and efficient CZE analyses.^{4,5} Because of the speed of these analyses, a unique optical-gating injection system is used to obtain injections that are rapid relative to the CZE analysis time. The "fast-CZE" system makes possible complete CZE analyses in as little as 3 s while high separation efficiency is maintained.

(1) Giddings, J. C. *HRC CC, J. High Resolut. Chromatogr. Chromatogr. Commun.* 1987, 10, 319–323.

(2) Majors, R. E., Jr. *J. Chromatogr. Sci.* 1980, 18, 571–579.

(3) Jorgenson, J. W.; Lukacs, K. D. *Anal. Chem.* 1981, 53, 1298.

(4) Monnig, C. A.; Jorgenson, J. W. *Anal. Chem.* 1993, 65, 802–807.

(5) Moore, A. W., Jr.; Jorgenson, J. W. *Anal. Chem.* 1993, 65, 3550–3560.

The high speed of the fast-CZE system makes it particularly well-suited for use as a second dimension in a 2D system. Because the second dimension separation is very fast, there is more freedom in control of the first dimension separation. The LC analysis need not be made unusually slow to allow time for the CZE analysis. In fact, the opposite is true. Because 2D methods have inherently high peak capacity, if not all of the peak capacity of a 2D separation is needed, the unneeded peak capacity can be traded for greater overall speed of analysis. Because the second dimension does part of the "work" of the separation, the first dimension can be run faster than normal. Thus, a separation that might be achieved in a 1D method in 1 h can be done with a 2D system in a few minutes, because peak capacity equivalent to that of a 1D system can be generated in a 2D system in a much shorter time.

Fast-CZE. In brief, fast-CZE is a means of performing CZE analyses in seconds rather than minutes. Characteristic CZE high-voltage levels (5–25 kV) are applied to short lengths of capillary, which results in very short CZE analysis times. The capillary is only 10- μ m internal diameter (i.d.) and low-concentration CZE buffers (10 mM) are used. Together these limit the current through the capillary at the high applied field, so that Joule heating is not a significant problem.

Because the fast-CZE analyses are done in seconds, a unique injection system is needed. Sample injections must be short relative to total analysis time, and mechanical fluidic valves are too slow for this purpose. A high-speed optical gating injection system was developed by Monnig and Jorgenson.⁴ This system is based on an argon ion laser operated at 350 mW. Samples to be analyzed are tagged with fluorescein isothiocyanate (FITC) to be sensitive to the 488-nm line of the laser. The beam from the laser is split into a gating beam, focused nearer the injection end of the capillary and containing 95% of the laser power, and a probe beam, focused nearer the exit end of the capillary and containing the remaining 5% of the laser power.

The optical-gating injection may be thought of as an "inverse" injection method. A constant high voltage is applied to the capillary, and sample is migrated continuously through the capillary by a combination of electroosmosis and electrophoresis. As long as the gating beam is focused on the capillary, the majority of sample passing through the beam is photodegraded by the intense light of the gating beam. Only a residual background fluorescence is seen at the probe beam further along the capillary. To make an "injection", the gating beam is momentarily blocked (usually for 5–50 ms) with a computer-controlled shutter. This allows a small slug of unbleached material to pass through into the region of the capillary between the beams, where its components are separated and detected by their fluorescence as they pass through the probe beam.

Figure 1 is a timing diagram for the optical-gating injection. The upper trace represents laser power at the gating beam. The sharp spike downward is the point of sample injection, when the beam is momentarily blocked by the shutter (here, for 20 ms). The lower trace is the fluorescence signal seen at the probe beam for an actual fast-CZE run of tryptic digest of cytochrome *c*. A dip in the background fluorescence signal is seen at the point of sample injection, because the mechanical shutter used to block the gating beam actually blocks the laser beam before it is split and thus blocks both beams. This dip in background fluorescence serves as a convenient injection marker in each run. Seconds

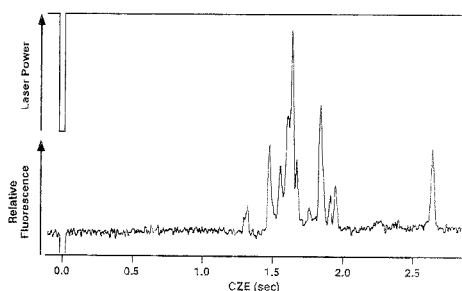


Figure 1. Timing diagram and fast-CZE analysis of tryptic digest of horse heart cytochrome *c*: injection time, 20 ms; 20 kV applied over total capillary length of 8 cm, with 2 cm between gating and probe beams. Data were smoothed with a five point moving average filter to reduce baseline noise.

after the injection, peaks are seen in the fluorescence trace as sample components separated between the beams pass through the probe beam.

EXPERIMENTAL SECTION

Samples and Reagents. Deionized water for all sample solutions and buffers was generated from distilled water with a Barnstead Nanopure system. All other reagents were used as obtained. All aqueous buffers were prepared with 0.005% (w/v) sodium azide as an antimicrobial agent. Buffers and samples to be injected directly into the fast-CZE system were first filtered with 0.2- μ m Acrodisc syringe filters (Gelman, Inc.). Methoxyarginine, horse heart cytochrome *c*, and trypsin were purchased from Sigma. Water-soluble sodium fluorescein was purchased from Aldrich. Fluorescein isothiocyanate was purchased from Molecular Probes (Eugene, OR) and Sigma. Acetone, pyridine, sodium phosphate, boric acid, and NaOH were purchased from Fisher Scientific. A solution of 0.01 M sodium phosphate, adjusted to pH 6.85 with NaOH, was used to optimize the operation of the CZE system. This buffer is hereafter referred to as CZE buffer.

Digest and FITC-Tagging Conditions. A 10 mg/mL solution of horse heart cytochrome *c* was prepared in 0.1 M boric acid buffer, pH 8.4. To 3 mL of this solution was added 1 mL of 0.1 mg/mL trypsin solution in the same buffer, and digestion was allowed to proceed for 24 h at 37 °C. The digest was then filtered with a 0.2- μ m syringe filter (Gelman, Inc.). A 50- μ L aliquot of FITC in a 90:10 (v/v) acetone/pyridine solution was added to 200 μ L of filtered digest solution and allowed to react in darkness for 24 h at room temperature. The concentration of the FITC solution was adjusted to give a 3-fold molar excess of tryptic peptides over FITC in the sample. The final concentration of FITC-tagged components in this sample was 4.4 mM. Samples were diluted 100-fold into CZE buffer before analysis by RPLC/fast-CZE. Methoxyarginine was tagged with FITC in a manner similar to that described above, with the methoxyarginine in 3-fold molar excess to the FITC tag. This procedure has been described in detail elsewhere.⁵ The resultant fluorescein thiocarbonyl (FTC) derivative, FTC-methoxyarginine, was used as a neutral marker to monitor electroosmotic flow in CZE.

Instrumentation. The fast-CZE instrument arrangement has been described in detail elsewhere.⁷ Figure 2 is a diagram of the 2D RPLC/fast-CZE instrument. The fast-CZE part of the system

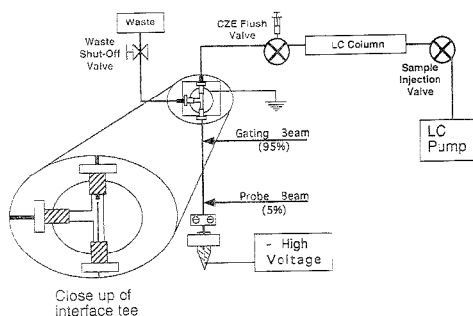


Figure 2. Two-dimensional RPLC/fast-CZE instrumental diagram.

is shown in the left side of the figure. The CZE capillary is mounted vertically, but there is no significant gravitationally driven flow because the capillary is only 10- μ m i.d.. A stainless steel tee (750- μ m i.d., Valco Instrument Co., Inc., Houston, TX) is connected to the top of the CZE capillary. The internal volume of the tee replaces the buffer reservoir normally seen in CZE, and the tee serves as a simple interface to the LC system. The tee is connected to ground, and negative high voltage is applied to the lower buffer reservoir so that electroosmotic flow is from top to bottom in the diagram. The positions of the gating and probe laser beams focused onto the CZE capillary are also shown. The laser is a 1-W Coherent Innova 70 argon ion laser (Coherent Inc., Palo Alto, CA) operated at 400 mW at a wavelength of 488 nm.

The right side of Figure 2 shows the LC system, made up of a gradient-capable HPLC pump (Hewlett-Packard Model 1050), a sample injection valve (Rheodyne) with a 20- μ L sample loop, and an LC column. Also shown is a post-LC flush valve (Valco Instrument Co., Inc.) between the LC column and the fast-CZE system and a shut-off valve (Alltech Associates Inc., Deerfield, IL) on the waste line from the fast-CZE tee. Connecting tubing between the outlet of the LC column and the flush valve is 0.005-in. (127- μ m) i.d. PEEK tubing (Upchurch Scientific, Oak Harbor, WA). The waste line on the fast-CZE tee is 0.040-in. (1-mm) i.d. PEEK tubing (Upchurch).

The waste line shut-off valve is used in the pretreatment of a new piece of fused-silica capillary before use in CZE. During 2D or fast-CZE analysis, this valve is open so that there is no significant back pressure on the waste line. When the waste valve is closed, the pump can be used to force liquids through the CZE capillary under pressure. The post-LC flush valve has a large (0.7 mL) sample loop which is filled using a 1-mL Glenco flushing syringe (Alltech Associates Inc.). It is used to send a slug of sample solution or base solution used in capillary pretreatment through the fast-CZE tee without going through the LC system.

Separation Conditions. The RPLC column was a Vydac 15 cm \times 2.1 mm i.d. protein and peptide C18 column, 5- μ m particle size, 300- \AA pores (The Nest Group, Inc., Southborough, MA). Solvent A for RPLC was CZE buffer. Solvent B for RPLC was 60% acetonitrile (Fisher Optima)/40% CZE buffer (v/v). The RPLC flow rate was 250 μ L/min, with a linear elution gradient from 10% B to 50% B over 5 min, hold 1 min at 50% B, and then return to initial conditions. This gave a linear gradient from 6 to 30% acetonitrile over 5 min.

The fast-CZE capillary was 10- μ m i.d., 350- μ m o.d., and 8 cm long. The high voltage is applied across the entire length of the

capillary, but the actual length available for CZE separation is less. Since the gating beam is the actual point of injection, and the probe beam is the point of detection, only the voltage dropped over that length of the capillary between the beams is actually available for the separation. Due to the design of the mount used to hold the capillary, for an 8-cm length of capillary, the maximum beam separation is about 2 cm. Thus, for 20 kV applied with 2 cm between the beams, only 25% or 5 kV is actually used in the CZE separation. Similarly with only 0.45 cm between the beams, only 5.6% or 1.1 kV is actually used in the CZE separation.

Data Acquisition. Two-dimensional systems inherently generate large amounts of data. For the LC/fast-CZE, because of the speed of the CZE analyses, that data must also be acquired rapidly. The data acquisition hardware (PMT, current amplifier, etc.) is as described previously for the fast-CZE system.^{4,5}

For 2D analysis, data acquisition is done at 400 Hz. A program written in LabVIEW2 (National Instruments, Austin, TX) running on a Macintosh II computer acquired data in double-buffered mode through a multipurpose A/D interface board (Model NB-M10-16X, National Instruments). In double-buffered mode, data are written to disk in the background as they are acquired in the foreground. The 2D data file is displayed using SpyGlass Transform and Format color raster imaging software (Spyglass, Inc.). Transform can be used to view the data as a two-dimensional color or gray-scale map. Only gray-scale plots are shown here. In these plots, RPLC time in minutes is on the Y-axis, fast-CZE time in seconds is on the X-axis, and fluorescence intensity of the sample peaks is shown by gray-scale intensity. Transform can also be used to generate three-dimensional surface plots of the 2D data set, similar to those shown in Figure 4. Plots of 1D data for individual CZE and LC analyses were done with IGOR plotting software (Wavemetrics Inc., Lake Oswego, OR).

Procedures. A new CZE capillary is prepared as follows. Eight centimeters of capillary is installed in the fast-CZE mount, and the polyimide coating is removed over about 4 cm using a heated nichrome wire device constructed in-house. The capillary mount is then installed into the system, and the fluid lines are connected. To fill the capillary, the LC column is replaced with a 1/16-in. union, and the LC pump is used to flow buffer through the tee and out the waste line. Then the waste valve is closed, and the pump back pressure is allowed to rise to 1000 psi. The maximum pressure safely applied to the tee is about 1000 psi, due to the constraints of the 1-mm i.d. PEEK (Upchurch Scientific) waste line. At 1000 psi, the pump is stopped but the pressure on the tee is not released. The back pressure slowly bleeds off as buffer flows through the small bore of the CZE capillary.

To pretreat the capillary, the flush valve loop is filled with 1 M NaOH solution and the valve is turned to the inject position. The waste valve is opened, and the base is pumped from the flush valve sample loop into the tee. Once the base is in the tee, the waste valve is closed and the pump is used to pressurize the tee as described above. In this way, 1 M NaOH solution is passed under pressure through the CZE capillary for 15 min. The waste valve is opened, the tee is flushed with CZE buffer, and the waste valve is closed again to pressurize the tee and flush the CZE capillary with buffer. This is done for 30 min, and the capillary is ready for use.

Before beginning a 2D analysis, the RPLC column is reinstalled and the fast-CZE optics are aligned using a solution of 1×10^{-6} M sodium fluorescein in CZE buffer. The post-LC flush valve can

be used to fill the CZE capillary without pumping a large volume of fluorescein solution through the LC column. The sample loop of the flush valve is filled with fluorescein solution, the pump is set to 50 $\mu\text{L}/\text{min}$ (no gradient), and the flush valve is turned to the inject position to send a constant flow of fresh fluorescein solution to the fast-CZE tee. The large sample loop and low flow rate allow fluorescein to be pumped through the tee for about 15 min. When the high voltage is on, a fraction of the fluorescein solution is continuously electromigrated into the CZE capillary. The optics that focus the laser beams can then be adjusted to give the maximum fluorescence signal. Fast-CZE analyses of this solution can also be done to check CZE system performance prior to a 2D analysis.

Fast-CZE is well-suited for use in a 2D LC/CZE instrument. In a 2D analysis, sample is injected with the sample injection valve and separated on the LC column, usually by gradient elution. Effluent from the LC column flows into the tee of the fast-CZE system. As shown in the inset in Figure 2, this effluent flows across the end of the fast-CZE capillary and out to waste. Because the waste line is 1-mm i.d., there is no significant pressure-induced flow through the 10- μm i.d. CZE capillary. As long as high voltage is applied to the capillary, a small fraction of the LC effluent is continuously electromigrated into the capillary. No automated switching valve is needed between the LC and fast-CZE systems, because the actual fast-CZE "injections" from the LC effluent are done with the gating beam. Fast-CZE analyses can be done so rapidly that second dimension analysis time plays a much smaller role in determining the first dimension LC analysis conditions.

LC Background Correction. The residual fluorescence background seen in fast-CZE is a result of the optical-gating injection method. When only CZE is being done, the background is constant for a given sample. However, in 2D analysis, the background level changes as peaks elute from the LC column. This makes interpretation of the 2D data difficult. To solve this problem, the original 2D data is digitally filtered with a moving median filter.⁶

The moving median filter is similar to a moving average filter except that, instead of calculating the average of a group of data points, it calculates the statistical median. The moving median discriminates against sharp momentary changes in signal level but retains slow changes and edgeline characteristics in a signal. In the 2D LC/fast-CZE data, the CZE peaks are less than 100 ms wide, while the LC peaks are 5–20 s wide. Thus the CZE peaks are very sharp relative to the LC peaks. In fact, the CZE peaks appear as spikes "riding" on the LC peaks.

Figure 3A shows 2D data the way it is actually collected, as one long array of data points, one CZE run after another. In these data, no LC column was present, but flow injection of a slug of fluorescein was done. The sharp spikes upward are the CZE peaks, while the spikes downward are the injection markers for each run. The broad "hill" is the change in background as the slug of fluorescein passes through the CZE tee. In Figure 3B, the data from (A) have been digitally filtered with a moving median filter of rank 32. The number of points in the filtering window is twice the rank plus 1, or 65 in this case. This removes the spikes due to the fast-CZE, leaving only the "LC part" of the data. In Figure 3C, the filtered data in (B) have been subtracted from the raw data in (A). This removes the changing background due to the LC peak and leaves only the CZE peaks.

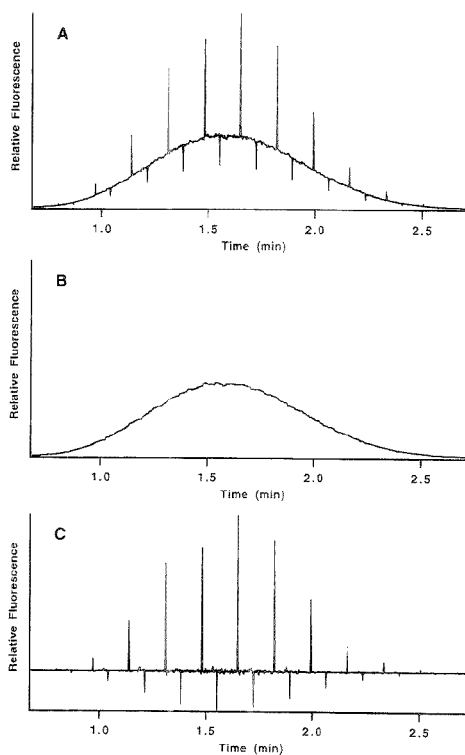


Figure 3. RPLC/fast-CZE background correction. (A) shows the raw data as it is actually acquired, as a series of 1D CZE analyses. (B) is the data from (A) after median filtering with filter of rank 32 (window width, 65 points). (C) is the difference data, the result of subtracting the filtered data in (B) from the raw data in (A).

The same data in a three-dimensional surface plot are shown in Figure 4. Figure 4A is the raw data. The broad "hill" is the peak in the LC dimension, while the sharp knifelike feature is the CZE peak. In the rear of the figure a "trench" is noticeable, which is the injection marker for each CZE analysis. Figure 4B is the data from Figure 3C, the result of subtracting the filtered data from the raw data. Notice that the knifelike CZE peak is now visible on a flat background, with the injection marker trench still seen in the rear of the figure.

RESULTS AND DISCUSSION

Because the LC analysis involves a solvent gradient, and because the LC effluent is the buffer used in fast-CZE, CZE times for analyses late in the LC run are not strictly comparable to those of CZE analyses early in the LC run. The increasing concentration of organic solvent (in this case acetonitrile) causes a decrease in electroosmotic flow. Thus, CZE analyses later in the LC gradient show later migration times than those earlier in the LC gradient. The data in Figure 5 were obtained by replacing the LC column with a tee (250- μm i.d., Valco) through which a small volume of FTC-methoxyarginine solution was continuously added to the effluent of the pump. In this way, FTC-methoxyarginine was present throughout the gradient. The same LC gradient was run,

(6) Moore, A. W., Jr.; Jorgenson, J. W. *Anal. Chem.* 1993, 65, 188–191.

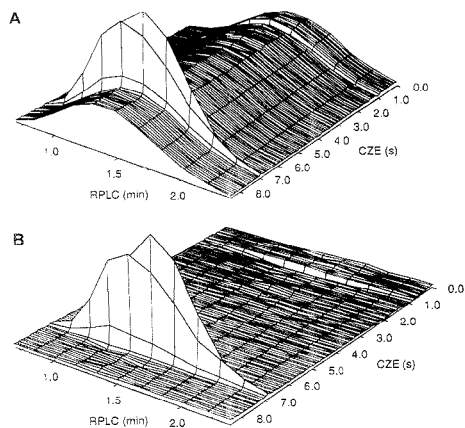


Figure 4. 2D surface plot of data from Figure 3. (A) is the raw data from Figure 3A, now plotted as a two-dimensional surface. (B) is the difference data from Figure 3C plotted as a two-dimensional surface.

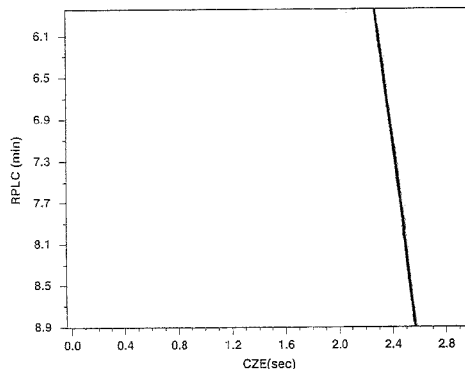


Figure 5. Effect of LC elution gradient on CZE electroosmotic flow. Sample is FTC-methoxyarginine continuously added to the RPLC mobile phase as a neutral marker of electroosmotic flow in CZE. RPLC conditions: 5-min linear gradient from 10% B to 50% B, hold 1 min at 50% B, and return to initial conditions over 0.1 min. CZE conditions: 20 kV applied over 8-cm total capillary length, with 2 cm between gating and probe beams. CZE injection time, 10 ms; total CZE analysis time, 2.5 s. The region of the 2D data set shown is the same as in Figure 6.

and the change in migration time of the FTC-methoxyarginine over the course of the LC gradient is obvious as the sloping dark gray line in the right side of the figure.

In practice, this change in CZE migration time does not change the use of the method. If standards were being analyzed to compare to migration and retention times in an unknown sample, the standards would be run in the same 2D system as the unknown. If the LC pump reproducibly forms the gradient each time, the shift in CZE migration times will be reproducible as well. Two-dimensional migration/retention times between standards and unknowns would still be directly comparable.

Figure 6 is a gray-scale plot of the 2D analysis of a tryptic digest of horse heart cytochrome *c*. The LC gradient is only 5 min long, but the actual times on the LC axis are longer because there is about 4.5 min of analysis "dead time". At a flow rate of 250 $\mu\text{L}/$

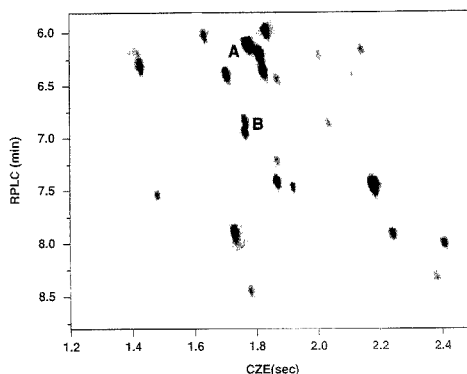


Figure 6. 2D RPLC/fast-CZE analysis with 5-min LC gradient. 2.5-s CZE analyses. Sample is FTC-tagged tryptic digest of horse heart cytochrome *c*. RPLC conditions: 5-min linear gradient from 10% B to 50% B, and hold 1 min at 50% B; return to initial conditions over 0.1 min. CZE conditions: 20 kV applied over 8-cm total capillary length, with 2 cm between gating and probe beams. CZE injection time, 10 ms; total CZE analysis time 2.5 s. Labeled peaks are for reference within the text but are not identified as specific compounds.

min, it takes 4.5 min for changes in solvent composition formed in the proportioning valve of the pump to pass through the LC column and connecting tubing to reach the head of the CZE capillary. In fact, sample injection is simultaneous with the start of the elution gradient, but data collection is not begun until four minutes after sample injection.

RPLC and CZE are truly complementary techniques. As shown in Figure 6, components unresolved in one dimension are often resolved in the other. To see this, consider first the LC dimension. Any peaks found on the same horizontal line through the data in Figure 6 are peaks with the same LC retention time. By summing horizontally, we get the reconstructed LC. Components represented by those peaks would not be resolved by LC alone. Similarly, peaks found on the same vertical line represent sample components with similar CZE migration times. Sample components responsible for those peaks would not be resolved by fast-CZE alone. The data in the timing diagram in Figure 1 is a fast-CZE analysis of the same digest sample showing a number of unresolved peaks. Clearly RPLC or CZE alone is unable to resolve the multiple sample components under these conditions. Through the combination of RPLC and CZE, most components in this sample are separated.

The peak capacity of a separation with unit resolution is defined as

$$n_c = L/4\sigma$$

where L is the total distance (or time) over which the sample zones (peaks) are distributed and σ is the average standard deviation of the peaks separated.⁷ Using the data shown in Figure 6, we can estimate the peak capacity of the 2D method. In Figure 6, the RPLC peaks elute over a range of 2.8 min, from 5.8 to 8.6 min. The average peak width in the RPLC dimension is 0.19 min

(7) Giddings, J. C. *Unified Separation Science*; John Wiley and Sons: New York, 1991.

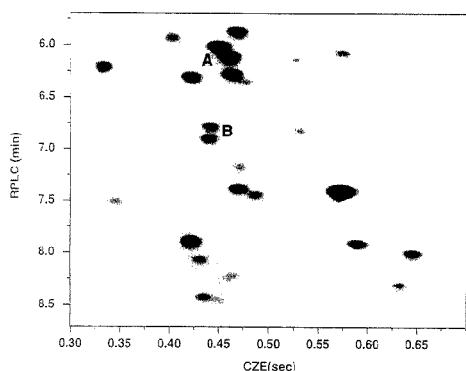


Figure 7. 2D RPLC/fast-CZE analysis with 5-min LC gradient, 0.7-s CZE analyses. Sample is FTC-tagged tryptic digest of horse heart cytochrome *c*. RPLC conditions: 5-min linear gradient from 10% B to 50% B, hold 1 min at 50% B, return to initial conditions over 0.1 min. CZE conditions: 20 kV applied over 8-cm total capillary length, with 0.45 cm between gating and probe beams. CZE injection time, 10 ms; total CZE analysis time, 0.7 s. Labeled peaks are for reference within the text but are not identified as specific compounds.

(4 standard deviations). Using eq 1 and assuming unit resolution, the number of peaks 0.19 min wide that fit into the 2.8-min space gives the peak capacity of the RPLC separation, or 15 in this case. Similarly for CZE, the peaks span 1.0 s, from 1.4 to 2.4 s. An average peak width is 0.023 s (4 standard deviations), and this gives a peak capacity with unit resolution of 43. The peak capacity of the 2D RPLC/CZE system is then $15 \times 43 \approx 650$.

One possible application of this method is the rapid fingerprinting of proteins. Tryptic digests of known and unknown proteins could be fluorescently tagged and analyzed by 2D RPLC/fast-CZE. The 2D data obtained act as a "fingerprint" of the protein structure based on its component peptides. Comparison of known proteins to unknowns could be done to identify unknowns as well as to assess protein purity. A contaminant in a sample protein or peptide should be visible as spurious peaks not found in the 2D data for that protein or peptide standard.

Sampling Considerations. In a continuous 2D system, the analysis time of the second dimension separation limits the rate at which the first dimension separation is sampled. As mentioned earlier, each entire analysis in the second dimension gives only a single "point" in the first. Sampling of the first dimension determines how well the first dimension separation is characterized. That is, if the first dimension is not sampled often enough, we do not make full use of the resolution obtained in that dimension. However, if the second dimension is made too rapid, we generally lose resolution in the second dimension.

In fast-CZE, with a given applied voltage and total capillary length, the actual CZE analysis time and separation efficiency are determined by the separation of the gating and probe beams. The distance between the beams can be adjusted to give the desired compromise between time of analysis and CZE separation efficiency. Greater distance between the beams gives a more effective CZE separation, because a greater fraction of the total applied voltage is used, but the analysis time is also greater. Thus the LC separation is sampled less often, and we may not take full advantage of the resolution obtained in the LC column. Alter-

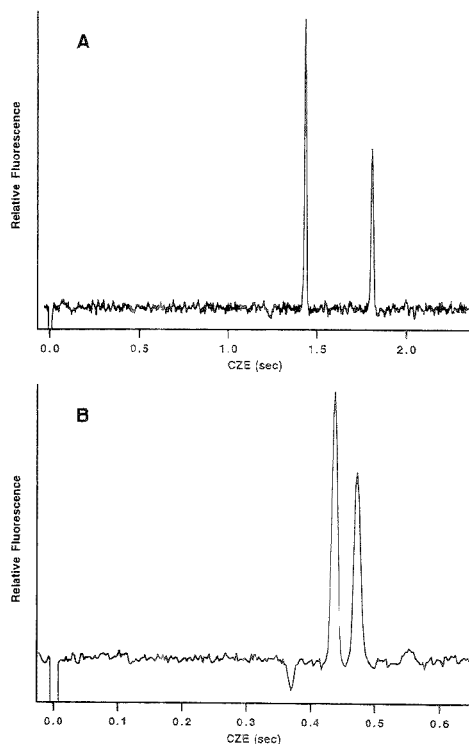


Figure 8. Individual fast-CZE analyses taken from 2D data sets. (A) is a CZE analysis taken from the data in Figure 6 at 6.3-min LC time, with 2 cm between the gating and probe beams and a total CZE analysis time of 2.5 s. (B) is a CZE analysis taken from the data in Figure 7 at the same LC time, with 0.45 cm between the beams and a total CZE analysis time of 0.7 s.

nately, less distance between the beams results in faster CZE analyses (so that the LC separation is sampled more rapidly) but less CZE separation efficiency.

In Figure 6, the fast-CZE analysis time is 2.5 s. This maximizes efficiency in the CZE analysis but somewhat undersamples the LC analysis. Figure 7 is an analysis of the same sample with a beam separation of 0.45 cm. The CZE analysis time is much shorter, only 0.7 s, so that the LC analysis is better sampled. This increase in sampling of the LC has come at the expense of lost efficiency in the CZE. Panels A and B of Figure 8 are individual CZE analyses taken from the 2D data sets in Figures 6 and 7 at 6.3-min LC time. The peaks are much sharper and much farther apart in the 2.5-s analysis than in the 0.7-s analysis, though they are still baseline resolved in the faster analysis.

Notice in Figure 7, the pair of peaks labeled B are fully baseline resolved in the LC. In Figure 6, these peaks are beginning to run together. The LC gradient is the same in both cases, but with the slower LC sampling rate (due to the longer CZE analysis time), the LC separation in Figure 6 is not as well characterized. In Figure 6, the LC resolution available is not completely utilized due to the slower CZE sampling rate. Compare also the cluster of peaks labeled A in Figures 6 and 7. In Figure 6, these peaks

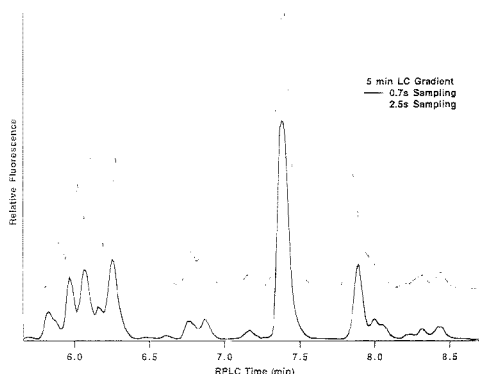


Figure 9. Reconstructed LC chromatograms for the 2D data shown in Figures 6 and 7. These plots are created by integrating (summing) the signal across each CZE analysis (each horizontal row) in the 2D data.

are well resolved by CZE but show some overlap in the LC dimension. In Figure 7, they are not as well separated by CZE but are better resolved in the LC. Again, the faster CZE analysis time makes more complete use of the LC resolution. The particular compromise chosen between the necessary sampling rate in the LC and the desired efficiency in the CZE will depend somewhat on the particular sample being analyzed.

Figure 9 shows the reconstructed LC chromatogram for the data shown in Figures 6 and 7. These plots are created by integrating (summing) the signal across each CZE analysis (each horizontal row) in the 2D data. Each data point in these plots then represents an entire fast-CZE analysis. The difference in CZE sampling of the LC chromatogram is more obvious in the data shown in this way. In Figure 9, there is a group of four peaks near 6.0 min in the LC chromatogram in which a small peak is visible between the last two large peaks in the analysis sampled every 0.7 s. At the same position in the analysis sampled every 2.5 s, the small peak is not seen. Here, because of the slower sampling of the LC by the CZE, resolution gained in the LC has been lost in the 2D analysis. Similarly, in the last peak near 8 min, a small shoulder on the larger peak is more distinctly visible as another peak in the lower trace than it is in the upper.

One means of dealing with the compromise between CZE analysis time and thorough sampling of the LC dimension is through overlapped injections. This technique has been described earlier.⁸ Figure 10A shows the entire 2D data set for the analysis shown in Figure 6 without overlapped injections. Notice in the far left of the figure a white vertical line is visible. This is the CZE injection marker described earlier. It is purposefully offset from the very edge of the 2D plot, but it is at zero time on the CZE axis. The unused part of the 2D separation space is obvious, because most of the sample components have CZE migration times in the last half of the CZE analysis. To make better use of the total 2D separation space, the injections in the second dimension may be overlapped. To do so, before the peaks from one injection have reached the detector, a second injection is done. This doubles the rate at which the LC analysis is sampled, with no loss in CZE efficiency. Figure 10B shows the same analysis

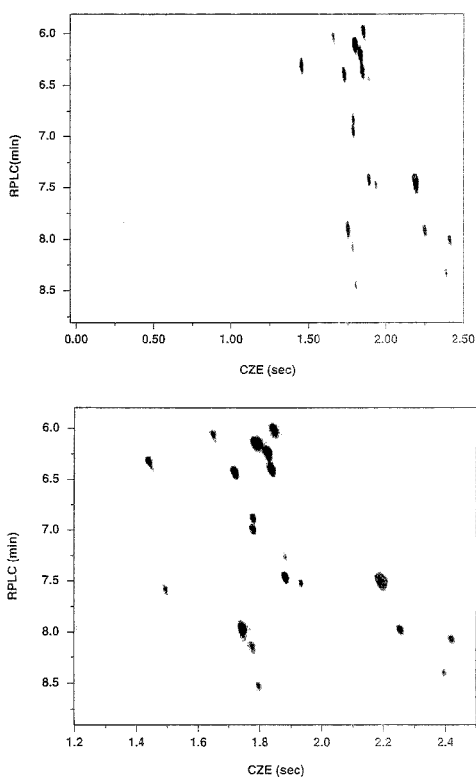


Figure 10. Overlapping of CZE injections to fill the 2D separation space. (A, top) is the same data as in Figure 6 but shows the entire 2D data set. The vertical white line at the left of the figure is the fast-CZE injection marker. (B, bottom) is the same tryptic digest sample, with the same LC and CZE conditions but with overlapped CZE injections. Notice that the vertical white injection marker is no longer at zero on the CZE axis.

with overlapped injections. The injection marker is also visible here, but no longer at zero because of the overlapped injections. The effect is to obtain the efficiency of 2.5-s CZE analyses, while sampling the LC run every 1.25 s. Figure 11 compares the sampling of the LC run every 2.5 s with that of every 1.25 s obtained through the use of overlapped injections. Overlapped injections may not be useful for all samples. A drawback of overlapped injections is the possibility of unusually late peaks from one CZE analysis "aliasing" into the following analysis, resulting in an incorrect CZE migration time for that peak.

Faster 2D Analysis. Because 2D methods have inherently higher peak capacity, they generate that peak capacity more rapidly. If not all of the peak capacity is needed, it can be exchanged for a decrease in analysis time. Figure 12 shows a 2D analysis in which the LC gradient is completed in only over 2 min. This is faster than optimum for the LC separation, but because it is part of a 2D system, the second dimension can be used to regain some of the resolution lost in the accelerated LC gradient. In Figure 12A, the fast-CZE beam separation is only 4.5 mm. This gives a rapid 0.7-s CZE analysis time, with 0.35-s sampling of the LC separation using the overlapped injection

(8) Larmann, J. P., Jr.; Lemmo, A. V.; Moore, A. W., Jr.; Jorgenson, J. W. *Electrophoresis* 1993, 14, 439-447.

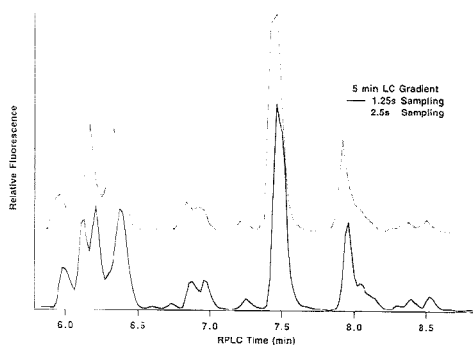


Figure 11. Reconstructed LC chromatograms from Figure 10A,B. The reconstructed LC separations allow comparison of sampling for nonoverlapped and overlapped injection 2D analyses.

technique. Unfortunately, with the gating and probe beams so close together, the CZE efficiency is low and does not adequately make up for the resolution lost in the LC. In Figure 12B, the beams are 2 cm apart. The greater beam separation gives greater CZE efficiency, which does begin to restore the resolution lost in the LC. The large peaks (labeled A) in the early part of the LC gradient had merged in Figure 12A to give an unresolved multiplet. We know from Figures 6 and 7 that this multiplet is actually three peaks. In Figure 12B, the high-efficiency CZE analyses have separated the multiplet into two components, so that at least some fraction of the lost LC resolution is compensated for in the second dimension.

An interesting artifact of the fast LC gradient is seen in Figure 12B. All of the peaks appear to be swept toward the lower right corner of the figure. This is because of the change in CZE migration time with the changing solvent gradient. Because the LC solvent composition is changing so rapidly, the migration times of peaks in the CZE are changing even over the course of a single peak in the LC. Thus, the front of an LC peak has a shorter CZE migration time than the rear of the same peak, and seen in two dimensions, the appearance is that of a peak slewed to the right. The same effect is present in Figure 12A, but is not as obvious because of the lower CZE separation efficiency. In practice this is an indicator that the gradient is changing too rapidly for the given LC column.

ACKNOWLEDGMENT

This research was supported by grants from the National Science Foundation (CHE 9215320) and the National Institute of Health (GM 39515) and by a gift from Hewlett-Packard. The

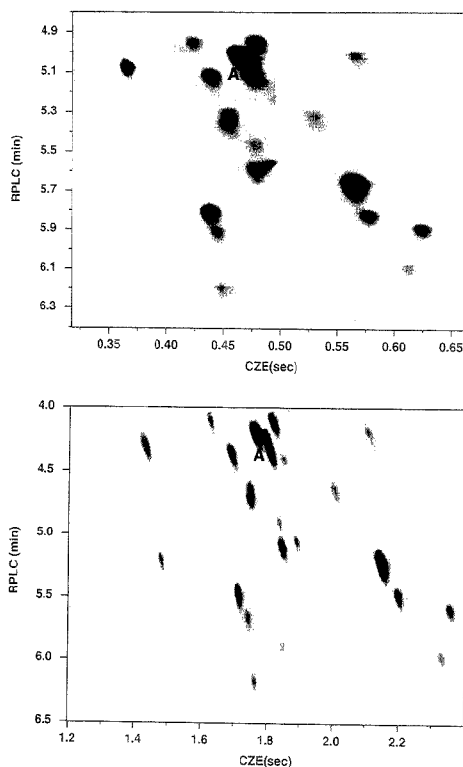


Figure 12. 2D RPLC/CZE analysis with 2-min LC gradient and overlapped injections. Sample is FTC-tagged tryptic digest of horse heart cytochrome c. RPLC conditions: 2-min linear gradient from 10% B to 50% B, hold 1 min at 50% B, and then return to initial conditions over 0.1 min. (A, top) 0.7-s CZE analyses, with CZE conditions as in Figure 7, but with overlapped injections. (B) 2.5-s CZE analyses, with CZE conditions as in Figure 6 but with overlapped injections. Labeled peaks are for reference within the text but are not identified as specific compounds.

HP1050 pump and UV absorption detector were donated by Hewlett-Packard.

Received for review October 25, 1993. Resubmitted July 7, 1995. Accepted July 14, 1995.*

AC9506793

* Abstrac: published in *Advance ACS Abstracts*, September 1, 1995.

Comprehensive Three-Dimensional Separation of Peptides Using Size Exclusion Chromatography/Reversed Phase Liquid Chromatography/Optically Gated Capillary Zone Electrophoresis

Alvin W. Moore, Jr., and James W. Jorgenson*

CB 3290, Department of Chemistry, University of North Carolina—Chapel Hill, Chapel Hill, North Carolina 27599

Multidimensional separation methods are attractive because of their potentially high peak capacities. Coupled-column systems in particular offer the advantages of on-line detection and automation. With the development of rapid two-dimensional (2D) analysis, it becomes possible to consider three-dimensional (3D) separation systems. In such a 3D system, effluent from a slow first dimension is repetitively sampled into a rapid 2D system. In the resultant data, each sample component has been subjected to three separative displacements, and the overall peak capacity is the product of that of each of the three dimensions. This paper demonstrates a comprehensive coupled-column 3D analysis of peptides. Size exclusion chromatography (SEC) is used as the first dimension to separate sample components by molecular weight, over an analysis time of several hours. The SEC effluent is repetitively sampled on-line into a rapid 2D reversed phase liquid chromatography/capillary zone electrophoresis (CZE) system with an analysis time of 7 min. Detection of sample zones is done only after the final CZE separation, by laser-induced fluorescence detection. Analysis data from this system consist of a series of 2D "slices" of the SEC effluent, which when stacked together give the 3D separation "volume".

In the previous paper, we described a method of doing rapid comprehensive two-dimensional (2D) analysis of peptides. This system used a coupled-column approach to link reversed phase liquid chromatography (RPLC) with optically gated capillary zone electrophoresis (CZE). In a coupled-column 2D system, effluent from the first column is repetitively sampled into the second, with detection usually only after the second dimension. If it is a comprehensive system,¹ the entire effluent from the first column is sampled into the second. This is in contrast to a heart-cutting technique, in which only small regions of interest from the first separation are sampled into the second.

For a comprehensive coupled-column system, each entire analysis in the second dimension yields only a single "point" in the first. Thus, if possible, it is advantageous to have the analysis time of the second method be much shorter than the first, so that the separation in the first dimension can be well sampled. This restriction usually results in overall analysis times of several hours for a 2D method. However, optically gated CZE makes possible rapid 2D analyses, with total analysis times of 5 min or

less. Because these 2D analyses can be done in only a few minutes, it becomes possible to consider comprehensive three-dimensional (3D) separations.

A coupled-column 3D system could be constructed by repetitively sampling effluent from a first dimension column into a subsequent two-dimensional system. If the entire effluent of the first column is sampled into the 2D method, the 3D method is likewise termed comprehensive. In a sequential 3D system of this kind, the separation data will consist of a series of 2D analyses of samples of the first column effluent. These 2D "slices" can then be "stacked" together to give a 3D separation "volume" in which each of the three axes represents a different separation method.

The motivation for development of 2D systems is the large gain in peak capacity of the 2D method over its component one-dimensional (1D) methods. Giddings has shown that the peak capacity of the 2D method is roughly the product of the peak capacities of the component 1D methods.² In the same work, he showed that this applies for a multidimensional system of any number of dimensions, n . Thus a 3D system is of interest because the total peak capacity will be roughly the product of all three component dimensions. Since the peak capacity of a 2D method is inherently high, even a modest peak capacity in the first dimension will make a significant difference in the peak capacity of the overall 3D method.

Giddings has reported a personal communication from J. F. K. Huber of a three-dimensional separation.³ This method relied on coupling three chromatographic columns in a 3D analysis requiring 102 h with over 6000 peaks. From the description, the method involved some heart-cutting of particular peaks and was not a comprehensive approach. In this paper, we demonstrate a comprehensive coupled-column 3D system. A size exclusion chromatography (SEC) column is used for the first dimension, to give a rough separation of peptides based on their molecular size. Effluent from this column is then sampled into a 2D RPLC/CZE system described in the previous paper. This system further separates the components based on their hydrophobicity and electrophoretic mobility. Detection of sample zones is done only at the end of the CZE analysis, after they have passed through all three separation modes.

(2) Giddings, J. C. *HRC CC, J. High Resolut. Chromatogr. Chromatogr. Commun.* 1987, 10, 319-323.

(3) Giddings, J. C. In *Multidimensional Chromatography*; Corcos, H. J., Ed.; Marcel Dekker, Inc.: New York, 1990; pp 1-28.

(1) Eushay, M. M.; Jorgenson, J. W. *Anal. Chem.* 1990, 62, 978-984.

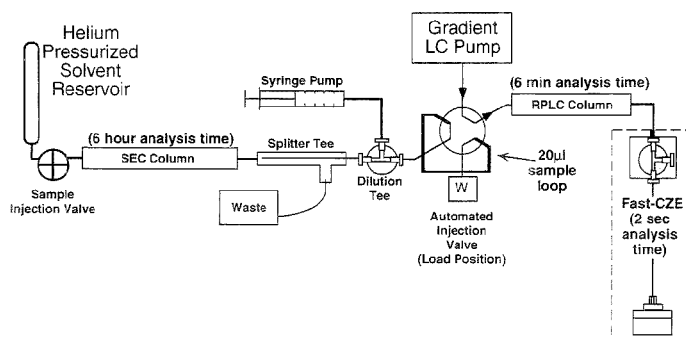


Figure 1. Schematic diagram of 3D SEC/RPLC/fast-CZE instrument. See text for explanation.

EXPERIMENTAL SECTION

Samples and Reagents. Only samples and reagents specific to this experiment are listed here. All components in common with the previous paper are as described therein. Hen ovalbumin was purchased from Sigma. Ammonium acetate and boric acid were purchased from EM Science (Gibbstown, NJ). Methanol (Fisher Optima grade) was purchased from Fisher Scientific (Fair Lawn, NJ).

Digest Conditions. A 10 mg/mL solution of hen ovalbumin was prepared in 100 mM borate buffer, pH 8.5. This solution was heated in a boiling water bath for 5 min to denature the protein. A 37 mg/mL solution of trypsin was prepared in the same borate buffer, and 5 μ L of this solution was added to 0.75 mL of the albumin solution. The mixture was allowed to react for 24 h at 37 $^{\circ}$ C, after which it was stored in the freezer. The ratio of ovalbumin to trypsin (w/w) in this solution was 41:1. Thirty-five peptide fragments of ovalbumin were expected in the digest if digestion was complete.⁴

Tagging Conditions. Fluorescein isothiocyanate (FITC) was dissolved in 95:5 (v/v) acetone/pyridine solution. A 65- μ L sample of this solution was added to 300 μ L of digest solution, and the mixture was allowed to react in darkness for 24 h at room temperature. The concentration of the FITC solution was adjusted to give a 3-fold molar excess of tryptic peptides over FITC in the sample. The final concentration of FITC-tagged components in this sample was 2.2 mM.

The tagged digest sample was diluted 1:50 into CZE buffer before analysis by 2D RPLC/fast-CZE. The tagged digest sample was diluted 1:10 in SEC mobile phase before analysis by SEC alone (with UV absorbance detection, for method development) or by 3D SEC/RPLC/fast-CZE.

Instrumentation. The 3D instrument is diagrammed in Figure 1. Reading from the left, the sample is injected onto the SEC column and separated by size, passes through into an SEC/RPLC interface in the center of the Figure, and then into the 2D RPLC/fast-CZE system on the right. The components of the individual separation systems will be described first, followed by a description of the interface between the SEC and RPLC systems.

SEC. The SEC column was slurry packed in-house. A 4.6 mm i.d. \times 25 cm column blank with 0.5- μ m Kel-f encased frits

(Alltech Associates Inc., Deerfield, IL) was packed⁵ with HEMA stationary phase (5- μ m particles, 100- Å pores) (Alltech Associates). HEMA is a hydrophilic macroporous copolymer of 2-hydroxyethyl methacrylate and ethylene dimethacrylate. For the SEC analysis, a 300-mL stainless steel solvent reservoir (Whitey Co., Highland Heights, OH) connected to a helium gas cylinder was used as an isocratic solvent pump. Solvent flow rate through the column was controlled by varying the applied gas pressure. The SEC solvent was 85% methanol/water (v/v), with 100 mM final concentration of ammonium acetate. This solvent was chosen on the basis of earlier work in our group⁶ to maximize ideal size exclusion behavior of the peptides and reduce other nonideal chemical interactions with the stationary phase. The solvent was filtered with 0.2- μ m syringe filters (Gelman, Inc.) before use, and a 0.5- μ m precolumn in-line filter was inserted between the sample injection valve and the head of the SEC column. For the data shown here, the SEC solvent flow rate was 11 μ L/min, driven by helium pressure of 3.1 bar (45 psi). Sample was injected onto the SEC column with a six-port Rheodyne valve fitted with a 20- μ L sample loop.

Initial method development work was done with the SEC column outlet connected directly to a Hewlett-Packard (HP) 1050 variable-wavelength UV absorbance detector. The absorbance was monitored at 488 nm to detect only the FITC-tagged components, with 2.0 absorbance units full scale (AUFS).

RPLC. The RPLC column was a 5 cm \times 2.1 mm i.d., 5- μ m particle diameter, 300RxC8 column (Rockland Technologies, Inc.). The elution gradient and the RPLC injection valve were the only other changes in the LC system from that described in the previous 2D paper. The LC pump flow rate was 250 μ L/min. Solvent A was 10 mM sodium phosphate buffer, pH 6.85. Solvent B was 40% acetonitrile/60% solvent A. The gradient was from initial conditions of 15% B to 75% B over 3.5 min and then a return to initial conditions from 3.5 to 3.6 min. This gave a change in acetonitrile from 6 to 30%. The gradient time was shorter than that of the 5-min gradient described in the previous paper to allow a faster overall LC cycle time without substantial loss of LC resolution. This allowed for more frequent sampling of the SEC effluent.

The manual Rheodyne valve used for RPLC injections in the previous paper was used here for sample injection onto the SEC

(4) Nisbet, A. D.; Saundry, R. H.; Moir, A. J. G.; Fothergill, L. A.; Fothergill, J. E. *Biochem. J.* **1981**, *115*, 335–345.

(5) Kennedy, R. T.; Jorgenson, J. W. *Anal. Chem.* **1989**, *61*, 1128–1135.

(6) Lammann, J. P., Jr. Ph.D. University of North Carolina—Chapel Hill, 1993.

column. Injections onto the RPLC column were done with an electrically actuated six-port valve (Valco Instrument Co. Inc., Houston, TX) fitted with a 20- μ L sample loop. In Figure 1, the automated valve is shown in the load position, in which the sample loop was slowly filled with a diluted fraction of the SEC effluent over the course of a 2D analysis. The valve was controlled by a digital output line of the data acquisition board, through an interface constructed in-house.

Fast-CZE. The fast-CZE system is described in detail in the previous paper and elsewhere.^{7,8} The CZE capillary was 8 cm \times 6 μ m i.d., 360- μ m o.d. with 1.7 cm between the gating and probe beams of the laser. The applied voltage was 20 kV to give an applied field of 2.5 kV/cm. Because the gating beam is the actual point of sample injection, and the probe beam is the point of sample detection, the voltage actually available for the separation is only the voltage between the beams or 4.25 kV. The gating and probe beams were generated by a 1-W Coherent Innova 70 argon ion laser (Coherent Inc., Palo Alto, CA) operated at 400 mW at 488 nm. The fast-CZE injection time was 15 ms.

SEC/LC Interface. (a) **SEC Flow Reduction.** Under ideal circumstances with a coupled-column system, the geometry and flow rates of the SEC and RPLC columns would be matched. That is, the amount of effluent generated by the SEC system during the time of a RPLC analysis would be equal to the injection volume of the RPLC column. In this way, all of the SEC effluent would be sampled into the LC system. In practice, this can be done by using a smaller internal diameter first dimension column and a larger internal diameter second dimension column. Then the optimum flow rate for the first is significantly smaller than for the second, and the ideal described above can be realized. For example, a SEC column with a flow rate of 1 μ L/min might be connected to a RPLC column which could receive a 10- μ L injection. Then RPLC analyses done every 10 min would inject the full effluent flow to the SEC column.

Smaller bore SEC columns, both 1- and 2.1-mm i.d., were packed in our laboratory, but the measured separation efficiencies of these smaller columns were far less than that obtained with the 4.6-mm-i.d. column. Thus, the 4.6-mm-i.d. column was used. Because the SEC column used in this system was of larger i.d. than the RPLC column, there was a flow incompatibility. Even with low SEC flow rates, the amount of effluent generated during the course of a RPLC analysis was more than could be stored in a sample loop and injected into the RPLC column. Thus, a discrete sampling approach was used, in which the repetitive RPLC analyses sampled some fraction of the SEC effluent and in which some fraction of the SEC effluent is lost between RPLC analyses.

Consider the case, for example, if the SEC flow rate was 10 μ L/min, the RPLC injection volume was 20 μ L, and the RPLC analysis time was 5 min. In 5 min, the SEC system generates 50 μ L of effluent, but the LC system can only inject 20 μ L. Thus 60% of the SEC effluent is lost. This is not a concern if the RPLC system can sample the SEC effluent rapidly relative to the SEC peak width, so that no SEC peaks will be missed in the SEC effluent lost between RPLC samplings. A better arrangement uses a flow splitter in which a fraction of the SEC effluent is diverted to waste before the LC system. In the example above, a 40:60 flow splitter between the SEC column and the RPLC column would divert 6 μ L/min to waste. Then only 4 μ L/min would go to the

LC sampling loop, or 20 μ L in the 5-min RPLC analysis time. This method has the advantage that the entire SEC effluent is analyzed by RPLC (there are no "lost" fractions of the SEC effluent), but some of the sample is lost in the flow splitter.

A flow-splitter arrangement similar to that described above was used to split off only a fraction of the SEC effluent for injection into the RPLC. The splitter itself was a 1/16-in. stainless steel tee (Swagelok), with an extension 2 cm long brazed onto one side of the tee. The splitter capillaries were referred to as the LC split (33 cm \times 50 μ m i.d.) and the waste split (37 cm \times 100 μ m i.d.). As shown in Figure 1, the LC split capillary passes through the tee and extension and is positioned very near the inlet of the SEC effluent. Effluent from the SEC column flows into the tee and across the end of the capillary. A fraction of the SEC effluent flows into the LC split, while the remainder flows out the waste split. The measured flow rates were 10 μ L/min for the waste split and 1 μ L/min for the LC split.

(b) **SEC Mobile Phase Dilution.** The high methanol content of the SEC mobile phase made it difficult to directly inject a fraction of the SEC effluent into the RPLC system. The initial RPLC solvent contained only 6% acetonitrile, while the SEC solvent was 85% methanol. Injection of as little as 5 μ L of sample in SEC solvent resulted in significant breakthrough of early-eluting peaks in the solvent front of the RPLC analysis. To circumvent this problem, the SEC mobile phase was diluted with CZE buffer before injection into the RPLC system.

Tests were done with varying dilution factors and injection volumes to find the best compromise between them. The SEC effluent was diluted 1:1 (v/v) with CZE buffer so that the organic concentration was 42.5% (with 10 μ L injected) and 1:3 (v/v) so that the organic concentration was 21.25% (with 20 μ L injected). It was found that the 1:1 dilution gave the most breakthrough, and the 1:3 dilution the least.

To dilute the SEC effluent on-line, a 250- μ m-i.d. tee (Valco Instruments Co. Inc.) was connected to the LC split line. A syringe pump (SAGE Instruments, Orion Research Inc, Boston, MA) with a 5-mL syringe was used to deliver 4 μ L/min CZE buffer to the tee to dilute the SEC effluent. This 1:4 dilution gave an approximately 17% methanol concentration in the solution entering the sample loop, and 20 μ L of this was injected onto the RPLC column. This gives a total flow into the RPLC sample loop of 5 μ L/min. With a RPLC analysis time of 6.35 min, this is 31.75 μ L. Because only 20 μ L is injected in each RPLC analysis, the remaining 11.75 μ L is lost. Again this is not a significant problem if the RPLC analyses are rapid relative to the peak width of the SEC peaks. Though some of the SEC effluent is missed, it is does not result in SEC peaks totally missed by the RPLC sampling.

Flow Rate Measurement. Flow rates through the splitter capillaries were measured using a piece of 320- μ m-i.d. capillary with two windows burned into the polyimide coating. The measured distance between the ends of the windows and the known capillary internal diameter give a known volume. The meniscus of the front of the flow of liquid through this capillary can be seen by the unaided eye, and the time taken to fill the region between the windows can be measured with a stopwatch. This time can be used to calculate a volumetric flow rate. The measurement capillary can be temporarily connected to the end of the splitter capillary with a Direct-Connect Capillary Connector union (Alltech Associates, Inc). After each measurement the measuring capillary was blown out with a flow of gas.

(7) Monnig, C. A.; Jorgenson, J. W. *Anal. Chem.* 1991, 63, 802-807.

(8) Moore, A. W., Jr.; Jorgenson, J. W. *Anal. Chem.* 1993, 65, 3550-3560.

RPLC/CZE Interface. The unique RPLC/fast-CZE interface is described in detail in the previous paper. RPLC effluent flows into a tee and across the end of the CZE capillary. A small fraction of the LC effluent is continuously electromigrated into the CZE capillary. No valve is needed, because the actual fast-CZE injections are done optically with the gating beam.

Data Acquisition, Timing, and Instrument Control. The detection optics and electronics for fast-CZE are described in detail in the previous paper and elsewhere.^{7,8} Data acquisition and instrument control software was written in-house using LabVIEW 2 software (National Instruments, Inc., Austin, TX). Data acquisition was done with a multifunction A/D interface board (Model NB-MIO-16X, National Instruments) in a Macintosh II computer.

Three-dimensional separations place unique demands on the data acquisition system and the instrument control mechanism. To acquire the 3D data set, a number of repetitive 2D "slices" of the SEC effluent were taken. As described in the previous paper, 2D data acquisition is done in double-buffered mode. Data are acquired in the foreground and written to disk in the background. While this method handles the large 2D data sets very well, it leaves the computer free to do nothing else. Thus, all instrument control functions must be accomplished between successive 2D data acquisitions.

To do repetitive RPLC gradients and synchronize the gradients with the data acquisition, the start of each gradient was triggered by the computer. To control the HP1050 pump with the computer, two digital input/output (I/O) lines on the data acquisition board were connected through a custom-made cable to the pump's nine-pin Analytical Products Group (APG) interface. This is the same interface used for local communication between individual Hewlett-Packard HPLC system components (pumps, detectors, auto-samplers) to signal analysis start and stop and error conditions. A 160-ms pulse from high to low on one line started the gradient, while a similar pulse on the other line stopped the gradient. The actual gradient elution parameters were programmed into the pump through the pump front panel, not through the computer.

The actual gradient covered only 3.6 min. After this time, the pump had returned to initial conditions and the column was reequilibrating. The gradient end time in the pump was set to 11 min, but the 2D analysis time was only 6.35 min. Thus, the pump waited at the initial conditions of the gradient for each start signal from the computer. The computer initially started the gradient in the pump and then stopped and restarted the gradient at the beginning of each new 2D data acquisition. The automated injection valve was controlled in a similar manner through another digital output line of the A/D board. High and low on the digital line corresponded to the inject and load positions on the valve, with timing controlled by the software.

Control of the instrument for a 3D analysis was as follows. The sample was injected onto the SEC column. After the appropriate amount of "dead time", 3D data acquisition was begun. The LabVIEW program would start the gradient, switch the valve to the inject position, and then return the valve to the load position after 10 s. A "slice" of 2D data was acquired over 6 min and written to disk. Immediately afterward, the pump gradient was stopped and restarted and the valve switched to the inject position to inject the next sample and repeat the entire process. The 3D data acquisition program ran the 2D data acquisition as a subroutine, repeated for the number of "slices" desired. The time

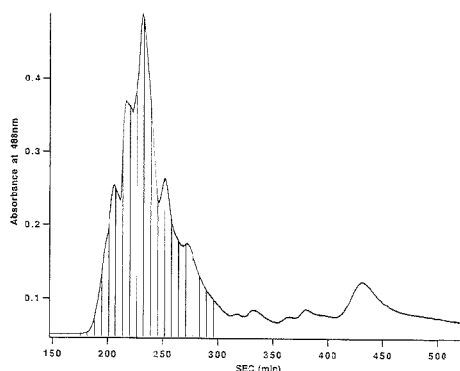


Figure 2. SEC analysis of FITC-tagged tryptic digest of hen ovalbumin. UV absorbance detection at 488 nm, 2.0 AUFS. Digest conditions and analysis conditions as described in text. Vertical lines indicate points of 2D sampling of the SEC effluent in a 3D analysis.

of each sample injection was written in the filename of each stored 2D data set.

Data Processing. All 2D slices were treated in exactly the same manner. First, all were moving median filtered with a moving median of rank 32 (see previous paper) with another LabVIEW program. Similarly, the data were smoothed with a five point linear smooth to reduce baseline noise. SpyGlass Transform, Format, and Dicer (SpyGlass Inc, Chicago, Illinois) were used to view the 2D and 3D data sets as color or gray-scale images. The LabVIEW data files were imported into Transform to generate 2D images and Format was used to annotate those images for publication. To examine the entire 3D data set, the individual 2D slices were combined into a 3D Dicer file. Dicer allows the display and manipulation of a 3D "volume" of data.

RESULTS AND DISCUSSION

Figure 2 shows the results of a 1D SEC analysis of the FITC-tagged ovalbumin digest sample. UV absorbance was monitored at 488 nm, so that only the FITC-tagged components were detected. The original tagged digest mixture was diluted 1:10 in SEC mobile phase and the injection volume was 20 μ L. The measured flow rate through the column and detector was 11 μ L/min. At this flow rate, with column dimensions of 4.6 mm \times 25 cm, a totally included peak eluted at 260 min. Only the last 5 h of a total 8-h analysis time is shown. Obviously, this is much slower than we would normally run a 1D SEC analysis. However, as the first dimension of a 3D separation, this slow SEC has two advantages. First, the SEC separation generally improves as the flow rate decreases. The extended time in the column will lead to increased diffusional broadening of sample zones, but there is also more time for equilibration of sample components with the pores of the stationary phase. During the SEC method development, resolution of sample components in successive analyses continued to improve as flow rate was decreased to 25 μ L/min. Below this point, increased diffusional band-broadening effects due to the greater analysis time began to counteract the improved SEC resolution. Second, the long SEC analysis time allows more frequent sampling of the SEC peaks by the 2D system because the SEC peaks are broader in time. The peaks in Figure 2 are 5–15-min wide. With a 2D RPLC/fast-CZE analysis time of 6.35

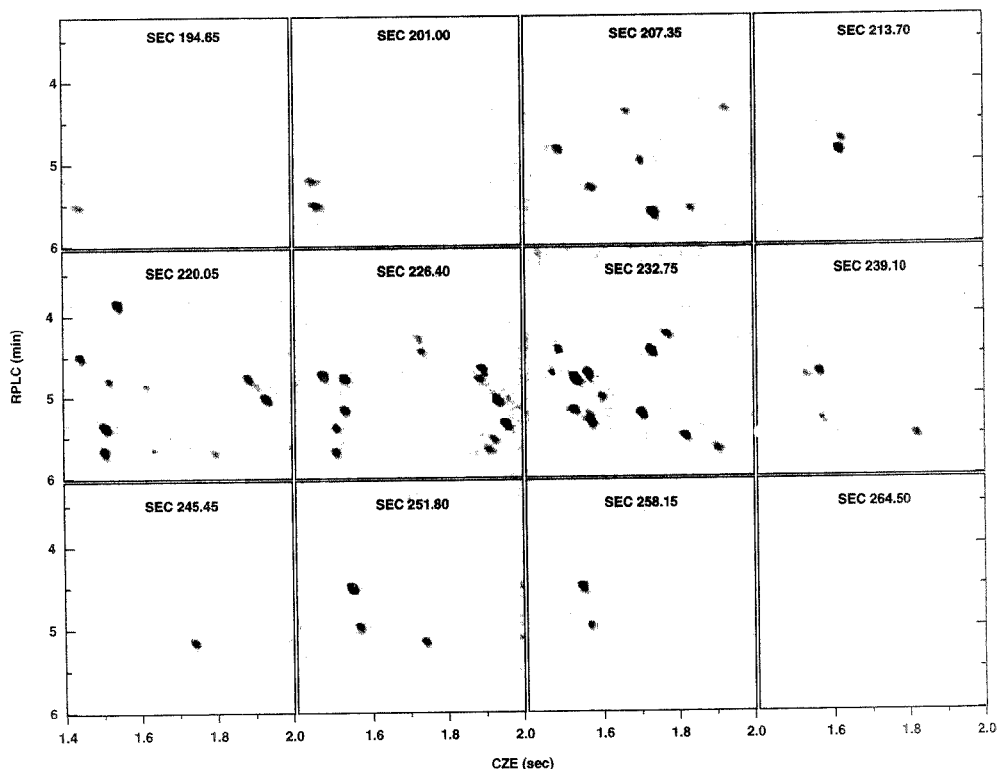


Figure 3. Individual 2D "slices" of 3D Analysis of FITC-tagged ovalbumin digest. Each square is data from a single 2D RPLC/fast-CZE analysis.

min, the broad SEC peaks ensure that each peak is sampled at least once into the 2D system.

The vertical bars on Figure 2 show where individual 2D samples were taken of the SEC effluent. Notice that most of the visible peaks are intersected by one or more 2D slices. 2D slices were also taken from 305 to 370 min but with no detectable peaks. Though some components are visible with the UV absorption detector, after dilution and injection into the RPLC (with further dilution in the LC column), the sample zones are apparently too dilute to be seen in fast-CZE. The latest peak at 430 min probably would have been detectable, but 2D data were not taken so late in the SEC run.

It should be noted that an injection of 0.1% formamide solution under the same conditions (with detection at 230 nm) resulted in a peak at 260 min. Since formamide should be totally included in the pores of the SEC stationary phase, all peaks after this point are separated by some mixed-mode mechanism. The multiple components visible early in the largest peak are probably larger peptides, separated by size exclusion. The components late in the down slope of the same peak, and the later eluting components, are resolved by some combination of SEC and other retention modes such as adsorption or ion exchange.

Figure 3 shows gray-scale plots of some of the actual 2D slices (samples) of the SEC analysis. The LC analysis time is 6 min, but the gradient formed in the pump requires 3 min to pass through the proportioning valve, pump, LC column, and connect-

ing tubing to reach the top of the fast-CZE capillary. Thus, there are no peaks in the LC dimension at times earlier than 3 min. The CZE analysis time is 2 s, but most of the CZE peaks occur in the last half of the CZE analysis. The slices in Figure 3 therefore focus on 3–6 min LC time (on the vertical axis) and 1.4–2.0 s CZE time (on the horizontal axis). The slices shown cover most of the major multicomponent SEC peak centered at about 230 min. The best signal to noise (S/N) ratio and the majority of the peaks are seen in the central slices at 220–240 min, corresponding to the maximum of the SEC peak. While in the earlier slices the SEC time reveals some information on the relative size of components seen in that slice, in the later slices we can only say that molecular size was one of the factors controlling its position. In the slices taken after 255 min, the SEC separation is mixed-mode.

Figure 4 is a 3D representation of a region of the 3D data set. The intensity of peaks is shown in inverted gray scale, so that lighter areas indicate peak maxima or larger peaks. Of the 20 2D slices taken, only 14 are included in this image. The peaks are shown as "stacks" of disks of varying gray-scale intensity. Because there are many more LC points than SEC points (14 slices = 14 points), and even more CZE points, Dicer is used to scale the values to give the 3D volume shown. In the 3D image, values between the actual data points are linearly interpolated to fill the desired volume. In this way, more than 14 horizontal surfaces can be drawn through the volume to better show the shape of

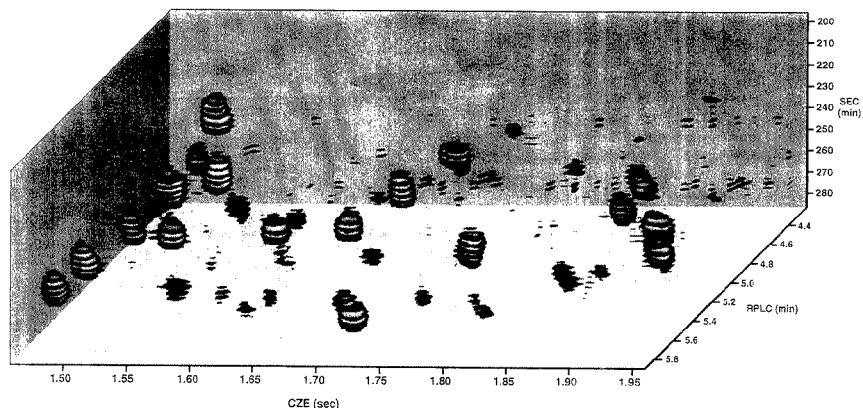


Figure 4. Three-dimensional representation of 3D data "volume" of tryptic digest of ovalbumin. Peaks are seen by making a series of planar slices through the data volume and so have the appearance of "stacks" of disks or ellipsoids.

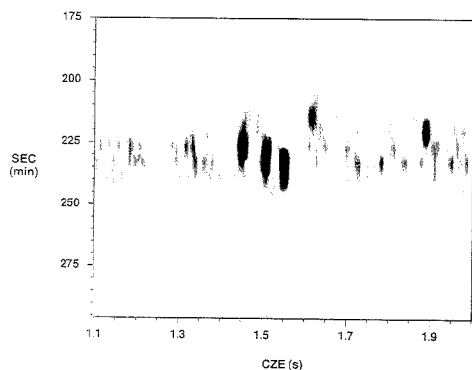


Figure 5. 2D SEC/CZE "slice" of the 3D data volume. All points in this 2D gray-scale plot correspond to a RPLC retention time of 4.76 min. Data for the entire SEC analysis are shown on the vertical axis. Only a portion of the CZE analysis data is shown on the horizontal axis.

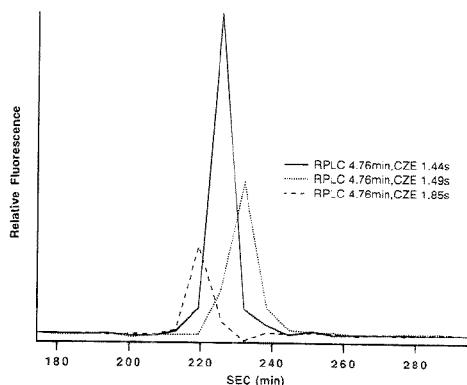


Figure 6. Individual SEC analyses taken from Figure 5 at particular CZE migration times. Three individual columns of data from Figure 5 are shown. These plots are individual SEC analyses of compounds whose RPLC retention time is 4.76 min and whose CZE migration times are 1.44, 1.49, and 1.85 s, respectively. As mentioned in the text, the SEC analysis is seriously undersampled.

the peaks in space. To see only the peaks, Dicer can be used to set some of the inverted gray-scale levels to be transparent. That is, the background gray level seen in the slices shown in Figures 3 and 4 can be set to be transparent, so that only the peaks are visible in the data volume. Without this feature, visualization of the entire data volume would result in a gray cube, with the peaks hidden behind baseline levels of gray above or in front of them. Only peaks intersecting the faces of the cube would be visible.

Though the 3D "volume" of data was collected as a series of horizontal RPLC/CZE "slices", other 2D "slices" of the data can be extracted in any combination of two dimensions to focus on distinct parts of the data set. Figure 5 is a SEC/CZE "slice" taken at a single RPLC retention time. All of the points shown in Figure 5 correspond to an RPLC retention time of 4.76 min. The entire range of the SEC analysis time sampled is given on the vertical axis. Remember that this is actually only 20 points. A region of the CZE analysis similar to that shown in Figure 3 is given on the horizontal axis. As in the other gray-scale plots, peaks are represented as dark spots on the gray background. There are

three darker spots (larger peaks) near the center as well as two lighter bands (smaller peaks) above and to the right of these bands. As would be expected, these spots correspond to those seen in Figure 3 at the appropriate RPLC and SEC retention times and CZE migration times. Notice that the three larger peaks near the center are well resolved in the CZE dimension but only partially resolved in the SEC dimension. If the data in this plot were summed horizontally, across the rows, it would give the equivalent SEC analysis with no CZE separation. Obviously, any peaks with the same SEC retention time would be unresolved by SEC alone. The three large peaks in the center would have very similar SEC retention times and would be largely unresolved. Similarly, summing vertically down the columns would give the equivalent CZE separation with no SEC separation.

Part of the power of the multidimensional approach can be realized by examining the data in a single column or row. A single column of data from Figure 5 gives the SEC analysis for all compounds of a particular RPLC retention time and a particular

CZE migration time. Similarly, a single row of data gives the CZE analysis for all compounds of particular SEC and RPLC migration times. Figure 6 shows three SEC analyses taken at the CZE times of the three large peaks in Figure 5. Obviously the peaks are extremely undersampled. The RPLC/CZE analysis time of 6.35 min limits how often the SEC separation can be sampled. However, even the smallest peak is sampled by at least two points. Though the undersampling limits the accurate determination of peak heights and retention times, some information can still be obtained. These peaks would probably be unresolved by SEC alone, and it would thus be difficult to estimate the number of components present. Also, rough estimates of the SEC peak width can be obtained from this figure. The smallest peak is roughly 20 min wide at the base, and the largest is roughly 30 min wide.

The 3D system relies on a flow splitter and a dilution tee after the SEC column to interface the SEC to the LC. Because a significant amount of sample is "lost" in the interface, some lower concentration components might not be detected in the 3D analysis. Also, we did not acquire data over the entire SEC analysis. To see small peaks possibly too dilute to detect in the 3D system, and to see which peaks might have been omitted because of their late SEC elution, we compared the 3D analysis to a 2D analysis of the same sample.

The original tagged ovalbumin digest was diluted 1:50 in CZE buffer, and 20 μ L was injected onto the RPLC column. The same 2D analysis conditions were used as in the 3D analysis. To compare this to the 3D separation, the 20 2D slices taken of the SEC were summed. A comparison of the direct 2D analysis and the summed slices is shown in Figure 7. Comparing panels A and B, the results of the 2D analysis and the summed data are largely what would be expected. Most of the larger peaks are present in both (A) and (B). Noticeably, a large peak in the 2D analysis at 1.82 s CZE time, 4.6 min LC time is missing from the summed data. Also two peaks from a group of three seen at 3.25–3.75 min LC time in the 2D analysis are not present in the summed data. Most of the peaks in the summed data are shifted to slightly later LC times than in the 2D analysis alone. There are a number of very faint spots (small peaks) seen in the 2D analysis which are not seen in the summed data. This is to be expected because of the greater sample dilution in the 3D analysis, as was mentioned earlier. Notice that for most of the components, the pattern seen in the summed data is very similar to that of the 2D analysis alone, both in peak position and intensity.

Peak Capacity. To estimate the peak capacity of the overall 3D method, we calculate the peak capacity of each dimension separately and take the product of the three values so obtained. The peak capacity of a separation with unit resolution is defined as

$$n_c = L/4\sigma$$

where L is the total distance (or time) over which the sample zones (peaks) are distributed and σ is the average standard deviation of the peaks separated.⁹ Calculation of the peak capacity for the RPLC and CZE is relatively straightforward, as shown below, but is more difficult for the SEC. In the SEC analysis shown in Figure 2, in the part of the run over which 3D data was

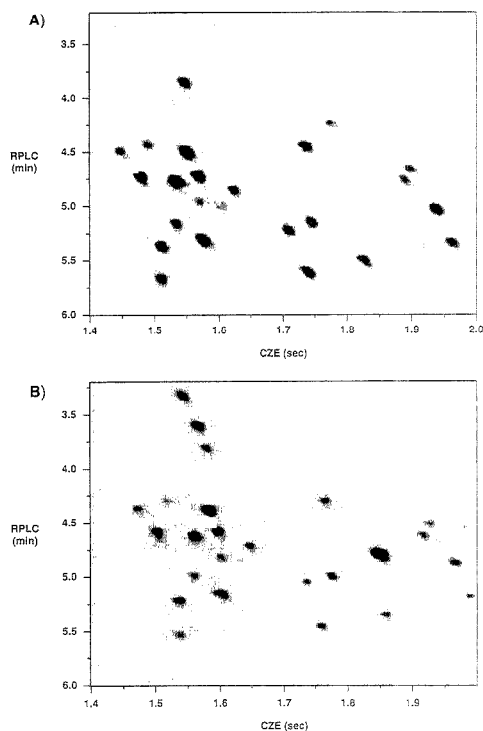


Figure 7. Comparison of summation of 2D slices taken in 3D analysis and same sample analyzed by 2D RPLC/fast-CZE alone: (A) Point-to-point summation of all 20 2D data slices, including those shown in Figure 3. (B) 2D RPLC/fast-CZE analysis of FITC-tagged ovalbumin digest.

collected, there are no baseline-resolved peaks from which an estimate of σ can be easily obtained. To estimate the peak capacity of the SEC separation, we use the data from Figure 6. Because peak widths there are 20–30 min, and data were acquired over about 125 min, a rough estimate of the SEC peak capacity is $n_{SEC} \approx 4-6$. In the calculations below we use the middle value of $n_{SEC} = 5$.

In Figure 7B, the RPLC peaks elute over a range of 2.3 min, from 3.2 to 5.5 min. The average peak width in the RPLC dimension is approximately 0.10 min (4 standard deviations). Based on eq 1, this gives a RPLC peak capacity of $n_{RPLC} = 23$. Similarly for CZE, the peaks span 0.60 s, from 1.4 to 2.0 s. An average peak width is approximately 0.025 s (4 standard deviations), and again with eq 1 this gives a CZE peak capacity with unit resolution of $n_{CZE} = 24$.

The peak capacity of the RPLC/CZE system alone is $23 \times 24 \approx 550$. When the SEC is added, the overall peak capacity of the 3D method is $5 \times 550 \approx 2800$. Though the peak capacity of the SEC dimension is small compared to the RPLC and SEC, it results in a substantial increase in the peak capacity of the overall method when multiplied by the RPLC/CZE peak capacity.

CONCLUSIONS

A three-dimensional separation identifies sample components by three different characteristics. Here, molecules are located in

(9) Giddings, J. C. *Unified Separation Science*; John Wiley & Sons: New York, 1991.

a 3D space by their size, hydrophobicity, and electrophoretic mobility. If there is sufficient resolution in each of the three dimensions, 3D "location" becomes a powerful means of component identification. As the number of separation methods increases, the possibility of two different molecules having the same location in each dimension decreases.

However, this identification is not without cost. In our present system, very concentrated samples are used to overcome dilution factors inherent in the design of the SEC/RPLC interface. This would be a problem in a sample-limited situation. Also, for elution/migration times in three dimensions to be strictly comparable, rigorous control of temperature in all three dimensions would be necessary. Thermostatic control of all three separation systems would avoid retention/migration time drift caused by changes in temperature over the course of the analysis. It would also be desirable to use a faster computer which would be able to acquire data and control the instrument simultaneously. This would enable not only more accurate timing but also better use of the 3D system. For example, the SEC analysis could be done more rapidly or be better characterized because LC analyses could be overlapped (see previous paper) to better sample the SEC.

The major advantage of a 3D method is of course the gain in peak capacity. As with a 2D system, the increase in peak capacity

is multiplicative. Because the peak capacity of a 2D system is already high, the addition of a third dimension with only a modest peak capacity can significantly increase the peak capacity of the overall method. As shown in the estimate of peak capacity above, addition of the SEC as a third dimension increases the peak capacity of the overall method by a factor of 5.

ACKNOWLEDGMENT

This research was supported by grants from the National Science Foundation (CHE 9215320) and the National Institute of Health (GM 39515) and by a gift from Hewlett-Packard. The HP1050 pump and UV absorption detector were donated by Hewlett-Packard. The HEMA stationary phase was donated by Alltech Associates. The RPLC column was donated by Rockland Technologies.

Received for review October 25, 1993. Resubmitted July 7, 1995. Accepted July 14, 1995.*

AC9506802

* Abstract published in *Advance ACS Abstracts*, September 1, 1995.

Resolution of Cis and Trans Isomers of Peptides Containing Proline Using Capillary Zone Electrophoresis

Alvin W. Moore, Jr., and James W. Jorgenson*

CB 3290, Department of Chemistry, University of North Carolina—Chapel Hill, Chapel Hill, North Carolina 27599

Capillary zone electrophoresis (CZE) is known for its high separation efficiency. Optically gated CZE is a form of CZE that allows rapid analyses while high separation efficiency is maintained. Analysis of peptides containing proline with CZE and optically gated CZE gives two peaks for dipeptides and multiple peaks for oligopeptides containing more than one proline. The multiple peaks are believed to be due to the cis and trans forms possible in peptide bonds containing proline. Isomerization between the cis and trans forms takes place at room temperature with a lifetime of seconds to minutes. Resolution of these peaks in CZE is found to be a function of separation efficiency and time of analysis. Rapid analyses with relatively lower separation efficiency give resolution equal to or better than that of longer analyses with much higher efficiency. This confirms the relationship between the multiple peaks and isomerization between the cis and trans forms. To extract kinetic information from the experimental data, a digital simulation is used to model the separation obtained experimentally. The equilibrium constant and rate constants that give the best fit of the simulated data to the experimental data are considered estimates of the actual values for the given experimental conditions.

In most peptide bonds, the bond exists almost exclusively in the trans configuration shown in Figure 1A. The cis form of the bond is energetically unfavorable, largely due to steric hindrance.¹ However, when proline is involved in the bond, both trans and cis forms are possible as shown in Figure 1B. The unique cyclic structure of the R group in proline lowers the steric hindrance and makes both cis and trans forms energetically stable. At room temperature, the cis and trans forms interconvert (isomerize) with rates on the order of seconds to minutes.²

The isomerization rate of the X-Pro bond, where X is another amino acid, has been studied extensively by NMR spectroscopy. Both ¹H and ¹³C NMR have been used to examine samples ranging from dipeptides to proteins,^{1,3} and there is considerable evidence that the rate of isomerization of the X-Pro bond is responsible for the slow step in protein-folding kinetics.² NMR has the advantage of a scan time that is rapid relative to the proline isomerization rate. Thus it is able to detect the individual cis and trans forms present at the time of the scan. Equilibrium concentrations of the two forms can be measured by assigning

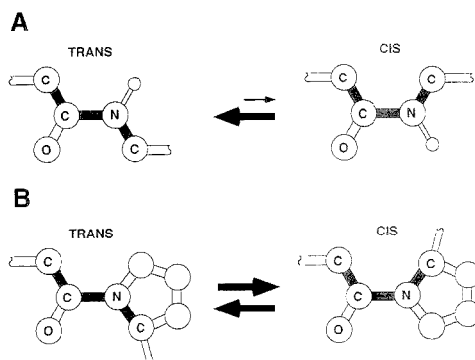


Figure 1. Cis and trans forms of the peptide bond. (A) represents the equilibrium between cis and trans forms for peptide bonds without proline. The trans isomer is energetically much more favorable than the cis isomer. (B) represents the equilibrium between cis and trans forms of the X-Pro bond. At room temperature, both cis and trans forms are present.

specific resonances to each form and comparing relative signal intensities. These can then be used to calculate K_{eq} , the equilibrium constant for the isomerization. The equilibrium constant is related to the kinetic rate constants by

$$K_{eq} = \frac{[\text{trans}]}{[\text{cis}]} = \frac{k_{C-T}}{k_{T-C}} \quad (1)$$

where k_{C-T} is the rate of isomerization from cis to trans (in units of s^{-1}) and k_{T-C} is the rate of isomerization from trans to cis (in units of s^{-1}). To measure kinetic rate constants for the interconversion, usually the change in signal is monitored over time after a temperature or pH jump is induced in the sample.

Previously in our laboratory, a number of fluorescamine derivatives of dipeptides were analyzed by capillary zone electrophoresis (CZE).⁴ In this analysis, one peak was unusually broad relative to other peaks with both earlier and later migration times. A portion of this electropherogram is reproduced in Figure 2. The broad peak (peak F) was identified as glycylproline (Gly-Pro) and the broad peak shape explained as the result of slow equilibration of the cis and trans forms of this dipeptide.⁵

To cause the broad peak, Gly-Pro must isomerize between cis and trans forms in the same order of time as is required to do

(1) Grathwohl, C.; Wuthrich, K. *Biopolymers* 1981, 20, 2623–2633.
 (2) Nall, B. T. *Comments Mol. Cell. Biophys.* 1985, 3, 123–143.
 (3) Grathwohl, C.; Wuthrich, K. *Biopolymers* 1976, 15, 2025–2041.

(4) Jorgenson, J. W.; Lukacs, K. D. *Anal. Chem.* 1981, 53, 1298.
 (5) Hiskey, R. G., personal communication, 1981.

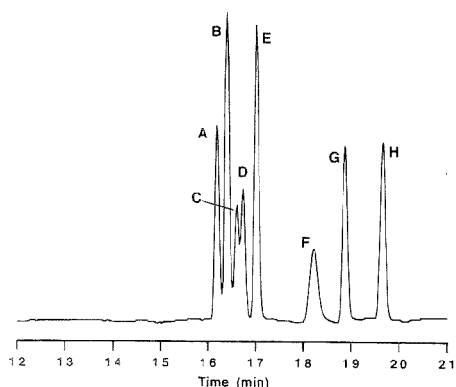


Figure 2. CZE separation of fluorescamine derivatives of dipeptides. Labeled peaks: A, phenylalanyl-leucine; B, phenylalanyl-valine; C, valyl-leucine; D, glycytyrosine; E, phenylalanyl-alanine; F, glycyproline; G, glycytylalanine; H, glycyglycine. Adapted with permission.⁴

the analysis. Because the cis to trans isomerization is a structural change, the two forms would be expected to have slightly different electrophoretic mobilities. Isomerization over the time of the analysis would result in an average mobility for the two forms. Similar behavior has been reported in many forms of chromatography in which equilibration between species occurs on the time scale of the analysis.⁶⁻⁸ Peak broadening in affinity CZE has also been noted as a result of equilibration between a protein and protein-ligand complex which occurs on the order of the CZE analysis time.⁹

NMR can resolve the two forms because of its rapid scan time. We have recently developed a method of doing rapid CZE analysis called fast-CZE.^{10, 11} Fast-CZE makes possible complete CZE analyses in as little as 2-3 s. This paper describes a unique method of monitoring the cis/trans isomerization rate of the X-Pro bond based on rapid CZE analysis. Because the isomerization rate of the X-Pro bond ranges from seconds to minutes, CZE analyses requiring only seconds can detect and resolve the individual trans and cis forms in some proline containing peptides.

If it is possible to resolve the cis and trans forms, an estimate of K_{eq} may be calculated from the relative peak areas of the two peaks. It is more difficult to directly obtain estimates of the individual rate constants $k_{C \rightarrow T}$ and $k_{T \rightarrow C}$. To estimate these values, a digital simulation of the separation was used. The simulation relied on experimentally measured migration times, separation efficiency, and K_{eq} and a user input value of $k_{C \rightarrow T}$ to model the separation. The value of $k_{C \rightarrow T}$ was adjusted until the simulation closely matched the experimental data to obtain an estimate of $k_{C \rightarrow T}$ for the experimental conditions.

Fast-CZE Analysis. CZE analysis time is a function of the capillary length squared. Thus, reduction of capillary length would

greatly decrease analysis time. However, with all other factors held constant, this would necessitate a reduction in the applied voltage to avoid heating effects. Reduction in the applied voltage would give lower CZE separation efficiency. If the analysis time were decreased but efficiency decreased as well, the cis and trans forms might remain unresolved. Even though the CZE analysis time would be rapid enough to "freeze out" the two forms as with NMR, the CZE resolution would not be great enough to separate them. The end result would again be a single broad peak.

Fast-CZE is a method of doing rapid high-efficiency CZE analyses. It relies on a high applied voltage and short capillaries to give fast and efficient CZE analyses. The heating problems normally associated with high voltages applied over short capillaries are surmounted by use of small-bore (6- μ m internal diameter, i.d.) capillaries and low-concentration (0.01 M) CZE buffers. These limit current through the capillary and thus limit Joule heating effects. The small capillary internal diameter also gives rapid diffusional averaging across the bore of the capillary, so that there are no significant band-broadening effects due to radial temperature gradients. Because of the small capillary bore, laser-induced fluorescence (LIF) detection is used and samples must be tagged with fluorescein isothiocyanate (FITC) before analysis. The system is completed by a unique optical-gating injection method which enables sample injections that are short relative to the fast-CZE analysis time. Fast and efficient CZE analyses enable resolution of the cis and trans isomers of some dipeptides.

EXPERIMENTAL SECTION

Samples and Reagents. All peptide samples were purchased from Sigma and used as obtained. Water-soluble sodium fluorescein salt was purchased from Aldrich. Fluorescein isothiocyanate was obtained from Molecular Probes (Eugene, OR). All water used in preparation of sample solutions and buffers was purified before use with a Barnstead Nanopure system. All aqueous buffers were prepared with 0.005% (w/v) sodium azide as an antimicrobial agent. Buffers for CZE were filtered with 0.2- μ m Acrodisc syringe filters (Gelman, Inc) before use. Acetone, pyridine, and sodium borate were obtained from Fisher Scientific. A 0.01 M borate buffer, pH 8.9, was used for all CZE analyses. This buffer is hereafter referred to as CZE buffer. A more concentrated borate buffer, 0.1 M, pH 9.1, was used for FITC-tagging reactions.

FITC-Tagging Conditions. A 3.8×10^{-3} M solution of each dipeptide studied was prepared in 0.1 M borate buffer, pH 9.1. To 0.8 mL of each dipeptide solution was added 200 μ L of a 6.0×10^{-3} M solution of FITC in acetone/pyridine (95/5, v/v), and the sample was allowed to react in darkness at room temperature for 4 h. These concentrations gave a 2.5-times molar excess of dipeptide over FITC. The product of the tagging reaction is the fluorescein thiocarbonyl (FTC) derivative of the dipeptide. The final concentration of FTC-dipeptide in each sample was 1.2 mM.

For the oligopeptides, a 0.3 mg was dissolved in 0.5 mL of the same borate buffer, and 30 μ L of the FITC solution was added. The final FTC-oligopeptide concentration was 0.34 mM. These tagged solutions, both dipeptides and oligopeptides, were diluted to 1×10^{-5} or 1×10^{-6} M before CZE analysis.

A 0.7 mM sodium fluorescein stock solution was prepared in water. This solution was diluted into CZE buffer, 40 μ L into 20 mL of buffer, to give a 1.4×10^{-6} M fluorescein solution used in alignment of the optics of the fast-CZE system. The fluorescein

(6) Giddings, J. C. *HRC CC, J. High Resolut. Chromatogr. Chromatogr. Commun.* **1987**, *10*, 319-323.

(7) Miller, J. M. *Chromatography: Concepts and Contrasts*; Wiley: New York, 1988.

(8) Braintwaite, A.; Smith, F. J. *Chromatographic Methods*; Chapman and Hall: New York, 1985.

(9) Avila, L. Z.; Chu, Y.-H.; Blosser, E. C.; Whitesides, G. M. *J. Med. Chem.* **1993**, *36*, 126-133.

(10) Moore Jr., A. W.; Jorgenson, J. W. *Anal. Chem.* **1993**, *65*, 3550-3560.

(11) Monnig, C. A.; Jorgenson, J. W. *Anal. Chem.* **1991**, *63*, 802-807.

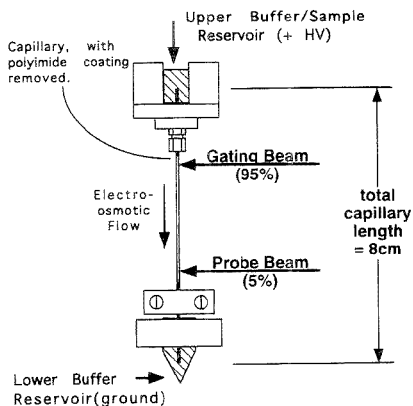


Figure 3. Fast-CZE instrumental diagram. Diagram is not drawn to scale. See text for explanation.

stock solution was also used to spike dipeptide samples with a fluorescein standard.

Instrumentation. Figure 3 is a diagram of the fast-CZE system. The operation of the fast-CZE system has been described in detail elsewhere.¹⁰ In Figure 3, the capillary is mounted vertically, but there is no significant gravitationally induced flow because the capillary is only 6- μm i.d. The total capillary length is 8 cm. Applied voltages of 5–25 kV give electric field strengths of 625–2500 V/cm. The high applied voltage and short capillary result in complete CZE analyses in as little as 2–3 s.

Because the analysis times are short, a unique injection system is needed. The beam from an argon ion laser (Innova 70 Model, Coherent, Inc., Palo Alto, CA) operated at 400 mW and 488-nm wavelength is split into two beams. One beam contains 95% of the laser power and is called the gating beam. The other contains only 5% of the laser power and is called the probe beam. As shown in Figure 3, the gating beam is focused high on the capillary and the probe beam is focused low on the capillary.

In fast-CZE, the upper buffer reservoir is also the sample reservoir. Samples are tagged with FITC so that they are fluorescent in the light of the 488-nm line of the laser. When high voltage is applied to the capillary, sample is migrated continuously into the capillary from the upper buffer reservoir. However, as long as the gating beam is on, the fluorescent tag is photodegraded by the intense light from the gating beam. Thus there is only a residual fluorescence seen at the probe beam. To make an injection, the gating beam is momentarily blocked with a mechanical shutter. This allows a small slug of unbleached material to pass through into the region of the capillary between the beams. Typical fast-CZE injection times are 5–50 ms. The components of the sample are separated by differential electromigration between the beams and detected by their fluorescence as they pass through the probe beam. The optical gating injections system enables sample injections that are short relative to the total CZE analysis time of seconds and that can be made with the applied voltage held constant at the CZE analysis voltage. Because the gating beam is the actual point of sample injection, and the probe beam is the point of sample detection, only the capillary length between the beams is actually used for the CZE separation. In this work, the distance between the beams was always 2 cm.

Table 1. Dimensions of Capillaries Used To Obtain Various CZE Analysis Times

	capillary		
	1	2	3
L (cm)	8.0	29.5	70.0
l (cm)	2.0	13.7	65.2
l/L^2	0.25	0.46	0.93

^a This value determines the fraction of the total applied voltage actually used in the CZE separation.

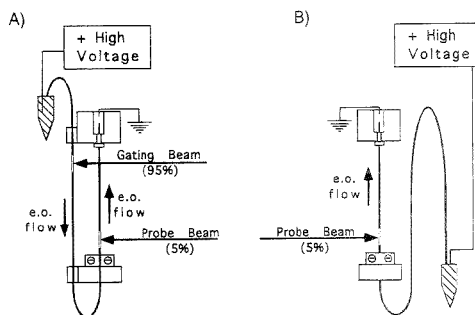


Figure 4. Fast-CZE mount with longer capillaries. (A) shows the installation of a 29.5-cm capillary, with optical-gating injection and 13.7 cm between the gating and probe beams. (B) shows the installation of a 70-cm capillary, with standard electromigration sample injection and 65.2 cm between point of injection (end of capillary) and point of detection.

Fast-CZE analyses have typical separation efficiencies of 50 000–150 000 theoretical plates. Analyses done with longer capillaries give longer analysis times and give higher separation efficiencies of 200 000–600 000 theoretical plates. In the longer analyses, the CZE separation efficiency is higher because more of the total capillary length (and thus more of the total applied voltage) is available for the CZE separation.

In this experiment, different lengths of capillary were used to obtain different CZE analysis times. For a given capillary length, analysis time can be increased by decreasing the applied voltage. However, this would also decrease the CZE separating efficiency. To increase the analysis time with equal or greater separation efficiency, the capillary length must be increased. Three lengths of capillary were used. While the voltage is applied over the total capillary length, L , only the capillary length from the point of sample injection to the point of sample detection, l , is used for the separation. Table 1 lists the capillary lengths used.

Capillary 1 was used in the fast-CZE mount shown in Figure 3. Capillary 2 was also used in the fast-CZE mount, but in an unusual configuration. Rather than one long window in the polyimide coating, two separate windows were created near opposite ends of the capillary. One end of the capillary was inserted in the mount as usual, with the window aligned with the location of the probe beam. The other end was passed through the lower mount and bent upward along the side of the mount. The gating beam was readjusted to focus on the window in this end of the capillary. This is shown in Figure 4A. For the longest capillary, shown in Figure 4B, only one window was created in the polyimide near one end of the capillary. The capillary was installed in the fast-CZE mount to align this window with the probe

beam. The other end of the capillary was placed in a buffer vial. Normal manual electromigration injections¹² were done with the longest capillary instead of optical-gating injections.

For the 70-cm capillary, 10- μ m-i.d. capillary was used because it gave less back pressure during pretreatment. All capillaries were pretreated before use by flushing for 15 min with 1 M NaOH and then 15 min with CZE buffer. No further treatment was necessary for capillaries in which the optical gating injection was used. For the 70-cm capillary, it was necessary to repeat the base and CZE buffer flushes for 10 min each after about every five analyses, when migration times would begin to drift to later times.

Detection and Data Acquisition. The data acquisition hardware (PMT, current amplifier, etc.) was as described previously for the fast-CZE system.^{10, 11} For fast-CZE analyses, with analysis times of 2–5 s, the time constant of the PMT current amplifier was set to 3 ms and data were acquired at 400 or 800 Hz. For the longer analyses, the amplifier time constant was increased and the data acquisition decreased. Details of specific amplifier time constants and data acquisition rates for the data presented are given in the figure captions.

Data were acquired through a multipurpose A/D interface board (Model NB-M10-16X, National Instruments, Austin, TX) with a program written in LabVIEW 2 (National Instruments) running on a Macintosh II computer. Plots of data were created with IGOR plotting software (Wavemetrics Inc, Lake Oswego, OR).

The digital simulation program was written in LabVIEW 2 and run on a Macintosh Centris 650 computer. The speed of this computer made it possible to repetitively run the simulation, changing parameters after each run to match the simulated data to the experimental data.

Calculation of Peak Attributes. Experimental values for peak retention times and peak variances were obtained from calculation of first statistical moments and second central statistical moments with another LabVIEW 2 program. The actual integration limits for each peak were set to be approximately equal to 6 standard deviations of the peak.

Digital Simulation. The simulation is based largely on the method of Avila et al.,⁹ used to model protein/ligand binding kinetics in affinity CE. Whereas their model simulated the interchange of free protein and protein–ligand complex, we use an adaptation of their model to simulate the isomerization of cis and trans forms of a dipeptide containing proline.

The digital model assumed a relative reference frame that traveled along the capillary at the velocity of the trans dipeptide (see Figure 5). Actual experimentally obtained migration times and measured peak efficiency (calculated via statistical moments; see Experimental Section) were entered into the simulation. The measured efficiency used in the simulation was that of the fluorescein standard migrating just before the cis and trans dipeptide peaks. This is explained as follows.

The simulation was used to model experimental data in which isomerization effects were causing the cis and trans peaks to begin to merge together. As such, the cis and trans peaks were distorted by the isomerization effects we were attempting to study, and their efficiencies could not be measured directly. Instead, the calculated efficiency of the fluorescein standard was used. The fluorescent tag, FITC, has a molecular mass of 389 g/mol, while the dipeptides also have molecular masses of 186 for Ala-Pro

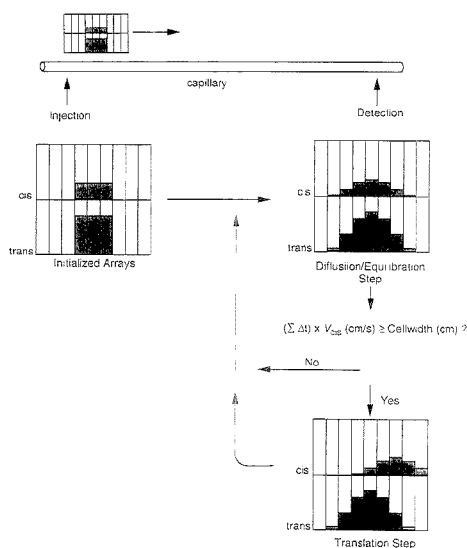


Figure 5. Digital simulation with relative reference frame. The reference frame consists of two parallel arrays of cells containing the concentrations of the cis and trans forms, respectively, of the dipeptide being modeled. The arrays are initialized with sample concentrations entered as plugs, with relative amounts of cis and trans based on the K_{eq} value of the peptide. The simulation consists of repetitive cycles of diffusion, by which the plugs eventually spread to Gaussian peaks, isomerization between the cis and trans forms, and translation of the cis array relative to the trans array. Since the reference frame is located relative to trans peak migration time, the trans peak is by definition stationary within the reference frame.

and 172 for Gly-Pro. Therefore, in the fluorescently tagged dipeptides, over 65% of the mass of the molecule is due to the tag. Because the fluorescein and the tagged dipeptides are of approximately the same molecular size, their diffusion constants should be similar. Thus, we may reasonably approximate the efficiency of the dipeptide peaks with the measured efficiency of the fluorescein peak.

The reference frame width was calculated from the position of migration of the trans peptide at its migration time (this is by definition equal to the distance from injector to detector, l) minus the position of migration of the cis peptide at that same time. This gave the peak separation in length units (cm) at the migration time of the trans peak. To ensure that the reference frame encompassed the full width of both peaks, a "margin" was added to each side. Without this margin added to each end, the simulation reference frame would start in the center of the first peak and end in the center of the second. The experimentally measured peak efficiency (N) and the distance from injector to detector (l) were used to calculate the variance (σ^2) based on

$$N = l^2 / \sigma^2 \quad (2)$$

From the variance, σ was obtained and the margin was set to five or six times σ . Since over 99.7% of a peak's area is contained by points 3σ on either side of the peak maximum (for a Gaussian peak),¹³ addition of $5-6\sigma$ ensured that virtually the full width of each peak was contained within the reference frame.

(12) Walbroehl, Y.; Jorgenson, J. W. *J. Microcolumn Sep.* 1989, 1, 41–43.

Because the reference frame traveled at the velocity of the trans peptide, the trans peak remained immobile in the reference frame by definition. The cis peptide was mobile within the reference frame, and its velocity within the reference frame was determined by the difference in migration times of the trans and cis forms and the distance between them at the trans migration time.

The reference frame was subdivided into two parallel linear arrays of cells: one array represented the cells for the trans form of the peptide and the other for the cis. The initial concentrations of cis and trans peptide were introduced as plugs. The width of the plugs was determined by the calculated linear velocity of the peptide and the injection time. From this injection width (in cm), the number of cells the initial plug would cover could be calculated from the known cell size. The initial relative concentrations of the cis and trans forms were calculated based on the equilibrium constant, K_{eq} .

The sample was introduced as a plug, and the effects of longitudinal diffusion were included in the simulation. To do this, the three-point derivative form of the differential equation describing diffusion (based on Fick's law) was used. This is taken from the treatment by Bard and Faulkner on the modeling of diffusion in electrochemical system.¹⁴ An equation of the form

$$C_{x,t+\Delta t} = C_{x,t} + D_m [C_{x+\Delta x,t} - 2C_{x,t} + C_{x-\Delta x,t}] - C_{x-\Delta x,t} \quad (3)$$

was used, where x represents a particular cell in the array and t is the time. Δx is the distance increment (the cell width in the simulation), and Δt is the time increment. Thus, $C_{x,t}$ is the concentration in cell x at time t , $C_{x+\Delta x,t}$ is the concentration in cell $x + \Delta x$ at time $t + \Delta t$ and so forth. In calculating the diffusion step, the concentration of each cell is adjusted according to eq 3 based on the concentrations in the cells immediately adjacent to it. D_m is the model diffusion coefficient and is a dimensionless variable. D_m is given by

$$D_m = D\delta t / \Delta x^2 \quad (4)$$

where D is the actual diffusion constant (in cm^2/s), Δt is the time increment in the simulation, and Δx is the distance increment in the simulation. Δx is equivalent to the cell size. Δx and Δt are related by the value of D in that Δx must not be so small that in time Δt the molecules could actually diffuse beyond Δx . If this is so, the model diverges from reality. Also, D_m has a maximum value of 0.5. For D_m greater than 0.5, this numerical model of diffusion is unstable and the simulation crashes. The closer D_m is to 0.5, the more accurately the simulation models real diffusion. Accurately modeling diffusion is given priority in the simulation; a value of D_m is chosen ($D_m = 0.45$ in all cases) and the Δt and Δx values are adjusted to fit this value of D_m . Here, D_m and Δt were chosen and Δx was calculated according to eq 4.

D , the diffusion coefficient, is actually an apparent diffusion coefficient calculated from the input peak efficiency. From the peak efficiency, the peak variance is obtained. The variance due to the injection is calculated from the theory of Sternberg,¹⁵ where

$$\sigma_{inj}^2 = V_{inj}^2 / K^2 \quad (5)$$

and σ_{inj}^2 is the injection variance, K is an injection shape factor, and V_{inj} is the injection volume. The actual value of V_{inj} used is in seconds, because the optical-gating injection is measured in seconds. From our earlier work¹⁰ the value of K for the optical-gating injection is 3.7. A perfect plug-shaped injection gives $K = 3.5$, while a Gaussian gives $K = 6.0$. Thus use of a plug-shaped injection in the simulation is supported. For the standard electromigration injections done with the longest capillary, the K value used was also 3.7 for consistency. Earlier work in our group has shown that the electromigration injection gives a plug-shaped injection.¹⁶ For these standard injections, done at a voltage lower than the CZE analysis voltage, the equivalent injection time at the analysis voltage was used. The injection variance is subtracted from the total variance to give the variance due to diffusion (and any other sources). This variance is used to back-calculate to an apparent diffusion constant using a rearrangement of the Einstein equation,

$$D = \sigma^2 / 2t \quad (6)$$

Here, t is the migration time of the trans peptide. We would expect different diffusion constants for the trans and cis peptides due to the structural differences between the two isomers. However, the difference between the two diffusion constant values is probably small because the structural difference between the two isomers is small. To simplify the simulation, we assume the difference is negligible and use the apparent diffusion constant of the trans peptide for both the trans and cis forms.

The main body of the simulation was a repetitive iteration cycle consisting of two steps: an equilibration/diffusion step and a translation step. The equilibration/diffusion step involved equilibration between paired cells in the cis and trans arrays and diffusion between adjacent cells within each array. The translation step simulated the movement of the cis molecules away from the trans within the reference frame of the simulation.

Remember that Δt was set by the user, along with D_m (always 0.45). From these two values and the apparent diffusion constant, Δx was calculated. The window width calculated earlier, divided by Δx , set the number of cells in the paired arrays. The migration time of the trans peptide divided by the Δt set the number of iterations of the simulation. Thus the simulation stopped when the elapsed simulation time equaled the migration time of the trans peak.

In the equilibration/diffusion step, the diffusion was done first. Each Δt , a diffusion step was done independently in the cells of the cis and trans arrays, gradually broadening the initial rectangular sample plug into a Gaussian peak. The equilibration step was then done, in which the concentrations of the cis and trans peptides were adjusted in each pair of corresponding cells in the cis and trans arrays (eqs 7-9).

$$\Delta[\text{trans}]_{x,\Delta t} = (k_{C \rightarrow T}[\text{cis}]_{x,t} - k_{T \rightarrow C}[\text{trans}]_{x,t})\Delta t \quad (7)$$

$$[\text{trans}]_{x,t+\Delta t} = [\text{trans}]_{x,t} + \Delta[\text{trans}]_{x,\Delta t} \quad (8)$$

$$[\text{cis}]_{x,t+\Delta t} = [\text{cis}]_{x,t} - \Delta[\text{trans}]_{x,\Delta t} \quad (9)$$

$\Delta[\text{trans}]_{x,\Delta t}$ in eq 7 represents the net change in concentration of the trans peptide in the x th paired compartments over the time

(13) Box, G. E. P.; Hunter, W. G.; Hunter, J. S. *Statistics For Experimenters*; John Wiley and Sons: New York, 1978.

(14) Bard, A. J.; Faulkner, L. R. *Electrochemical Methods*; John Wiley and Sons: New York, 1980.

interval Δt . Equations 8 and 9 update the concentration in each compartment of the cis and trans arrays to reflect the new cis and trans concentration after time Δt using the value of $\Delta(\text{trans})_{x,\Delta t}$ from eq 7. Because K_{cis} , $k_{\text{C} \rightarrow \text{T}}$, and $k_{\text{T} \rightarrow \text{C}}$ are related by eq 1, values of $k_{\text{C} \rightarrow \text{T}}$ and K_{cis} were input into the simulation and $k_{\text{T} \rightarrow \text{C}}$ was calculated from these values. K_{cis} could be estimated from the relative peak area of the cis and trans peaks. $k_{\text{C} \rightarrow \text{T}}$ could be estimated initially using literature values from NMR studies.¹

The translation step was achieved by shifting the cis array relative to the trans. The content of the x th cell of the cis array was shifted to the $(x + 1)$ th cell every time interval equivalent to the time required by the cis peptide to travel the distance Δx (the width of a cell of the reference frame). This time is based on the difference in linear velocity of the cis and trans forms, which sets the velocity of the cis form within the reference frame, and the width of the cells of the reference frame (Δx). In this way, the cis was mobile within the reference frame while the trans, by definition, was not.

At the end of the simulation (based on the number of iterations, above), the contents of each pair of compartments (cis and trans) were summed and then plotted vs distance from the origin of the moving reference frame. This gave a "snapshot" approximation of the spatial separation of the sample zones at the migration time of the trans dipeptide. Seen in the same way, the experimental electropherogram was a real-time record of the fluorescence of the tagged peptide cis and trans forms as they moved past the detector in the hypothetical reference frame.

The simulation modeled the separation of the sample zones spatially, while the experimental data recorded the separation of the sample zones temporally at a specific point in space (the point of detection). The two methods are not interchangeable. In the experimental data, the signal is acquired by monitoring a specific point in space over time, and the cis peak continues to broaden even after the trans peak is detected. Because the simulation is stopped at the migration time of the trans peak, the cis peak experiences less diffusional broadening in the simulation than in the experimental data. However, the difference in the experimental cis and trans migration times is 7.7 s (for Ala-Pro), which is only 1.7% of the total migration time of 440.25 s (for the trans peak). Similarly for the Gly-Pro, the difference in the experimental cis and trans migration times is 2.8 s, which is only 0.60% of the total migration time of 463.5 s (for the trans peak). Thus, the error introduced by stopping the simulation at the trans migration time is small, and the simulation data (though modeling a spatial separation) can be compared directly to the experimental data (a temporal separation).

The number of cells in the simulation was generally several times greater than the number of points in the equivalent region of the experimental data. The region of the experimental data array covered by the cis and trans peptide peaks would usually contain 75–120 points, while the simulation always had 500 or more cells. To compare the two arrays, the simulation data array was "sampled" at the same times as the experimental data. This gave a simulation array and an experimental data array of equal number of data points and identical time axes. The initial concentration actually used in the simulation was a value of 1, split between the cis and trans injection plugs according to the

input K_{cis} value. The area of the simulation array was normalized to that of the same region of the experimental data array after the sampling process described above. To judge the fit of the simulation to the experimental data, the two arrays were plotted on the same graph. To obtain a numerical estimate of the match between the simulated and experimental data, the amplitude difference between the experimental data array and the simulation data array was calculated. This was called the residual array. The residuals were squared and summed, and the square root was expressed as a percentage of the total area of the experimental array. The best fit was then obtained by minimizing the residuals.

RESULTS AND DISCUSSION

To investigate the cis/trans isomerization effect, we performed the following experiment. Several CZE analyses of a dipeptide sample were done, each with different analysis times. The analysis conditions were such that separation efficiency for the longer analyses was greater than or equal to that of the shorter analyses. Two peaks were seen for the dipeptide in the fastest analyses. These were due to separation of the cis and trans forms of the molecule. As analysis time was increased, these peaks eventually merged together due to averaging of the cis and trans forms over the time of the analysis.

If the second peak seen in the fastest analyses was simply an impurity, it should be present in the longer analyses as well. In fact, if an impurity, it should be better resolved in a longer analysis time (with equal or greater separation efficiency) than in a short analysis time. Only if an isomerization effect were present would more rapid analyses of lower separation efficiency give better resolution than slower analyses of higher separation efficiency. Even though the analyses at longer times have higher separation efficiency, the peaks became less resolved because the molecules had more time to interchange back and forth between cis and trans forms.

Unlike NMR, CZE does not give specific structural information. For the dipeptides examined in this paper, the earlier migrating peak was larger and was assigned as trans. This is based on NMR studies in the literature, in which the trans form of the dipeptide was the major component under similar conditions (aqueous buffer, basic pH).¹ The later migrating smaller peak was similarly assigned as cis.

Isomerization vs Analysis Time. Figure 6 shows the results of a number of analyses of Ala-Pro, with analysis time increasing from top to bottom. Figure 6A is a fast-CZE analysis of Ala-Pro done at 20 kV with an 8-cm capillary. The total analysis time is less than 3 s, and the two peaks are well resolved. The two peaks are the cis and trans isomers of the dipeptide, with the larger peak designated the trans isomer as mentioned earlier. Figure 6B–D shows longer analyses of Ala-Pro. A fluorescein standard is spiked into these samples because the two Ala-Pro peaks are not fully resolved. The fluorescein peak in each run migrates just before the Ala-Pro peaks, and the calculated theoretical plates for fluorescein are also shown. Figure 6B is a fast-CZE at 15 kV with a 30-cm capillary. The separation efficiency is higher but the analysis time has grown to 90 s. Though the trans and cis Ala-Pro peaks remain well separated, there is a noticeable rise in the baseline between the trans and cis peaks. Figure 6C shows an analysis at 28 kV with a 70-cm capillary. The separation efficiency is considerably higher but the analysis time is now 9 min. The resolution of the two Ala-Pro peaks is significantly worse, and the fill-in between the peaks is now quite obvious. Figure 6D shows

(15) Sternberg, J. C. In *Advances in Chromatography*; Giddings, J. C., Keller, R. A. Eds.; Marcel Dekker: New York, 1966; pp 205–270.

(16) Walboecki, Y., Ph.D. Thesis, University of North Carolina at Chapel Hill, 1985.

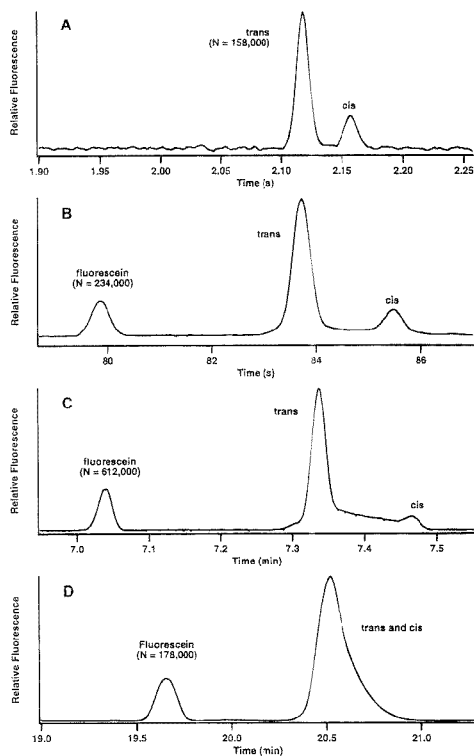


Figure 6. CZE analyses of Ala-Pro with varying analysis times. (A) is the fast-CZE analysis of Ala-Pro with $L = 8$ cm, $l = 2$ cm, 20 kV applied voltage, injection time 5 ms, and data acquisition rate 800 Hz. (B) is the fast-CZE analysis of Ala-Pro and a fluorescein standard, with $L = 29.5$ cm, $l = 13.7$ cm, 15 kV applied voltage, injection time 200 ms, and data acquisition rate 40 Hz. (C) is the CZE analysis of Ala-Pro and a fluorescein standard, with $L = 70$ cm, $l = 65.2$ cm, 28 kV applied voltage, electromigration injection for 5 s at 1 kV (equivalent to 179-ms injection at 28 kV), and data acquisition rate 20 Hz. (D) is the CZE analysis of Ala-Pro and a fluorescein standard, with $L = 70$ cm, $l = 65.2$ cm, 10 kV applied voltage, electromigration injection for 30 s at 2 kV (equivalent to 2.14 s injection at 28 kV), and data acquisition rate 2.5 Hz. Separation efficiency is less than optimum in the analysis in Figure 6D due to overinjection of the sample.

a 21-min analysis at 10 kV with the 70-cm capillary. The efficiency here is less than a third of that in (C) but almost the same as in (B). However, even though the efficiency is roughly equal, the resolution of the cis and trans forms of Ala-Pro is much worse. Only a single tailed peak is seen.

Though the calculated peak efficiency increases from panel A in Figure 6 to panel C, the resolution of the two Ala-Pro peaks decreases. In (D), with efficiency near to that of (B), the Ala-Pro gives only one tailed peak. This behavior confirms the cis/trans relationship between the two peaks seen for Ala-Pro. If isomerization kinetics were not involved, the separation of these two peaks should improve with increasing separation efficiency. Likewise we would expect the peaks to be less well resolved in the faster analyses, where the separation efficiency is lower. In fact, exactly the opposite is true. The 3-s analysis in Figure 4A

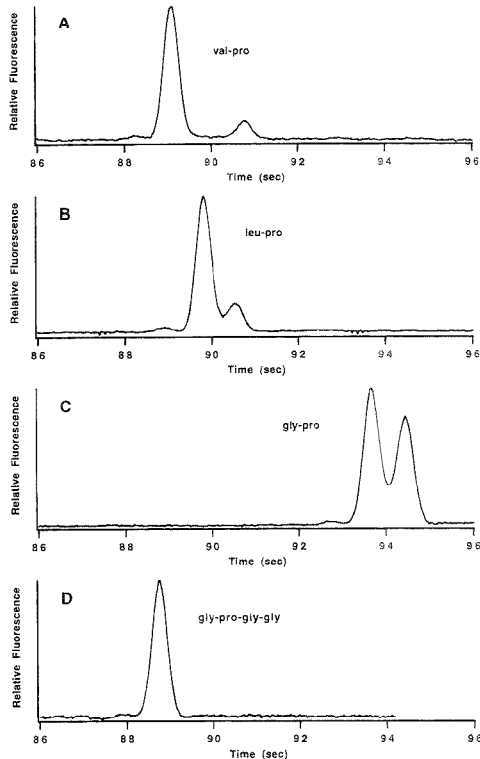


Figure 7. Fast-CZE analyses of other dipeptides. All analyses in this figure are done with $L = 29.5$ cm, $l = 13.7$ cm, 15 kV applied voltage, and data acquisition rate of 40 Hz. In (A–C), the injection time is 100 ms. In (D), the injection time is 50 ms.

gives baseline resolution of the cis and trans forms with $N \approx 160\,000$ plates, while resolution is much worse in Figure 4C with $N \approx 600\,000$ plates and an analysis time of 8 min.

For comparison, Figure 7 shows data of intermediate analysis time for other dipeptides. Some interesting comparisons can be made. Leu-Pro is less well resolved than Ala-Pro, indicating either more rapid isomerization kinetics or that the mobilities of the cis and trans forms of Leu-Pro are more similar and thus the two forms are more difficult to resolve. NMR studies of various dipeptides containing proline have shown the isomerization rate of the X-Pro bond to be very sensitive to the nature of the X residue.¹ Val-Pro is very similar to Ala-Pro. All three of these compounds have similar ratios of trans to cis peak area, approximately 4:1. Gly-Pro is unique in that the cis/trans ratio of peak areas appears closer to 1:1. For Gly-Pro-Gly-Gly, only a single peak is seen. Because this is a longer peptide, we might expect a greater difference in structure between the cis and trans forms, and that it thus would be easier to resolve them by CZE. However, experimentally this is not the case, and the difference may be explained by the length of the peptide chain. The presence of another residue beyond the proline, so that the proline is no longer the carboxyl terminus of the peptide, is known to increase the isomerization rate as much as 20-fold.¹

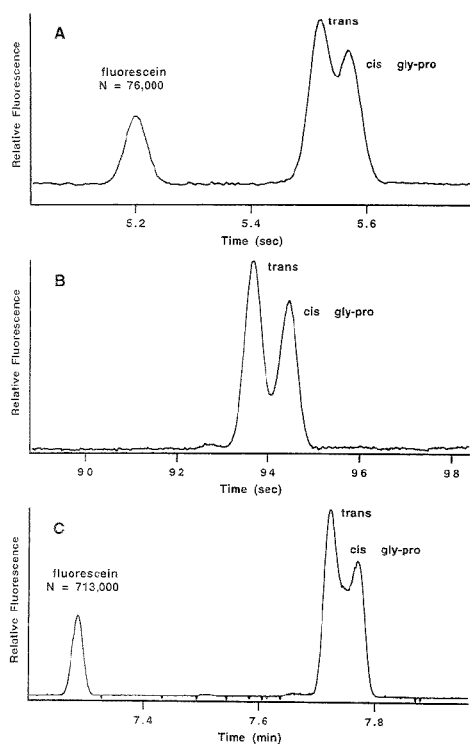


Figure 8. CZE analyses of glycyl proline with varying analysis times. (A) is a fast-CZE analysis of Gly-Pro and fluorescein standard, with $L = 8$ cm, $l = 2$ cm, 10 kV applied voltage, injection time of 20 ms and data acquisition rate of 200 Hz. (B) is a fast-CZE analysis of Gly-Pro with $L = 29.5$ cm, $l = 13.7$ cm, 15 kV applied voltage, injection time of 100 ms, and data acquisition rate of 40 Hz. (C) is a CZE analysis of Gly-Pro and fluorescein with $L = 70$ cm, $l = 65.2$ cm, 28 kV applied voltage, electromigration injection of 10 s at 2 kV (this is equivalent to 714 ms at 28 kV), and data acquisition rate of 10 Hz.

The poorer resolution of the two forms of Leu-Pro is due either to faster kinetics or to more similarity between the mobilities of the cis and trans forms. The latter explanation is more feasible in this case. If resolution is insufficient due to a lack of separation efficiency, the two peaks begin to merge as in Figure 7B. When efficiency is high but isomerization kinetics are rapid, the tendency is to see the "fill-in" between the peaks increase as for Ala-Pro in Figure 6C. This results in a peak with a shoulder or tail, rather than a close doublet.

Gly-Pro appears to be another example of the same effect. Figure 8 shows analyses of Gly-Pro at three different analysis times. In (A), the analysis is complete in about 5 s. The two peaks seen for Gly-Pro are not fully resolved. Because the separation efficiency for this analysis is only about 80 000 theoretical plates (based on the fluorescein peak), the lack of resolution is most likely due to the low separation efficiency. Notice that the valley between the two Gly-Pro peaks is relatively sharp. In Figure 8B, the analysis time is much longer. The data in Figure 6B were acquired under the same conditions, and the separation efficiency was over 200 000 plates. The Gly-Pro peaks are much

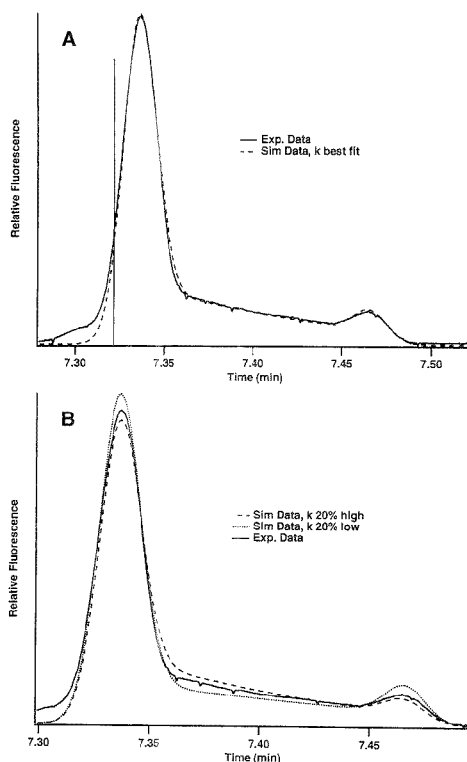


Figure 9. Comparison of experimental and simulated data for alanylproline. (A) shows the experimental data and best-fit simulated data. The experimental data are the same as in Figure 6C. The simulation parameters were as follows: trans migration time 440.21 s (experimental value 440.25 s); cis migration time, 448.22 s (experimental value 447.95 s); separation efficiency, 618 000 plates (measured from fluorescein peak); capillary length, 65.2 cm; number of cells in simulation array, 1164; number of iterations, 2201; simulation step size (Δt), 200 ms; injection time, 179 ms (experimental injection was 5 s at 1 kV; 179 ms is equivalent time at 28 kV), best fit $k_{C \rightarrow T} = 3.0 \times 10^{-3} \text{ s}^{-1}$; $K_{eq} = 4.2$ (experimental $K_{eq} = 4.4$, calculated from ratio of peak areas of data in Figure 6A). (B) shows the experimental data with the simulation $k_{C \rightarrow T}$ value adjusted 20% above and below the best-fit value used in (A).

better separated, and the valley between the peaks remains sharp. Any effects of the isomerization between the cis and trans forms are not obvious in this analysis. Finally, in Figure 8C, a much longer analysis is done with an efficiency for the fluorescein peak of over 700 000 plates. Again, the cis and trans forms of Gly-Pro are unresolved, but notice that the valley between the peaks is no longer sharp. There is now visible a flat fill-in region between the peaks, which is indicative of an isomerization effect. Because the separation efficiency is higher in (C) than in (B), without isomerization effects we would expect the resolution in (C) to be at least as good as in (B).

Comparison of Simulation and Experimental Data. Figure 9A shows a comparison of the experimental analysis of the Ala-Pro at an analysis time of about 8 min. These data were well suited for modeling with the simulation because the two peaks

are well resolved, but there is a significant amount of fill-in between them. This is seen as a noticeable rise in the baseline between the peaks. The fill-in is caused by the isomerization of the cis and trans forms over the time of the analysis. As shown in Figure 6, this fill-in increases as the analysis time increases, until eventually the peaks merge into one peak. We have found that the match of the simulation to the experimental data is more sensitive to changes in $k_{C \rightarrow T}$ values when the data being modeled has more fill-in between the peaks.

To model these data with the simulation, we input the migration times of the trans Ala-Pro (earlier) and cis Ala-Pro (later) peaks, the efficiency of the fluorescein standard that migrates just before the peptide peaks, and an initial K_{eq} value based on the relative areas of the cis and trans peaks. To get the best estimate of K_{eq} , the relative areas of the well-separated peaks run under fast-CZE conditions (Figure 6A) were used. An initial value of $k_{C \rightarrow T}$ was obtained from the literature,¹ and a value of Δt was input based on the magnitude of the migration time. If Δt is large, the simulation runs quickly but the approximation to the experimental data is always poor. If Δt is very small, the simulation more closely approximates the actual data but the time taken to run the simulation is excessively long. In most cases, Δt was adjusted to give 500–1000 cells in the simulation array and 2000 or more iterations. The specific values are given in the figure captions.

The simulation was operated as follows. First, the K_{eq} value was adjusted to match the peak heights in the simulated and experimental data. Because electromigration injections were done in all cases, the trans form would be preferentially injected over the cis because it has the higher electrophoretic mobility. This would experimentally cause the ratio of the trans and cis peak areas to give an artificially high K_{eq} value. In practice, this is confirmed in that the K_{eq} value was usually adjusted downward to raise the height of the simulated cis peak to that of the experimental data. However, for Gly-Pro, the simulation K_{eq} value was actually adjusted upward from that measured experimentally.

Second, the cis migration time input to the simulation was increased to align the peak maxima of the simulated and experimental data. For the short analysis times, where the trans and cis peptides were fully resolved, the measured cis peptide migration time could be assumed to be very close to the "true" value. However, for longer analysis times, where the trans and cis peaks were beginning to merge together, the experimentally measured cis migration time would be early. The cis and trans forms are beginning to average together over the course of the analysis, and as such, the trans will have a slightly later migration time, and the cis form a slightly early migration time. The extent of this depends on the equilibrium constant between the two forms. Consider for example Ala-Pro, where the trans is preferred 4 to 1 over the cis. As analysis time becomes large, the trans form will eventually have a 20% later migration time, and the cis 80% earlier (at this point they will have merged into one peak). Reasoning similarly, in analyses of intermediate length, the trans migration time will be gradually later (a smaller effect) and the cis migration time gradually earlier (a larger effect). In running the simulation, we found that a small adjustment (<0.1%) of the cis migration time to a later time resulted in a better fit of the simulated data to experimental data.

Finally, the $k_{C \rightarrow T}$ value was adjusted to match the fill-in between the peaks in the simulation data to that of the experimental data. Figure 9A shows the experimental data as a solid line and

simulated data as a dashed line. The vertical line indicates the point at which area scaling was begun. Notice that there is a small unresolved contaminant peak in the experimental data just before the trans Ala-Pro peak. There is no provision in the simulation to account for the additional area from a contaminant peak, so this area must be omitted when the simulation data are scaled. Thus, the area of the experimental array to the left of the vertical line was not included when the simulation data were scaled. This results in a better fit of the simulation data to the experimental data it was designed to model. Figure 9B shows the sensitivity of the simulation to changes in $k_{C \rightarrow T}$. The solid line is again the experimental data, and the dashed lines are simulated data with $k_{C \rightarrow T}$ values 20% above and below the value used in Figure 9A. The agreement is obviously much worse.

As mentioned earlier, to accurately use the simulation, it is best to have experimental data in an analysis time that makes obvious the isomerization contribution to the peak shapes. Figure 10 is similar to Figure 9 but shows data for Gly-Pro. Gly-Pro was never fully resolved, even with the fast-CZE analyses. To estimate K_{eq} for Gly-Pro, Gaussian curves were fit to the data in Figure 8B. The ratio of the areas of these Gaussians gave a K_{eq} of 1.3. This was the initial value used in the simulation to model the data in Figure 8C. Figure 10A is a closeup view of the Gly-Pro peaks from Figure 8C. The vertical line again is where the area scaling of the experimental to simulation data was begun. In this case there is no obvious contaminant peak, but this point is chosen to omit the baseline just before the Gly-Pro peaks. Here again the separation efficiency is high and the lack of resolution between the peaks is largely due to isomerization effects. The solid line is the experimental data and the dashed line is the simulation data with the input $k_{C \rightarrow T}$ value adjusted to give the best match to the experimental. In Figure 10B, the experimental data (solid) are compared to simulation data using $k_{C \rightarrow T}$ values 20% above and below the value used in Figure 10A. The difference here with a 20% variation is even greater than in Figure 9.

Panels A and B of Figure 11 show the individual cis and trans arrays from the simulation data plotted in Figures 9A and 10A, respectively. These are representative of molecules that were in the cis or trans state at the end of the simulation. The peak shapes are intuitively what one would expect with the isomerization behavior. For Ala-Pro, the equilibrium ratio of trans isomer to cis is about 4:1. In Figure 11A, the cis array shows a peak with a large and unusual fronting shape. At injection, the cis and trans start out as identical plugs of sample, differing only in amplitude. Over the simulation time, the cis migrates away from the trans (within the relative reference frame) but the trans is the energetically preferred form. Any cis molecules that isomerize to trans become immobile during the simulation, only moving further if they convert back to cis. The cis peak shows the large front of molecules that spent a significant portion of their time as trans. Similarly, the trans shows a sharp peak with a long low tail. The tail is due to the small fraction of the trans molecules that spent a significant amount of time initially as cis. In the final simulation array, the tail of the trans peak and the front of the cis peak add together to give the fill-in area between the peaks.

For Gly-Pro, the equilibrium ratio of trans isomer to cis is lower, about 1.3:1. Figure 11B shows the individual cis and trans arrays, which are almost mirror images. Because the trans and cis are almost equally preferred, the skew in the peak shapes is not as great. Also, the difference in mobility between the cis and

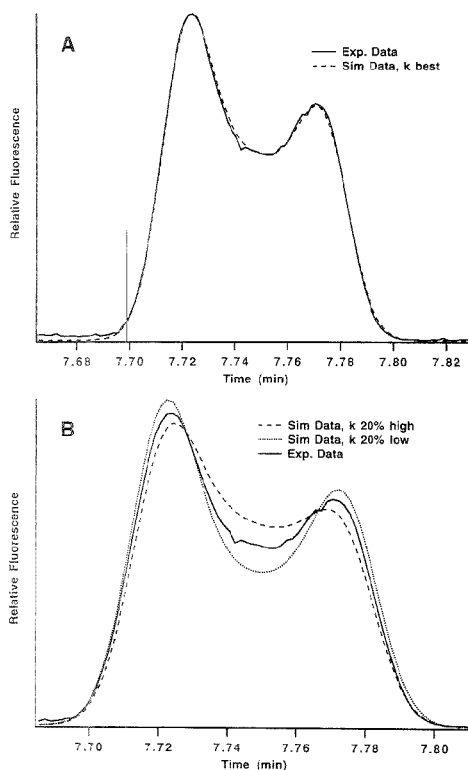


Figure 10. Comparison of experimental and simulated data for glycylproline. (A) shows the experimental data and best-fit simulated data. The experimental data are the same as in Figure 7C. The simulation parameters were as follows: trans migration time, 463.28 s (experimental value, 463.5 s); cis migration time, 466.625 s (experimental value, 466.3 s); separation efficiency, 705 000 plates (measured from fluorescein peak); capillary length, 65.2 cm; number of cells in simulation array, 878; number of iterations, 2316; simulation step size (Δt), 200 ms; injection time, 715 ms (experimental injection was 10 s at 2 kV; 715 ms is equivalent time at 28 kV); best-fit $k_{C-T} = 1.95 \times 10^{-5} \text{ s}^{-1}$; $K_{eq} = 1.28$ (experimental $K_{eq} = 1.23$, calculated from ratio of peak areas of data in Figure 7B. Because the peaks in Figure 7B are not fully resolved. Gaussian curves were fit to the experimental data and the ratio of the areas of the Gaussians was used). (B) shows the experimental data with the simulation k_{C-T} value adjusted 20% above and below the best-fit value used in (A).

trans isomers is small, so molecules that isomerize from cis to trans do not move far from their original position over the course of the simulation.

Heating Effects. Originally we expected that the same K_{eq} and k_{C-T} values should apply for all analyses of a particular compound, such as Ala-Pro, no matter what the analysis time. We did not find this to be the case. Rather, exactly the opposite was true and the values were different for each analysis time. However, the calculated electrophoretic mobility for the trans peak also varied with the analysis time. Because other experimental conditions had not changed, changes in the temperature of the CZE buffer were suspected as the cause of changes in electrophoretic mobility.

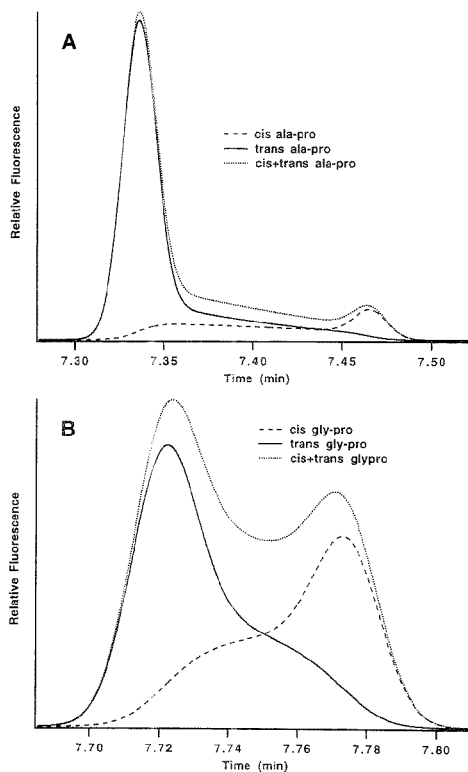


Figure 11. Cis and trans arrays from best-fit simulation data. (A) shows the simulation cis and trans arrays from the best-fit Ala-Pro data in Figure 9A. The sum of the cis and trans arrays gives the simulation data which is matched to the experimental data. (B) similarly shows the simulation cis and trans arrays from the best-fit Gly-Pro data in Figure 10A. See text for discussion.

Our CZE system was constructed in-house, and no provision was made for thermostating the capillary. Indeed this would be especially difficult with the fast-CZE system. However the applied electric field strength varied with the analysis time. For the fast-CZE analyses, the field was extremely high (625–2500 V/cm) and it varied from 200 to 500 V/cm for the other analyses. Though the capillaries used were small bore, so that radial temperature gradients were unlikely, overall heating of the buffer was certainly possible. If Joule heating was occurring, the electrophoretic mobility should increase with applied field strength. However, the experimental data were taken over several days, with significant fluctuations in room temperature over that time. The combination of room temperature changes and applied field changes gave unpredictable changes in electrophoretic mobility, which is equivalent to unpredictable changes in the temperature inside the capillary. The kinetics information we obtain is of the same magnitude as obtained in studies done by NMR, but careful temperature control would be necessary to make a detailed comparison. A comparison of K_{eq} and k_{C-T} obtained here with those of similar compounds measured by NMR is shown in Table 2.

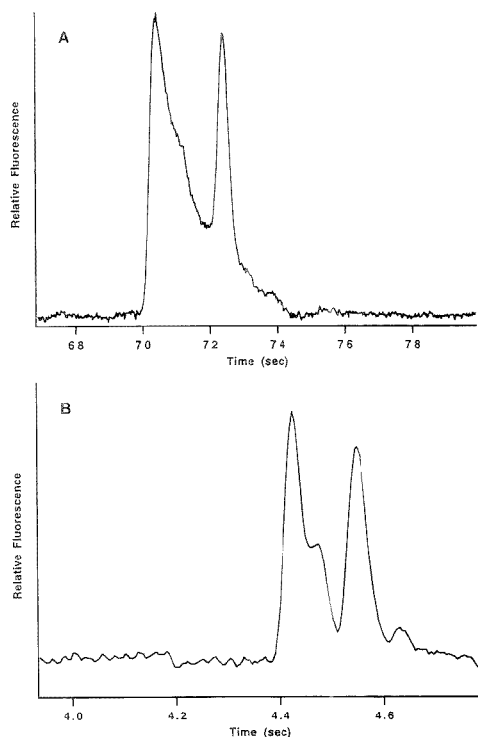
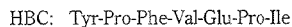
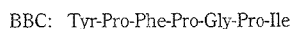


Figure 12. Fast-CZE analyses of FTC-tagged bovine β -casomorphin. (A) is an analysis with $L = 29.5$ cm, $l = 13.7$ cm, 15 kV applied voltage, 200-ms injection, and data acquisition rate of 40 Hz. (B) is the same sample with $L = 8$ cm, $l = 2$ cm, 10 kV applied voltage, 15-ms injection, and data acquisition rate of 200 Hz. A three-point linear smooth was performed to reduce baseline noise.

Of course an exact match with NMR values would not be expected. The large FTC tag undoubtedly has some effect on the isomerization kinetics of the dipeptides. This same experiment could be done with a UV absorbance detector, where no fluorescent label would be necessary. UV detection would require the use of larger diameter capillaries. Because high separation efficiency is needed, high applied voltages are necessary, and with larger bore capillaries this would make heating effects more of a concern. Most commercial CZE instruments are designed to thermostat the capillary, which would solve the unknown temperature problem described above. Temperature control would also allow the use of higher voltages on the larger bore capillaries needed for UV detection, since excess heat could be removed by the capillary temperature control system.

Analysis of Longer Peptides. For comparison, we tagged some longer peptides containing proline. Bovine β -casomorphin (BBC) and human β -casomorphin (HBC) are heptamers containing respectively three and two proline residues. Their structures are



Considering their structures, we might expect eight peaks for BBC (three X-Pro bonds, each with two possible configurations)

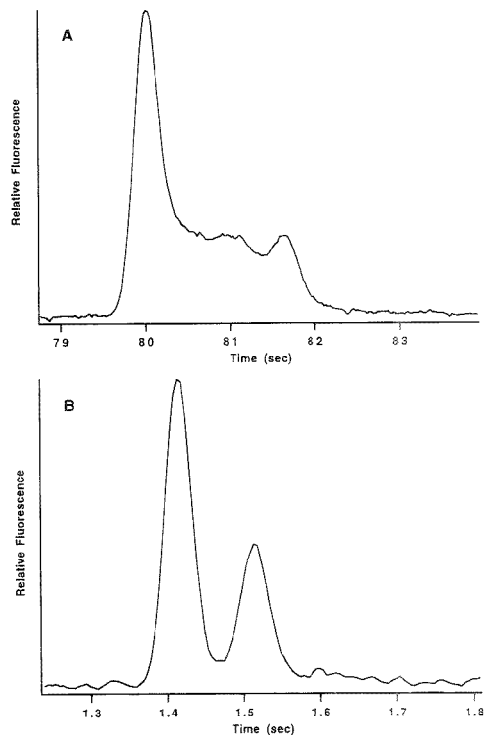


Figure 13. Fast-CZE analyses of FTC-tagged human β -casomorphin. (A) is an analysis with $L = 29.5$ cm, $l = 13.7$ cm, 15 kV applied voltage, 200-ms injection, and data acquisition rate of 40 Hz. (B) is the same sample with $L = 8$ cm, $l = 2$ cm, 10 kV applied voltage, 15-ms injection, and data acquisition rate of 200 Hz. A three-point linear smooth was performed to reduce baseline noise.

Table 2. Comparison of Equilibrium Constants (K_{eq}) and Rate Constants ($k_{C \rightarrow T}$ and $k_{T \rightarrow C}$) Measured by CZE (with Best-Fit Simulation) to Those Measured by NMR

analyte	K_{eq} (measd)	K_{eq} (used in simul)	$k_{C \rightarrow T}$ ($\times 10^{-3} \text{ s}^{-1}$)	$k_{T \rightarrow C}$ ($\times 10^{-3} \text{ s}^{-1}$)
FTC-Ala-Pro (CZE)	4.4 ^a	4.2	3.0	0.71
Ala-Pro (NMR)	1.6 ^b		2.4	1.5
FTC-Gly-Pro (CZE)	1.2 ^a	1.3	2.0	1.5
Gly-Pro (NMR)	1.7 ^c		2.2	1.3

^a Calculated from relative peak areas of trans and cis peaks in data in Figure 6A. Peak areas were calculated from peak width at 6 standard deviations. Buffer conditions are 0.01 M borate buffer, pH 8.9.

^b Calculated from relative areas of Gaussian curves fit to experimental data in Figure 8B, because peaks in (B) were not fully resolved.

^c Calculated from pD jump experiments done with ¹³C NMR.¹ Final conditions after pD jump were pD = 7.5 in 0.1 M solution of peptide in D₂O. ^d Calculated using eq 1 from K_{eq} and $k_{C \rightarrow T}$.

and four peaks for HBC (two X-Pro bonds, reasoning similarly). Results for these samples at two different analysis times are shown in Figures 12 and 13.

In the longer analysis of 70 s, BBC shows an unresolved multiplet with two prominent peaks (Figure 12A). The efficiency here is high enough to resolve some of the isomers (as shown by the sharp peak at 72.5 s), but the long analysis time allows

others to average together. In the faster analysis of 5 s shown in Figure 12B, more individual component peaks are seen. While the resolution is still less than we would like, the broad tail from the first peak seen in Figure 12A is better resolved and there are clearly at least four peaks in the multiplet.

Figure 13A shows an intermediate length analysis of HBC. Again, the longer analysis has higher plates and multiple forms are seen. The appearance is that of a large peak with a shoulder containing multiple components. In the faster analysis shown in (B), only two distinct peaks are seen. The faster analysis involves some loss of efficiency, so that the multiple smaller peaks expected from Figure 13A may not all be visibly resolved in (B). These smaller forms might comigrate with the larger peaks. Indeed, the second peak in (B) is larger than expected from (A), and might be the sum of several smaller peaks.

Initially, eight peaks were expected for BBC and four were seen, and four peaks were expected for HBC and two were seen. This may not be unreasonable after further consideration of the structures of these peptides. NMR studies by Grathwohl and Wuthrich¹ found that amino acids with aromatic R groups in the X position of the X-Pro bond can cause a 10-fold decrease in the rate of isomerization of the X-Pro bond. In BBC, two of the X-Pro bonds it contains have aromatic amino acids in the X position. If the isomerization rates for these bonds were significantly slower than that of the last X-Pro bond, only four peaks would be expected. The fastest BBC analysis gave approximately four peaks. Though they are not well resolved, it is obviously much closer to four peaks than to eight.

Similarly, with HBC, the aromatic Tyr residue might significantly slow the isomerization rate of the Tyr-Pro bond. If the isomerization rate of the other X-Pro bond is significantly faster,

only two peaks would be seen. This fits the experimental data for the fastest HBC analysis. The resolution may be incomplete because the overall kinetic rates for longer peptides are faster than those for shorter peptides.¹ This is the opposite of what one might intuitively expect. The nature of the amino acid beyond the proline residue, on the right side of the X-Pro bond, has comparatively little effect on the isomerization rate of the X-Pro bond. However, the presence of any residue beyond the proline, so that the proline is not the carboxyl terminus of the peptide, results in a significant increase in the isomerization rate relative to that of a dipeptide.¹ Thus it is not unreasonable to assume that the last X-Pro bonds in HBC and BBC might have isomerization rates beyond those we are able to study with this method.

The unusual peak shapes seen here have implications for a wide range of CZE analyses of peptides and proteins. If the efficiency is high enough and the analysis time short enough, additional peaks, peak shoulders, or peak tails could be misinterpreted as impurities in the original compound. While the supplier might be accused of selling impure product, in fact the product is pure but cis and trans forms are being detected.

ACKNOWLEDGMENT

This research was supported by grants from the National Science Foundation (CHE 9215320) and the National Institute of Health (GM 39515), and by a gift from Hewlett-Packard.

Received for review October 25, 1993. Resubmitted July 7, 1995. Accepted July 14, 1995.[⊗]

AC950678A

[⊗] Abstract published in *Advance ACS Abstracts*, September 1, 1995.

Analysis of Organophosphate Pesticides by a Trochoidal Electron Monochromator Mass Spectrometer System

James A. Laramée, Peter C. H. Eichinger, Paul Mazurkiewicz, and Max L. Deinzer*

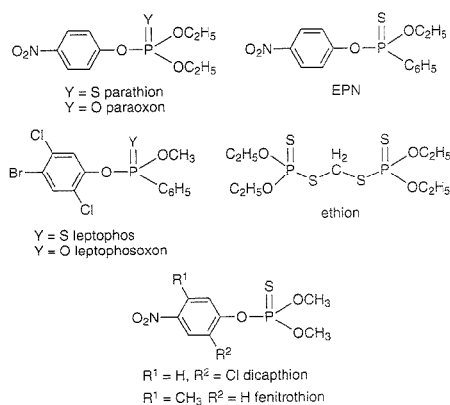
Department of Agricultural Chemistry and Environmental Health Sciences Center, Oregon State University, Corvallis, Oregon 97331

An electron monochromator mass spectrometer was used to study the resonant electron energies versus negative ion masses of the organophosphate insecticides dicapthion, EPN, ethion, fenitrothion, leptophos, leptophosoxon, paraoxon, and parathion. Each compound yielded a unique two-dimensional electron energy/mass spectrum. The most abundant ions are produced with electrons of energies between 0.03 and 1 eV, but ions result also from capture of electrons with energies ranging to 8.5 eV. Both resonance electron capture ions and dissociative electron capture ions are produced with electrons of energies ranging from 0.03 to 8.5 eV, and ions may have as many as three observable resonance states from which they are formed. Substituted thiophenoxide ions are postulated to arise by rearrangement of the parent thiophosphate ions through a spiro intermediate. Most fragment ions can be rationalized as arising through simple homolytic cleavage of the parent radical anions.

The use of organophosphate pesticides in agriculture is widespread. As a result, there is considerable concern about the level of residues and their entry into biological systems, which include animal and plant tissues as well as food, groundwater, and air. The most recent effort to improve on the sensitivity for detection of these residues and to improve on their quantification uses electron capture negative ion mass spectrometry (ECNIMS). The method generally provides greater sensitivity than positive ion chemical ionization or electron impact ionization¹ for this class of compounds as well as for other analytes of environmental and biomedical significance.

It was recently shown that ECNIMS can be performed without buffer gas to moderate electron energies to thermal and epithermal levels by using an electron monochromator.^{2,3} This device provides distinct advantages over the standard practice of moderating high-energy electrons with a buffer gas. First, the electron energy is tunable to give just the right energy for ionizing specific compounds or isomers. Second, because no chemical ionization plasma is present, the plethora of radicals, cations, anions, and high-energy electrons is eliminated along with spurious adduct ions from ion/molecule and ion/wall reactions that are largely responsible for causing a lack of spectral reproducibility. Con-

Chart 1. Structures of Organophosphate Pesticides



sequently, the ion source remains clean and free of contamination. Third, the monoenergetic beam of electrons produces only anions from the analyte, and none are produced from GC helium carrier gas or residual air and water within the ion source. Fourth, the electron monochromator promises to provide another analytical dimension which, in addition to the traditional GC/MS data, can be used to uniquely distinguish electron-absorbing compounds.

The sensitivity of the present prototype instrument has been conservatively established at around 5 pg of hexachlorobenzene.³ Important classes of environmental compounds including polychlorodibenzodioxins,⁴ *sym*-triazine herbicides,² and polychloro compounds from Arctic trout,³ as well as some explosives,^{3,4} have already been investigated with this instrument. The widely distributed organophosphate insecticides have the ability to absorb low-energy electrons and produce unique energy/mass fingerprints. These spectra are rich in negative ion resonance bands, on which we wish to report at this time.

EXPERIMENTAL SECTION

Electron Monochromator/Mass Spectrometer System.

Electron energy measurements and mass analysis of negative ion resonances (NIRs) were performed on an electron monochromator/mass spectrometer system^{2,3} which creates a well-defined and

(1) Knighton, W. B.; Mock, R. S.; McGrew, D. S.; Grimsrud, E. P. *J. Phys. Chem.* 1994, 98, 3770-3776.

(2) Laramée, J. A.; Koehler, C. A.; Deinzer, M. L. *Anal. Chem.* 1992, 64, 2316-2322.

(3) Laramée, J. A.; Deinzer, M. L. *Anal. Chem.* 1994, 66, 719-724.

(4) Laramée, J. A.; Deinzer, M. L. *Proceedings of the 40th ASMS Conference on Mass Spectrometry and Allied Topics*; Washington, DC, May 31-June 5, 1992; pp 995-996.

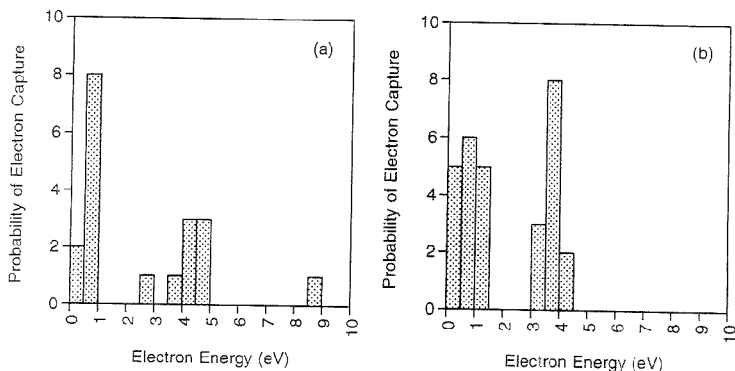


Figure 1. $P_{ec}(E)$ vs E (eV) distributions for (a) dicapthion and (b) fenitrothion.

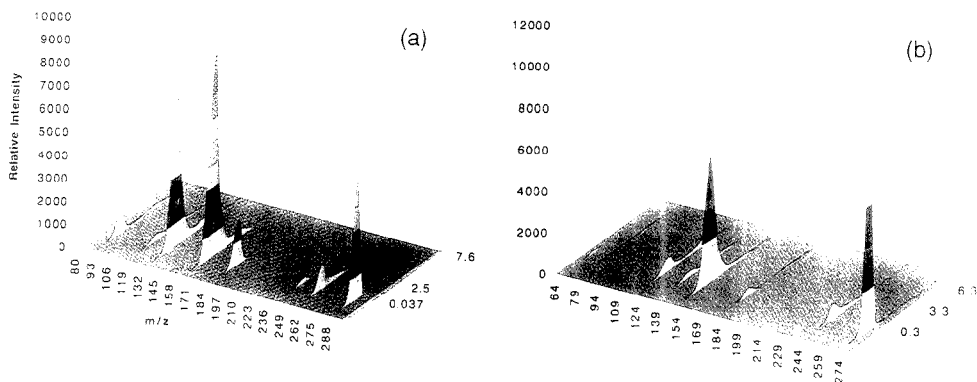


Figure 2. Three-dimensional spectra of ion intensity vs mass vs electron energy for (a) parathion and (b) paraoxon.

narrow beam of electrons whose energy can be freely varied from 0.03 to 30 eV either by computer or by operator control. The electron beam is magnetically confined to a diameter of 1.0 mm and dispersed in a crossed electric (E) and magnetic (B) field with a drift velocity of $(E \times B)/B^2$. The electron energy distribution was measured using hexafluorobenzene, which has generally accepted electron attachment energies.⁵ Thermal energy electrons (0.025 eV) and the fractional electron energy distribution, $\Delta E/E$, were defined with the sharply peaked resonance for capture of an electron to produce the molecular radical anion of hexafluorobenzene. The energy spread of the beam was 0.36 ± 0.07 eV (fwhm) at the 99% confidence level. The electron energy scale was calibrated using the NIR's at 0.03, 4.5, and 8.3 eV. The latter two resonances correspond to the process $C_6F_6 + e^- \rightarrow C_6F_5^- + F^*$. Calibration was performed immediately before and after data acquisition to check for drift in the energy scale, which averaged 0.17 ± 0.10 eV at the 99% confidence level. Electron energy spectra were acquired by scanning the filament potential from -5 to 12 eV while a fixed quadrupole rf/dc level transmitted each ion of interest. Solutions of samples were evaporated into a disposable crucible from pesticide grade acetone. A direct-insertion probe was used to introduce the sample into the ion source.

(5) Fenzlaff, H.-P.; Ilenberger, E. *Int. J. Mass Spectrom. Ion Processes* 1984, 59, 185-202.

Data Acquisition and Analysis. A special high-gain/low-noise spiraltron (DeTech Model 450) detected ions, which were counted and stored in a multichannel scaler.^{2,3} Spectra were acquired until counting statistics were better than $\pm 0.3\%$ for the largest peak in the electron energy spectrum and $\pm 1\%$ for the smallest. All electron energies refer to the peak electron energy (mode average) of the negative ion resonance as determined by nonlinear curve fitting (Peakfit, Jandel Scientific). Two-dimensional (2-D) mass/energy maps were obtained by plotting the electron energy corresponding to the maximum ion production rate at the top of the negative ion resonance versus the mass of the ion transmitted by the quadrupole to the detector. Three-dimensional (3-D) spectra were obtained by plotting the anion intensity data recorded as a function of electron energy with respect to the corresponding ion mass using commercial plotting software (Excel, Microsoft).

Chemicals and Toxicity. All samples were acquired from AccuStandard and analyzed for purity on a Finnigan 4023 GC/MS using a $30 \text{ m} \times 0.25 \text{ mm}$ i.d. DB-5 silica capillary column with splitless injection. The samples were found to be $>99.9\%$ pure. These organophosphates are potent inactivators of acetylcholinesterase, an enzyme responsible for terminating the transmitter action of acetylcholine.⁵ Routes of entry into the body include skin contact, skin absorption, inhalation, and ingestion. Permissible exposure limits in air are 0.05 mg/m^3 for the most

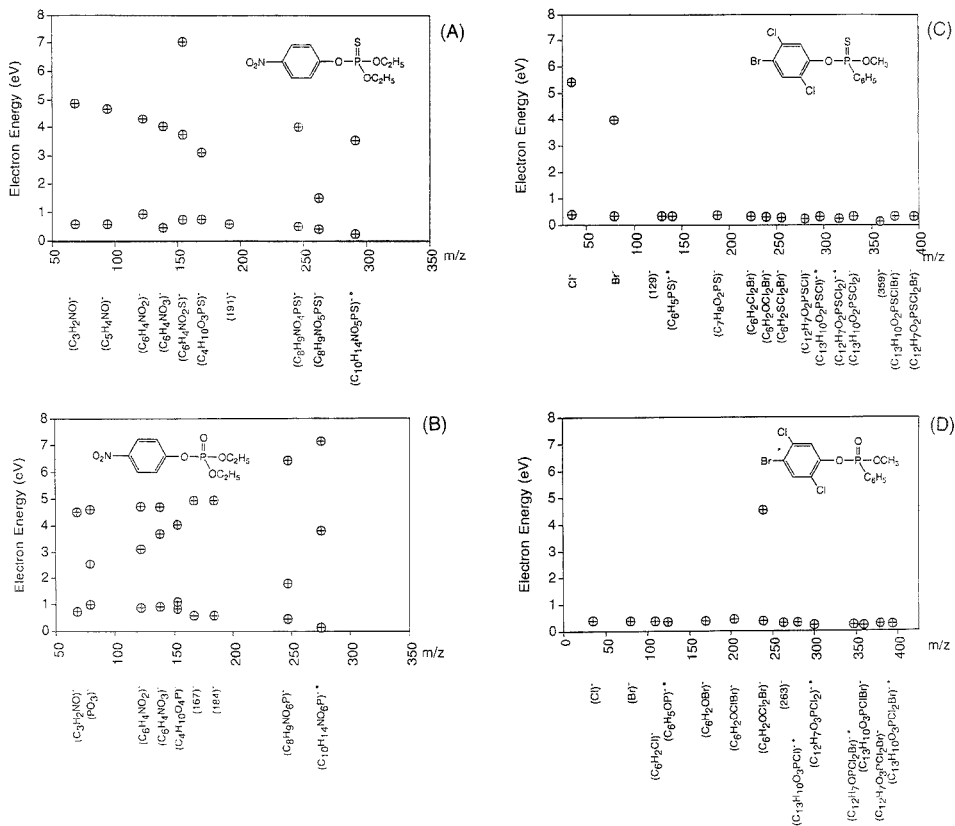


Figure 3. Two-dimensional electron energy/mass maps showing the NIR states for (A) parathion, (B) paraoxon, (C) leptophos, and (D) leptophosoxon.

toxic of the compounds examined, though all were handled in a fume hood. The LD₅₀ values for oral doses in rats are 2 mg/kg for parathion and paraoxon, 24 mg/kg for fenitrothion, 26 mg/kg for EPN, 53 mg/kg for leptophos and leptophosoxon, 208 mg/kg for ethion, and 400 mg/kg for dicapthion. For comparison, the LD₅₀ for sarin is 0.04 mg/kg.

RESULTS AND DISCUSSION

NIRs for all resonance and dissociative electron capture processes can be plotted as a function of electron energy to obtain an overview of the electron energies needed to ionize sample molecules (Figure 1). These plots constitute a total electron capture cross section with respect to electron energy but without designation of the anions formed. Therefore, they represent the probability of electron capture [$P_{ec}(E)$] versus electron energy (E) for the sample compound and can be thought of as the instrument response from a gas chromatographic electron capture detector (ECD) with respect to electron energy. These distributions are useful because they reflect differences in the electronic nature of different molecules and indicate which electron energies are

needed to observe various ions. For example, the difference between fenitrothion and dicapthion is a methyl group versus a chlorine atom at the ortho position of the ring (Chart 1). These molecules have different electronic states and, accordingly, show distinctly different NIR bands (compare parts a and b of Figure 1). All of the compounds examined in this study show unique $P_{ec}(E)$ vs E distributions.

A 3-D presentation of electron energy versus mass versus ion abundance readily shows the distinguishing spectral features of parathion (Figure 2a) and paraoxon (Figure 2b). Such spectra are anticipated to be different for each compound or congener and are likely to provide potentially useful information to help in the identification of unknowns in environmental samples. In all cases, the predominant ions observed resulted from capture of electrons with energies of <1 eV, which is consistent with Wigner's threshold law for electron capture processes.⁷ Thus, very weak ions at higher energies might be missed if the observation threshold were set too high. Such limitations, however, should not preclude the use of the full range of electron/ion information in these spectra, because modern mass spectrom-

(6) Sittig, M. *Handbook of Toxic and Hazardous Chemicals*; Noyes Publishers: Park Ridge, NJ, 1981.

(7) Wigner, E. P. *Phys. Rev.* **1948**, *73*, 1002-1009.

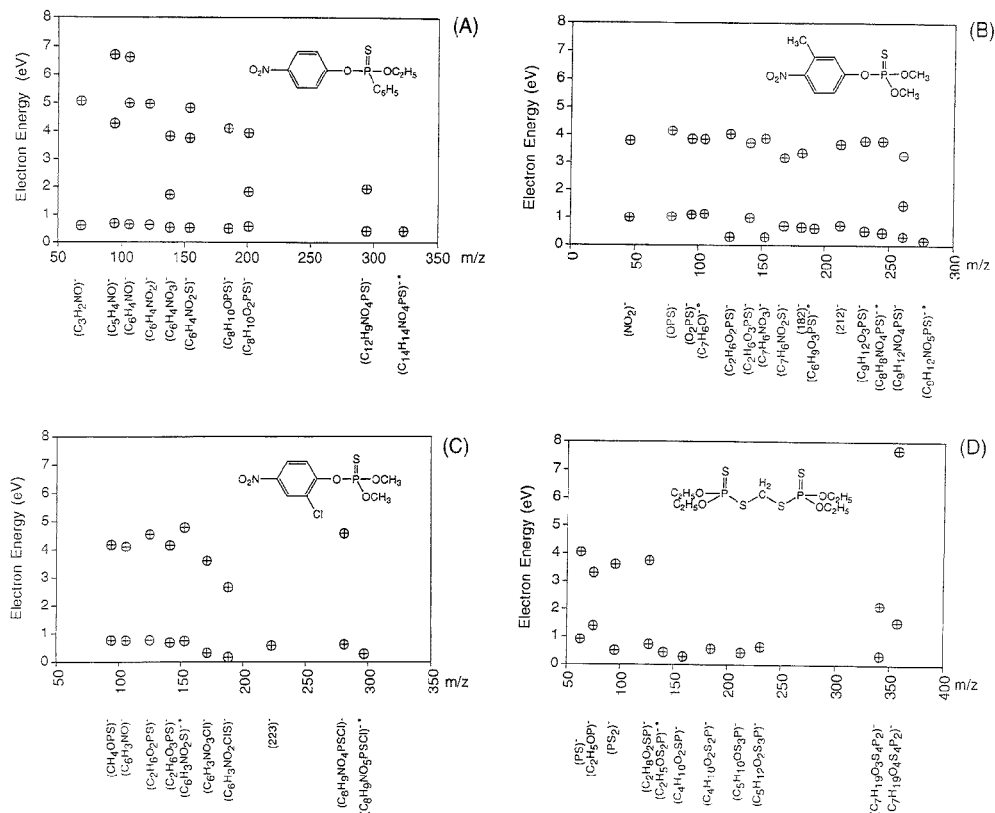


Figure 4. Two-dimensional electron energy/mass maps showing the NIR states for (A) EPN, (B) fenitrothion, (C) dicapthion, and (D) ethion.

etry systems have the capability to record data of very large dynamic ranges.

A 2-D plot consisting only of mass versus electron energy information provides a unique fingerprint for any electron-absorbing compound. Such information could be used in conjunction with traditional ECNIMS data for the analyses of structurally similar compounds whose spectra might otherwise contain too little information to distinguish them. A peak was considered real in these 2-D plots when its intensity was at least 10 times the background noise level. The spectra of all eight organophosphates are readily distinguished on this basis (Figures 3 and 4). Parathion and paraoxon, for example, yield similar ECNI mass spectra, but their 2-D maps are clearly different (compare parts A and B of Figure 3). Likewise, leptophosoxon, leptophosoxon (compare parts C and D of Figure 3), and EPN (Figure 4A) are easily distinguished from one another by their 2-D plots. The difference in substituents on fenitrothion and dicapthion results in a large difference in their electronegativities, which in turn yields significantly different energy/mass maps (compare parts B and C of Figures 4). It remains to be determined what effect minor differences in the polarity of functional groups may have on the energy states reflected in these maps.

All but one of the organophosphates studied possess an electrophilic aromatic ring containing either halogens or a *p*-nitro

group (Chart 1). This series of compounds allows for some interesting comparisons (Table 1). Ethion, for example, does not yield a molecular ion, despite the presence of the electronegative phosphorothioate moiety, which would be expected to capture an electron. The reason for the absence of the molecular ion could be related to the lack of a conjugated π -electron system into which an electron can be captured and secured against autodetachment. Leptophos does not show a molecular ion, either, despite the aromatic rings in the molecule, but leptophosoxon does (Table 1). The apparent stabilizing role of the phosphoryl oxygen is also observed to enhance the molecular ion intensity of paraoxon in comparison to that of parathion (Figure 2).

Two of the more important dissociative electron capture events involve formation of phenoxide and thiophenoxide ions. These might arise from a common ion X, produced by capture of an electron into a π -orbital, which rearranges to a spiro intermediate, followed by fragmentation via pathways a and b to give the thiophenoxide and phenoxide ions, respectively (Scheme 1). Of the organophosphates studied, only EPN produces both thiophenoxide and phenoxide ions with the same electron energies (Table 1). The others are produced with electrons of significantly different energies, suggesting that different mechanisms are involved.

Table 1. Resonance Electron Energies (eV) for Ion Formation from Organophosphate Pesticides

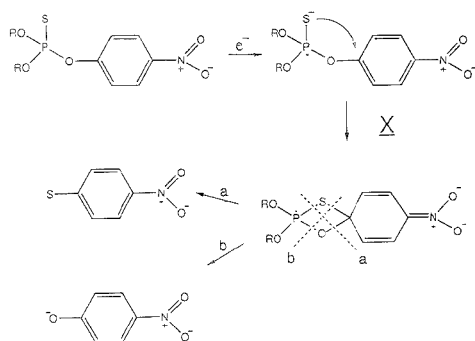
organophosphate/MW	ϵ_{M^-}	$\epsilon_{\text{phenoxide ion}}$	$\epsilon_{\text{thiophenoxide ion}}$
parathion/291	0.24	0.80	0.74
	3.5	2.6	3.7
		4.3	7.0
paraoxon/275	0.14	0.92 ^a	
	3.8	3.7 ^a	
	7.1	4.7 ^a	
leptophos/410	<i>b</i>	0.34	0.31
		4.6	4.4
		8.0	8.1
leptophosoxon/394	0.26	0.30 ^a	
	0.28	0.32	0.17
	0.87	3.6	2.7
fenitrothion/277	0.18	0.83	0.7
		3.7	3.2
		5.3	5.3
EPN/323	0.42	3.8	4.8
			3.8
			4.8
ethion	<i>b</i>		

^a Oxygens not distinguishable on phenoxide ion. ^b No molecular ion.

Table 2. Negative Ion Resonances (eV) for Fragment Anions Arising from Different Precursors

	$C_6H_5NO_2^-$	$C_6H_4NO^-$
parathion	0.94, 3.9	<i>a</i>
paraoxon	0.88, 3.1, 4.7	<i>a</i>
EPN	0.63, 4.9	0.64, 5.0, 6.6
	$(CH_3O)_2PS^-$	$(CH_3O)_2PSO^-$
fenitrothion	0.32, 4.0	1.0, 3.7
dicapthion	0.75, 4.5	0.67, 4.2
		$(C_2H_5O)_2PS^-$
ethion		0.31
parathion		0.75, 3.7, 7.0
		$C_6H_5P(S)OC_2H_5^-$
EPN		0.51, 4.1
leptophos		0.37

^a Anion not observed.

Scheme 1

Since the most abundant ions are produced from the lowest energy NIR states, a rearrangement mechanism must be considered for production of thiophenoxide ions from phosphorothioic ester precursors and for phenoxide ions when oxons are the parent molecules. A rearrangement mechanism involves bond formation in addition to bond cleavage, and the activation energy for such a process would be expected to be lower than that for a simple cleavage mechanism.⁸ If one assumes that the thiophenoxide ion arises after rearrangement (Scheme 1) and the phenoxide ion arises from direct cleavage, then the thiophenoxide ion should form with lower energy electrons. In every case except for EPN, where the energies are the same, the thiophenoxide ion is, in fact, formed with electrons of energies lower than those of the electrons producing the phenoxide ions (Table 1). The differences in the electron energies for rearrangements versus simple bond cleavages are usually not large.⁵ In the present examples, energies differ by as little as a few hundredths of an electronvolt (0.5–1.0 kcal/mol) for leptophos or as much as 0.15 eV (3.5 kcal/mol) for dicapthion. These are reasonable values.

(8) Levsen K. *Fundamental Aspects of Organic Mass Spectrometry*, Verlag Chemie: Weinheim, 1978; Chapter 3.

Oxons may rearrange and fragment via a spiro intermediate (Scheme 1) as well, but oxygen labeling experiments will be needed to unambiguously establish the mechanism. The present data, however, suggest this is not the case, and if so, then a plausible argument for the stability of the molecular ions in oxons is related to the absence of a low-energy rearrangement pathway. Thiophosphates, on the other hand, appear to rearrange readily and follow a lower energy channel, through which the energy is disposed. This also makes sense from the point of view that the thiolate anion is a softer nucleophile and the polarization of the para carbon of the phenyl ring in the thiophosphates, as opposed to those in oxons, is less severe, hence producing also a softer electrophile for the negatively charged sulfur atom to attack.

In addition to phenoxide and thiophenoxide ions, other ions can easily be accounted for by invoking intermediate X (Scheme 1). Thus, the loss of an alkyl or alkoxy radical, or the aromatic ring, involves simple homolytic cleavage and pairing of the electrons. For example, cleavage of the P–O bond in intermediate X would yield $(M-R)^\cdot$, $(M-OR)^\cdot$, or $(M-Ar)^\cdot$. Other simple mechanisms could be written to account for most of the ions observed (Figures 3 and 4). A conceptually more challenging problem is how to account for $C_3H_2NO^-$ and $C_6H_4NO^-$ or their equivalents because production of these ions appears to involve breaking up aromatic rings with low-energy electrons.

It should be noted that all these ions (Figures 3 and 4) are also observed in standard ECNIMS scans using methane buffer gas, and data from such experiments were used for selecting the ions to follow in these experiments. Ions were also selected by setting the electron energy to 0.03 eV and scanning the rf/dc ratio of the quadrupole until a peak was found. Most of the ions have resonances around 0.03 eV, but this method will not locate negative ion resonances which occur at nonzero electron energies. As in the present case, such resonances have been observed in spectra of other compounds.⁴

Fragment ions of the same mass but arising from different precursors can also be distinguished on the basis of the electron energies producing them. This is advantageous because it allows for the possibility of deconvoluting coeluting GC peaks on the basis of their NIR states and greatly improves the chances for

correct compound identification and confirmation. Nitrobenzene anions of identical empirical formula, for example, are formed by simple cleavage of the carbon-oxygen bond in parathion, paraoxon, and EPN, and yet they can be distinguished from one another on the basis of their electron energies (Table 2). The phosphorothioic ion, $(C_2H_5O)_2PS^-$, is formed from one NIR state centered at 0.31 eV when originating from ethion and from three states with energies of 0.75, 3.7, and 7.0 eV when formed from parathion (Table 2).

CONCLUSIONS

An ion source which uses a trochoidal electron monochromator to generate ultralow-energy electrons is ideally suited to ionize organophosphates in the negative ion mode. Two- and three-dimensional plots composed of energy versus mass and ion intensities are unusually rich in information and provide unique spectral profiles of these compounds. In addition, the electron energy can be tuned to enhance a particular fragment ion and separate it from competing processes. These additional analytical dimensions can be used to complement standard ECNIMS data.

It was previously reported³ that the electron monochromator filament potential can be ramped rapidly (3–300 ms) over the requisite electron energy range while recording either total ion

currents or mass-resolved ion currents. Broad-band electron energies were generated and used to acquire complete mass spectra of compounds eluting from the gas chromatograph. The organophosphates studied in this application show a wide distribution of NIR states, and broad-band electron energies would be needed for their analysis by GC/MS. Additional refinements in the electron monochromator design to improve sensitivity and the stabilization of molecular radical anions against autodetachment by introduction of a nonionizing buffer gas should lead to a powerful and reliable method for the analyses of organophosphates and other environmental compounds.

ACKNOWLEDGMENT

This work was supported by grants from the National Institutes of Health (NIEHS 00040 and NIEHS 00210). This is Technical Report No. 10686 from the Oregon Agricultural Experiment Station.

Received for review March 15, 1995. Accepted July 6, 1995.*

AC950265+

* Abstract published in *Advance ACS Abstracts*, August 15, 1995.

Use of a Nitrocellulose Film Substrate in Matrix-Assisted Laser Desorption/Ionization Mass Spectrometry for DNA Mapping and Screening

Yan-Hui Liu, Jian Bai, Xiaoli Liang, and David M. Lubman*

Department of Chemistry, The University of Michigan, Ann Arbor, Michigan 48109-1055

Patrick J. Venta

College of Veterinary Medicine, Michigan State University, East Lansing, Michigan 48824-1314

A nitrocellulose film is used as a substrate in matrix-assisted laser desorption/ionization mass spectrometry (MALDI MS) studies of DNA. PCR products and DNA fragment digests obtained from biochemical procedures can be analyzed with the use of a nitrocellulose substrate in MALDI MS whereas no signal is observed with the use of a stainless steel substrate. In this method, on-probe purification allows for effective elimination of the interfering effects of salts, buffers, and other contaminants that are usually present in DNA samples, which serve as important limiting factors in the DNA molecular ion yield in the MALDI process. The use of the nitrocellulose film substrate also appears to improve the shot-to-shot and sample-to-sample reproducibility of the ion yield due to the more homogeneous coverage of matrix/analyte over the sample surface. With the use of the nitrocellulose substrate, DNA fragments of up to 622 base pairs in complex mixtures provide mass spectra with minimal sample purification. Although only species corresponding to single-stranded DNA were detected, a mass calibration scheme was established allowing an accuracy of within one base pair for fragments of <250 bp under the experimental conditions. Despite the low mass resolution of the spectra obtained, the method has been successfully used for rapid DNA screening for sample disease genes and PCR products.

The size of DNA fragments is presently determined by gel electrophoresis, which is the basis for DNA sequencing, mapping, and screening. However, electrophoresis is time-consuming and occasionally susceptible to errors due to possible irregularities of both the gel and the migration behavior of certain fragments. The development of rapid, accurate, and cost-effective methods for large-scale characterization of both synthetic and natural genetic materials has become an important area of research for the human genome initiative in terms of mapping genes, detection of gene defects/mutations for diagnostic purposes, and drug development.

Mass spectrometry is one potential alternative method for DNA sequencing and screening. In the past, mass spectrometric

methods have been limited in both mass range and sensitivity.¹⁻³ More recently, matrix-assisted laser desorption/ionization mass spectrometry (MALDI MS), introduced by Karas and Hillenkamp in 1988,⁴ has become an attractive method for DNA analysis due to its high sensitivity, its high mass range, and the capability of analyzing mixtures with minimal sample preparation.⁵⁻⁹ MALDI MS thus has the potential of replacing gel electrophoresis for direct analysis of DNA sequencing reaction mixtures, enzymatic digests of DNA, and polymerase chain reaction (PCR) products for sequencing, mapping, and screening.

Early studies in the MALDI MS analysis of DNA were limited to oligonucleotides smaller than 50 bases in size.¹⁰⁻¹² This was due to the difficulty of efficiently desorbing/ionizing DNA molecules intact with commonly used matrices, where fragmentation of DNA during the MALDI process was a major limitation. However, over the last several years new matrices have been identified and successfully used for the analysis of larger oligodeoxyribonucleotides.^{5,6,13,14} In particular, the use of 3-hydroxypicolinic acid (3-HPA) as a matrix for DNA, identified and characterized by Becker and co-workers,^{6,14} represented a major breakthrough in the area, where mixed-base oligonucleotides as large as a 76- and 89-mer were initially detected. Tang et al. subsequently succeeded in using 3-HPA to detect mixed-base single-stranded oligonucleotides up to a 150-mer⁸ and restriction enzyme-digested double-stranded PCR mixtures up to 91 base

- (1) Grotjahn, L.; Steinert, H. *Biochem. Soc. Trans.* **1987**, *15*, 164-170.
- (2) McNeal, C. J.; Narang, S. A.; Macfarlane, R. D.; Hsiung, H. M.; Brousseau, R. *Proc. Natl. Acad. Sci. U.S.A.* **1980**, *77*, 735-739.
- (3) Beavis, R.; Ens, W.; Nemer, M. J.; Ogilvie, K. K.; Standing, K. G.; Westmore, J. B. *Int. J. Mass Spectrom. Ion Phys.* **1983**, *46*, 475-478.
- (4) Karas, M.; Hillenkamp, F. *Anal. Chem.* **1988**, *60*, 2299-2301.
- (5) Curie, G. J.; Yates, J. R., Jr. *J. Am. Soc. Mass Spectrom.* **1993**, *4*, 955-963.
- (6) Wu, K. L.; Steding, A.; Becker, C. H. *Rapid Commun. Mass Spectrom.* **1993**, *7*, 142-146.
- (7) Schneider, K.; Chait, B. T. *Org. Mass Spectrom.* **1993**, *28*, 1353-1361.
- (8) Tang, K.; Alliman, S. L.; Chen, C. H. *Rapid Commun. Mass Spectrom.* **1993**, *7*, 943-948.
- (9) Fitzgerald, M. C.; Zhu, L.; Smith, L. M. *Rapid Commun. Mass Spectrom.* **1993**, *7*, 895-897.
- (10) Spengler, B.; Parr, Y.; Cotter, R. J.; Kang, L. S. *Rapid Commun. Mass Spectrom.* **1990**, *4*, 99-102.
- (11) Huith-Fehre, T.; Gosine, J. N.; Wu, K. J.; Becker, C. H. *Rapid Commun. Mass Spectrom.* **1992**, *6*, 209-213.
- (12) Hettich, R.; Buchanan, M. J. *Am. Soc. Mass Spectrom.* **1991**, *2*, 402-412.
- (13) Schieltz, D. M.; Chou, C.-W.; Luo, L.-W.; Thomas, R. M.; Williams, P. *Rapid Commun. Mass Spectrom.* **1992**, *6*, 631-636.
- (14) Wu, K. J.; Shaler, T. A.; Becker, C. H. *Anal. Chem.* **1994**, *66*, 1637-1645.

pairs, though only segments corresponding to single-stranded components were obtained.¹⁵ Tang et al. also detected DNA segments as large as 500 nucleotides using picolinic acid (PA) and 3-HPA mixtures as the matrix.¹⁶ MALDI MS of oligonucleotides has also been performed using IR radiation (2.94 μm),^{17,18} where oligothymidylic acid up to a 100-mer was detected using succinic acid and urea matrices. Recently, RNA molecules of up to 461 nucleotides in length have also been successfully analyzed using 3-HPA as the matrix with 355 nm radiation.¹⁹

Another major issue concerning the MALDI MS analysis in general is the presence of impurities. It has been shown that impurities present in typical biological samples can complicate the MALDI sample preparation process and cause degradation of the MALDI MS spectrum even though MALDI is tolerant toward certain impurities.¹⁷ The degradation may take the form of a combination of reduced signal intensity, poor persistence, or peak broadening. The effects of impurities on the MALDI process are varied but can be summarized as those affecting the matrix materials, the analytes, or both. Some contaminants, such as surfactants, may lead to total loss of ion signal if present above a certain concentration. Cations in buffering salts can lead to cation attachment product formation, a leading source of peak broadening.²¹ All the impurities present can affect the crystallization process of the analyte/matrix mixture, which appears to be a critical aspect of MALDI experiments.

The presence of impurities in DNA samples may create serious fundamental problems for the MALDI process. DNA molecules contain strong acidic phosphate groups. The high polarity of the DNA molecules and the strong interactions among the DNA molecules may explain the general difficulty in desorbing those species intact, as experienced by several desorption/ionization techniques. In aqueous solutions, DNA molecules are highly dissociated, carrying multiple negative charges. Surprisingly, singly charged ions are dominant in desorption mass spectrometry, such as FAB MS,¹ PD MS,² and MALDI MS.¹⁰ It seems that before/during the desorption, excessive charges of DNA molecules are counterbalanced by positively charged counterions, which are often present in typical biological samples, such as in buffers, or in other ingredients introduced during sample preparation and purification steps.

The most commonly encountered and observed counterions in DNA samples and in the mass spectra are Na^+ and K^+ , and their presence can lead to extensive adduct ion formation in the mass spectrum. The degree of the adduct ions observed depends on the size of the DNA molecules and the level of counterions present in the sample, as determined by the purification procedures employed. It has been observed that in MALDI MS analysis of relatively pure DNA samples, such as the synthetic ss-DNA oligomers, sodium or potassium adduct ions often dominate the

molecular ion signal in the mass spectra.¹⁷ The formation of these adduct ions not only degrades the sensitivity by distributing the signal over several ions but also deteriorates the resolution if those multiple peaks cannot be resolved. The presence of these counterions and their interactions with the DNA molecules may also affect the volatility of the DNA molecules. This may well account for the fact that, in the MALDI MS analysis of DNA, the sensitivity drops dramatically as the size of the DNA increases, limiting the size of DNA molecules that can be analyzed. Other buffering reagents in DNA samples can also lead to the total suppression of the analyte signals in MALDI MS.

The problem associated with impurities, particularly sodium and potassium ions, in mass spectrometric analysis of DNA has been realized and addressed in FAB,²¹ PD,²² ESI,^{23,24} and MALDI MS.¹⁷ Various schemes have been used for the removal of sodium and potassium ions in DNA samples, including the use of ion exchange beads,¹⁷ addition of ammonium base,^{23,24} and complexation reagents.²⁵ It has been shown that DNA molecules present in the $\text{M}[\text{H}]_n$ or $\text{M}[\text{NH}_4]_n$ forms often result in enhanced sensitivity in mass spectrometric analysis.²²⁻²⁵ In MALDI MS, an improvement in signal response was observed by converting the DNA oligomers to their ammonium salts using ion exchange beads.¹⁷ Recently, Bai et al.²⁶ reported a method to enhance MALDI MS analysis of DNA oligomers using a Nafion substrate which enabled the detection of ds-DNA up to 267 base pairs. This method is based on the on-probe purification capability of the Nafion film.²⁷

Nitrocellulose (NC) has long been used as a blotting matrix for protein immobilization,²⁸ and the NC film has been used as a sample backing for PD MS studies²⁹ of peptides and proteins. The selective adsorption of peptides and proteins from solution onto the NC film allows effective removal of salts by washing, which can result in improved signals. NC has also been used as a substrate for the immobilization of proteins for MALDI MS analysis.^{30,31} In these cases, hydrophobic interactions between proteins and the NC are mainly responsible for the adsorption of proteins onto the nitrocellulose, while impurities such as cations can be removed by washing. Nitrocellulose is also negatively charged, which may result in other interactions of the NC and impurities.

In the present study, DNA mapping and screening methods with MALDI MS analysis have been studied using a nitrocellulose film substrate, where double-stranded DNA in enzymatic digest mixtures ranging from 9 to 622 base pairs can be routinely detected. Improvements in detection efficiency of DNA using a

(15) Tang, K.; Allman, S. I.; Chen, C. H.; Chang, L. Y.; Schell, M. *Rapid Commun. Mass Spectrom.* **1994**, *8*, 183-186.

(16) Tang, K.; Tarantenko, N. I.; Allman, S. L.; Chang, L. Y.; Chen, C. H. *Rapid Commun. Mass Spectrom.* **1994**, *8*, 727-730.

(17) Nordhoff, E.; Ingendoh, A.; Cramer, R.; Overberg, A.; Stahl, B.; Karas, M.; Hillenkamp, F.; Crain, P. F. *Rapid Commun. Mass Spectrom.* **1992**, *6*, 771-776.

(18) Nordhoff, E.; Cramer, R.; Karas, M.; Hillenkamp, F.; Kirpekar, F.; Kirstiansen, K.; Roepstorff, P. *Nucleic Acids Res.* **1993**, *21*, 3347-3357.

(19) Kirpekar, F.; Nordhoff, E.; Kristiansen, K.; Roepstorff, P.; Lezius, A.; Hahner, S.; Karas, M.; Hillenkamp, F. *Nucleic Acids Res.* **1994**, *22*, 3866-3870.

(20) Ling, V.; Cuzzetta, A. W.; Canova-Davis, E.; Stults, J. T.; Hancock, W. S.; Covey, T. R.; Shushan, B. I. *Anal. Chem.* **1991**, *63*, 2909-2915.

(21) Nollmer, D. L.; Gross, M. L. *J. Mass Spectrom.* **1995**, *30*, 113-118.

(22) Macfarlane, R. D.; McNeal, C. J. *J. Am. Chem. Soc.* **1986**, *108*, 2132-2139.

(23) Smith, R. D.; Loo, J. A.; Edmonds, C. G.; Barinaga, C. J.; Udseth, H. R. *Anal. Chem.* **1990**, *62*, 882-889.

(24) Potier, N.; Dorsselaer, A. V.; Cordier, Y.; Roch, O.; Bischoff, R. *Nucleic Acids Res.* **1994**, *22*, 3895-3903.

(25) Fujii, I. *J. Chem. Soc., Chem. Commun.* **1985**, 405-406.

(26) Bai, J.; Liu, Y. H.; Siemieniak, D.; Lubman, D. M. *Rapid Commun. Mass Spectrom.* **1994**, *8*, 687-691.

(27) Bai, J.; Liu, Y. H.; Cain, T. C.; Lubman, D. M. *Anal. Chem.* **1994**, *66*, 3423-3430.

(28) Southerr, E. M. *J. Mol. Biol.* **1975**, *98*, 503-571.

(29) Jonsson, G. P.; Hedin, A. B.; Hakansson, P. L.; Sundqvist, B. U. R.; Save, B. G. S.; Nielson, P. F.; Roepstorff, P.; Johansson, K.-E.; Kamensky, I.; Lindberg, M. S. L. *Anal. Chem.* **1986**, *58*, 1084-1087.

(30) Mock, K. K.; Sutton, C. W.; Cottrell, J. S. *Rapid Commun. Mass Spectrom.* **1992**, *6*, 233-238.

(31) Zhao, S.; Somayajula, K. V.; Sharkey, A. G.; Hercules, D. M. *Fresenius J. Anal. Chem.* **1990**, *338*, 588-592.

NC substrate compared to an inert stainless steel probe tip and Nafion substrate are demonstrated. PCR products derived from the canine and human genomes up to 455 bp can be detected on a routine basis with this method. This method is also successfully applied for the typing of human and canine genetic polymorphisms in combination with PCR and restriction endonuclease digestion, which may become a valuable alternative to electrophoresis for the diagnosis of genetic diseases and for linkage studies. The technical and experimental aspects of DNA mapping and screening involving the use of active substrates for MALDI MS are discussed in this work.

EXPERIMENTAL SECTION

Instrumental Setup. The linear TOF mass spectrometer used in these studies was a modified Wiley-McLaren design with an acceleration capability of ± 20 kV (manufactured by R.M. Jordan Co., Grass Valley, CA) and has been described elsewhere.²⁶ The laser source was a DCR-11 Nd:YAG laser system (Spectraphysics, Mountain View, CA) which produces 355 nm radiation used to acquire the mass spectra in this work. The laser beam was focused onto the probe tip at a 45° angle to the probe surface with a single 12.5 in. focal length quartz lens to a spot size of ~ 0.2 mm \times 0.5 mm. The power density at this spot was generally between $\sim 5 \times 10^6$ and 1×10^7 W/cm² at 355 nm in these experiments. The sample probe tip was inserted through a vacuum lock and into the acceleration region such that the front end of the stainless steel surface was flush with the first acceleration plate. The detector was a triple microchannel plate (MCP) detector with a Cu-Be conversion dynode with postacceleration capability up to ± 15 kV.³² The use of the triple MCP detector with the postacceleration stage enhanced the efficiency for detection of heavy species significantly and was found to be important for effective detection in these experiments, but at the expense of resolution. The voltages were maintained constant for all experiments except that of the 5-mer in this work, as the following: -15 kV for repeller, -10 kV for extraction, and +12 kV for postacceleration. In order to obtain improved resolution for the 5-mer ss-DNA, -17 kV was used for the repeller and -10 kV for extraction, and no postacceleration was applied. Data were recorded using a LeCroy 9350M digital oscilloscope and subsequently transferred to an IBM 486 compatible PC for processing. Each mass spectrum in this work consisted of an average of 50–100 single-shot spectra.

Materials. 3-HPA, PA, HPLC grade acetone, methanol, and acetonitrile were purchased from Aldrich Chemical Co. (Milwaukee, WI) and used without further purification. Pure NC blotting membrane (Immobilon) was obtained as a gift from Dr. Janet E. Tice of the Millipore Corp. (Bedford, MA), and *MspI* digest of pBR322 DNA was from New England Biolabs, Inc. (Beverly, MA). PCR products used in these experiments were amplified from the canine genome or the human genome using standard PCR conditions.³³

Sample Preparation. The DNA digest mixture was available at a concentration of 1 mg/mL, which was obtained by digesting double-stranded pBR322 DNA to completion with *MspI*. The mixture [in 15 μ L of 10 mM Tris-HCl (pH 8.0) and 1 mM EDTA]

contains 26 fragments ranging from 9 to 622 base pairs. In this experiment, 225 μ L (~ 80 pmol) of the digest mixture was subjected to chloroform/isoamyl alcohol and phenol extraction. After the extraction, the DNA was precipitated with the addition of 0.1 volume of 3 M sodium acetate and 2 volumes of ice-cold ethanol by incubating in dry ice overnight. The sodium acetate introduced here may potentially interfere with the MALDI MS analysis using the conventional MALDI sample preparation method. The longer incubation time was used to avoid the loss of smaller fragments as experienced previously.³⁶ The precipitated DNA was pelleted in a microcentrifuge at a speed of 17 000 rpm for 15 min, washed with 70% ethanol, and lyophilized. The dried DNA was resuspended in 150 μ L of deionized water for MALDI MS analysis.

The PCR products used in this work were initially derived from the human and dog genomes. The amplification was obtained by PCR using a thermal cycler (MJ Research, Watertown, MA) in either 50 or 100 μ L reactions under routine conditions. The amplified products were purified using a commercial PCR purification kit (Qiagen, Chatsworth, CA) following the manufacturer's protocol. The size of the PCR products was estimated by gel electrophoresis to be 199, 225, and 455 base pairs for the human genome products (data not shown). The PCR digest samples bearing DNA polymorphism were obtained by directly digesting the PCR products of the thermal cycled reactions with *HincII* and *BstVI*, and the resulting digests were purified using the commercial PCR purification kit.

3-HPA/PA mixture has been reported to enhance the MALDI MS analysis of ds-DNA.^{16,34} Either a 60–70 mg/mL 3-HPA solution or a mixture of 3-HPA and PA with a molar ratio of 4:1 (60–70 mg/mL 3-HPA) dissolved in 10–50% acetonitrile and water mixture solvent was used as a matrix for these experiments.

Preparation of Nitrocellulose Substrate. Two procedures were used for the preparation of the NC substrate in these experiments. One of them involves the application of NC solution in appropriate solvents onto the stainless steel probe tip followed by air-drying. The nitrocellulose solution was obtained by dissolving a piece of Immobilon-NC pure membrane in organic solvents, such as acetone, methanol, or acetonitrile, at concentrations in the range of 10–32 mg/mL. Usually a concentration of ~ 16 mg/mL was used for these experiments. Approximately 5 μ L of this solution was applied to a stainless steel probe tip using a glass pipet. After the initial application, the excess liquid (~ 4 μ L of the solution) was taken away by the same pipet and the remaining part was allowed to air-dry. A thin and homogeneous layer of NC film covering an area of ~ 12 mm² was obtained. Then 2 μ L of the DNA sample was applied to the hydrophobic surface followed by air-drying. A 4 μ L aliquot of the matrix was then applied to the sample spot and air-dried.

A second method tested for preparation of the NC substrate involved the direct use of an untreated NC blotting membrane. In the case of the untreated NC membrane substrate, 3 μ L of DNA sample was applied to the center of the membrane ($\sim 2 \times 2$ mm²). After drying, 6 μ L of the matrix was deposited onto the same side of the membrane as where the sample was applied. The dried membrane was then attached to the stainless steel probe tip using double-sided tape for MALDI MS analysis.

(32) Liu, Y. H.; Bai, J.; Lubman, D. M. *Proceedings of the 42nd ASMS Conference on Mass Spectrometry and Allied Topics*, Chicago, IL, 1994, p 791.

(33) Saiki, R. K.; Gelfand, D. H.; Toffel, S.; Scharf, S. J.; Higuchi, R.; Horn, G. T.; Mullis, K. B.; Erlich, H. A. *Science* **1988**, *239*, 487–491.

(34) Wu, K. J.; Shafer, T. A.; Becker, C. H. *Proceedings of the 42nd ASMS Conference on Mass Spectrometry and Allied Topics*, Chicago, IL, 1994, p 970.

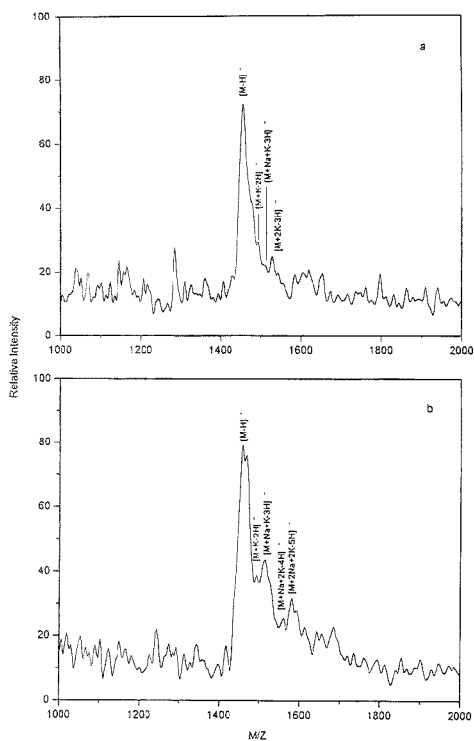


Figure 1. Negative ion MALDI mass spectra of a 5-mer ss-DNA (5'-TTTTT-3') with 3-HPA matrix on (a) NC film substrate and (b) stainless steel probe. Acceleration voltage, -17 kV. No postacceleration voltage applied.

RESULTS AND DISCUSSION

Nitrocellulose as a substrate for sample preparation has been widely used for PD MS of peptides and proteins due to its effective removal of salt contaminants by washing with ultrapure water or diluted acid.²⁹ The mechanism of protein binding to NC is complex and not entirely understood. It has been claimed that the binding of a protein to NC is nonionic at pH ~ 7 and is dominated by hydrophobic interactions.^{35,36} NC has also been examined as a substrate for MALDI MS analysis of peptides and proteins.^{30,31,37} In recent work,³⁷ it was noted that in the MALDI process the signal from free alkali metal ions obtained with the addition of NC is suppressed even though the sample was not rinsed to eliminate these impurities. This may be explained by the fact that NC binds cations, such as metal ions, since NC is negatively charged.³³ This arises since the nitrate ester groups of NC are polarized, forming dipoles with the "negative" oxygen atoms directed toward the outer surface.

In Figure 1 is shown a comparison of the negative ion mass spectra of a 5-mer single-stranded oligonucleotide obtained on

both a NC film and stainless steel probe tip using 3-HPA as the matrix, demonstrating the effect of the NC substrate on sodium and potassium adducts. It can be seen that adduct ions due to sodium and potassium are greatly reduced with the use of the NC film substrate. It appears that NC effectively binds the inorganic cation contaminants to its "negative" site and limits/eliminates their interference during the MALDI process for oligonucleotides even though the deposited sample was not washed. The procedure used in this work for applying the DNA sample prior to the matrix may further enhance this effect since the analyte sample is in direct contact with the active NC surface and the impurities can access the "negative" sites and bind. DNA molecules are highly hydrophilic and negatively charged, so that their interactions with the NC surface are minimal.

In this work, an important finding is that the success of using NC as a substrate for MALDI MS analysis of ds-DNA is highly dependent on the preparation of the NC film. Among the important factors are the concentration of the original NC solution and the solvent used. A wide range of concentrations of the NC solution was tested in this work. NC solutions at concentrations in the range of ~ 10 – 32 mg/mL generate a colorless, thin, and homogeneous film. This range of concentration provides the most consistent results for molecular ion yields of DNA using the substrate preparation method described herein. A concentration of ~ 16 mg/mL was generally used for the solution in this work, which is similar to that in PD MS where usually a 25 – 50 μ L NC solution with a concentration of 2 mg/mL was electrosprayed onto a target.³⁸ NC solutions with too high or too low concentrations usually provide less satisfactory results. When the concentration of the solution was too high, the application of NC solution by glass pipet was difficult and usually resulted in a wrinkled, thick film from which quality spectra could not be obtained. If the NC concentration was too low, the capacity of the NC film substrate prepared appears to be insufficient to have any apparent effect. Acetone, methanol, and acetonitrile were good solvents for dissolving the NC membrane. However, acetone with the lowest boiling point was ultimately used as the solvent for the NC solution because it has the fastest evaporation rate and produces a homogeneous film.

The choice of the solvent system for the matrix is another factor that needs to be considered because of its potential damage to the nitrocellulose film substrate upon matrix application. The conventional solvent for the matrix is a mixture of acetonitrile/water (v/v, 1:1). However, this solvent composition can partially degrade the NC film. By examining the dissolution of the NC blotting membrane by matrix solutions in different solvent systems ranging from 10 to 50% of acetonitrile in water and comparing the quality of the spectra obtained, $\sim 36\%$ acetonitrile in water was selected as the solvent for the matrix in this work. A further decrease in the proportion of acetonitrile will eventually limit the solubility of the matrix materials.

Analysis of Enzymatic Digests of ds-DNA. The challenges of using MALDI MS for DNA sequencing and mapping rely on its ability to analyze mixtures containing DNA fragments from several base pairs to several hundred base pairs. Mixture analyses have been demonstrated for ss-DNA oligomers shorter than 60-mers with a variety of matrices, and recently for a ds-DNA mixture

(35) Gershoni, J. M.; Palade, G. F. *Anal. Biochem.* **1983**, *131*, 1–15.

(36) Andrews, A. T. *Electrophoresis*; Clarendon Press: Oxford, U.K., 1986; pp 59–61.

(37) Preston, I. M.; Murray, K. K.; Russell, D. H. *Biol. Mass Spectrom.* **1993**, *22*, 344–350.

(38) Roepstorff, P. *Methods in Enzymology*; Academic Press, Inc.: New York, 1993; Vol. 193, pp 432–441.

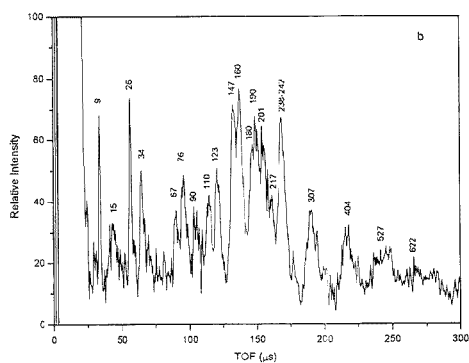
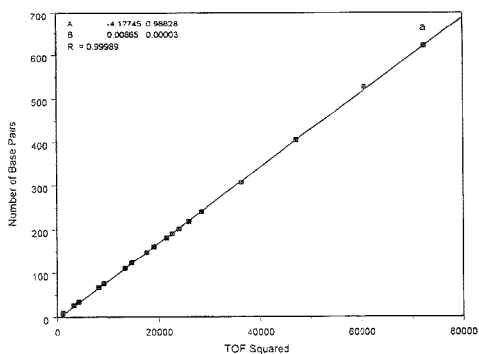


Figure 2. (a) Calibration curve of number of bases vs the TOF squared and (b) negative ion MALDI mass spectrum of *MspI* digest of pBR322 on NC film substrate. Matrix, 3-HPA/PA with molar ratio of 4:1.

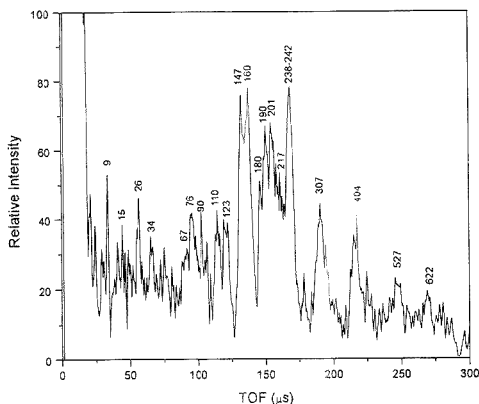


Figure 3. Negative ion MALDI mass spectrum of *MspI* digest of pBR322 on NC film substrate with laser power increased by 10%. NC film substrate; matrix, 3-HPA/PA with molar ratio of 4:1.

from 22 to 267 bp by using a Nafion substrate.²⁶ In Figures 2 and 3 are shown the MALDI MS spectra of a DNA digest mixture obtained using NC film as the substrate. All fragments ranging from 9 to 622 bp are detected with this method. Table 1 summarizes the double-stranded fragments generated from the

Table 1. Fragments in the *MspI* Digest of the pBR322 DNA

fragment no.	base pairs	daltons ($\times 10^3$)	fragment no.	base pairs	daltons ($\times 10^3$)
01	622	4.04	14	147	0.96
02	527	3.42	15	123	0.80
03	404	2.62	16	110	0.72
04	307	2.00	17	90	0.59
05	242	1.57	18	76	0.49
06	238	1.55	19	67	0.44
07	217	1.41	20	34	0.22
08	201	1.31	21	34	0.22
09	190	1.24	22	26	0.17
10	180	1.17	23	26	0.17
11	160	1.04	24	15	0.10
12	160	1.04	25	9	0.06
13	147	0.96	26	9	0.06

DNA pBR322 after *MspI* digestion and those detected by MALDI MS. Due to the relatively low resolution, mixtures of different fragments with the same number of base pairs, such as 9, 26, 34, 147, and 160 bp, cannot be resolved. However the intensities of these peaks are considerably higher than those of the other peaks with only one single fragment as expected. In Figure 2, the DNA fragments of up to 404 bp are clearly detectable, whereas larger fragments may be lost due to the S/N. However, an enhancement of the signal intensity of higher mass fragments could be achieved by increasing the laser power by ~10% as shown in Figure 3, where fragments at 527 and 622 bp are observed. The accompanying calibration of the spectrum as a function of the number of base pairs is shown in Figure 2a, and the various fragment peaks are observed in the TOF mass spectrum as expected.

MALDI MS of DNA mixtures with the NC film substrate was found to be highly reproducible and uniform in desorption of all of the fragments in the mixture. In comparison, the use of a stainless steel substrate resulted in a much degraded spectrum, where DNA fragments of >100 bp could not be detected. This may be due to interference by salts introduced during the precipitation such as sodium acetate and residue buffer ingredients in the sample, which can disturb the crystallization process. In Figure 4 is shown the MALDI MS spectrum of the same DNA mixture from a Nafion substrate under the same conditions. In both Figures 2 and 4, three separate mass spectral runs have been averaged together to improve the S/N for larger fragments. All the fragments ranging from 9 to 242 bp are clearly detected with the Nafion substrate. The larger species appear to be present, but the S/N is too low to provide unambiguous identification. It is observed that the sample preparation is more uniform with the NC film substrate than with the Nafion substrate, and the ion yield from the NC film substrate is consistently more reproducible.

Mass Calibration. One of the limitations affecting the applicability of MALDI MS for DNA analysis is the low mass resolution. In addition, ds-DNA is only observed as single-stranded fragments in MALDI MS. It is impossible with the present resolution to resolve the signals from the two strands with different but complementary sequences. The peak originating from a ds-DNA may represent the average of the two complementary ss-DNA. Based on this assumption, linear regression was performed by taking the number of base pairs of the fragments and the corresponding TOF squared measured from the mass spectrum. Figure 2a and 4a show the linear regression

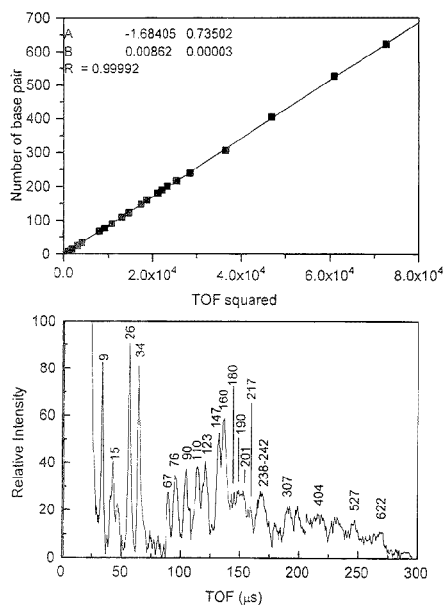


Figure 4. (a) Calibration curve of number of bases vs the TOF squared and (b) negative ion MALDI mass spectrum of *MspI* digest of pBR322 on Nafion substrate. Matrix, 3-HPA/PA with molar ratio of 4:1.

curves obtained using both the NC film substrate and the Nafion substrate. The difference of the two regression parameters may be caused by the different surface charging and insulating effects of the two substrates. Residue and statistical analyses of the linear regressions indicate that the precision using this method is within 2 bp in the range of 9–622 bp, and within 1 bp (usually <0.5 bp) in the range of 9–250 bp. The poorer precision in the broader mass range is caused by the increasing difficulty in determining the peak centroid of the larger fragments. However, the precision may be sufficiently high to be useful for DNA screening, and further improvements can be expected as the resolution increases. The existence of excellent linearity between the number of base pairs and the TOF squared is not surprising. Even though the mass difference between the sum of the complementary pairs, A + T, and G + C, is only 1, making it possible to correlate the mass of a fragment peak to its number of base pairs. For a DNA fragment of n bp, if the four bases are evenly distributed, the average mass of the two strands can be expressed as $M = nk$, where k is the average mass of the four nucleotides. For any ds-DNA, the average molecular weight of the two strands will be $n(k \pm 0.25)$, by a mass deviation of only $\pm 0.25n$. In this way the variations of the average mass of the two complementary strands of any ds-DNA should be within 0.08%, which at present is not a limiting factor for the mass determination accuracy using TOF MS. The validity of the above assumption is also shown by the unresolved peak originating from fragments of 238 and 242 bp. Based on the mass calibration method, the measured size corresponding to the peak is 240 bp, which is the average of 238 and 242 bp.

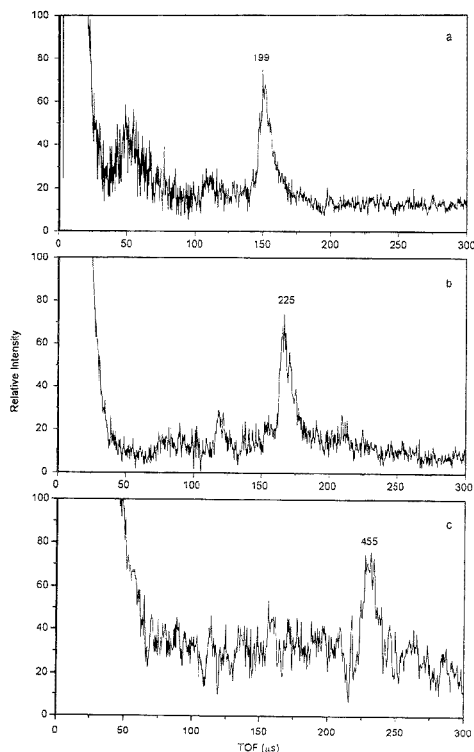


Figure 5. Negative ion MALDI mass spectra of ds-DNA of human genome on NC film substrate: (a) 199, (b) 225, and (c) 455 bp; matrix, 3-HPA/PA with molar ratio of 4:1.

DNA Screening. Several PCR products derived from the canine and human genomes ranging from 100 to 450 bp were analyzed using both the NC film substrate and the stainless steel probe tip. Figure 5 shows the MALDI MS spectra of a 199, 225 and 455 bp double-stranded DNA from the human genome obtained by using a NC film substrate. Only signals corresponding to single-stranded DNA were detected for all of the PCR products. Generally, no discernible signal could be observed by MALDI from a stainless steel substrate. The use of the NC film substrate greatly enhances the ion yields, the reproducibility of the signal, and the signal persistence. A much more homogeneous crystallization of the matrix/sample was obtained with the NC substrate, where long and thin needlelike crystals uniformly cover the probe tip for relatively pure samples such as the synthetic ss- and ds-oligonucleotides, and dot/needlelike crystals for samples containing more contaminants. With the stainless steel probe tip, dramatically different matrix/sample "crystals" were formed, where a thick foamy rim of no distinct structure with very little dotlike crystals in the center is formed, and virtually no signal can be observed. It appears that the formation of distinct matrix/sample crystals is necessary for the observation of the DNA signals. This may imply that NC binds alkali metal ions through ionic interactions and some other buffer impurities by hydrophobic adsorption, so they are partially excluded from the matrix/analyte during crystallization. It is also possible that NC acts as a

Table 2. Sequence of Part of the CA II Gene and the PCR-Amplified Region for Typing of the *Bst*NI Polymorphism^{a-c}

ATTCAAGTG AAGCTCGTAA TTCTTTTATT TGTGCCAGT GATATAGAAC	50
CCCGTTTTT AAAAAGTGT TTTGACCATC AGAGGGGAGT ATACCTATTT	100
<u>GTGCTGCTG CTCTCCTACC TTCCTCCTAC TCTGTCAATG TGRTTGTTTG</u>	150
primer 1	
AAGTGCCTA TTTGCCTTGT TCTAGGGCAA GAGTGTGAC TTCCTACT	200
TCGATCCTCG TGGCCTCTTT CCTGAATC* <u>ACGATTACTG GACCTACCTG</u>	250
<u>CTCCTACTGA CCACCCCTCC TCTTCTGGAA TGTGTGAGCCGATTTGCT</u>	300
primer 2	
CAAGGAACCC ATCAGCGTCA GCAGCGAGCA GTTTGTGTTT GTAATGACAG	350
GTCTGTTTAC GGTGGAGCA TTTAGTCAAG GCAGAAGACC TTGGCCTCCA	400
GAGTGAAGA GACCTGAGAT TTAATCCTTC TCC	433

^a The sequences underlined are primer regions for PCR. ^b Asterisk at position 230 indicates polymorphism site, where T is replaced by C in another allele, in which case, the resulting sequence CCTGG (shaded box) can be cleaved by *Bst*NI. ^c Sequence in shaded box can be cleaved by *Bst*NI.

crystallization moderator, either as a crystal nucleation site or by suppressing nucleation at surface defect sites on the stainless steel probe tip surface. It is not clear yet which effect is most important, but the use of the NC film substrate consistently results in matrix/sample crystals different from those formed on a stainless steel probe tip. An untreated NC blotting membrane was also tested as a substrate for the 97 bp DNA of a dog gene. However, no molecular ion was observed. This may be due to the fact that the NC membrane is too thick as a substrate, where the DNA molecules are buried within the NC membranes and become inaccessible for MALDI.

Analysis of PCR Digests and Typing of DNA Polymorphisms. One particular area where MALDI MS may find immediate use is the typing of genetic polymorphisms for linkage studies and for diagnosis of genetic diseases. These problems are presently accomplished by comparing restriction endonuclease maps, sequencing, annealing properties, or the thermal stability of the hybrid duplexes formed between family members.³⁹ In this experiment, MALDI MS is used for the typing of polymorphisms by analyzing the PCR products or the restriction enzyme digests of the corresponding PCR products. PCR products amplified from genes coding for carbonic anhydrase II (CA II) and III (CA III) located on human chromosome 8 were digested with *Bst*NI⁴⁰ and *Hinc*II,⁴¹ respectively. The fragments representing the two polymorphic alleles are 133 and 152 bp in length for the CA II, and 60 and 86 bp for the CA III. Table 2 lists the gene sequence coding for the CA II and the PCR-amplified region defined by primers 1 and 2. Polymorphism arises when the base at the position 230 is present as T for one allele and C for the other, which can be recognized by cleavage with the enzyme *Bst*NI (CCTGG/

(39) Singer, M.; Berg, P. *Genes & Genomes*; University Science Books: Mill Valley, CA, 1991; pp 624–625.

(40) Venta, P. J.; Tashian, R. E. *Nucleic Acids Res.* **1991**, *19*, 479.

(41) Venta, P. J.; Hewett-Emmett, D.; Tashian, R. E. *Am. J. Hum. Genet.* **1991**, *49*, 445A.

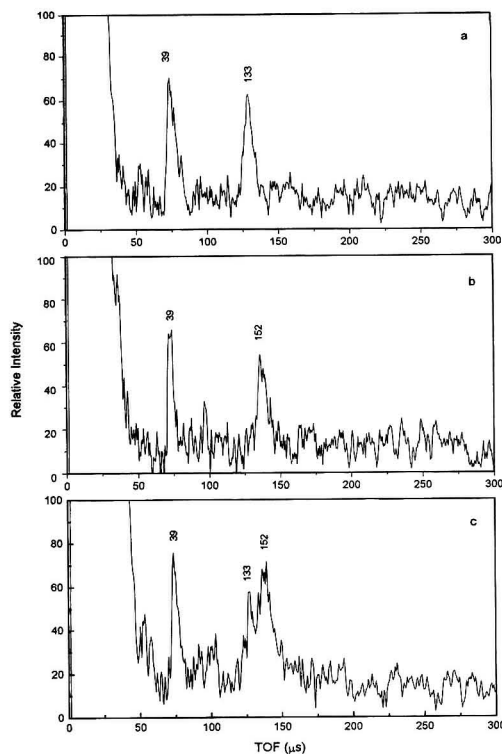


Figure 6. Negative ion MALDI mass spectra of *Bst*NI digest of the (a) homozygous, (b) homozygous, and (c) heterozygous PCR products from CA II locus on human chromosome 8. NC film substrate; matrix, 3-HPA/PA with molar ratio of 4:1.

CCAGG). If the base at the position 230 is T for both alleles, the *Bst*NI digest of the PCR product will contain fragments of 152, 39, and 19 bp, whereas, fragments of 133, 39, and two 19 bp will be generated by the *Bst*NI if T is replaced by C for both alleles. For the heterozygous population, all of the fragments can be found, and heterozygosity can be detected by the presence of both the 133 and 152 bp fragments by MALDI MS. Figure 6 shows the MALDI MS spectra obtained from samples containing the *Bst*NI digest of the PCR products from CA II. For the homozygous PCR products, only one related fragment (133 or 152 bp for CA II) can be detected, while both polymorphic fragments (133 and 152 for CA II) can be detected in the heterozygous samples.

Table 3 lists the genes coding for the CA III. A slightly different PCR process is used for the amplification of the DNA region containing the polymorphic site, where three primers are used. One primer (primer 2) has a mismatched base at base position 140 (G in place of C) near the polymorphic site to create a possible *Hinc*II cut for the amplified PCR product. Figure 7 shows the MALDI MS spectra of *Hinc*II digests of the PCR products from CA III. For the homozygous individual, after *Hinc*II digestion, the presence of G at base position 135 results in fragments of 26 and 60 bp. In this case, incomplete digestion can also lead to the formation of a fragment of 86 bp as shown in Figure 7a, while the presence of A at base position 135 will lead

Table 3. Sequence of Part of the CA III Gene and the PCR-Amplified Regions for Typing of the *HincII* Polymorphism^{a-c}

GGGAGAGAGA AGCAGGAGCC GTCCAGCAGC GAGGAAGGCA GACCATGGCC	50
AAGGAGTGGG GCTAGCCCRG TCACACCGGT CCTGACCACT GGCATGAACT	100
primer 1	
TTTCCCAARAT GCCAAGGGGG AAAACCAGTC GCCC <u>ATTGAG</u> CTGCMTACTA	150
primer 2	
AAGACATCAG GCATGACCCT TCTCTGCRGC CATGGTCTGT GTCATTATGAT	200
GGTGGCTCTG CCAAGACCAT CCTGATAAT GGGAGACCT GCCGATTGT	250
primer 3	
ATTTGATGAT ACTTATGATA GGTCAATGCT GAGAGGGGGT CCTCTCCCTG	300
GACCTACCG ACTTCGCCAG TTTCATCTTC ACTGGGGCTC TTCGGATGAT	350
CATGGCTCTG	360

^a The sequences underlined are primer regions for PCR. ^b Asterisk at position 135 indicate the polymorphic site, where G can be replaced by A in another allele. ^c Asterisk at position 140 indicate the mismatched base for primer 2, where it is replaced by C, so the resulting sequence GTTGAC (shaded box) can be cleaved by *HincII*.

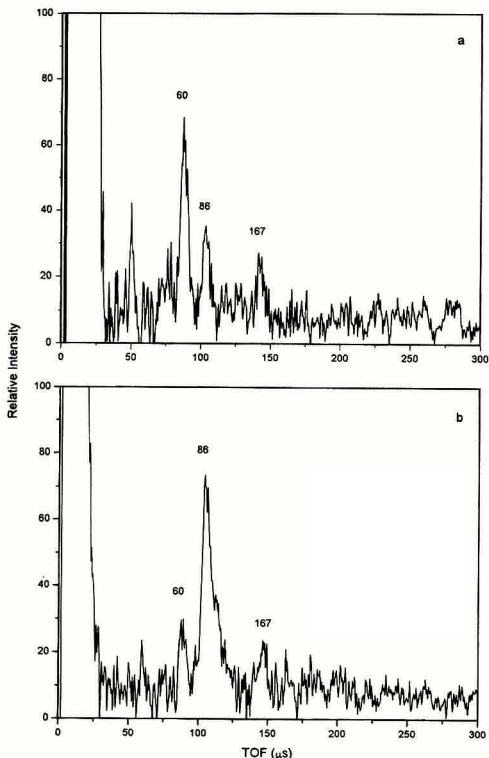


Figure 7. Negative ion MALDI mass spectra of *HincII* digest of the (a) homozygous and (b) heterozygous PCR products from CA III locus on human chromosome 8. NC film substrate; matrix, 3-HPA/PA with molar ratio of 4:1.

to the formation of only a fragment of 86 bp after digestion with *HincII*.

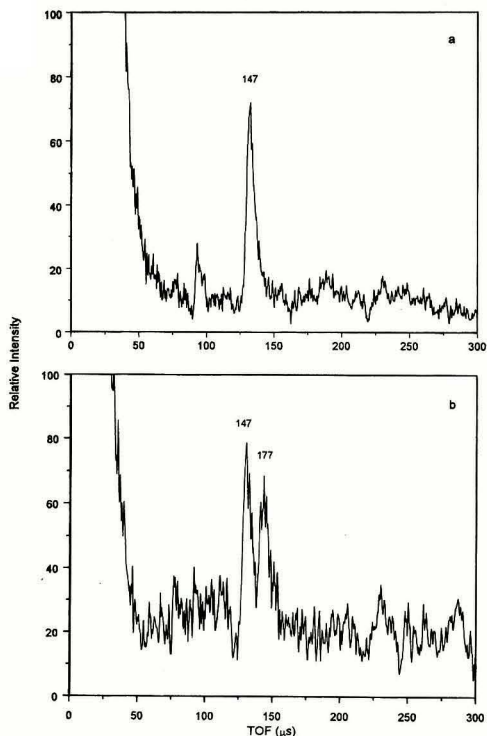


Figure 8. Negative ion MALDI mass spectra of the PCR products from the genes of (a) Siberian husky (homozygous) and (b) mixed-breed dog (heterozygous). NC film substrate; matrix, 3-HPA/PA with molar ratio of 4:1.

Polymorphism arises when the base at position 135 is G for one allele and A for the other and is detected by the presence of fragments of 60, 86, and 167 bp and by examining the relative intensities of fragments of 60 and 86 bp (Figure 7b). The relative intensities of the fragments become important in this case, where for heterozygous population, the ratio of the cut that generates fragments of 60 bp to fragments of 86 bp is 1:3, because of the presence of a heteroduplex generated during the PCR process which cannot be cleaved by *HincII*.

Another type of polymorphism is due to the variation of the copy numbers of a segment of DNA in the gene. In this work, the copy number of a hexamer repeat sequence (AGGAAT) in intron 40 of the canine von Willebrand's factor gene was detected by screening the PCR products directly.⁴² Figure 8 shows the spectra of the PCR products obtained from the genes of a Siberian husky and a mixed-breed dog. Figure 8a was obtained from the Siberian husky, which is homozygous containing nine repeats of AGGAAT, and the PCR fragment is 147 bp in length. Figure 8b is from the mixed-breed dog which is heterozygous containing both 9 and 14 repeats of AGGAAT, and the PCR fragments obtained are 147 and 177 bp in length.

An external mass calibration using the parameters established from the DNA digest mixture was used to estimate the sizes of

(42) Shibuya, H.; Collins, B. K.; Huang, T. H.-M.; Johnson, G. S. *Animal Genet.* 1994, 25, 122.

the fragments detected, which allows an accuracy of ± 2 bp. The relative intensities of the polymorphic fragments observed from the gel (data not shown) are also semiquantitatively conserved in the MALDI mass spectra with the NC film substrate, and the results are quite reproducible. These preliminary results together with that observed in Figure 2 imply that reproducibility and more uniform desorption of each component by MALDI MS are achieved with the use of the NC film substrate.

The resolution for the molecular ion peaks is on the order of ~ 5 –40, and the total amounts of sample loaded for the analysis are in the range of 1 pmol for the *Msp*I digest of pBR322 DNA, and between 200 and 500 fmol for the PCR products and the restriction enzyme digests of the PCR products based on 100% recovery. The sample consumed to obtain the MALDI MS spectra in this work is only a very small fraction of the total sample deposited. It should be possible to decrease the total sample loading considerably by minimizing the sample spot, so that sensitive detection and rapid characterization of DNA by MALDI MS will become a method of choice for genetic screening of PCR products.

CONCLUSION

The use of a nitrocellulose film substrate has been demonstrated for enhancing the molecular ion yield in MALDI MS analysis of DNA. This method resulted in more uniform crystallization of the matrix/analyte mixture, which is essential for success in these MALDI experiments. The NC film substrate greatly improved the reproducibility in desorption/ionization of DNA fragments in mixtures. Double-stranded DNA fragments ranging from 9 to 622 bp from restriction enzyme digests of DNA

and PCR products up to 455 bp can be detected routinely by using this method. The results reported here represent an important development for rapid genetic screening using MALDI/MS. This work demonstrates that, through the use of certain active substrates, large DNA fragments in complex mixtures can be detected. The mass accuracy using the mass calibration scheme established is sufficient to determine the size of the DNA fragments of < 622 bp within 2 bp. DNA samples obtained from biochemical procedures can be routinely analyzed with high reproducibility using the NC film substrate. Indeed, the method has been successfully demonstrated for rapid typing of genetic polymorphism despite the relatively low resolution available. The method may eventually prove to be a valuable alternative to gel electrophoresis for screening problems such as searching for gene defects.

ACKNOWLEDGMENT

We thank Mr. David Siemieniak of The University of Michigan Medical Center for his help in sample purification and Dr. Vilma Yuzbasiyan-Gurkan of the Michigan State University for supplying DNA samples for some of the preliminary work. We gratefully acknowledge support for this work from the National Institute of Health under the National Center for Human Genome Research under Grant 1R21HG00685-01A2.

Received for review April 3, 1995. Accepted July 13, 1995.*

AC9503318

* Abstract published in *Advance ACS Abstracts*, September 1, 1995.

Identification of Alkylbenzenes and Direct Determination of BTEX and (BTEX + C₃-Benzenes) in Oils by GC/MS

Zhendi Wang,* Merv Fingas, Michael Landriault, Lise Sigouin, and Nanni Xu

Emergencies Science Division, ETC, Environment Canada, 3439 River Road, Ottawa, Ontario, Canada, K1A 0H3

A rapid, reliable, and effective method for direct determination of benzene, toluene, ethylbenzene, and *o*-, *m*-, and *p*-xylenes (BTEX) and alkyl-substituted benzene components in oil has been developed using GC/MS in selected ion monitoring mode. Using this method, 58 alkyl-substituted benzene components in a light crude oil, Alberta Sweet Mixed Blend, were positively identified, and the concentrations of the individual BTEX compounds and C₃-benzene isomers in over 200 different crude and weathered oils were quantified. The effects of weathering on compositional changes of alkylbenzenes were also studied. The plots of the concentrations of BTEX and BTEX + C₃-benzenes versus weathering percentages can be used to estimate the weathering extent of weathered oil samples, especially for those short-term weathered oils for which the loss of BTEX and C₃-benzenes is significant.

For environmental and toxicity concerns, BTEX levels in oil are a very important parameter. BTEX is the collective name of benzene, toluene, ethylbenzene, and the xylene isomers (*p*-, *m*-, and *o*-xylenes). BTEX compounds are the most common aromatic compounds in petroleum (the amount of BTEX can be up to a few percent of the total weight for some crude oils) and often occur in greater amounts than other aromatics. BTEXs constitute the most soluble, most mobile fraction of crude oil and many petroleum products. BTEXs have many chemical applications and are widely used in the manufacture of paints, synthetic rubber, agricultural chemicals, and chemical intermediates. The concentration of BTEX in petroleum can directly affect the physical and chemical properties of petroleum such as density, viscosity, flash points, dispersibility, emulsion stability, solubility, and weathering processes. On the other hand, BTEX compounds frequently enter soil, sediments, and groundwater because of accidental oil spill, leakage of gasoline and other petroleum fuels from underground storage tanks and pipelines, and improper oil-related waste disposal practices. In these cases, BTEX compounds can also be used as markers in identifying the presence and determining the composition of these weathered fuels originating from leaking underground fuel tanks or pipelines. BTEXs are hazardous carcinogenic and neurotoxic compounds and are classified as priority pollutants regulated by Environment Canada¹ and the U.S. Environment Protection Agency (EPA),² especially benzene, which has a very low tolerance standard in drinking water of 5 µg/L.

Analytical techniques for volatile organic compounds (VOCs) including BTEX have made major advances in recent years. The U.S. EPA has developed a series of matrix-specific methods for VOC analysis based on the original work of Bellar and Lichtenberg in the early 1970s.³⁻⁷ Although there are minor differences among the methods, all employ a dynamic headspace or purge and trap technique to extract the analyte from the matrix and introduce it into a gas chromatograph (GC). GC separation was originally accomplished using a nonpolar packed column, and although this is still specified in most of the methods, substitution of a 0.53-mm-i.d. capillary column is widely accepted. The most common method of detection for BTEX and other volatile compounds involves a series combination of a photoionization and a flame ionization or a mass spectrometer. In most European countries, requirements to use specific analytical methods for environmental analyses of VOC compounds are not very common. Rather, the analyst is allowed to use professional judgment to specify performance criteria. Several different sample extraction and introduction techniques are used there, including solvent extraction and injection, static headspace analysis, dynamic headspace analysis, and closed-loop stripping with the solvent-extraction being the most common.^{8,9} The American Society for Testing and Materials (ASTM) developed a series of test methods specially for determination of BTEX in gasolines, such as method D4420¹⁰ for determination of BTEX content in finished gasoline by GC, method D3606¹¹ for determination of benzene and toluene in finished motor and aviation gasoline by GC, and methods D3797 and D3798¹² for determination of benzene, toluene, and ethylbenzene impurities in xylene by GC. All ASTM standard test methods employ packed or capillary columns and a gas chromatograph coupled with either a thermal conductivity or hydrogen flame ionization detector.

(3) Bellar, T. A.; Lichtenberg, J. J. *J. Am. Water Works Assoc.* 1974, 66, 702.

(4) *Methods for Organic Chemical Analysis of Municipal and Industrial Wastewater*, U.S. Environment Protection Agency, 1982, EPA-600/4-82-057.

(5) *Methods for the Determination of Organic Compounds in Drinking Water*, U.S. Environment Protection Agency, 1985, EPA-600/4-85-039.

(6) *U.S. EPA Contract Laboratory Program Statement of Work for Organics Analysis*, U.S. Environment Protection Agency, Document No. 0LM01.0.

(7) *Test Methods for Evaluating Solid Waste*, U.S. Environment Protection Agency, 3rd ed.; 1986; SW-846.

(8) *Deutsche Einheitsverfahren zur Wasser-, Abwasser-, und Schlammuntersuchung: Gemeinsam erfassbare Stoffgruppen (Gruppe F)*, Deutsches Institut für Normung, 1991; DIN 38 407, Teil 4, 5, und 9.

(9) Voice, T. C.; Kolb, B. J. *Chromatogr. Sci.* 1994, 32, 306-311.

(10) *1993 Annual Book of ASTM Standards*; ASTM: Philadelphia, PA, 1993; Vol. 05.02, D4420-89.

(11) *1993 Annual Book of ASTM Standards*; ASTM: Philadelphia, PA, 1993; Vol. 05.02, p D3606-92.

(12) *ASTM Manual on Hydrocarbon Analysis*, 5th ed.; Drews, A. W., Ed.; ASTM: Philadelphia, PA, 1992; pp D3797-88 and D3798-89.

(1) Fingas, M.; Laroche, N.; Sergy, G.; Mansfield, B.; Cloutier, G.; Mazerolle, P. *Proceedings of The 8th Technical Seminar on Chemical Spills*, Environment Canada: Ottawa, 1991; pp 223-332.

(2) *List of Lists*, U.S. Environment Protection Agency, July 1987.

Petroleum is exceedingly complex in composition. There is no simple and direct method to determine BTEX and alkyl-substituted benzene constituents in crude oil, weathered oil, and oil spill-related sediment or soil samples. Obviously, there is a gap for determination of BTEX between petroleum and the light petroleum product, gasoline. Due to the low boiling points and very volatile nature of BTEX compounds, analytical methods for determination of BTEX in crude oil and oil spill-related samples are therefore required to be specific, preferably without a solvent evaporation and concentration step which may result in the loss of BTEX compounds.

In recent years, the Emergencies Science Division (ESD) of Environment Canada has conducted projects to investigate various countermeasures in responding to oil spills. The goals of one such project are to develop analytical methods to characterize individual oil components and component groups in various oil samples.¹³⁻¹⁷ In this paper, we report our attempt to develop a rapid, reliable, and effective method for identification and direct determination of BTEX and alkyl-substituted benzene components in oil using capillary gas chromatography/mass spectrometry (GC/MS) in selected ion monitoring (SIM) mode. The efficiency and reproducibility of the method were demonstrated by separation and determination of a standard aromatic alkylbenzene mixture with the alkyl group ranging from C₁ to C₇. Using this method, 58 alkyl-substituted benzene components in a light crude oil Alberta Sweet Mixed Blend (ASMB) were identified and characterized. Quantitation of BTEX and BTEX + C₃-benzenes was accomplished using an internal standard method. The extensive qualitative and quantitative information pertaining to alkylbenzenes obtained from this oil is very useful because the ASMB oil is often used by other laboratories in Canada as a reference. In addition, BTEX and BTEX + C₃-benzenes concentrations in over 200 different crude oils were quantified to supply more complete information on distribution of monoring aromatic compounds in different oils. The correlations between the concentrations of alkylbenzenes and the weathering percentages for several weathered oils were also studied.

EXPERIMENTAL SECTION

Materials. All solvents including *n*-pentane and dichloromethane were distilled chromatographic grade and were used without further purification. Silica gel used to fractionate oil into saturate and aromatic fractions was purchased from Fisher Scientific (Fair Lawn, NJ). Before use, 200–300 g of silica gel (100–200 mesh, pore size 150 Å, pore 1.2 cm³/g, active surface 320 m²/g) was placed in a 900 × 41 mm i.d. chromatographic column with a coarse-porosity fritted disk. The column was serially rinsed with approximately 3 × 250 mL of acetone, *n*-hexane, and dichloromethane. The silica gel was left in a fume hood overnight and then completely dried at 40–50 °C. The dried silica gel was then activated at 180 °C for 20 h in a shallow tray that was loosely covered with aluminum foil.

Table 1. Relative Response Factors Determined by the Internal Standard Method

compounds	mr w	target ion	quali- fying ion	internal standard		
				av RRF ^a	SD ^b	RSD ^b (%)
ethylbenzene-d ₁₀	116	116	98			
benzene	78	78	77	7.21	0.38	5.3
toluene	92	91	92	7.18	0.23	3.1
ethylbenzene	92	91	106	6.27	0.17	2.7
<i>m</i> -xylene	92	91	106	8.13	0.22	2.7
<i>o</i> -xylene	92	91	106	6.57	0.15	2.3
isopropylbenzene	120	105	120	7.84	0.20	2.5
propylbenzene	120	91	120	10.48	0.23	2.2
3-ethyltoluene	120	105	120	6.84	0.13	1.9
1,3,5-trimethylbenzene	120	105	120	7.03	0.16	2.3
2-ethyltoluene	120	105	120	7.83	0.19	2.5
1,2,4-trimethylbenzene	120	105	120	6.87	0.15	2.2
butylbenzene	134	105	134	7.53	0.17	2.3
1,2,4,5-tetramethylbenzene	134	119	134	6.52	0.18	2.8
amylbenzene	148	91	148	6.48	0.14	2.2
pentamethylbenzene	148	133	148	8.19	0.18	2.1
1-phenylheptane	176	91	92	4.94	0.13	2.6
hexamethylbenzene	162	147	162	5.96	0.18	3.1

^a Values represent eight determinations. ^b RRF, relative response factor; SD, standard deviation; RSD, relative standard deviation.

Alkylbenzene standards (the purities of most standards are greater than 95%) with the alkyl groups ranging from C₁ to C₇ and the internal standard ethylbenzene-d₁₀ were purchased from Aldrich (Milwaukee, WI) and Supelco (Bellefonte, PA).

ASMB oil is the reference oil used for dispersant testing in the ESD. Other oils were obtained from various sources during the period of 1985–1994 and stored in the cold room of this laboratory.

Weathered Oils. The oil weathering system consists of a Wheaton N-10 Spin Vap with a 10 L flask, an integral Haake F3-CH circulating water bath (capacity 14 L), and a Millipore vacuum pump. The bath temperature can be controlled to ±0.5 °C and the thermal control range is 1–120 °C. The rotation speed can be continuously varied from 10 to 135 rpm.

Please refer to the ref 16 for details of the evaporative weathering procedures that were used to obtain weathered oils with varying weathered percentages (% of weight loss).

Column Chromatographic Fractionation. Details of the column chromatographic fractionation procedure were presented in the literature.¹³ The only difference is that *n*-pentane and dichloromethane were exclusively used in this work instead of *n*-hexane and benzene throughout the fractionation process. Oil was fractionated into saturated (*n*-pentane fraction) and aromatic (50% dichloromethane in *n*-pentane fraction, v/v) fractions only for identification purpose. In this way, the identification of alkylbenzene components from the total ion chromatogram of the aromatic fraction will not be interfered with and complicated by saturated components of oil. As for quantitation of alkylbenzenes in the SIM mode, no prefractionation step was needed and performed.

Capillary Gas Chromatography/Mass Spectrometry (GC/MS). The analysis of BTEX and alkylbenzene compounds was performed on a Hewlett-Packard (HP) 5890 equipped with a Model 5972 mass selective detector (MSD). System control and data acquisition was achieved with a HP G1034C MS ChemStation (DOS series). The MSD was operated in the scan mode to obtain spectral data for identification of alkylbenzene components and

- (13) Wang, Z. D.; Fingas, M.; Li, K. J. *Chromatogr. Sci.* **1994**, *32*, 361–366.
 (14) Wang, Z. D.; Fingas, M.; Li, K. J. *Chromatogr. Sci.* **1994**, *32*, 367–382.
 (15) Wang, Z. D.; Fingas, M.; Sergy, G. *Environ. Sci. Technol.* **1994**, *28*, 1733–1746.
 (16) Wang, Z. D.; Fingas, M. *Proceedings of The 17th Arctic and Marine Oil Spill Program (AMOP) Technical Seminar*, June 8–10, 1994, Vancouver, BC, Canada: Environment Canada: Ottawa, 1994; pp 133–172.
 (17) Wang, Z. D.; Fingas, M. *Environ. Sci. Technol.*, in press.

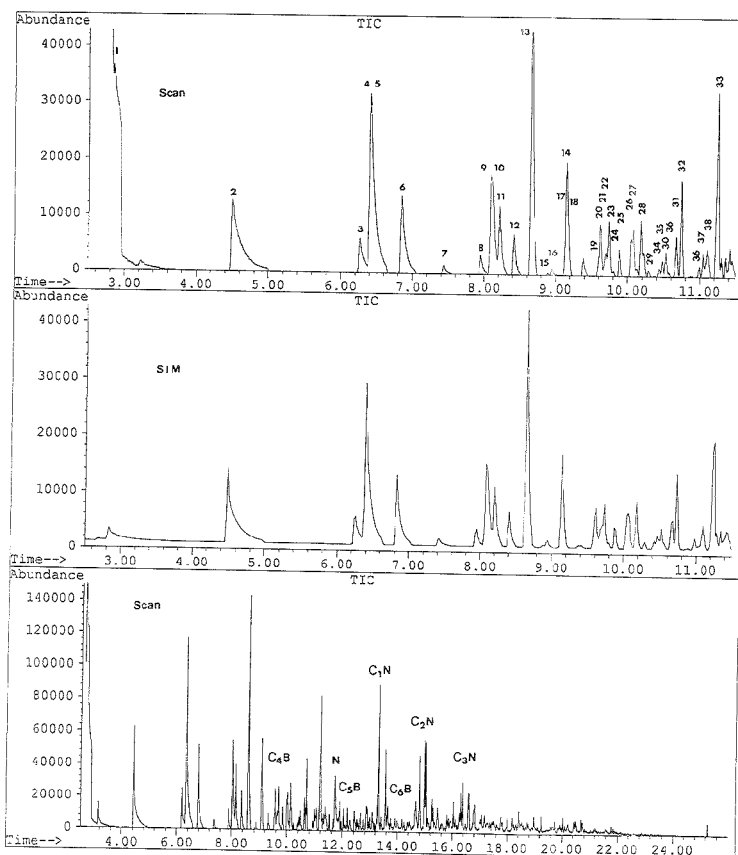


Figure 1. GC/MS chromatograms of alkylbenzene compounds (A, top, scan; B, middle, SIM) and the aromatic fraction (C, bottom, scan). See Table 2 for identification of alkylbenzene components.

in selected ion monitoring (SIM) mode for quantitation of BTEX and other target alkylbenzene compounds. An HP-5 fused-silica column with dimensions of 30 m \times 0.25 mm i.d. (0.25- μ m film) was used. The chromatographic conditions were as follows: carrier gas, helium (1.0 mL/min); injection mode, splitless; injector and detector temperature, 290 and 300 $^{\circ}$ C, respectively. The following temperature program was used for analysis of BTEX and target alkylbenzenes: 35 $^{\circ}$ C for 2 min, ramp at 10 $^{\circ}$ C/min to 300 $^{\circ}$ C, and hold for 10 min.

Table 1 lists the selected characteristic ions used for analysis of target BTEX and alkylbenzene homologues. Prior to sample analysis, the instrument was calibrated using a standard solution that was composed of five BTEX compounds, six C_3 -benzene compounds, two C_4 , two C_5 , one C_6 , and one C_7 -benzene compounds. Ethylbenzene- d_{10} was used as the internal standard. A five-point calibration curve that demonstrated the linear range of the analysis was established for each target compound. All these 17 target alkylbenzene compounds showed good linearity from 0.01–200 ppm. The relative response factors (RRF) for each compound were calculated relative to the internal standard. The relative standard deviations (RSDs) obtained from eight determi-

nations of RRF were under 3.2% except for the RSD for benzene, which was 5.3% (Table 1), this clearly demonstrated the satisfactory reproducibility of the instrument performance. In addition to being used for quantitation of themselves, the RRF of *m*-xylene and 1,2,4-trimethylbenzene were also used for quantitation of *p*-xylene and 1,2,3-trimethylbenzene, respectively.

In order to avoid any possible loss of volatile alkylbenzenes because of fractionation or concentration, all oil samples were directly weighed and dissolved in *n*-pentane to an approximate concentration of 2 mg/mL. Prior to analysis, the tightly capped oil solutions in *n*-pentane were put in a refrigerator for 30 min to precipitate the asphaltenes to the bottoms of the vials in order to avoid performance deterioration of the column.

Retention indexes for alkylated benzene hydrocarbons were calculated using the following formula:¹⁸

$$I_A = 100N + 100 \frac{\log t'_{R(A)} - \log t'_{R(N)}}{\log t'_{R(N-1)} - \log t'_{R(N)}} \quad (1)$$

where I_A is the retention index of component A, $t'_{R(A)}$ is the

(18) Kovats, E. In *Advances in Chromatography*; Giddings, J. C., Keller, R. A., Eds.; M. Dekker: New York 1965; Vol. 1, pp 229–247.

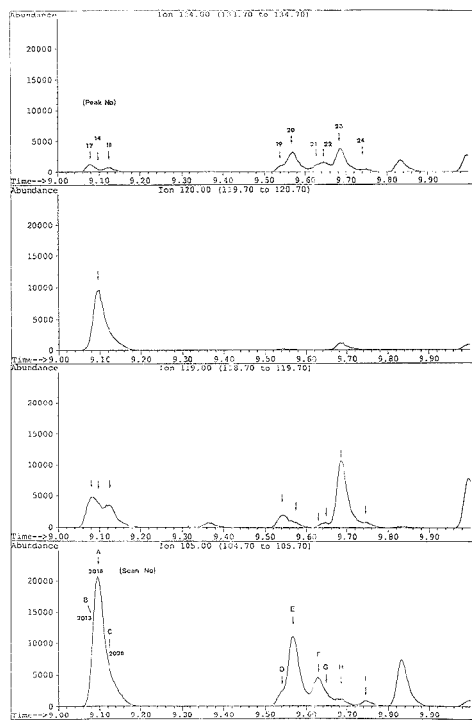


Figure 2. Examination of one peak (scan 2018) in the TIC, showing that there are actually three components, (peaks 14, 17, and 18; from examination of the extracted ions m/z 134, 120, 119, and 105) coeluting under one TIC peak.

adjusted retention time of component A, and $t'_{R(N)}$ and $t'_{R(N+1)}$ are the adjusted retention times of the n -paraffins with carbon number N and $N + 1$, respectively.

RESULTS AND DISCUSSION

Identification and Characterization of Alkylbenzene Homologues. Panels A and B of Figure 1 show the GC/MS scan and SIM chromatograms of alkylbenzene compounds in the retention time range of 2.5–11.5 min obtained from the aromatic fraction of the ASMB oil. For comparison purposes, Figure 1C shows the GC/MS scan chromatogram of the aromatic fraction in the time range of 2.5–25 min.

It can be clearly seen from Figure 1 that (1) using the current temperature program, no aromatic hydrocarbons with notable abundance were detected after 25 min; (2) a significant feature of the alkylated benzene series is their higher concentrations relative to the polycyclic aromatic hydrocarbons (PAHs); it is especially true for the early-eluting C_2 - and C_3 -benzenes (the sums of BTEX + C_3 -benzenes and target alkylated naphthalene, phenanthrene, dibenzothiophene, fluorene, and chrysenes homologous series were determined to be 1.88 and 1.36% of ASMB oil, respectively¹⁴); (3) the PAH hydrocarbons in ASMB oil are mainly comprised of alkylated naphthalene, phenanthrene, and dibenzothiophene series, with the alkylated naphthalene series being the most

abundant¹⁴; (4) the BTEX compounds and homologues of the C_6 -benzene family in the ASMB oil (starting from the simplest aromatic compound benzene, peak 1, with a retention time of 2.84 min to 1,2,3-trimethylbenzene, peak 13, with a retention time of 9.15 min) are significantly more abundant than the late-eluting highly alkylated benzene components; (5) the benzene peak is hardly distinguished from the solvent peak in the scan chromatogram because of masking of the huge coeluted solvent (n -pentane and dichloromethane) peak. In the SIM chromatogram, however, the benzene peak is well resolved with no interference from solvents and, therefore, can be accurately quantitated.

The structural identification and characterization of alkylbenzenes were based on mass spectral data in both full-scan and SIM modes, comparison of GC retention data with reference standards, and calculation of retention index (RI) values verified by comparison with literature RI values. Comparison of the RI values with those reported in the literature¹⁹ enables the assignment of some positional isomers. For example, the mass spectrum for peak 13 (Figure 1) at scan 1875 shows that the compound has a molecular ion at m/z 120 and major fragment ions at m/z 105 and 91. Such successive losses of one 15-amu fragment (CH_3) and one 14-amu fragment (CH_2) are highly characteristic of trimethylbenzene. A match of the retention time and the mass spectrum with those of standard compounds permits the peak to be assigned as 1, 2, 4-trimethylbenzene. However, a few peaks in the total ion chromatogram (TIC) of this sample look like a single compound, but they are actually not. For such peaks, very careful and extensive examination of the mass spectra should be performed. For example, the fairly symmetrical peak 14 (Figure 1) in the TIC at scan 2018 looks like a single component, but it is actually due to three closely eluting compounds. As illustrated in Figure 2, the mass spectrum taken at scan 2018 (point A, peak 14) is closely matched to the standard spectrum of 1,2,3-trimethylbenzene, but the appearance of a significantly abundant ion at m/z 134 is difficult to interpret. Examination of the extracted ion (m/z 134, 120, 119, and 105) mass spectra on the two sides of peak 14 proves that it is not due to a single component. The earlier and later mass spectrum at point B (scan 2013, peak 17) and C (scan 2028, peak 18) indicates a C_7 -benzene compound with a molecular ion of 134, respectively. The extracted ion chromatograms at m/z 134, 120, 119, and 105 very clearly indicate the existence of three compounds with 1,2,3-trimethylbenzene at scan 2018 being the most abundant and dominant. The two components at the sides of 1,2,3-trimethylbenzene were identified to be *m*-cymene (1-methyl-3-isopropylbenzene) and *p*-cymene (1-methyl-4-isopropylbenzene), respectively. Comparison of retention times, retention indexes and mass spectra with those of standard compounds confirms the assignment. This example indicates the power of the data system of GC/MS to further resolve compounds that are not completely separated by chromatograph. Using the same mass spectrum processing technique, the chromatographically resolved four peaks between scans 2140 and 2220 were identified as six components (peaks 19–24, Figure 2): 1,3-diethylbenzene, 1-methyl-3-propylbenzene, 1-methyl-4-propylbenzene, butylbenzene, 1-ethyl-3,5-dimethylbenzene, and 1,2-diethylbenzene.

In the ASMB oil, 58 alkyl-substituted benzene compounds in total were positively identified (Table 2). These 58 compounds

(19) Lubeck, A. J.; Sutton, D. L. *J. High Resolut. Chromatogr. Chromatogr. Commun.* **1983**, *6*, 328–332.

Table 2. Alkyl-Substituted Benzene Compounds Identified in ASMB Oil

peak no.	RT (min)	compound identified	MW	RI		std RT (min)	std RI					
				calc	lit. ^a							
1	2.840	benzene	C ₆ -Benzene 78	671.3	670.6	2.836	671.0					
			C ₇ -Benzene 92	771.2	772.7			4.492	771.3			
2	4.490	toluene	C ₆ -Benzene 106	868.1	867.4	6.264	867.9					
			106	875.3	874.8			6.405	875.0			
			106	875.8	875.4			6.410	875.3			
			106	896.5	898.7			6.847	896.3			
			C ₆ -Benzene 120	930.7	931.4			7.437	931.1			
			120	960.7	959.9			7.959	960.8			
3	6.268	ethylbenzene	106	868.1	867.4	6.264	867.9					
4	6.411	<i>m</i> -xylene	106	875.3	874.8	6.405	875.0					
5	6.421	<i>p</i> -xylene	106	875.8	875.4	6.410	875.3					
6	6.852	<i>o</i> -xylene	106	896.5	898.7	6.847	896.3					
7	7.430	isopropylbenzene	C ₆ -Benzene 120	930.7	931.4	7.437	931.1					
			120	960.7	959.9			7.959	960.8			
			120	967.4	967.2			8.086	967.8			
			120	968.5	969.0			8.096	968.3			
			120	974.7	974.0			8.214	974.6			
			120	985.5	985.7			8.423	985.7			
			120	997.5	998.8			8.655	997.6			
			120	1028.2	> 1000			9.135	1028.1			
			C ₆ -Benzene 134	1012.1	> 1000			8.868	1010.9			
			134	1015.2	> 1000			8.920	1014.3			
			134	1027.1				9.122	1027.3			
			134	1030.3				9.162	1029.8			
			134	1056.3				9.573	1055.3			
			134	1058.1				9.613	1057.7			
134	1061.3		9.685	1062.0								
134	1062.9		9.710	1063.5								
134	1065.9		9.746	1065.6								
134	1068.8		9.793	1068.4								
134	1074.1		9.885	1073.8								
134	1083.5		/	/								
134	1085.2		10.060	1084.2								
134	1091.0		10.188	1091.4								
134	1097.1		10.300	1097.7								
134	1113.1		10.530	1113.2								
134	1123.2		10.687	1124.0								
134	1127.9		10.725	1126.6								
134	1161.4		/	/								
34	10.430	C ₆ -benzene	C ₆ -Benzene 148	1106.3		11.306	1165.0					
			148	1109.8								
			148	1114.6								
			148	1144.5								
			148	1150.3								
			148	1154.1								
			148	1160.1								
			148	1164.9								
			148	1168.5								
			148	1172.6								
			148	1174.8								
			148	1182.2								
			148	1204.5								
			148	1217.6								
			148	1227.5								
			148	1290.4								
			50	12.334	C ₆ -Benzene			C ₆ -Benzene 162	1234.5		12.800	1267.3
								162	1245.0			
								162	1251.9			
								162	1267.2			
162	1274.6											
162	1281.3											
162	1284.6											
C ₇ -Benzene 176	1408.8											
58	15.522	C ₆ -Benzene				C ₆ -Benzene 190	1473.0					

^a The literature RI values listed here are the values after correction of the temperature's effect on RI according to the temperature coefficient given in ref 19.

Table 3. Analysis Results of Individual BTEX and C₃-Benzene Compounds in Representative Light, Medium, and Heavy Oils^a

compounds	target ion	RT (min)	ASMB	Maya (% weathered)				Bunker C
				0.0	9.4	14.9	22.2	
ethylbenzene- <i>d</i> ₁₀	116	6.14	2.00	2.00	2.00	2.00	2.00	2.00
benzene	78	2.82	1.50	0.50	0.10	0.05	0.05	0.10
toluene	91	4.47	4.35	1.35	0.66	0.00	not found	0.10
ethylbenzene	91	6.24	0.82	0.77	0.46	0.05	0.00	0.05
<i>m</i> -xylene + <i>p</i> -xylene	91	6.37	3.48	1.85	1.27	0.15	0.00	0.20
<i>o</i> -xylene	91	6.81	1.50	1.04	0.66	0.15	0.00	0.15
isopropylbenzene	105	7.41	0.19	0.14	0.10	0.05	0.00	0.00
propylbenzene	91	7.98	0.39	0.27	0.20	0.10	0.00	0.10
3-/4-ethyltoluene	105	8.06	1.50	1.17	1.07	0.39	0.00	0.70
1,3,5-trimethylbenzene	105	8.20	0.92	0.36	0.30	0.15	0.00	0.30
2-ethyltoluene	105	8.39	0.43	0.63	0.51	0.25	0.00	0.20
1,2,4-trimethylbenzene	105	8.64	3.09	1.40	1.17	0.59	0.00	1.09
1,2,3-trimethylbenzene	105	9.12 ^a	0.72	0.41	0.20	0.10	0.00	0.25
BTEX			11.64	5.50	3.15	0.39	0.05	0.60
C ₃ -benzenes			7.25	4.37	3.55	1.63	0.00	2.64
BTEX + C ₃ -benzenes			18.89	9.87	6.70	2.02	0.05	3.23

^a Units, milligrams per gram of oil.

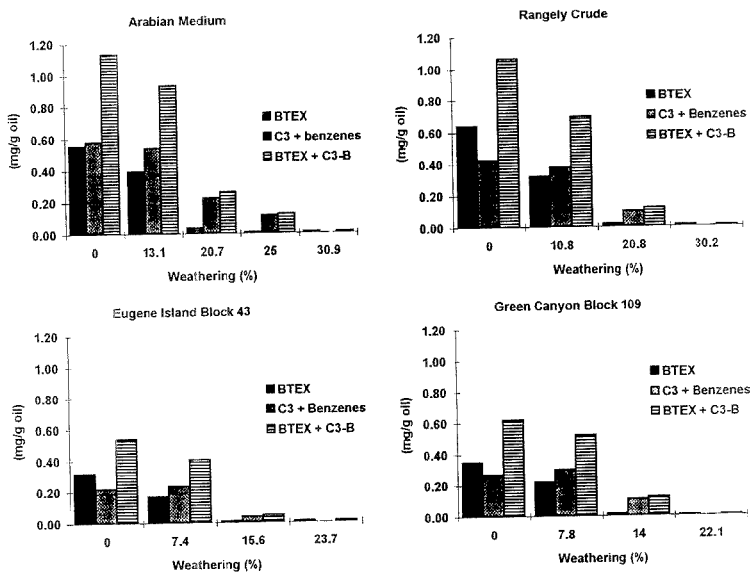


Figure 3. Contents of BTEX, C₃-benzenes, and BTEX + C₃-benzenes at varying weathered percentages for four different oils.

in benzene series include 8 C₇-benzene isomers (theoretically, only 8 C₇-benzene isomers exist), 19 C₇-benzene compounds, 16 C₅-benzene compounds, 7 C₆-benzene compounds, and 1 C₇- and 1 C₈-benzene, in addition to 6 common BTEX compounds. For comparison purposes, the calculated RI values for all 58 identified alkylbenzene compounds, the literature RI values of the BTEX and C₃-benzenes,¹⁹ and the RI values calculated from the chromatographic data of the BTEX and alkylbenzene (from C₃ to C₆) standards are also listed in Table 2. These three series of RI values are in excellent agreement with each other.

Quantitation of BTEX and Alkylbenzenes. Sample handling can greatly affect analytical precision and accuracy of alkylbenzene compounds in oil because of the volatility of the lighter

alkylbenzenes. In order to achieve improved analytical precision and accuracy, the following refinements were implemented in addition to the routine quality control measures:

(1) Oil was directly weighed and dissolved in *n*-pentane and tightly sealed to avoid any possible loss of alkylbenzene compounds, especially the BTEX compounds.

(2) Tightly capped oil sample vials were put into a refrigerator to precipitate asphaltene bottoms in order to avoid deterioration of performance of the capillary GC column by the introduction of asphaltene.

(3) Blanks and calibration check standards were analyzed before and after each sample batch (about 10 samples) to monitor analysis accuracy and precision.

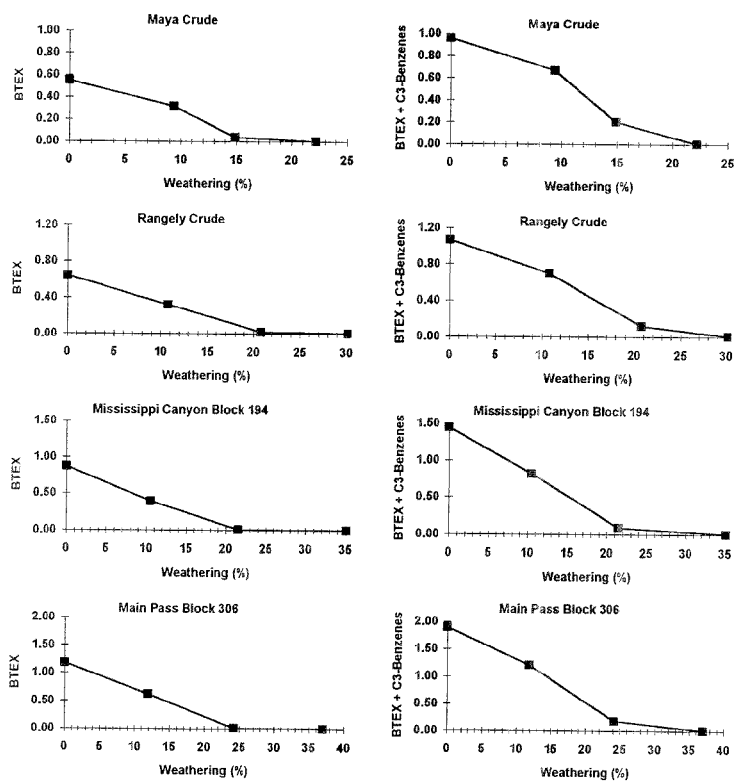


Figure 4. Plots of concentrations (mg/g of oil) of BTEX and BTEX + C₃-benzenes versus weathered percentages for four weathered oil series.

(4) C₃-benzenes in oil were quantitated using the RRFs directly obtained from the respective individual C₃-benzene standards instead of using the RRFs obtained from benzene or C₁/C₂ substituted benzenes.

Individual BTEX compounds and eight C₃-benzene compounds in over 200 oils were quantified. As an example, Table 3 presents the detailed quantitation results of individual BTEX compounds and C₃-benzene isomers in representative light ASMB oil (density 0.839), medium Maya oil (density 0.923), and heavy Bunker C oil (density 0.974). Table 4 summarizes the quantitation results of total BTEX, C₃-benzenes, and BTEX + C₃-benzenes in these 200 oils. The contents of BTEX and BTEX + C₃-benzenes vary from oil to oil. They can range from 0 to 6% for BTEX and from 0 to 7% for BTEX + C₃-benzenes, depending on the nature and origin of the oil. In general, however, the dominance of BTEX and C₃-benzenes in the alkyl-substituted benzene category is obvious. For the ASMB oil, the sums of BTEX and BTEX + C₃-benzenes were determined to be 11.6 and 18.9 mg/g of oil, respectively. The most abundant alkylbenzenes in ASMB are toluene (4.3 mg/g of oil), *m*-xylene plus *p*-xylene (3.5 mg/g of oil), and 1,2,4-trimethylbenzene (3.1 mg/g of oil). Also, a trend is seen that the sums of C₇, C₈, C₉, and C₁₀-benzenes in the ASMB oil dramatically decrease as the carbon numbers of the substituted alkyl groups increase. It is noted that among the 16 identified C₇-benzene isomers, 1,2,3,4-tetramethylbenzene (the last eluted compound in

the C₇-benzene family) is the most abundant with a concentration of 1.35 mg/g of oil. In sharp contrast, for example, the concentrations of BTEX and BTEX + C₃-benzenes in the heavy Bunker C oil were determined to be only 0.6 and 2.6 mg/g of oil, respectively.

Effect of Weathering on the Composition of Alkylbenzenes. Figure 3 depicts graphically the concentrations of BTEX, C₃-benzenes, and BTEX + C₃-benzenes at varying weathering degrees for four different oils (Arabian Medium, Rangely Crude, Eugene Island Block 43, and Green Canyon Block 109). The major changes in alkylbenzene composition relating to increase of the weathering percentage are summarized as follows:

- (1) The loss rate is significantly correlated to the molecular weight and boiling points of alkylbenzene compounds. Relative to C₃-benzenes, the low molecular weight and the most volatile BTEX compounds are lost more quickly through weathering.
- (2) The homologous group shows the clear evaporation trend: C₀ > C₁ > C₂ > C₃ > C₄. For example, when the Green Canyon Block 109 Crude was weathered from 0 to 7.8%, 50% of benzene and toluene was lost, C₂-benzenes showed approximately 25% loss, C₃-benzene compounds isopropylbenzene, propylbenzene, and 3-/4-ethylmethylbenzene did not show any obvious loss, and the other four late-eluting C₂-benzenes even showed slight increase in their concentrations.

Table 4. Summary of BTEX Analysis Results in Various Oils

oil	BTEX (%)	C ₃ -benzene (%)	BTEX + C ₃ -benzene (%)	oil	BTEX (%)	C ₃ -benzene (%)	BTEX + C ₃ -benzene (%)
Adgo	0.04	0.05	0.09	Hondo	0.68	0.41	1.10
Alberta Sweet Mixed Blend	0.02	0.00	0.02	Hondo 16.67%	0.14	0.25	0.39
Arnauligak	0.54	0.68	1.21	Hondo 32.29%	0.00	0.00	0.00
Arabian Light	0.80	0.74	1.54	IFO 180 No. 4	0.06	0.10	0.16
Arabian Light GS 12.05%	0.60	0.67	1.27	Iranian Heavy	0.98	0.76	1.73
Arabian Light GS 24.20%	0.02	0.24	0.27	Iranian Heavy 13.68%	0.64	0.56	1.19
Arabian Medium	0.56	0.58	1.13	Iranian Heavy 24.84%	0.02	0.15	0.17
Arabian Medium 13.15%	0.39	0.54	0.94	Irving Whale	0.02	0.06	0.08
Arabian Medium 20.77%	0.04	0.22	0.26	Issunak Crude Oil	0.65	0.67	1.32
Arabian Medium 25.00%	0.01	0.11	0.12	Lago	0.59	0.50	1.09
Arabian Medium 30.90%	0.01	0.00	0.01	Lago Medio	0.24	0.17	0.41
ASMB Crude Oil No. 5	1.16	0.72	1.89	Lube Oil	0.00	0.00	0.00
ASMB California API = 11.0	0.74	0.54	1.27	Lucula	0.36	0.27	0.62
Atkinson Crude Oil	0.09	0.15	0.24	Louisiana	0.91	0.57	1.48
Avalon J-34	0.77	0.49	1.26	Louisiana 9.65%	0.60	0.54	1.14
Barrow Island	0.67	0.60	1.27	Louisiana 31.89%	0.00	0.00	0.00
BCF-24	0.52	0.33	0.85	Main Pass Block 37	1.28	0.75	2.03
BCF-24 9.23%	0.25	0.30	0.56	Main Pass Block 37 16.22%	0.61	0.69	1.30
Belridge Heavy Crude	0.01	0.00	0.01	Main Pass Block 37 30.27%	0.02	0.21	0.23
Bent Horn A02	0.29	0.27	0.55	Main Pass Block 37 50.19%	0.00	0.00	0.00
Bent Horn	0.08	0.13	0.21	Main Pass Block 306	1.18	0.71	1.89
Bent Horn 20.6%	0.07	0.16	0.23	Main Pass Block 306 11.84	0.62	0.59	1.21
Beta Crude	0.11	0.12	0.23	Main Pass Block 306 24.15%	0.02	0.17	0.18
Bitumen diluent	5.72	1.09	6.81	Main Pass Block 306 37.04%	0.00	0.00	0.00
Boscan	0.07	0.07	0.14	Malongo	0.45	0.24	0.69
Brent Crude	1.81	0.63	2.44	Marine Intermediate Fuel Oil	0.01	0.19	0.20
Deasphaltized Brend Crude	0.01	0.00	0.01	Maya Crude	0.55	0.44	0.99
Bunker C	0.06	0.26	0.32	Maya 9.38%	0.31	0.36	0.67
Bunker C Light	0.03	0.06	0.08	Maya 14.85%	0.04	0.16	0.20
Bunker C (fuel oil No.)	0.04	0.06	0.09	Maya 22.15%	0.00	0.00	0.00
California API 11.0	0.12	0.17	0.29	Mississippi Canyon Block 194	0.87	0.57	1.44
California API 15.0	0.31	0.22	0.53	Mississippi Canyon Block 10.47%	0.39	0.43	0.82
Carpenteria	0.35	0.31	0.66	Mississippi Canyon Block 21.49%	0.01	0.08	0.09
Carpenteria 10.31%	0.25	0.33	0.58	Mississippi Canyon Block 35.06%	0.00	0.00	0.00
Carpenteria 14.87%	0.01	0.10	0.11	Nektorlik K-59	0.38	0.33	0.71
Cat Cracking Feed	0.03	0.02	0.06	Nerterk	0.26	0.23	0.49
Cat Cracking Feed 2.06%	0.02	0.02	0.04	Ninian 15.26%	0.90	0.67	1.58
Cohasset A-52 28.1%	0.03	0.02	0.06	Ninian 30.22%	0.06	0.14	0.20
Combined Gas Oil	0.00	0.00	0.00	Nobe No. 1	0.26	0.33	0.59
Dilbit Blend	0.87	0.18	1.05	Nobe Oil Fresh Truck 1	0.28	0.31	0.60
Dos Cuadras Crude	0.27	0.51	0.78	Nobe Oil Fresh Truck 2	0.26	0.31	0.57
Dos Cuadras 11.17%	0.26	0.52	0.78	Nobe Oil Fresh Truck 3	0.24	0.30	0.54
Dos Cuadras 20.30%	0.02	0.11	0.12	Nobe Oil Fresh Truck 1 + 3	0.30	0.34	0.64
Empire	0.61	0.40	1.01	Nobe Oil Fresh Truck 2 + 3	0.27	0.32	0.59
Empire 10.05%	0.59	0.52	1.11	Nobe Oil Weathered Truck 1	0.30	0.32	0.62
Empire 20.25%	0.02	0.10	0.12	Nobe Oil Weathered from Apex of FB	0.26	0.32	0.58
Endicott	1.10	0.43	1.53	Norman Wells	0.51	0.52	1.03
Eugene Island Block 32	0.61	0.27	0.88	NQ 2 Fuel Oil	0.25	0.73	0.98
Eugene Island Block 32 6.00%	0.27	0.27	0.54	Nugini	1.63	0.92	2.55
Eugene Island Block 32 13.18%	0.00	0.03	0.03	Nugliomo 31.61%	0.60	1.09	1.69
Eugene Island Block 20.04%	0.00	0.00	0.00	Offshore ASMB-1	0.47	0.45	0.93
Eugene Island Block 43	0.32	0.22	0.54	Offshore Mousse Mix No. 2	0.42	0.37	0.79
Eugene Island Block 43 7.40%	0.17	0.24	0.40	Orimulsion	0.00	0.00	0.00
Eugene Island Block 43 15.56	0.01	0.04	0.05	Orimulsion 26.06%	0.00	0.00	0.00
Eugene Island Block 43 23.65%	0.01	0.00	0.01	Oseberg	1.20	0.61	1.81
Eugene Island Block 224	3.63	1.62	5.26	Oseberg 13.99%	0.45	0.43	0.88
Exxon Valdez Oil Emulsion	0.01	0.00	0.01	Oseberg 27.47%	0.05	0.13	0.18
FCC	0.01	0.05	0.06	Panuk	0.16	0.48	0.64
FCC Light	0.03	0.06	0.09	Pitas Point	1.05	1.54	2.59
FCC Heavy	0.45	1.02	1.47	Pitas Point 23.56%	0.45	1.21	1.66
FCC Heavy 4.17%	0.17	0.74	0.91	Point Arguello Comingled	0.47	0.48	0.94
Federated 1994	1.05	0.84	1.89	Point Arguello Heavy	0.44	0.43	0.86
Federated	1.03	0.86	1.89	Point Arguello Light	0.54	0.64	1.18
Green Canyon Block 65	0.17	0.16	0.33	Port Hueneme	0.03	0.07	0.09
Green Canyon Block 66 7.70%	0.15	0.20	0.35	Port Hueneme 4.16%	0.02	0.04	0.05
Green Canyon Block 66 13.13%	0.06	0.15	0.21	Port Hueneme 8.37	0.01	0.00	0.01
Green Canyon Block 65 22.91%	0.01	0.00	0.01	Propylene Tetramer	0.00	0.00	0.00
Green Canyon Block 109	0.35	0.27	0.62	Propylene Tetramer 82.66%	0.00	0.00	0.00
Green Canyon Block 109 7.83%	0.22	0.30	0.52	Prudhoe Bay	0.99	0.47	1.46
Green Canyon Block 109 14.01%	0.01	0.11	0.12	Rangely Crude	0.64	0.43	1.07
Green Canyon Block 109 22.11%	0.00	0.00	0.00	Rangely 10.75%	0.36	0.38	0.70
Gulllaiks Crude	1.35	0.64	1.99	Rangely 20.84%	0.02	0.10	0.12
Heavy Reformate	0.08	0.08	0.15	Rangely 30.20%	0.01	0.00	0.01
Hibernia	1.08	0.39	1.47	Residue between F.B. + B.B	0.01	0.00	0.01
Hibernia Poured Oct. 18, 1994	1.56	0.55	2.11	Residue from side of boats	0.00	0.00	0.00
High Viscosity Fuel Oil	0.10	0.16	0.25	Santa Clara	0.24	0.24	0.48
Hog Oil	0.05	0.07	0.12	Santa Clara 11.40%	0.17	0.18	0.35

Table 4. Continued

oil	BTEX (%)	C ₇ -benzene (%)	BTEX + C ₇ -benzene (%)	oil	BTEX (%)	C ₇ -benzene (%)	BTEX + C ₇ -benzene (%)
Ship Shoal Block 239	0.21	0.15	0.36	Sumatran Heavy (DURI)	0.04	0.10	0.14
Ship Shoal Block 239 16.75%	0.09	0.19	0.28	Synthetic Crude	0.96	0.60	1.56
Ship Shoal Block 239 42.57%	0.01	0.06	0.07	Taching	0.11	0.10	0.21
Ship Shoal Block 239 53.15%	0.00	0.00	0.00	Takula	0.28	0.23	0.51
Ship Shoal Block 269	1.29	0.62	1.91	Takula 10.58%	0.23	0.24	0.47
Ship Shoal Block 269 13.23%	1.06	0.97	2.02	Takula 18.42%	0.02	0.11	0.13
Ship Shoal Block 269 26.27%	0.05	0.34	0.38	Terra Nova	0.90	0.46	1.36
Ship Shoal Block 269 38.95%	0.00	0.00	0.00	Thevenard	0.58	0.65	1.23
Sockeye	0.86	0.69	1.55	Transmountain Blend Crude Oil	0.43	0.55	0.98
Sockeye 12.50%	0.44	0.65	1.10	Transoil 10 AEC Pipelines	0.02	0.01	0.03
Sockeye 22.10%	0.02	0.07	0.09	Udang	0.01	0.00	0.01
South Pass Block 60	1.14	0.46	1.60	Waxy Gas Oil Crude	0.01	0.00	0.01
South Pass Block 60 16.51%	0.40	0.60	1.00	Waxy Light Heavy Blend	0.40	0.23	0.63
South Pass Block 60 24.61%	0.02	0.21	0.23	Waxy residuum Crude	0.01	0.00	0.01
South Pass Block 60 38.12%	0.00	0.00	0.00	West Delta Block 30	0.02	0.00	0.02
South Pass Block 67	0.63	0.26	0.89	West Delta Block 30 23.76%	0.01	0.00	0.01
South Pass Block 67 22.17%	0.08	0.20	0.28	West Delta Block 30 42.16%	0.01	0.00	0.01
South Pass Block 67 44.56%	0.01	0.03	0.04	West Delta Block 30 61.34%	0.00	0.00	0.00
South Pass Block 67 63.99%	0.01	0.00	0.01	West Delta Block 97	2.30	0.90	3.20
South Pass Block 93	0.55	0.33	0.88	West Delta Block 97 23.38%	1.80	1.43	3.23
South Pass Block 93 11.03%	0.31	0.43	0.75	West Delta Block 97 47.99%	0.08	0.48	0.57
South Pass Block 93 21.38%	0.05	0.24	0.29	West Delta Block 97 72.68%	0.01	0.00	0.01
South Pass Block 93 33.70%	0.01	0.00	0.01	Western Sweet Blend Crude 30./3/9	1.67	1.11	2.77
South Timbalier Block 130	1.12	0.82	1.94	Western Sweet Blend Crude 30./10/	1.74	1.14	2.88
South Timbalier Block 130 11.11%	0.40	0.56	0.96	West Texas Intermediate	0.96	0.59	1.56
South Timbalier Block 130 21.95%	0.01	0.18	0.19	West Texas Intermediate 14.14%	0.74	0.54	1.27
South Timbalier Block 130 35.07%	0.00	0.00	0.00	West Texas Intermediate 28.47%	0.03	0.21	0.24
St-Amable Tire Fire Oil	0.60	0.29	0.89	West Texas Sour	2.05	0.74	2.80
Statfjord Crude	1.94	0.63	2.57	West Texas Sour 14.74%	1.32	0.79	2.12
Deasphaltized Stratford Crude	0.00	0.00	0.00	West Texas Sour 29.90%	0.02	0.09	0.11
Sumatran Light Minas	0.15	0.17	0.32	Zaire	0.31	0.24	0.55
Sumatran Heavy 5.26%	0.01	0.03	0.04				

(3) When oil was weathered to a certain degree (approximately in the range of 20–25% weathered percentages for the six oils shown in Figure 3), the BTEX and C₇-benzenes were completely lost.

It should be understood that there are two opposing factors which can affect the concentration changes of alkylbenzene compounds during the weathering process: the first factor is evaporation, which results in the concentration decrease of the alkylbenzenes; the second is volume reduction by evaporation, which results in the concentration increase of remaining compounds. The chemical composition changing behavior is the combined result of these two opposing effects. At the starting stage of weathering (say, the weathering degree under 10%), the second factor played a slightly larger role than the first one for C₇-benzenes: therefore, C₇-benzene compounds showed no noticeable loss and even slight increase in their concentrations. As the weathering process continued, more and more C₇-benzene compounds were lost, resulting in pronounced reduction in the sum of BTEX plus C₇-benzenes.

Figure 4 presents the plots of the concentrations of BTEX and BTEX + C₇-benzenes versus weathered percentages for four weathered oil series. Two pronounced features which can be demonstrated from the plots are that (1) before complete loss, the concentrations of BTEX and BTEX + C₇-benzenes are obvious in proportion to the weathering degrees, the relation between the abundances of BTEX and BTEX + C₇-benzenes and the weathered percentages can be described by a linear equation for each oil, and (2) each oil in Figure 4 shows a break point at which the BTEX and BTEX + C₇-benzenes are completely lost. Figure 4 offers a useful way to estimate the weathering extent and degree

of weathered oil samples through the determination of BTEX and BTEX + C₇-benzenes concentrations in the weathered oils.

CONCLUSION

For analysis of volatile hydrocarbons (for example, BTEX compounds and C₇-benzenes) in complex matrices such as crude oils, two criteria must be met in order to provide both qualitative and quantitative information on composition of monoring aromatic components: (1) simplicity; (2) reliability. The simplicity and directness of the method is obvious. The reliability of the method has been demonstrated by separation and determination of the standard aromatic alkylbenzene mixtures with the alkyl group ranging from C₁ to C₇ and guaranteed by strict analysis quality control measures (including running of blanks and calibration check standards before and after each sample batch). The distribution fingerprints of alkylbenzene homologues vary from oil to oil and can be easily affected by sample treatment processing due to the volatility of the compounds. However, this method needs neither fractionation nor concentration. Also, by using the GC/MS technique in the SIM mode, the interference from light saturated compounds to the determination of target aromatic compounds (each compound has its own characteristic target and qualifying ions at different retention times) can be largely minimized. Thus, the required analytical accuracy and precision is obtained.

Using this method, the concentrations of BTEX and C₇-benzenes in over 200 oils were quantified. In addition, the effects of weathering on compositional changes of alkylbenzenes were studied, and the plots of the concentrations of BTEX and BTEX

+ C₂-benzenes versus weathering percentages for several weathered oil series were graphically depicted, which can be used to estimate the weathering extent and degree of weathered oils especially for those oils weathered for short term where the loss of BTEX and C₂-benzenes is significant.

Received for review February 15, 1995. Accepted June 29, 1995.[®]

AC950168G

[®] Abstract published in *Advance ACS Abstracts*, August 1, 1995.

LC/MS/MS of Carbohydrates with Postcolumn Addition of Metal Chlorides Using a Triaxial Electro spray Probe

Martin Kohler and Julie A. Leary*

College of Chemistry, University of California, Berkeley, California 94720-1460

A new technique for on-line postcolumn addition (PCA) formation and tandem electro spray mass spectrometry of carbohydrate-metal complexes is presented. A metal chloride solution is added to a carbohydrate sample directly within the ion source of the mass spectrometer. Using a triaxial electro spray probe, this technique can be applied to form carbohydrate-metal complexes on-line, without the need of previously mixing the carbohydrate and metal chloride. Two basic tasks may be accomplished: structural analysis and sensitivity enhancement. The performance of this approach is demonstrated through PCA of LiCl, NaCl, KCl, RbCl, CsCl, and CoCl₂, introduced via the triaxial probe after chromatographic separation of two four-component carbohydrate mixtures. Each metal-carbohydrate complex is subsequently analyzed by on-line MS and MS/MS. This technique is used to enhance sensitivity and also, in the case of cobalt coordination, to assist in carbohydrate structural elucidation. On-line LC/MS with PCA of LiCl was achieved with as little as 1.7 pmol of oligosaccharide (average consumed amount, 1.7 pmol with 1 μ L of a 10 pmol/ μ L carbohydrate test mixture injection).

The growing interest in the biological role and pharmaceutical application of carbohydrates has led to an increasing demand for faster and better analytical methodology.¹ As parts of cell-surface glycoproteins, oligosaccharides play an important role in molecular recognition processes and determine, to a large extent, a variety of the biochemical properties of these proteins.² Mass spectrometric methods are among the most widely used techniques for carbohydrate analysis. Despite the fact that on-line liquid chromatography/tandem mass spectrometry (LC/MS/MS) is recognized as a powerful tool for peptide analysis, few LC/MS studies on carbohydrates, in and of themselves, are currently found in the literature.^{3,4} More notable are studies using LC/MS/MS in the area of determining posttranslational modifications of proteins that have been glycosylated⁵⁻⁸ and phosphorylated.⁹ Although a

variety of ionization techniques, such as continuous-flow fast atom bombardment,¹⁰ thermospray,^{2,11} and electro spray (ESI)^{4,12} can be suitably interfaced to a liquid chromatograph for carbohydrate analysis, ESI has the advantage of high sensitivity and low background noise. In light of the new developments in these hyphenated techniques, we have investigated a method for on-line LC/MS/MS of metal-coordinated oligosaccharides using ESI.

We have shown previously that FAB and ESI MS/MS of metal-coordinated oligosaccharides is a useful technique for oligosaccharide analysis.¹³⁻¹⁷ On the basis of recent work in our laboratory on differentiating calcium- and magnesium-coordinated trisaccharides using ESI MS/MS,¹⁵ a method for on-line formation of carbohydrate-metal complexes was developed. The multiple-step process of purification, separation, postcolumn complexation and tandem mass spectrometry was implemented by an LC/MS/MS system using a triaxial electro spray probe for on-line formation of carbohydrate-metal complexes (Figure 1). After purification by liquid chromatography, the sample is mixed with a sheath liquid¹⁸ directly within the electro spray ion source, where a carbohydrate-metal complex is immediately formed. Unlike postcolumn derivatization,^{19,20} this process is fast and does not require a postcolumn reactor.²¹ In ESI mass spectrometry, addition of a sheath liquid such as 2-methoxyethanol/2-propanol is effective in obtaining stable electro spray of solutions containing solvents with high surface tension, such as water and buffers treated with trifluoroacetic acid.²² In work presented herein, the same principle is employed to form carbohydrate-metal com-

* E-mail: leary@garnet.berkeley.edu.

- (1) Borman, S. *Chem. Eng. News* 1993, (June 28), 27-34.
- (2) Rademacher, T. W.; Parekh, R. B.; Dwek, R. A. *Annu. Rev. Biochem.* 1988, 57, 785-853.
- (3) Simpson, R. C.; Fencselau, C. C.; Hardy, M. R.; Townsend, R. R.; Lee, Y. C.; Cotter, R. J. *Anal. Chem.* 1990, 62, 243-252.
- (4) Conboy, J. J.; Henion, J. *Biomol. Mass Spectrom.* 1992, 21, 397-407.
- (5) Carr, S. A.; Huddleston, M. J.; Bean, M. F. *Protein Sci.* 1993, 2, 183-196.
- (6) Lewis, D. A.; Guzzetta, A. W.; Hancock, W. S. *Anal. Chem.* 1994, 66, 585-595.
- (7) Medzihradsky, K. F.; Maltby, D. A.; Hall, S. C.; Settineri, C. A.; Burlingame, A. L. *J. Am. Soc. Mass Spectrom.* 1994, 5, 350-358.

- (8) Conboy, J. J.; Henion, J. D. *J. Am. Soc. Mass Spectrom.* 1992, 3, 804-814.
- (9) Huddleston, M. J.; Antan, R. S.; Bean, M. F.; Carr, S. A. *J. Am. Soc. Mass Spectrom.* 1993, 4, 710-717.
- (10) Boulenger, P.; Leroy, Y.; Alonso, J. M.; Montreuil, J.; Ricart, G.; Colbert, C.; Duquet, D.; Dewaele, C.; Fournet, B. *Anal. Biochem.* 1988, 168, 164-170.
- (11) Niessen, W. M. A.; van der Hoeven, R. A. M.; van der Greef, J.; Schois, H. A.; Voragen, A. G. J. *Rapid Commun. Mass Spectrom.* 1992, 6, 197-202.
- (12) Duffin, K. L.; Welby, J. K.; Huang, E.; Henion, J. D. *Anal. Chem.* 1992, 64, 1440-1448.
- (13) Hofmeister, G. E.; Zhou, Z.; Leary, J. A. *J. Am. Chem. Soc.* 1991, 113, 5964-5970.
- (14) Staempfli, A.; Zhou, Z.; Leary, J. A. *J. Org. Chem.* 1992, 57, 3590-3594.
- (15) Fura, A.; Leary, J. A. *Anal. Chem.* 1993, 65, 2805-2811.
- (16) Fura, A.; Leary, J. A., manuscript in preparation.
- (17) Zhou, Z.; Ogden, S.; Leary, J. A. *J. Org. Chem.* 1990, 55, 5444-5446.
- (18) Smith, R. D.; Barinaga, C. J.; Udseth, H. R. *Anal. Chem.* 1988, 60, 1948-1952.
- (19) Del Nozal, M. J.; Bernal, J. L.; Gamez, F. J.; Antolin, A.; Toribio, L. *J. Chromatogr.* 1992, 607, 191-198.
- (20) Coquet, A.; Veuthey, J.-L.; Haerdli, W. *J. Chromatogr.* 1991, 553, 255-263.
- (21) Brinkman, U. A. T.; Frei, R. W.; Lingeman, H. *J. Chromatogr.* 1989, 492, 251-298.
- (22) Griffin, P. R.; Cofman, J. A.; Hood, L. E.; Yates, J. R., III. *Int. J. Mass Spectrom. Ion Processes* 1991, 111, 131-149.

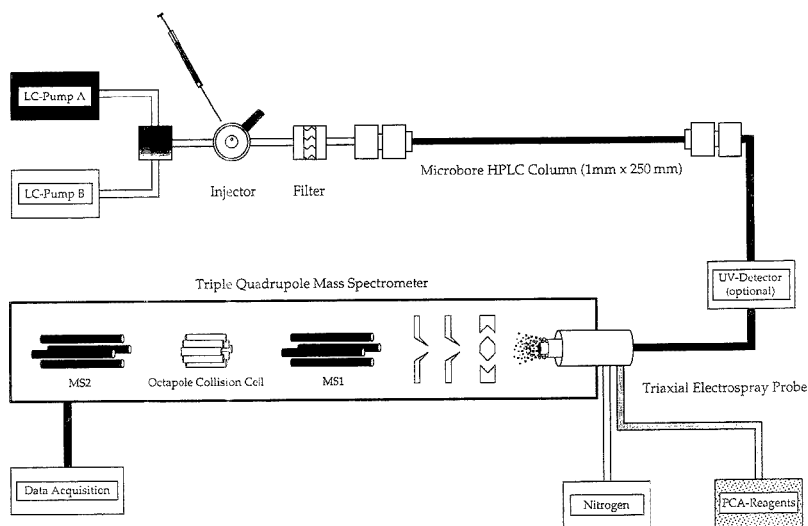


Figure 1. Setup of LC/MS/MS system for postcolumn addition of metal chlorides using a triaxial electro spray probe.

plexes on-line, directly within the ion source by adding a metal chloride solution as a sheath liquid.

LC separations were carried out on an aminopropyl stationary phase, a standard technique for separation of small oligosaccharides. Although high-performance anion-exchange chromatography (HPAE) is the method of choice for complex oligosaccharides, high pH, high sodium concentration, and the need of postcolumn desalting of the mobile phase make on-line HPAE/MS a nontrivial task.^{3,4}

Here, we present data that demonstrate the applicability of this new approach to two four-component test mixtures. Depending on the metal chosen, one observes either increased sensitivity in detecting the carbohydrate or informative MS/MS data for structural analysis.

EXPERIMENTAL SECTION

Chromatography. The mobile phase was delivered by a Phoenix 20 CU LC pump (Carlo Erba/Fisons Instruments, Beverly, MA). The sample mixture was injected using a 8125 low-dispersion injector (Rheodyne, Cotati, CA) with a 5 μ L probe loop. After passing a 0.5 μ m precolumn filter (Upchurch Scientific, Oak Harbor, WA), the sample mixture was separated on a microbore HPLC column (Spherisorb s5-NH₂, 25 cm \times 1 mm; Phase Separations, Norwalk, CT). All experiments were performed at a flow rate of 20 μ L/min employing gradient elution (mobile phase, acetonitrile/water, gradient: 0 min 100% acetonitrile, 10 min 50% acetonitrile, 20 min 12% acetonitrile, 30–60 min 0% acetonitrile). Before each run, the column was conditioned for 30 min with acetonitrile. Retention time reproducibility was found to be $\pm 0.7\%$ (retention time, 25–30 min, average of 10 separations). Usually, between 10 pmol and 1 nmol of the sample mixture was injected using a 2.5 μ L syringe (Hamilton, Reno, NV). The injection volumes were maintained between 0.1 and 1 μ L by adjusting the sample concentration. The triaxial electro spray probe was operated at a sample flow rate of 20 μ L/min (no splitting).

Mass Spectrometry. Conventional (MS) and tandem electro spray mass spectra (MS/MS) were collected on a VG-BioQ (Fisons Instruments, Beverly, MA) triple-quadrupole electro spray mass spectrometer, equipped with an octapole collision cell. The potential of the capillary was set to 4 kV and the counter electrode was held at 1.25 kV. All spectra were measured at a cone voltage of 70 V. The ion source temperature was set to 80 $^{\circ}$ C. Argon was used as a collision gas at a pressure of $(1.0\text{--}1.2) \times 10^{-3}$ mbar. The collision energy (E_{lab}) was set to 20 eV for cellobiose, nigerose, and Lewis a, to 40 eV for di-*N*-acetylchitobiose, tri-*N*-acetylchitotriose, and Lewis X, to 60 eV for LNFP-V, and to 80 eV for LNFP-I. A mass range between m/z 380 and 940 was scanned for conventional mass spectra and the scan time was set to 2.5 s. The data system was set up to acquire on-line MS/MS data over the mass range of each individual oligosaccharide–metal complex (e.g., the instrument was scanned from m/z 100 to 400 for cellobiose and then switched to scan from m/z 100 to 500 for di-*N*-acetylchitobiose). The MS/MS scan time was set to 5 s. After a solvent delay of 15 min, MS and MS/MS scans were performed alternately (2.5 s MS, 4 \times 5 s MS/MS for each individual compound) for 30 min. The average amount of sample consumed for a particular spectrum was calculated by dividing the amount of sample injected by the size of the elution time window (peak width at base, typically 60 s) multiplied by the total scan time (number of scans \times scan time, typically one or two scans, 5 s each). Data were baseline subtracted and smoothed using the MassLynx 2.0 software (Fisons Instruments, Beverly, MA). Reference spectra of the carbohydrate test mixtures I and II were taken by direct infusion of 5 μ L of a solution of each component, mixed with an equal amount of CoCl₂ at a concentration of 1.5 nmol/ μ L in acetonitrile/water 1:1.

Postcolumn Addition: Setup and Optimization. A commercially available triaxial electro spray probe (Fisons Instruments) was used for the experiments described. This probe consists of three coaxial stainless steel tubes (outer diameters, 0.034, 0.018,

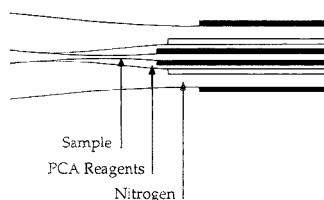


Figure 2. Tip of the triaxial electrospray probe.

and 0.010 in.). The sample is delivered to the innermost tube, the metal chloride solution flows through the tube in the middle, and the nebulizer gas (nitrogen) is delivered by the outermost tube (see Figure 2). As postcolumn addition (PCA) reagents, 1 nmol/ μ L solutions of the corresponding metal chloride in acetonitrile/water (1:1) were prepared. The metal chloride solution was transferred to the triaxial probe by a syringe pump (Harvard, S. Natick, MA) at flow rates between 1.67 and 5 μ L/min. Both the sample and the PCA reagent were sprayed at the same time, thus ensuring in-source mixing. The flow rate of the PCA reagent as well as of the nebulizer and bath gas was previously optimized to obtain maximum abundances of the carbohydrate-metal complexes.

Samples. Cellobiose and nigerose were purchased from Sigma (St. Louis, MO), di-*N*-acetylchitobiose and tri-*N*-acetylchitotriose were obtained from Seikagaku (Rockville, MD). Lewis X, Lewis a, and LNFP-V were purchased from Oxford GlycoSystems (Rosedale, NY). HPLC-grade water, acetic acid, and CoCl_2 were obtained from Fisher Scientific (Pittsburgh, PA). LiCl was purchased from Allied Chemical (Morristown, NJ). NaCl and RbCl were obtained from Aldrich (Milwaukee, WI). KCl and CsCl were purchased from Alfa Inorganics (Beverly, MA). The sample mixtures were prepared by dissolving 2 μ L of a 10 nmol/ μ L stock solution of each of the four carbohydrates in 12 μ L of HPLC-grade water (carbohydrate test mixture I, cellobiose, di-*N*-acetylchitobiose, Lewis X, LNFP-V; carbohydrate test mixture II, nigerose, tri-*N*-acetylchitotriose, Lewis a, LNFP-I). All reagents were used without further purification.

RESULTS AND DISCUSSION

Postcolumn addition of metal chlorides using a triaxial electrospray probe can be used to accomplish two goals in on-line carbohydrate analysis: sensitivity enhancement and structural analysis. This is demonstrated using two oligosaccharide test mixtures, each consisting of four oligosaccharides with different linkages, branch points, substitution patterns, and size (structures provided on Figures 6B and 7B). After separation on a microbore HPLC column, on-line PCA and electrospray tandem mass spectrometry (LC/MS/MS) of the individual components was carried out. Sensitivity enhancement was obtained by forming lithiated complexes through PCA of LiCl, taking advantage of the high affinity of lithium to oligosaccharides¹⁵⁻¹⁷ and the high ionization efficiency of the $[\text{M} + \text{Li}]^+$ adduct.²³ However, tandem mass spectrometry of lithiated branched oligosaccharides,¹⁵ and particularly those containing *N*-acetyl functionalities, does not lend itself to detailed structural analysis as it does when the oligosaccharides are straight-chain hexose polymers. For these particular

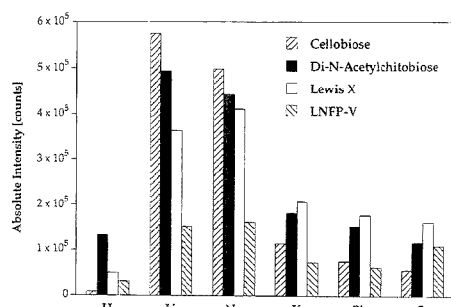


Figure 3. Abundance of the protonated carbohydrate and the carbohydrate-metal complexes of Li, Na, K, Rb, and Cs, generated with postcolumn addition of a solution of the corresponding metal chloride to carbohydrate test mixture I ($c = 100$ pmol/ μ L).

types of carbohydrates, we have found that cobalt is much more effective as the coordinating metal.¹⁶

The work presented herein focusses on three issues using electrospray ionization: (1) sensitivity enhancement of the oligosaccharide-alkali metal complexes versus the protonated species, (2) application of postcolumn addition of LiCl to enhance the detection limits in LC/MS, and 3) use of postcolumn addition of CoCl_2 and on-line LC/MS/MS in obtaining specific structural information.

Carbohydrate Complexes with Alkali Metals Generated by PCA of Metal Chlorides. The formation of oligosaccharide-alkali metal complexes using PCA of the metal chlorides of lithium, sodium, potassium, rubidium, and cesium was investigated. Test mixture I containing cellobiose, di-*N*-acetylchitobiose, Lewis X, and LNFP-V (100 pmol each) was first separated by HPLC. The eluents then enter the inner capillary of the triaxial probe whereupon the metal chloride is simultaneously introduced via the middle tube of the probe (Figure 2). The mixed sprays of both analytes and PCA reagents are then introduced into the ion source via the probe and undergo electrospray ionization. For comparison with the alkali metals, the same experiment was carried out using a 1% solution of acetic acid as the PCA reagent, again introduced via the middle capillary of the probe. The absolute intensities of the ions representing the oligosaccharide-metal complexes, $[\text{M} + \text{metal}]^+$, along with the protonated ion $[\text{M} + \text{H}]^+$, are shown in Figure 3. The abundances of the oligosaccharide-alkali metal ions are notably higher than those for the protonated ions, even though there is a large excess of protons available for complexation (1% acetic acid corresponds to a H^+ concentration of 167 nmol/ μ L).

The most significant increase in intensity was observed for cellobiose. The signal of the $[\text{M} + \text{Li}]^+$ ion was found to be approximately 70 times more abundant than the corresponding $[\text{M} + \text{H}]^+$ signal. Lithium was found to have the highest affinity to cellobiose and di-*N*-acetylchitobiose, whereas Lewis X and LNFP-V showed a slightly higher affinity to sodium. This is not surprising, since earlier investigations have shown that lithium coordinates quite well to straight-chain oligomers but is less tightly held by branched oligosaccharides.¹³⁻¹⁷ Although the difference between the coordination affinity of these four oligosaccharides for lithium and sodium is small, a sharp drop in affinity is found when alkali metals of larger ionic radii, such as potassium, rubidium, and cesium, are used as the PCA reagent. All four

(23) Leary, J. A.; Pedersen, S. F. *J. Org. Chem.* **1989**, *54*, 5650-5651.

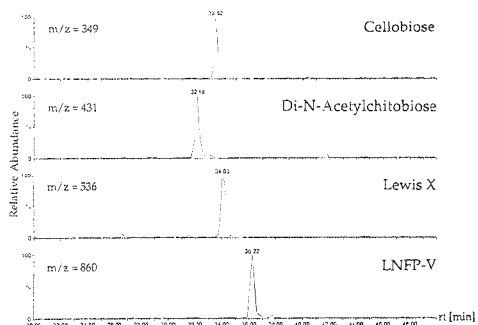


Figure 4. LC/MS of 100 pmol of carbohydrate test mixture I (amount injected) with postcolumn addition of LiCl ($c = 1 \text{ nmol}/\mu\text{L}$; flow rate, $5 \mu\text{L}/\text{min}$) as a function of time. Reconstructed ion chromatograms of the $[\text{M} + \text{Li}]^+$ adducts (m/z 349, 431, 536, and 860).

oligosaccharides investigated show a gradual decline in affinity in going down the group I metals. The only case where a slight perturbation in this trend is observed is for the pentasaccharide LNFP-V. In this case, cesium is preferred over rubidium and potassium but is still less favored than lithium and sodium.

The high abundance of the $[\text{M} + \text{Li}]^+$ complexes obtained compared to the corresponding $[\text{M} + \text{H}]^+$ species clearly indicates the potential of postcolumn addition of lithium and sodium for enhancing the detection of oligosaccharides. The results found for PCA of LiCl are comparable to those of an ESI study of polyether antibiotics (lasalocid), where the presence of 5 mM NaCl was reported to increase the instrumental response for 100 ng of lasalocid by 75-fold.²⁴

LC/MS with Postcolumn Addition of LiCl. In order to demonstrate the sensitivity enhancement obtained by postcolumn addition of LiCl using a triaxial electrospray probe, a series of LC/MS/MS experiments were undertaken to investigate the efficiency of the formation of the $[\text{M} + \text{Li}]^+$ ion. An LC/MS analysis of 100 pmol of test mixture I with PCA of LiCl is shown in Figure 4. The mass chromatogram shows separation of all four components along with strong signals for the lithium adducts at m/z 349, 431, 536, and 860. The same LC/MS experiment was repeated with 10 pmol of test mixture I, in which case an $[\text{M} + \text{Li}]^+$ ion was detected at a total consumption of 1.7 pmol as shown in Figure 5 (cellobiose is not shown due to high background noise for this component).

These data demonstrate that the process of formation of the lithium-oligosaccharide complex with PCA using the triaxial probe is quite effective. We have determined that thresholds for the concentration of the PCA reagent and detection sensitivities of the oligosaccharide are in the same range and, in some cases, better than that obtained when an individual carbohydrate is premixed with LiCl without use of the triaxial probe. Clearly, the postcolumn addition technique is more advantageous in that the sample can be chromatographed; i.e., the chromatography of the mixture can be accomplished without the deleterious effects of having metal salts present prior to separation. Higher sensitivities for alkali metal-oligosaccharide complexes can be obtained by electrospray ionization as compared to thermospray (TSP) ioniza-

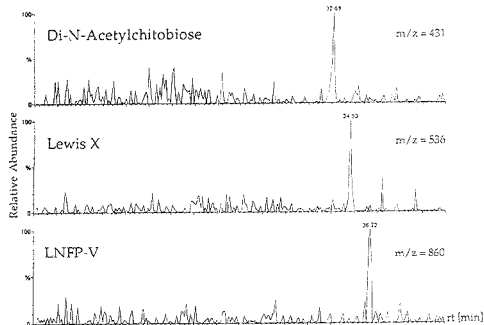


Figure 5. LC/MS of 10 pmol of carbohydrate test mixture I (amount injected) with postcolumn addition of LiCl ($c = 1 \text{ nmol}/\mu\text{L}$; flow rate, $5 \mu\text{L}/\text{min}$) as a function of time. Reconstructed ion chromatograms of the $[\text{M} + \text{Li}]^+$ adducts (m/z 431, 536, and 860). Scan time, 10 s; one scan; sample consumption, 1.7 pmol.

tion. Niessen et al.¹¹ reported data in an on-line LC/TSP-MS study where 20 μg of a maltodextrin mixture (multiple ion detection of the $[\text{M} + \text{Na}]^+$ adducts) was required for analysis. The authors claim that the same sensitivity was observed for the lithiated adducts. Similarly, in a study using HPAE/TSP-MS by Simpson et al.,³ the authors reported detection limits of 2.5 nmol for GlcNAc, ManNAc, and LacNAc.

LC/MS/MS with PCA of CoCl_2 . We have shown previously that MS/MS of lithium-coordinated branched trisaccharides does not provide enough information to determine glycosidic linkage position.¹⁵ This is also the case with *N*-acetylhexosamines containing oligosaccharides. In order to obtain linkage-specific fragmentation for branched oligosaccharides and structures containing *N*-acetyl functionalities, experiments with postcolumn addition of CoCl_2 were carried out.¹⁶

Using a 100 pmol/ μL solution of cellobiose in acetonitrile/water (1:1) as a test compound, the flow rates of the sample (1–50 $\mu\text{L}/\text{min}$), the postcolumn addition reagent (1.67–20 $\mu\text{L}/\text{min}$), the nebulizer gas (0–40 L/h), and the bath gas (0–500 L/h) were optimized to obtain a maximum abundance of the $[\text{M} + \text{Co} - \text{H}]^-$ precursor ion. Optimum flow rates found were the following: sample, 20 $\mu\text{L}/\text{min}$; postcolumn addition reagents, 1.67 $\mu\text{L}/\text{min}$; nebulizer gas, 40 L/h and bath gas, 300 L/h. During the course of these optimizations, it was observed that the ratio of $[\text{M} + \text{Co} - \text{H}]^+$ to $[\text{M} + \text{CoCl}]^+$ decreases significantly with increasing flow rate of the postcolumn reagent (also the absolute intensity of $[\text{M} + \text{Co} - \text{H}]^+$ decreases by approximately 50%). A low flow rate of 1.67 $\mu\text{L}/\text{min}$ was chosen to enhance the abundance of the $[\text{M} + \text{Co} - \text{H}]^-$ species. The sensitivity of the mass spectrometer (absolute intensity divided by flow rate) as a function of sample flow rate was studied with the same experimental setup. The response of the instrument drops less than 10% if the sample flow rate is increased from 4 to 20 $\mu\text{L}/\text{min}$. Therefore, splitting of the sample flow after chromatography to obtain higher sensitivity was not considered necessary.

The reconstructed ion chromatograms and MS/MS spectra of the LC/MS/MS run of carbohydrate test mixture I with PCA of CoCl_2 are shown in Figure 6. All four components could be separated, although cellobiose and di-*N*-acetylchitobiose elute shortly after each other (Figure 6A). Generally, the specificity of reconstructed ion chromatograms is high; however, some

(24) Schneider, R. P.; Lynch, M. J.; Ericson, J. F.; Fouda, H. G. *Anal. Chem.* 1991, 63, 1789–1794.

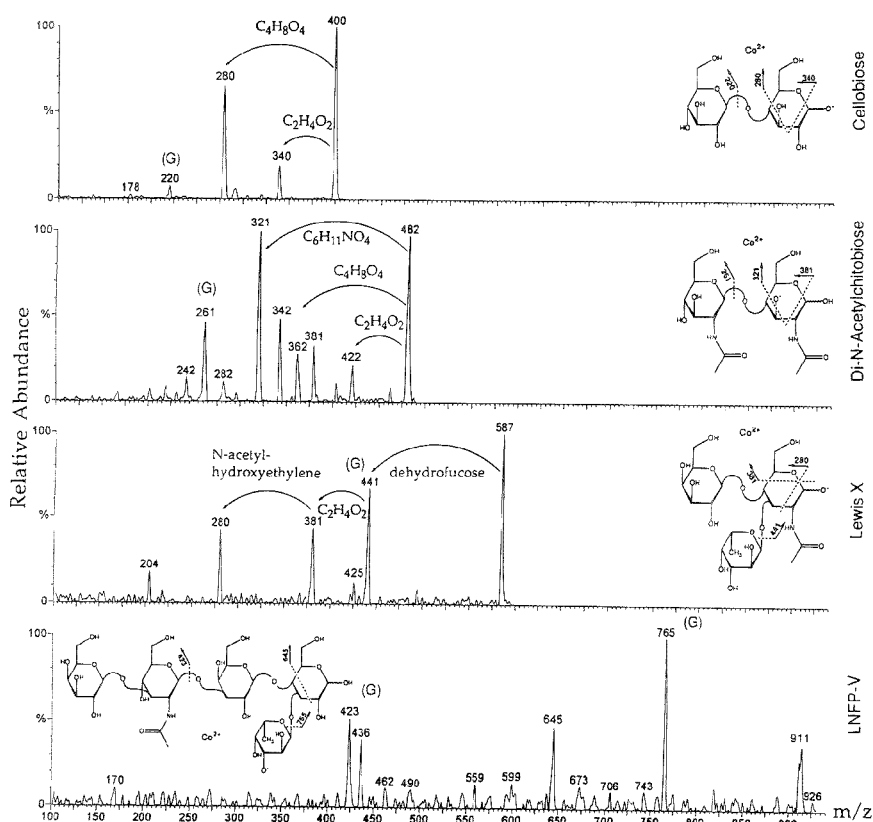
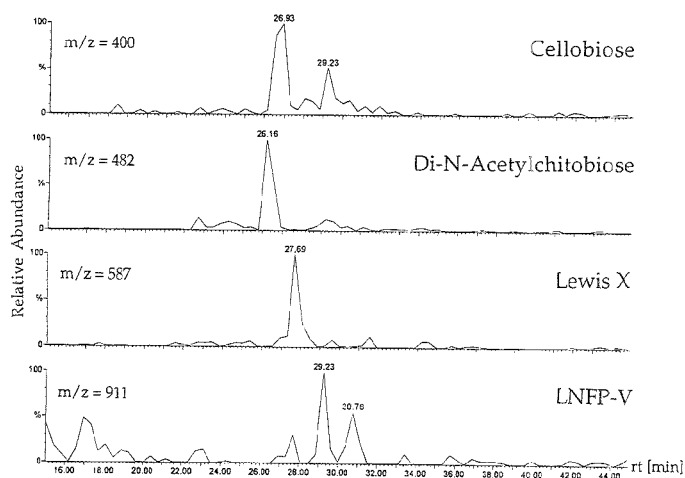


Figure 6. LC/MS/MS of 1 nmol of carbohydrate test mixture I (amount injected) with postcolumn addition of $CoCl_2$ ($c = 1 \text{ nmol}/\mu\text{L}$; flow rate, $1.67 \mu\text{L}/\text{min}$). (A, top) Reconstructed on chromatograms of the $[M + Co - H]^+$ adducts (m/z 400, 482, 587, and 911). (B, bottom) On-line LC/MS/MS spectra of $[M + Co - H]^+$. Collision energies: 20 eV for cellobiose and Lewis X, 40 eV for di-*N*-acetylchitobiose, and 60 eV for LNFP-V. The pressure was set to 1.1×10^{-3} mbar (argon); scan time, 2.5 s for MS, 5 s for MS/MS; (G), glycosidic cleavages; sample consumption, 83 pmol (one scan).

interferences are observed. For example, the cellobiose-cobalt adduct $[M + Co - H]^+$ at m/z 400 elutes at 26.93 min, while a second peak representing an ion at m/z 400 was observed at 29.23 min. This species was found to be a minor fragment of LNFP-V, generated by in-source CID. This is confirmed by the fact that the retention time of this component is the same as the retention time of LNFP-V. Further evidence is given by the MS/MS spectra of this species, showing characteristic neutral losses of 60 and 120 amu. The signal at 30.76 min could not be readily explained by analyzing the MS and MS/MS spectra, and is attributed to the high noise level of the reconstructed ion chromatogram of LNFP-V.

The MS/MS spectra, corresponding to the four components of carbohydrate test mixture I are shown in Figure 6B. All spectra presented correspond to a sample consumption of 83 pmol (one scan). Collision-induced dissociation (CID) of the $[M + Co - H]^+$ complexes yields cross ring fragmentation, which allows determination of the specific linkages.¹³⁻¹⁷ For cellobiose, losses of $C_2H_4O_2$ (m/z 340) and $C_4H_8O_4$ (m/z 280) are observed which are characteristic of a 1,4-linkage. A glycosidic cleavage ion is also observed at m/z 220.

The MS/MS spectrum of di-*N*-acetylchitobiose, a β (1,4)-linked disaccharide possessing two *N*-acetyl functionalities, shows losses of $C_2H_4O_2$ (m/z 422) and $C_4H_8O_4$ (m/z 362) as well as the loss of carbons 1 and 2 (the numbering system for saccharides follows the conventional nomenclature: i.e., carbon 1 (C1) is the reducing-end anomeric position with subsequent numbering proceeding clockwise) together with the *N*-acetyl group (m/z 381). A glycosidic cleavage ion is observed at m/z 261. This dissociation is quite different from what we have observed previously. In this particular case it would appear that C5 and C6 are lost in the first $C_2H_4O_2$ dissociation (m/z 422). Whereas, the losses of C1 and C2 with the *N*-acetyl function and then subsequent losses of C5 and C6 are the typical cleavages observed for 1,4-linked metal-coordinated oligosaccharides.¹³⁻¹⁷ The ion at m/z 362 is also puzzling and would appear to be an additional loss of $C_2H_4O_2$ from m/z 422. If this is the case, then clearly the only other location containing a contiguous $C_2H_4O_2$ ene-diol or aldehyde is on the nonreducing ring. This also applies for the ion detected at m/z 342; i.e., the only contiguous-four carbon chain that is not tied up in a linkage and/or does not contain an *N*-acetyl group is on the nonreducing ring. Since this is the first time we have looked at oligomers containing two *N*-acetyl functionalities on adjacent rings, we plan to carry out ^{18}O and 2H labeling studies in addition to precursor ion scans to determine the specific sites of cleavage.

The third compound, Lewis X, features a loss of dehydrofucose (m/z 441), followed by elimination of $C_2H_4O_2$ (m/z 381) and *N*-acetylhydroxyethylene ($C_4H_7O_2N$, m/z 280). The signal at m/z 204 represents either $[HexNAc]^+$ or $[dehydrofucose + Co - H]^+$. Due to the fact that we have never observed the loss of the metal employing low-energy CID during earlier experiments, we assume this ion to be the latter, generated through a second reaction channel from the $[M + Co - H]^+$ precursor. The loss of $C_2H_4O_2$ and $C_4H_7O_2N$ after the initial dehydrofucose loss suggests that this monosaccharide is 1,4-linked to the nonreducing ring and the fucose ring is branched off C3 of the reducing ring. These pathways are similar to those observed for other branched trisaccharides studied which were ^{18}O and 2H labeled and studied in detail.¹⁵

The MS/MS spectrum of LNFP-V shows an immediate loss of dehydrofucose (m/z 765) and subsequent cleavage of the adjacent ring (m/z 645). The signal at m/z 423 represents a glycosidic cleavage. For a complete analysis of this pentasaccharide, further MS/MS spectra of the individual fragments obtained from the $[M + Co - H]^+$ complex through in-source CID are required (MS/MS/MS). These can be obtained by a second LC/MS/MS run of the sample at high cone voltage.

The data collected for the first three compounds are in good agreement with reference spectra, verified by ESI-MS of the single compounds previously premixed with an equivalent amount of $CoCl_2$. The last compound of this mixture, LNFP-V, turned out to be the most challenging species in terms of both sensitivity and structural delineation. The LC/MS/MS spectra of cellobiose, di-*N*-acetylchitobiose and Lewis X were acquired using as little as 200 pmol. However, at least 500 pmol to 1 nmol of LNFP-V was needed to obtain spectra containing sufficient detail for complete structural analysis. It is quite likely that a different metal ion would coordinate better with the higher molecular weight oligosaccharides and give more structural detail. A parallel study is currently underway in which a survey of different metals and their coordination to high mannose core pentasaccharides are being investigated. We anticipate that these experiments will provide more insight into obtaining structural information of these larger, branched oligomers. We are also investigating the collision conditions needed to dissociate these larger oligosaccharides. In fact, the ESI and MS/MS conditions optimized for the first three compounds in the mixture are not quite optimal for the LNFP pentasaccharides.

A second example of an LC/MS/MS analysis with postcolumn addition of $CoCl_2$ is provided in Figure 7. Both the reconstructed ion chromatograms and the MS/MS spectra of test mixture II are shown. All four components were clearly separated (Figure 7A). The reconstructed ion chromatogram for m/z 400 again shows two peaks. The first signal at 26.54 min represents the nigerose-cobalt adduct, $[M + Co - H]^+$, while the second signal at 29.61 arises from in-source CID of LNFP-I. Again, MS/MS spectra of this species show characteristic neutral losses of 60 and 120 amu. The signals at 26.93 and 31.14 min could not be explained by analyzing the MS and MS/MS spectra and are attributed to the significantly higher noise level of the reconstructed ion chromatogram of LNFP-I.

The MS/MS spectra of the $[M + Co - H]^+$ adducts of each of the four components of test mixture II are shown in Figure 7B. The spectra of nigerose and tri-*N*-acetylchitotriose correspond to a sample consumption of 83 pmol (one scan). For Lewis a and LNFP-I, 167 pmol was consumed (two scans). The MS/MS spectrum of nigerose, an α (1,3)-linked disaccharide, shows losses of $C_2H_6O_3$ (m/z 310) and $C_4H_8O_4$ (m/z 280), characteristic of a 1,3-linkage.¹³⁻¹⁷ For Lewis a, loss of dehydrofucose (m/z 441), followed by a loss of $C_4H_8O_4$ (m/z 321) is observed. The striking difference of this MS/MS spectrum compared with that for Lewis X is the fact that there is no observed loss of C1 and C2 (containing the *N*-acetyl functionality) as was the case with Lewis X. Given the fact that the only difference in these two isomers is the reversal of the fucose and galactose rings, this difference in dissociation is surprising. It is possible that the geometry of the structure of the cobalt-Lewis a complex leads to stabilization of the *N*-acetyl group, thus hindering dissociation.

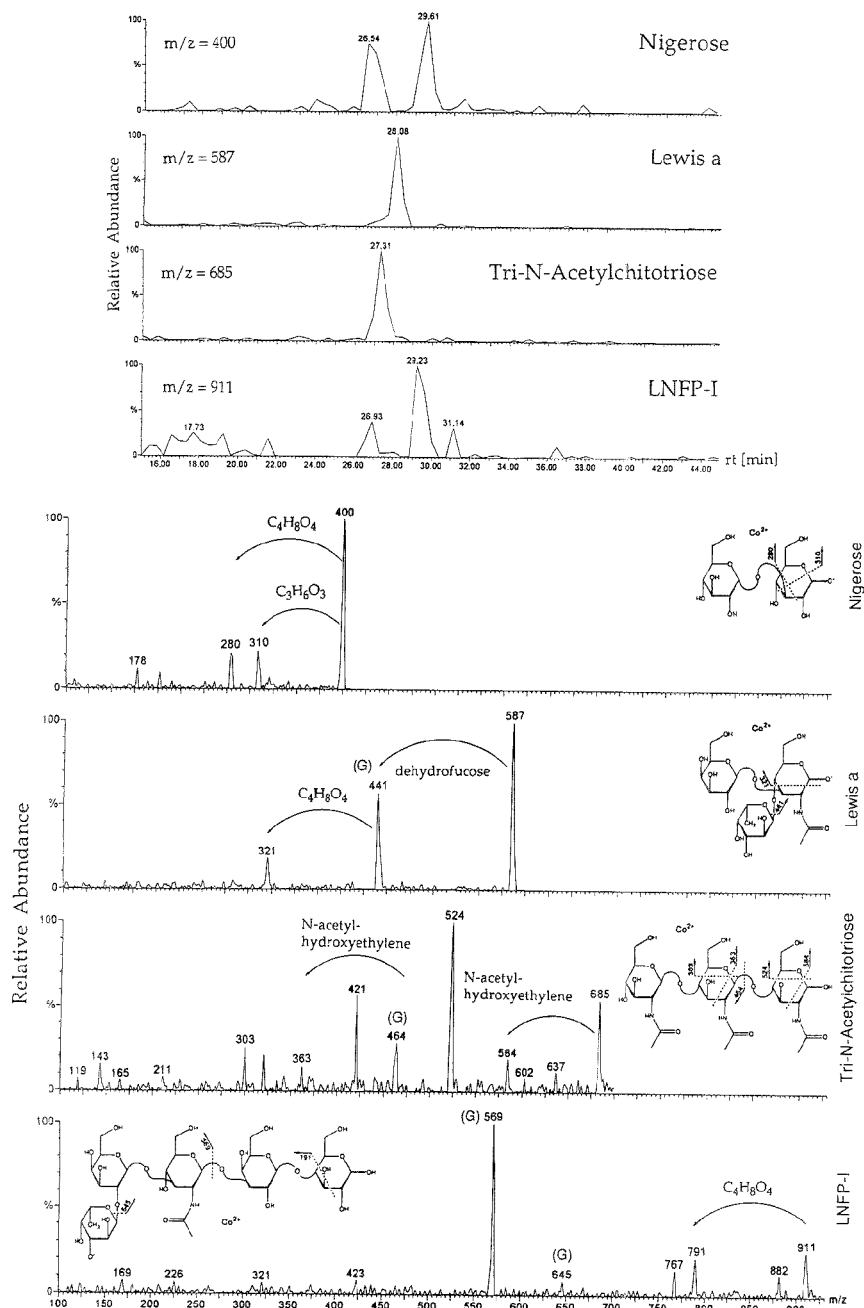


Figure 7. LC/MS/MS of 1 nmol of carbohydrate test mixture II (amount injected) with postcolumn addition of $CoCl_2$ ($c = 1 \text{ nmol}/\mu\text{L}$; flow rate, $1.67 \mu\text{L}/\text{min}$) as a function of time. (A, top) Reconstructed ion chromatograms of the $[M + Co - H]^-$ adducts (m/z 400, 587, 685, and 911). (B, bottom) On-line LC/MS/MS spectra. Collision energies: 20 eV for nigerose and Lewis a, 40 eV for tri-*N*-acetylchitotriose, and 80 eV for LNFP-I. The pressure was set to 1.1×10^{-5} mbar (argon); scan time, 2.5 s for MS, 5 s for MS/MS; (G), glycosidic cleavages; sample consumption, 83 pmol (one scan) for nigerose and tri-*N*-acetylchitotriose and 167 pmol for Lewis a and LNFP-I (two scans).

The MS/MS spectrum of tri-*N*-acetylchitotriose shows losses of *N*-acetylhydroxyethylene (m/z 584) followed by the loss of $C_2H_4O_2$ (m/z 524) as expected for a 1,4-linkage. This pattern is repeated for the middle ring with losses again corresponding to $C_4H_8O_2N$ (m/z 363) and $C_2H_4O_2$ (m/z 303), indicating that the linkage between the nonreducing and middle rings is also 1,4-linked. A glycosidic cleavage ion is also detected at m/z 464. Unfortunately, placement of the *N*-acetyl group on the nonreducing ring could not be determined.

For LNFP-I, a cross-ring cleavage ion at the reducing ring is observed at m/z 791 and the signal at m/z 645 results from the loss of dehydrofucose. A prominent ion is observed at m/z 569, indicating glycosidic cleavage. LNFP-I was the most difficult species to analyze. Not all signals found in the corresponding reference spectrum are found in the MS/MS spectrum of LNFP-I; however, some of the important fragments can be clearly identified. The spectrum shown in Figure 7B corresponds to a sample consumption of 167 pmol, which represents the lower sample limit required for the given instrumental setup.

CONCLUSIONS

Postcolumn addition of metal chlorides using a triaxial electrospray probe was found to be a versatile technique to form metal complexes of carbohydrates for subsequent on-line MS and MS/MS analysis. Thresholds for the concentration of the PCA reagent and detection sensitivities for carbohydrates were found to be in the same range or better when the sample is directly mixed with the postcolumn addition reagent before analysis (off-line). Compared to the conventional way of adding the postcolumn reagents using a mixing tee, the technique presented in this work does not increase the dead volume of the chromatographic system and

may be accomplished by a low-pressure syringe pump. Furthermore, on-line postcolumn addition allows use of standard chromatographic procedures because the reagents are added after the separation process and thus have no influence on the chromatography.

Two different metals, lithium and cobalt, were used to obtain high sensitivity and structure-specific fragmentation of carbohydrates. LC/MS/MS data (using postcolumn addition of $CoCl_2$) were obtained for sample amounts ranging from 1 nmol (Lewis X, LNFP-V) to 200 pmol (cellobiose, di-*N*-acetylchitobiose), corresponding to sample consumptions of 83 and 17–33 pmol, respectively. LC/MS experiments using postcolumn addition of LiCl showed carbohydrate detection limits of 10 pmol, corresponding to a sample consumption of 1.7 pmol.

The application of this technique is not limited to carbohydrates. Application of postcolumn addition using a triaxial electrospray probe for metal coordination and analysis of other compounds like peptides is considered to be straightforward.

ACKNOWLEDGMENT

M.K. thanks the Swiss National Science Foundation for fellowship support during 1994. J.A.L. acknowledges NIH (GM 47356) for their support. This work was first presented at the 7th Tandem Mass Spectrometry Workshop, Chateau Lake Louise, Canada, November 1994.

Received for review March 29, 1995. Accepted June 29, 1995.*

AC950315A

* Abstract published in *Advance ACS Abstracts*, August 1, 1995.

Direct Analysis of Enzymatic Reactions of Oligosaccharides in Human Serum Using Matrix-Assisted Laser Desorption Ionization Mass Spectrometry

Randy M. Whittal, Monica M. Palcic, Ole Hindsgaul, and Liang Li*

Department of Chemistry, University of Alberta, Edmonton, Alberta, Canada T6G 2G2

Matrix-assisted laser desorption ionization mass spectrometry has been developed for direct mass analysis of enzymatic reaction products of oligosaccharides in human blood serum without the use of extraction or chromatographic separation. Molecular labeling of the substrate is used to achieve both the detection sensitivity and selectivity required in rapid analysis of reaction products in serum. It is found that tetramethylrhodamine (TMR)-labeled oligosaccharides provide 100-fold sensitivity enhancement over the corresponding underivatized oligosaccharides. In order to selectively retain the TMR-labeled molecules on the sample probe while washing away contaminants in a serum sample, a sample/matrix preparation method is developed. This technique provides detection sensitivity of labeled oligosaccharides in the range of hundreds of femtomoles per microliter. The mass measurement accuracy is better than 0.01% when a linear time-of-flight mass spectrometer is used. The application of the technique is illustrated for the subpicomole detection and quantitation of the conversion of the disaccharide $\alpha\text{Fuc}(1\rightarrow2)\beta\text{Gal-TMR}$ to the blood group B active trisaccharide $\alpha\text{Fuc}(1\rightarrow2)[\alpha\text{Gal}(1\rightarrow3)]\beta\text{Gal-TMR}$, catalyzed by the blood group B galactosyltransferase present in human serum.

Mass spectrometry using fast atom bombardment (FAB), electrospray, and matrix-assisted laser desorption ionization (MALDI) has recently been developed for the analysis of products of enzymatic reactions in biological fluids. For example, FAB mass spectrometry has been reported for analyzing endogenous met-enkephalin and β -endorphin from their respective precursors in human cerebrospinal fluid¹ and dynorphin A, dynorphin B, and α -neodynorphin from the prodynorphin precursor in human pituitary.² More recently, MALDI time-of-flight (TOF) mass spectrometry has been shown to be an effective method for mass analysis of the products of *in vitro* processing involving dynorphin A³ and cyclosporin A⁴ in human blood and neuropeptide Y in human cerebrospinal fluid.⁵ Electrospray mass spectrometry has been used as an assay for peptidyl- α -hydroxyglycine α -amidating

lyase enzyme.⁶ Although these techniques require an extensive sample cleanup (except that of Costello et al.⁵) through extraction, filtration, or chromatographic separation, the mass spectrometric approach provides high molecular specificity for the detection and identification of the reaction products.

We are exploring the use of the MALDI technique in the area of glycobiology. One of the major observations driving research in this new field is that the structures of the carbohydrate chains present on cell-surface glycoproteins and glycolipids present sites for the binding of viruses and bacteria, in addition to their roles in both normal and abnormal development and in cell-cell adhesion. In particular, developing embryonic cells, activated cells, and tumor cells all produce altered carbohydrate sequences on their cell surfaces, whose functions are only beginning to be understood.⁷ These altered carbohydrate structures appear to be the product of abnormal expression of the class of enzymes termed glycosyltransferases, the enzymes that control the assembly of oligosaccharides.⁸ The ability to monitor changes in the activity of these enzymes in cells and tissues is of prime importance in understanding the regulation of their expression, and ideally, the required assays of enzyme activities should be simple and applicable to crude cell or tissue homogenates, including blood and serum.

The assay of glycosyltransferases in cells or tissues usually involves quantitation of the transfer of ³H- or ¹³C-labeled sugars from their sugar nucleotides to either an isolated or a synthetic oligosaccharide acceptor.^{9,10} While the technique is sensitive (down to ~1 pmol), there is no product characterization. This means that one cannot decide if one or more sugars have been added to the acceptor or if it is a degradation product of the acceptor that in fact becomes a substrate for another interfering glycosyltransferase. To partially overcome these difficulties, radioactive products can be separated by high-performance liquid chromatography (HPLC) and characterized by coelution with authentic standards, if these are available.^{11,12} There are distinct

(1) Liu, D.; Wood, G. W.; Desiderio, D. M. *J. Chromatogr.* 1990, 530, 235-252.

(2) Silberring, J.; Brostedt, P.; Thornwall, M.; Nyberg, F. *J. Chromatogr.* 1991, 554, 83-90.

(3) Chou, J. Z.; Kreek, M. J.; Chait, B. T. *J. Am. Soc. Mass Spectrom.* 1994, 5, 10-16.

(4) Muddiman, D. C.; Gusev, A. I.; Proctor, A.; Hercules, D. M.; Venkataraman, R.; Diven, W. *Anal. Chem.* 1994, 66, 2362-2368.

(5) Costello, C. E.; Juhasz, P.; Ekman, R.; Heilig, M.; Agren, H. *Proceedings of the 42nd ASMS Conference on Mass Spectrometry and Allied Topics*, Chicago, Illinois, May 29-June 3, 1994; p 25.

(6) Unsworth, E. J.; Treston, A. M. *Proceedings of the 42nd ASMS Conference on Mass Spectrometry and Allied Topics*, Chicago, Illinois, May 29-June 3, 1994; p 154.

(7) Varki, A. *Glycobiology* 1993, 3, 97-130.

(8) Schachter, H. In *Molecular Glycobiology*; Fukuda, M., Hindsgaul, O., Eds.; IRL Press: Oxford, UK, 1994; pp 88-162.

(9) Sadler, J. E.; Beyer, T. A.; Oppenheimer, C. L.; Paulson, J. C.; Prieels, J. P.; Rearick, J. I.; Hill, R. L. *Methods Enzymol.* 1982, 83, 458-514.

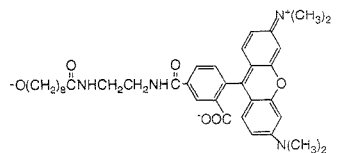
(10) Palcic, M. M.; Heerze, L. D.; Pierce, M.; Hindsgaul, O. *Glycoconjugate J.* 1988, 5, 49-63.

advantages to such chromatographic methods, but they remain very time consuming. Replacement of the radiolabels with fluorescent probes can result in dramatic increases in sensitivity, but again, either HPLC or electrophoresis is needed to gain evidence for formation of the expected products.¹³⁻¹⁶ Finally, immunological-based methods, where product formation is both detected and structurally characterized by a specific protein, are very powerful and sensitive (100 fmol). Such methods, however, require the production of either a refined polyclonal antiserum or a monoclonal antibody or the availability of a sequence-specific lectin.¹⁷⁻²¹

Reported herein is the development of a MALDI method for the rapid and sensitive detection of the product of a glycosyltransferase enzyme reaction. Blood group B galactosyltransferase enzyme occurs naturally in the serum of blood group B individuals. This enzyme transfers a galactose residue from uridine diphosphogalactose (UDP-Gal) in α -linkage to OH-3 of the galactose residue in oligosaccharide chains terminating in the sequence α Fuc(1 \rightarrow 2) β Gal producing the blood group-B antigenic determinant α Fuc(1 \rightarrow 2)[α Gal(1 \rightarrow 3)] β Gal. This is an ideal model system for the development of sensitive assays for the products of enzymes involved in oligosaccharide biosynthesis or degradation since this enzyme is present in very low abundance in an extremely crude sample: human serum. Serum of individuals lacking this enzyme activity, e.g., blood group O or A individuals, is additionally available as a control.

The fast MALDI assay presented in this report represents one of the so-called mass tracer methods we are currently developing. By analogy to well-established radioassay tracer and fluorescent tracer techniques, mass tracer methods are based on mass spectrometry for monitoring chemical, enzymatic, or other changes in biological systems, with no or minimal sample preparation in detection. In this MALDI method, an appropriate functional group is linked to the target molecules, and then the MALDI technique is used to follow the transformation of the labeled molecular species. After experimenting with different labeling groups, we find that tetramethylrhodamine (TMR) derivatives of oligosaccharides are \sim 100-fold more sensitive than underivatized oligosaccharides. Moreover, we have developed a sample preparation method for mixing samples and matrix for on-probe sample cleanup. With this method, salts, buffers, and other potential interfering contaminants in serum are washed away, and yet the TMR-labeled species are selectively retained on the sample probe.

Chart 1

Structure	Abbreviation
α Fuc(1 \rightarrow 2) β Gal —	disac-
α Fuc(1 \rightarrow 2)[α Gal(1 \rightarrow 3)] β Gal —	B-
α Fuc(1 \rightarrow 2) β Gal(1 \rightarrow 3)[α Fuc(1 \rightarrow 4)] β GlcNAc —	Le ^b -
$\cdot\text{O}-(\text{CH}_2)_6\text{COOCH}_3$	-MCO
	-TMR

MATERIALS AND METHODS

Preparation of Labeled Oligosaccharides. Chart 1 lists the structures and their respective abbreviations for the labeled oligosaccharides that pertain to this work. Le^b-OCH₃²¹ and Le^b-MCO²¹ as well as α Fuc(1 \rightarrow 2) β Gal-MCO (disac-MCO) and α Fuc(1 \rightarrow 2)[α Gal(1 \rightarrow 3)] β Gal-MCO (B-MCO),²² were available from earlier work. The conversion of MCO glycosides to their TMR derivatives was performed as previously described.^{15,16}

Enzyme Reactions. Five nanomoles of α Fuc(1 \rightarrow 2) β Gal-TMR (acceptor) in aqueous solution at 1 mg mL⁻¹ was added to an Eppendorf tube and lyophilized to dryness. After drying, 50 μ L of human serum (blood group B), 2 μ L of 2.5 mM UDP-Gal (donor), 0.6 μ L of 0.5 M MnCl₂, and 5 μ L of 0.5 M sodium cacodylate buffer (pH 7.1) were added. The mixture was incubated at 37 $^{\circ}$ C for 90 min, and an aliquot was used to check for the presence of product through MALDI analysis. The introduction of the TMR substituent has a minor effect on the galactosyltransferase reaction. Under the conditions employed for the in vitro conversion, the rate of reaction of the labeled species was found to be 90% that of the parent α Fuc(1 \rightarrow 2) β Gal-O(CH₂)₇CH₃ by standard radiochemical assay methods.¹⁰

MALDI Sample Preparation. All nonserum samples were prepared for MALDI analysis using the dried droplet method of sample preparation (see, for example, Hillenkamp et al.²³). 2,5-Dihydroxybenzoic acid (2,5-DHB) matrix solution was prepared at a concentration of 10 mg mL⁻¹ in 30% acetonitrile/water. α -Cyano-4-hydroxycinnamic acid (4-HCCA) matrix solution was prepared as a saturated solution (\sim 7 mg mL⁻¹) in 30% acetonitrile/water. The matrix solutions were mixed on a vortex mixer for 1 min and then centrifuged to remove undissolved matrix crystals. A 0.5 μ L aliquot of matrix solution and 0.5–1.0 μ L of analyte solution were placed on the sample probe and allowed to dry.

For samples analyzed from buffered human serum, 4-HCCA was used as the matrix. 4-HCCA matrix solution was prepared at a concentration of 20 mg mL⁻¹ in 70% acetonitrile/water. A 0.5 μ L aliquot of matrix solution was applied to the probe tip and allowed to dry. The high-concentration matrix solution produced a dense layer of matrix on the sample probe of \sim 2 mm diameter, giving a surface density of 17 nmol/mm². The serum sample was

- Koenderman, A. H. L.; Wijermans, P. W.; Van den Eijnden, D. H. *FEBS Lett.* **1987**, *222*, 42–46.
- Brockhausen, I.; Carver, J. P.; Schachter, H. *Biochem. Cell. Biol.* **1988**, *66*, 1134–1151.
- Honda, S.; Iwase, S.; Makino, A.; Fujiwara, S. *Anal. Biochem.* **1989**, *176*, 72–77.
- Lee, K. B.; Desai, U. R.; Paleic, M. M.; Hindsgeul, O.; Linhardt, R. J. *Anal. Biochem.* **1992**, *205*, 108–114.
- Zhao, J. Y.; Dovichi, N. J.; Hindsgeul, O.; Gosselin, S.; Paleic, M. M. *Glycobiology* **1994**, *4*, 238–242.
- Zhang, Y.; Le, X.; Dovichi, N. J.; Compston, C. A.; Paleic, M. M.; Diedrich, P.; Hindsgeul, O. *Anal. Biochem.*, in press.
- Stults, C. L.; Wilbur, B. J.; Macher, B. A. *Anal. Biochem.* **1988**, *174*, 151–156.
- Paleic, M. M.; Ratcliffe, R. W.; Lamontagne, L. R.; Good, A. H.; Alton, G.; Hindsgeul, O. *Carbohydr. Res.* **1990**, *196*, 133–140.
- Crawley, S. C.; Hindsgeul, O.; Alton, G.; Pierce, M.; Paleic, M. M. *Anal. Biochem.* **1990**, *185*, 112–117.
- Zatta, P. F.; Nyame, K.; Cormier, M. J.; Mattox, S. A.; Prieto, P. A.; Smith, D. F.; Cummings, R. D. *Anal. Biochem.* **1991**, *194*, 185–191.
- Spohr, U.; Morishima, N.; Hindsgeul, O.; Lemieux, R. U. *Can. J. Chem.* **1985**, *63*, 2664–2668.

(22) Lemieux, R. U. *Chem. Soc. Rev.* **1978**, *7*, 423–452.

(23) Hillenkamp, F.; Karas, M.; Beavis, R. C.; Chai, B. T. *Anal. Chem.* **1991**, *63*, 1193A–1203A.

diluted in half with 50% ethanol/water. On top of the matrix solution, 0.5–1.0 μL of the serum supernatant was applied. Just before the sample dried (~ 1 min), the probe tip was dipped into pure room temperature water for 45 s. Excess water was removed by gently touching a wiper to the edge of the sample probe. Washing the probe tip just before the sample dries proved more effective at removing the high concentration of buffers and other species present in serum. The washed probe tip was then inserted into the mass spectrometer.

TOFMS. A linear, time-lag focusing TOF mass spectrometer was used to collect all mass spectra. The MALDI instrument was designed and constructed at the University of Alberta. A detailed description of this system will be reported elsewhere. In brief, it consists of an acceleration region containing a repeller plate and an ion extraction plate to which 12 kV voltages are applied. After the laser desorption/ionization takes place, a pulsed voltage (1 kV) is applied to the repeller for ion extraction. The time delay between the ionization and ion extraction events is optimized at 280 ns and used throughout the work presented herein. The total flight tube length is about 1 m. A nitrogen laser (Photochemical Research Associates LN1000) is used to generate the MALDI ions. The mass spectrum is captured using either a LeCroy 9310M or 9350M digital oscilloscope. The major difference is the sampling rate. The 9350M scope provides a sampling rate of up to 1×10^9 samples/s or a time resolution of 1 ns/point, whereas the 9310M scope has a time resolution of 10 ns/point. High-resolution mass spectra are collected on the 9350M oscilloscope. All mass spectra are the result of signal averaging of 100 laser shots. Signal averaging was performed on the oscilloscope without selection. The averaged mass spectrum was then downloaded to a PC for processing.

RESULTS AND DISCUSSION

It has been shown that underivatized oligosaccharides can be ionized by MALDI.²⁴ However, the limit of detection for underivatized carbohydrates is 100 fmol (for reference standards in clean samples), which is somewhat higher than that obtained for peptides of similar mass.²⁵ For direct analysis of reaction products in serum, the detection sensitivity of MALDI needs to be improved. It has been found that peracetylation of neutral oligosaccharides enhances the detection sensitivity 10-fold²⁶ and permethylation enhances the sensitivity of glycolipids 100-fold.²⁶ After experimenting with different labeling groups, we find that TMR derivatives of oligosaccharides are ~ 100 -fold more sensitive than underivatized oligosaccharides.

Figure 1 shows the MALDI mass spectrum of a mixture of three derivatives of a model Le^b blood group active tetrasaccharide: 10 pmol of Le^b-OCH₃ (a simple methyl glycoside derivative), 1 pmol of Le^b-MCO (a more lipophilic derivative with an 8-methoxycarbonyloctyl aglycon), and 0.2 pmol of Le^b-TMR (with the TMR label attached to the MCO group). The spectra shown in Figure 1 are obtained by using 2,5-DHB as the matrix. 2,5-DHB has been reported to be a superior matrix among several substituted benzoic acids, cinnamic acids, and coumarins, including 4-HCCA and 3-amino-4-hydroxybenzoic acid.²³ The neutral sugars in the spectrum show two peaks due to cationization with both sodium and potassium. The peak observed for Le^b-TMR

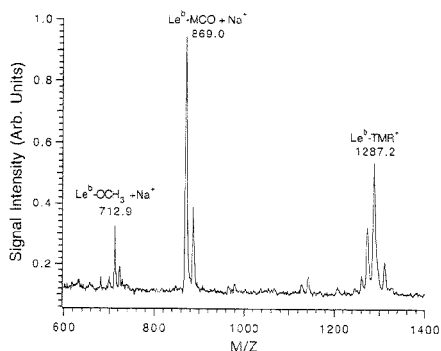


Figure 1. MALDI mass spectrum of a mixture of three derivatives of an oligosaccharide using 2,5-DHB as the matrix: 10 pmol of Le^b-OCH₃, 1 pmol of Le^b-MCO, and 0.2 pmol of Le^b-TMR.

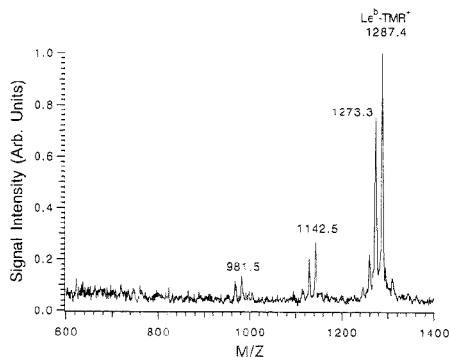


Figure 2. MALDI mass spectrum of 0.2 pmol of Le^b-TMR obtained using 4-HCCA as the matrix.

arises from protonation of the TMR zwitterion, although at this time it is unknown whether protonation occurs in the gas phase or if the TMR ion is desorbed preformed (see Chart 1). There is also a predominant peak (at $M - 14$), possibly due to the loss of CH₂ from TMR.²⁷ The signal/background ratios for Le^b-OCH₃, Le^b-MCO, and Le^b-TMR are 21, 82, and 42, respectively. The mass spectra obtained from more concentrated or more diluted solutions of the mixture used in Figure 1 display similar relative detection responses. Le^b-TMR is generally about 2–3-fold more sensitive than Le^b-MCO and 100-fold more sensitive than Le^b-OCH₃ with 2,5-DHB.

We find that the cinnamic acid derivative 4-HCCA can also provide good MALDI spectra for the TMR-labeled oligosaccharides. Figure 2 shows the MALDI spectrum of 0.2 pmol of Le^b-TMR acquired using 4-HCCA as the matrix. The peak at ($M - 14$) intensifies, and additional fragment peaks are observed at m/z 1142.5 (loss of fucose) and 981.5 (loss of fucose and galactose). This finding is not surprising in light of the fact that others have noted fragmentation increases with 4-HCCA matrix in reflectron TOF systems.²⁸ Fragmentation can take place during the time-

(24) Stahl, B.; Steup, M.; Karas, M.; Hillenkamp, F. *Anal. Chem.* **1991**, *63*, 1463–1466.

(25) Harvey, D. J. *Rapid Commun. Mass Spectrom.* **1993**, *7*, 614–619.

(26) Juhasz, P.; Costello, C. E. *J. Am. Soc. Mass Spectrom.* **1992**, *3*, 785–796.

(27) The study of several rhodamine derivatives using laser desorption/ionization mass spectrometry reveals a predominant peak for the loss of a single alkyl from the alkylamine on tetraalkylrhodamines. Whitall, R. M.; Li, L. unpublished results.

lag period (280 ns) in our instrument. Figure 2 also shows that the signal/background ratio improves to 60, a 50% improvement over that with 2,5-DHB. On the other hand, for $\text{Le}^b\text{-OCH}_3$ and $\text{Le}^b\text{-MCO}$, the signal/background ratio drops below 3 if the same quantity of neutral oligosaccharide is loaded, as in Figure 1. Several other TMR-labeled oligosaccharides have been examined, and similar results are obtained. In general, with a sample loading in the range of 100–200 fmol or a concentration of 100–200 fmol μL^{-1} , a well-defined molecular ion signal (analyte signal/background signal > 50) can be obtained for TMR-labeled species using 4-HCCA.

In order to analyze these labeled species in a buffered serum sample, sample/matrix preparation becomes very important. The MALDI technique is known to be able to tolerate salts and buffers to some extent. This is particularly true for peptide and protein analysis.²³ The dried droplet method for preparing matrix crystals followed by on-probe sample washing is a simple technique, but it is often not very effective in removing a high concentration of contaminants. In the case of buffered serum, the dried droplet method using either 2,5-DHB or 4-HCCA fails to form crystals, and a spectrum of only background noise is obtained (not shown). There are several other refined methods reported to wash away potentially interfering contaminants on the probe. In particular, the fast evaporation method of Vorm et al.²⁹ and the pressed crystal sample cleanup method developed by Xiang and Beavis³⁰ are effective for removing salts and glycerol from peptide and protein samples. However, using these methods, positive results are not obtained for analyzing oligosaccharides in buffered serum. For all of the matrices tested, the underlying matrix layer completely redissolves upon deposition of sample and does not recrystallize.

We have developed a two-step sample preparation method, which is a modification of the method described by Vorm et al.,²⁹ to analyze labeled oligosaccharides in serum. In preparing the matrix layer on the probe, a high surface density of matrix is necessary to prevent the complete redissolution of the matrix layer when serum is added. Deposition of matrix (i.e., 4-HCCA) from a 20 mg mL^{-1} 70% acetonitrile solution provides small matrix crystals with a high surface density (17 nmol/ mm^2). To prepare the analyte, an aliquot of serum is diluted with an equal amount of 50% ethanol/water, which precipitates some of the serum proteins. This is an effective first step in the sample analysis procedure, since proteins cannot be readily washed away from the matrix/analyte mixture on the sample probe. The supernatant is then deposited directly on top of the matrix layer. The matrix layer partially redissolves and then recrystallizes, presumably entrapping the analyte. On-probe sample washing then follows. It should be noted that matrices such as 2,5-DHB that have a high solubility in aqueous solution are unsuccessful with this approach.

For the analysis of the labeled oligosaccharides from serum, this method is found to be facile and effective for removing salts and other contaminants in serum. As an example, Figure 3 shows the MALDI spectrum of a mixture of 30 pmol of $\text{Le}^b\text{-OCH}_3$, 10 pmol of $\text{Le}^b\text{-MCO}$, and 0.5 pmol $\text{Le}^b\text{-TMR}$ spiked into human serum with buffers and other reagents added. Of the three sugars loaded, only $\text{Le}^b\text{-TMR}$ (m/z 1287.4) is detected from this buffered

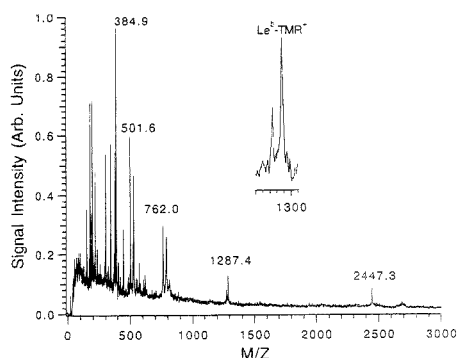


Figure 3. MALDI mass spectrum of a mixture of 30 pmol of $\text{Le}^b\text{-OCH}_3$, 10 pmol of $\text{Le}^b\text{-MCO}$, and 0.5 pmol of $\text{Le}^b\text{-TMR}$ spiked into human serum with buffers and other reagents added. 4-HCCA is used as the matrix with the new sample/matrix preparation method. $\text{Le}^b\text{-TMR}$ is the only oligosaccharide derivative observed. The inset graph is an expansion of the peak at m/z 1287.4.

serum sample with a signal/background ratio of 11. Therefore, the signal/background ratio for serum samples decreases by a factor of 14 over the nonserum samples. Peaks are observed at m/z 384.9, 501.6, and 762.0, along with a significantly weaker peak at 2447.3. These peaks are from unidentified serum components. Other TMR-labeled di-, tri-, and tetrasaccharides have also been studied, and similar findings are obtained. Note that the TMR derivatives are very soluble in water, whereas the 4-HCCA matrix is not. The TMR derivatives may preferentially either form cocrystals with the matrix or adsorb onto the matrix crystals. During the sample washing step, salts, buffers, and other potential contaminants are effectively washed away. In the example of Figure 3, $\text{Le}^b\text{-OCH}_3$ and $\text{Le}^b\text{-MCO}$ may also be washed away. This illustrates that by properly designing the label group in conjunction with an optimal sample/matrix preparation protocol, selective analyte retention and ionization can be achieved.

High mass measurement accuracy is essential for unambiguous identification of chemical species on the basis of molecular weight information. In MALDI, the presence of impurities in a sample can potentially degrade the mass resolution and mass accuracy. Thus, an ideal sample preparation method must be able to remove interfering contaminants that would reduce mass accuracy. The mass measurement accuracy for the detection of oligosaccharides was investigated using our linear TOFMS. Figure 4A shows the molecular ion region of the MALDI mass spectrum of the blood group B active TMR-labeled trisaccharide (B-TMR) obtained with a pure reference sample using the 1 gigasample/s digitizer (LeCroy 9350M oscilloscope). The total sample loaded is 200 fmol or 1.0 μL of a sample solution with a concentration of 2×10^{-7} M. As Figure 4A illustrates, the isotope peaks are well resolved. With a signal/background ratio of 34 for the major isotope peak, the mass resolution is 2600 fwhm. The theoretical exact mass of B-TMR is 1099.50 Da. The measured mass of the monoisotopic peak utilizing a two-point external calibration is 1099.45 Da; thus, the error in mass measurement is 46 ppm. For comparison, the mass spectrum of B-TMR obtained from buffered serum, using the sample preparation method described above, is shown in Figure 4B. To maintain a comparable signal/background ratio B-TMR is spiked into

(28) Karas, M.; Bahr, U.; Ehring, H.; Strupat, K.; Hillenkamp, F. *Proceedings of the 42nd ASMS Conference on Mass Spectrometry and Allied Topics*, Chicago, Illinois, May 29–June 3, 1994; p 7.

(29) Vorm, O.; Roepstorff, P.; Matthias, M. *Anal. Chem.* **1994**, *66*, 3281–3287.

(30) Xiang, F.; Beavis, R. C. *Rapid Commun. Mass Spectrom.* **1994**, *8*, 199–204.

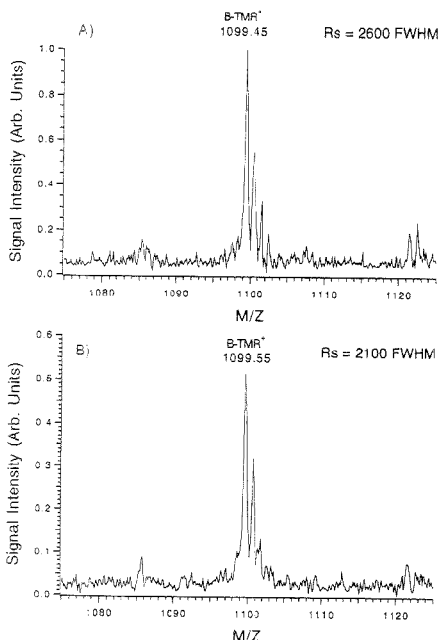


Figure 4. MALDI mass spectra of B-TMR obtained (A) with a pure sample and (B) from buffered serum spiked with B-TMR. 4-HCCA is used as the matrix with the new sample/matrix preparation method. Spectra were collected with a 1 ns/point digitizer. The theoretical exact mass of B-TMR is 1099.50 Da.

human serum to a concentration of 6×10^{-7} M. One microliter of the sample is loaded to the probe, followed by washing. The MALDI spectrum shown in Figure 4B has a mass resolution of 2100 fwhm. The observed mass of the monoisotopic peak is 1099.55 Da, giving an error in mass measurement of 52 ppm using a two-point external calibration. More generally, repeat measurements ($n = 8$) show a mass accuracy of 50 ± 20 ppm. The calibrants used for Figure 4 are disac-TMR and Le^b-TMR dissolved in water at a concentration of 1×10^{-6} M. This example shows that there is a degradation in mass resolution between the pure reference sample and the buffered serum sample, but not to the point where mass accuracy suffers.

Direct monitoring of the *in vitro* α Gal(1 \rightarrow 3)transferase (blood group B galactosyl transferase) enzyme reaction is accomplished using this MALDI analysis technique. This enzyme uses UDP-Gal as the donor and α Fuc(1 \rightarrow 2) β Gal-TMR (disac-TMR) as the acceptor to produce B-TMR. A known amount of disac-TMR (5 nmol in 57.6 μ L of serum solution), along with sodium cacodylate buffer (45 mM, pH 7.1) and manganese chloride (5 mM), is added to the serum. The mixture is incubated for 90 min. Figure 5A shows the MALDI spectrum when no UDP-Gal donor is added to the incubation. As expected, product ion is not present in this spectrum. The peaks at m/z 938.1 and 960.0 are for the molecular ions of the starting material disac-TMR due to protonation and sodium cationization, respectively. The peak at m/z 1039.4 is found only in the incubated samples. The origin of this peak is unknown. Figure 5B shows the spectrum taken when 5 nmol of

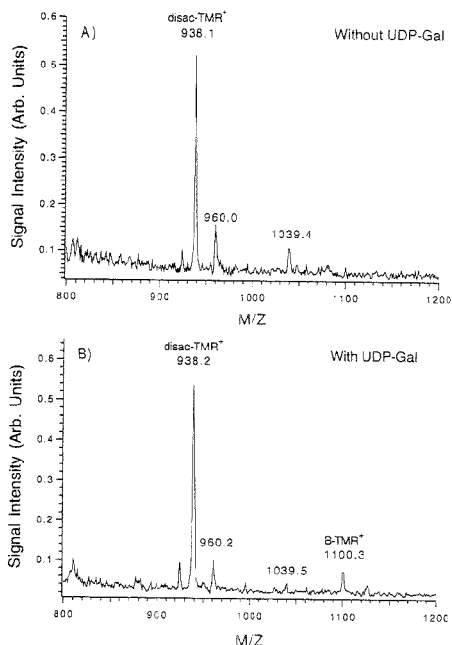


Figure 5. MALDI for monitoring the α Gal(1 \rightarrow 3) transferase enzyme reaction *in vitro*. MALDI mass spectra of the serum samples after a 90-min incubation with no UDP-Gal donor added (A) and with UDP-Gal donor added (B). 4-HCCA is used as the matrix with the new sample/matrix preparation method.

UDP-Gal donor is added to the starting mixture and incubated for 90 min. In this case, a new peak appears at m/z 1100.3. B-TMR is the expected reaction product from the transferase enzyme reaction with a theoretical average mass of 1100.2 Da. For the B-TMR peak, the signal/background ratio is 3, and the intraspectral S/N ratio is 15.

This example illustrates that the MALDI technique can be used for monitoring an enzymatic reaction directly from crude serum without the use of traditional time-consuming separation processes. While this enzymatic reaction can be studied by other tracer techniques, the mass spectrometric technique shown here provides chemical identification. In monitoring an enzymatic reaction in a biological sample, there are concerns that the reaction conditions used, or the presence of other unanticipated enzymes, may change the course of the reaction of interest. For example, in the case of the incubation analyzed in Figure 5, fucosidase-catalyzed hydrolysis of the starting material may take place to form free fucose and the TMR-labeled monosaccharide β Gal-TMR. Radiochemical assay methods would not detect this hydrolysis. HPLC would also fail to identify the products unless mass spectrometry is used for detection. Under the reaction conditions used for Figure 5, there are no other detectable peaks that can be assigned to possible reaction products. The example shown in Figure 5 also illustrates the importance of running a parallel control experiment in identifying the source of the unknown peak at m/z 1039.4. One limitation of the MALDI technique with the current setup is the lack of extensive fragment ions for structural

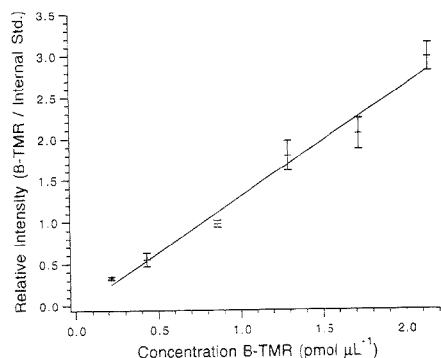


Figure 6. Calibration curve for quantitation of B-TMR product. The peak intensity of B-TMR is measured relative to Le^b-TMR. The error bars represent ± 2 SD for five samples at each concentration.

analysis. In this regard, MALDI combined with MS/MS can be very powerful in analyzing unexpected peaks. This type of instrument is now commercially available.

An ideal mass tracer method should be able to provide quantitative information rapidly. Quantitative information, with regard to the reaction products, can be provided with MALDI if an internal standard is used.^{4,25,31} To quantify the yield of B-TMR formed in Figure 5, a calibration curve was generated using the relative signal intensity of B-TMR with respect to the signal intensity of Le^b-TMR. The disac-TMR ion intensity was not used because the concentration of disac-TMR changes during incubation. To develop the calibration curve, shown in Figure 6, B-TMR and Le^b-TMR are spiked to buffered human serum and analyzed. The concentration of B-TMR was varied between 0.22 and 2.1 pmol μL^{-1} , while the concentration of Le^b-TMR was fixed at 2.1 pmol μL^{-1} . The relative intensity of the molecular ion peak of B-TMR to Le^b-TMR is plotted as a function of B-TMR concentration. A linear response is obtained ($r = 0.99$). The error bars represent ± 2 SD for five samples at each concentration. For the sample analysis, Le^b-TMR is spiked to the sample, followed by immediate MALDI analysis. From the calibration curve, the concentration of B-TMR formed after the 90 min incubation of disac-TMR is 0.50 ± 0.09 pmol μL^{-1} , or a total product yield of 29 ± 5 pmol. Also, from the calibration curve, the concentration detection limit

of B-TMR in human serum can be estimated as 0.11 pmol μL^{-1} (detection limit defined as 3 SD of the background signal level/sensitivity).

It should be noted that the ability to perform analyte quantitation directly from a crude sample as illustrated in this example is very significant. This method averts the problems of possible sample loss or quantitative variations often associated with conventional sample cleanup, extraction, and chromatographic procedures. In addition, the calibration curve can be constructed in a much shorter period of time. We are currently in the process of performing a detailed investigation on the quantitative aspect of this mass tracer method. In particular, the linear dynamic range and the rational selection of internal standards in the calibration curve method will be studied. The possibility of using standard addition for quantitation will also be investigated. In addition, a correlation study between the MALDI work and other quantitative methods will be carried out in establishing the validity of these methods. The MALDI approach for the study of enzyme kinetics as well as for the determination of enzyme concentration in crude samples will also be investigated.

In summary, we have developed a tracer method based on the MALDI technique for the assay of glycosyltransferases in human serum. We anticipate that this rapid, sensitive, and molecular-specific detection system will be very useful for reaction monitoring and enzyme kinetic studies of oligosaccharides from crude samples including crude cell tissue and organ extracts. This work also demonstrates the importance of the molecular structure and other physical and chemical properties of the analyte in sample preparation or crystal formation in MALDI. We plan to investigate this phenomenon further in the future in order to design better mass tracers and extend this work to other biomolecules.

ACKNOWLEDGMENT

We thank Mr. Paul Diedrich and Mr. Richard Beever for preparing the TMR conjugates, Le^b-OCH₃, and the MCO glycosides were generous gifts from Prof. R. U. Lemieux. This work was supported in part by the Natural Sciences and Engineering Research Council of Canada (NSERC). R.M.W. thanks NSERC for a postgraduate scholarship.

Received for review March 28, 1995. Accepted July 6, 1995.⁹

AC950307U

(31) Nelson, R. W.; McLean, M. A.; Hutchens, T. W. *Anal. Chem.* **1994**, *66*, 1408-1415.

⁹ Abstract published in *Advance ACS Abstracts*, August 15, 1995.

Capillary Isoelectric Focusing-Electrospray Mass Spectrometry for Protein Analysis

Qing Tang, A. Kamel Harrata, and Cheng S. Lee*

Department of Chemistry and Ames Laboratory, Iowa State University, Ames, Iowa 50011

On-line combination of capillary isoelectric focusing (CIEF) with electrospray mass spectrometry (ESMS) as a two-dimensional separation system is demonstrated. Mixtures of model proteins including cytochrome *c* (horse heart), myoglobin (horse heart), and carbonic anhydrase II (bovine erythrocyte) are focused and cathodically mobilized in a polyacrylamide-coated capillary. At the end of CIEF capillary, the mobilized protein zones are analyzed by mass spectrometry coupled on-line to an electrospray interface with a coaxial sheath flow configuration. The effects of carrier ampholyte concentration on the CIEF separation and the protein electrospray ionization mass spectra are presented and discussed. In this study, the focusing effect of CIEF permits analysis of very dilute protein samples. A typical concentration factor of 50–100 times is observed. The concentration detection limit of myoglobin for a full-scan CIEF-ESMS analysis is in the range of 10^{-7} M, 2 orders of magnitude over that possible with normal capillary zone electrophoresis ESMS.

The traditional biochemical approach to protein characterization has been the use of two-dimensional gel electrophoresis. All the sample proteins are separated first by charge and then by size in a two-dimensional gel.¹ The separation by charge is carried out by isoelectric focusing in a column filled with a pH gradient medium. The medium does not contain sodium dodecyl sulfate (SDS) and separates the native proteins according to their overall charge. The gel containing the charge-separated sample is then applied to the top of a flat gel containing SDS, and the denatured proteins are electrophoretically separated by molecular weight in a second dimension. When the proteins are radiolabeled, their positions in the gel can be detected by autoradiography. As many as several thousand different protein chains—virtually the total protein content of *Escherichia coli*—can be detected and separated by a two-dimensional gel electrophoresis.

Despite the selectivity and sensitivity of two-dimensional gel electrophoresis, this technique as practiced today is the collection of manually intensive procedures. Casting of gels, application of samples, running of gels, and staining of gels are time-consuming tasks prone to irreproducibility and poor quantitative accuracy. The objective of this study is, therefore, to combine the strengths of both capillary isoelectric focusing (CIEF)^{2–5} in the ease and speed of separation and electrospray mass spectrometry (ESMS)^{6–9}

in the accuracy of mass determination. In analogy to a two-dimensional separation system, CIEF separates proteins on the basis of their differences in isoelectric point (pI). The fused silica capillary contains not only ampholytes for the creation of a pH gradient but also proteins. The proteins are focused into discrete and narrow zones with local pHs corresponding to their isoelectric points. ESMS as the second dimension allows the formation of multiply-charged, high molecular weight ions and the precise mass determination of $\pm 0.01\%$ for proteins up to 30 kDa. The integration of CIEF with ESMS exhibits superior resolving power, speed, and sensitivity for protein characterization in biological and biomedical studies.

Various instrumentation arrangements for interfacing capillary zone electrophoresis (CZE) and MS, including the use of metalized capillary terminus, sheath (coaxial) interface, liquid junction, and gold wiring, have been introduced and demonstrated.^{10–15} The purpose of any CZE-MS interface is to establish the electrical connection at the CZE capillary terminus, which serves to define the electric field along the CZE capillary. The electrical connection at the capillary terminus also serves as the electrospray source by having a 3–6-kV difference in applied voltage between the terminus and the sampling aperture of the mass spectrometer. The comparison between sheath interface and liquid junction has been made by Pleasance et al.,¹⁶ and the coaxial sheath flow appeared to have several advantages. The coaxial sheath flow interface is therefore employed in this study to increase the stability of the electrospray process in CIEF-ESMS.

Mass detection of proteins in CZE-MS is typically in the high femtomole range.^{13,17} When the concentration of the sample injected is considered, the detection level in the range of 10^{-5} M is frequently insufficient for various biological and biomedical studies. An obvious approach to improving CZE-MS detection limits is to perform sample stacking during the injection step¹⁸

(6) Yamashita, M.; Fenn, J. B. *J. Phys. Chem.* **1984**, *88*, 4671–4675.

(7) Fenn, J. B.; Mann, M.; Meng, C. W.; Wong, S. F. *Mass Spectrom. Rev.* **1990**, *9*, 37–70.

(8) Ikononou, M. G.; Blades, A. T.; Kebarle, P. *Anal. Chem.* **1991**, *63*, 1989–1998.

(9) Kebarle, P.; Tang, L. *Anal. Chem.* **1993**, *65*, 972A–986A.

(10) Olivares, J. A.; Nguyen, N. T.; Yonker, C. R.; Smith, R. D. *Anal. Chem.* **1987**, *59*, 1236–1232.

(11) Smith, R. D.; Barinaga, C. J.; Udseth, H. R. *Anal. Chem.* **1988**, *60*, 1948–1952.

(12) Lee, E. D.; Muck, W.; Henion, J. D.; Covey, T. R. *J. Chromatogr.* **1988**, *458*, 313–321.

(13) Smith, R. D.; Wahl, J. H.; Goodlett, D. R.; Hofstadler, S. A. *Anal. Chem.* **1993**, *65*, 574A–584A.

(14) Wahl, J. H.; Gale, D. C.; Smith, R. D. *J. Chromatogr.* **1994**, *659*, 217–222.

(15) Fang, L.; Zhang, R.; Williams, E. R.; Zare, R. N. *Anal. Chem.* **1994**, *66*, 3696–3701.

(16) Pleasance, S.; Thibault, P.; Kelly, J. J. *J. Chromatogr.* **1992**, *591*, 325–339.

(17) Thibault, P.; Paris, C.; Pleasance, S. *Rapid Commun. Mass Spectrom.* **1991**, *5*, 484–490.

(1) Creighton, T. E. *Protein Structure: A Practical Approach*; IRL Press: New York, 1990; Chapter 3.

(2) Hjerten, S.; Zhu, M. D. *J. Chromatogr.* **1985**, *346*, 265–270.

(3) Hjerten, S.; Liao, J. L.; Yao, J. J. *J. Chromatogr.* **1987**, *387*, 127–138.

(4) Klar, F.; Hjerten, S. *Electrophoresis* **1989**, *10*, 23–29.

(5) Mazzeo, J. R.; Krull, I. S. *Anal. Chem.* **1991**, *63*, 2852–2857.

by dissolving the sample in water or low-concentration buffer. A particularly useful approach involving on-column isotachophoretic sample preconcentration has recently been reported by Tinke et al.¹⁹ and by Karger and co-workers.^{20,21} With the proper selection of running buffers and the on-column combination of capillary isotachopheresis (CITP) and CZE, the concentration detection limits for a full-scan CZE-MS analysis are decreased by a factor of 100, to $\sim 10^{-7}$ M.²¹ In this study, the focusing effect of CIEF permits analysis of very dilute samples with a typical concentration factor of 50–100 times. It will be shown that CIEF-ESMS provides a concentration detection level competitive with that obtainable with CITP-CZE-MS but 2 orders of magnitude over that possible with normal CZE-MS.

EXPERIMENTAL SECTION

Capillary Isoelectric Focusing: UV Measurement. The capillary isoelectric focusing apparatus was constructed in-house using a CZE 1000R high-voltage (HV) power supply (Spellman High-Voltage Electronics, Plainview, NY). Fused silica capillaries with 50 μm i.d. and 192 μm o.d. (Polymicro Technologies, Phoenix, AZ) were coated internally with linear polyacrylamide for the elimination of electroosmotic flow.⁴ The proteins, including cytochrome *c* (horse heart), myoglobin (horse heart), and carbonic anhydrase II (bovine erythrocyte), were obtained from Sigma (St. Louis, MO). A 20-cm-long capillary was filled with a solution containing proteins and carrier ampholyte, pharmalyte 3–10 (Pharmacia, Uppsala, Sweden). Focusing was performed at a 10-kV constant voltage for 15 min with the use of 20 mM phosphoric acid and 20 mM sodium hydroxide as the anolyte and the catholyte, respectively. Cathodic mobilization was initiated by replacing the sodium hydroxide catholyte with a solution containing methanol/water/acetic acid in a volume ratio of 50:49:1 at pH 2.6. A constant voltage of 10 kV was applied during the mobilization. The protein zones were monitored by UV detection (Linear Instruments, Reno, NV) at 280 nm. The distance between the injection point and the UV detector was 14 cm. All chemicals, including phosphoric acid, sodium hydroxide, acetic acid, and methanol, were purchased from Fisher (Fair Lawn, NJ). All solutions were filtered through a 1- μm filter (Whatman, Maidstone, England).

Mass Spectrometer and Electrospray Interface. The mass spectrometer was a Finnigan MAT TSQ 700 (San Jose, CA) triple quadrupole equipped with an electrospray ionization source. The Finnigan MAT electrospray adapter kit, containing both gas and liquid sheath tubes, was used to perform the direct infusion experiment and also to couple CIEF with ESMS without any modifications. The electrospray needle was maintained at a 5 kV for all direct infusion and CIEF-ESMS measurements. The first quadrupole was used for the mass scanning of protein ions, while the second and third quadrupoles were operated in the radio frequency only mode. The electron multiplier was set at 1.3 kV, with the conversion dynode at -15 kV. Tuning and calibration of the mass spectrometer were established by using an acetic acid solution (methanol/water/acetic acid, 50:49:1 v/v/v) containing myoglobin and a small peptide of MRFA.

Flow Injection and Capillary Isoelectric Focusing: Electrospray Mass Spectrometry. The solution mixtures of protein and pharmalyte were infused at 5 $\mu\text{L}/\text{min}$ in 50% methanol, 49% water, and 1% acetic acid (v/v/v) by using a Harvard Apparatus 22 syringe pump (South Natick, MA). The nitrogen sheath gas was operated at a flow rate of 2 L/min. The first quadrupole was scanned from m/z 200 to 2000 at a scan rate of 3 s/scan.

For the combination of CIEF with ESMS, a 20-cm-long CIEF capillary was mounted within the electrospray probe. The outlet reservoir containing 20 mM sodium hydroxide as the catholyte was located inside the electrospray housing during the focusing step. The inlet reservoir containing 20 mM phosphoric acid as the anolyte was kept at the same height as the outlet reservoir. The capillary dimensions and applied focusing voltage were the same as in CIEF-UV measurements. Once the focusing was completed, the electric potential was turned off and the outlet reservoir removed. The capillary tip was fixed about 0.5 mm outside the electrospray needle. The sheath liquid consisted of 50% methanol, 49% water, and 1% acetic acid (v/v/v) and was delivered at a flow rate of 3 $\mu\text{L}/\text{min}$ with use of a Harvard Apparatus 22 syringe pump. During the mobilization step, two HV power supplies (Spellman) were used for delivering the electric potentials at the inlet electrode and at the electrospray needle. Because most HV power supplies are not designed to operate as current sinks, a resistor ladder in parallel with the HV electrode connecting with the electrospray needle was incorporated. A constant electric field of 500 V/cm was applied for the mobilization of focused proteins in the CIEF capillary. The first quadrupole was scanned from m/z 700 to 1800 at a scan rate of 3 s/scan. No sheath gas was employed during the CIEF-ESMS measurements.

RESULTS AND DISCUSSION

In a focusing experiment, the capillary tubing contains not only carrier ampholytes but also proteins. The carrier ampholytes are small amphoteric molecules with different p/s. When an electric potential is applied, the negatively charged acidic ampholytes migrate toward the anode and decrease the pH at the anodic section, while the positively charged basic ampholytes migrate toward the cathode and increase the pH at the cathodic section. These pH changes will continue until each ampholyte species has come to its isoelectric point, where it will then become concentrated. Because each ampholyte has its own buffering capacity, a virtually continuous pH gradient will be formed in the capillary. Because the proteins are amphoteric macromolecules, protein analytes will also focus at their pI values in narrow zones in the same way as the individual carrier ampholytes. To prevent the ampholytes from migrating into the inlet and outlet reservoirs by either diffusion or gradient drift,³ the 20 mM phosphoric acid and 20 mM sodium hydroxide are generally used as the anolyte and the catholyte, respectively.

To investigate the effect of carrier ampholyte concentration on protein separation in CIEF, the polyacrylamide-coated capillary was filled with a solution containing pharmalyte 3–10, myoglobin, and carbonic anhydrase II. The concentration of pharmalyte 3–10 was varied between 5% and 0.1%. The final protein concentration in the solution was 0.2 mg/mL for each protein analyte before the focusing. The focused protein zones were mobilized by replacing the sodium hydroxide catholyte with a solution containing methanol/water/acetic acid (50:49:1 v/v/v) at pH 2.6. The catholyte used in cathodic mobilization was the same as the sheath liquid later employed in the electrospray interface.

(18) Chien, R. L.; Burgi, D. S. *Anal. Chem.* **1992**, *64*, 489A–496A.

(19) Tinke, A. P.; Reinhoud, N. J.; Niessen, W. M. A.; Tjaden, U. R.; van der Greef, J. *Rapid Commun. Mass Spectrom.* **1992**, *6*, 560–563.

(20) Foret, F.; Szoko, E.; Karger, B. L. *J. Chromatogr.* **1992**, *608*, 3–12.

(21) Thompson, T. J.; Foret, F.; Vouros, P.; Karger, B. L. *Anal. Chem.* **1993**, *65*, 900–906.

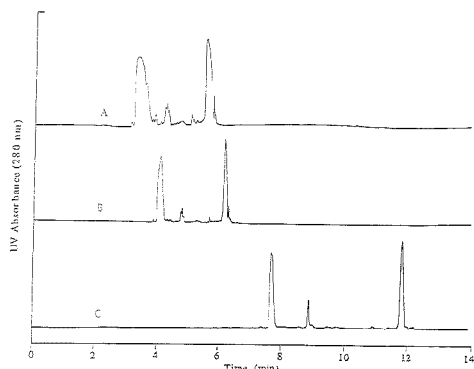


Figure 1. CIEF separation of myoglobin and carbonic anhydrase II in the presence of various pharmlalyte concentration. Capillary, 20 cm total length, 50 μm i.d. and 192 μm o.d.; length to detector, 14 cm; voltage, 10 kV for focusing and mobilization; UV detection at 280 nm. Concentrations: (A) 0.1% pharmlalyte, (B) 0.5% pharmlalyte, and (C) 5% pharmlalyte.

Table 1. Effect of Pharmlalyte Concentration on Protein Separation in Capillary Isoelectric Focusing^a

pharmlalyte 3-10 concn (%)	separation resoln. myoglobin/carbonic anhydrase	peak height ^b (%)	
		myoglobin	carbonic anhydrase
0.1	3.8	19.5	21.3
0.5	9.8	65.5	66.8
1	10.0	76.0	74.2
2	10.4	92.8	83.0
5	12.5	100	100

^a The experimental error in measuring the values of separation resolution and peak height was about 4–8% for various ampholyte concentrations for over five runs. ^b The peak heights of myoglobin and carbonic anhydrase, measured by UV absorbance at 280 nm, were set to be 100% in the presence of 5% ampholyte.

The electropherograms of CIEF separation under the influence of various pharmlalyte concentrations are shown in Figure 1. The elution order was myoglobin (pI 7.2 and 6.8), followed by carbonic anhydrase II (pI 5.9). The migration time of protein zones during the cathodic mobilization step increased with increasing pharmlalyte concentration. A significant increase in band broadening of protein analytes was observed when the pharmlalyte concentration was reduced to 0.1%. The quantitative dependence of pharmlalyte concentration on the separation resolution and the peak height of focused proteins in CIEF is summarized in Table 1. In comparison with protein separation at 5% pharmlalyte, a 22% loss in the separation resolution and a 34% reduction in the UV absorbance intensity were measured in CIEF with 0.5% carrier ampholyte. Significant deterioration in both the separation and the peak intensity was observed when the pharmlalyte concentration was further reduced to 0.1%. Clearly, a 0.1% ampholyte solution was insufficient to provide a smooth and continuous pH gradient for CIEF protein separation.

Electrospray ionization is a highly effective means for producing gas phase peptide and protein ions from the solution.^{22,23} The

mass spectra of these electrosprayed ions are characterized by the distribution of peaks, where each component peak of the distribution corresponds to a different charge state of the intact protein. The shapes of these charge distributions are determined by different factors, including protein conformation,^{21,23} solution pH,²⁶ solvent composition,²⁷ instrumentation conditions,²⁸ temperature,²⁹ solution ionic strength,^{30,31} and the number of basic or acidic sites.³² A strong correlation has been observed between the number of basic amino acid residues present in the protein and the distribution of charge states seen in the positive electrospray ionization spectrum.

To combine CIEF with ESMS, the effect of carrier ampholyte concentration on the charge distribution of protein analytes in the electrospray ionization has to be determined. In the direct infusion experiments, three model proteins of cytochrome *c*, myoglobin, and carbonic anhydrase II were dissolved separately in the solution containing methanol/water/acetic acid (50:49:1 v/v/v) at pH 2.6. The positive electrospray ionization mass spectra of cytochrome *c* at various pharmlalyte concentrations are shown in Figure 2. The average charge states and the ion counts of cytochrome *c*, myoglobin, and carbonic anhydrase II at various pharmlalyte concentrations are summarized in Table 2 for comparison.

The ions of pharmlalyte 3-10 were observed in the low *m/z* range up to *m/z* 800. The presence of pharmlalyte not only caused a marked reduction in the protein peak intensity but also resulted in a decrease of the net charge of protein ions in the mass spectra compared to the average charge state measured in the absence of carrier ampholyte. Protein peak intensities in the mass spectra decreased as the solution pharmlalyte concentration increased. The ion intensity of cytochrome *c* in Figure 2C was amplified 10-fold after the mass scan of pharmlalyte ions. Thus, the pharmlalyte ions similar to simple electrolyte ions led to higher solution conductivity and contributed to the establishment of the charge excess known to exist in droplets formed during the electrospray process. The suppression of protein ion intensity due to the addition of pharmlalyte ions could be qualitatively accounted for by the theories of Tang and Kebarle^{33,34} and Wang and Cole.³⁰

Furthermore, the pharmlalyte ions seemed to participate in the process of charge attachment to protein analytes. As demonstrated by Mirza and Chait,³¹ certain anionic species in the electrospray solution could cause a marked decrease in the average charge state of peptide and protein ions in the mass spectra. This charge neutralization effect was found to depend solely on the nature of the anion species and was independent of the source of the anion. A charge reduction mechanism was proposed that involved as the first step anion pairing with a

- (23) Fenn, J. B. *J. Am. Soc. Mass Spectrom.* **1993**, *4*, 524–535.
 (24) Katta, V.; Chait, B. T. *Rapid Commun. Mass Spectrom.* **1991**, *5*, 214–217.
 (25) Loo, J. A.; Ogorzalek Loo, R. R.; Udseth, H. R.; Edmonds, C. G.; Smith, R. D. *Rapid Commun. Mass Spectrom.* **1991**, *5*, 101–105.
 (26) Chowdhury, S. K.; Katta, V.; Chait, B. T. *J. Am. Chem. Soc.* **1990**, *112*, 9012–9013.
 (27) Edmonds, C. G.; Loo, J. A.; Barinaga, C. J.; Udseth, H. R.; Smith, R. D. *J. Chromatogr.* **1989**, *474*, 21–39.
 (28) Ashton, D. S.; Beddel, C. R.; Cooper, D. J.; Green, B. N.; Oliver, R. W. A. *Org. Mass Spectrom.* **1993**, *28*, 579–583.
 (29) Mirza, U. A.; Cohen, S. L.; Chait, B. T. *Anal. Chem.* **1993**, *65*, 1–6.
 (30) Wang, G.; Cole, R. B. *Anal. Chem.* **1994**, *66*, 3702–3708.
 (31) Mirza, U. A.; Chait, B. T. *Anal. Chem.* **1994**, *66*, 2898–2904.
 (32) Smith, R. D.; Loo, J. A.; Ogorzalek Loo, R. R.; Busman, M. *Mass Spectrom. Rev.* **1991**, *10*, 339–451.
 (33) Tang, L.; Kebarle, P. *Anal. Chem.* **1991**, *63*, 2709–2715.
 (34) Tang, L.; Kebarle, P. *Anal. Chem.* **1993**, *65*, 3654–3668.

(22) Fenn, J. B.; Mann, M.; Meng, C. K.; Whitehouse, C. M. *Science* **1989**, *246*, 64–71.

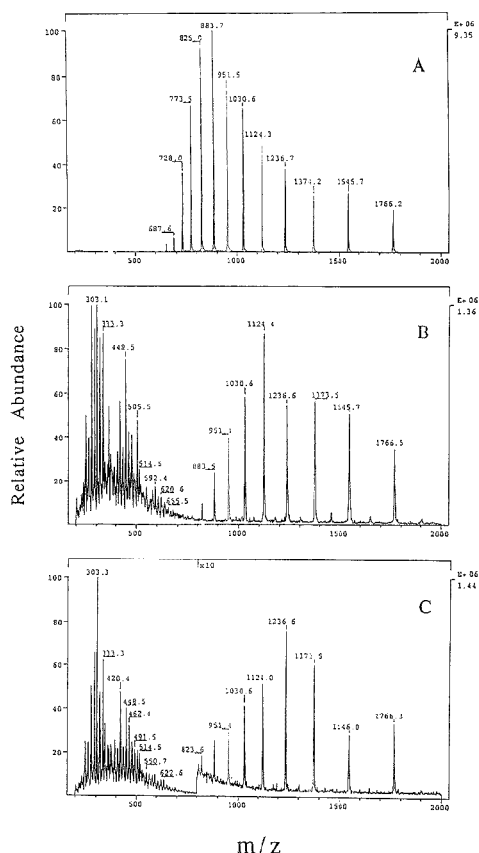


Figure 2. Positive electrospray ionization mass spectra of cytochrome *c* obtained at different pharmalyte concentrations: (A) 0% pharmalyte, (B) 0.5% pharmalyte, and (C) 2% pharmalyte. Cytochrome *c* concentration, 0.2 mg/ml. The solution mixture of cytochrome *c* and pharmalyte was infused at 5 $\mu\text{L}/\text{min}$ in 50% methanol, 49% water, and 1% acetic acid (v/v/v).

Table 2. Effect of Pharmalyte Concentration on Average Charge State and Ion Count of Protein Mass Spectra^a

pharmalyte 3-10 concn (%)	average charge state ^a			ion count ($\times 10^5$) ^b		
	CYT	MYO	CAB	CYT	MYO	CAB
0	13.0	18.0	26.5	47.5	74.2	8.86
0.5	11.0	15.0	23.0	11.1	23.1	5.12
1	11.0	15.0	22.5	5.2	10.8	0.07
2	11.0	14.5	21.0	1.1	2.1	0.01

^a CYT, cytochrome *c*; MYO, myoglobin; CAB, carbonic anhydrase II. ^b The ion counts were measured for cytochrome *c*, myoglobin, and carbonic anhydrase II at m/z 1124, 1304, and 1320, respectively.

positively charged basic amino acid of protein in the solution. The second step occurred during the process of desolvation or in the gas phase, where the ion pair dissociated to yield the neutral acid and the protein with reduced charge state. The different propensities for charge neutralization of the different anionic species were

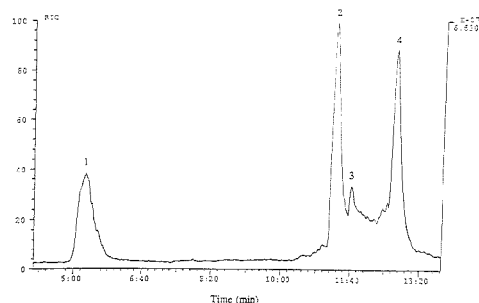


Figure 3. CIEF-ESMS reconstructed ion electropherogram of 0.1 mg/mL each of (1) cytochrome *c*, (2) myoglobin (pI 7.2), (3) myoglobin (pI 6.8), and (4) carbonic anhydrase II. Capillary, 20 cm total length, 50 μm i.d. and 192 μm o.d.; applied voltages, 10 kV for focusing and mobilization, 5 kV for electrospray; sheath liquid, methanol/water/acetic acid (50:49:1 v/v/v) at pH 2.6, 3 $\mu\text{L}/\text{min}$.

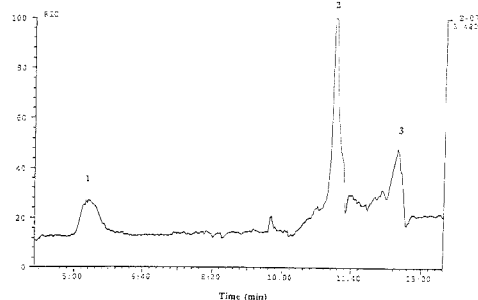


Figure 4. CIEF-ESMS reconstructed ion electropherogram of 0.01 mg/mL each of (1) cytochrome *c*, (2) myoglobin (pI 7.2), and (3) carbonic anhydrase II. Other conditions are the same as in Figure 3.

assumed to reflect the avidity of the anion-protein interaction. These findings from Mirza and Chair³¹ could be used to support the possible ion pair formation between the anionic moiety of carrier ampholyte and a positively charged basic amino acid of protein. The ion pair formation, in combination with the subsequent desolvation and dissociation processes, produced the charge neutralization effect and the observed shift in the charge distribution of protein mass spectra.

Considering the effect of ampholyte concentration on the CIEF separation and the protein electrospray ionization mass spectra, a solution containing 0.5% pharmalyte and standard proteins was used in the CIEF-ESMS measurements. The reconstructed ion electropherograms of the protein mixture with final concentrations of 0.1 and 0.01 mg/mL for each protein analyte are shown in Figures 3 and 4, respectively. The reconstructed ion electropherograms were obtained from the mass scan between m/z 700 and 1800 at a scan rate of 3 s/scan. All protein peaks were directly identified on the basis of mass spectra of protein analytes taken from the average scans under the peaks. There was no measurable protein mass spectrum by averaging the scans between peak 3 (myoglobin, pI 6.8) and peak 4 (carbonic anhydrase II) in Figure 3. An example of the mass spectra obtained from the average scans under the peaks of Figure 4 is shown in Figure 5 for carbonic anhydrase II with a concentration of 0.01 mg/mL, or 3.45×10^{-7} M. Initial preconcentration during the focusing step

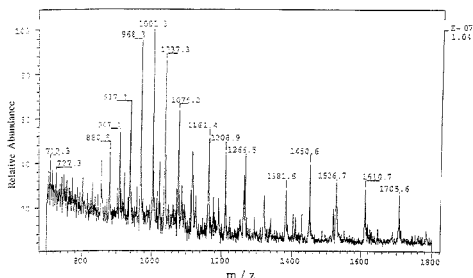


Figure 5. Positive electrospray ionization mass spectrum of carbonic anhydrase II taken from the average scans under the peak in Figure 4.

was responsible for improving detection limit by 2 orders of magnitude in comparison with that obtained with normal CZE-MS.

In comparison with CIEF-UV experiments (see Figure 1), the longer migration distance from the focused regions to the end of the capillary in CIEF-ESMS accounted for the increase in the migration time. However, the average velocity of myoglobin (8 cm/11.2 min = 0.71 cm/min) during the cathodic mobilization

in CIEF-ESMS was faster than that of myoglobin in CIEF-UV (2 cm/4.05 min = 0.49 cm/min). This difference in the average migration velocity contributed to a smaller Δt of 1.6 min between the myoglobin and carbonic anhydrase II peaks in CIEF-ESMS than that of 2.2 min in CIEF-UV.

In CIEF-ESMS, the scan rate of MS might be insufficient to truly reflect the high separation efficiency of CIEF. The reduced elution speed method, as demonstrated by Goodlett et al.,³⁵ could be applied to circumvent the speed limitations of scanning mass spectrometry. It is known that selected ion monitoring (SIM) of quadrupole mass spectrometry yields significantly enhanced detection limits compared with those obtained with scanning MS operation because of the greater dwell time for signal acquisition at each selected m/z value. For samples with prior known analyte molecular weights and m/z values, SIM can further reduce the detection limits of CIEF-ESMS.

ACKNOWLEDGMENT

Support for this work by the Microanalytical Instrumentation Center of the Institute for Physical Research and Technology at Iowa State University is gratefully acknowledged. C.S.L. is a National Science Foundation Young Investigator (BCS-9258652).

Received for review April 7, 1995. Accepted July 11, 1995.[®]

AC950348Q

(35) Goodlett, D. R.; Wahl, J. H.; Udseth, H. R.; Smith, R. D. *J. Microcolumn Sep.* **1993**, *5*, 57-62.

[®] Abstract published in *Advance ACS Abstracts*, August 15, 1995.

Capillary Electrophoresis/Frontal Analysis for Microanalysis of Enantioselective Protein Binding of a Basic Drug

Toshio Ohara, Akimasa Shibukawa,* and Terumichi Nakagawa

Faculty of Pharmaceutical Sciences, Kyoto University, Sakyo-ku, Kyoto 606, Japan

A new HPCE method was developed for the enantioselective determination of the unbound concentration of a basic drug under plasma protein binding equilibrium. The racemic basic drug verapamil (VER) and human serum albumin mixed solution was used as a model sample solution. The sample solution was introduced into a fused-silica capillary hydrodynamically or electrokinetically. During the electrophoresis following hydrodynamic injection, the unbound drug zone migrated apart from the sample zone and was separated into two zonal peaks with a plateau due to enantiomers by a chiral selector (trimethyl- β -cyclodextrin) dissolved in the acidic running buffer solution (pH 2.5). By the electrokinetic introduction of the same sample solution from the anodic end, only the unbound drug entered the capillary and was separated into the enantiomers, which also gave the zonal peaks with plateau. The unbound concentration of each enantiomer was determined from the plateau peak height. The results obtained by the different methods for sample introduction agreed well with those determined by conventional ultrafiltration-chiral HPLC, which was employed as a reference method. The unbound concentration of (S)-VER was 1.7 times higher than that of the antipode. The sample size used in the present method was ~200 nL, which is about one-thousandth of that in the reference method. The electrokinetic introduction gave a better peak shape than the hydrodynamic introduction.

A drug dosed to the body enters the blood stream, where it reaches an equilibrium of binding to plasma proteins such as albumin and α_1 -acid glycoprotein. The protein binding is a reversible and kinetically rapid process. Unbound drug transfers freely to the target organ, whereas it is hard for the bound drug to penetrate the blood vessel wall. Consequently, protein binding of a drug affects significantly the disposition and the exertion of its pharmaceutical effect. This is why the quantitative investigation of protein binding is essential to pharmacokinetics and a therapeutic dosing regimen.¹⁻³ The protein binding of a chiral drug is potentially different between the optical isomers because of the inherent chirality of protein.^{4,5} Therefore, a stereoselective protein binding study is necessary.

So far, equilibrium dialysis and ultrafiltration followed by HPLC analysis have been commonly used for the determination of unbound drug concentration. However, these methods involve adsorption of drug to the membrane, leakage of bound drug through the membrane, and a long time to attain equilibrium. In contrast, the Hummel-Dreyer method and the gel filtration frontal analysis method, based on size exclusion chromatography,⁶ are free from these problems. Recently, we developed another chromatographic method called high-performance frontal analysis (HPFA).⁷⁻¹⁷ The advantages of HPFA over the conventional methods are as follows: (1) Sample solution containing drug and protein can be directly applied without pretreatment. (2) Errors due to leakage of protein through the membrane and adsorption of drug to the membrane can be avoided. (3) The total drug concentration and the unbound drug concentration in the protein binding equilibrium can be simultaneously determined from the peak area and peak height, respectively, following a single injection.⁸ (4) HPFA can be easily incorporated into an on-line HPLC system. By coupling with a chiral HPLC column, the unbound concentration of a chiral drug can be determined stereoselectively. (5) As low as a few nanomolar or lower unbound drug concentration can be determined with good reproducibility.¹⁵⁻¹⁷

The injection volume required for HPFA becomes smaller as protein binding of the drug becomes stronger.¹⁶ For instance, the strong binding of warfarin and human serum albumin (HSA) (the bound drug fraction was ~99%) could be analyzed using 40 μ L of sample solution injected,⁹ whereas the analysis of carbamazepine and HSA mixed solution (the unbound drug fraction was ~30%) required 1.4 mL of sample.⁸ To reduce the injection volume, we developed a micro-HPFA method where a microbore

(1) Meyer, M. C.; Guttman, D. E. *J. Pharm. Sci.* 1968, 57, 895-918.
(2) Vallner, J. J. *J. Pharm. Sci.* 1977, 66, 447-465.

(3) Kwong, T. C. *Clin. Chem. Sci.* 1985, 151, 193-213.

(4) Tucker, G. T.; Lennard, M. S. *Pharmacol. Ther.* 1989, 45, 309-329.

(5) Noctor, T. *Drug Stereochemistry*, 2nd ed.; Wainer, I. W., Ed.; Dekker: New York, 1993; Chapter 12.

(6) Korpela, T. K.; Hirmanen, J.-P. *Aqueous Size-Exclusion Chromatography*; Dubin, P. L., Ed.; Elsevier: Amsterdam, 1988; Chapter 13.

(7) Shibukawa, A.; Nakagawa, T.; Nishimura, N.; Miyake, M.; Tanaka, H. *Chem. Pharm. Bull.* 1989, 37, 702-706.

(8) Shibukawa, A.; Nishimura, N.; Nomura, K.; Kuroda, Y.; Nakagawa, T. *Chem. Pharm. Bull.* 1990, 38, 443-447.

(9) Shibukawa, A.; Nagao, M.; Kuroda, Y.; Nakagawa, T. *Anal. Chem.* 1990, 62, 712-716.

(10) Nishimura, N.; Shibukawa, A.; Nakagawa, T. *Anal. Sci.* 1990, 6, 355-359.

(11) Shibukawa, A.; Terakita, A.; He, J.; Nakagawa, T. *J. Pharm. Sci.* 1992, 81, 710-715.

(12) Terakita, A.; Shibukawa, A.; Nakagawa, T. *Anal. Sci.* 1993, 9, 229-232.

(13) Shibukawa, A.; Nagao, M.; Terakita, A.; He, J.; Nakagawa, T. *J. Liq. Chromatogr.* 1993, 16, 903-914.

(14) Terakita, A.; Shibukawa, A.; Nakagawa, T. *Anal. Sci.* 1994, 10, 11-15.

(15) Shibukawa, A.; Nakao, C.; Sawada, T.; Terakita, A.; Morokoshi, N.; Nakagawa, T. *J. Pharm. Sci.* 1994, 83, 868-873.

(16) Shibukawa, A.; Kadobara, M.; He, J.; Nishimura, M.; Naito, S.; Nakagawa, T. *J. Chromatogr.* 1995, 694, 81-89.

(17) Shibukawa, A.; Sawada, T.; Nakao, C.; Izumi, T.; Nakagawa, T. *J. Chromatogr.* 1995, 697, 337-343.

HPFA column is used,^{12,14} by which the injection volume was reduced to one-tenth. Further reduction of the sample size could be achieved by incorporating frontal analysis in the HPCE format (HPCE/FA).^{15,19}

So far, a few HPCE methods have been reported for the estimation of drug-protein binding. Kraak et al. applied the Hummel-Dreyer method, vacancy peak method, and frontal analysis method in HPCE format for the estimation of warfarin-bovine serum albumin interaction.¹⁹ In the Hummel-Dreyer method, protein is electrophoresed in the running buffer containing drug, and the bound drug concentration is calculated from the area of the vacant peak. In the vacancy peak method, the capillary is filled with buffer containing drug and protein, and a small plug of buffer is injected. The bound and unbound drug concentrations are calculated from the areas of two negative vacant peaks. However, these methods are reported to be less preferable than the HPCE/FA method.¹⁹

Affinity HPCE has been used for the estimation of the interaction between enzyme and cofactors,²⁰ lectin and sugar,²¹ peptides and drugs,^{22,23} and protein and ligands.²⁴ Recently, Lloyd et al. applied affinity HPCE to the analysis of drug-plasma protein binding,²⁵ where protein solution is added to a running buffer. The binding constant was calculated from the subsequent change in electrophoretic mobility of the drug. Affinity HPCE allows the simultaneous protein binding assay of plural drugs by injecting the drugs together. This method is practically beneficial to the stereoselective binding study, because the binding constant of each optical isomer can be calculated by using racemates. In addition, the location of binding site on the protein molecule can be identified by using a displacer with a known binding site location. However, the affinity HPCE method has the following problems: (1) Strong UV absorption of protein in the running buffer may interrupt the detection of drug. (2) The binding constant is calculated on the basis of a stoichiometrical assumption. Usually, 1:1 binding is supposed. However, the number of binding sites is often more than unity and may be different between the optical isomers. (3) Sometimes the drug peak becomes broadened, which may lead to error in estimation of the binding constant.²⁵ (4) Once protein is adsorbed to the inner surface of capillary, the drug binds to protein not only in the running buffer but also on the inner surface,²⁶ which may complicate the numerical analysis.

In contrast, HPCE/FA can avoid the above mentioned problems. Since drug is separated from protein, the strong UV absorption of the protein does not disturb the analysis. HPCE/FA followed by Scatchard analysis gives both the binding constant and the number of binding sites.¹⁸ The coating of the inner surface of capillary serves to avoid the adsorption of protein.¹⁸ In addition, unlike other HPCE binding assay methods, HPCE/FA

allows the determination of the unbound drug concentration.

This paper expands the application of the HPCE/FA method to the enantioselective determination of unbound concentrations of a chiral basic drug. Sample was introduced into a fused-silica capillary electrokinetically or hydrodynamically. In HPCE/FA with electrokinetic injection, the principle of frontal analysis effects the selective introduction of the unbound drug into the capillary. In contrast, in HPCE/FA following hydrodynamic injection, frontal analysis occurs inside the capillary to generate the unbound drug zone.

EXPERIMENTAL SECTION

Reagents and Materials. Verapamil (VER) hydrochloride and sodium dodecyl sulfate (SDS) were purchased from Wako Pure Chemicals (Osaka, Japan). HSA (globulin and fatty acid free; Catalog No. A-3782) was purchased from Sigma (St. Louis, MO) and was used without further purification. Heptakis(2,3,6-tri-O-methyl)- β -cyclodextrin (TM- β -CD; Catalog No. H-4645) was purchased from Sigma. Racemic VER and HSA mixed solutions were made up in sodium phosphate buffer (pH 7.4, ionic strength (I) = 0.17) and were shaken gently at 25 °C for 1 h before analysis.

Apparatus. A capillary electrophoresis instrument (CAPI-3000, Otsuka Electronics Co. Ltd., Osaka, Japan) was equipped with a fused-silica capillary (75 μ m i.d.; GL science Inc., Tokyo, Japan) and a UV absorption detector: temperature, 25 °C; detection, 200 nm. After each electrophoretic run, the capillary was sequentially rinsed with 30 mM SDS in phosphate buffer (pH 7.4) and 50 mM sodium phosphate buffer (pH 2.5).

Optimization of Running Buffer Condition. Among the three chiral selectors examined (β -CD, DM- β -CD, TM- β -CD), TM- β -CD was found to give a base-line separation of VER enantiomers in acidic running buffer (pH 2.5) but not in neutral buffer (pH 7.4). TM- β -CD (40 mM) gave a better enantioseparation than 10 or 20 mM TM- β -CD. Thus, the running buffer condition was optimized as 50 mM sodium phosphate buffer (pH 2.5, adjusted by phosphoric acid) containing 40 mM TM- β -CD. Similar HPCE conditions for the chiral separation of VER have been reported.^{27,28}

Electrokinetic Sample Injection. After the capillary (total length 63 cm, effective length 50 cm) was filled with the running buffer, a small volume of neutral buffer (pH 7.4, I = 0.17) was introduced by suction (3 s) into the capillary. Then, the injection end of the capillary was immersed into the sample solution, and a positive voltage (+18 kV) was applied for 30 s. After sample introduction, the injection end of the capillary was transferred to the running buffer, and a positive voltage (+18 kV) was applied to start the electrophoresis.

Hydrodynamic Sample Injection. After the capillary (total length 83 cm, effective length 75 cm) was filled with the running buffer, neutral phosphate buffer (pH 7.4, I = 0.17) was introduced into the capillary by suction (15 s for 300 μ M VER-550 μ M HSA solution or 18 s for 200 μ M VER-550 μ M HSA solution). Then, the sample solution was introduced hydrodynamically (10 s for 300 μ M VER-550 μ M HSA solution or 7 s for 200 μ M VER-550 μ M HSA solution). After sample introduction, the injection end of the capillary was transferred to the neutral phosphate buffer (pH 7.4, I = 0.17), and a positive voltage (+22 kV) was applied to start the electrophoresis.

(18) Shibukawa, A.; Yoshimoto, Y.; Ohara, T.; Nakagawa, T. *J. Pharm. Sci.* **1994**, *83*, 615-619.

(19) Kraak, J. C.; Busch, S.; Poppe, H. J. *Chromatogr.* **1992**, *608*, 257-264.

(20) Chu, Y.-H.; Avila, L. Z.; Biebuyck, H. A.; Whitesides, G. M. *J. Med. Chem.* **1992**, *35*, 2915-2917.

(21) Honda, S.; Taga, A.; Suzuki, K.; Suzuki, S.; Kakehi, D. *J. Chromatogr.* **1992**, *597*, 377-382.

(22) Carpenter, J. L.; Camilleri, P.; Dhanak, D.; Goddard, D. A. *J. Chem. Soc., Chem. Commun.* **1992**, 804-806.

(23) Chu, Y.-H.; Whitesides, G. M. *J. Org. Chem.* **1992**, *57*, 3524-3525.

(24) Liu, J.; Volk, K. J.; Lee, M. S.; Pucci, M.; Handwerker, S. *Anal. Chem.* **1994**, *66*, 2412-2416.

(25) Lloyd, D. K.; Li, S.; Ryan, P. *Chirality* **1994**, *6*, 230-238.

(26) Yang, J.; Hage, D. S. *Anal. Chem.* **1994**, *66*, 2719-2725.

(27) Soiri, H.; Riekkola, M.-L.; Novotny, M. V. *J. Chromatogr.* **1992**, *608*, 265-274.

(28) Dethy, J.-M.; De Broux, S.; Lesne, M.; Longstreth, J.; Gilbert, P. J. *Chromatogr. B* **1994**, *554*, 121-127.

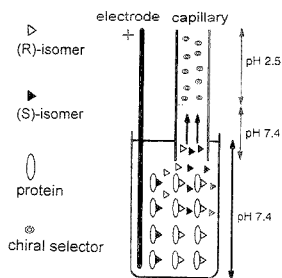


Figure 1. Schematic diagram of the electrokinetic injection.

Calibration Lines. A series of racemic VER standard solutions (50, 100, 200, and 300 μM) dissolved in phosphate buffer (pH 7.4, $I = 0.17$) were used to prepare calibration lines. In the case of electrokinetic injection, these calibration standards were introduced according to the same procedure as mentioned above. In the case of hydrodynamic injection, the injection times of the neutral buffer and the calibration standards were 5 and 20 s, respectively. The plateau height of each enantiomer was measured in duplicate, and the averaged value was used to make the calibration lines. Good linearity was obtained ($r > 0.998$).

Determination of Unbound VER Concentrations by a Ultrafiltration-Chiral HPLC Method. A disposable ultrafiltration kit (Molcut II, UFPILGC, Millipore) was used as a reference standard method to determine the unbound concentration of the VER enantiomer. To suppress the adsorption of the drug on the filter membrane, 1 mL of the sample solution was put into the filtration kit and the membrane was saturated with VER by filtration of $\sim 200 \mu\text{L}$ portion of 1 mL sample solution. After discarding the sample solution remaining in the kit, another 1 mL of the same sample solution was applied, and a $\sim 200 \mu\text{L}$ portion of the filtrate containing the unbound drug was obtained. The filtration was performed at 25 $^{\circ}\text{C}$. A 100 μL portion of the filtrate was subjected to chiral HPLC under the following conditions: Ultron ES-OVM column (15 cm \times 6 mm i.d., Shinwa Chemical Industries, Kyoto, Japan); mobile phase of 20 mM NaH_2PO_4 -ethanol, 97:3 (v/v); flow rate, 1.2 mL/min; UV detection 275 nm; injection volume, 80 μL ; column temperature, 37 $^{\circ}\text{C}$.

RESULTS

HPCE/FA with Electrokinetic Injection. Figure 1 illustrates the electrokinetic sample introduction process. Since electroosmotic flow is not generated under the acidic running buffer condition (pH 2.5), only the unbound drug with a positive net charge is introduced into the capillary from the anodic end, keeping the same *R/S* ratio as in the sample solution. The unbound drug was then separated into two zones of enantiomers by the chiral selector in the running buffer. The unbound concentration of each enantiomer was calculated from the respective plateau height.

In a protein binding study, it is important to investigate the bindability under physiological conditions. Therefore, phosphate buffer of physiological pH (=7.4) was used to prepare the sample solution. However, the optimal pH of the running buffer solution (pH 2.5) was far lower than the physiological pH, as mentioned above. Thus, it was feared that direct contact of the sample solution with the running buffer during the sample injection

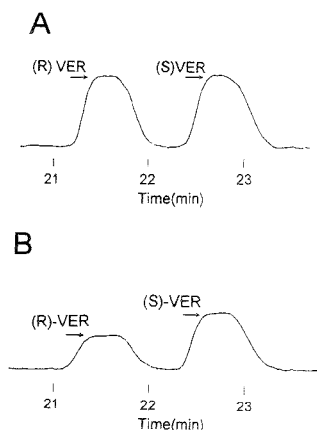


Figure 2. Electropherograms of (A) 200 μM racemic VER solution and (B) 200 μM racemic VER in 550 μM HSA solution obtained by HPCE/FA with electrokinetic injection.

Table 1. Unbound Concentrations of VER Enantiomers Determined by HPCE/FA with Electrokinetic Injection and by an Ultrafiltration (UF)-Chiral HPLC Method

	HPCE/FA ^b		UF-chiral HPLC ^{b,c}
	within-run ^d	day-to-day ^d	
Racemic 300 μM VER-550 μM HSA			
Cu(<i>R</i>) (μM)	60.6 (2.81)	60.9 (4.54)	60.6 (8.92)
Cu(<i>S</i>) (μM)	100 (3.45)	104 (5.06)	103 (5.06)
Cu(<i>S</i>)/Cu(<i>R</i>)	1.66 (2.29)	1.71 (2.80)	1.70 (3.81)
Racemic 200 μM VER-550 μM HSA			
Cu(<i>R</i>)	44.5 (1.77)	43.7 (6.78)	44.3 (3.19)
Cu(<i>S</i>) (μM)	74.7 (2.71)	75.2 (9.31)	77.5 (2.01)
Cu(<i>S</i>)/Cu(<i>R</i>)	1.68 (2.33)	1.72 (3.47)	1.75 (1.27)

^a Cu(*R*) and Cu(*S*) represent the unbound concentration of (*R*)-VER and (*S*)-VER, respectively. ^b Mean and % CV (in parentheses). ^c $n = 5$. ^d $n = 15$.

process might disturb the protein binding equilibrium because of the pH difference. To avoid this trouble, a small volume of the neutral phosphate buffer (pH 7.4, $I = 0.17$) was introduced by suction (3 s) prior to sample introduction. After the sample injection, the anodic end of capillary was immersed in the running buffer, and the electrophoresis was carried out.

Panels A and B of Figure 2 show the electropherogram of 200 μM racemic VER solution and 200 μM racemic VER-550 μM HSA mixed solution, respectively. VER enantiomers were completely separated by the chiral selector (TM- β -CD). The peak heights in Figure 2A represent the total drug concentration, and those in Figure 2B represent the unbound drug concentration. In Figure 2B, the plateau heights of both peaks are different from each other, indicating enantioselective protein binding.

As shown in Table 1, the unbound concentrations of VER enantiomers in 200 or 300 μM racemic VER and 550 μM HSA mixed solution determined by this method agree with those determined by the ultrafiltration-chiral HPLC method. The enantioselectivity in VER-HSA binding can be quantitatively estimated as the enantiomeric ratio of the unbound concentration. The *S/R* ratio is ~ 1.7 , which agrees with the literature reporting that (*R*)-VER is bound with HSA more tightly than (*S*)-VER.²⁹

When a small volume of the neutral buffer was not introduced prior to the sample injection, the *S/R* ratio of unbound VER concentration in 200 μM VER and 550 μM HSA mixed solution was estimated as 1.4, which is $\sim 20\%$ lower than the value (1.7) estimated under neutral conditions (pH 7.4). Our preliminary experiment suggested that VER–HSA binding exhibited no enantioselectivity with the acidic buffer. Therefore, the underestimation of the enantioselectivity is ascribable to the disturbance in the protein binding equilibrium caused by contact with the acidic running buffer (pH 2.5).

The appearance of a plateau region corresponding to the unbound drug concentration indicates that the binding equilibrium near the capillary injection end does not deviate during sample introduction. The decrease in the amount of unbound drug due to the introduction into the capillary can be supplied by the electrophoretic migration of unbound drug from the bulk sample and/or by the sample diffusion.

A relatively long-time injection (30 s) was applied in this study to obtain plateau peaks. For HPCE/FA with electrokinetic injection, the appearance of a plateau region is not essential in principle but convenient in practice. The plateau peak gives us the maximum UV response. Determination of unbound drug concentration from the plateau height is not influenced by the variation in migration time and the error in injection volume, unlike the determination using the peak area or the height of the drug peak without the plateau region. Since a small volume of the neutral buffer preliminarily sucked into the capillary would produce a slight electroosmotic flow, a small volume of the sample solution (total drug + protein) may be introduced into the capillary. This leads to overestimation of the unbound drug concentration, if the peak area or the height of the drug peak without a plateau region is used for the determination. In contrast, plateau height is free from this problem, because the introduced sample solution is subjected to frontal analysis to produce the unbound drug zone with the same plateau height as that of the unbound drug zone introduced electrokinetically.

After every run, the capillary was washed sequentially with 67 mM phosphate buffer (pH 7.4) containing 30 mM SDS and with 50 mM phosphate buffer (pH 2.5). Washing with SDS solution is indispensable to obtain good reproducibility. Without SDS washing, the unbound concentrations of VER enantiomers in 300 μM racemic VER–550 μM HSA mixed solution were determined as 64.1 ± 19.9 and 96.4 ± 30.4 μM for (*R*)- and (*S*)-VER, respectively ($n = 5$). The % CV was as large as 31.0% and 31.5%, although the mean value was almost the same as that obtained with SDS washing. The % CV was improved to 1.7% and 3.5%, respectively, by the SDS washing.

This method was applied to plasma sample. Figure 3 shows the electropherograms of (A) a human plasma blank and (B) 200 μM racemic VER spiked in human plasma. VER enantiomers were separated well from each other and from endogenous plasma components. In the case of electrokinetic injection, the peak response is dependent on the buffer concentration in the sample solution.³⁰ Therefore, the unbound drug concentration in plasma cannot be determined precisely. The calibration by using the drug standard dissolved in plasma ultrafiltrate would allow the determination. However, the enantioselectivity in plasma protein

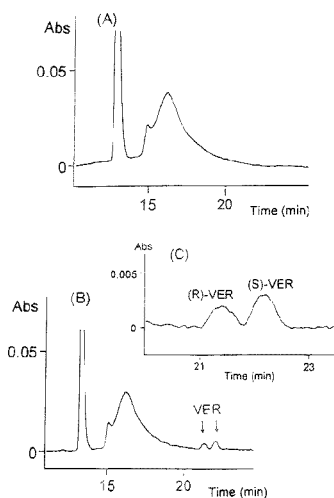


Figure 3. Electropherograms of (A) human plasma, (B) 200 μM racemic VER in human plasma obtained by HPCE/FA with electrokinetic injection, and (C) the expanded electropherogram of (B).

binding can be quantitatively analyzed as the peak height ratio between the enantiomers. The *S/R* ratio of unbound VER concentration in the plasma sample was 1.59 ± 0.08 ($n = 4$), which is close to the enantioselectivity in the HSA solution (see Table 1).

HPCE/FA Following Hydrodynamic Injection. After a plug of drug–protein mixed solution (~ 200 nL) was introduced hydrodynamically into the capillary, positive voltage was applied on the sample injection side. Neither negatively charged protein nor the bound drug migrated toward this direction, and only the unbound drug with a positive charge migrated toward the cathodic end (detection end), being separated from protein. During this separation process, the drug–protein mixed zone became shorter, and the zone containing only protein became longer. The binding equilibrium in the drug–protein mixed zone remained constant because of the quick release of bound drug from protein. Finally, the whole drug came out of the protein zone and migrated as a zone of the unbound form. The unbound drug zone was then separated into two zones of enantiomers by the chiral selector in the running buffer. The unbound concentration of each enantiomer was calculated from the respective plateau height. Similarly to the above mentioned electrokinetic injection, a small volume of the neutral phosphate buffer (pH 7.4, $I = 0.17$) was introduced by suction prior to the hydrodynamic sample injection. After the sample injection, the anodic end of capillary was immersed in the neutral phosphate buffer (pH 7.4, $I = 0.17$), and electrophoresis was carried out. Electrophoresis stopped when the anodic end was wrongly put in the acidic running buffer, probably due to the denaturation of the protein by the acidic running buffer.

Figure 4A shows the electropherogram of 200 μM racemic VER solution, and Figure 4B shows that of 200 μM racemic VER in 550 μM HSA solution. VER enantiomers were completely separated by the chiral selector (TM- β -CD). The peak height of each enantiomer in Figure 4B was lower than that in Figure 4A because of the protein binding. Figure 4B shows that the plateau heights of both peaks are different from each other. This indicates

(29) Eichelbaum, M.; Somogyi, A.; von Unruh, G. E.; Dengler, H. J. *Eur. J. Clin. Pharmacol.* **1981**, *19*, 133–137.

(30) Huang, X.; Gordon, M. J.; Zare, R. N. *Anal. Chem.* **1988**, *60*, 375–377.

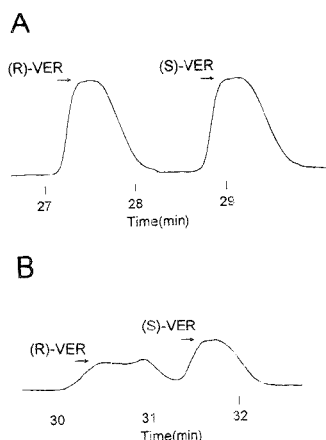


Figure 4. Electropherograms of (A) 200 μM racemic VER solution and (B) 200 μM racemic VER in 550 μM HSA solution obtained by HPCE/FA following hydrodynamic injection.

Table 2. Unbound Concentrations of VER Enantiomers^a Determined by HPCE/FA Following Hydrodynamic Injection

	within-run ^{b,c}	day-to-day ^{b,d}
Racemic 300 μM VER–550 μM HSA		
Cu(R) (μM)	61.3 (3.59)	65.0 (7.09)
Cu(S) (μM)	105 (3.53)	114 (7.04)
Cu(S)/Cu(R)	1.71 (0.65)	1.75 (3.41)
Racemic 200 μM VER–550 μM HSA		
Cu(R) (μM)	38.6 (5.18)	36.9 (7.03)
Cu(S) (μM)	69.3 (1.59)	65.8 (9.48)
Cu(S)/Cu(R)	1.80 (3.65)	1.78 (5.29)

^a Cu(R) and Cu(S) represent the unbound concentration of (R)-VER and (S)-VER, respectively. ^b Mean and % CV (in parentheses). ^c $n = 5$. ^d $n = 15$.

that the protein binding is enantioselective. Since both enantiomers were introduced in the same amount, the zonal peak of (R)-VER with the lower plateau height became broader than that of (S)-VER.

Table 2 lists the unbound concentration of VER enantiomers determined by this method. These values almost agree with the results determined by HPCE/FA with electrokinetic injection and by the ultrafiltration-HPLC method (Table 1).

DISCUSSION

In this paper, two chiral HPCE/FA methods with different injection procedure were used for the stereoselective binding assay of a basic drug. The common advantage is the small sample size. The sample volume introduced hydrodynamically was ~ 200 nL. Estimated from the peak area, the sample size for the electrokinetic injection was almost the same as that for the hydrodynamic injection. This sample size is about one-thousandth of that for the conventional ultrafiltration method.

Although both HPCE/FA methods gave similar results, electrokinetic injection seems to be more convenient than hydrodynamic injection. The HPCE/FA following hydrodynamic injection may confront the overlap of enantiomer peaks, because a lower

unbound drug fraction gives rise to a wider plateau range. In case the unbound fraction is different between enantiomers, the enantiomer with the higher unbound fraction is separated from protein faster than the antipode, and thereafter the binding equilibrium between the protein and the antipode remaining in the sample zone may be varied. Since this change leads to disturbance in the rear part of the plateau, the height should be measured at the front part of the plateau. In contrast, HPCE/FA with electrokinetic injection produces two zonal peaks of enantiomers with similar peak widths regardless of the unbound drug fraction. This is advantageous to analyze a series of samples with a wide range of bound drug fractions under a single separation condition. In addition, electrokinetic injection does not cause a disturbance in the rear part of the plateau. As found from the comparison between Figures 2b and 4b, electrokinetic injection gave better peak shapes than hydrodynamic injection.

HPCE/FA with electrokinetic injection is applicable only when drug and protein migrate the direction opposite to each other. Since most plasma proteins are negatively charged, only a positively charged drug can be applied. On the other hand, HPCE/FA following hydrodynamic injection is, in principle, applicable not only to a basic drug but also to an acidic drug and a neutral drug, as long as we can obtain enough difference in the electrophoretic mobility between drug and protein.

Detectability is the common problem in both methods. The S/N of 10 μM racemic VER was roughly estimated as 3. However, the therapeutic concentration of VER is much lower (the maximum concentration of VER in human plasma after oral administration of 80 mg of VER is ~ 80 nM). The on-capillary preconcentration using absorbent packed in a capillary is expected to improve the detectability.³¹ Some devices to prolong optical path length using a Z-shaped flow cell,³² multireflection flow cell,³³ and extended light path capillary³⁴ are also considered to benefit the detectability. Although these devices increase peak broadening, this will not be a serious problem, because HPCE/FA does not need a very high separation efficiency.

The affinity HPCE method and the HPCE/FA method have their own advantages and disadvantages. Affinity HPCE allows the enantioselective estimation of binding constants by using a racemate sample, while HPCE/FA requires a series of samples of each enantiomer to estimate the binding constants based on Scatchard analysis. In contrast, unlike affinity HPCE, HPCE/FA allows the direct determination of unbound concentrations of enantiomers. The enantioselectivity can be quantitatively estimated as the enantiomeric ratio of the unbound drug concentration. Because binding parameters may change depending on the protein concentration,^{35,36} the bindability should be estimated under physiological protein concentrations. If the physiological concentration of HSA (~ 550 μM) is applied in affinity HPCE, several problems, such as large UV absorbance, protein adsorption onto the capillary inner wall, high viscosity, and broadening of the drug peak, will interfere with the analysis. In contrast, HPCE/

(31) Swartz, M. E.; Merion, M. *J. Chromatogr.* 1993, 632, 209–213.

(32) Chervet, J. P.; van Soest, R. E. J.; Ursem, M. *J. Chromatogr.* 1991, 543, 439–449.

(33) Wang, T.; Aiken, J. H.; Huie, C. W.; Hartwick, R. A. *Anal. Chem.* 1991, 63, 1372–1376.

(34) Heiger, D. N. *High-performance capillary electrophoresis, an introduction*; Hewlett-Packard: Palo Alto, CA, 1993; pp 100–101.

(35) Boobis, S. W.; Chignell, C. F. *Biochem. Pharmacol.* 1979, 28, 751.

(36) Igari, Y.; Sugiyama, Y.; Awazu, S.; Hanano, M. *J. Pharm. Sci.* 1981, 70, 1049.

FA is applicable to the sample solution with a high protein concentration.

CONCLUSION

HPCE/FA with electrokinetic injection and HPCE/FA following hydrodynamic injection allow the simple and quantitative estimation of the enantioselectivity in protein binding of VER, a model basic drug. The unbound concentrations of VER enantiomers in a high concentration of HSA solution can be directly determined. The reliability of these methods was confirmed by comparison with a conventional ultrafiltration-chiral HPLC method.

The chiral HPCE with electrokinetic injection gives a better peak shape than HPCE/FA following hydrodynamic injection. The small sample size (~200 nL) will benefit the stereoselective binding study of plasma proteins, which are precious and difficult to obtain.

Received for review April 25, 1995. Accepted July 6, 1995.*

AC9504001

* Abstract published in *Advance ACS Abstracts*, August 15, 1995.

Determination of the Binding of Ligands Containing the *N*-2,4-Dinitrophenyl Group to Bivalent Monoclonal Rat Anti-DNP Antibody Using Affinity Capillary Electrophoresis

Mathai Mammen, Frank A. Gomez,[†] and George M. Whitesides*

Department of Chemistry, Harvard University, 12 Oxford Street, Cambridge, Massachusetts 02138

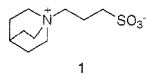
Affinity capillary electrophoresis has been used to determine the two dissociation constants of the complex between anti-DNP rat monoclonal IgG_{2b} antibody and charged ligands that contained a *N*-dinitrophenyl group. Singly and multiply charged ligands were used to establish the influence of the charge on the mobility of the complex between Ig and its ligand(s). Zwitterionic buffer additives lessened adsorption of protein to the walls of the capillary. A form of analysis of the binding data is derived that is more useful than Scatchard analysis for certain multivalent systems where cooperativity of binding is in question, but where it is also possible to make plausible assumptions about electrophoretic mobilities of protein and protein-ligand complexes. The uncertainties and assumptions of this analysis are contrasted with those of Scatchard analysis. For this antibody and these monovalent ligands, the dissociation of the ligands from the antibody occurred noncooperatively. The charge on IgG_{2b} at pH 8.3 is estimated to be -8.0 ± 0.2 ; this value is obtained by analysis of the electrophoretic mobilities of complexes IgG_{2b}L₂, where the ligands L are structurally similar but have different charges (the charges on the ligands were also determined by CE).

Nature uses polyvalency—the cooperative association of a receptor, or aggregate, having multiple recognition sites with a molecule containing multiple complementary ligands—to mediate many classes of biological interactions: between two surfaces (cell-cell,¹ cell-pathogen²⁻⁴); between a surface and a soluble species (cell-protein,⁵ pathogen-protein,^{6,7} pathogen-polysaccharide,⁸ cell-polysaccharide⁹); and between two soluble species (protein-protein,¹⁰ drug-ligand¹¹). We wish to quantitate the contribution of simultaneous, multivalent binding to these interactions. As a first, preliminary step in developing analytical methods

applicable to polyvalent interactions, we have explored the use of affinity capillary electrophoresis (ACE)¹²⁻¹⁵ to examine binding of monovalent ligands to bivalent antibodies. Polyvalent interactions can be either cooperative or noncooperative: the binding at one site may or may not influence binding at another site. We require methods applicable to cooperative systems and capable of yielding multiple dissociation constants. This study demonstrates a method for using ACE to extract dissociation constants of ligands from antibodies. It requires an assumption about the influence of binding of the ligand on the electrophoretic mobility of the protein and is, therefore, not completely general. This assumption, or its generalization, will, however, probably be met in many systems of interest. This system therefore models a common class of interactions involving an important class of proteins—immunoglobulins—that interact polyvalently.

We illustrate this method using ligands containing *N*-(2,4-dinitrophenyl)amino (DNP) groups and bivalent antibodies (rat myeloma monoclonal antibody, IgG_{2b}, hereafter referred to as Ig) that bind to DNP groups. These antibodies are well characterized and readily available.¹⁶⁻¹⁸

Proteins with high molecular mass (greater than ~50 kDa) and *pI* (greater than ~6.0) tend to give peaks on capillary electrophoresis under many conditions that are broad and unsymmetrical in shape (or to give no peaks at all) as a result of interactions with the wall of the capillary. The molecular mass of Ig is 150 kDa and its *pI* is 6.5; its peaks in simple buffers are broad. Use of zwitterionic additives to a simple buffer gives sharper, more symmetrical and highly reproducible peaks. We added 500 mM 3-quinuclidinopropanesulfonate (1) and 10 mM



K₂SO₄ to the buffer in all the experiments. This type of zwitterionic additive was originally proposed by Jorgensen.¹⁹

[†] Present address: California State University, Los Angeles, Department of Chemistry and Biochemistry, 5151 State University Drive, Los Angeles, CA 90032-8202.

- (1) Cepek, K.; Brenner, M. B. *Nature* 1994, 372, 190.
- (2) Sparks, M. A.; Williams, K. W.; Whitesides, G. M. *J. Med. Chem.* 1993, 36, 778-783.
- (3) Cohen, J. A.; Williams, W. V. *Microbiol. Sci.* 1988, 5, 265-270.
- (4) Collono, R. J. *Adv. Exp. Med. Biol.* 1992, 312, 61-70.
- (5) Pantoliano, M. W.; Horlick, K. A. *Biochemistry* 1994, 33, 10229-10248.
- (6) Roche, A. C.; Midoux, P. *Res. Virol.* 1990, 141, 243-249.
- (7) Karlsson, K. A. *Trends Pharm. Sci.* 1991, 12, 265-272.
- (8) Spear, P. G.; Shieh, M. T. *Adv. Exp. Med. Biol.* 1982, 313, 341-353.
- (9) Mora-Perez, I.; Porres-Cubero, J. C. *Rev. Clin. Esp.* 1985, 176, 1-4.
- (10) Dalgleish, A. G.; Kennedy, R. C. *Vaccine* 1988, 6, 215-220.
- (11) Christian, B.; Waring, M. J. *Biochem. J.* 1994, 300, 165-173.

- (12) Kuhr, W. G.; Monnig, C. A. *Anal. Chem.* 1992, 64, 389-407.
- (13) Chu, Y. H.; Lees, W. J.; Stassinopoulos, A.; Walsh, C. T. *Biochemistry* 1994, 33, 10616-10621.
- (14) Liu, J.; Volk, K. J.; Lee, M. S.; Kerns, E. H.; Rosenberg, I. E. *J. Chromatogr. A* 1994, 680, 395-403.
- (15) Liu, J.; Volk, K. J.; Lee, M. S.; Pucci, M.; Handwerker, S. *Anal. Chem.* 1994, 66, 2412-2416.
- (16) Bazin, H. *Proteins and Biological Fluids, 29th Colloquium*; Pergamon Press: Oxford, U.K., 1982; pp 615-618.
- (17) Koolstra, D. A.; Richards, J. H. *Biochemistry* 1978, 17, 345-351.
- (18) Brunger, A. T.; Leahy, D. J.; Hynes, T. R.; Fox, R. O. *J. Mol. Biol.* 1991, 221, 239-256.

ACE yields dissociation constants by analysis of the change in electrophoretic mobility of a protein on binding a small charged ligand.^{20,21} We derive these changes in electrophoretic mobility from changes in the time that the protein requires to reach the detector (the time of appearance, t_{app}) relative to the time required for several internal standards that are not influenced by the ligand. The change in the time of appearance (Δt_{app}) of a protein on binding a ligand must be greater than the width of its peak to be measured reliably. A typical width at half-height of the peaks in this study is ~ 10 s. The Δt_{app} is approximately proportional to the charge on the ligand, Z_L , and inversely proportional to the mass, M , of the protein (eq 1). Ig has a high molecular mass (150

$$\Delta t_{app} \propto Z_L/M^\alpha \quad (1)$$

kDa). To achieve the required Δt_{app} , the value of Z_L for the ligand must therefore be relatively large. In this study, if $Z_L = -1$, $\Delta t_{app} \sim 3$ s; if $Z_L = -3$, $\Delta t_{app} \sim 9$ s. We synthesized and used ligands where $Z_L = -1, -2, -3$, and -9 .

There have been several reports of positive cooperativity between the binding sites of antibodies that bind monovalent ligands, particularly for antibodies that bind DNP groups;²²⁻²⁴ we could not, therefore, assume that binding of monovalent ligands to Ig occurred noncooperatively. Cooperativity would yield a curved plot in Scatchard analysis, and values for the two dissociation constants are not readily extracted from such a plot. Scatchard analysis, which was acceptable in monovalent systems previously studied by ACE (e.g., carbonic anhydrase,²³ vancomycin,²⁶ and SH3 domain²⁷), is thus not useful here. We derive a form of analysis (different from Scatchard analysis) in which there is no assumption regarding cooperativity: for all types of cooperativity (positive, negative, none), this analysis yields a line from which we extract dissociation constants.

As with many affinity experiments, we measure degree of complexation as a function of the concentration of ligand; analysis of these data yields dissociation constants. Our analysis requires that we determine the mobility of the complex of protein bound to ligand experimentally. In Scatchard analysis, fully saturating conditions of ligand need never be used experimentally. In a later section, we discuss the potential error introduced into the dissociation constants as a function of the experimental uncertainty in the mobility of the Ig complexed to two ligands. If the value for a dissociation constant is micromolar or less, we can achieve conditions experimentally that make this error acceptably small (10–20%).

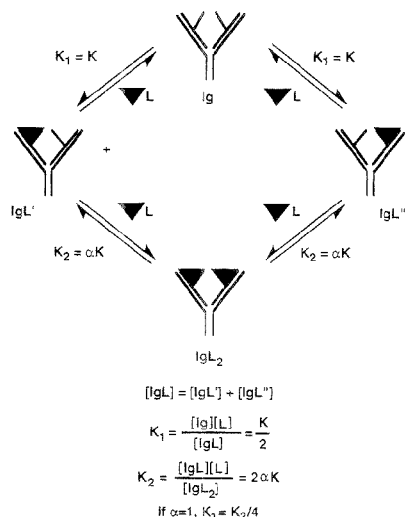


Figure 1. Equilibria involved in Ig–antigen interactions. K_1 is the dissociation constant between the singly occupied Ig and the unoccupied Ig. K_2 is the dissociation constant between the doubly occupied Ig and the singly occupied Ig. We denote the degree of cooperativity between K_1 and K_2 as α . Antibodies that bind DNP do so mainly through interaction with the light chain; the binding site is represented as localized on this chain.

DERIVATION OF ANALYSIS

We define two dissociation constants, K_1 and K_2 , for the complex between Ig and two ligands (Figure 1).^{18,23} The total mobility, μ^{total} , of a molecule, X, is a sum of the mobility due to electroosmotic (EO) flow, μ^{EO} , and the mobility due to electrophoretic flow, $\mu^{electro}$. Total mobility is inversely proportional, with proportionality constant C_t , to the total time of appearance, t_{app} , that X takes to move from the injection port to the detector (eq 2). We calculate $\mu^{electro}$ by subtracting the EO mobility of the

$$\mu^{total} = \mu^{EO} + \mu^{electro} = C_t/t_{app,X} \quad (2)$$

neutral marker (in our case, mesityl oxide, MO), μ^{EO} , from μ^{total} (eq 3). ACE relates the changes in $\mu^{electro}$ of a receptor (Ig) on

$$\mu^{electro} = \mu^{total} - \mu^{EO} = C_t \left(\frac{1}{t_{app,X}} \right) - C_t \left(\frac{1}{t_{app,MO}} \right) \quad (3)$$

complexation with a ligand (L) present in the electrophoresis buffer to the dissociation constant (K_d). When the concentration of ligand is zero, $\mu^{electro}$ is that of free Ig, μ_{Ig} . When the concentration of ligand is sufficiently high that both of the binding sites of the Ig are occupied, the electrophoretic mobility is μ_{IgL_2} . When intermediate concentrations of ligand are present, bivalent Ig receptors exist in three forms: unoccupied (Ig), singly occupied (IgL), and doubly occupied (IgL₂). In the present system, we assume (and infer from the line widths of the peaks) that the rates of dissociation (k_{off}) are sufficiently fast (>0.1 s⁻¹) that we observe

(28) Bunting, J. R.; Cathou, R. E. *J. Mol. Biol.* **1973**, *77*, 223–235.

- (19) Bushley, M. M.; Jorgenson, J. W. *J. Chromatogr.* **1989**, *480*, 301–310.
 (20) Chu, Y. J.; Avila, L. Z.; Gao, J.; Whitesides, G. M. *Acc. Chem. Res.*, submitted for publication.
 (21) Gomez, F. A.; Avila, L. Z.; Chu, Y.; Whitesides, G. M. *Anal. Chem.* **1994**, *66*, 1785–1791.
 (22) Lancet, D.; Pecht, I. *Biochemistry* **1977**, *16*, 5150–5157.
 (23) Zidovetzki, A. L.; Pecht, I. *Proc. Natl. Acad. Sci. U.S.A.* **1979**, *76*, 5848–5852.
 (24) Zidovetzki, K.; Light, A.; Pecht, I. *Mol. Immunol.* **1981**, *18*, 491–497.
 (25) Avila, L. Z.; Chu, Y.; Blosssey, E. C.; Whitesides, G. M. *J. Med. Chem.* **1993**, *36*, 126–133.
 (26) Chu, Y.; Whitesides, G. M. *J. Org. Chem.* **1992**, *57*, 3524–3525.
 (27) Gomez, F. A.; Chen, J. K.; Tanaka, A.; Schreiber, S. L.; Whitesides, G. M. *J. Org. Chem.* **1994**, *59*, 2885–2886.

a concentration-weighted average electrophoretic mobility for all three species (we only see one peak at all concentrations of ligand).²⁹ If we define the total concentration of all forms of Ig as $[Ig_0]$, then the fraction of Ab in form "i" is θ_i .³⁰ The electrophoretic mobility, μ^{electro} , is the weighted mobility of all three species of Ig (eq 4). The θ_i can be rewritten in terms of K_1 , K_2 , and $[L]$ by

$$\mu^{\text{electro}} = \frac{[Ig]}{[Ig_0]} \mu_{Ig} + \frac{[IgL]}{[Ig_0]} \mu_{IgL} + \frac{[IgL_2]}{[Ig_0]} \mu_{IgL_2} \quad (4)$$

using the definitions from Figure 1. The results are shown in eqs 5–7 and are similar to the equations derived for the

$$\theta_{Ig} = 1 / \left(\frac{[L]^2}{K_1 K_2} + \frac{[L]}{K_1} + 1 \right) \quad (5)$$

$$\theta_{IgL} = 1 / \left(\frac{[L]}{K_2} + \frac{K_1}{[L]} + 1 \right) \quad (6)$$

$$\theta_{IgL_2} = 1 / \left(\frac{K_1 K_2}{[L]^2} + \frac{K_2}{[L]} + 1 \right) \quad (7)$$

dissociation of a diacid.³⁰

The charge on the protein with n ligands, $Z_{P(L)_n}$, is the sum of all charges on the amino acid residues of the protein and all tightly bound species (cofactors, coenzymes, ligands). Z_P is the charge on the uncomplexed protein; Z_L is the charge on the ligand. The electrophoretic mobility of the Ig, μ_{ig} , is approximately proportional to Z_P and inversely proportional to its hydrodynamic drag with a proportionality constant $C_{\mu,ig}$. This drag is often set proportional to M^α (eq 8); this equation fits the experimental data relating

$$\mu_{ig} = C_{\mu,ig} (Z_P / M^\alpha) \quad (8)$$

electrophoretic mobility to mass for a number of globular proteins.^{31,32} The binding of one or two ligands, each with mass m ($\ll M$), and charge Z_L , gives species having electrophoretic mobilities given by eqs 9 and 10, respectively. The proportionality

$$\mu_{IgL} = C_{\mu,IgL} \frac{Z_{P(L)}}{(M+m)^\alpha} = C_{\mu,IgL} \frac{Z_P + Z_L}{(M+m)^\alpha} \approx (Z_P + Z_L) \frac{C_\mu}{M^\alpha} \quad (9)$$

$$\mu_{IgL_2} = C_{\mu,IgL_2} \frac{Z_{P(L)_2}}{(M+2m)^\alpha} = C_{\mu,IgL_2} \frac{Z_P + 2Z_L}{(M+2m)^\alpha} \approx (Z_P + 2Z_L) \frac{C_\mu}{M^\alpha} \quad (10)$$

constant C_μ is related to, but not the same as, C_1 from eq 2. The

(29) If the time for a single dissociation event is, on average, much shorter than the time by which the two peaks due to two species are separated, we expect to observe an average weighted peak. If this time for dissociation is much longer than the time of separation, then we expect to observe two individual peaks. If the dissociation rate is intermediate in magnitude, then we expect to observe a broad single peak; we expect this peak to be especially broad at $[L] = K_0$.

(30) Connors, K. A. *Binding Constants: The Measurement of Molecular Complex Stability*; John Wiley & Sons, New York, 1987.




			
Charge on complex, $Z_{P(L)_n}$	Z_P	$Z_P + Z_L$	$Z_P + 2Z_L$
Approximate Mass	M	M	M
Electrophoretic Mobility	μ_{Ig}	μ_{IgL}	μ_{IgL_2}
Determined:	experimentally at $[L] = 0$	using eq 16	experimentally asymptotically at high $[L]$ ($[L] > 30K_2$)

Figure 2. Electrophoretic mobilities of the various protein and protein–ligand complexes.

numerical values of C_μ , $C_{\mu,Ig}$, $C_{\mu,IgL}$, and C_{μ,IgL_2} are not important in this study because they all cancel in the final analysis.

The value for α is $\sim 2/3$ for small proteins.^{31,32} The exact value of α in this work is not important since we assume that M^α will be a constant so long as the bound ligand contributes negligibly to the hydrodynamic drag of its complex with Ig (that is, if m and $2m \ll M$). If, in addition, $C_{\mu,Ig} = C_{\mu,IgL} = C_{\mu,IgL_2} = C_\mu$, then the change in the mobility of the Ig on binding one ligand ($\mu_{IgL} - \mu_{Ig}$) is half the change in mobility on binding two ligands ($\mu_{IgL_2} - \mu_{Ig}$) (Figure 2). Equations 4–10 can be combined and rearranged to give eq 11. Plotting the left-hand side of eq 11 against the

$$\frac{\mu^{\text{electro}} - 1/2(\mu_{IgL_2} + \mu_{Ig})}{\mu^{\text{electro}} - \mu_{Ig}} [L] = \left(\frac{\mu_{IgL_2} - \mu^{\text{electro}}}{\mu^{\text{electro}} - \mu_{Ig}} [L]^2 \right) \frac{1}{K_2} - K_1 \quad (11)$$

coefficient of the term $1/K_2$ gives a line with slope equal to $1/K_2$ and y intercept equal to $-K_1$.

As $[L]$ increases, μ^{electro} asymptotically approaches μ_{IgL_2} (Figures 2 and 3). Experimentally, we expect that when increasing $[L]$ does not *observably* increase the value of μ^{electro} , then we have reached $\mu^{\text{electro}} \approx \mu_{IgL_2}$. In order to estimate how close our observed electrophoretic mobility is to μ_{IgL_2} , we perform the following iterative experiment: We use some arbitrary value of (or best guess for) the maximum concentration of ligand, $[L]^{\text{max}}$. We calculate dissociation constants K_1 and K_2 based on these data using eq 11. We then ask if $[L]^{\text{max}} > 30K_2$. If $[L] > 30K_2$, greater than 97% of the Ig is bound to two ligands (and therefore we are very close to μ_{IgL_2}). If $[L]^{\text{max}} < 30K_2$, then we collect more data using higher $[L]$ and repeat the analysis using eq 11. We iterate until $[L]^{\text{max}} > 30K_2$. This procedure guarantees that we are within $\sim 3\%$ of the actual value of μ_{IgL_2} .³³ A 3% error in μ_{IgL_2} translates into a maximum error of 5% in K_1 and 10% in K_2 . There are, of course, other sources of error that further increase the uncertainty in K_1 and K_2 ; some of these are discussed in more detail in a later section.

(31) (a) Cantor, C. R.; Schimmel, P. R. *Biophysical Chemistry*; W. H. Freeman: New York, 1980. (b) The application of Henry's equation to proteins yields that the μ^{electro} becomes independent of mass. Whether or not μ^{electro} is inversely dependent on mass or independent of mass, however, has little impact on the current work.

(32) Grossman, P. D.; Colburn, J. C. *Capillary Electrophoresis: Theory and Practice*; Academic Press, Inc.: San Diego, CA, 1992.

(33) Achieving the condition $[L]^{\text{max}} > 30K_2$ is not possible if this concentration either exceeds the solubility of the ligand in the buffer or significantly changes M^α , C_μ , or C_1 .

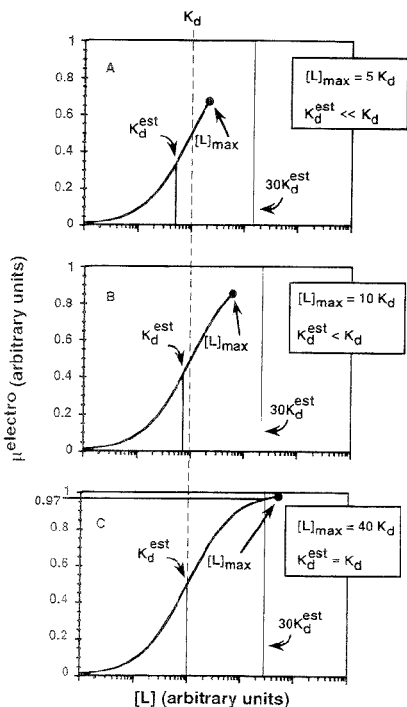


Figure 3. $[L]$ vs μ_{electro} . (A) The highest experimental value of $[L]_{\text{max}}$ is much less than $30K_d$ and not sufficiently high to give a reliable value of μ_{ligL_2} . (B) The value of $[L]_{\text{max}}$ is less than $30K_d$ and is still not sufficiently high to give a reliable value of μ_{ligL_2} . (C) The value of $[L]_{\text{max}}$ is greater than $30K_d$ and is sufficiently high that the lg is within 3% of complete saturation (i.e., $\theta_{\text{ligL}_2} \geq 0.97$; eq 5). The error in the estimate of μ_{ligL_2} is less than 3%.

In the case of noncooperative binding, K_d is the dissociation constant for one site and is related to K_1 and K_2 according to eq 12 (Figure 1). A Scatchard plot (eq 13), yields straight lines in

$$K_d = 2K_1 = 1/2K_2 \quad (12)$$

$$\frac{\mu_{\text{electro}} - \mu_{\text{lg}}}{[L]} = -K_d^{-1}(\mu_{\text{electro}} - \mu_{\text{lg}}) + K_d^{-1}(\mu_{\text{ligL}_2} - \mu_{\text{lg}}) \quad (13)$$

$$\Delta\mu = \mu_{\text{electro}} - \mu_{\text{lg}} = \frac{\mu_{\text{ligL}_2} - \mu_{\text{lg}}}{1 + (K_d/10^{\log[L]})} \quad (14)$$

cases of noncooperative binding (rearranging eq 13 gives eq 14; plotting $\Delta\mu$ against $\log [L]$ gives a regular sigmoid). In all other cases (positively or negatively cooperative binding), Scatchard plots are curved. As it is difficult to detect curves by eye, we advocate plotting the data using eq 11 in *all* cases where cooperativity is in question.

The uncertainties in values for K_2 and K_1 are less than 10 and 20%, respectively. For each of the experimental quantities (observables) in our experiment ($[L]$, μ_{electro} , μ_{lg} , μ_{ligL_2}), there is an uncertainty in its value ($\sigma_{[L]}$, $\sigma_{\mu_{\text{electro}}}$, $\sigma_{\mu_{\text{lg}}}$, and $\sigma_{\mu_{\text{ligL}_2}}$, respectively).

In our analysis (eq 11), we use these experimental quantities to calculate and plot a pair of points (X, Y) , where Y is the left-hand side of eq 11 and X is the coefficient of the term $1/K_d$. The experimental uncertainties in the observables gives rise to uncertainties in X and Y : σ_X and σ_Y .³⁷ The mathematical relationship between X (or Y) and the observables determines how strongly uncertainties in the observables influence σ_X (or σ_Y). In eq 11, for example, the X value depends on $[L]$ and the $\sigma_X^{[L]}$ increases with increasing $[L]$ and $\sigma_{[L]}$ (eq 15). Thus we expect

$$\sigma_X^{[L]} = 2[L]\sigma_{[L]} \quad (15)$$

that data obtained using high concentrations of ligand will display greater scatter than those derived from low concentrations of ligand (this expectation is consistent with our observations shown in Figure 7). This expectation is different when Scatchard analysis is used. In Scatchard analysis, the Y value, Y^{Scat} , is $\Delta\mu/[L]$ (eq 13). The error in Y^{Scat} that is due to uncertainty in $[L]$, $\sigma_{Y^{\text{Scat}}}^{[L]}$, decreases rapidly with $[L]$ and increases with $\sigma_{[L]}$ (eq 16). In

$$\sigma_{Y^{\text{Scat}}}^{[L]} = \sigma_{[L]}/[L]^2 \quad (16)$$

Scatchard analysis, we expect more scatter in data derived from low concentrations of ligand; one therefore should take more data points from *high* concentrations of ligand. With our analysis, one should, in contrast, use more data from *low* concentrations of ligand (as discussed earlier in Figure 3, we also need to collect several data from *very* high concentrations of ligand to determine μ_{ligL_2} reliably).

The portion of the uncertainty in the X value that is due to $\sigma_{\mu_{\text{ligL}_2}}$, $\sigma_X^{\mu_{\text{ligL}_2}}$, is given in eq 17. The portion of the uncertainty in Y that is due to μ_{ligL_2} , $\sigma_Y^{\mu_{\text{ligL}_2}}$, is given in eq 18.

$$\sigma_X^{\mu_{\text{ligL}_2}} = \sigma_{\mu_{\text{ligL}_2}} [L]^2 \left(\frac{1}{\mu_{\text{obs}} - \mu_{\text{lg}}} \right) \quad (17)$$

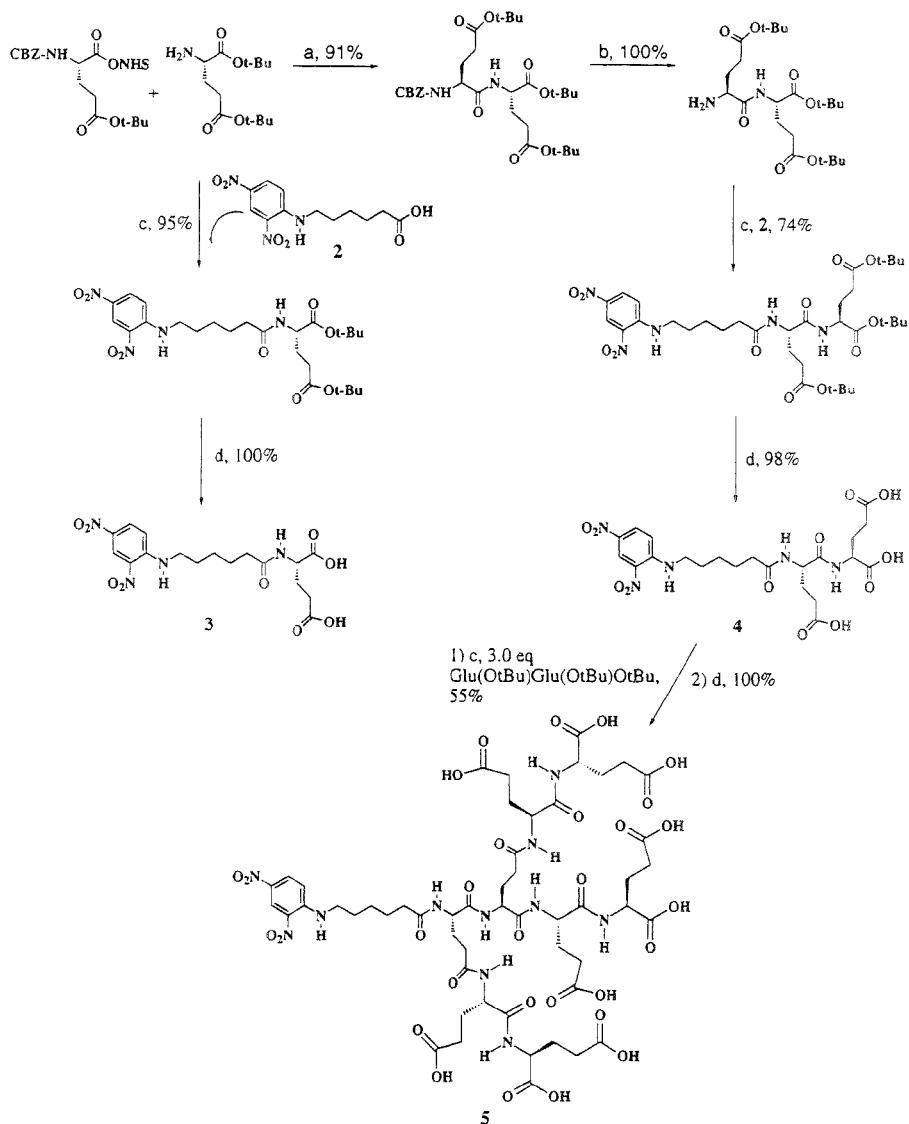
$$\sigma_Y^{\mu_{\text{ligL}_2}} = \sigma_{\mu_{\text{ligL}_2}} \left(\frac{[L]}{2(\mu_{\text{obs}} - \mu_{\text{lg}})} \right) \quad (18)$$

There are also uncertainties in the plotted data introduced by $\sigma_{\mu_{\text{electro}}}$, $\sigma_{\mu_{\text{lg}}}$, and $\sigma_{\mu_{\text{ligL}_2}}$. These uncertainties were calculated by mathematically propagating reasonable values for $\sigma_{[L]}$, $\sigma_{\mu_{\text{electro}}}$, $\sigma_{\mu_{\text{lg}}}$, and $\sigma_{\mu_{\text{ligL}_2}}$. We conclude that the *total* uncertainties in the slope ($1/K_d$) and Y intercept ($-K_1$) are, in our experiments and analysis, approximately 5–10 and 15–20%, respectively.

EXPERIMENTAL SECTION

Materials. Rat monoclonal anti-dinitrophenol antibody (Zymed, Clone LO-DNP-11, 1994 Catalog No. 04-8500, purchased in 10 mM phosphate-buffered saline (PBS) at 0.6 mg/mL) was used after ultracentrifugal filtration (molecular weight cutoff 10 000) and lyophilization. Bovine carbonic anhydrase (CA; EC 4.2.1.1, containing CAA and CAB isozymes, from bovine erythrocytes), bovine α -lactalbumin (LA; type I, from bovine milk), the tripeptide Arg-Gly-Asp (RGD), 2, and mesityl oxide (MO) were purchased from Sigma Chemical Co. and used without further purification. All solutions containing protein were prepared by dissolving

Scheme 1. Synthesis of Ligands 2–5^a



^a Reagent: (a) CH_2Cl_2 ; (b) H_2 , 10% activated Pd on carbon; (c) dicyclohexylcarbodiimide (DCC), hydroxybenzotriazole (HOBT), and diisopropylethylamine (DIPEA) in dimethylformamide (DMF); (d) trifluoroacetic acid (TFA)– CH_2Cl_2 1:1.

lyophilized protein into buffer. Organic reagents used in the syntheses of 1–5 were purchased from Aldrich and used without purification. Reaction solvents were distilled from an appropriate drying agent before use. Reaction mixtures were stirred magnetically and monitored by thin-layer chromatography on silica gel precoated glass plates (Merck). Flash column chromatography was carried out at medium pressure on silica gel 60_{F254} (230–400 mesh, E. Merck) using the solvents that are indicated. Compound 1 was synthesized as previously described.²¹ The procedures for

synthesizing and characterizing compounds 2–5 and all intermediates are available as supporting information.

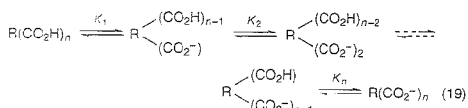
Equipment. Proton and carbon NMR spectra were measured on a Bruker AM-400 MHz NMR spectrometer. Chemical shifts are reported in ppm relative to TMS for the proton spectra and relative to $\text{dms}\text{-}d_6$ at 39.5 ppm for the carbon spectra. The analysis of dissociation constants was performed using an ISCO Model 3140 CE system. The titration of ligands 4 and 5 was performed using a Beckman P/ACE System 5010. The capillary

tubing (Polymicro Technologies, Phoenix) was of uncoated fused silica with an internal diameter of 50 μm , a total length of 57 cm, and a length from inlet to detector of 47 cm.

Procedure for CE. The sample for injection into the electrophoresis capillary consisted of the Ig (0.6 mg/mL), 20 μM mesityl oxide (MO), carbonic anhydrase (CA, 1 mg/mL), α -lactalbumin (LA, 1 mg/mL), and RGD (1 mg/mL). The sample solution (~ 8 nL) was introduced into the capillary by vacuum injection. The conditions used during each CE experiment were as follows: voltage, 30 kV; current uncontrolled, but generally 20 μA ; buffer, 25 mM Tris-HCl, 192 mM glycine (pH 8.3), 0.5 M 1, 10 mM K_2SO_4 ; detection, 200 nm; temperature 25 ± 2 $^\circ\text{C}$.

RESULTS AND DISCUSSION

Scheme 1 summarizes the syntheses of DNP analogs 3–5. We expected that, at pH 8.3, the charges on 2–5 would be -1 , -2 , -3 , and -9 , respectively. We validated this expectation for ligands 4 and 5 by monitoring the electrophoretic mobility of these ligands as a function of pH.³⁴ That is, we titrated the ligands using electrophoretic mobilities as the experimental variable being monitored. The charges on ligands 4 and 5 remain constant at pH > 7 ; all carboxylic acids in these molecules are fully deprotonated at pH > 7 (Figure 4). The titration curves fit the theoretical equations³⁵ that are derived for polyacids in which the values of pK_a for each acidic residue are independent of one another, and identical. K_a is the microscopic dissociation constant for one acidic residue (its value may change with different buffers and different ionic strengths). For a polyacid with n independent sites (eq 19), each with microscopic dissociation constant K_a , the molecular dissociation constants, K_m , are defined according to eq 20. The



$$K_m = \frac{n - (m - 1)}{m} K_a \quad m = 1 - n \quad (20)$$

statistical distribution of dissociation constants for the nonacid molecule, 5, is $9K_a$, $4K_a$, $(1/2)K_a$, $(1/2)K_a$, K_a , $(1/3)K_a$, $(1/3)K_a$, $(1/4)K_a$, and $(1/4)K_a$; for the triacid 4, the distribution is $3K_a$, K_a , and $(1/3)K_a$. The theoretical titration curves³⁵ derived using these statistics fit the experimental mobilities relatively well when the values of the two microscopic dissociation constants are 4.1 and 5.6 for 4 and 5, respectively. In the present study, we have insufficient data to determine whether the polyacids are truly statistical in their ionization; we suspect that they are not.

We used MO as an indicator of EO flow in these experiments, and CAB, CA, and LA as charged noninteracting (ostensibly) reference materials. These reference materials represent a range of molecular surfaces (uncharged to highly charged) and molecular masses (0.40–30 kDa). Any large systematic change in the mobilities of these species with changing [L] would suggest potential problems with the experiment. For example, if the mobilities of any of the reference materials varied as a function

(34) Cleveland, J. A.; Benko, M. H.; Gluck, S. J.; Walbroehl, Y. M. *J Chromatogr.* 1993, 652, 301–308.

(35) We use a manual iterative procedure to arrive at the fit shown.

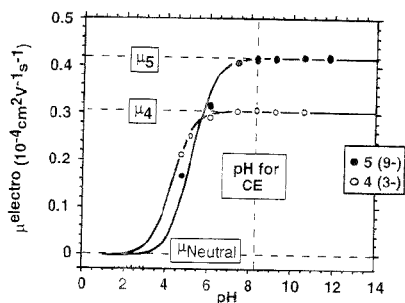


Figure 4. pH vs μ^{electro} . The value of μ^{electro} of ligands 4 and 5 are measured as a function of the pH of the phosphate buffer (from pH 4.69 to 11.76) using CE (see Experimental Section for exact details). The μ^{electro} of 4 (●) and 5 (○) are approximately constant at pH > 7 ; all carboxylic acids in these ligands are fully deprotonated at pH > 7 . The curves drawn through the data represent theoretical titration curves for polyacids in which there are no interactions between acidic groups: the microscopic values for pK_a for 4 and 5 are assigned values of 4.1 and 5.6, respectively. These curves are guides to the eye—they demonstrate only that the data can be fit to a single microscopic pK_a , not that only a single microscopic pK_a is involved.

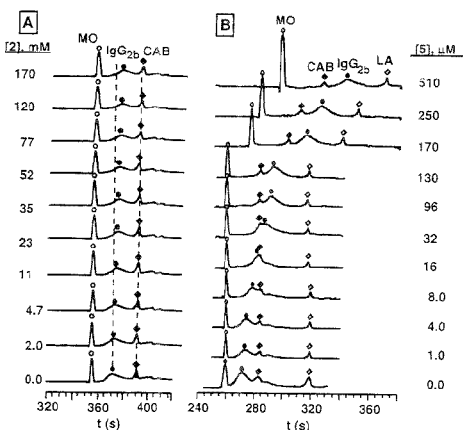


Figure 5. MO as an indicator of rate of EO flow, and CAB and LA as internal references. ACE of IgG_{2b} (see Experimental Section for exact conditions): (A) increasing [2], with charge -1 ; (B) increasing [5], with charge -9 .

of [L], we might have concluded that these materials interacted with the charged ligand.

Figure 5 shows a representative series of electropherograms of Ig in buffer containing various concentrations of 2 and 5. As expected, the more negatively charged ligand 5 shifts the antibody by a larger amount than the less negatively charged ligand 2. The broadness of the peak due to Ig may be due to its heterogeneity (possibly due to different states of glycosylation). Figure 6A shows the change in electrophoretic mobilities of Ig, CA, and LA on increasing the concentration of 5. The approximately horizontal lines for LA and CA indicate that 5 has no affinity for these species. Figure 6B shows the electrophoretic mobility as a function of log [5]. Using the values of values for K_1 and K_2 derived later, and eqs 6–10 and

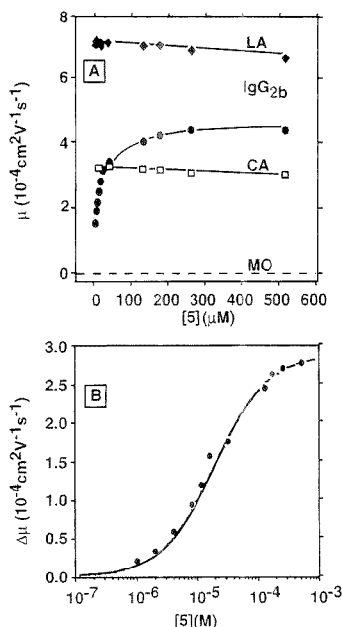


Figure 6. (A) The μ^{electro} of IgG_{2b}, MO, LA, and CAB for increasing concentration of 5 (see Experimental Section for exact conditions). The electrophoretic mobility of MO is taken as zero. (B) Change in the electrophoretic mobility of IgG_{2b}, plotted against $\log [5]$. The sigmoidal curve drawn through the data represent the theoretical fit, assuming that the binding sites are independent (eq 14) and that the microscopic dissociation constant $K_2 = 20 \mu\text{M}$ ($K_1 = 10 \mu\text{M}$ and $K_2 = 40 \mu\text{M}$; Table 1).

19, we calculate the observed electrophoretic mobility as a function of $\log [5]$; the calculated curve fits the experimental data.

In addition to the iterative procedure illustrated in Figure 3, a further check to the experimental value of $\mu_{i:L_2}$ is possible in the case where analysis using eq 11 is consistent with noncooperative binding: we plot the data using eq 13. The X intercept yields a value for $\mu_{i:L_2}$. The experimental values of $\mu_{i:L_2}$ (obtained from high concentrations of ligand) were within 3% of the value calculated using eq 11.

Figure 7 is a plot of the data from Figure 5 based on eq 11. Table 1 gives the values for K_1 and K_2 that describe the interactions between charged ligands 2–5 and IgG_{2b}. Experiments in 0.2, 0.5, and 1.0 M 1 all yielded the same values of K_1 and K_2 (although we can make no more general statement concerning the dependence of dissociation constants on zwitterions).³⁶

As is consistent with noncooperative binding, all our systems yield a ratio of K_2/K_1 of ~ 4 (Figure 1). We conclude that binding of monovalent ligands 2–5 to IgG_{2b} is noncooperative.

Defining Charge: $Z_{P(L)}$, Z_{exp} , Z_{calc} , Z_{eff} . The charge on a protein can be a theoretical construct, a calculated value, or an experimentally determined value. We define $Z_{P(L)}$ as the sum of all charges on the amino acid residues of a protein, P, plus all charges on tightly associated molecules including ligands (L), cofactors, and coenzymes (Figure 8). The charges on L and the

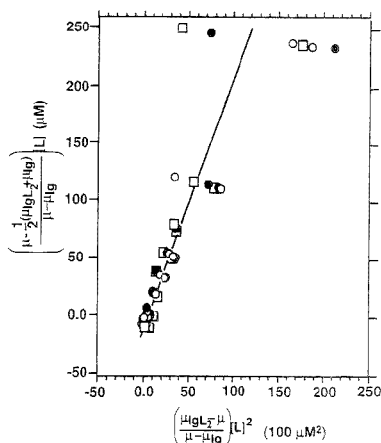


Figure 7. Binding of 5 to IgG_{2b} using eq 11. The plot yields a straight line from which one obtains dissociation constants K_1 and K_2 . The data include duplicate trials for three different days (different sample and buffer preparations).

charge on P that is uncomplexed to L are, analogously, Z_L and Z_P , respectively.

The effective charge on a protein, Z_{eff} , is treated as a perturbation on Z_P and is an experimental parameter that describes the response of the protein to an electrical field. If the protein is in a solution containing ions, Z_{eff} tacitly includes the charges of the ions in the Stern–Helmholtz layer³⁸ (the stationary boundary layer) surrounding the protein (Figure 8). Z_{eff} is in general (but need not necessarily be) lower than Z_P (as a result of “charge shielding”). The relationship between Z_P and Z_{eff} is given by eq 21. The term q (eq 21) reflects the degree of shielding of Z_P by

$$Z_{\text{eff}} = Z_P / (1 + q) \quad (21)$$

ions in solution and is approximately proportional to the ionic strength of the solution: if $q \ll 1$, then shielding is negligible.

The μ^{electro} is linearly proportional to Z_{eff} (eq 22). Using eq 21,

$$\mu^{\text{electro}} = C_{\mu}^{\text{eff}} \frac{Z_{\text{eff}}}{M^{\alpha}} = \frac{C_{\mu}^{\text{eff}}}{(1 + q)} \frac{Z_P}{M^{\alpha}} = C_{\mu} \frac{Z_P}{M^{\alpha}} \quad (22)$$

μ^{electro} is also linearly proportional to Z_P (eq 22). The proportionality constants that relate Z_P and Z_{eff} to μ^{electro} are C_{μ} and C_{μ}^{eff} , respectively; C_{μ} and C_{μ}^{eff} are consequently related by eq 23.

$$C_{\mu} = C_{\mu}^{\text{eff}} / (1 + q) \quad (23)$$

We use CE to estimate experimentally the charge on a protein, Z_{exp} , from the mobilities of a protein and its complexes with differently charged ligands (described in detail

(37) In general, if X is a function of the two experimental observables a and b ($X = f(a, b)$), then $(\sigma_X)^2 = (\sigma_a^2)^2 + (\sigma_b^2)^2 = (aX/ua)^2(\sigma_a)^2 + (bX/ub)^2(\sigma_b)^2$; Skoog, D. A. *Principles of Instrumental Analysis*; Saunders College Publishing: Fort Worth, TX, 1985; pp 5–22.

(38) Knox, J. H. J. *Chromatogr.* 1994, 680, 3–13.

(36) Cordova, E.; Gomez, F. A.; Whitesides, G. M., in progress.

Table 1. Dissociation Constants of the IgG2b Complexes with Ligands 2-5^a

ligand	charge ^b	K_1^c (μM)	K_2^d (μM)	K_2/K_1
2	-1	1.9 ± 0.4	8.5 ± 0.9	4.5 ± 0.9
3	-2	2.8 ± 0.6	9.5 ± 1.0	3.4 ± 0.7
4	-3	5.8 ± 1.2	19 ± 1.9	3.3 ± 0.7
5	-9	9.0 ± 1.8	40 ± 4.0	4.4 ± 0.9

^a 192 mM Tris, 25 mM glycine, 10 mM K_2SO_4 , 0.5 M 1. ^b Charge on the ligand in aqueous solution, pH 8.3. ^c Probable error in K_1 is 20%. ^d Probable error in K_2 is 10%.

below). We will show that if the values of q , M , and C_μ^{eff} remain constant for the protein and its complexes, then $Z_{\text{exp}} \approx Z_p$ (Figure 8).

We may also calculate a charge on the protein from values of pK_a and pH. We refer to this calculated charge on the protein as Z_{calc} . If the values of pK_a and pH are known exactly, then $Z_{\text{calc}} \approx Z_p$ (Figure 8).

The experimental charge (Z_{exp}) of this IgG2b is -8.0 at pH 8.3. It has been difficult to estimate the charge, Z_p , on a protein.³⁹⁻⁴² We recently reported a method of inferring the charge, Z_{exp} , experimentally for small (MW < 50 000) proteins.⁴² In that analysis, we acylate the protein partially under nondenaturing conditions to create a family of differently acylated derivatives, that is, a charge ladder. Analysis of the electrophoretic mobilities of the differently acylated derivatives yields Z_{exp} . We are, however, unable to use this method for proteins of high molecular weight ($\text{MW}_{\text{ig}} = 150\,000$) because we are unable to separate the components of the charge ladder with resolution that is sufficient for analysis.

In this paper, we use the change in electrophoretic mobility of the protein in complexing charged ligands to evaluate Z_{exp} . This method has been used previously to determine the value of Z_{exp} for carbonic anhydrase at various pH values.⁴² This method also requires the syntheses of multiple ligands with different values of charge and is therefore less convenient than the method based on charge ladders. It is free of some of the limitations due to the molecular weight of the protein. The electrophoretic mobility of the complex, μ_{igL_2} , is proportional to the charge of the ligand, Z_L (eqs 9-11). A ratio of μ_{igL_2} to μ_{ig} is only dependent on the charges of the protein, Z_p , and the ligand, Z_L , if the mass, M , and the proportionality constant, C_μ^{eff} , and the correction for effective charge, $(1+q)$,⁴³ all cancel (eq 24). In general, however, we do

$$\frac{\mu_{\text{igL}_2}}{\mu_{\text{ig}}} \approx \left(\frac{1+q_p}{1+q_{p(L_2)}} \right) \left(\frac{M^\alpha}{(M+2m)^\alpha} \right) \left(\frac{C_{\mu,P(L_2)}}{C_{\mu,P}} \right) \frac{Z_p + 2Z_L}{Z_p} \approx 1 + \frac{2Z_L}{Z_{\text{exp}}} \quad (24)$$

not know that all these values cancel, and thus we refer to Z_p in eq 24 as Z_{exp} (an experimental estimate of Z_p). Rearranging eq

(39) Ojtag, G.; Lundahl, P.; Wolgast, M. *Biochim. Biophys. Acta* **1989**, *991*, 317-323.

(40) Nozaki, Y.; Tanford, C. *Methods Enzymol.* **1967**, *11*, 715-734.

(41) Ford, C. L.; Winzor, D. J. *Biochim. Biophys. Acta* **1982**, *703*, 109-112.

(42) Gao, J.; Gomez, F. A.; Hartner, R.; Whitesides, G. M. *Proc. Natl. Acad. Sci. U.S.A.* **1994**, *91*, 12027-12030.

24 yields eq 25. Plotting the left side of eq 25 (corresponding to

$$2Z_L = Z_{\text{exp}} \left((\mu_{\text{igL}_2} / \mu_{\text{ig}}) - 1 \right) \quad (25)$$

the total charge of ligand bound to the protein) against the coefficient of the term Z_{exp} gives a line with a slope equal to Z_{exp} .⁴⁴ From the analysis of the data for the binding of Ig to ligands 2-5 by this method, we determine that for Ig (MW 150 000), $Z_{\text{exp}} = -8.0 \pm 0.2$ at pH 8.3 (Figure 9); we therefore estimate that $Z_p \approx -8.0 \pm 0.2$ at pH 8.3.

The linearity of this plot further indicates that the experimental estimate of μ_{igL_2} (using very high concentrations of ligand) was acceptably good; if the experimental value of μ_{igL_2} underestimated its actual value, then the plot would appear curved downward at higher values of $2Z_L$. The linearity also validates $Z_{p(L)} = Z_p + Z_L$; the data point for μ_{ig} would have deviated from the line if this relation did not hold.

CONCLUSIONS

Use of ACE To Study Interactions of Antibodies with Ligands. Quantifying the interaction between bivalent antibodies and the ligands to which they bind is central to molecular immunology. Enzyme-linked immunosorbent assays (ELISA)⁴⁵ radioimmunoassays (RIA)⁴⁵ equilibrium dialysis,⁴⁶ and immunoprecipitation (the Farr method⁴⁷) are widely used to quantify these interactions. These methods yield a single relative binding constant with a substantial error.⁴⁸ Other methods—fluorescence,⁴⁹ surface plasmon resonance (SPR),⁵⁰ and stopped-flow kinetics⁵¹—often require modifying the antibody; they are also time-consuming. This study demonstrates that ACE can be used to estimate both dissociation constants—regardless of cooperativity—for the interaction of Ig antibodies and monovalent ligands of low molecular weights. The use of Jorgensen buffers¹⁹ gave acceptable (although still broad) line shapes. We believe that although the concentrations of zwitterionic additives in these buffers (500 mM) give solutions of higher ionic strength and viscosity than normally used for biological assays, the results are still relevant to biology. We estimate the ionic strength of the interior of a cell to be between 0.5 and 1.1 M.⁵² In addition, the interior of a cell contains a large number and high concentration of organic

(43) The value of q is unknown in this experiment. Theoretically, it is dependent to differing degrees on the characteristics of both the molecule and the solution. The value of q is strongly dependent on the ionic strength of the solution. If all measurements are done in buffer of constant ionic strength, then the assumption that q remains constant for the protein and its complexes may be a good one.

(44) If the relationship between $Z_{p(L)}$ and Z_L (eq 11) is different for the different L (that is, the values of $q_{\text{L}2}$, $q_{\text{L}3}$, $q_{\text{L}4}$, and $q_{\text{L}5}$ differ), then the measured value of charge using eq 24 will be different from Z_p .

(45) Goldberg, M. E.; Djavad, O. L. *Curr. Opin. Immunol.* **1993**, *5*, 278-281.

(46) Gopalakrishnan, P. V.; Karush, F. *Immunochemistry* **1974**, *11*, 279-283.

(47) Farr, R. S. *J. Infect. Dis.* **1958**, *103*, 329.

(48) The uncertainty in these techniques is not better than a factor of 2-4.

(49) Dandliker, W. B. *Methods Immunol. Immunochem.* **1971**, *3*, 435-453.

(50) Malmqvist, M. *Curr. Opin. Immunol.* **1993**, *5*, 282-286.

(51) Kitano, H.; Hasegawa, J.; Iwai, S.; Okubo, T. *Polym. Bull. (Berlin)* **1986**, *16*, 89-93.

(52) In 1000 g of HeLa cells, there are 10 g of small inorganic ions (MW = 40; 0.25 M), 80 g of small molecules (MW = 400; 0.28 M); 19 g of cytoplasmic RNA (effective molarity ranges from 0 to 0.06 M); 225 g of protein (effective molarity ranges from 0.01 to 0.48 M). The total effective molarity then ranges from 0.53 to 1.07 M. The total concentration of organic molecules is approximately 300 g (30%). Data drawn from: Darnell, J.; Lodish, H.; Baltimore, D. *Molecular Biology*, 2nd ed.; W. H. Freeman and Co.: New York, 1990; pp 114-115.

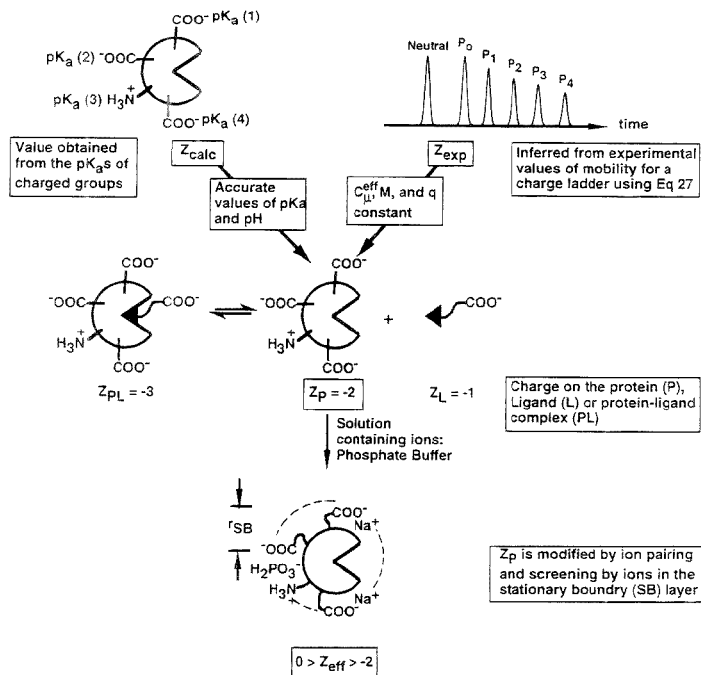


Figure 8. Summary of terms referring to the charge of a protein. $Z_{P(L)}$ represents the total charge on the protein plus the charge on all tightly associated ligands, cofactors, and coenzymes. Z_P and Z_L are, analogously, the charges on the uncomplexed protein and the ligand, respectively. In the hypothetical example used here for illustration, $Z_{P(L)}$, Z_P , and Z_L are -3 , -2 and -1 , respectively. The effective charge of the protein, Z_{eff} , is Z_P minus the average net charge of counterions in the stationary boundary layer (Stern–Helmholtz layer) of solvation (represented here by a sphere of radius r_{SB}). The counterions in the stationary boundary layer exchange slowly with the other ions in solution. We do not know the value of r_{SB} in our experiments and therefore, do not know the difference in magnitude between the values of Z_{eff} and Z_P . In the hypothetical example shown here, the net charge of the counterions in the sphere of radius r_{SB} is $+1$ and Z_{eff} is -1 . Z_{calc} is the charge on the protein calculated from values of pK_a of the amino acid residues and the value of pH. If the values of pK_a and pH are known exactly, then $Z_{calc} \approx Z_P$. Z_{exp} is the charge on the protein that is inferred from experiment; if the coefficients that relate Z_P to mobility (C_{μ}^{eff} , M , and q) remain constant, then $Z_{exp} \approx Z_P$.

materials ($\sim 300 \text{ g/L}^{52}$). The complex buffers used in this study (having high ionic strength— 500 mM —and high concentrations of organic materials— 110 g/L), in our opinion, more closely simulate intracellular conditions than do the simple buffers often used for biological assays.

The rate of electroosmotic flow changed substantially on increasing the concentration of ligands (especially **4** and **5**). By using internal standards and mobilities (rather than absolute appearance times, t_{app}), we believe that we have successfully corrected for these changes.²¹ We therefore did *not* need to have highly reproducible values of t_{app} in our experiments. The use of internal standards to correct for changes in EO flow is central to the success of these analyses.

Ligands that were highly charged clearly shifted the electrophoretic mobility of the Ig; even, however, a ligand with a *single* charge gave shifts that were detectable and reproducible. The association of a ligand with one unit of charge to the Ig (that is, two units per bivalent Ig) changes the mobility by $\sim 25\%$ since $Z_{exp} \approx -8$. This change is detectable even with the broad lines that we observe. Other Igs will have similar (although not identical) changes. We feel that, in principle, one can quantify the binding of Ig to *any* low molecular weight ligand that is either

naturally charged or contains a site for attaching a charged group: extension of the analysis to ligands large enough that the antibody–ligand complex and the antibody alone have different hydrodynamic drag should be possible, but requires exploration.

Monitoring the electrophoretic mobilities of the *ligands* as a function of the pH of the buffer allowed us to determine the degree of ionization. Such an experiment allows the determination of pK_a in some cases.³⁴

Analysis of the Data. The analysis used here is useful (and may be more appropriate than Scatchard analysis) for polyvalent systems in which cooperativity between binding events is in question. There were five assumptions used in this analysis: (i) the mobility of the fully complexed antibody, μ_{IgL_n} , can be estimated experimentally at high values of $[L]$ to within 3% of its value; (ii) binding of the ligands to the protein affected the hydrodynamic drag of the protein negligibly; (iii) the values of k_{on} and k_{off} are sufficiently large that the observed mobility is a concentration-weighted average of the mobilities of all complexes containing Ig; (iv) the proportionality constants $C_{\mu,Ig}$, C_{μ,IgL_n} , and C_{μ,IgL_n} (eqs 8–10) that relate electrophoretic mobility to mass and charge are equal in magnitude; (v) the hydrodynamic drag (M^e) is constant for Ig and its complexes.

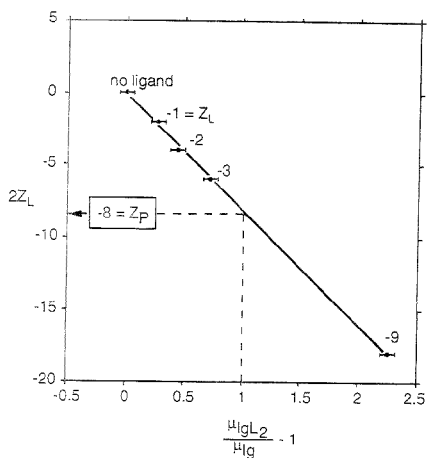


Figure 9. Total charge of the bound ligands, $2Z_L$, against the coefficient of the experimental charge on Ig, Z_{exp} (eq 25). The plot gives a line whose slope yields Z_{exp} . Z_{exp} on IgG_{2b} (MW 150 000) at pH 8.3 is -8.0 . The horizontal error bars represent a 3% uncertainty in the X value. When the value of $X = 1$, then $Y = Z_{exp}$ (indicated by a dashed line). The labels on the points of data represent values for Z_L .

Our analysis indicates that the binding of two ligands to this Ig is noncooperative (independent). Noncooperative binding between a bivalent antibody and two small monovalent ligands is intuitively reasonable. Noncooperative binding is less obviously indicated for ligands in which charge-charge interactions might be significant.³³ The previously reported positively cooperative binding between monovalent DNP-containing ligands and an anti-

(33) The binding sites in the bivalent antibody are approximately 100 Å apart and one ligand, therefore, is not likely to hinder the binding of the other ligand sterically: Schref, T.; Hiller, R.; Naider, F.; Levitt, M.; Anglister, J. *Biochemistry* **1992**, *31*, 6884-6897

DNP antibody was rationalized through conformational changes on binding the first ligand.²²⁻²⁴ Since these groups used different antibodies, we can make no comment on their results.

Use of ACE To Estimate the Charge of an Antibody in Solution. A useful method of estimating the charge, Z_p , on large proteins uses analysis of binding to a family of ligands that differ in charge. This method is based on one used by Gao¹² and yields a value for the experimental charge, Z_{exp} , of a protein in solution at a given pH. The mobilities of Ig and its complexes are linearly related if all other terms in the equation relating mobility to charge—namely, C_{μ}^{eff} , M , and q —remain constant: Z_{exp} is an estimate of Z_p . The method of estimating Z_p using covalent charge ladders is currently most useful for proteins with molecular mass less than 50 kDa; that based on examining relative mobilities of a series of protein-ligand complexes with different charges is more laborious, but is also applicable to higher molecular weight proteins. Neither a crystal structure nor information on the sequence exists for the Ig studied here. Thus, our prediction of the charge for the IgG_{2b} used in this study ($Z_p \approx -8.0$ at pH 8.3) is the first of which we are aware.

ACKNOWLEDGMENT

The authors gratefully acknowledge fruitful discussions with Jiming Gao. This work was supported by the National Institutes of Health Grant GM51559. M.M. was supported by an Eli Lilly predoctoral fellowship and F.A.G. by a Damon Runyon-Walter Winchell Cancer Research Fund postdoctoral fellowship.

SUPPORTING INFORMATION AVAILABLE

Detailed procedures for the synthesis and characterization of compounds 2-5 and all intermediates (5 pages). See any current masthead page for ordering information.

Received for review April 13, 1995. Accepted June 27, 1995.*

AC950368S

* Abstract published in *Advance ACS Abstracts*, August 1, 1995.

Structure Determination of Polymeric Materials by Pyrolysis Gas Chromatography

Frank Cheng-Yu Wang,* Bruce B. Gerhart, and Patrick B. Smith

Analytical Sciences Laboratory, Michigan Division, The Dow Chemical Company, Midland, Michigan 48667

A pyrolysis gas chromatography method has been developed to investigate the microstructure of emulsion polymers. The number-average sequence length, which reflects the monomer arrangement in the polymer, was calculated using the proper formulas that incorporate the pure trimer peak intensities and hybrid trimer peak intensities. In this study, styrene and *n*-butyl acrylate copolymer systems were used to measure “the degree of structure” (i.e., the number-average sequence length for styrene and *n*-butyl acrylate repeat units) and compared to a homogeneous nonstructured (or random) copolymer. The number-average sequence length information was further extended to calculate the composition. For the emulsion polymers examined in this study, the composition elucidated from the number-average sequence length matched the preparation recipe and/or what was measured by ¹³C NMR.

The structure of a polymeric system usually can be determined by a spectroscopic method, such as NMR spectroscopy,¹ and by a structural degradation method, such as pyrolysis gas chromatography (Py-GC).² Both methods have been developed for more than 20 years. There are many different polymeric systems that have been studied. Occasionally, the choice of which method to use mainly depends on which specific polymeric system is being studied and what kind of information needs to be generated.

The number-average sequence length is most commonly used as an indicator of the degree of polymer structure. A structured copolymer, by our definition, contains regions within a polymer chain or polymer domain that are largely composed of one monomeric type. A nonstructured (or random) polymer would be one containing a completely homogeneous and random distribution of the monomeric types. The statistical method to calculate the number-average sequence length from the trimer distributions is well established.¹ The method is widely used in NMR spectroscopic analysis because NMR (especially ¹³C NMR) can supply triad molar fractions. In a copolymer system containing monomers A and B, the number-average sequence length of both monomers is expressed as

$$\bar{n}_A = \frac{N_{AAA} + N_{AAB+BAA} + N_{BAB}}{(1/2)N_{AAB+BAA} + N_{EAB}} \quad (1)$$

(1) Randall, J. C. *Polymer Sequence Determination*; Academic Press: New York, 1977; pp 41–69.

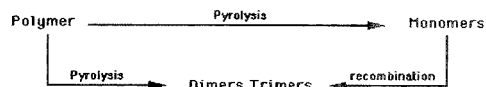
(2) Jones, C. E. R.; Reynold, G. E. J. *Br. Polym. J.* 1969, 1, 197.

$$\bar{n}_B = \frac{N_{BBB} + N_{ABB+BBA} + N_{ABA}}{(1/2)N_{ABB+BBA} + N_{EBA}} \quad (2)$$

where \bar{n}_A and \bar{n}_B are the number-average sequence lengths of monomers A and B. N_{AAA} , $N_{AAB+BAA}$, N_{BAB} , N_{ABA} , $N_{ABB+BBA}$, and N_{BBB} are the experimentally derived six distinguishable triad molar fractions or numbers of molecules. From the formulas above, if all six triad molar fractions or numbers of molecules can be generated, the number-average sequence lengths of monomers A and B can be calculated. The higher value for the number-average sequence length implies a longer run of a particular monomer. Using a flame ionization detector in GC, the peak intensity is a direct reflection of concentration³ (molar fraction or number of molecules/unit volume). Thus, the peak intensity has been used as concentration or molar fraction.

The number-average sequence length can be further used to calculate the mole percent of monomer in the copolymer. Utilization of the monomer-type molecular weights will allow for conversion to weight percent, which is the commonly used unit when emulsion polymers are designed and synthesized. Additionally, the weight percent of the monomers calculated from the number-average sequence length can serve as a check of the experimental procedure and the empirical determination. Similarities between these values assure the accuracy of the number-average sequence value for each monomer.

Pyrolysis followed by gas chromatographic separation is a mechanism utilizing thermal energy to break down a polymeric structure to monomers and oligomers and separation of those units for quantitation. Because of the temperature limitations of the common silicone capillary column, only the dimer and trimers of the system studied here can be reliably separated and detected. The major mechanism of producing dimers and trimers with pyrolysis can be attributed to thermal degradation. A relatively small amount of dimers and trimers is formed as a result of a recombination of monomers. This mechanism is demonstrated as follows:



The intensity of the various dimer and trimer peaks in a pyrolysis gas chromatogram will reflect the monomer sequence

(3) Irwin, W. J. *Analytical Pyrolysis*; Marcel Dekker, Inc.: New York, 1982; pp 135.

and polymer structure when two conditions are met: (1) recombination contributes little to the pyrolysis products and (2) the formation of pyrolysis products is proportional to their existence in the copolymer. The literature⁴⁻⁴ discusses the determination of the structural sequence from dimer and trimer peak intensities. Since the probability of monomer recombination to trimers is considerably less than the same recombination to dimers, the determination of the number-average sequence length will be little affected by peak intensities that result from inter- or intramolecular recombination. Thus, the use of all trimer peaks will provide more accurate and reliable results as compared to use of dimer peak intensities.

Styrene and *n*-butyl acrylate emulsion polymers have been widely used in numerous coating and adhesive applications in the paper, paint, and construction industries. Mechanical and physical properties are an important aspect of the use of these polymers and can be governed by not only the composition but also by the structure of the polymeric molecules and the existence of homopolymer domains. Thus, the understanding of the relationship between mechanical, physical, and chemical properties becomes critically important. The polymer structure has a direct effect on such properties as modulus, glass transition temperature, film porosity, and minimum film formation temperature. By varying the monomer feed rates, initiator concentration, and chain transfer agent concentration, such properties as monomer sequence, molecular weight distribution, and particle size distribution can be affected. By knowing the monomer sequence in the final product, the emulsion polymer chemist will have a powerful tool for understanding to what degree an experimental parameter affects the polymer structure.

There are several NMR spectroscopy studies dealing with determining the polymeric structure of *n*-butyl acrylate copolymer systems^{15,16} as well as *n*-butyl acrylate/styrene copolymers¹⁷ which are based on the same theory of determining the number-average sequence length from peak intensities corresponding to triads. However, the NMR structure determination becomes difficult due to broadened peaks which result from high molecular weight.

Pyrolysis gas chromatography of styrene (STY)/alkyl acrylate systems have very clear and distinguishable trimer peaks that can be used in the determination of the number-average sequence length. The trimer peaks of STY/*n*-BA were identified by Py-GC/MS in both electron ionization (EI) and chemical ionization (CI) mode. The number-average sequence length was then calculated on the basis of eqs 1 and 2 and those trimer peak intensities. The weight percents of the monomers were eluci-

dated. These values were compared with recipe amounts and ¹³C NMR results, when available.

EXPERIMENTAL SECTION

Sample Preparation. (1) Emulsion Polymer. All homogeneous emulsion polymers were synthesized in our laboratories. The homogeneous polymer was synthesized on the basis of procedures given in an experimental polymer textbook.¹⁸ The structured polymer was synthesized in a similar way except monomers were fed in series.

(2) Pyrolysis-GC and Pyrolysis-GC/MS. Samples of emulsion polymer (~1.5 μg) were deposited on the Pt ribbon and equilibrated for 10 min in a 250 °C interface connected to the injection port of a HP5890 gas chromatograph equipped with a flame ionization detector (FID). Samples were pyrolyzed (CDS 120 Pyroprobe Pt coil) at a set temperature of 500 °C. The coil was heat to 500 °C with 20 °C/ms and hold at 500 °C for a 20-s interval. The pyrolysis products were split in the 250 °C injection port, with 10 psi head pressure, 50:1 split ratio, separated on a fused-silica capillary column (J&W DB-5, 30 m × 0.25 mm i.d., 1.0-μm film thickness) using a linear temperature program (40 °C/4 min, 20 °C/min, to 120 °C/10 min and then 20 °C/min ramp to 300 °C/23 min), and detected by a FID.

In the GC/MS system, the FID was replaced with a VG Trio-1 mass spectrometer. The output from GC was transferred through a transfer line (280 °C) to the ion source of the mass spectrometer. The electron ionization mass spectrum was obtained every second over the mass range of 29–500 amu. Methane was used as reagent gas in the chemical ionization mode.

RESULTS AND DISCUSSION

The reproducibility of pyrolysis data is always a concern when the technique is applied to any kind of quantitative study. Table 1 shows the average and relative standard deviation of a number-average sequence length calculation based on six consecutive runs of a 48%/52% STY/*n*-BA emulsion copolymer. Most of the terms show a relative standard deviation below 1%, which demonstrates the reliability of the pyrolysis method applied to the analysis of STY/*n*-BA copolymer.

Pyrolysis of an emulsion polymer is performed on the dried film. The liquid emulsion is heated in the pyrolysis chamber at 250 °C for 10 min and allowed to coalesce to a solid. A volatility experiment showed there were no detectable materials released during this period. For the homogeneous emulsion polymers where every latex particle has a uniform composition and structure, the film formation process will not alter the copolymer structure. For the blend emulsion polymer, the film formation process will have a significant effect on the interface volume of the polymers. The latex G with 50% styrene particles and 50% *n*-butyl acrylates particles will have no interface volume in the emulsion state, but after coalescence, an interface volume of styrene and butyl acrylate polymer will form.

The response of the FID detector is assumed equal for all three styrene-centered trimers and for all three *n*-butyl acrylate-centered trimers in this study. Essentially, FID is a carbon atom counter; any components having the same number of carbon atoms should have the same response. The styrene-centered trimers have 22–24 carbon atoms; the difference in carbon atoms is less than ±5%

- (4) Tsuge, S.; Ito, H.; Takeuchi, T. *Bull. Chem. Soc. Jpn.* **1970**, *17*, 3341.
- (5) Yamamoto, Y.; Tsuge, S.; Takeuchi, T. *Kobunshi Kagaku* **1972**, *29* (6), 407.
- (6) Alekseeva, K. V.; Khranova, L. P.; Solomatina, L. S. *J. Chromatogr.* **1973**, *77* (1), 61.
- (7) Wallisch, K. L. *J. Appl. Polym. Sci.* **1974**, *18*, 203.
- (8) Braun, D.; Canji, E. *Angew. Makromol. Chem.* **1974**, *36*, 75.
- (9) Tsuge, S.; Hiramitsu, S.; Horibe, T.; Yamaoka, M.; Takeuchi, T. *Macromolecules* **1975**, *6*, 721.
- (10) Káel, J.; Sevc, F.; Zachoval, J.; Kubat, J. *J. Polym. Sci., Polym. Lett. Ed.* **1979**, *17*, 691.
- (11) Shimono, T.; Tanska, M.; Shono, T. *J. Anal. Appl. Pyrolysis* **1979**, *1*, 77.
- (12) Blazzo, M.; Varhegyi, G.; Jakab, E. *J. Anal. Appl. Pyrolysis* **1980**, *2*, 177.
- (13) Tanaoka, A.; Akhiro, I.; Ishitani, Y.; Nishimura, H. *Asahi Gakka Kenkyu Hokoku* **1987**, *37* (2), 263.
- (14) Rao, M. R.; Sebastian, T. V.; Radhakrishnan, T. S.; Ravindran, P. V. *J. Appl. Polym. Sci.* **1991**, *42*, 753.
- (15) Picot, C.; Liaro, M. *J. Polym. Sci., Polym. Lett. Ed.* **1981**, *42*, 2619.
- (16) Brar, A. S.; Sunita, S. C. V. *Polymer* **1993**, *34*, 3391.
- (17) Brar, A. S.; Sunita, S. C. V. *Polym. J.* **1992**, *24*, 879.

(18) Collins, E. A.; Bares, J.; Billmeyer, F. W., Jr. *Experiments in Polymer Sciences*; John Wiley & Sons: New York, 1973; pp 337–345.

Table 1. Multiple Runs for Number-Average Sequence Length Determination in One Emulsion Polymer from Pyrolysis Gas Chromatography Method

	H1	H2	H3	H4	H5	H6	av	RSD (%)
normalized peak intens								
SSS	0.136	0.129	0.136	0.142	0.132	0.150	0.14	0.73
SSB+BSS	0.288	0.288	0.291	0.284	0.284	0.289	0.29	0.27
BSB	0.576	0.583	0.573	0.574	0.584	0.561	0.58	0.83
<i>N</i> (S)	1.39	1.38	1.39	1.40	1.38	1.42	1.39	1.50
BBB	0.052	0.051	0.049	0.051	0.055	0.054	0.05	0.23
BB+SBB	0.343	0.348	0.343	0.348	0.348	0.346	0.35	0.25
SBS	0.605	0.602	0.608	0.601	0.597	0.599	0.60	0.41
<i>N</i> (B)	1.29	1.29	1.28	1.29	1.30	1.29	1.29	0.51
mol %								
S	52	52	52	52	52	52	0.52	0.28
B	48	48	48	48	48	48	0.48	0.28
wt %								
S	47	46	47	47	46	47	47	0.28
B	53	54	53	53	54	53	53	0.28
std wt %								
S	48	48	48	48	48	48	48	
B	52	52	52	52	52	52	52	
grouped (%)								
S	42	42	43	43	42	44	42	0.83
B	39	40	39	40	40	40	40	0.41
group								
<i>N</i> (S)	2.95	2.90	2.94	3.00	2.92	3.03	2.96	5.00
<i>N</i> (B)	2.30	2.29	2.28	2.29	2.31	2.31	2.30	1.27

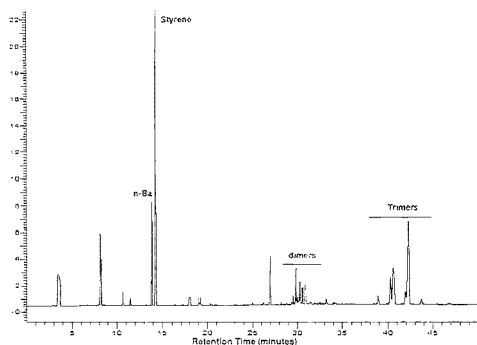


Figure 1. Typical pyrogram of a 50%/50% by weight STY/*n*-BA homogeneous emulsion polymer.

around those trimers. This fact makes the equal response assumption valid. The same argument also applied to *n*-butyl acrylate-centered trimers.

The 500 °C pyrolysis temperature was chosen to obtain a higher yield of trimer for both styrene and *n*-butyl acrylate. Figure 1 shows the typical pyrogram of a 50%/50% by weight STY/*n*-BA homogeneous emulsion polymer. The identification of pure trimers was accomplished by comparing retention times with both 100% styrene polymer and 100% *n*-butyl acrylate polymer as well as Py-GC/MS in the electron ionization mode and chemical ionization mode. The identification and assignment of hybrid trimers (isomers) was accomplished by Py-GC/MS(EI), Py-GC/MS(CI), interpretation of EI spectra, and comparison made to similar structural compound spectra in the NIST library. Figure 2 shows an expansion of the trimer area of Figure 1 with trimer assignments.

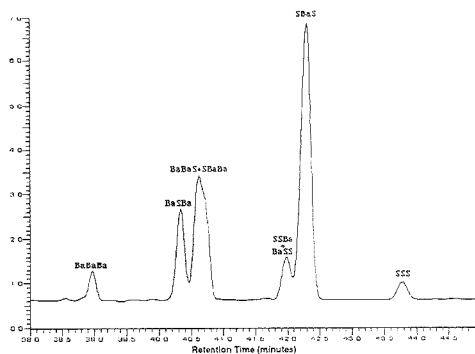


Figure 2. Trimer area of 50%/50% STY/*n*-BA homogeneous emulsion polymer with trimer assignments, where Ba = *n*-butyl acrylate and S = styrene.

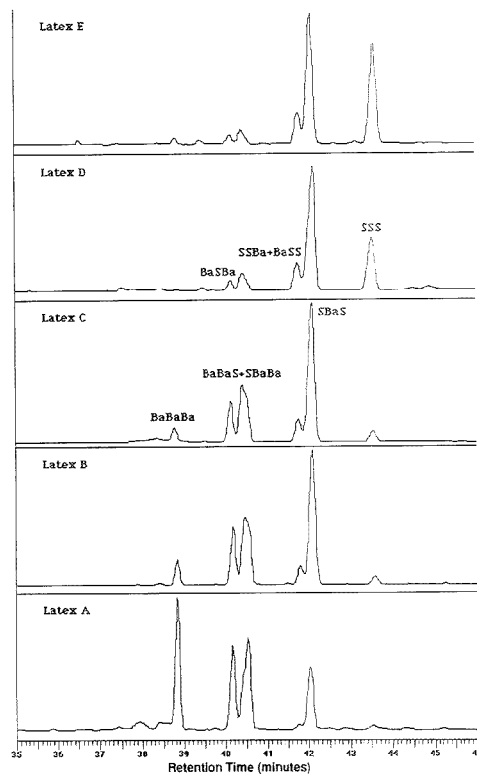


Figure 3. Pyrogram of the trimer area for five different compositions of STY/*n*-BA. The pure trimer peaks directly reflect the relative abundance of the monomers, where Ba = *n*-butyl acrylate and S = styrene.

Figure 3 shows the pyrogram of the trimer area for five different compositions of STY/*n*-BA. The number-average sequence lengths were calculated for all five polymers. The peak areas were normalized on the basis of the summation of $N_{SSBa+BaSS}$, N_{BaSBa} equaling 1 and the summation of N_{BaBaBa}

Table 2. Number-Average Sequence Length for Different Compositions of Homogeneous Emulsion Polymers from Pyrolysis Gas Chromatography Method

	A	B	C	D	E
normalized peak intens					
SSS	0.069	0.116	0.168	0.610	0.733
SSB+BSS	0.058	0.221	0.322	0.305	0.210
BSE	0.872	0.663	0.511	0.085	0.057
$N(S)$	1.11	1.29	1.49	4.21	6.17
BBB	0.374	0.076	0.058	0.005	0.031
BBS+SBB	0.401	0.379	0.323	0.123	0.106
SBS	0.224	0.545	0.620	0.872	0.863
$N(B)$	2.35	1.36	1.28	1.07	1.09
mol %					
S	32	49	54	80	85
B	68	51	46	20	15
expt wt %					
S	28	44	49	76	82
B	72	56	51	24	18
std wt %					
S	25	43	50	74 ^a	82
B	75	57	50	26 ^a	18
grouped (%)					
S	13	34	49	91	94
B	78	46	38	13	14
grouped					
$N(S)$	4.39	3.05	3.04	6.00	8.98
$N(B)$	3.86	2.40	2.36	2.08	2.59

^a Weight percentage determined by ¹³C NMR analysis.

$N_{S(Ba+B)} = N_{B(S)} = 1$. All normalized peak areas were then used in eqs 1 and 2 to calculate the number-average sequence length for both styrene and *n*-butyl acrylate. The mole percentage and weight percentage were also calculated to compare with the weight percentage obtained by preparation recipe or by the NMR technique.

Table 2 lists results of the normalized peak intensities, the calculated number-average sequence length, and the calculated weight percent composition. All of the emulsion polymers (A–E) were homogeneously polymerized and considered nonstructured (random). Thus, the number-average sequence length is strictly a reflection of the composition of the polymer. When the calculation is extended to obtain the monomer weight percent of the polymer, a match is made to that expected from the recipe or an NMR determination to within $\pm 3\%$. This assures the accuracy and precision of the number-average sequence length value.

Figure 4 shows the pyrogram of the trimer area for three different structures of STY/*n*-BA emulsion polymers all having the same 50/50 wt % composition. The first polymer (G) consists of a physical blend of an all-styrene and an all-*n*-butyl acrylate emulsion. The second (F) consists of core/shell emulsion particles made with two distinct domains, a *n*-butyl acrylate core and a styrene shell. The third (C) is a homogeneous STY/*n*-BA polymer made by the simultaneous feed of the individual monomers. The significant differences in the pyrograms can be seen in the hybrid trimer peak intensities. These peak intensities decrease from the completely homogeneous polymer system (C), to the core/shell particle structure with a finite interface (F), to the physical blend of particles with no distinct polymer interface (G).

Table 3 shows the data for the three structured polymers (C, F, G). The number-average sequence length strongly reflects the "structural differences" of the polymers, and concurrently, the

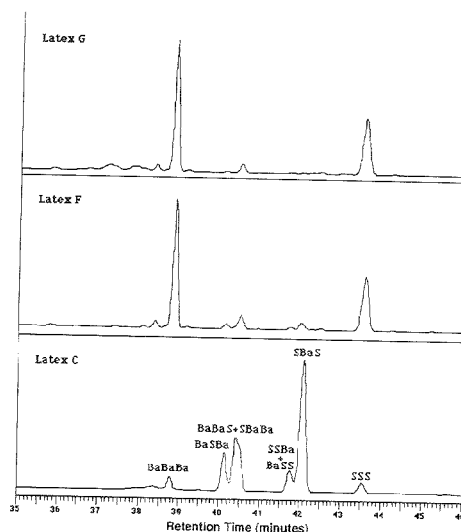


Figure 4. Pyrogram of the trimer area for three different structures of STY/*n*-BA emulsion polymers all having the same 50/50 wt % composition, where Ba = *n*-butyl acrylate and S = styrene.

Table 3. Number-Average Sequence Length for the Same Composition but Different Structural Emulsion Polymers from Pyrolysis Gas Chromatography Method

	C	F	G
normalized peak intens			
SSS	0.168	0.909	0.973
SSB+BSS	0.322	0.030	0.014
BSB	0.511	0.061	0.013
$N(S)$	1.49	13.20	49.77
BBB	0.058	0.847	0.956
BBS+SBB	0.223	0.106	0.037
SBS	0.620	0.047	0.006
$N(B)$	1.28	9.977	39.775
mol %			
S	54	57	53
B	46	43	44
S	49	52	50
B	51	48	50
std wt %			
S	50	50	50
B	50	50	50
grouped (%)			
S	49	94	99
B	38	95	99
grouped			
$N(S)$	3.04	62.22	143.47
$N(B)$	2.36	17.93	53.08

weight percent monomer composition matches the composition based on monomer feed. This is a strong demonstration that the number-average sequence length can be used as a measure of the degree of structure and composition.

Advances in emulsion polymerization technology have allowed the polymer chemist to synthesize the emulsion polymer with a degree of structure. Variation in the monomer feed sequence can produce emulsion polymers with the same composition but vastly different physical and mechanical properties as a result of

structural differences. A prime example is the comparison of the homogenous polymer and the monomer domain separated (core/shell) polymer. The number-average sequence length can be an important measurement of the degree of structure. Additionally, it may be important to determine the percent of two or more of the same type of monomers bonded together. Such parameters are termed the percent of grouped monomers and the number-average sequence length of grouped monomers. For monomer A in the AB copolymer, these two terms are expressed as follows:

$$\% \text{ group of monomer A} = \frac{(N_{AAA} + N_{AAB+BAA})}{100} \times 100\% \text{ or } (1 - N_{BAB}) \times 100\%$$

$$\text{number-average sequence length of grouped monomers} = \frac{N_{AAA} + N_{AAB+BAA}}{(1/2)N_{AAB+BAA}}$$

For the emulsion polymers studied, the information pertaining to the percent of grouped monomers is shown in Tables 1 and 2.

Examination of the percent number of grouped monomers and the number-average sequence length of grouped monomers as calculated using the previous formulas reveals the relationship between the relative monomer concentration and the structure of the polymer chains. This is shown in Table 2, where the percent of grouped monomers varies with composition as one might expect. This mainly results from the relative concentration of the monomers under the homogeneous polymerization conditions. Table 3 values of percent of grouped monomers is even more dramatic. Here the variation is strictly related to the degree

of structure in the emulsion polymer, not to composition. The differences are extreme as the homogeneous emulsion polymer (C) reveals 49% of the styrene as grouped, the core/shell (F) reveals 94% of the styrene as grouped, and the blend is what one would expect with 99% of the styrenes grouped.

CONCLUSIONS

By applying the proper statistical formula and the data obtainable from pyrolysis gas chromatography, the number-average sequence length as well as the monomer composition of an emulsion copolymer can be explored. The structure of a copolymer of two monomeric types can be quantified by deriving the percent of grouped monomers and the number-average length of grouped monomers. This method could be extended to any copolymer system as long as all six trimer peaks can be identified and the peak intensities obtained by assuming that these intensities represent the polymer compositions. This method extends the capabilities of pyrolysis not only in the quantitative study of monomer composition but also in the realm of polymer structure investigation.

Received for review May 30, 1995. Accepted July 18, 1995.⁶

AC950515M

⁶ Abstract published in *Advance ACS Abstracts*, September 1, 1995.

Supercritical Fluid Extraction-Gas Chromatographic Analysis of Organic Compounds in Atmospheric Aerosols

Kristen J. Hansen,^{†*} Brian N. Hansen,^{‡,§} Eric Cravens,^{†,‡} and Robert E. Sievers^{*,†,‡}

Global Change and Environmental Quality Program, Cooperative Institute for Research in Environmental Science, Department of Chemistry and Biochemistry, University of Colorado, Boulder, Colorado 80309-0216

An integrated sampling and supercritical fluid extraction (SFE) cell has been designed for whole-sample analysis of organic compounds on tropospheric aerosol particles. The low-volume, polymer-free, temperature-controlled extraction cell has been interfaced with a sampling manifold for aerosol collection in the field. After sample collection, the entire SFE cell was removed, transferred, and coupled to a gas chromatograph; after on-line extraction, the cryogenically focused sample was separated and the volatile compounds were detected with either a mass spectrometer or a flame ionization detector. A 20-min extraction at 450 atm and 90 °C with pure supercritical CO₂ is sufficient for quantitative extraction of most volatile compounds in aerosol samples. A comparison between SFE and thermal desorption, the traditional whole-sample technique for analyses of this type, was performed using ambient aerosol samples, as well as samples containing known amounts of standard analytes.

Organic compounds are emitted into the atmosphere as products of many biogenic and anthropogenic processes. A significant fraction of this organic material ends up as inhalable particulate matter, or aerosols, as a result of physical condensation processes, emission processes, or photochemical reactions.^{1–3} Determining the organic composition of tropospheric aerosols and monitoring how this composition changes on a time scale of meteorological changes is fundamental to understanding many chemical and physical processes in the atmosphere.

In the past, studies designed to determine the role of organic aerosols in the atmosphere have utilized liquid solvent extraction or thermal desorption to separate the organic component from the aerosol for analysis. Liquid extractions typically require large volumes of solvent (100–500 ml) and extended extraction times (8–48 h); these characteristics make the technique inconvenient for analyzing a large number of samples. Liquid extraction results in an aliquot of sample extract (~40 µL), only a fraction of which, typically 1 µL, can be utilized in a single gas chromatographic analysis.^{1,4} Due to this inherent dilution factor, liquid extraction

techniques require 24–72 h sample collection periods.⁴ Because the composition of an air mass can change on a time scale of minutes to hours, it has been difficult to elucidate chemical and physical relationships in aerosol composition using analysis techniques based on liquid extraction with long sample collection times.^{5–7}

Thermal desorption has been used to monitor short-term changes in the organic content of aerosols. In this method, whole aerosol samples are heated for a short period of time at 250–300 °C; the entire volatile component of the aerosol is swept into a cryogenically cooled gas chromatograph. Short sampling times result from the increased sensitivity of the whole-sample desorption technique.^{8–10} However, thermal desorption is known to create some analysis artifacts; the high desorption temperatures required by the technique can cause some unstable organic compounds to polymerize, char, or pyrolyze.^{11,12} In addition, thermal desorption may not adequately remove extremely low-volatility, high molecular weight compounds from the aerosol matrix.

Supercritical fluid extraction (SFE), a whole-sample analysis technique, provides a low-temperature alternative to liquid solvent extraction and thermal desorption. A supercritical fluid, often characterized as a dense gas, has a mass transfer coefficient similar to that of a liquid; for this reason, SFE efficiencies for many analytes are comparable with those achieved using liquid extraction.¹³ In addition, analytes in a supercritical fluid have diffusivities characteristic of those in a gas; as a result, the time required for SFE is on the order of that required for thermal desorption (minutes).¹⁴ The critical parameters of carbon dioxide, the solvent

(4) Stephanou, E. G. *Atmos. Environ.* 1992, 26A, 2821–2829.

(5) Parrish, D. D.; Hahn, C. H.; Fahey, D. W.; Williams, E. J.; Bollinger, M. J.; Hubler, G.; Buhr, M. P.; Murphy, P. C.; Trainer, M.; Hsie, E. Y.; Liu, S. C.; Fehsenfeld, F. C. *J. Geophys. Res.* 1990, 95, 1817–1835.

(6) Fehsenfeld, F. C.; Bollinger, M. J.; Liu, S. C.; Parrish, D. D.; McFarland, M.; Trainer, M.; Kley, D.; Murphy, P. C.; Albritton, D. L. *J. Atmos. Chem.* 1983, 1, 87–105.

(7) Jacob, D. J.; Wofsy, S. C. *J. Geophys. Res.* 1988, 93, 1477–1486.

(8) Greaves, R. C.; Barkley, R. M.; Sievers, R. E. *Anal. Chem.* 1985, 57, 2807–2815.

(9) Greaves, R. C.; Barkley, R. M.; Sievers, R. E.; Meglen, R. R. *Atmos. Environ.* 1987, 21, 2549–2561.

(10) Veitkamp, P. R.; Hanson, K.; Barkley, R. M.; Sievers, R. E. *J. Geophys. Res.*, in press.

(11) Cachier, H.; Bremond, M.-P.; Buat-Menard, P. *Aerosol Sci. Technol.* 1989, 10, 358–364.

(12) Lioussé, C.; Cachier, H.; Jennings, S. G. *Atmos. Environ.* 1993, 27A, 1203–1211.

(13) Hawthorne, S. B.; Miller, D. J. *J. Chromatogr.* 1986, 24, 258–264.

(14) Lohleit, M.; Bachmann, K. *J. Chromatogr.* 1990, 505, 227–235.

[†] Global Change and Environmental Quality Program.

[‡] Department of Chemistry and Biochemistry.

[§] Permanent address: Department of Chemistry, National Institute of Standards and Technology, Boulder, CO 80303.

(1) Rogge, W.; Hildemann, L. M.; Mazurek, M. A.; Cass, G. R. *Environ. Sci. Technol.* 1994, 28, 1375–1388.

(2) Yokouchi, Y.; Ambe, Y. *Atmos. Environ.* 1985, 19, 1271–1276.

(3) Grosjean, D.; Seinfeld, J. H. *Atmos. Environ.* 1989, 23, 1733–1747.

used in this work, are 78 atm and 31 °C.¹⁵ As SFE does not require high temperatures, thermally labile compounds are less likely to be pyrolyzed during SFE than they are during thermal desorption analysis.

A method and apparatus for removing organic compounds from tropospheric aerosols using supercritical fluid extraction is described here. In this method low-volume air sampling is used, followed by SFE of the aerosol with pure CO₂ with the solution formed being transferred directly into a cryogenically cooled gas chromatographic column. The CO₂ vaporizes as the pressure is lowered, leaving the analytes focused at the head of the capillary column. Aerosols are collected by passing 200–2000 L of air through a quartz-fiber filter positioned on a support screen. Following collection, the sample and support are placed in the SFE cell. The SFE cell has a low volume and contains no polymer seals; both of these characteristics minimize the possibility of system contamination. The SFE cell is designed to be easily adapted to a sampling manifold for aerosol collection in the field.

During extraction, the SFE cell is interfaced with a cryogenically cooled GC column through the on-column injection port. The sample extraction, carried out at 450 atm and 90 °C, is completed in 20 min. After extraction, the GC oven is temperature-programmed and organic compounds are separated and detected with either a mass spectrometer (MS) or with a flame ionization detector (FID). Previous studies on the effectiveness of SFE have discussed extraction efficiencies for a variety of compounds; this work provides an apparatus and a method optimized specifically for routine whole-sample analysis of ambient aerosols.^{13,6}

The purpose of this study was to determine whether SFE is a viable alternative to liquid extraction and thermal desorption for removing organic compounds from tropospheric aerosols for subsequent separation and detection. Standard solutions of some representative compounds found on atmospheric aerosols were prepared and spiked onto quartz-fiber filters. Recovery of these compounds using SFE and thermal desorption was compared. Chromatograms obtained by SFE and by thermal desorption of parallel aerosol samples collected in an urban environment are presented.

EXPERIMENTAL SECTION

Chemicals and Instrumentation. All solvents were purchased from Mallinckrodt Specialty Chemical Co. (Paris, KY) and were used as received. The *n*-carboxylic acids and the 1-alcohols were obtained from Sigma Chemical Co. (St. Louis, MO); guaiacol, nicotine, and vanillin were purchased from Aldrich Chemical Co. (Milwaukee, WI). Carbon dioxide, research grade-FID certified, was purchased from Scott Specialty Gases (Plumsteadville, PA). Quartz-fiber filters used for spike recovery studies and collection of ambient samples were from Pallflex Products Corp. (Putnam, CT). Pyrex 5-mL weighing vials were used for holding the SFE sample support containing the sample after aerosol particle collection, while Pyrex screw-cap culture tubes were used for holding the thermal desorption sampling tubes with aerosol samples. Both types of samples were desiccated over Drierite anhydrous calcium sulfate from W. A. Hammond Drierite Co. (Xenia, OH). The thermal desorption tubes were constructed from 40–60- μ m fritted straight sealing tubes, 202 mm \times 14 mm,

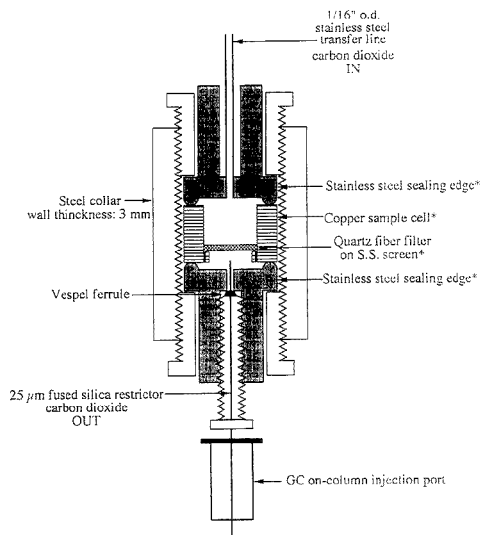


Figure 1. Supercritical fluid extraction cell for SFE-GC analysis of tropospheric aerosols. Parts machined specifically for the cell are marked with an asterisk. All others are commercially available.

from VWR Scientific (Brisbane, CA). Further details concerning construction of thermal desorption tubes are available elsewhere.⁸

Parts specially designed and constructed for the SFE cell are indicated with an asterisk in Figure 1. The extraction cell was machined from 316 stainless steel; the sample support (external diameter 2 cm; internal diameter 1.4 cm; height 0.9 cm) was constructed from brass. The high-pressure seal between sample support and extraction cell is achieved when the stainless steel cell is tightened firmly against the more malleable copper or brass sample support. The screen in the sample support is stainless steel. The internal volume of the extraction cell, measured with CO₂ at 100 atm, is 1.95 mL. The SFE cell restrictor is ~7 cm long, with an internal diameter of 25 μ m; this internal diameter provides good chromatographic peak shape while maintaining acceptable extraction flow rates.¹⁷ The outside diameter of the restrictor is 150 μ m, small enough to easily pass through the on-column injection port on the gas chromatograph into the capillary GC column. The fused silica restrictor was purchased from Polymicro Technologies Inc. (Phoenix, AZ). A high-pressure syringe pump, manufactured by Isco (Lincoln, NE) was used for pressurizing and delivering CO₂.

Gas chromatography with flame ionization detection was accomplished with a Hewlett-Packard Model 5890 gas chromatograph (Wilmington, DE). Separation of aerosols and standards was achieved using a 25 m \times 0.32 mm internal diameter column packed with 5% phenylmethylsiloxane (phase thickness 0.52 μ m) from Hewlett-Packard. A 5 m \times 0.32 mm internal diameter, uncoated, deactivated fused-silica capillary (Hewlett-Packard) preceded the analytical column as a retention gap (Hewlett-

(15) Vannoort, R. W.; Chervet, J. P.; Lingeman, G. L.; DeJong, G. J.; Brinkman, U. A. J. *Chromatogr.* **1990**, *505*, 45–77.

(16) Hawthorne, S. B.; Miller, D. J. *Anal. Chem.* **1987**, *59*, 1705–1708.

(17) Hawthorne, S. B.; Miller, D. J. *J. Chromatogr.* **1987**, *403*, 63–76.

Packard) and was joined to the analytical column by a Hewlett-Packard Chromfit glass connector. The on-column injection port was unheated during SFE; for thermal desorption analyses, the desorption port was thermostated at 250 °C. The detector temperature was 285 °C for both analysis methods. Identification of compounds in ambient samples was carried out with a Model 5890A GC/MS from Hewlett-Packard. The same capillary column was used in GC/MS analysis as that used in GC/FID. The GC/MS analyses were performed by electron impact ionization with an electron energy of 70 eV. Both chromatographic systems used helium as the carrier gas; the linear flow velocity in the GC/FID system was 1.45 mL/min at 80 °C and in the GC/MS system was 2.41 mL/min at 80 °C, as measured by the retention time of an unretained compound (butane).

Ambient aerosol samples were collected using a manifold sampling system designed to ensure isokinetic sample flows. Flow into the manifold was maintained with a brushless blower from Ametek (New York, NY). Aerosols were sampled under isokinetic conditions from the manifold using an oil-free pump manufactured by GAST Manufacturing (Benton Harbor, MI). Flow rates through matched, duplicate samples were adjusted and monitored with a flowmeter and flow controller from Omega Technologies Co. (Stamford, CT).

Procedure for Spike Recovery Studies by SFE and Thermal Desorption. Aliquots (1 μ L) of standard solutions were injected onto a clean quartz-fiber filter positioned in the thermal desorption tube or in the SFE extraction cell. The solutions were desorbed or extracted immediately after spiking under conditions identical to those used in ambient aerosol analysis. Compound responses were compared to those from 1- μ L on-column injections of each standard.

Procedure for Ambient Aerosol Collection. Aerosol samples were collected at a sampling site maintained by the Colorado Department of Health on the University of Colorado campus in Boulder. Simultaneous aerosol samples were collected from within a manifold under isokinetic sampling conditions. Sample supports for SFE and thermal desorption sample collection tubes were each connected to the manifold by a 5-cm section of 1/4-in.-o.d. stainless steel tubing. The thermal desorption tube was connected to the tubing with 1/4-in. Teflon ferrules and fittings while the SFE sampling system was connected with 1/4-in. stainless steel fittings. Samples for both SFE and thermal desorption were positioned vertically within the manifold and collected at flow rates of 5–8 L/min. To collect duplicate samples, the sample collection flow rate through each sample filter was matched with a mass flow controller and a series of needle and shutoff valves (see Figure 2). Once collected, the samples were removed from the manifold, sealed in aluminum foil-wrapped glass containers, and stored in a desiccator at 3 °C until analysis. The samples were analyzed within 48 h of collection to minimize potential sample degradation. Field blanks were collected by this same method, except after flow matching, the shutoff valve to the blank thermal desorption tube or the blank SFE sample support was closed. The SFE sample support and thermal desorption tubes were handled with tweezers or cotton gloves to minimize the possibility of contamination.

Procedure for SFE of Aerosols. The sample collection support was removed from the glass storage container with tweezers and placed into the SFE cell. The SFE cell was sealed and then connected via 1/16-in.-o.d. stainless steel transfer line to

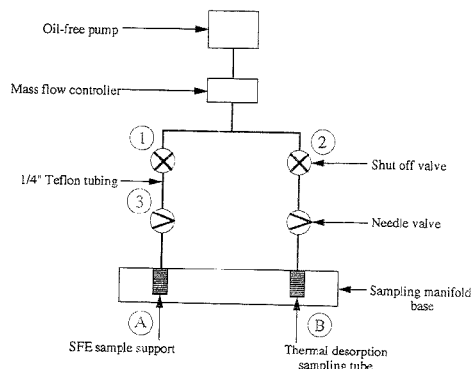


Figure 2. (A) and (B), duplicate sampling procedure detailed in text. To collect duplicate samples, the sample collection flow rate through each sample filter was matched using a mass flow controller and a series of needle and shutoff valves, depicted above. Flow through one of the sample collection lines, marked A, was interrupted by closing valve 1. Total flow through the remaining sample, B, was recorded on the digital readout of the mass flowmeter. Subsequently, sample line B was closed (valve 2 shut) and sample line A opened. Flow through line A was matched to line B by adjusting a needle valve (valve 3). Flow through each sample line was monitored and adjusted, as necessary, with the corresponding needle valve. When both flow rates were identical, the sample lines were opened to begin aerosol collection. Flow rates through each line was checked at the end of the sampling period to ensure that no significant drift occurred during collection.

the high-pressure syringe pump. Immediately prior to extraction, the SFE cell was placed in the heating block and the exit restrictor threaded through the on-column injection port ~6 cm into the retention gap (refer to Figure 1). The SFE cell was then pressurized, and the aerosol sample was extracted for 20 min by passing the dissolved solutes through the pressure restrictor directly into the cryogenically cooled GC column. The gas chromatograph oven was cooled to -30 °C to sharply focus extracted compounds onto a narrow band at the head of the column as the CO₂ vaporized at the reduced pressure of the restrictor outlet. Others have determined that this temperature is sufficient for trapping even low molecular weight compounds such as α -pinene and camphene.¹⁸ In addition, the use of the low temperature prolongs column lifetime as interaction between the stationary phase in the column and the CO₂ is minimized. Although the FID is extinguished by the CO₂ almost immediately, reignition is possible moments after removing the restrictor from the injection port after extraction.

A 5-m retention gap precedes the analytical column in order to trap nonvolatile compounds that may be extractable but not volatile enough to be eluted. In addition, the retention gap protects the analytical column from the CO₂ which is violently expelled from the end of the restrictor. Incorporation of uncoated column to serve as a retention gap is the only instrumental modification to the GC required for the SFE-GC/FID analysis of aerosols.

The GC was held at -30 °C for 3–5 min after extraction to ensure that all of the CO₂ had been flushed from the column.

(18) Hawthorne, S. B.; Krieger, M. S.; Miller, D. J. *Anal. Chem.* **1988**, *60*, 472–477.

After extraction, the GC was temperature-programmed from -30 to 60 °C at 30 °C/min; the temperature program was continued at 4 °C/min to 300 °C. The column remained at 300 °C for 20 min. In order to ensure that the SFE cell stayed clean, after aerosol extraction the quartz-fiber filter was removed from the SFE sample support. The SFE cell, with an empty support screen, was extracted for 20 min at 475 atm and 90 °C.

RESULTS AND DISCUSSION

The results of this study have shown that SFE of atmospheric aerosols allows quantitative measurement of compounds from several classes. Furthermore, information that is complementary to that gained by the thermal desorption technique can be obtained by SFE. These conclusions are based upon the following comparative analyses of spiked samples and of ambient aerosol particle samples between thermal desorption and SFE. The results also indicate that SFE with CO_2 can be validated as an alternative to thermal desorption for quantitation of several organic compounds.

A variety of anthropogenic and biogenic processes contribute particulate phase organic compounds to the lower atmosphere. Gasoline- and diesel-powered vehicles, residential wood burning, surface abrasion of plant leaves, meat-cooking operations, natural gas appliances, and cigarette smoke are some sources that contribute to the organic content of ambient aerosol samples.^{19–21} Each of these sources emits a complex mixture of organic compounds; as a result, ambient aerosols typically contain several hundred compounds. Some classes of compounds found in aerosol samples include alkanes, carboxylic acids, alkanols, polycyclic aromatic hydrocarbons (PAHs), monoterpenes, furans, phenols, and alkylated benzenes, as well as pesticides.^{1,9,22} It is the complex nature of the organic composition of the aerosols which complicates whole-sample analysis.

The 250 – 300 °C temperature range utilized in thermal desorption analysis is optimized to maximize volatility and minimize pyrolysis of organic compounds.^{8,11} Nonetheless, at these temperatures, not all compounds are fully volatilized and some compounds may be pyrolyzed.^{11,12} Other references contain details about the optimization and full characterization of the thermal desorption technique.^{8,11}

Supercritical fluid extraction provides an alternative means of removing organic compounds from aerosol particles. SFE has been used to remove organic compounds from a variety of environmental matrices, some with near 100% efficiency with respect to liquid solvent extraction.^{13,14,16,17,23} In some instances, SFE extracts more of some compounds from NIST standard reference materials than organic solvents can by Soxhlet extraction techniques requiring more time.^{24–26} SFE is easily coupled to a GC equipped with either mass spectrometric or flame ionization

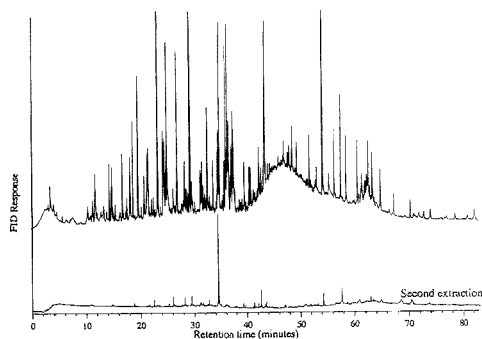


Figure 3. First SFE-GC/FID of an atmospheric aerosol sample (a, top), followed by a second extraction of the same sample (b, bottom). Both 20-min extractions were carried out at 450 atm of pure CO_2 at 90 °C; the vertical scale is the same in both chromatograms. Chromatographic conditions are reported in the text.

detection, a characteristic that makes SFE ideal for whole-sample measurement of trace organic species.¹⁷ Although a variety of compounds and mixtures of compounds, for example, CO_2 , CO_2 /methanol, N_2O , and ethane, make acceptable supercritical solvents, pure CO_2 was used in this work, for safety and simplicity. Pure CO_2 has easily achievable supercritical parameters (78 atm, 31 °C); it is inexpensive, environmentally sound, and relatively nonreactive.^{18,27,28} SFE can usually also be effected much more rapidly than solvent extraction using organic liquid solvents (minutes vs hours).

Optimal extraction conditions were determined from literature reviews of extraction efficiencies, results of standard extraction recoveries, and qualitative tests performed on aerosol samples. The solvating strength of a supercritical fluid is related to its density, a parameter primarily dependent upon pressure.^{18,28} A literature review of extraction efficiencies from a variety of matrices indicates that the recoveries for some compounds, such as PAH, increase as extraction pressure increases up to 450 atm.^{24,25,28,29} Extraction efficiency also increases with temperature;^{25,28} however, temperatures in this study were kept below 90 °C to minimize degradation of thermally labile compounds. This temperature is well above the critical temperature of CO_2 (31 °C). Figure 3a shows a chromatogram of an aerosol sample extracted according to the conditions described above. A second extraction of the same sample (Figure 3b) shows that these extraction conditions provide nearly quantitative removal of organic compounds from the aerosol sample.

Spike Recovery Studies of Standards by SFE and Thermal Desorption. A comparison between SFE and thermal desorption was conducted using standard solutions of compounds previously shown to be present on atmospheric aerosols.^{30–32} The recoveries

(19) Simoneit, B. R. T.; Mazurek, M. A. *CRC Crit. Rev. Environ. Control* **1981**, *11*, 219–276.

(20) Simoneit, B. R. T. *Atmos. Environ.* **1984**, *18*, 51–67.

(21) Hildemann, L. M.; Mazurek, M. A.; Cass, G. R. *Environ. Sci. Technol.* **1991**, *25*, 1311–1325.

(22) Rogge, W. F.; Hildemann, L. M.; Mazurek, M. A.; Cass, G. R.; Simoneit, B. R. T. *Environ. Sci. Technol.* **1991**, *25*, 1112–1125.

(23) Hawthorne, S. B.; Miller, D. J.; Krieger, M. S. *J. High Resol. Chromatogr.* **1989**, *12*, 714–720.

(24) Hawthorne, S. B.; Miller, D. J. *Anal. Chem.* **1994**, *66*, 4005–4012.

(25) Burford, M. D.; Hawthorne, S. B.; Miller, D. J. *Anal. Chem.* **1993**, *65*, 1497–1505.

(26) Langenfeld, J. J.; Hawthorne, S. B.; Miller, D. J.; Pavluszyn, J. *Anal. Chem.* **1993**, *65*, 338–344.

(27) Hawthorne, S. B.; Krieger, M. S.; Miller, D. J. *Anal. Chem.* **1989**, *61*, 736–740.

(28) Levy, J. M.; Dolata, L. A.; Ravey, R. M. *J. Chromatogr. Sci.* **1993**, *31*, 349–352.

(29) Rein, J.; Cork, C. M.; Furton, K. G. *Journal of Chromatographic Science* **1991**, *545*, 149–160.

(30) Graedel, T. E.; Hawkins, D. T.; Claxton, L. D. *Atmospheric Chemical Compounds: Sources, Occurrence, and Bioassay*; Academic Press: Orlando, FL, 1986.

(31) Rogge, W. F.; Hildemann, L. M.; Mazurek, M. A.; Cass, G. R. *Environ. Sci. Technol.* **1993**, *27*, 636–651.

Table 1. Recoveries of Spiked Compounds Using SFE-GC/FID and Thermal Desorption (TD)-GC/FID

compound	% recovered	
	by SFE ^{a,b}	by TD ^{a,b}
1-tridecanol	105 ± 2	27 ± 9
1-octadecanol	100 ± 5	8 ± 6
1-octacosanol	78 ± 8	0
<i>n</i> -nonanoic acid	68 ± 14	30 ± 13
<i>n</i> -dodecanoic acid	71 ± 13	18 ± 5
<i>n</i> -octadecanoic acid	105 ± 11	16 ± 6
<i>n</i> -eicosanoic acid	100 ± 12	9 ± 6
guaiaicol	17 ± 5	44 ± 12
nicotine	15 ± 13	55 ± 3
vanillin	29 ± 13	85 ± 10
9-fluorenone	77 ± 12	81 ± 5
pyrene	87 ± 13	75 ± 3

^a Averages of four replicate analyses. ^b Recoveries were normalized to the average of four replicate on-column injections of each compound. For the injected standards, the standard deviation was <5% in all cases.

of these spiked compounds from filters by SFE and by thermal desorption are shown in Table 1; recoveries are normalized to peak areas resulting from on-column injections of the standard solutions of these compounds. The comparison was performed in order to elucidate general differences between the two techniques with respect to atmospheric aerosol analysis.

It should be noted that the matrix of the filter is significantly different from that of atmospheric aerosol particles. Others have reported that methods of sample spiking are rarely indicators of extraction efficiencies from environmental samples in which one can place much confidence.²⁵ The inorganic compounds and elemental and organic carbon composition of the aerosol matrix vary greatly depending upon emission source, aerosol age, local meteorology, and transport conditions of the air mass.^{11,12,33,34} For this reason, it is difficult to create in the laboratory samples that mimic actual atmospheric particles. Nevertheless, taking into account the difficulties inherent in extraction of organic compounds and the character of the constantly changing aerosol matrix, a general comparison of recoveries for spiked standards can provide some indication of the effectiveness of each technique for the removal of these compounds from atmospheric aerosol samples.

Recoveries of two series of standards, primary alcohols, from 1-tridecanol to 1-octacosanol, and *n*-carboxylic acids, from *n*-nonanoic acid to *n*-eicosanoic acid, were measured; compounds in both classes are present in atmospheric aerosols.^{30,32,35} The remaining compounds included in the comparison, nicotine, guaiaicol, vanillin, 9-fluorenone, and pyrene, were chosen to reflect a variety of compounds known to be emitted from various sources into the atmosphere. Nicotine and guaiaicol have been identified as unique source tracers for cigarette smoke and wood smoke, respectively. Vanillin has been identified in wood smoke as well as in particle samples collected in forested areas;^{8,36} 9-fluorenone is emitted into the atmosphere by a number of combustion

processes such as wood burning, petroleum combustion in vehicles, and natural gas appliances.^{31,35,36} Pyrene is a PAH emitted to the atmosphere primarily as a result of petroleum combustion by vehicles.³¹

The spiked primary alcohol standards were quantitatively recovered from the filter by SFE, with the exception of 1-octacosanol, which showed a 76% recovery. Significantly lower recoveries of the primary alcohols were achieved using thermal desorption, in part due to thermal decomposition of these compounds. A typical chromatogram of thermally desorbed alcohol standards contains several peaks in addition to those of the spiked standards. Mass spectral analysis and retention time matching have identified the decomposition products as alkenes produced by thermal dehydration of the parent alcohol. Neither 1-octacosanol, the highest molecular weight primary alcohol standard investigated, nor its corresponding alkene decomposition product was detected in the thermal desorption analysis.

Supercritical fluid extraction was also more effective than thermal desorption in recovering the spiked *n*-carboxylic acids. Recovery efficiency by SFE increases as the polarity of the acid decreases (68% for *n*-nonanoic acid; 100% for *n*-eicosanoic acid). The *n*-carboxylic acids with molecular weights higher than that of eicosanoic acid, although expected to be soluble in supercritical CO₂, are not reproducibly analyzed by the GC temperature program utilized in this study. The low volatility of the acids is apparent in the low recoveries achieved using thermal desorption analysis.

Extraction/Desorption of Ambient Aerosols. Table 2 contains a list of compounds identified in the ambient air in Boulder during the autumn of 1994. Duplicate samples were collected and analyzed by either SFE-GC/MS or by thermal desorption-GC/MS. Organic compounds identified in the samples subjected to SFE analysis and not in the duplicate samples analyzed by thermal desorption are indicated with an asterisk. Similarly, there were some compounds identified in the thermal desorption analysis that were not found in the SFE analysis that are marked by a dagger.

Several possibilities may be considered to account for the apparent differences in the duplicate samples analyzed by the two techniques. The first possibility is that the compound identified by one technique and not by the other may have been selectively removed from the sample matrix only by one removal technique. For this to be a valid explanation, there must be reason to expect that the compound in question was actually present in the aerosol sample and not an artifact, such as a thermolysis product arising from a step in the analytical procedure. In addition, there should also be a chemical or physical reason for why the compound was not removed from the sample matrix by one, but only one, of the two techniques. For example, a compound with extremely low vapor pressure may not be removed by thermal desorption; similarly, a very polar molecule might not be effectively removed from an aerosol particle upon which it is strongly adsorbed by SFE using only CO₂, a nonpolar solvent.

Under the conditions studied, SFE and thermal desorption are similar in their effectiveness for removing *n*-alkanes, carboxylic acids, furanones, and several PAHs from atmospheric aerosol particles. Methyl esters of tetradecanoic and hexadecanoic acid, as well as some molecular markers of softwood combustion such

(32) Rogge, W. F.; Hildemann, L. M.; Mazurek, M. A.; Cass, G. R. *Environ. Sci. Technol.* 1993, 27, 2700-2711.

(33) Hildemann, L. M.; Klinedinst, D. B.; Klouda, G. A.; Currie, L. A.; Cass, G. R. *Environ. Sci. Technol.* 1994, 28, 1565-1576.

(34) Harrison, R. M.; Pio, C. A. *Atmos. Environ.* 1983, 17, 1733-1738.

(35) Rogge, W. F.; Hildemann, L. M.; Mazurek, M. A.; Cass, G. R. *Environ. Sci. Technol.* 1993, 27, 2736-2744.

(36) Hawthorne, S. B.; Miller, D. J.; Langenfeld, J. J.; Krieger, M. S. *Environ. Sci. Technol.* 1992, 26, 2251-2262.

Table 2. Organic Compounds Identified in Urban Tropospheric Aerosols Using Low-Volume Sampling with Either Thermal Desorption- or SFE-GC/FID^{a,c}

<i>n</i> -carboxylic acids	PAHs
<i>n</i> -hexanoic acid	fluoranthene
<i>n</i> -heptanoic acid	pyrene
<i>n</i> -octanoic acid	chrysene
<i>n</i> -nonanoic acid	benzo[<i>a</i>]anthracene
<i>n</i> -decanoic acid	benzo[<i>ghi</i>]perylene
<i>n</i> -undecanoic acid	ketones
<i>n</i> -dodecanoic acid	6,10,14-trimethyl-2-pentadecanone
<i>n</i> -tetradecanoic acid	(9 <i>ff</i>)-fluorenone
<i>n</i> -hexadecanoic acid	2-heptadecanone ^e
<i>n</i> -octadecanoic acid	methyl esters of carboxylic acids
<i>n</i> -eicosanoic acid [*]	1-methyl ester of tetradecanoic acid
<i>n</i> -alkanes	1-methyl ester of hexadecanoic acid
<i>n</i> -pentadecane	alkylbenzenes
<i>n</i> -hexadecane	1,3-methyl-2-ethylbenzene ^f
<i>n</i> -heptadecane	1,2,3-trimethylbenzene ^g
<i>n</i> -octadecane	alcohols
<i>n</i> -nonadecane	2-(2-butoxyethoxy)ethanol ^h
<i>n</i> -eicosane	2-ethoxy-1-propanol ^h
<i>n</i> -heneicosane	1-pentacosanol ⁱ
<i>n</i> -docosane	1-hexacosanol ⁱ
<i>n</i> -tricosane	1-octacosanol ⁱ
<i>n</i> -tetracosane	phthalates
<i>n</i> -pentacosane	bis(1-methylethyl) phthalate
<i>n</i> -hexacosane	bis(2-methyl propyl) phthalate
<i>n</i> -heptacosane	bis(2-ethyl hexyl) phthalate
<i>n</i> -octacosane	aldehydes
<i>n</i> -nonacosane	1-nonanal
<i>n</i> -triacontane	benzaldehyde ^f
<i>n</i> -hentriacontane	vanillin
<i>n</i> -dotriacontane	alkenes
<i>n</i> -tritriacontane	1-nonacosene ^f
<i>n</i> -tetraatriacontane	miscellaneous
branched alkanes	1,5-diethyl-2,3-dimethylcyclohexane ^g
b-C ₂₂ ^b	3-methyl-2-butaneamine ^g
b-C ₂₅ ^b	guaiacol
b-C ₂₁ ^b	camphor
b-C ₂₅ ^b	retene
b-C ₂₆ ^b	PAHs
b-C ₂₇ ^b	

^a These are all compounds identified in at least one of three sets of duplicate samples collected between August 4 and December 2, 1994 in Boulder, CO; all samples represent 600–2400 liters of air sampled over 2 to 12 h. Compounds were identified by comparison of their mass spectra to mass spectra reported in the literature, and by retention time matching that of an authentic standard. ^b No authentic standards were available, so tentative identification was based on comparison of mass spectra. ^c Asterisk indicates compound was removed and detected only in the aerosol sample analyzed by SFE with CO₂. ^d Dagger indicates the compound was removed and detected only in the aerosol sample analyzed by thermal desorption.

as retene, guaiacol, and vanillin,^{36,37} were identified in samples analyzed by both techniques.

Several compounds identified in the sample analyzed by thermal desorption were not seen in the sample analyzed by SFE. These compounds included two alkylated benzene compounds, benzaldehyde, and 1-nonacosene. Alkylbenzene compounds and benzaldehyde are emitted to the atmosphere from a variety of sources, including petroleum combustion, tobacco smoking, and some growing vegetation;³⁰ these low molecular weight compounds have been identified in aerosol samples in past studies.⁹ Hawthorne et al. have shown that a variety of terpenes, hydrocarbons with molecular weights and polarities similar to substituted benzene compounds, are soluble in supercritical CO₂ and are effectively trapped in the cryogenically cooled analytical column under the conditions used in this analysis.^{18,23} Given the

relatively small concentration of these compounds in ambient aerosols, however, it is likely that the total amount extracted was below the detection limit of the FID. Thermal desorption is probably more effective than SFE for removing the alkylated benzene compounds from the aerosol. 1-Nonacosene, another compound removed and identified by thermal desorption analysis but not seen in the SFE analysis, has not, to our knowledge been previously reported to be present in tropospheric samples. It is unlikely that this compound was actually present in our ambient aerosol particles, as it is expected to be quite soluble in supercritical CO₂ under the conditions utilized in this analysis. Alkenes have been shown to be generated as a result of alcohol dehydration during thermal desorption (see above). The presence of nonacosene in the sample analyzed by thermal desorption may be due to dehydration of 1-nonacosanol during desorption; 1-nonacosanol is contributed to the atmosphere by vascular plants,³² but it was not observed in the sample analyzed by SFE.

Compounds identified in the sample treated by SFE, but not in the sample treated by thermal desorption, include several high molecular weight alcohols (e.g., 1-pentacosanol, 1-hexacosanol, and 1-octacosanol) and eicosanoic acid. These alcohols and this acid are present in suspended particulates formed by abrasion of plant leaves;^{32,38} they are also found, to a lesser extent, in cigarette smoke.¹ These compounds all have fairly low vapor pressures relative to much of the organic material identified in aerosols. It is unlikely that the temperature used for thermal desorption in this study was sufficiently high to volatilize the compounds from the aerosol. Again, analysis of alcohol standards indicates that some thermal degradation does occur at these temperatures. It is likely that the alcohols and acids were actually present on the aerosols, were removed by SFE, and either were not desorbed or were thermally degraded during the thermal desorption analysis.

Qualitative Comparison of Desorbed and Extracted Ambient Aerosol Samples. A qualitative comparison of SFE vs thermal desorption was also conducted on duplicate samples by performing two analyses on each sample (SFE followed by thermal desorption on one sample and thermal desorption followed by SFE on the duplicate). Chromatographic separation and detection followed each step of the two analyses in the sequence in order to compare the peaks with those in the duplicate sample analyzed in the opposite sequence.

A matched pair of ambient aerosol samples was collected simultaneously from an urban air mass and analyzed in the following manner. One sample was first thermally desorbed into the gas chromatograph for GC/FID analysis. After thermal analysis, this sample was extracted into the gas chromatograph using supercritical CO₂. The other matched sample was first extracted with supercritical CO₂ and the extract was analyzed on-line by GC/FID; then, in a second step, the sample was subjected to thermal desorption-GC/FID analysis. The desorption and extraction steps were performed under conditions earlier determined empirically to be optimal for the removal of most of the organic compounds from the aerosol. Therefore, any organic compounds detected in the second step of the analysis sequence must not have been quantitatively removed in the first analysis. Chromatograms of the two-step analysis of each matched sample are shown in Figure 4.

(37) Ramdahl, T. *Nature* 1983, 306, 580–582.

(38) Simoneit, B. R. T.; Mazurek, M. A. *Atmos. Environ.* 1982, 16, 2139–2159.

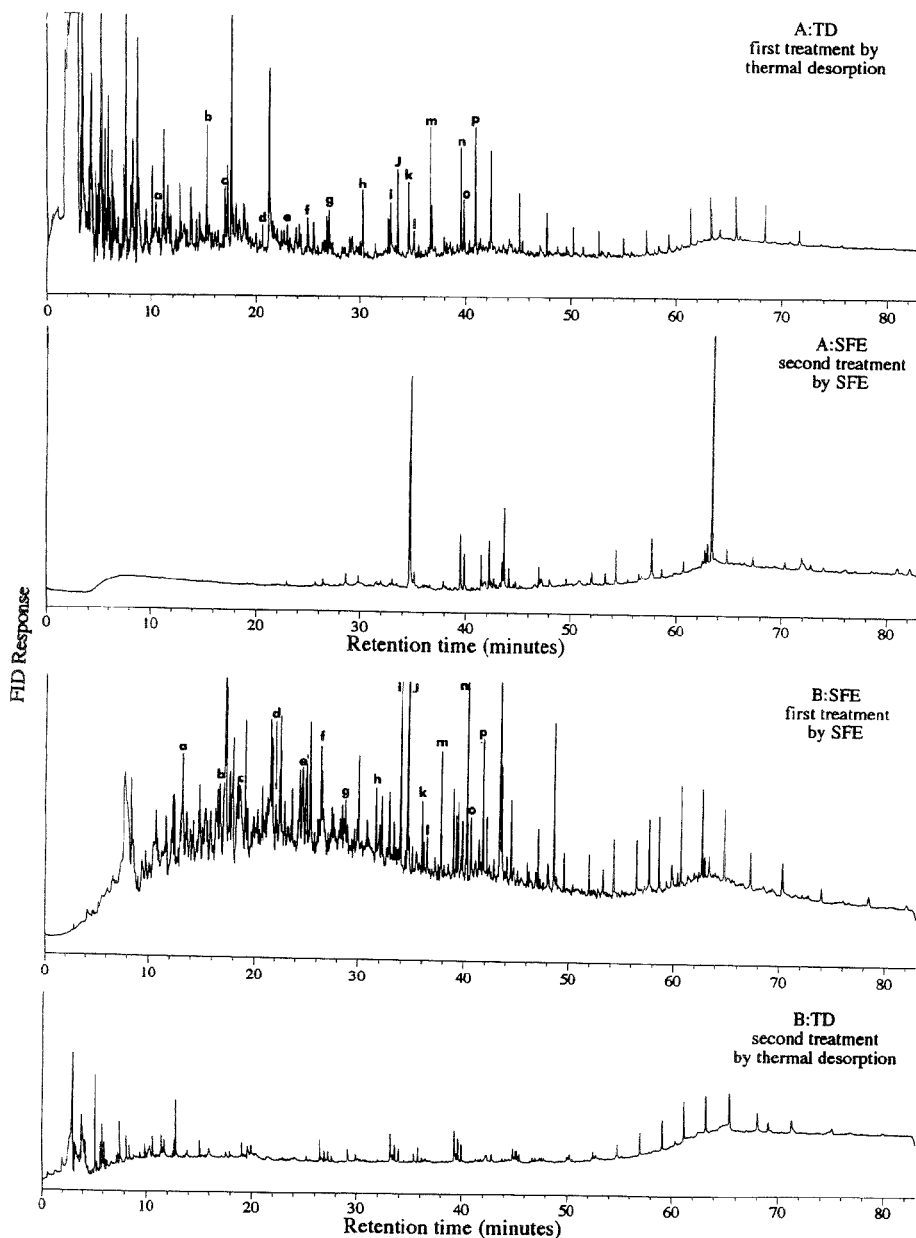


Figure 4. Chromatographic traces of analyses of two duplicate ambient aerosol samples from 200 L of air. Chromatogram A:TD results from a thermal desorption-GC/FID analysis of one sample; chromatogram A:SFE is the result of a subsequent SFE-GC/FID analysis of the previously desorbed filter. Chromatogram B:SFE is the result of the first treatment of the duplicate sample, by SFE-GC/FID analysis. B:TD results from the second step, thermal desorption-GC/FID analysis of the previously extracted filter.

The results in Figure 4 show that most compounds are removed by either SFE or thermal desorption; the chromatograms for the first treatment steps are similar. More than 90% of the

volatile/extractable organic compounds are removed in one step by either technique. Sixteen peaks present in both A:TD and B:SFE were selected at random from the middle portion of the

Table 3. Recoveries of Randomly Selected Compounds from Duplicate Particle Samples Analyzed by Either Thermal Desorption (TD)- or SFE-GC/FID

peak indicator ^a	compd desorbed A:TD ^b (ng)	compd extracted B:SFE ^b (ng)	mean mass of compd (ng) ^b	% of mean mass removed	
				TD	SFE
a	13.7	19.2	16.4	83	117
b	17.4	10.6	14.0	124	76
c	12.4	10.2	11.3	110	90
d	4.8	3.2	4.0	120	80
e	6.0	11.3	8.6	69	130
f	8.8	8.7	8.8	100	100
g	7.6	5.6	6.6	115	85
h	10.6	6.1	8.4	127	73
i	14.2	14.2	14.2	100	100
j	25.7	22.1	18.9	83	117
k	14.3	5.2	9.8	147	53
l	6.1	2.5	4.3	141	59
m	16.7	10.4	13.6	124	76
n	14.2	18.6	16.4	87	113
o	10.0	5.9	7.9	126	74
p	19.1	9.5	14.3	134	66

^a Selected peaks are indicated, according to letter, in Figure 4 chromatogram A:TD and chromatogram B:SFE. ^b Mass is calculated by multiplying the integrated peak area for each compound by the FID response for 1 ng of *n*-docosane.

chromatograms, and the integrated peak areas of each were compared on a peak-by-peak basis. The results, presented in Table 3, show that many compounds are effectively removed from the aerosol particles by either SFE or thermal desorption. In most cases, there was reasonably good agreement between the two analytical methods. The most dramatic differences were by slightly greater than a factor of 2.

There are some important differences in the early and late stages of the chromatogram that will be discussed in more detail. The trace A:TD, in Figure 4, is the result of a 15-min thermal desorption of one of the original matched aerosol samples. The large, off-scale, unresolved peak near the beginning of the chromatographic trace is characteristic of thermal desorption of an ambient aerosol sample and may arise in part from thermal degradation of some unstable compounds. The trace A:SFE, in Figure 4, was obtained by SFE of the aerosol sample immediately after the thermal desorption-GC/FID analysis (A:TD). Supercritical fluid analysis of the previously desorbed filter extracted additional organic compounds from the aerosol particles; most of the compounds present in A:SFE were eluted in the later half of the chromatographic trace.

Sample B:SFE resulted from the SFE-GC/FID analysis of the second original, matched aerosol analysis. Relatively few compounds are present in the first quarter of the chromatogram B:SFE compared to the chromatogram from the matched sample first analyzed by thermal desorption (A:TD). The later half of B:SFE contains a significantly more integrated area than the later half of A:TD. Following the initial SFE, sample B was transferred to a desorption tube for subsequent analysis by thermal desorption-GC/FID; the results of this analysis are shown in trace B:TD in Figure 4. In B:TD, additional organic compounds have been desorbed from the previously extracted aerosol sample; most of the compounds desorbed were eluted early in the chromatogram.

There are several possible explanations for the abundance of early-eluting compounds in the sample analyzed initially by thermal desorption (A:TD) that are not present in the duplicate

sample analyzed initially by SFE (B:SFE). These compounds give rise to the large unresolved peak that dominates the beginning of chromatogram A:TD. The unresolved peak could arise from a group of volatile compounds that are poorly soluble in supercritical CO₂ but are effectively separated from the aerosol particles by thermal desorption. This conclusion seems unlikely, however, in light of the fact that the sample analyzed first by SFE and second by thermal desorption (B:TD) has a much smaller unresolved peak at the same retention time. If the compounds were truly insoluble in supercritical CO₂, they would remain on the aerosol particles until the subsequent thermal desorption analysis. It is also possible that during SFE some compounds were removed from the aerosol but not effectively trapped in the analytical column. Others have reported that the trapping temperature utilized in this study should be sufficiently low to trap most compounds;¹⁸ nevertheless, some of the most volatile compounds present in trace amounts on the particles may have been lost or incompletely transported to and collected in the capillary column. A third possibility is that the early-eluting compounds were absorbed to strong active sites on the aerosol particle. It is possible that the relatively low temperatures utilized in the SFE technique do not supply sufficient energy for certain analytes to overcome the "barrier of desorption" necessary to free the analyte from these active sites.²⁶ Langenfeld et al. hypothesized this to be one factor contributing to the increased recoveries of some compounds from environmental matrices observed in high-temperature SFE over recoveries achieved at lower temperatures more characteristic of those used in this study.^{26,39}

The unresolved peak in A:TD may be thermal degradation products generated during the desorption. Thermally labile organic compounds on or in the aerosol particles are less likely to be degraded in the relatively low-temperature SFE analysis; this would explain the lack of a corresponding unresolved peak in B:SFE. The presence of some resolved peaks in the beginning of B:TD may indicate that the unresolved peak in A:TD is a combination of both volatile organic compounds that are insoluble in CO₂ and thermal degradation products.

To further characterize the unresolved peak observed in the thermal desorption analysis, we performed a lower (130 °C) or a higher (300 °C) temperature thermal desorption analysis on two different fractions of the same aerosol particle sample and repeated this analysis with two different samples. Within every set analyzed, the first peak in the chromatogram resulting from the thermal desorption conducted at the lower temperature was dramatically smaller than the first peak in the chromatogram from the higher temperature thermal desorption. Though this observation does not conclusively identify compounds within the first peak as thermal degradation products of the desorption analysis, it is consistent with that conclusion.

Both chromatograms resulting from SFE analysis, A:SFE and B:SFE, contain more late-eluting compounds than the corresponding thermal desorption analysis. Compounds eluted in this region may either be thermally labile, and therefore destroyed during thermal desorption, or have low volatilities, and thus are preferentially removed from the aerosol by SFE but not by thermal desorption. This is not unexpected as SFE with carbon dioxide is known to be an effective solvent for some high molecular weight

(39) Langenfeld, J. J.; Hawthorne, S. B.; Miller, D. J.; Pawliszyn, J. *Anal. Chem.* 1994, 66, 909-916.

compounds with low volatilities. Others have shown that SFE may extract some compounds, such as anthracene and phenanthrene, more efficiently from standard reference materials than NIST has certified to be present when a standard method such as Soxhlet extraction is used.^{13,24,25} This indicates that some fraction of certain compounds may be very difficult to remove from particular matrices.

CONCLUSIONS

Supercritical fluid extraction with pure CO₂ has been shown to provide quantitative recovery of many compounds present in atmospheric aerosol samples. The SFE technique is a whole-sample analysis that can be coupled directly to a gas chromatograph for separation and on-line detection of complex organic samples. Optimal extraction conditions have been determined and extraction can be completed in 20 min. The sensitivity afforded by the SFE technique is sufficient to accommodate low-volume sample collection; the composition of organic compounds in atmospheric aerosol particles can be monitored on a short-term (2 h rather than 24 h) basis. Recoveries of standards, spiked onto filters, by SFE and by thermal desorption, a well-characterized method of whole-sample aerosol analysis, have been determined.

In addition, duplicate aerosol samples have been analyzed by SFE and thermal desorption in order to further demonstrate differences and similarities between the two techniques. The SFE technique uses relatively low temperatures; as a result, thermal degradation of labile compounds during analysis is minimized. Thermal desorption is a more effective technique for the removal of certain more volatile compounds and, possibly, those compounds that interact strongly with active sites from the aerosol particles. The two analytical methods offer complementary advantages and can also be used in combination.

ACKNOWLEDGMENT

The authors thank the Colorado Department of Health and the City of Boulder for extending the use of their local air monitoring facility. Dr. Barbara Watkins, Dr. Tom Ryerson, and Dr. Craig Perman provided helpful comments on this work; the technical assistance of Paul Frazey is gratefully acknowledged.

Received for review April 20, 1995. Accepted July 18, 1995.*

AC950393Y

* Abstract published in *Advance ACS Abstracts*, September 1, 1995.

Predicting Drug–Membrane Interactions by HPLC: Structural Requirements of Chromatographic Surfaces

Hanlan Liu,[†] Shaowei Ong,[†] Louis Glunz,[‡] and Charles Pidgeon^{*,†}

Department of Medicinal Chemistry, School of Pharmacy, Purdue University, West Lafayette, Indiana 47907, and Regis Technologies Inc., 8120 Austin Avenue, Morton Grove, Illinois 60053

Drug–membrane interactions have recently been studied by immobilized artificial membrane (IAM) chromatography (Pidgeon, C.; et al. *J. Med. Chem.* 1995, 38, 590–595. Ong, S.; et al. *Anal. Chem.* 1995, 67, 755–762), and the molecular recognition properties of IAM surfaces toward drug binding/partitioning appear to be remarkably close to the molecular recognition properties of fluid membranes. The structural requirements of chromatography surfaces to emulate biological partitioning are unknown. To begin to elucidate the surface structural requirements needed to predict drug partitioning into membranes, three bonded phases were prepared. The chromatography bonded phases were prepared by immobilizing (i) a single-chain analog containing the phosphocholine (PC) headgroup (IAM.PC.DD), (ii) a long-chain alcohol containing polar OH groups protruding from the surface (12-OH-silica), and (iii) a long-chain fatty acid containing OCH₃ groups protruding from the surface (12-MO-silica). The 12-OH-silica surface can be considered as an immobilized “octanol” phase with OH groups protruding from the surface and is therefore a solid phase model of octanol/water partitioning systems. As expected, improved capability of predicting solute–membrane interactions as found for the chromatographic surface containing the PC polar head-group because the PC headgroup is also found in natural cell membranes. For instance, the IAM.PC.DD column predicted drug partitioning into dimyristoylphosphatidylcholine liposomes ($r = 0.864$) better than 12-OH-silica ($r = 0.812$), and 12-MO-silica ($r = 0.817$). IAM. PC.DD columns also predicted intestinal drug absorption ($r = 0.788$) better than 12-OH-silica ($r = 0.590$) and 12-MO-silica ($r = 0.681$); reversed phase octadecylsilica (ODS) columns could not predict intestinal absorption ($r = 0.10$). Collectively, these results suggest that chromatographic surfaces containing interfacial polar groups, i.e., PC, OH, and OCH₃, model drug–membrane interactions, but surfaces lacking interfacial polar functional groups (e.g., ODS surface) are poor models. Most interestingly, drug partitioning into octanol/water systems does not correlate with drug binding to the immobilized octanol phase. However, drug partitioning into immobilized octanol

correlates with drug partitioning into liposomes ($r = 0.812$).

Immobilized artificial membranes (IAMs) are solid phase membrane mimics whereby phospholipid molecules are covalently bonded to silica particles at a monolayer density.^{3–5} Recently, we have developed IAMs as a novel method for rapidly predicting drug–membrane partitioning and drug–membrane transport by using IAMs as a stationary phase in high-performance liquid chromatography (HPLC) systems.^{1,2}

The success of IAM chromatography in predicting drug–membrane interactions is based on the structural similarities between the immobilized ligand comprising IAMs and the phospholipids comprising membrane bilayers.² Most interestingly, the phospholipids found in cell membranes contain predominantly diacylated phosphocholine (PC) lipids, but all of the IAM surfaces shown in Chart 1 are prepared from PC ligands. One ligand is a PC diacylated ester, and the other ligands are single-chain PC analogs with and without the glycerol backbone. In spite of these structural differences, all of the IAM surfaces shown in Chart 1 give virtually identical results in predicting drug partitioning into fluid dimyristoylphosphatidylcholine (DMPC) liposomes.^{2,6} Thus the glycerol backbone, the linkage between the glycerol backbone, the acyl chain linkage (ether linkage or ester linkage), and the number of acyl chains are not critical structural features of surfaces that are intended to model drug–membrane interactions. The most important structural components of IAMs are a phospholipid headgroup and a hydrocarbon chain.

A natural question arising from the above finding is whether surfaces prepared by immobilized ligands with polar groups other than PC protruding from the surface can be good membrane models. In particular, since the octanol/water partitioning system has previously been extensively used to predict drug–membrane interactions prior to IAM chromatography, we speculated that immobilized octanol may create a surface that is a good membrane

[†] Purdue University.

[‡] Regis Technologies, Inc.

(1) Pidgeon, C.; Ong, S.; Liu, H.; Qiu, X.; Pidgeon, M.; Dantzig, A.; Munroe, J.; Hornback, W. J.; Kasher, J. S.; Glunz, L.; Szezerba, T. *J. Med. Chem.* 1995, 38, 590–594.

(2) Ong, S.; Liu, H.; Qiu, X.; Bhat, G.; Pidgeon, C. *Anal. Chem.* 1995, 67, 755–762.

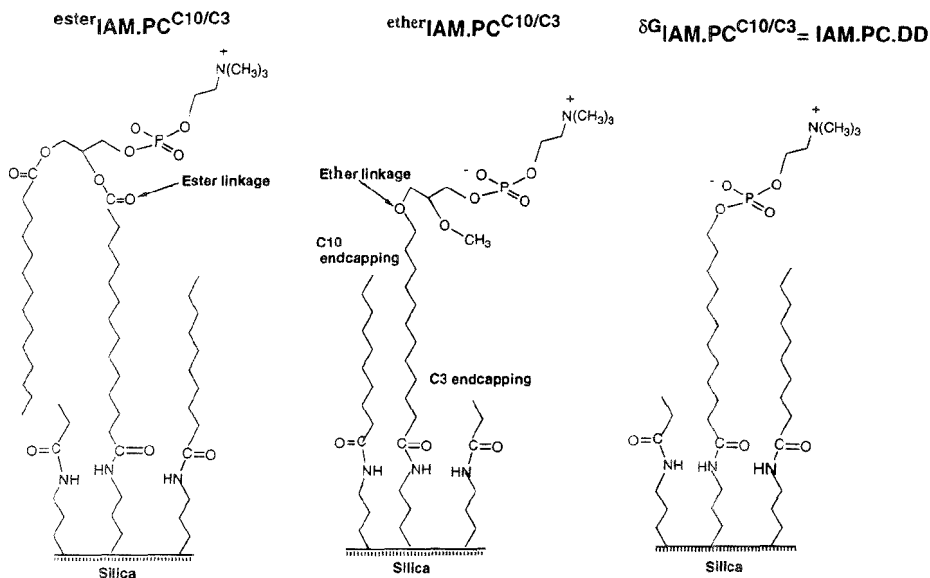
(3) Pidgeon, C. U.S. Patent 4,927,879, 1990.

(4) Pidgeon, C. U.S. Patent 4,931,498, 1990.

(5) Pidgeon, C.; Venkatarum, U. V. *Anal. Biochem.* 1989, 176, 36–47.

(6) Ong, S.; Pidgeon, C. *Anal. Chem.*, submitted for publication.

Chart 1. Structures of Three IAM.PC Bonded Phases

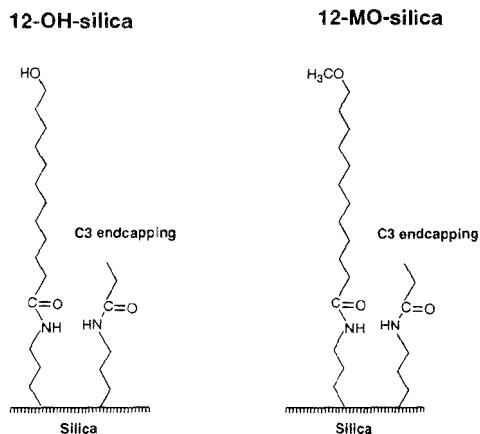


model. To address this question, we synthesized 12-hydroxydodecanoic silica propyl amide (denoted as 12-OH-silica) and evaluated the ability of this surface to predict drug partitioning into *n*-octanol/water phases and also to predict drug partitioning into fluid membranes. 12-OH-silica is effectively immobilized alcohol and can be considered as a solid phase model of the *n*-octanol/water partitioning system. 12-OH-silica contains both hydrogen bond donor and acceptor capabilities at the surface. To probe the effect of hydrogen bonding at the chromatographic interface, a surface lacking hydrogen bond donor capabilities was also prepared by immobilizing 12-methoxydodecanoic acid (12-MO) on silica propyl amine (SPA) to form 12-MO-silica. The general structures of 12-OH-silica and 12-MO-silica are shown in Chart 2 which shows that monolayers of OH groups form on the 12-OH-silica surface and monolayers of OCH₃ groups form on the 12-MO-silica surface.

EXPERIMENTAL SECTION

Chemicals. 12-Bromododecanoic acid, 12-hydroxydodecanoic acid, sodium methoxide (25 wt % solution in methanol), tetrahydrofuran, alcohol-free chloroform, and propionic anhydride were purchased from Aldrich Chemical Co. (Milwaukee, WI). Tetrahydrofuran was dried by refluxing over sodium under nitrogen. Methanol was from Mallinckrodt Inc. (Paris, KY) and was distilled over CaH₂. The following chemicals were ordered from Sigma Chemical Co. (St. Louis, MO): xylometazoline, oxymetazoline, naphazoline, tetrahydrozoline, clonidine, propranolol hydrochloride, alprenolol, oxprenolol, metoprolol, pindolol, nadolol, atenolol, tramazoline, phosphate buffered saline (PBS) tablets, 1,1'-carbonyldiimidazole (CDI), salicylic acid, *m*-nitrobenzoic acid, acetylsalicylic acid, benzoic acid, phenol, acetanilide, theophylline, *p*-nitroaniline, antipyrine, *m*-nitroaniline, aniline, and *p*-toluidine. The imidazolidine derivatives ST608, ST475, ST476, ST603, STH2224,

Chart 2. Structures of 12-OH-silica and 12-MO-silica Bonded Phases

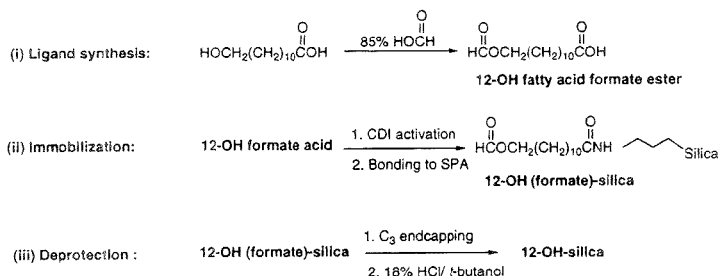


STH2100, ST585, ST600, ST606, and ST590 were kind gifts from Boehringer-Ingelheim Co. Hydrochloric acid and formic acid were from Fisher Scientific (Pittsburgh, PA). SPA chromatography particles were kindly provided by Regis Technologies Inc. (Morton Grove, IL). Chromatography columns were prepared by bonding synthetic ligands to the SPA. The SPA particles were 12 μm for preparing both 12-MO-silica and 12-OH-silica chromatography surfaces and 5 μm for preparing the IAM.PC.DD column.

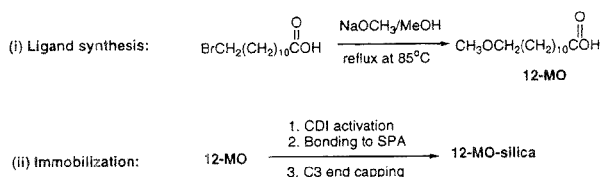
Syntheses. (i) Synthesis of IAM.PC.DD. The single-chain PC ligand that lacks a glycerol backbone (⁶IAM.PC^{C10/C3}, shown in Chart 1) is commercially produced as an IAM.PC.DD column

Scheme 1. Syntheses of 12-OH-silica and 12-MO-silica Surfaces

A. Synthetic Route for Preparing 12-OH-Silica



B. Synthetic Route for Preparing 12-MO-Silica



(where "DD" stands for drug discovery), supplied by Regis Technologies Inc.

(ii) **Synthesis of 12-OH-silica.** A linear bifunctional lipid was required that contained an OH group on one end of the alkyl chain and a carboxyl group at the other end of the chain. Octanol is an eight-carbon primary alcohol with an ω -methyl that cannot be used to immobilize octanol with the orientation of the OH groups protruding from the surface. The eight-carbon bifunctional analog of octanol, ω -carboxyl-1-octanol, was not commercially available. Consequently, we used ω -carboxyl-1-undecanol as the bifunctional lipid. Although ω -carboxyl-1-undecanol contains four additional carbons compared to octanol, immobilization of the ω -carboxyl-1-undecanol causes orientation of the lipid such that the four additional carbons contribute only $\sim 5\text{--}6$ Å of hydrophobic thickness to the surface.

Scheme 1A shows the synthetic pathway for preparing 12-OH-silica. The ligand required for preparing this surface was ω -carboxyl-1-undecanoyl formate (12-OH fatty acid formate ester). To prepare this ligand, 10 mL of formic acid (88 wt %) and 2.0 g (9.24 mmol) of 12-hydroxydodecanoic acid were dissolved in 20 mL of *tert*-butyl alcohol and heated at 65°C for 1.5 h. TLC on silica gel ($\text{CHCl}_3/\text{MeOH} = 9:1$) showed that there is only one spot ($r_f = 0.49$) which differed from the starting material ($r_f = 0.31$). A new peak at 1725 cm^{-1} was found in the IR spectrum of the reaction mixture, indicating that an ester bond was formed between formic acid and 12-hydroxydodecanoic acid. Flash chromatography was used to purify the product (12-OH fatty acid formate ester) with 400 mL of organic solvent ($\text{CHCl}_3/\text{MeOH} = 9:1$). Fractions containing the 12-OH fatty acid formate ester were pooled, rotary evaporated, and vacuum pumped to dryness, to give 1.969 g of 12-OH fatty acid formate ester (87.2% yield): $^1\text{H NMR}$ (CDCl_3) δ 8.80 (s, 1H), 4.14 (t, 2H), 2.31 (t, 2H), 1.66–1.62 (m, 4H), and 1.25 (br s, 14H).

The procedure for immobilization of the 12-OH fatty acid formate ester on SPA, followed by propionyl (C3) endcapping to

form 12-HO-silica, was the same as that for the synthesis of IAMs described previously.^{7,8} Briefly, 1.5 g of 12-OH fatty acid formate ester was activated by 0.50 g of CDI in chloroform and then bonded to 5.0 g of SPA, followed by C3 endcapping. The density of the immobilized ligand (i.e., 12-OH fatty acid formate ester) was $110\ \mu\text{mol/g}$ of silica, measured using elemental analysis.⁷ The formate group was deprotected on the surface as follows: 5.0 g of ω -propylamide 1-undecanoyl formate silica (12-OH(formate)-silica) was suspended in 30 mL of *tert*-butyl alcohol, 30 mL of concentrated HCl (37%) was slowly added, and the mixture stirred mildly at 50°C for 2 h. The suspension was filtered, and the particles were washed with 120 mL of methanol, 40 mL of chloroform, and 40 mL of acetone. The chromatography packing material was dried by vacuum pumping at 40°C overnight.

(iii) **Synthesis of 12-MO-silica.** Scheme 1B shows the synthetic pathway for preparing 12-MO and the immobilization strategy used to tether 12-MO to SPA. 12-MO was synthesized as described.⁹ The procedure for immobilization of 12-MO on SPA, followed by C3 endcapping to form 12-MO-silica, was the same as that for the synthesis of IAMs described previously.^{7,8} The 12-MO-silica bonded phase contains the polar OCH_3 group protruding from a silica surface. Briefly, 1.0 g of 12-MO was activated by 0.70 g of CDI in THF and then bonded to 12.0 g of SPA, followed by C3 endcapping. The density of immobilized ligand (i.e., 12-MO) was $171\ \mu\text{mol/g}$ of silica, by elemental analysis and FT-IR spectroscopy.⁷

Chromatography. All HPLC columns containing IAM stationary phases were packed at Regis Technologies Inc. The columns were (i) a 0.46×3.0 cm IAM.PC.DD column ($5\ \mu\text{m}$), (ii) a 0.46×3.0 cm 12-OH-silica column ($12\ \mu\text{m}$), and (iii) a 0.46×15 cm

(7) Ong, S. W.; Cai, S.-J.; Bernal, C.; Rhee, D.; Qiu, X.; Pidgeon, C. *Anal. Chem.* **1994**, *66*, 782–792.

(8) Rhee, D.; Markovich, R.; Chae, W. G.; Qiu, X.; Pidgeon, C. *Anal. Chim. Acta* **1994**, *297*, 377–386.

(9) Pidgeon, C.; Markovich, R. J.; Liu, M. D.; Helzer, T. J.; Novak, R. M. *J. Biol. Chem.* **1993**, *268*, 7773–7778.

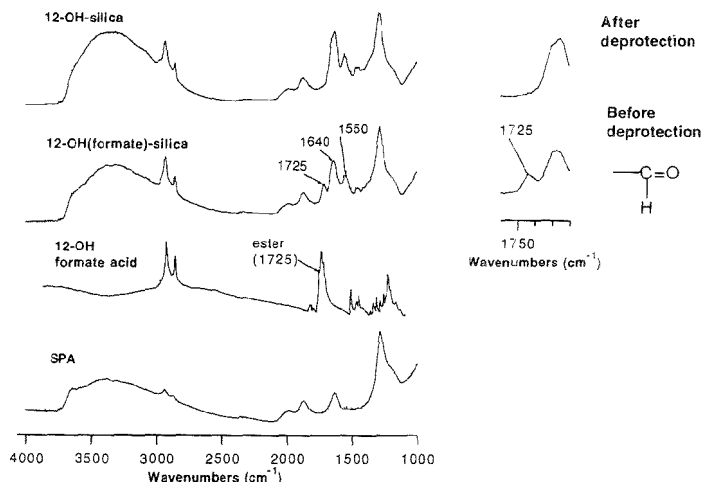


Figure 1. FT-IR spectra of SPA, 12-OH fatty acid formate ester, 12-OH(formate)-silica, and 12-OH-silica. The amide I band at 1640 cm^{-1} and the amide II band at 1550 cm^{-1} in the IR spectrum of 12-OH(formate)-silica indicate that the ligand (12-OH fatty acid formate ester) was covalently bonded to SPA. The characteristic absorptions of the formate group at 1725 cm^{-1} (C=O of ester) completely disappeared in the IR spectrum of 12-OH-silica. The insets below the spectra show the intensity of the ester carbonyl band at 1725 cm^{-1} before and after deprotection.

12-MO-silica column (12 μm). For all studies, the injection volume was $\sim 15 \mu\text{L}$ of an aqueous solution of the drug ($\sim 0.1 \mu\text{g}/\mu\text{L}$) dissolved in 0.01 M PBS buffered at pH 7.4 or the same buffer with pH adjusted to 5.4. The flow rate was 1 or 2 mL/min, and solute detection was at 220 nm. Chromatograms were obtained using a Rainin HPLC pumping system equipped with a Knauer Model 87 detector and interfaced with a Macintosh computer. Rainin Dynamax software was used to record the chromatograms on the computer.

The retention times (t_r) of solute molecules on IAM chromatography columns were used to calculate the solute capacity factors (k'_{IAM}) using eq 1, where t_r is the retention time (in

$$k' = (t_r - t_0)/t_0 \quad (1)$$

minutes) of the test compound and t_0 corresponds to the column dead time or void volume. In our laboratory, solute retention times exhibit a day-to-day variation of less than 4%. The capacity factor, k' , is linearly proportional to the equilibrium partition coefficient, K , of a solute that partitions between the stationary phase and the mobile phase,

$$k' = (V_s/V_m)K \quad (2)$$

where V_s is the total volume of solvent within the HPLC column and V_m is the volume of the IAM surface created by the immobilized ligands. The phase ratio V_s/V_m is constant for a given column. Furthermore, the membrane partitioning coefficient K_m is directly related to the drug permeability across the membrane by eq 3, where P_m is the permeability, D_m is the diffusion

$$P_m = D_m K_m / L \quad (3)$$

coefficient of the solute, and L is the thickness of the membrane.

D_m is related to the molecular size and to a first approximation is inversely proportional to molecular weight. Thus, drug retention behavior on columns can be used to test the capability of predicting drug-membrane permeability since the k' measured by chromatography is linearly related to K_m .^{1,2}

RESULTS AND DISCUSSION

All of the bonded phases used in this work, IAM.PC.DD, 12-OH-silica, and 12-MO-silica, contain a monolayer of immobilized lipid. IAM synthetic strategies are well established,^{7,8} and the synthesis of the IAM.PC.DD column is available.² The synthesis of 12-MO-silica shown in Scheme 1 was straightforward because protection/deprotection strategies were unnecessary. However, the synthesis of the 12-OH-silica surface was more difficult because the free surface hydroxy groups required protection before the immobilization step in the preparation of the surface. The free OH's were protected with a formate group. The characteristic IR band of formate at 1725 cm^{-1} (Figure 1) was used to monitor the integrity of the formate group during (i) immobilization of 12-OH fatty acid formate ester to SPA, (ii) endcapping with C3 anhydride, and (iii) deprotection with acid to generate free surface OH groups. Figure 1 is a typical set of IR spectra which demonstrate our method of monitoring the bonding and deprotection. The intensity of the formate IR band did not change after endcapping (not shown), indicating that the formate protecting group was stable to the endcapping reaction conditions. Acid deprotection of the formate groups generated surface OH groups. The IR band intensity of the formate groups decreased $\sim 90\%$ in the IR spectra after deprotection (Figure 1, compare upper two spectra), which indicates that the deprotection reaction was $>90\%$ efficient.

Figure 2 shows the correlations between drug partitioning into DMPC liposomes¹⁰⁻¹² and drug partitioning into the three bonded

(10) Betageri, G. V.; Rogers, J. A. *Int. J. Pharm.* 1987, 36, 165-173.

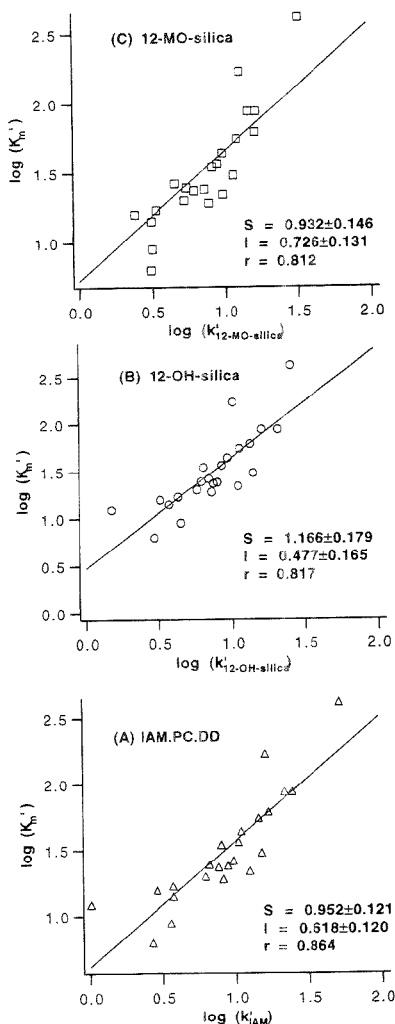


Figure 2. (A) Correlation of drug partitioning in IAM.PC.DD ($\log K_{IAM}$) and in liposome ($\log K_m$) for 23 drugs including seven β -blockers, six imidazoline derivatives, and 10 imidazolidine derivatives. The liposome partition coefficients of these 23 drugs were measured using DMPC liposomes in 0.01 M PBS buffer (pH 7.4).¹⁰⁻¹² IAM capacity factors, K_{IAM} , were measured on a 0.46×3.0 cm IAM.PC.DD column using a mobile phase of 0.01 M PBS (pH 7.4). The same correlation was done on a 0.46×3.0 cm 12-OH-silica column (B) and a 0.46×15 cm 12-MO-silica column (C).

phases: IAM.PC.DD, 12-OH-silica, and 12-MO-silica. The structures of the 23 solutes used for the partitioning studies are shown in Table 1. As shown in Figure 2, IAM.PC.DD columns predicted drug partitioning into DMPC liposomes ($r = 0.886$, Figure 2A) better than 12-OH-silica ($r = 0.812$, Figure 2B) and also better than 12-MO-silica ($r = 0.817$, Figure 2C). Similar results were

found for comparing the abilities of these bonded phases to predict intestinal transport in *in situ* tissue models. For instance, the correlation between solute intestinal absorption and solute partitioning using IAM.PC.DD ($r = 0.788$, Figure 3A) was better than the correlation using the 12-OH-silica column ($r = 0.590$, Figure 3B), the 12-MO-silica column ($r = 0.681$, Figure 3C), and the *n*-octanol/water partitioning system. Most importantly, solute partitioning into nonpolar octadecylsilica (ODS) did not correlate with solute intestinal absorption ($r = 0.10$).¹

The above results indicate that IAM.PC.DD better predicts solute-membrane interactions than 12-OH-silica and 12-MO-silica columns. This is because solute-IAM interactions involve not only hydrogen-bonding van der Waals interactions but also electrostatic interactions. Although 12-OH-silica and 12-MO-silica have hydrogen bond acceptors and donors, these surfaces cannot model electrostatic interactions common between molecules and membranes that occur during the partitioning process. IAM.PC.DD contains the zwitterionic PC headgroup and thus can model virtually all of the molecular interactions found in cell membranes during drug partitioning (Chart 3C). It was thus expected that the IAM.PC.DD phase would model the partitioning process because this phase contains the PC headgroup found in biological membranes. However, it was very surprising that 12-OH-silica and 12-MO-silica could model drug-membrane interactions better than ODS reversed phase columns. This suggests that polar groups on the chromatographic surface might be important for modeling the solute-membrane interaction for some compounds (Chart 3D).

12-OH-silica is effectively immobilized alcohol on silica surface, and a key question is whether drug partitioning into *n*-octanol/water systems correlates with drug partitioning into the 12-OH-silica bonded phase. Drug partitioning into 12-OH-silica is compared to drug partitioning into *n*-octanol/water systems¹⁰⁻¹² in Figure 4. Surprisingly, a poor correlation between drug partitioning into 12-OH-silica and drug partitioning into *n*-octanol/water was found for a total of 22 compounds studied ($r = 0.297$, Figure 4). Although it is known that in octanol/water systems, water-saturated *n*-octanol is tied up in a tetrahedral hydrogen-bonded complex (A,W) that retains a high degree of hydrophobicity because of the four eight-carbon nonpolar chains surrounding the polar water center,¹³ the *n*-octanol molecules in the water-saturated octanol phase are virtually randomly oriented (Chart 3A). In contrast, 12-OH-silica bonded phases have immobilized alcohol molecules arranged in a monolayer structure with OH groups protruding from the silica surface. It has been recognized that the ordered structure of the membrane bilayer is important in drug-membrane interactions. The 12-OH-silica surface is an ordered liquid containing a polar region and a nonpolar region (Chart 3B). Obviously, the physical-chemical properties of the immobilized alcohols on the 12-OH-silica surface should be different compared to the nonbonded randomly oriented octanol molecules in the *n*-octanol/water system. Therefore, drug-12-OH-silica interactions are not expected to be similar to the drug-octanol interactions in the octanol/water system, as shown in Figure 4.

(13) Hansch, C.; Muri, R. M.; Fujita, T.; Maloney, P. P.; Geiger, F.; Streich, M. *J. Am. Chem. Soc.* **1963**, *85*, 2817-2824.

(14) De Young, L.; Dill, K. A. *Biochemistry* **1988**, *27*, 5281-5289.

(15) Schanker, L. S.; Tocco, D. J.; Brodic, E. B.; Hogben, C. A. M. *Pharmacol. Exp. Ther.* **1958**, *123*, 81-88.

(16) Leo, A.; Hansch, C.; Elkins, D. *Chem. Rev.* **1971**, *71*, 523-612.

(11) Betageri, G. V.; Rogers, J. A. *Pharm. Res.* **1993**, *10*, 913-917.

(12) Choi, Y. W.; Rogers, J. A. *Pharm. Res.* **1990**, *7*, 508-512.

Table 1. Structures of Drugs Used To Compare Drug Partitioning into DMPC Liposomes with Drug Partitioning into Bonded Phases

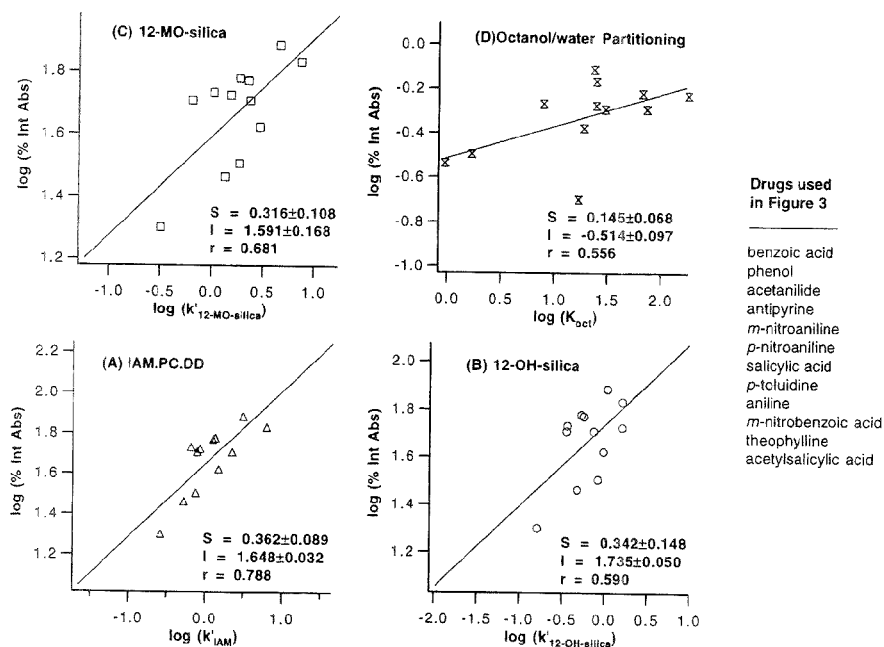
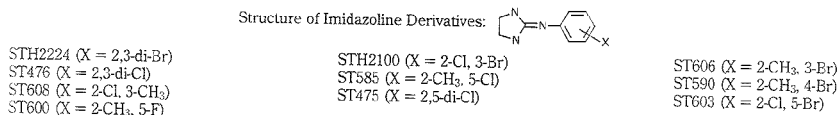
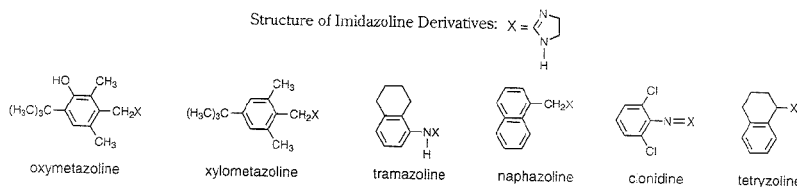
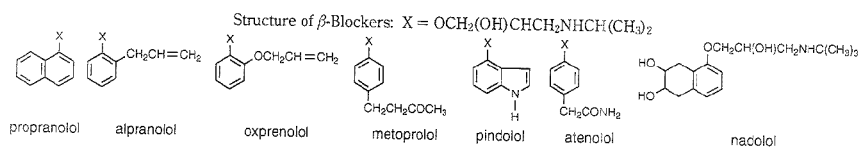
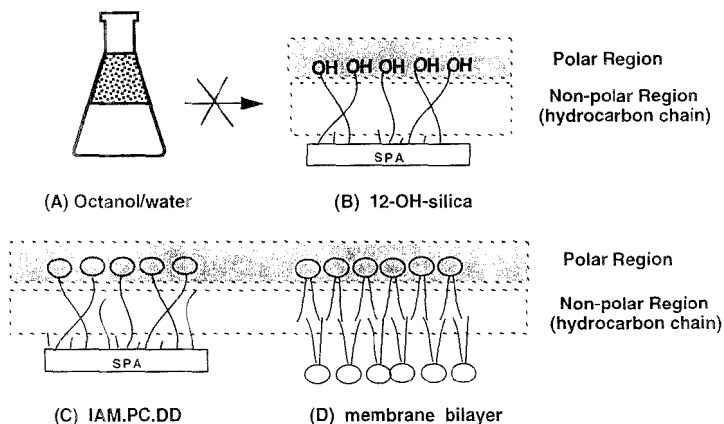


Figure 3. Correlation of rat intestinal drug absorption with drug partitioning into an IAM.PC.DD ($\log K'_{IAM}$) column (A), a 12-OH-silica ($\log K'_{12\text{-OH-silica}}$) column (B), a 12-MO-silica ($\log K'_{12\text{-MO-silica}}$) column (C), and the *n*-octanol/water system (D). The intestinal absorption of the drugs from rat small intestine was measured by Schanker et al.,¹⁵ and the effective pH at the surface of the intestinal epithelial is about 5.4. The partitioning coefficients of these compounds in *n*-octanol/water system were measured using distilled water and *n*-octanol suspensions.¹⁶ IAM capacity factors, K'_{IAM} , were measured on a 0.46×3.0 cm IAM.PC.DD column. $K'_{12\text{-OH-silica}}$ values were measured on a 0.46×3.0 cm 12-OH-silica column, and $K'_{12\text{-MO-silica}}$ values were measured on a 0.46×15 cm 12-MO-silica column. The mobile phase of 0.01 M PBS (pH 5.4) was used in the all of capacity factor measurements.

Chart 3^a



^a The solvent structure of octanol in the octanol/water partitioning system (A) is fundamentally different compared to the monolayer structure of 12-OH-silica (B). The interfacial polarity of 12-OH-silica is similar to that of IAM.PC.DD (C) and the membrane bilayer (D).

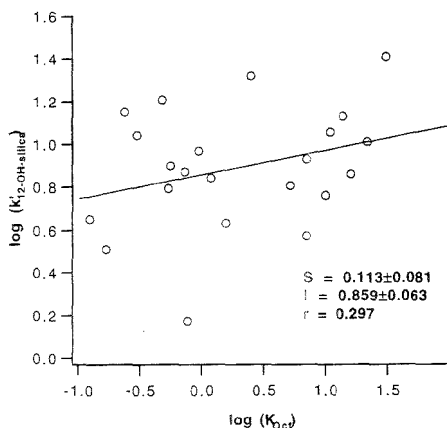


Figure 4. Comparison of drug partitioning in 12-OH-silica ($\log K_{12\text{-OH-silica}}$) and in the *n*-octanol/buffer phase for 22 drugs including six β -blockers, six imidazole derivatives, and 10 imidazolidine derivatives. 12-OH-silica capacity factors, $K_{12\text{-OH-silica}}$, were measured on a 0.46×3.0 cm 12-OH-silica column using a mobile phase of 0.01 M PBS (pH 7.4). The *n*-octanol/buffer partition coefficients of these drugs were measured elsewhere¹⁰⁻¹² using a 0.01 M PBS (pH 7.4) buffer.

We have previously postulated that drug-membrane interactions on IAM surfaces are a bulk phase property of the immobilized lipids. In other words, individual functional groups of the immobilized lipids are not critical for the membrane-drug interaction. This was based on the observation that IAM drug-membrane interactions did not depend on interfacial ester vs ethers, the number of fatty acid chains, etc. The molecule-membrane interaction was thus proposed to be a property of the structure of the interface. The importance of the bulk interfacial properties of the IAM surface in monitoring solute-membrane interaction was also demonstrated in this report. Thus the 12-OH-silica and the 12-MO-silica have polar interfacial properties and a ~ 15 Å hydrocarbon environment for the partitioning

process, and both of these surfaces were able to model to some degree of success the partitioning process.

Critical experimental data supporting the importance of the polar interfacial region in membrane-solute interaction is found by comparing the data obtained with use of the *n*-octanol/water system to those from the 12-OH-silica system (Figure 4). The partitioning in the octanol/water system of the 22 drugs does not correlate with the partitioning into 12-OH-silica ($r = 0.297$). Similarly, drug partitioning into the octanol/water system does not correlate with drug partitioning into DMPC liposomes for the 23 drugs shown in Table 1 ($r = 0.483$).² However, drug partitioning into the immobilized alcohol phase gives a good prediction ($r = 0.812$). The fact that immobilized alcohol can mimic partially the solute-membrane interaction but nonimmobilized octanol cannot (i.e., *n*-octanol/water partitioning) strongly supports the idea that the interface created by the lipid molecules, not the individual lipid molecules themselves, controls the solute-membrane interactions.

CONCLUSION

In conclusion, an ordered monolayer of immobilized lipids containing both a polar and a nonpolar region is critical for a chromatographic surface to accurately monitor the interaction between solutes and biological membranes. Differences in the interfacial polar functional groups do not eliminate the ability of the surface to predict drug-membrane interactions, i.e., surface PC headgroups, surface OH groups, and surface OCH_3 groups all provide the interfacial properties necessary to predict drug-membrane interactions better than reversed phase C18 surfaces. However, when the interfacial polar region is comprised of the phospholipid headgroup found in biological membranes (i.e., not monolayers of OH groups or OCH_3 groups), further improved capabilities of predicting solute-membrane interactions are found for that surface. Thus IAM.PC.DD was a better *in vitro* screen for predicting drug-membrane interactions than 12-OH-silica or 12-MO-silica column.

ACKNOWLEDGMENT

We are very grateful for the support from Eli Lilly and Co. This work was also supported by NSF (CTS 9214794), NIH (AI33031), and Regis Technologies Inc. (2R446M3022-02). We are also very grateful for the gifts of the imidazolidine derivatives (ST drugs) from Boehringer-Ingelheim Co.

Received for review March 16, 1995. Accepted June 24, 1995.*

AC950267U

* Abstract published in *Advance ACS Abstracts*, August 1, 1995.

Simultaneous Determination of Total and Free Metal Ion Concentration in Solution by Sorption on Iminodiacetate Resin

Maria Pesavento* and Raffaella Biesuz

Dipartimento di Chimica Generale, Università di Pavia, Viale Taramelli, 12-27100 Pavia, Italy

A method for determining the total concentration of a metal ion originally present in a solution (c_{tot}) and the ratio of total to free metal ion (Z_M) is proposed. It consists of putting different aliquots of the sample (V) in contact with the resin (w) in batch, by keeping the acidity constant, and determining the concentration of the sorbed metal ion c . Then $1/c$ is plotted against V/w , and c_{tot} and Z_M are calculated from the straight line obtained. The chemical model that allows evaluation of the ratio of total to free metal ion is illustrated and discussed. Some synthetic systems are examined to demonstrate the validity of the procedure.

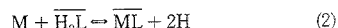
The iminodiacetate resins, for example, the commercially available Chelex 100, are widely used for separation and preconcentration purposes, and after the pioneering work of Riley and Taylor,¹ a large number of papers have been published on the subject.^{2–6} However, only recently have the distribution equilibria of metal ions on Chelex 100 been investigated in detail.⁷ It has been found that, for a number of metal ions at trace level, three kinds of complexes are formed in the resin, i.e., ML , ML_2 , and $M(HL)_2$, depending mainly on the acidity of the solution. Thus the fraction of sorbed metal ion f is given by the following relation:

$$f = \frac{[\overline{ML}]w + [\overline{ML}_2]w + [\overline{M(HL)_2}]w}{[M]VZ_M + [\overline{ML}]w + [\overline{ML}_2]w + [\overline{M(HL)_2}]w}$$

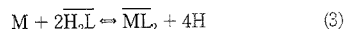
$$= 1 / \left(1 + \frac{Z_M}{\frac{\beta_{10\text{exM}} [\overline{H_2L}]w}{[H]^2V} + \frac{\beta_{20\text{exM}} [\overline{H_2L}]^2w}{[H]^4V} + \frac{\beta_{22\text{exM}} [\overline{H_2L}]^2w}{[H]^2V}} \right) \quad (1)$$

where the species with the overbars are those in the resin phase, w indicates the grams of water in the resin, and V indicates the grams of water in the solution phase. The concentrations are in moles per kilogram of solvent in both phases, and $\beta_{10\text{exM}}$, $\beta_{20\text{exM}}$, and $\beta_{22\text{exM}}$ are the exchange coefficients pertinent to the three possible reactions:

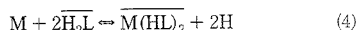
- (1) Riley, J. P.; Taylor, D. *Anal. Chim. Acta* **1968**, *40*, 479–485.
- (2) Florence, T. M.; Batley, G. E. *Talanta* **1976**, *23*, 179–186.
- (3) Figura, P.; McDuffie, B. *Anal. Chem.* **1979**, *51*, 120–125.
- (4) Boniforti, R.; Ferraroli, R.; Frigieri, P.; Hellai, D.; Queirazza, G. *Anal. Chim. Acta* **1984**, *162*, 33–46.
- (5) Pai, S. U.; Whung, P. Y.; Lai, R. L. *Anal. Chim. Acta* **1988**, *211*, 257–270.
- (6) Vermeiren, K.; Vandecasteele, C.; Dams, R. *Analyst* **1990**, *115*, 17–22.
- (7) Pesavento, M.; Biesuz, R.; Gallorini, M.; Profumo, A. *Anal. Chem.* **1993**, *65*, 2522–2527.



$$\beta_{10\text{exM}} = \frac{[\overline{ML}][H]^2}{[M][\overline{H_2L}]}$$



$$\beta_{20\text{exM}} = \frac{[\overline{ML}_2][H]^4}{[M][\overline{H_2L}]^2}$$



$$\beta_{22\text{exM}} = \frac{[\overline{M(HL)_2}][H]^2}{[M][\overline{H_2L}]_2}$$

It has also been shown⁷ that the exchange coefficients are related to the intrinsic complexation constant of the active group in the resin, β_{npiM} , by the relationship obtained from the Gibbs–Donnan model

$$\beta_{npi\text{exM}} = \beta_{npiM} (\gamma_M \gamma_{HL}^n \{C\}^{(m-s)} / \gamma_{MH} \gamma_{H_2L}^n \gamma_H^s \{C\}^{(m-s)}) \quad (5)$$

where n is the number of ligand molecules (L), p the number of protons per mole of complex, s the number of protons exchanged, and m the charge of the metal ion. γ indicates the activity coefficient of the species, and $\{C\}$ the activity of the counterion. As expected on the basis of the Gibbs–Donnan model of the resin,⁸ the intrinsic complexation constants have values very near to the complexation constants of the metal ions with soluble substances bearing a chelating group similar to that present in Chelex 100. Z_M is the fraction of the total to free metal ion in the solution phase, which can be estimated only if the composition of the sample solution is completely known. In this case, eq 1 allows one to predict the amount of metal ion sorbed on a resin by a batch procedure under given conditions. However, the main problem when dealing with real samples is that their composition is often unknown. For example, in seawater strong ligands of unknown nature and concentration are present.^{9–11} The aim of the present paper is to show that eq 1 can be used for determining the total and free metal ion concentration in aqueous solution of unknown composition, by considering in particular the case of seawater. When a metal ion is separated from a real sample solution by sorption on a chelating resin by a batch procedure, the quantity experimentally accessible is the concentration of sorbed metal ion (c), not the total concentration c_{tot} , even if they can coincide.

- (8) Marinsky, J. A.; Miyajima, T.; Hogfeldt, E.; Muhammed, M. *React. Polym.* **1989**, *11*, 279–289.
- (9) Johnson, K. S.; Coale, K. H.; Jannash, H. W. *Anal. Chem.* **1992**, *64*, 1065A–1075A.
- (10) Midorikawa, T.; Tanoue, E. *Anal. Chim. Acta* **1994**, *284*, 605–619.
- (11) Mackey, D. J.; Zirino, A. *Anal. Chim. Acta* **1994**, *284*, 635–647.

Remembering that f is the fraction of sorbed to total metal ion, i.e., $f = c/c_{\text{tot}}$, only the two quantities c_{tot} and Z_M in eq 1 are unknown, when it is used for samples of unknown composition.

For better evidence, eq 1 can be rewritten as

$$1/c = 1/c_{\text{tot}} + Z_M V / (w c_{\text{tot}} K^*) \quad (6)$$

where, in the case of Chelex 100

$$K^* = \beta_{10\text{exM}} [\overline{\text{H}_2\text{L}}] / [\text{H}]^2 + \beta_{20\text{exM}} [\overline{\text{H}_2\text{L}}]^2 / [\text{H}]^4 + \beta_{22\text{exM}} [\overline{\text{H}_2\text{L}}]^2 / [\text{H}]^2 \quad (7)$$

K^* depends only on the metal ion considered, on the nature of the resin, on the concentration of free active groups in the resin, and on the acidity of the solution. Thus, it is constant at constant pH and $[\text{H}_2\text{L}]$, as is the case when a large excess of resin is used for sorption. K^* can be evaluated if the exchange coefficients and the concentration of biprotonated free active groups are known.

Z_M is constant at fixed pH when it is equal to 1 (not any complex formed in solution) or when the concentration of the ligand in solution is constant, for instance, when it is buffered or when it is present in large excess with respect to the metal ion. In this case, the plot of $1/c$ against V/w is a straight line, from which c_{tot} and Z_M can be evaluated. This procedure can be considered as a titration of the unknown solution with the chelating resin, from which c_{tot} is always evaluable. Z_M can be obtained only if K^* is correctly evaluated, i.e., if the sorption equilibria of the considered metal ion are completely known, as is often the case for Chelex 100. The feasibility and the accuracy of this procedure will be illustrated in the present work with some examples concerning the determination of total and free bivalent heavy metal ions in a solution of known composition.

EXPERIMENTAL SECTION

Reagents. All chemicals were of analytical reagent grade. Chelex 100 (Bio-Rad Laboratories, Richmond, CA), with a particle size of 100–200 mesh was delivered in sodium form. It was converted to the H^+ form, which is believed to have the lowest "blank" values.¹² The resin in the acidic form was air-dried as previously described.⁷ Known amounts were sealed in tubes, and their water content was determined by drying a known amount in an oven at 80 °C to constant weight. The capacity (millimoles of active groups per gram of dry resin, Q) of Chelex 100 was determined as described elsewhere,⁷ and it was found to be 1.6 mmol/g of dry resin in the H^+ form.

The ionic medium simulating the ionic composition of seawater was prepared at the following concentrations: NaCl 0.471 mol kg^{-1} , $\text{MgCl}_2 \cdot 6\text{H}_2\text{O}$ 0.0539 mol kg^{-1} , and CaSO_4 0.010 mol kg^{-1} . Carbonate was not added.

The selected aqueous soluble complexing agent was iminodiacetic acid (IDA, disodium salt, Sigma). It was added directly into the titration vessel in a calculated amount of concentrated solution.

Apparatus. A PHM 84 Research pH meter, Radiometer Copenhagen, and a combined Orion glass electrode (9102 SC) were used. The potentiometric cell for the determination of the

pH values was standardized in H^+ concentration by a previously described procedure.¹³ A small N_2 overpressure was applied in the vessel which was thermostated at 25 ± 0.3 °C.

A Perkin-Elmer 1100 B flame AAS was used for metal ion determinations. Analysis were carried out under standard conditions of flame AAS determinations.

Determination of the Concentration of Sorbed Metal Ions

c. A known volume of aqueous solution (25–800 mL) with a certain ionic composition and containing a known amount of metal ion was equilibrated with a known amount of Chelex 100 (0.10–1.0 g of dry resin). The amount of resin was selected to always have a large excess of active groups compared to the amount of heavy metal ion. The pH was adjusted by adding small amounts of acid or base. After equilibration (usually 3–4 h), the pH of the aqueous solution was measured potentiometrically with a glass electrode standardized in H^+ concentration, and a small amount (50–100 μL) was diluted to 5 mL with 0.1 mol kg^{-1} HNO_3 and analyzed. The amount of metal sorbed on the resin was calculated by difference. Otherwise the resin was separated by filtration on porous glass, and the sorbed metal ion was eluted with 10 mL of 0.1 mol kg^{-1} HNO_3 and determined in this solution by flame AAS.

Procedure for the Determination of c_{tot} and Z_M . According to eq 6, the ratio V/w was changed by keeping constant the acidity of the solution, and c was determined by the procedure reported above. Practical values of V/w range from around 30 to 4000. For instance, using a fixed amount of 1 g of dry resin, different volumes of aqueous solution from 100 to 800 mL are stirred with the resin for 3 h or until the equilibrium is believed to be reached. Higher volumes are difficult to handle by using a batch procedure. At least four samples with different V/w must be treated in order to obtain a meaningful regression line when plotting $1/c$ vs V/w . c_{tot} is obtained from the first parameter of the regression line, and Z_M/K^* from the second. Z_M is then calculated if K^* is known or can be evaluated. An important point is that the pH of the solution must be kept constant. In the present investigation, Chelex 100 in the H^+ form was used, so that the acidity of the solution increased because of the ion exchange. During the equilibration, the pH was controlled with the glass electrode and adjusted to the original value by small additions of acid or base. However, for some applications it is desirable to keep the pH of the solution constant without any adjustment. Here Chelex 100 must be used in a form which does not change the acidity of the solution. For instance, when considering seawater, the resin should bear as counterion calcium or magnesium (resin in seawater form), or ammonium, which is probably less contaminated by heavy metal ions.^{4,12}

Evaluation of K^* . The following quantities must be known when eq 7 is to be used for the evaluation of K^* : (1) the acidity of the aqueous solution, which is measured with the glass electrode standardized in H^+ concentration;¹³ (2) the exchange coefficients of the considered metal ion, β_{specM} , which can be either known from previous investigations or evaluated by eq 5 from the complexation constants of similar systems in aqueous solution; (3) the concentration of the free active group $\overline{\text{H}_2\text{L}}$ in the resin.

In the presence of trace amounts of metal ions, $[\overline{\text{H}_2\text{L}}]$ depends only on the acidity of the solution,⁷ being $[\overline{\text{H}_2\text{L}}] = c_1 / Z_{\overline{\text{H}_2\text{L}}}$, where c_1 is the concentration of the free active groups inside the resin (in mol kg^{-1}) and $Z_{\overline{\text{H}_2\text{L}}}$ indicates the ratio of the

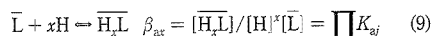
(12) Baffi, F.; Cardinale, A. M.; Bruzzone, R. *Anal. Chim. Acta* 1992, 270, 79–86.

(13) Pesavento, M.; Profumo, A.; Biesini, R.; Höglfeldt, E. *Ann. Chim. (Rome)* 1990, 80, 265–270.

concentration of the total free active group inside the resin to that of the biprotonated form $[\overline{H}_2L]$:

$$Z_{\overline{H}_2L} = \sum \beta_{ax} [H]^x / \beta_{a2} [H]^2 \quad (8)$$

The summation is extended from $x = 0$ to $x = 3$, the maximum number of protons linked to the iminodiacetic active group. β_{ax} are the global x -protonation coefficients of the group inside the resin ($\beta_{a0} = 1$), pertinent to the following equilibria:



The product \prod is extended from $j = 1$ to $j = x$, and K_{aj} are the protonation coefficients referred to each protonation step:

$$K_{aj} = [\overline{H}_jL] / [\overline{H}_{(j-1)}L] [H] \quad (10)$$

According to the Gibbs–Donnan model of the resin the protonation coefficients are related to the intrinsic protonation constants by⁷

$$K_{aj} = K_{aj}^0 \{ \overline{C} \}^j \gamma_{\overline{H}_{(j-1)}L} / \{ C \} \gamma_{\overline{H}_jL} \quad (11)$$

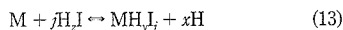
Equation 11 shows that the protonation coefficients usually change with the composition of the resin and the acidity and the composition of the aqueous solution, and they must be evaluated at each condition.

When in the presence of high amounts of metal ions, which can be sorbed by complexation to the active groups, as calcium and magnesium in seawater, the concentration of free ligand inside the resin is much lower. The mass equilibrium of the ligand in the resin phase is

$$\begin{aligned} c_L = & [\overline{H}_2L] Z_{\overline{H}_2L} + 2[\overline{Ca(HL)_2}] + 2[\overline{CaL}_2] + [\overline{CaL}] + \\ & 2[\overline{Mg(HL)_2}] + 2[\overline{MgL}_2] + [\overline{MgL}] = [\overline{H}_2L] Z_{\overline{H}_2L} + \\ & 2\beta_{22exCa} c_{Ca} [\overline{H}_2L]^2 / [H]^2 Z_{Ca} + 2\beta_{20exCa} c_{Ca} [\overline{H}_2L]^2 / [H]^4 Z_{Ca} + \\ & \beta_{10exCa} c_{Ca} [\overline{H}_2L] / [H]^2 Z_{Ca} + 2\beta_{22exMg} c_{Mg} [\overline{H}_2L]^2 / [H]^2 Z_{Mg} + \\ & 2\beta_{20exMg} c_{Mg} [\overline{H}_2L]^2 / [H]^4 Z_{Mg} + \beta_{10exMg} c_{Mg} [\overline{H}_2L] / [H]^2 Z_{Mg} \end{aligned} \quad (12)$$

$[\overline{H}_2L]$ can be evaluated from this second-order equation, where c_{Ca} and c_{Mg} indicate the concentration of calcium and magnesium in solution. This can be considered as the total concentration if a sufficiently low amount of resin is used. Here too, $Z_{\overline{H}_2L}$ is evaluated according to eq 8.

Evaluation of the Fraction of Total to Free Metal Ion in Aqueous Solution Z_M . Suppose that a substance I is present in solution, which is able to complex the metal ion of interest M, according to the equilibrium



$$K_{jM,I} = [MH_jI] [H]^x / [M] [HI]^j$$

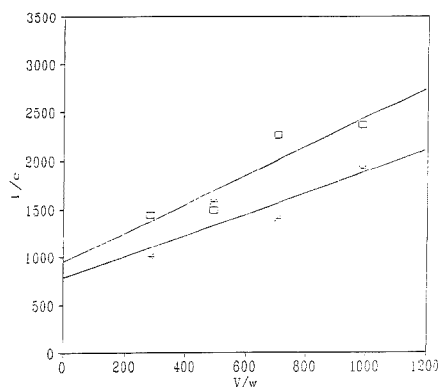


Figure 1. Sorption of cadmium(II) from 0.1 mol kg⁻¹ NaNO₃ on Chelex 100: determination of the total concentration and the fraction of total to free metal ion according to eq 6. Chelex 100, 0.071 g; total concentration of cadmium(II), 1.11 × 10⁻³ mol kg⁻¹; (*) pH 3.4, regression line 1/c = 790(222) + 1.11(0.42)V/w, R² = 0.773; (□) pH 3.1, regression line 1/c = 966(236) + 1.50(0.45)V/w, R² = 0.845; standard error of the parameter in parentheses.

The fraction of total to free metal ion Z_M is

$$Z_M = \sum [MH_nI] / [M] = \sum K_{pM,I} [HI]^p / [H]^p \quad (14)$$

where the summation is extended from $n = 0$ to $n = P$, the maximum number of ligand moles in the complex, and $K_{pM,I}$ is the formation constant of the complex MH_nI ($K_{0M,I}$ is equal to 1). For instance, in seawater one of the most important complexing substances, because of its high concentration, is chloride. Cadmium, copper, and manganese are linked by chloride, and Z_M can be calculated from the complexation constants reported in the literature.

RESULTS AND DISCUSSION

The use of eq 6 is illustrated by the two examples reported in Figures 1 and 2. The first one refers to the sorption of cadmium(II) from a 0.1 mol kg⁻¹ sodium nitrate solution not containing any ligand, but at acidities for which the sorption is not quantitative, as can be deduced by calculating f at the considered conditions from eq 1. Cadmium(II) is present in solution only as an aquo ion ($Z_M = 1$). Its exchange coefficients are known from previous investigations^{7,14,15} and are reported in Table 1.

The second example is the sorption of copper(II) from a 0.1 mol kg⁻¹ sodium nitrate solution containing a chelating agent of copper(II), the iminodiacetic acid (IDA), in large excess with respect to the metal ion. In this case too, the exchange coefficients are known^{7,15} and they are reported in Table 1. In this example, copper(II) is present in aqueous solution mainly as the complex with IDA, so that Z_M is much higher than 1. Its values can be estimated making use of eq 14 with the stability constants

(14) Pesavento, M.; Biesuz, R.; Cortina, J. L. *Anal. Chim. Acta* 1994, 298, 225–232.

(15) Pesavento, M.; Biesuz, R. *XI Congresso Nazionale di Chimica Analitica*. Cagliari, Italy, 12–16 September 1994; p 318.

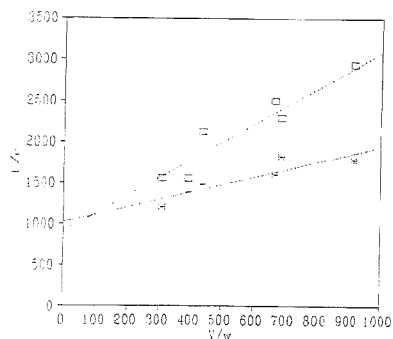


Figure 2. Sorption of copper(II) from 0.1 mol kg⁻¹ NaNO₃ on Chelex 100, in the presence of 0.0515 mol kg⁻¹ IDA: determination of the total concentration and the fraction of total to free metal ion according to eq 6. Total concentration of copper(II); 1.11 × 10⁻³ mol kg⁻¹; (*) pH 3.9, regression line 1/c = 1010(112) + 0.95(0.22)V/w, r² = 0.823; (□) pH 2.9, regression line 1/c = 870(189) + 2.28(0.37)V/w, r² = 0.904; standard error of the parameter in parentheses.

Table 1. Protonation Coefficients of Chelex 100 and Extraction Coefficients of Some Divalent Metal Ions on Chelex 100

metal	log β _{1MxM}		log β _{2MxM}		log β _{2ZxM}	
	exp	est ^a	exp ^b	est ^b	exp	est ^c
Cu(II)	-0.75 ^a	-0.68	-6.7 (in 0.1 M nitrate)	-5.61		-2.37
Cd(II)		-5.00	-11.7 (in sw)	-11.02	-3.47 ^e	-3.50
Mn(II)		-6.37	-14.5 (in sw)	-14.0	-4.2 ^e	-3.94
Mg(II)		-8.33			-4.94 ^e	
Ca(II)		-8.02			-5.08 ^e	-5.39 ^e
H	log K ₀₁ = 9.12 ^f		log K ₀₂ = 3.2 ^f			

^a Values estimated from the complexation constants of the 1:1 complexes with methyliminodiacetic acid (MIDA) in aqueous solution.¹⁶ ^b Values estimated for aqueous solutions containing 1 mol kg⁻¹ counterion from the 1:2 complex with MIDA.¹⁶ ^c Values estimated from the complex formation constants of the 1:2 complex metal/acetate,¹⁷ as described in refs 7 and 14. ^d Values previously obtained.⁷ ^e From data reported in ref 5. ^f Values previously reported by Szabadka.¹⁸ ^g Value obtained previously, recalculated for a 1 mol kg⁻¹ counterion solution.¹⁵

found in the literature¹⁹ and are shown in Table 2. In Figures 1 and 2, the function 1/c vs V/w is reported according to eq 6. As expected, straight lines are obtained in both cases, from which c₀₁ and Z_M are evaluated. The statistical characteristics of the regression lines are reported in the captions of the figures. Table 2 shows the results obtained. The values of c₀₁ calculated from the intercepts are in good agreement with the concentration originally present. Also Z_M can be evaluated from the slope of the straight lines, since K* is a quantity that depends only on the particular combination resin-metal ion considered and can be calculated independently. The values of K* pertinent to the conditions considered in the experiments are given in Table 2,

last column. The evaluation of K* was done by assuming that in 0.1 mol kg⁻¹ NaNO₃ and at pH lower than 3 log K₀₂ = 3.2,⁷ since other counterions are sorbed on the resin only by diffusion when the active groups are completely protonated, so that {Na} = {Na}. Thus, according to eq 1, the protonation coefficient is independent of the concentration of the counterion in solution. On the contrary, at pH higher than 3.9 sodium penetrates into the resin to neutralize the deprotonated active groups, and its concentration in the resin is mainly determined by the deprotonation degree, its activity being around unity.⁷ As a consequence, the protonation coefficient strongly depends on the concentration of the counterion in solution. The value of log K₀₂ = 3.9 was previously found⁷ for a 0.1 mol kg⁻¹ sodium nitrate solution. The values of Z_M obtained experimentally are compared with those expected in Table 2, showing an acceptable agreement, at least as a magnitude order.

Two examples regarding the sorption on Chelex 100 of manganese(II) and cadmium(II) from a simulated seawater are reported in Table 3. The regression lines obtained by plotting 1/c vs V/w are given in Table 3, while the values of c₀₁ and Z_M are reported in Table 2. In the case of manganese(II), where no chelating agent was present in the aqueous phase, values of Z_M very near to 1, as expected, are obtained. In the example here discussed, where the sorption is from a simulated seawater, the counterions inside the resin are mainly calcium and magnesium. Indeed, these two metal ions are present in the simulated seawater sample in large excess with respect to the active groups in the resin and are sorbed by the iminodiacetate resins at pH higher than about 3, by formation of undissociated complexes.^{5,7} The value of K* in Table 2 was calculated by taking into account this point, according to eq 12. The exchange coefficients of calcium and magnesium on Chelex 100 must be known. That of calcium has been determined previously⁷ and that of magnesium was evaluated from the data of Pai⁵ obtaining the value reported in Table 1. As expected, it is very similar to that of calcium. Also, the concentration of calcium and magnesium remaining in solution must be evaluated. However, in the experiments reported in Table 3, the concentration of calcium and magnesium in solution was practically unaffected by the presence of the resin, since the total amount of active groups in the resin was lower than that of the alkaline earth metal ions in solution.

As no complexing agents for calcium and magnesium are present in the simulated seawater at the considered pH, Z_{Ca} and Z_{Mg} are both equal to 1. The second protonation coefficient of the iminodiacetic group inside the resin must be known for evaluating Z_{H2L}. As discussed above, in the simulated seawater at pH higher than 3, practically all the active groups of the resin are combined with Ca²⁺ and Mg²⁺ and some uncomplexed counterion is present only because of the diffusion from the external solution. It is reasonable to assume that {C} = {C̄}, so that the protonation coefficients are independent of the counterion concentration, as seen from eq 11. Thus, it can be reasonably assumed that log K₀₂ = 3.2. For the same reason, the amount of water in the resin is constant and is very similar to that of the completely protonated resin (0.5 g of water/g of dry resin in the case of Chelex 100).⁷ Here the total concentration of active groups inside the resin is c₁ = Q/0.5, where Q = 1.6 mequiv/g is the capacity of Chelex 100.

The example concerning the sorption of cadmium(II) from a simulated seawater sample shows the effect of the presence of

(16) Schwarzenbach, G.; Anderegg, G.; Schneider, W.; Senn, H. *Helv. Chim. Acta* 1955, 38, 1147-1151.

(17) Archer, D. W.; Morik, C. B. *J. Chem. Soc.* 1964, 3117-3121.

(18) Szabadka, O.; Inczedy, J. *J. Chromatogr.* 1980, 201, 59-66.

(19) Anderegg, G. *Helv. Chim. Acta* 1964, 47, 1801-1809.

Table 2. Results Obtained from the Experiments of Figures 1 and 2, and of Table 3: Concentration of Total Metal Ion (c_{tot}) and Ratio of Total to Free Metal Ion (Z_M) in Aqueous Solution

	c_{tot} (exp value and diff from the expected)	Z_M exp value	eval by eq 14	K^* (eval by eq 7)
Cd(II) from NaNO ₃ 0.1 mol kg ⁻¹ , pH 3.1	1.03×10^{-3} (-7.20%)	0.68	1.00	4.43×10^2 (log $K_{\text{Cd}} = 3.2$) ^c
Cd(II) from NaNO ₃ 0.1 mol kg ⁻¹ , pH 3.4	1.26×10^{-3} (+13.5%)	2.82	1.00	8.73×10^2 (log $K_{\text{Cd}} = 3.2$) ^c
Cu(II) from NaNO ₃ 0.1 mol kg ⁻¹ , IDA 0.0515 mol kg ⁻¹ , pH 2.9	1.15×10^{-3} (+3.6%)	3.24×10^2	5.44×10^{2c}	1.24×10^3 (log $K_{\text{Cu}} = 3.2$) ^c
Cu(II) from NaNO ₃ 0.1 mol kg ⁻¹ , IDA 0.0515 mol kg ⁻¹ , pH 3.9	9.90×10^{-4} (-10.8%)	1.55×10^4	9.07×10^{3c}	1.65×10^7 (log $K_{\text{Cu}} = 3.9$) ^c
Mn(II) from simulated seawater, pH 3.55	1.98×10^{-3} (+1.0%)	1.33	1.00	5.20×10^1 (log $K_{\text{Mn}} = 3.2$) ^b
Mn(II) from simulated seawater, pH 4.32	2.12×10^{-3} (+6.0%)	0.95	1.00	7.19×10^1 (log $K_{\text{Mn}} = 3.2$) ^b
Mn(II) from simulated seawater, pH 4.83	2.14×10^{-3} (+7.0%)	0.81	1.00	1.04×10^2 (log $K_{\text{Mn}} = 3.2$) ^b
Cd(II) from simulated seawater, IDA 0.050 mol kg ⁻¹ , pH 5.45	1.75×10^{-4} (-2.8%)	21.5	17.7 ^e	6.91×10^4 (log $K_{\text{Cd}} = 3.2$) ^b

^a See ref 7. ^b The resin is in the seawater from (alkaline earth metal ions as counterions). ^c Formation constants of the complex M-IDA from ref 17.

Table 3. Determination of the Concentration of Total Metal Ion (c_{tot}) and Ratio of Total to Free Metal Ion (Z_M) in Simulated Seawater^a

composition of soln	regression line: $1/c$ vs V/w
Mn(II) in simulated seawater pH 3.55	$1/c = 503(35) + 12.9(0.9)V/w$ $r^2 = 0.990$
Mn(II) in simulated seawater pH 4.32	$1/c = 469(31) + 6.2(0.8)V/w$ $r^2 = 0.966$
Mn(II) in simulated seawater pH 4.83	$1/c = 467(14) + 3.6(0.4)V/w$ $r^2 = 0.978$
Cd(II) in simulated seawater IDA 0.05 mol kg ⁻¹ , pH 5.45	$1/c = 5719(153) + 1.79(0.06)V/w$ $r^2 = 0.996$

^a Regression lines $1/c$ vs V/w for the sorption of manganese(II) and cadmium(II) on Chelex 100 (standard error of the parameters in parenthesis). Range of V/w , 25–80 for manganese(II) and 500–3000 for cadmium(II).

an excess of IDA at pH 5.45. This acidity was selected to avoid hydrolysis. Again a straight line was obtained by plotting $1/c$ vs V/w , whose characteristics are reported in Table 3. The total concentration was found to be 1.75×10^{-4} mol kg⁻¹, in acceptable agreement with that originally present in the considered sample. Z_M was obtained from the slope of the experimental straight line, using the value of K^* reported for cadmium(II) in Table 2. It is in acceptable agreement with that evaluated by considering that cadmium(II) is complexed both by IDA ($Z_{\text{Cd,IDA}} = 5.2$) and by chloride ($Z_{\text{Cd,Cl}} = 12.5$). The presence of a high chloride concentration in seawater is of particular relevance in the case of cadmium, which is more strongly complexed (log $K_{10\text{Cd,Cl}} = 0.74$,²⁰ log $K_{10\text{Mn,Cl}} = 0.04$,²¹ log $K_{10\text{Cu,Cl}} = 1.30$ ²¹). The examples reported above show that the total concentration of the metal ion can be determined by the proposed procedure with good accuracy, independent of its value. As far as the evaluation of Z_M is concerned, the proposed treatment is of utility only when eq 1 holds, i.e., if the sorption of the considered metal ion takes place according to the model found in diluted solutions. This has been found to be true also in the case of complicated matrices such as seawater.¹³

If the working conditions of the described procedure are such that $Z_M V/w K^*$ is much lower than 1, the concentration of sorbed metal ion c does not depend on V/w , since of course it is the total concentration originally present, c_{tot} . In this case, the

procedure simply gives a demonstration that $c = c_{\text{tot}}$, but it is impossible to evaluate Z_M . In this case, the slope of the straight line obtained by plotting $1/c$ vs V/w is lower than 0.1, very near to 0. This does not mean that the metal is not complexed in solution, but only that Z_M is much lower than $K^* V/w$. If, on the contrary, $Z_M V/w K^*$ is much higher than 1, i.e., if the slope of the straight line is higher than around 10, the metal ion is not sorbed on the resin. Thus, to obtain the required information, c_{tot} and Z_M , V/w would range between $10K^*/Z_M$ and $10^{-1}K^*/Z_M$. This is not always obtainable in practice with a given resin and at given acidity. The "titrant" resin and the conditions must be properly selected.

For instance, suppose that one wants to use Chelex 100 for the titration of copper in a solution at pH 7.5 (NaNO₃ 0.1 mol kg⁻¹), and with V/w of around 1000. Under these conditions only Z_M values ranging from around 4.8×10^{10} to 4.8×10^{12} can be evaluated, since $K^* = 4.8 \times 10^{11}$. If Z_M is higher, copper(II) is not sorbed at all, and a resin with a higher exchange coefficient must be used in order to be able to at least partially sorb the metal ion. If Z_M is lower, the metal ion is quantitatively sorbed, and a resin with lower exchange coefficients must be selected to evaluate Z_M .

CONCLUSIONS

It has been shown that the total concentration of metal ion in a sample can be determined by sorption on a chelating resin even in the presence of unknown complexing substances which can reduce the sorption of the metal ion on the resin only to a part of the total. At the same time, the fraction of total to free metal ion can be evaluated. The concentration of free metal ion originally present in the sample is calculated from these quantities. This method, which is based on eq 6, can be considered as a titration of the metal ion with the resin. Since it is based on the sorption on the chelating resin, it is particularly suitable for determination at very low concentration and in complex matrices. Indeed, a separation and preconcentration can be easily performed using the proposed procedure. The method is helpful in that it allows one to distinguish unambiguously between the free metal ion and that linked to complexing substances. This information can be of interest in the speciation procedures. As a matter of fact, many speciation procedures previously proposed are based on the use of Chelex 100, which should sorb the free metal ion and that metal ion which is linked to the so-called "labile complexes". This is a merely operational definition, not only in a kinetic sense, as it is

(20) Lister, M. W.; Rosenblum, P. *Can. J. Chem.* 1960, 38, 1827–1833.
(21) Bixler, J. W.; Larson, T. M. *J. Inorg. Nucl. Chem.* 1974, 36, 224–229.

widely recognized, but also from a thermodynamic point of view. For example, the same complex can appear as "labile" in freshwater, and "not labile" in seawater, for the only reason that in seawater Chelex 100 contains alkaline earth metal ions as counterions, forming strong complexes with the iminodiacetic groups. On the contrary, the method here proposed gives information about the concentration of free metal ion, a well-defined quantity, independent of the experimental details. An important point is that the accuracy of this information depends on the accuracy with which the distribution equilibria of the metal ion on the resin are known. Of course here too the kinetics of the sorption process is of importance. The equilibrium in the distribution of metal ions between the solution and Chelex 100 is reached in about 3 h at 25 °C, by batch procedure, under stirring and practical values of the ratio V/w (30–4000).⁷ However the

dissociation of the unknown complexes present in real samples, such as seawater, can be much slower.¹¹ In the procedure here proposed, the contact time may be selected at will,¹² and in this way even complexes kinetically very inert can be allowed to reach equilibrium conditions.

ACKNOWLEDGMENT

This work has been financially supported by the Italian Ministry of University and Scientific and Technological Research (MURST, 40%).

Received for review September 8, 1994. Accepted June 21, 1995.[⊗]

AC940897G

[⊗] Abstract published in *Advance ACS Abstracts*, August 1, 1995.

Application of Potential-Modulated UV-Visible Reflectance Spectroscopy to Electron Transfer Rate Measurements for Adsorbed Species on Electrode Surfaces

Zhi Qiang Feng, Takamasa Sagara,*[†] and Katsumi Niki*

Electrochemistry Laboratory, Department of Physical Chemistry, Yokohama National University, Tokiwadai, Hodogaya-ku, Yokohama 240, Japan

The electrode reaction rate constant of an electrochemically active species adsorbed on an electrode surface was determined by potential-modulated UV-visible reflectance spectroscopy. In-phase and 90° out-of-phase components of the electroreflectance signal at an electrode/adsorbed layer interface in response to a sinusoidal modulation of the electrode potential were formalized as a function of the modulation frequency. The heterogeneous rate constant k_s (the overall rate constant) of the electrode reaction of a dye adsorbed on a glassy carbon electrode surface was determined by analyzing the frequency dependence of the electroreflectance signal. The electrode reaction rate constant k_s were $4.9 \times 10^3 \text{ s}^{-1}$ for hemin and $5.4 \times 10^2 \text{ s}^{-1}$ for Nile Blue A.

Modification of electronically conductive substrates with a monolayer or a thin film of electrochemically active molecules has been extensively studied. It has been shown that the redox properties of the adsorbed species are often different from those in the bulk solution¹ and that the electrode reaction of the species in the bulk solution is strongly influenced by the species present at the electrode surface. Electrode surfaces modified by electrochemically active substances provide novel functions which cannot be achieved at a bare electrode surface. It is, therefore, quite important to investigate the electrode reactions of the species present at the electrode surface and the interaction between the modified surface and bulk species. The electrode reaction rate of the redox species immobilized on the electrode surface is one of the most important characteristics of the modified electrode. Recently, electrode reaction rates of the redox species immobilized on long-chain thiol-modified electrodes have been extensively studied.^{2,3}

Spectroelectrochemical techniques have several advantages over traditional electrochemical techniques in situ measurements of the redox processes of the species at the electrode interface.⁴ They enable us to investigate both dynamics and

structures of the redox species at the electrode surfaces simultaneously at a molecular level.

Traditional electrochemical techniques used to evaluate the electrode reaction rate constants of the adsorbed species at the electrode reaction include dc cyclic voltammetry, ac impedance spectroscopy, and potential step chronoamperometry. When the dc voltammetric peak potential is measurable as a function of scan rate without the influence of ohmic drop, the formula derived by Laviron et al.^{5,6} is applicable to evaluate the electrode reaction rate constant k_s (the turnover rate constant). Matsuda and co-workers modified Laviron's theoretical treatment and applied it to the determination of k_s at an LB film-modified electrode.⁷ Rapid scan dc voltammetry at an ultramicroelectrode became available for the determination of k_s of rapid electrode reactions,⁸ and He et al. measured the k_s values of the order of 10^5 s^{-1} for dyes adsorbed on a mercury electrode at scan rates over 100 kV s^{-1} .⁹ The determination of k_s by using ac impedance spectroscopy, ac polarography, or ac voltammetry has been discussed.¹⁰⁻¹⁴ In the case of irreversibly adsorbed redox species, k_s has been obtained by the ac impedance method. However, large double-layer capacitance and solution resistance make the determination of k_s by ac impedance spectroscopy difficult. Laviron and colleagues predicted theoretically that the upper limit of k_s measurable by using the ac method is as high as $2 \times 10^4 \text{ s}^{-1}$.¹⁴ In the case of chronoamperometry, discrimination of the faradaic current from the nonfaradaic one is not easy.

The potential-modulated UV-visible reflectance spectroscopic technique (electroreflectance spectroscopy, ER) is an ac techniques in which the ac reflectance response originating from the

* Present address: Department of Applied Chemistry, Nagasaki University, Bunryo-cho, Nagasaki 852, Japan.

(1) Hinnen, C.; Parsons, R.; Niki, K. *J. Electroanal. Chem.* **1983**, *147*, 329.
(2) Song, S.; Clark, R. A.; Bowden, E. F.; Tarlov, M. *J. Phys. Chem.* **1993**, *97*, 6564.
(3) (a) Finklea, H. O.; Hanshew, D. D. *J. Am. Chem. Soc.* **1992**, *114*, 3173. (b) Becka, A. M.; Miller, C. J. *J. Phys. Chem.* **1992**, *96*, 2657. (c) Chidsey, C. E. D. *Science* **1991**, *251*, 919. (d) Miller, C.; Graetzl, M. *J. Phys. Chem.* **1991**, *95*, 5225. (e) Bunding Lee, K. A. *Langmuir* **1990**, *6*, 709.

(4) (a) For review, see: Ryan, M. D.; Chamdrés, J. Q. *Anal. Chem.* **1992**, *64*, 79R. (b) Gutierrez, C.; Meléndez, C., Eds. *Spectroscopic and Diffraction Techniques in Interfacial Electrochemistry*; Kluwer Academic Publishers: Amsterdam, 1990. (c) Gale, R. J., Ed. *Spectroelectrochemistry*; Plenum Press: New York, 1988.
(5) Laviron, E. *J. Electroanal. Chem.* **1979**, *101*, 19.
(6) Laviron, E.; Roullier, L.; Degrand, C. *J. Electroanal. Chem.* **1980**, *112*, 11.
(7) Daifuku, H.; Aoki, K.; Tokuda, K.; Matsuda, H. *J. Electroanal. Chem.* **1985**, *183*, 1.
(8) Andrieux, C. P.; Hapiot, P.; Saveant, J.-M. *Chem. Rev.* **1990**, *90*, 723.
(9) Chen, X.-M.; Zhuang, J.-H.; He, P.-X. *J. Electroanal. Chem.* **1989**, *271*, 257.
(10) MacDonald, J. R. *Impedance spectroscopy*. John Wiley & Sons: New York, 1987.
(11) Sluyters-Rehbach, M.; Sluyters, J. H. In *Electroanalytical Chemistry*; Bard, A. J., Ed.; Marcel Dekker: New York, 1970; pp 1-128.
(12) (a) Kakutani, T.; Senda, M. *Bull. Chem. Soc. Jpn.* **1979**, *52*, 3236. (b) Laviron, E. *J. Electroanal. Chem.* **1979**, *105*, 25; 35. (c) Laviron, E.; Roullier, L. *J. Electroanal. Chem.* **1983**, *157*, 7.
(13) Laviron, E. *J. Electroanal. Chem.* **1979**, *97*, 135.
(14) Lelievre, D.; Plichon, V.; Laviron, E. *J. Electroanal. Chem.* **1980**, *112*, 137.

electrode reactions (redox reaction, adsorption/desorption reaction, or field effect) at the electrode surface is measured instead of ac current response.¹⁵⁻¹⁷ The ac reflectance response (ER response) measured in the vicinity of the formal potential E° of the adsorbed species originates from its redox reaction.¹⁸ The potential modulation in the vicinity of E° gives rise to the change in the fractions of oxidized and reduced forms of the species present at the electrode surface, and the difference spectrum between the oxidized and reduced forms is expected as the ER response. It is important to note that the amplitude of the ac reflectance response is proportional to the amount of the redox species interconverted between oxidized and reduced forms in response to the potential modulation.¹⁸

We have demonstrated two types of ER measurements for monolayers of dyes and redox proteins at electrode surfaces.¹⁶⁻¹⁹

(1) ER response as a function of the electrode potential in the course of a potential scan at a constant wavelength, viz., ER voltammetry, and (2) ER response as a function of the wavelength at a constant electrode potential, viz., ER spectrum. It was shown that ER voltammetry is a sensitive technique for detection of the electrode reaction of the species at the electrode surface without interference of the nonfaradaic process.^{16,18,20} The sensitivity is so high that the redox reaction of a monolayer of a heme protein is detectable at a gold electrode, even though the dc cyclic voltammetric response is immeasurable.²¹

When the amplitude of the ac potential modulation ΔE_{ac} is much smaller than RT/nF (R is the gas constant, T is the temperature, n is the number of electrons involved in the electrode reaction, and F is the Faraday constant), a linear approximation is applicable to the ac reflectance signal from the electrode surface. When the electrode potential is modulated by a sinusoidal wave,

$$E = E_{dc} + \Delta E_{ac} \sin(\omega t) \quad (1)$$

the reflectance signal, R , which is the sum of dc and ac components, can be written

$$\begin{aligned} R &= R_{dc} + R_{ac} \\ &= R_{dc} + \Delta R_{ac} \sin(\omega t - \phi) \end{aligned} \quad (2)$$

where E_{dc} is the dc electrode potential, ΔE_{ac} is the modulation amplitude, ω is the angular frequency, t is the time, R_{dc} and R_{ac} are dc and ac components of R , respectively, and ΔR_{ac} is the amplitude of the ac reflectance signal. The phase shift ϕ of R_{ac} with respect to ΔE_{ac} is not zero unless the electrode reaction is reversible and the cell time constant is negligible. When the electrode reaction is quasi-reversible, ϕ is a function of the electrode reaction rate. Therefore, it is expected that the analysis of the ER response, ϕ in particular, in the frequency domain enables us to determine the electrode reaction rate.

There are few reports on the frequency domain analysis of the ac optical responses from the electrode in the presence of

electroactive species.²² A practical application of the complex plane analysis of the ac transmission light intensity through an optically transparent electrode has been reported.²³ An advantage of the ER spectroscopic method over UV-vis transmission, IR reflection spectroscopies, and SERS is that any electrode material which reflects light can be used in the ER measurements. In 1973, Yeager et al. first proposed the complex plane analysis of ER response.²⁴ However, the use of the frequency domain analysis of ER response in the study of the redox reaction of a monolayer at the electrode surface has not been reported, probably because the sensitivity of the ER measurement was insufficient.

In our previous paper, we discussed the ER voltammetric determination of k_s of the electrochemical systems whose cell time constants are negligible.¹⁶ In the present paper, the frequency dependence of the ER response at an electrode/adsorbed layer interface is derived by taking into consideration a finite cell time constant. The resulting formulation is applied to the determination of k_s of the species adsorbed on a glassy carbon electrode.

EXPERIMENTAL SECTION

A glassy carbon rod (GC30S, Tokai Materials Co.) was sheathed by an epoxy cement resin (Torr Seal, Barian Co.). The electrode surface was mechanically polished with 0.06 μm alumina powder to a mirror finish, and then the electrode was sonicated in water to remove alumina particles embedded in the electrode. The electrode area was 0.283 cm^2 . Hemin (iron(III) protoporphyrin IX chloride, Tokyo Kasei Co.) and Nile Blue A (3-amino-7-(dimethylamino)-1,2-benzophenoxazine, Eastman Kodak Co.) were of the highest grade commercially available and were used without further purification. Water was purified by a Milli-Q system (Millipore Co.) and its resistivity was $>18 \text{ M}\Omega \text{ cm}$. All other chemicals were of reagent grade and were used as received. All electrode potentials were measured with respect to the Ag/AgCl electrode in a saturated KCl solution. A platinum electrode with a large surface area served as a counter electrode. The cell configuration and the instrumentation for ER measurements were the same as described in our previous publications.^{16,20} The in-phase (real part) and 90° out-of-phase (imaginary part) components of R_{ac} were measured by a lock-in amplifier (Model 5210, EG&G PARC). The ac components (the real and imaginary parts) of the reflected light intensity divided by an average intensity of the reflected light (dc component of the reflected light intensity) were given as the ER responses, the real and imaginary parts of which are represented by $\text{Re}(R_{ac})/R_{dc}$ and $\text{Im}(R_{ac})/R_{dc}$, respectively.

Electrochemical and spectroelectrochemical measurements were performed at $25 \pm 2^\circ\text{C}$ in argon atmosphere. Two electrode systems have been used in the present investigations.

I. Hemin/Glassy Carbon Electrode. The glassy carbon surface was wetted with a drop of saturated hemin solution (100 mM Na_2HPO_4 aqueous solution containing 30% ethanol) for 30 min. The electrode was then rinsed thoroughly to remove free hemin from the electrode surface before being placed in the cell filled with a base solution (0.5 M NaF solution at pH 6.85, buffered by 30 mM phosphate solution).

(15) (a) Pieth, W. *J. Phys. Chem.* **1992**, *96*, 223. (b) Kolb, D. M. *Science* **1991**, *95*, 87.

(16) Sagara, T.; Igarashi, S.; Sato, H.; Niki, K. *Langmuir* **1991**, *7*, 1005.

(17) Sagara, T.; Niki, K. *Langmuir* **1993**, *9*, 831.

(18) Sagara, T.; Iizuka, J.; Niki, K. *Langmuir* **1992**, *8*, 1018.

(19) Sagara, T.; Murakami, H.; Igarashi, S.; Sato, H.; Niki, K. *Langmuir* **1991**, *7*, 3190.

(20) Sagara, T.; Sato, H.; Niki, K. *Bunseki Kagaku* **1991**, *40*, 641.

(21) Ikeda, T.; Kobayashi, D.; Maisushita, F.; Sagara, T.; Niki, K. *J. Electroanal. Chem.* **1993**, *361*, 221.

(22) (a) Hutton, R. S.; Kalaji, M.; Peter, L. M. *J. Electroanal. Chem.* **1989**, *270*, 429. (b) Gabrielli, C.; Kuddam, M.; Takenouti, H. *Electrochim. Acta* **1990**, *35*, 1553.

(23) Amemiya, T.; Hashimoto, K.; Fujishima, A. *J. Phys. Chem.* **1993**, *97*, 4187.

(24) Adzic, R.; Cohan, B.; Yeager, E. *J. Chem. Phys.* **1973**, *58*, 1780.

II. Nile Blue A/Glassy Carbon Electrode. Nile Blue A was immobilized on the polished glassy carbon electrode by soaking the electrode in a saturated solution of Nile Blue A, followed by rinsing the electrode thoroughly with the base solution to remove free Nile Blue A before mounting the electrode in the experimental cell. The base solution used for the spectroelectrochemical measurements was 30 mM phosphate buffer solution at pH 7.14.

THEORY

We assume that an electrode surface is covered with a monolayer or submonolayer of an electrochemically active species, which undergoes a quasi-reversible electron transfer reaction, and that there is no electrochemically active species in the solution phase. We also assume that the sum of the surface concentrations of the oxidized and reduced forms of the adsorbed species, Γ_1 , is independent of time.

When the adsorbed species are equivalent and noninteracting, the rate of the electrode reaction is given by eq 3, where k_s is the

$$\frac{d\Gamma_{\text{red}}}{dt} = k_s \{ (\Gamma_1 - \Gamma_{\text{red}}) \exp\{-\alpha nF(E - E^\circ)/RT\} - \Gamma_{\text{red}} \exp\{(1 - \alpha)nF(E - E^\circ)/RT\} \} \quad (3)$$

reaction rate constant (turn-over reaction rate constant), Γ_{red} the surface concentration of the reduced form, E° the formal potential of the adsorbed species, α the transfer coefficient, and n the number of electrons involved in the electrode reaction.

When the adsorbed molecules are interacting, the formal potentials of the adsorbed molecules are no longer unique, and the apparent number of electrons, n_a , involved in the electrode reaction calculated from the Nernst slope is different from n . When an intermolecular interaction is repulsive, $n_a < n$; when it is attractive, $n_a > n$. In the case of methylene blue adsorbed on a pyrolytic graphite electrode, the apparent number of electrons involved in the electrode reaction is calculated from the peak widths at half-maximum of the dc cyclic voltammogram and ER voltammogram to be 0.96 instead of 2.¹⁶ These results clearly suggest that methylene blue molecules adsorbed on the graphite electrode are interacting (repulsive interaction) and nonequivalent sites. That is, the Nernst equation for the methylene blue adsorbed on a graphite is given by

$$(\Gamma_1 - \Gamma_{\text{red}})/\Gamma_{\text{red}} = \exp\{n_a F(E - E^\circ)/RT\} \quad (4)$$

The rate equation given by eq 3 leads to eq 5 for the interacting sites.

$$\frac{d\Gamma_{\text{red}}}{dt} = k_s \{ (\Gamma_1 - \Gamma_{\text{red}}) \exp\{-\alpha n_a F(E - E^\circ)/RT\} - \Gamma_{\text{red}} \exp\{(1 - \alpha)n_a F(E - E^\circ)/RT\} \} \quad (5)$$

The equivalent circuit of the electrode reaction of molecules adsorbed on an electrode surface is represented by Figure 1, where R_s is the solution resistance, C_d the double-layer capacitance, R_{ct} the charge transfer resistance, and C_a the capacity invoked by the reactant adsorbed on the electrode surface.^{2,10,14,25,26}

(25) (a) Niki, K.; Yagi, T.; Inokuchi, H.; Kimura, K. *J. Electrochem. Soc.* **1977**, *124*, 1889. (b) Niki, K.; Yagi, T.; Inokuchi, H.; Kimura, K. *J. Am. Chem. Soc.* **1979**, *101*, 3335. (c) Fan, K.; Akutsu, H.; Niki, K. *J. Electroanal. Chem.* **1990**, *178*, 295.

(26) Sagara, T.; Niwa, K.; Sone, A.; Hinneen, C.; Nishi, K. *Langmuir* **1990**, *6*, 254.

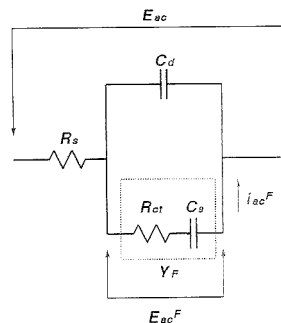


Figure 1. Equivalent circuit of an electrode/monolayer of adsorbed species/solution interface. For notations, see text. The circuit directly responsible for the ER response, the faradaic component of the equivalent circuit, is shown within a broken line.

When the electrode potential is modulated by a sinusoidal wave at $E_{dc} = E^\circ$ with a modulation amplitude ΔE_{ac} which is much smaller than $RT/n_a F$, the charge transfer resistance R_{ct} and the capacitance due to the adsorbed reactant C_a are given by eqs 6 and 7 by a linear approximation,^{13,14,26} where n is the number of

$$R_{ct} = 2RT/nn_a F^2 k_s \Gamma_1 \quad (6)$$

$$C_a = nn_a F^2 \Gamma_1 / 4RT \quad (7)$$

electrons involved in the electrode reaction. Therefore, the rate constant k_s is given by

$$k_s = (2R_{ct} C_a)^{-1} \quad (8)$$

The current flowing through the faradaic component of the equivalent circuit by the application of the potential modulation given by eq 1 is represented by eq 9, where E_{ac}^F is the ac voltage

$$i_{ac}^F = Y_F E_{ac}^F \quad (9)$$

across the faradaic component of the equivalent circuit and Y_F is the faradaic admittance, which is equal to $[R_{ct} - j(\omega C_a)^{-1}]^{-1}$ [where $j = (-1)^{1/2}$]. By analogy with eq 9, for the equivalent circuit shown in Figure 1, reflectance of the faradaic component of the equivalent circuit Y_{AF} is defined as

$$R_{ac} = Y_{AF} E_{ac}^F \quad (10)$$

The ac component of the apparent absorbance of the adsorbed layer on the electrode surface A_{ac} is given by

$$A_{ac}(t) = (\epsilon_{\text{red}} - \epsilon_{\text{ox}}) \Gamma_1 f(t) \quad (11)$$

where ϵ_{red} and ϵ_{ox} are the apparent absorption coefficients of the reduced and oxidized forms of the adsorbed layer, respectively, and $f(t) = \Gamma_{\text{red}}/\Gamma_1$.¹⁶ Since i_{ac}^F is given by

$$i_{ac}^F = nF \Gamma_1 \frac{df(t)}{dt} \quad (12)$$

$A_{ac}(t)$ is obtained by substituting eq 12 into eq 11:

$$A_{ac}(t) = \frac{\Delta\epsilon}{nF} \int i_{ac}^F dt = -(\Delta\epsilon/j\omega nF) Y_F E_{ac}^F \quad (13)$$

where $\Delta\epsilon = \epsilon_{\text{red}} - \epsilon_{\text{ox}}$. The apparent absorbance of the adsorbed layer is much smaller than unity, and R_{ac} can be written as

$$R_{ac} = (Kj/\omega) Y_F E_{ac}^F \quad (14)$$

and

$$Y_{AF} = (Kj/\omega) Y_F \quad (15)$$

where $K = \Delta\epsilon/nF$ is a constant at a given wavelength. Note that the relationship between Y_F and Y_{AF} expressed by eq 15 is valid not only for the particular equivalent circuit shown in Figure 1, but also for any other systems where Y_F can be analytically expressed.

In the lock-in detection of the ac reflectance signal, the phase reference is E_{ac} but not E_{ac}^F . The reflectance of the whole circuit Y_A is thus defined, similar to eq 10, as

$$R_{ac} = Y_A E_{ac} \quad (16)$$

The reflectance Y_A in the equivalent circuit shown in Figure 1 can be solved first by substituting E_{ac}^F , which is expressed in terms of E_{ac} , R_{ct} , C_a , R_s , and C_d , into eq 14 and then by comparing the resulting equation with eq 16. The real and imaginary parts of Y_A are given by eqs 17 and 18, respectively.

$$\text{Re}(Y_A) = -KC_a(1 - \omega^2 R_s R_{ct} C_a C_d) / \xi \quad (17)$$

$$\text{Im}(Y_A) = KC_a \omega (R_{ct} C_c + R_s C_a + R_s C_d) / \xi \quad (18)$$

where

$$\xi = (1 - \omega^2 R_s R_{ct} C_a C_d)^2 + \omega^2 (R_{ct} C_c + R_s C_a + R_s C_d)^2 \quad (19)$$

When R_s is negligible, the trajectory of the complex plane plot of R_{ac} is a semicircle, and the angular frequency at its peak is equal to $2k_s$. A rigorous treatment of the ER response in the case of $R_s = 0$ was described in our previous publication.¹⁶ When $R_s \neq 0$, the product of $\omega/2$ and the ratio of the magnitude of the real part of R_{ac} to that of the imaginary part of R_{ac} , viz., $\omega/2 |\text{Re}(R_{ac})/\text{Im}(R_{ac})|$, is independent of frequency and is equal to k_s .¹⁶

Figure 2A represents the complex plane plots of the ER response simulated by using eqs 17–19. When the values of k_s are either greater than 10^5 s^{-1} or less than 1 s^{-1} , the complex plane plot of the ER response becomes a semicircle, as shown in Figure 2A, but it is in a different frequency domain. When the rate constant is in the range between 1 and 10^5 s^{-1} , the phase angle of R_{ac} with respect to E_{ac} is $>90^\circ$ at higher frequencies, as shown in Figure 2A. The sign of $\text{Re}(R_{ac})$ is inverted at $\omega = (2k_s/R_s C_a)^{1/2}$. The larger the difference between $R_s C_d$ and k_s , the greater the phase shift expected.

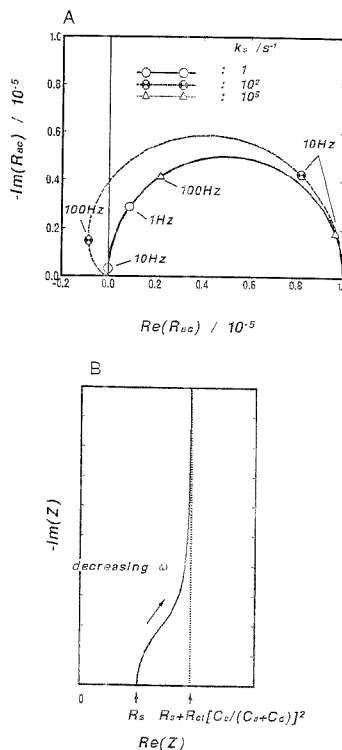


Figure 2. (A) Simulated complex plane plot of the ER response for the equivalent circuit shown in Figure 1 according to eqs 17–19. The parameters are $C_d = 20 \mu\text{F cm}^{-2}$, $R_s = 100 \Omega \text{ cm}^2$, $C_a = 10 \mu\text{F cm}^{-2}$, $K = 10^5 \text{ cm}^2 \text{ C}^{-1}$, and $\Delta E_{ac} = 10 \text{ mV}$. (B) Schematic complex plane plot of the ac impedance for the equivalent circuit shown in Figure 1.

Figure 2B represents the Cole–Cole plot for the equivalent circuit shown in Figure 1. The extrapolated value at $\omega = 0$ to the $Re(Z)$ axis shifts toward R_s with an increase in the rate constant, and it becomes difficult to determine the charge transfer resistance, R_{ct} .

The frequency dependence of ϕ can be represented by using the relation $\cot \phi = \text{Re}(Y_A)/\text{Im}(Y_A)$ and eqs 17–19 as

$$-\omega \cot \phi = (1 - \omega^2 R_s R_{ct} C_a C_d) / (R_{ct} C_c + R_s C_a + R_s C_d) \quad (20)$$

Among the parameters in eq 20, R_s and C_d are measurable parameters. That is, R_s can be measured by the ac impedance at a high frequency limit, and C_d by either the double-layer charging current of the dc voltammetry or the ac impedance at low frequencies. Therefore, R_{ct} and C_a can be determined from the plot of $\omega \cot \phi$ against ω^2 . Then, one can evaluate k_s from eq 8.

RESULTS AND DISCUSSION

I. Hemin/Glassy Carbon Electrode. The dc cyclic voltammetric measurement at the hemin/glassy carbon electrode system was carried out. The hemin monolayer is so stable that

the desorption of hemin with time is negligible, and only the electrode reaction of adsorbed hemin is to be considered. The peak current is proportional to the scan rate, which suggests that the adsorbed hemin is involved only in the redox reaction. The formal potential is -310 mV. The amount of hemin adsorbed on the electrode surface is estimated to be $\Gamma_1 = 5 \times 10^{-11}$ mol cm^{-2} from the charge of the voltammetric peak. This value of Γ_1 is much less than the monolayer coverage (3×10^{-10} mol cm^{-2}). Both anodic and cathodic peak potentials are independent of the scan rate in the range of 10 – 200 mV s^{-1} . By use of eq 4, the current–potential curve of a reversible reaction of adsorbed species is given as

$$i = \frac{nn_a F^2 v A \Gamma_1}{RT} \frac{\exp[n_a F(E - E^{\circ})/RT]}{\{1 + \exp[n_a F(E - E^{\circ})/RT]\}^2} \quad (21)$$

where v is the scan rate and A is the electrode surface area. The peak width at half-maximum is determined to be $3.53RT/n_a F$ from eq 21, and n_a in the present electrode system is calculated to be 0.4 from the peak width of 220 mV.

The broadening of the peak is due to the scattering of the formal potential of the adsorbed hemin, which can be explained in terms of the interactions between the adsorbed molecules and/or between the electrode and the adsorbed molecules. We examined the cyclic voltammetric behavior of the adsorbed hemin with a surface concentrations Γ_1 less than the monolayer coverage and found that the peak width at half-maximum was not influenced significantly by Γ_1 . That is, the broadening of the formal potential of the adsorbed hemin is due mainly to the interaction with the glassy carbon electrode surface. Further investigations are necessary to understand the intermolecular interaction of the adsorbed species and the interaction with the electrode surface, which is evidenced by the ER spectra.^{16,27} The value of C_d evaluated from the sweep rate dependence of the double-layer charging current is $55.2 \mu\text{F cm}^{-2}$.

Figure 3A shows the ER spectrum at $E_{dc} = -310$ mV. Since the background of the ER response from the glassy carbon electrode was negligibly small compared with the ER response due to the redox reaction of hemin, the background correction was unnecessary. The ER spectrum shown in Figure 3A is nearly the same as that at a basal plane pyrolytic graphite in phosphate buffer solution at pH 7.0.²⁷ The maximal ER response is obtained at 433 nm in the wavelength region of the Soret band of the adsorbed hemin.

Figure 3B shows the ER voltammogram measured at 433 nm. The peak potential of the real part is -325 mV, identical with that of the imaginary part.

The fact that the ER voltammetric peak shape is symmetrical with respect to the peak potential supports that eq 5 can be used in this electrode system. If the distribution of E is asymmetrical about E° , the ER voltammetric peak shape should be asymmetrical.

Figure 4 shows the complex plane plot of the ER response measured at 44 different frequencies at -325 mV with the modulation amplitude of $\Delta E_{ac} = 14.5$ mV. A linear approximation of the ER response is valid at this amplitude. The ER response at a given frequency remains unchanged throughout the measurement.

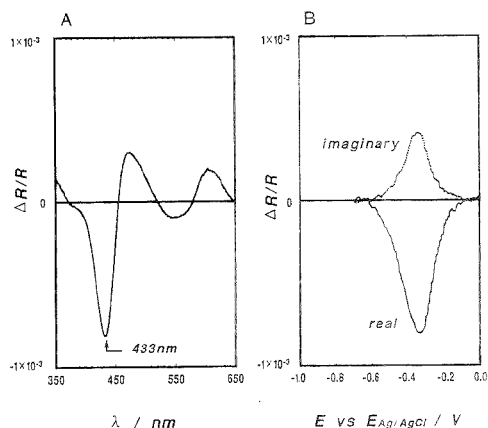


Figure 3. ER spectrum (A) and ER voltammogram (B) of the glassy carbon electrode covered with the hemin monolayer in the base solution (0.5 M NaF + 30 mM phosphate buffer) at pH 6.85. (A) ER spectrum at $E_{dc} = -310$ mV, $f = 14.27$ Hz, and $\Delta E_{ac} = 14.5$ mV. (B) ER voltammogram at $\lambda = 433$ nm, $f = 14.27$ Hz, and $\Delta E_{ac} = 14.5$ mV; sweep rate, -2 mV s^{-1} .

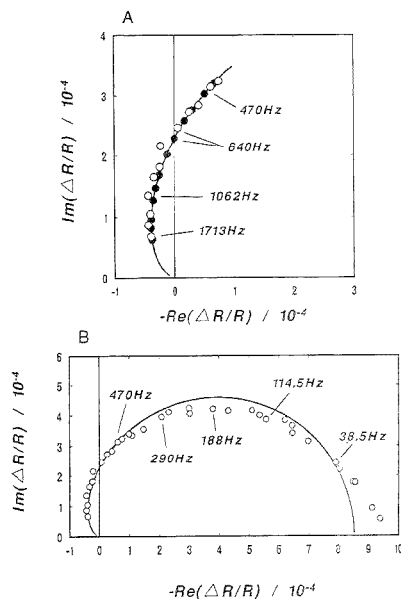


Figure 4. Complex plane plot of the ER response at the glassy carbon electrode covered with hemin monolayer in the base solution (0.5 M NaF + 30 mM phosphate buffer) at pH 6.85, $E_{dc} = -325$ mV, $\Delta E_{ac} = 10.25$ mV, and $\lambda = 433$ nm, (A) in high-frequency region and (B) in a wide frequency region. Open circles are experimental values; closed circles in A and full lines in both A and B are simulated by the use of the best-fit parameters.

Figure 5 shows the complex plane plot of ac impedance Z , which is measured simultaneously with the measurement of the frequency dependence of the ER response. A small modulation amplitude, $\Delta E_{ac} = 4.43$ mV, is used in the ac impedance

(27) Sagara, T.; Takagi, S.; Niki, K. *J. Electroanal. Chem.* 1993, 349, 159.

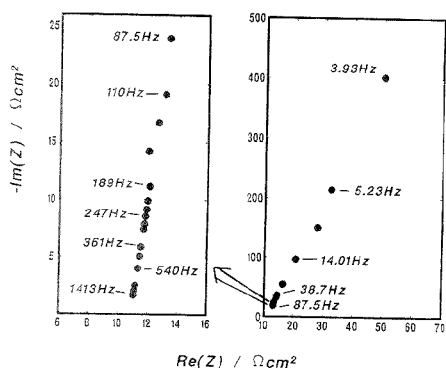


Figure 5. Complex plane plot of ac impedance at the glassy carbon electrode covered with hemin monolayer in the base solution (0.5 M NaF + 30 mM phosphate buffer) at pH 6.85, $E_{dc} = -325$ mV and $\Delta E_{ac} = 4.43$ mV.

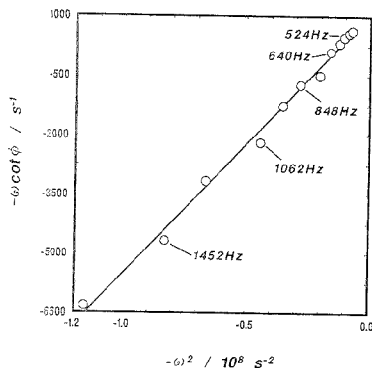


Figure 6. Plot of $-\omega \cot \phi$ against $-\omega^2$ for the ER response shown in Figure 4. Open circles are experimental values; full line is simulated by the use of the least-squares fitting calculation.

measurement in order to determine the solution resistance R_s . The trajectory of the impedance plot is a straight line and nearly perpendicular to the abscissa, indicating that R_s and C_d play dominant roles in the ac impedance. This fact suggests that k_s is too large to be determined from the ac impedance data, and a rate constant of $k_s > 2 \times 10^3$ s $^{-1}$ is estimated. The value of R_s is determined to be 10.9 Ω cm 2 by extrapolating the plot at higher frequencies to the abscissa. The plot of $\text{Im}(Z)$ against the reciprocal of ω gives rise to a straight line at lower frequencies, and the reciprocal of the slope is 55 μF cm $^{-2}$. This value agrees with C_d obtained from the dc voltammogram.

Figure 6 shows a plot of $-\omega \cot \phi$ against $-\omega^2$ for the ER response represented in Figure 4. The plot shows a linear relationship between $\omega \cot \phi$ and ω^2 , as expected from eq 20. The least-squares fitting calculation in the range from 1710 to 439 Hz yields the slope of the straight line as $(6.6 \pm 0.1) \times 10^{-5}$ s and the intercept as $(1.1 \pm 0.2) \times 10^3$ s $^{-1}$. Using eq 20 and the values of R_s (10.9 Ω cm 2) and C_d (55.2 μF cm $^{-2}$) obtained in separate measurements, k_s is calculated to be 4.9×10^3 s $^{-1}$. The parameters obtained in the present measurements are listed in Table 1. Substituting the values of C_d obtained from the frequency

dependence of the ER response and Γ_1 obtained from the dc voltammogram into eq 7, n_2 is calculated to be 0.44, which is in accord with the value obtained from the peak width at half-maximum of the dc voltammogram.

The ER response simulated using the parameters given in Table 1 is shown on the complex plane in Figure 4 by a solid line and closed circles. On the other hand, the value of $R_{ct}[C_a/(C_a + C_d)]^2$ in the present experiment is only 3.4% of R_s , so the evaluation of R_{ct} from the ac impedance data was impossible, as expected from Figure 2B. The reversible dc voltammetric response of hemin adsorbed on a glassy carbon electrode in the scan range measured is expected on the basis of the reaction rate constant of 4.9×10^3 s $^{-1}$.⁵ Brown and Anson previously used an open circuit charge injection technique to measure k_s of hemin adsorbed on a basal plane pyrolytic graphite electrode.²⁸ The electrode reaction was so rapid that the reaction rate constant was predicted to be $> 2 \times 10^4$ s $^{-1}$.

II. Nile Blue A/Glassy Carbon Electrode. The dc cyclic voltammogram at a glassy carbon electrode covered with a monolayer of Nile Blue A is measured in the sweep rate range between 10 and 200 mV s $^{-1}$. The midpoint potential between anodic and cathodic peaks is -380 mV. The peak separation depends on the scan rate. The peak width at half-maximum at lower scan rate is 175 mV, from which n_2 is calculated to be 0.52. This result suggests that the electrode reaction of Nile Blue A adsorbed on a glassy carbon electrode involves two consecutive one-electron reactions with two closely spaced formal potentials.¹⁶ The intermolecular repulsive interaction between the adsorbed Nile Blue A molecules and the interaction between Nile Blue A molecules and the electrode may also be present.

In the present work, we applied the theory delivered in the previous section to the analysis of the frequency dependence of ER response to calculate the overall rate constant.

The ER spectrum measured at $E_{dc} = -380$ mV with a modulation frequency of 14.1 Hz shows a positive peak at 600 nm and a negative peak at 703 nm, and the wavelength at which no ER response is observed is 668 nm. This ER spectrum is similar to that of Nile Blue A adsorbed on a basal plane pyrolytic graphite electrode.¹⁸ The ER voltammogram at 600 nm exhibits a peak at -380 mV.

Figure 7 represents the complex plane plot of the ER response at $\lambda = 592$ nm and $E_{dc} = -380$ mV.

The solution resistance determined by the ac impedance method is 270 Ω cm 2 . The double-layer capacitance estimated from the double-layer charging current in the dc voltammetry agrees with the value measured by the ac impedance method and is 37.5 μF cm $^{-2}$. The plot of $\omega \cot \phi$ against ω^2 is analyzed by using these values. The plot gives rise to a straight line in the frequency range between 5.24 and 123.4 Hz. From the slope and intercept of this line at $\omega = 0$, k_s is determined to be 5.4×10^2 s $^{-1}$. The other parameters are listed in Table 1. The value of n_2 is calculated by using the values $C_d = 70.6$ μF cm $^{-2}$ and $\Gamma_1 = 7 \times 10^{-11}$ mol cm $^{-2}$ as being 0.57, which is in accord with the value estimated from the peak width at half-maximum of the dc voltammogram.

In the case of the Nile Blue A/glassy carbon electrode system, the modulation amplitude was larger than that used in the hemin/glassy carbon electrode system, namely 21.9 mV. In the ER measurement, the use of a larger modulation amplitude leads to

(28) Brown, A. P.; Anson, F. C. *J. Electroanal. Chem.* 1978, 92, 133.

Table 1. Electrode Reaction Parameters Obtained from ER Response, ac Impedance, and dc Voltammogram

system ^a	ER response				ac impedance and dc voltammogram			
	R_{ct} , $\Omega \text{ cm}^2$	C_d , $\mu\text{F cm}^{-2}$	n_a	k_s , s^{-1}	Γ , mol cm^{-2}	R_s , $\Omega \text{ cm}^2$	C_d , $\mu\text{F cm}^{-2}$	n_a
GC/Hm	5.0	20.6	0.44	4.9×10^3	5×10^{-11}	10.9	55.2	0.4
GC/NB	13.1	70.6	0.57	5.4×10^2	7×10^{-11}	270	37.5	0.5

^a GC, glassy carbon; Hm, hemin; NB, Nile Blue A.

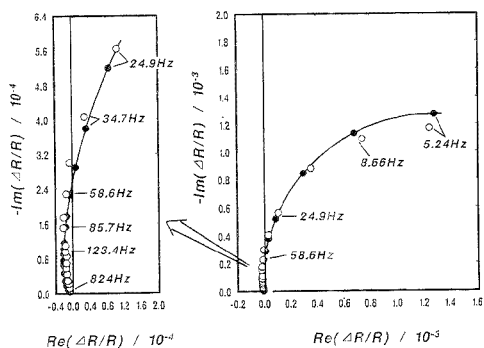


Figure 7. Complex plane plot of the ER response at the glassy carbon electrode covered with the Nile Blue A adsorbed layer in the base solution (30 mM phosphate buffer) at pH 7.14, $E_{oc} = -390 \text{ mV}$, $\Delta E_{ac} = 21.9 \text{ mV}$, and $\lambda = 592 \text{ nm}$. Open circles are experimental values; closed circles and full line are simulated by the use of the best-fit parameters.

a higher sensitivity but is inferior in ensuring the validity of a linear approximation. Nevertheless, consistency between the experimental and simulated complex plane plots of the ER response is achieved, as shown in Figure 7. This fact connotes that the use of a value of ΔE_{ac} which is comparable to $RT/n_a F$ does not generate inappropriate significant errors in the electrode kinetic parameters.

III. Limitation of the Measurable k_s . The intercept of the trajectory on the $\text{Im}(Y_A)$ axis, denoted by I_0 , can be measured with a reasonable accuracy. The value of I_0 is a function of C_d and R_s , and the maximum value, I_0^{max} , is attained when $C_d = (R_{ct} + R_s)C_d/R_s$. When C_d is either larger or smaller than $(R_{ct} + R_s)C_d/R_s$, the value of I_0 becomes smaller. The maximum value of I_0^{max} can be derived from eqs 17–19:

$$I_0^{\text{max}} = KC_d R_{ct}^{1/2} / 2(R_{ct} + R_s)^{1/2} \quad (22)$$

The upper limit of the measurable electrode reaction rate constant can be calculated from eq 23.

$$k_s < K^2 C_d^2 / 8R_s C_d I_0^2 \quad (23)$$

where I_0 is the minimum value of I_0^{max} to be measured.

The minimum value of I_0^{max} with a reasonable accuracy in the present ER measurement is $5 \times 10^{-4} \text{ V}^{-1}$. In the case of the monolayer adsorption of dyes such as hemin, the magnitudes of the K and C_d are of the orders of $10^3 \text{ cm}^2 \text{ C}^{-1}$ and $10^{-5} \text{ F cm}^{-2}$, respectively. The upper limit of the rate constant is calculated from eq 23 to be $50/R_s C_d$. When the cell time constant $R_s C_d$ is 0.6 ms, as in the case of the present experiment (the hemin/glassy carbon electrode system), the upper limit of the measurable

k_s would be $8 \times 10^4 \text{ s}^{-1}$. On the other hand, the upper limits of the electrode reaction rate constant evaluated by the ac impedance method are 1.6×10^3 and $1.0 \times 10^2 \text{ s}^{-1}$ for the hemin/glassy carbon and the Nile Blue A/glassy carbon electrode systems, respectively.

CONCLUSION

A new spectroelectrochemical technique is proposed to evaluate a rapid electrode reaction rate of the species adsorbed on electrode surfaces. This technique is applicable to the redox systems which have an absorption band in the UV-visible region at any electrode system which reflects light. The present method is one of the ac techniques. The faradaic current of the dye molecule adsorbed on the electrode surface is measurable as the response of an electroreflectance from the electrode instead of the total current through an electrochemical cell in the ac impedance method. The feature of the complex plane plot of the ER response generated by the modulation of the electrode potential by a sinusoidal wave is entirely different from that of the ac impedance. We found that the upper limit of the rate constant measured by the complex plane analysis of the ER response is much larger than those measurable by a traditional ac impedance method, because we can exclude a non-faradaic process, whereas in the traditional method, only the faradaic process at the electrode can be measured as the ER response.

ACKNOWLEDGMENT

We are gratefully indebted to the Ministry of Education, Science and Culture, Japan, for the financial support of Grant-in-Aids for Scientific Research on Priority Area of New Development of Organic Electrochemistry (No. 236 for K.N.) and for Developmental Scientific Research (No. 04555196 for K.N.) and also Encouragement of Young Scientist (No. 03855168 for T.S.). K.N. is grateful to the NEDO (New Energy and Industrial Technology Development Organization) for financial support. T.S. gratefully acknowledges the financial support of the Kanagawa Academy of Science and Technology. We thank Dr. T. Kakuchi for his valuable advice on the data analysis and Dr. H. Nakagawa (Nakagawa Applied Research Co.) and Mr. Y. Karatsu (Fuso Co.) for their technical advice in the construction of the ER instrument's electric circuits.

Received for review July 5, 1994. Accepted July 3, 1995.[®]
AC940668U

[®] Abstract published in *Advance ACS Abstracts*, August 15, 1995.

Square-Wave Voltammetric Stripping Analysis of Mercury(II) at a Poly(4-vinylpyridine)/Gold Film Electrode

Jyh-Myng Zen* and Mu-Jye Chung

Department of Chemistry, National Chung-Hsing University, Taichung, Taiwan 402, Republic of China

A novel poly(4-vinylpyridine)/gold film electrode (PVP/GFE) was developed for the determination of trace mercury(II) in real samples by Osteryoung square-wave anodic stripping voltammetry. Mercury is preconcentrated, as the anionic forms in the chloride medium, onto the modified electrode by the ion-exchange effect of the PVP. The high solubility of mercury in gold also helps to increase the preconcentration effect. The preparation of the PVP/GFE is performed by first spin-coating a solution of the PVP polymer onto the electrode surface. Subsequently, gold is plated onto the electrode. Various factors influencing the determination of mercury(II) were thoroughly investigated in this study. In comparison with the conventional gold film electrode, this modified electrode showed improved resistance to interferences from surface-active compounds and common ions, especially for copper(II), which is generally considered as a major interference in the determination of mercury(II) on gold film electrode. The PVP/GFE also showed increased sensitivity and better mechanical stability of the gold film when used in conjunction with the square-wave voltammetric method. In addition, detection can be achieved without deoxygenation, and the electrode can be easily renewed. The analytical utility of the PVP/GFE is demonstrated by application to various water samples.

It is well known that mercury is one of the most toxic metals, and its determination in trace level quantities is very important in environmental and biological analyses.^{1,2} Several previous studies concluded that gold is the preferable electrode material for detecting mercury by anodic stripping voltammetry (ASV). For example, gold disk or rod electrodes,³⁻⁹ gold fiber electrodes,^{10,11} gold twin disk electrodes,^{12,13} and gold film carbon electrodes¹⁴⁻¹⁶

have already been developed for this purpose. Unfortunately, similar to the main disadvantage of using a mercury film electrode in many applications,^{17,18} the most common problem in applying the bare-type gold electrode in ASV is the interference effect caused by surface-active compounds and several metal ions.⁹⁻¹³ A convenient way to improve the problem is to coat the working electrode with a permselective membrane to protect the surface from these interferences. Although many permselective membranes have been introduced, in practice, a compromise between the exclusion of the interference matter and the unhindered transport of the metal ions must be considered. Overall, the key issue in making an electrochemical analytical technique one of the conventional methods for detecting mercury in the category associated with high sensitivity, such as cold vapor atomic absorption spectrometry, cold vapor atomic fluorescence spectrometry, and neutron activation analysis, is the availability of a suitable working electrode.

The modification of electrode surfaces with polymer films has received considerable attention because of the many advantageous properties of polymers.¹⁹ However, most of the previous studies related to this topic were cation-oriented, and hence cation permselective membranes were particularly explored. We have also sought to exploit the advantages of polymer-modified electrodes for the determination of cationic metals such as nickel, lead, copper, and cadmium.²⁰⁻²³ In reality, however, many species of analytical interest exist in the form of anions in sample solutions. Thus, anion exchangers are promising for the determination of such analytes. This is the case for mercury(II) in a solution acidified with hydrochloric acid. Recently, indeed, a carbon paste electrode modified with a liquid anion exchanger (Amberlite LA2) was reported for the voltammetric determination of mercury(II) in a chloride medium.²¹ Nevertheless, the addition of Amberlite LA2 apparently can provide an improvement only in the sensitivity aspect. As a result, a medium change procedure was needed to separate many components that may interfere with the detection. Even so, this method still required a fairly long accumulation time

(1) Von Burg, R.; Greenwood, M. R. In *Mercury*; Merian, E., Ed.; VCH: Weinheim, Germany, 1991; pp 1045-1088.
(2) Niessner, R. *Trends Anal. Chem.* 1991, 10, 310.
(3) Vydra, F.; Stulikova, M.; Petak, P. *J. Electroanal. Chem.* 1972, 49, 99.
(4) Luong, L.; Vydra, F. *J. Electroanal. Chem.* 1974, 50, 379.
(5) Ulrich, L.; Rueggsegger, P. *Z. Anal. Chem.* 1975, 277, 349.
(6) Fukai, R.; Hoynh-Ngoc, L. *Anal. Chim. Acta* 1976, 83, 375.
(7) Taddia, M. *Microchem. J.* 1978, 23, 64.
(8) Golimowski, J.; Gustavsson, I. *Z. Anal. Chem.* 1984, 317, 481.
(9) Jagner, D.; Josefson, M.; Aren, K. *Anal. Chim. Acta* 1982, 141, 147.
(10) Huang, H.; Jagner, D.; Renman, L. *Anal. Chim. Acta* 1987, 201, 1.
(11) Huang, H.; Jagner, D.; Renman, L. *Anal. Chim. Acta* 1987, 201, 269.
(12) Sipos, L.; Nurnberg, H. W.; Valenta, P.; Branica, M. *Anal. Chim. Acta* 1980, 115, 25.
(13) Sipos, L.; Valenta, P.; Nurnberg, H. W.; Branica, M. *J. Electroanal. Chem.* 1977, 77, 263.
(14) Allen, R. T.; Johnson, D. C. *Talanta* 1973, 20, 799.

(15) Lo, J.-M.; Lee, J.-D. *Anal. Chem.* 1994, 66, 1242.
(16) Gl, E. P.; Ostapczuk, P. *Anal. Chim. Acta* 1994, 293, 55.
(17) Brezonic, F. L.; Brauner, P. A.; Stumm, W. *Water Res.* 1976, 10, 635.
(18) Hoyer, B.; Florence, T. M.; Batley, C. E. *Anal. Chem.* 1987, 59, 1608.
(19) Murray, R. W. In *Electroanalytical Chemistry*; Bard, A. J., Ed.; Marcel Dekker: New York, 1984; Vol. 13, p 191.
(20) Zen, J.-M.; Lee, M.-L. *Anal. Chem.* 1993, 65, 3238.
(21) Zen, J.-M.; Huang, S.-Y. *Anal. Chim. Acta* 1994, 296, 77.
(22) Zen, J.-M.; Chi, N.-Y.; Hsu, F.-S.; Chung, M.-J. *Anal. Chem.* 1995, 67, 511.
(23) Zen, J.-M.; Hsu, F.-S.; Chi, N.-Y.; Huang, S.-Y.; Chung, M.-J. *Anal. Chim. Acta* 1995, 310, 407.
(24) Cai, X.; Kallcher, K.; Diwald, W.; Neuhold, C.; Maceo, R. J. *Fresenius' Z. Anal. Chem.* 1993, 345, 25.

of 15 min to achieve a detection limit of 1 ppb. Several other carbon paste electrodes modified with zeolite,²⁵ crown ether,²⁶ diphenylcarbazone,²⁷ 1,5-diphenylcarbazide,²⁸ or tetraphenylborate²⁹ were also reported for the determination of mercury. Unfortunately, either these methods suffer from a fairly high detection limit²⁵⁻²⁷ or the electrode surface cannot be easily regenerated.²⁷⁻²⁹ Apparently, more sensitive and selective chemically modified electrodes are still needed to be developed for the determination of mercury, due to its environmental and biological significance.

Based on the same concept as our previous studies using polymer-modified electrodes for the detection of metal cations,²⁰⁻²³ we expect that similar advantages should also be achieved if a suitable anion permselective membrane is used for the detection of mercury(II) in the chloride medium. As part of our continuing interest in the analytical application of chemically modified electrodes, we report here the use of a poly(4-vinylpyridine)/gold film electrode (PVP/GFE) for the determination of mercury(II). Protonated and quaternized PVPs have been examined extensively as matrices for immobilization of negatively charged redox centers near electrodes since the first work by Oyama and Anson.³⁰⁻³³ The cross-linked PVP polymer is chemically inert, nonelectroactive, hydrophilic, and insoluble in water and thus possesses almost ideal properties for the preparation of chemically modified electrodes. In this paper, the preparation and regeneration of the PVP/GFE and the various factors influencing the determination of mercury(II) are investigated. Typical interferences that can occur in water samples are discussed. The analytical utility of the PVP/GFE is demonstrated by application to various water samples.

EXPERIMENTAL SECTION

Chemicals and Reagents. Poly(4-vinylpyridine) (MW 50 000) solution in methanol containing ~20 wt % polymer was obtained from Aldrich. Gold(III) standard solution (0.100 g, AAS grade) was purchased from RDH. All buffers and supporting electrolyte solutions were prepared from Merck Suprapur reagents. The standard metal solutions used in the interference studies were also obtained from Merck. All the other compounds (ACS-certified reagent grade) were used without further purification. Aqueous solutions were prepared with doubly distilled deionized water.

Apparatus. Electrochemistry was performed on a BAS CV-50W electrochemical analyzer. A BAS Model VC-2 electrochemical cell was employed in these experiments. The three-electrode system consists of one of the following working electrodes, gold film electrode (GFE), PVP-coated glassy carbon electrode (PVP/GCE), and PVP/GFE; a Ag/AgCl reference electrode (Model RE-5, BAS); and a platinum wire auxiliary electrode.

Electrode Preparation. The glassy carbon disk electrode (3 mm diameter, BAS) was polished on a polishing cloth sequentially with diamond of decreasing particle size (15, 3, 1,

and 0.05 μm) to a shiny surface. It was then rinsed with deionized water and further cleaned ultrasonically in 1:1 nitric acid and deionized water successively. The three kinds of working electrodes, GFE, PVP/GCE, and PVP/GFE, used in this work were prepared as follows. Gold was deposited onto a glassy carbon substrate by adding 50 ppm AuCl_4^- to the 0.05 M HCl and 0.05 M KCl supporting electrolyte medium at -0.1 V vs Ag/AgCl for either 3 or 6 min in the preparation of the GFE. For the PVP/GCE, 4 μL of the coating solution was first spin-coated onto the glassy carbon electrode surface at 3000 rpm. A 0.25 wt % solution of PVP in methanol was used as the spin-coating solution. The solution also contained 7% (vs the pyridine moiety) of 1,5-dibromopentane as a cross-linking agent. A uniform thin film was formed after about 3 min of spinning. The coated electrodes were then heated in an oven at 90 °C for about 2 h in order to hasten the cross-linking process and to prevent dissolution of the films in aqueous solutions. Finally, for the preparation of the PVP/GFE, gold was deposited onto the PVP/GCE under the same conditions as those used in the preparation of the GFE, except that the deposition time was varied as required.

Procedure. The freshly prepared PVP/GFE was dipped into the stirred analyte solution containing mercury(II) at $+0.3$ V vs Ag/AgCl for the required time for preconcentration. Quantitative determinations were then performed in the square-wave (SW) mode. The potential range was set from -0.2 to $+0.7$ V vs Ag/AgCl in the anodic direction for most cases. Actually, after the deposition at $+0.3$ V, scanning the potential from -0.2 or from $+0.3$ to $+0.7$ V produces the same result. The reason for changing the potential in the analytical procedure from -0.2 to $+0.7$ V was only for the convenience of examining the interference effect. Unless stated otherwise, a medium containing 0.025 M sulfuric acid and 0.005 M KCl was used in the electrochemical experiments. Solutions and samples were detected without deoxygenation. After the voltammogram was recorded, the electrode was regenerated with 0.1 M H_2SO_4 at $+0.7$ V vs Ag/AgCl for 100 s. The renewed electrode was then checked in the supporting electrolyte to ascertain that it did not show any peak within the potential range before the next measurement.

Groundwater and electroplating waste solution were collected and prepared as reported previously.²⁰ Seawater was collected from the harbor of Taichung, Taiwan. After being filtered through membrane filters (0.45 μm), the sample was stored in the dark at 4 °C. Photooxidation of seawater was accomplished by exposing the sample to a 1-kW UV lamp for 12 h. The standard addition method was used to evaluate the content of mercury in the water samples.

RESULTS AND DISCUSSION

Electrochemical Behavior of Mercury(II) on the PVP/GFE. For the purpose of complexing Hg(II) into anionic forms, the detection was chosen to proceed in the chloride medium since the cumulative formation constants for HgCl_3^- and HgCl_4^{2-} are 1.2×10^{14} and 1.2×10^{15} , respectively.³¹ In this way, in the preconcentration step of the electrochemical stripping determination of mercury(II), the mercurate(II) anions can be accumulated by the anion exchanger (PVP) of the PVP/GFE. In order to confirm the above expectation, the responses of the proposed method for the determination of mercury(II) in different

(25) Hernandez, P.; Alda, E.; Hernandez, L. *Fesentis' Z. Anal. Chem.* **1987**, *327*, 676.

(26) Wang, J.; Bonkadar, M. *Talanta* **1988**, *35*, 277.

(27) Labuda, J.; Plaskon, V. *Anal. Chim. Acta* **1990**, *228*, 259.

(28) Navaratilova, Z. *Electroanalysis* **1991**, *3*, 799.

(29) Hua, C.; Smyth, M. R. *Talanta* **1992**, *39*, 391.

(30) Oyama, N.; Anson, F. C. J. *Electroanal. Chem.* **1980**, *127*, 640.

(31) Doblhofer, K.; Braun, H.; Lange, R. J. *Electroanal. Chem.* **1986**, *206*, 93.

(32) Lindholm, B. J. *Electroanal. Chem.* **1988**, *250*, 341.

(33) Oh, S.-M.; Faulkner, L. R. J. *Electroanal. Chem.* **1989**, *269*, 77.

(34) Dean, J. A. *Lange's Handbook of Chemistry*, McGraw-Hill Inc.: New York, 1973.

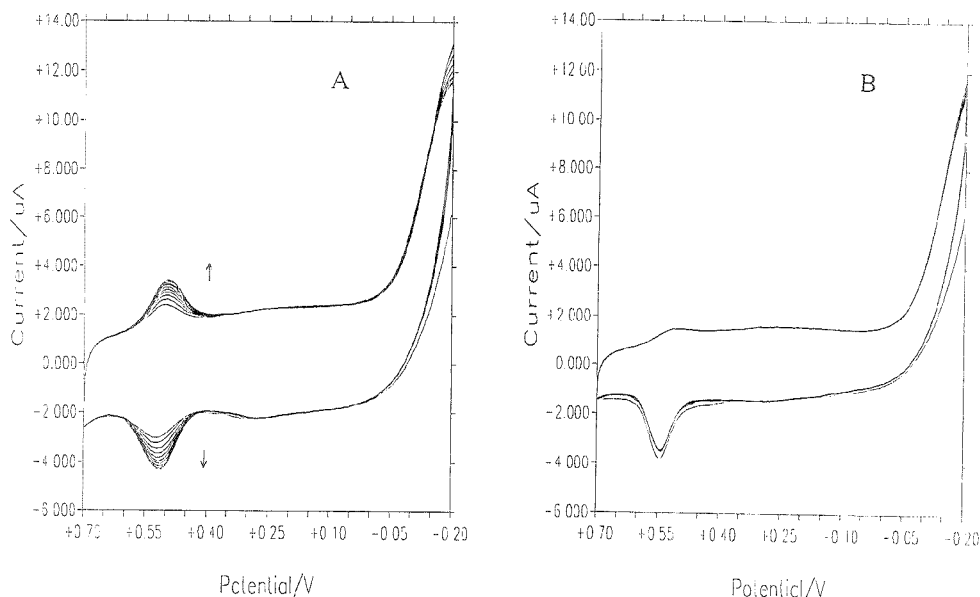


Figure 1. Cyclic voltammograms for 1 ppm mercury(II) in 0.025 M H₂SO₄ and 0.05 M KCl supporting electrolyte on (A) PVP/GFE and (B) GFE. Gold deposition time, 3 min; scan rate, 100 mV/s for 20 cycles.

supporting electrolyte media were studied. The results showed that no voltammetric response at all was detected in a medium containing both the nitrate and the sulfate anions, while a well-defined oxidation peak of mercury(II) at about +0.51 V vs Ag/AgCl was observed in the 0.05 M chloride medium. These results confirm that Hg(II) is complexed into anionic forms in the chloride medium. Note that, in contrast to the results obtained with the PVP/GFE, similar voltammetric responses were observed for the GFE in all three supporting electrolyte media. The results further confirmed the proper complexation of mercury(II) in the chloride medium.

The function of the PVP polymer in the detection of mercury(II) was further studied by cyclic voltammetry. For comparison, Figure 1 shows the cyclic voltammetric behavior of mercury(II) at the GFE and the PVP/GFE. As shown in Figure 1A, for the PVP/GFE, the growth in voltammetric response for the anionic forms of mercury(II) is clear as the film loads. Obviously, the mercurate(II) anions are incorporated into the PVP film by cycling at 100 mV/s between -0.2 and +0.7 V vs Ag/AgCl, a range that encompasses the standard potential of the redox mercury couple. On the contrary, no loading effect was observed at the GFE, as shown in Figure 1B. Actually, the ion-exchange process between the mercurate(II) anions and PVP was once again confirmed by these results. Most importantly, however, the redox mercury couple shows a more reversible behavior at the PVP/GFE than that at the GFE. It is well known that the sensitivity of square-wave anodic stripping voltammetry (SWASV) of adsorbed species is proportional to the degree of reversibility of the electrochemical reaction.^{35,36} Therefore, a clear advantage of using

the PVP/GFE in the SW mode with respect to the sensitivity of detection is expected.

Optimum Conditions for Analysis. In order to arrive at the optimum conditions for mercury(II) determination, two aspects should be considered: the electrode and the detection. As to the electrode aspect, the principal factors governing the performance of the PVP/GFE are the thickness of the PVP film and the deposition of gold. As to the detection aspect, the governing factors consist of the solution pH, the chloride concentration, the preconcentration time, the preconcentration potential, and the SW parameters.

Electrode Aspect. Effect of Film Thickness. The thickness of the PVP film directly controls the electrode performance. The optimum film thickness depends on both the diffusion process of the mercurate(II) anions in the film and the maximum mercury(II) loading that does not affect the adhesion of the film to the glassy carbon surface. The film thickness was varied by preparing the electrodes with different percent weights in methanol of PVP at a 3000 rpm spin-coating rate. The coating solution also contained 7% (vs the pyridine moiety) of 1,5-dibromopentane as a cross-linking agent. The electrode prepared with 0.25 wt % in methanol of PVP shows the best performance. Electrodes prepared with the optimum coating solution of 0.25 wt % in methanol of PVP at a 3000 rpm spin-coating rate were therefore used in all subsequent works.

Effect of Gold Deposition. Gold electrodeposited onto the glassy carbon/PVP substrate from gold(III)-containing solutions could be clearly seen as a golden deposit formed. The amount of gold plated depends on the deposition time. The peak current increases as the deposition time increases and reaches a maximum after 10 min. However, there is a reproducibility problem for

(35) Lovric, M.; Pranica, M. *J. Electroanal. Chem.* **1987**, *226*, 239.

(36) Lovric, M.; Komorsky-Lovric, S. *J. Electroanal. Chem.* **1988**, *248*, 239.

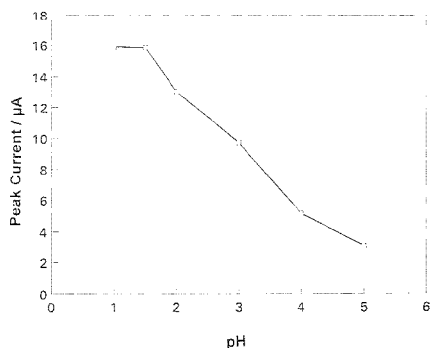


Figure 2. Effect of pH on the peak current of mercury(II) determination obtained at the PVP/GFE. $[\text{Hg}^{2+}] = 1.2$ ppm; preconcentration time (t_p), 200 s. Solution was unstirred during preconcentration. Gold deposition time, 3 min. SW parameters: modulation amplitude, 25 mV; modulation frequency, 15 Hz; effective scan rate, 60 mV/s.

electrodes prepared with a gold deposition time longer than 8 min. This phenomenon is similar to that observed in our previous study of fabricating nickel-sensitive Nafion/dimethylglyoxime mercury film electrode.²⁰ It is believed that the reduction of gold ions and the growth of the gold phase might take place at the glassy carbon/PVP interface. Hence, there is a possibility that the gold may fill up the pores of the PVP coating and extend beyond it. Indeed, such a process can still help to increase the electrode area and hence the detection signal. However, apparently, it can also cause a problem of reproducibility. A deposition time of 6 min was therefore used in most of the subsequent work.

Detection Aspect. Effect of pH and Chloride Concentration. In order to increase the anion-exchange capacity of the protonated PVP, the pH effect of the chloride solution should be evaluated first. By fixing the chloride concentration at 0.05 M, the dependence of the peak current on the acidity of the analyte solutions was studied, and the results obtained are shown in Figure 2. As can be seen, the modified electrode shows an optimum performance when pH is lower than 1.5. This is because the PVP polymer can be protonated more completely in more acidic solution. On the other hand, the mercury(II) solution starts to undergo hydrolysis reaction between pH 2 and pH 6 and eventually forms a hydroxide precipitate at pH > 6. This effect also contributes to the poor performance of the modified electrode at pH > 2, as shown in Figure 2. An acid solution of 0.025 M H_2SO_4 is therefore used in the subsequent experiments.

The effect of changing the chloride concentration in the medium was studied next. As previously mentioned, there must be a complexing reaction between Hg(II) and Cl^- in the solution to form the anionic forms of mercury(II). Figure 3 presents the effect of changing the chloride concentration on peak current (solid line) and peak potential (dashed line) for Hg(II) determination. As can be seen, the optimum concentrations of Cl^- lie in the range of 0.05–0.005 M in the analyte solution. Higher concentrations of Cl^- cause a depression of the peak current, which indicates a competitive effect between chloride ions and mercurate(II) anions. Lower concentrations of Cl^- are also unfavorable, due to the need of a reasonable excess of chloride ions for converting HgCl_2 into its anionic forms. As a matter of fact, the shifting of the mercury oxidation potential with increasing

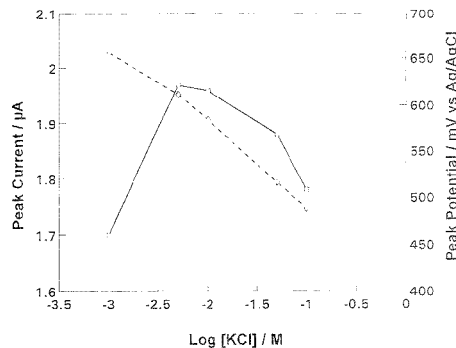


Figure 3. Effect of chloride concentration on peak current (left scale, solid line) and peak potential (right scale, dash line) of mercury(II) determination obtained at the PVP/GFE. $[\text{Hg}^{2+}] = 0.1$ ppm; gold deposition time, 6 min. Other conditions as in Figure 2.

amounts of chloride indicates a proper complexation of Hg(II) and Cl^- . A 0.005 M concentration of Cl^- was therefore used in the subsequent experiments.

Effect of Preconcentration Time and Potential. The effect of preconcentration potential on the SW response for mercury(II) is shown in Figure 4A. As can be seen, the peak current increases as the potential of the electrode becomes more positive between -0.6 and $+0.3$ V vs Ag/AgCl. This behavior is explained by the fact that mercurate(II) anions bear a negative charge; as a result, the adsorption of mercury(II) is favored at more positive potentials. However, the peak current drops rapidly as the potential becomes more positive than $+0.3$ V. As the preconcentration potential moves closer to the redox potential of the mercury couples, more of the deposited mercury was oxidized, causing a decrease in peak current. A preconcentration potential of $+0.3$ V vs Ag/AgCl was therefore chosen in all subsequent work.

The effect of preconcentration time on the SW response for mercury(II) is shown in Figure 4B. For 10 ppb mercury(II), the peak current increases as the preconcentration time increases and starts to level off around 14 min. It takes an even longer time for the peak current to level off for a lower concentration of mercury(II). This phenomenon is as expected and further confirms the ion-exchange process between PVP and mercurate(II) anions. Therefore, in order to increase the sensitivity of detection, longer times are needed for lower concentrations of mercury(II).

Effect of SW Parameters. The SW parameters that were investigated were the frequency, the pulse height, and the pulse increment. These parameters are interrelated and have a combined effect on the response. The response for mercury(II) increases with SW frequency, but at frequencies higher than 75 Hz, sloping background current renders the measurement difficult. An increase in the pulse height causes an increase in the mercury(II) peak up to 40 mV. The scan increment, together with the frequency, defines an effective scan rate; hence, an increase in either the frequency or the pulse increment results in an increase in the effective scan rate. Overall, the best signal-to-background current characteristics can be obtained with the following instrument settings: modulation amplitude, 40 mV; modulation frequency, 75 Hz; effective scan rate, 300 mV/s.

Analytical Characterizations. Reproducibility of the Modified Electrode. To characterize the reproducibility of the modified

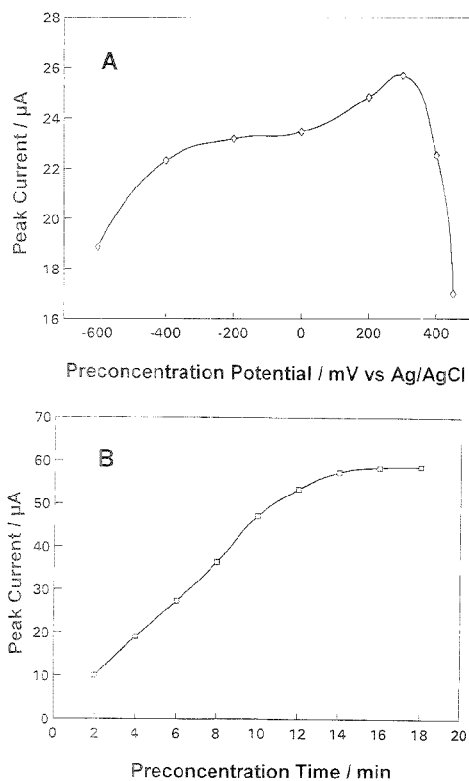


Figure 4. Effect of (A) preconcentration potential ($t_p = 6$ min) and (B) preconcentration time ($p_p = +0.3$ V vs Ag/AgCl) on the peak current of 10 ppb mercury(II) obtained at the PVP/GFE. Solution was stirred during preconcentration. SW parameters: modulation amplitude, 40 mV; modulation frequency, 75 Hz; effective scan rate, 300 mV/s.

electrode, repetitive preconcentration–measurement–regeneration cycles were carried out. The electrode was regenerated in 0.1 M H_2SO_4 at +0.7 V vs Ag/AgCl for 100 s. The result of 10 successive measurements showed a relative standard deviation of 4.4% for 10 ppb mercury(II) with a preconcentration time of 6 min. Thus, the electrode renewal gives a good reproducible surface.

Sensitivity, Linear Range, and Detection Limits. Calibration data were obtained under the optimum experimental conditions mentioned above. Figure 5 presents SW voltammograms for the PVP/GFE after having been contacted with mercury for a 6-min preconcentration time at concentrations of 1 (a), 10 (b), 20 (c), 30 (d), and 40 ppb (e). In all cases, a stripping response was observed at a potential in the vicinity of +0.61 V vs Ag/AgCl. The observed peak currents were then used for the construction of the calibration plot. The plot shows a very linear behavior with slope ($\mu\text{A/ppb}$), intercept (μA), and correlation coefficient of 2.60, 0.51, and 0.9998, respectively. The linear range for a 6-min preconcentration is from 0.5 to 40 ppb mercury(II), and the detection limit is 0.1 ppb ($S/N = 3$). The sensitivity started to decrease when the concentration of mercury(II) was higher than

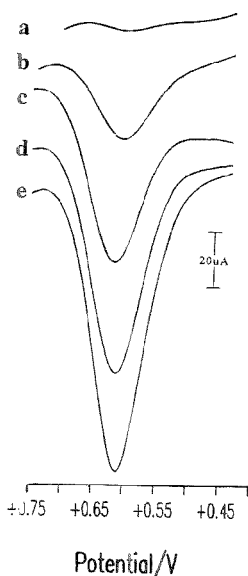


Figure 5. Dependence of the SWASV peak current on increasing mercury concentrations of (a) 1, (b) 10, (c) 20, (d) 30, and (e) 40 ppb. $t_p = 6$ min. Other conditions as in Figure 4.

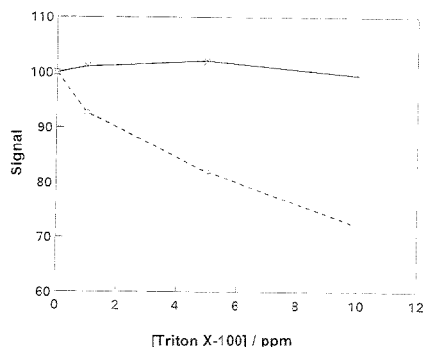


Figure 6. Effect of the surfactant Triton X-100 at different concentrations on the SW stripping response for 10 ppb mercury(II) with the PVP/GFE (solid line) and the GFE (dashed line). $t_p = 4$ min, $p_p = +0.3$ V vs Ag/AgCl. Other conditions as in Figure 4. Peak currents are given relative to those obtained with no added Triton X-100.

40 ppb. An even lower detection limit could be achieved for mercury(II), provided that the preconcentration time was longer than 6 min, as indicated by Figure 4B.

Interferences. Various ions were examined with respect to their interference with the determination of mercury. For the GFE, elements which can be reduced to the elemental state on the gold electrode and at the same time are soluble in gold are likely interferents. For the PVP/GFE, the number of species interacting in this manner is limited to those present in the anionic form due to the presence of the PVP film. For 10 ppb mercury(II) with a 4-min preconcentration time, the results showed that over 1000-fold excess concentration of zinc(II), nickel(II), and tin(II) did

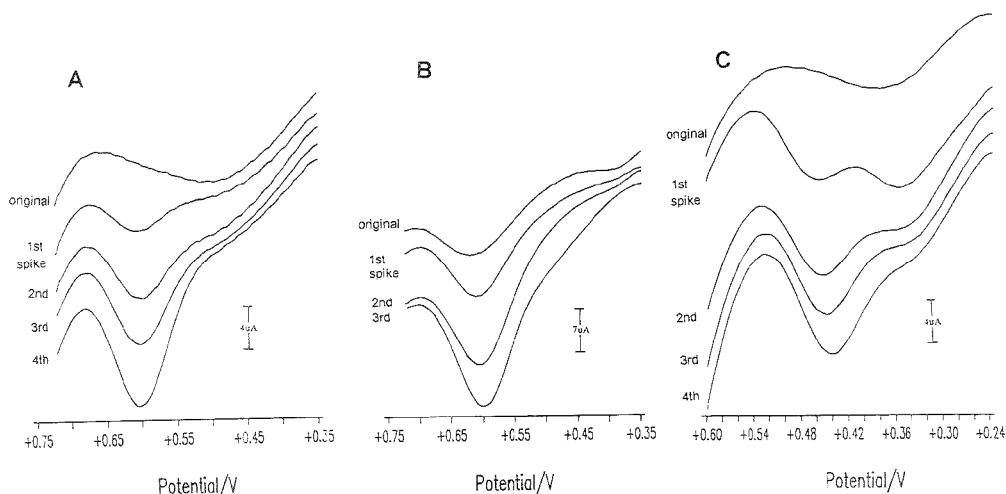


Figure 7. Typical SW voltammograms of the three water samples obtained by the PVP/GFE: (A) The original and spiked (1 ppb/spike) groundwater, (B) the original and spiked (2 ppb/spike) electroplating wastewater, and (C) the original and spiked (1 ppb/spike) seawater.

Table 1. Determination of Mercury(II) in Groundwater, Electroplating Wastewater, and Seawater

	ground-water	electroplating wastewater	sea-water
original detected value (ppb)		2.31 ± 0.16	
spike (ppb)	1.0	2.0	1.0
detected value after spike (ppb)	1.01 ± 0.03	4.27 ± 0.18	1.01 ± 0.04
recovery (%)	101	98	101
real value ^a (ppb)		23.1 ± 1.6	

^a Real value is obtained by multiplying the detected value and the dilution factor. Number of samples assayed, 6.

not influence the mercury response. Copper(II), lead(II), thallium(III), cobalt(II), and arsenic(III) were found to interfere at a 1000-fold excess, and selenium(IV), chromium(VI), arsenic(V), vanadium(V), silver(I), and bismuth(III) interfered at a 100-fold excess. Note that copper(II) is generally considered as a major interference in the determination of mercury(II) on a gold film electrode.⁹⁻¹³ The mercury peak may be easily overlapped or even shielded by the peak of copper, provided that the copper concentration is in great excess of the mercury concentration in the sample investigated. However, this problem can actually be largely overcome by using the proposed modified electrode as indicated above.

The interference effects caused by surface-active compounds in ASV when bare-type gold electrodes are used are well recognized. One function of the PVP membrane coating on the GFE is to prevent the organic interferences from reaching the interface at which the deposition/stripping takes place. Triton X-100 was used to simulate the effect of a typical nonionic surfactant, and Figure 6 shows how the 10 ppb mercury(II) stripping peak current is affected by different concentrations of Triton X-100. As can be seen, the detection can tolerate the presence of Triton X-100 at least up to 10 ppm with the PVP/GFE (Figure 6, solid line). Compared to the same experiments

carried out with the GFE (Figure 6, dashed line), the tolerance was largely improved.

Practical Applications. The analytical utility of the PVP/GFE was assessed by applying it to the determination of mercury(II) in groundwater, electroplating wastewater, and seawater. The results summarized in Table 1 are those for the original and spiked water samples. Typical SW voltammograms for the original and spiked water samples are provided in Figure 7. As can be seen, the mercury stripping peaks are clearly displayed for all three spiked water samples. The recovery of the spiked mercury was also observed to be high in all three different water samples. These results provide sufficient evidence of a high feasibility of the PVP/GFE employed for determining mercury for the different water samples. Note that the dilution factors used for detection were 1.1, 10, and 5 for groundwater, electroplating wastewater, and seawater, respectively. The amount of mercury(II) that occurs in natural waters is typically below 0.1 ppb,³⁷ and this is indeed the case for groundwater and seawater in this study. The amount of mercury(II) therefore cannot be detected by the proposed method with a 6-min preconcentration time. Actually, even with a 30-min preconcentration time, the amount of mercury(II) in groundwater and seawater was still not detectable. Nevertheless, since the 0.1 ppb mercury stripping peak was clearly displayed for these two water samples with a 30-min preconcentration time, the amount of mercury(II) in groundwater and seawater was therefore believed to be well below 0.1 ppb. Finally, the shift in peak potential for mercury in seawater was due to the presence of a large amount of chloride ions, and the direction of the shift was quite reasonable, as can be seen in Figure 3.

CONCLUSIONS

The results show that the application of the PVP/GFE in the determination of trace mercury(II) in real samples is very

(37) Von Burg, R.; Greenwood, M. R. In *Metals and Their Compounds in the Environment. Occurrence, Analysis and Biological Relevance*; Merian, E., Ed.; VCH: Weinheim, Germany, 1991; Chapter II.20.

promising. The recovery of the spiked mercury was observed to be good in three different water samples of groundwater, electroplating wastewater, and seawater. The PVP/GFE not only offers considerably higher resistance to organic interferences and common ions than the conventional gold film electrode but also yields higher sensitivity when used in conjunction with the SW voltammetry. The PVP/GFE also possesses good selectivity and can be easily regenerated with exposure to sulfuric acid by electrochemical means. Finally, the mechanical stability of the gold film is also improved.

ACKNOWLEDGMENT

The authors gratefully acknowledge financial support from the National Science Council of the Republic of China under Grants NSC 84-2732-M-005-001 and NSC 84-2113-M-005-015.

Received for review February 17, 1995. Accepted June 29, 1995.*

AC950179+

* Abstract published in *Advance ACS Abstracts*, August 15, 1995.

Imaging of Immobilized Antibody Layers with Scanning Electrochemical Microscopy

Gunther Wittstock,[†] Ke-jia Yu,[‡] H. Brian Halsall, T. H. Ridgway, and William R. Heineman*

Department of Chemistry, University of Cincinnati, P.O. Box 210172, Cincinnati, Ohio 45221-0172

Visualization of immobilized antibodies can be achieved with scanning electrochemical microscopy (SECM) by saturation of the antigen binding sites with an alkaline phosphatase–antigen conjugate, which catalyzes hydrolysis of the redox-inactive 4-aminophenyl phosphate to the redox-active 4-aminophenol (PAP). PAP was detected in the collection mode at an amperometric SECM tip. The tip current reflects the density of active binding sites in the immobilized antibody layer. The application of this approach for immunosensing research has been demonstrated with the optimization of a covalent immobilization procedure of antibodies on glass. The special advantages and present limitations of the procedures are discussed.

Immunoassays and immunosensors with electrochemical detection schemes are being developed in many laboratories.¹ Because highly specific antibodies can be raised against a wide variety of substances, much attention has been focused on the application of antibodies as selective agents for analytical purposes. The immobilization of the antibodies on a surface represents one preferred way in immunosensing to facilitate the separation of the formed Ag–Ab complexes from the sample.

The optimization of assay or sensor surfaces is complicated by a lack of suitable methods to characterize their properties. Until now, layers of immobilized immunoglobulins have been investigated with spectroscopic and ellipsometric techniques.^{2–9} These techniques detect the presence of proteins at the surface but do not allow one to determine whether the immobilized biomolecules still exhibit their binding function. The same limitations apply to electrochemical inhibition measurements¹⁰ or impedance measurements,¹¹ which might be carried out if the antibodies were immobilized directly on an electrode surface. The optimization

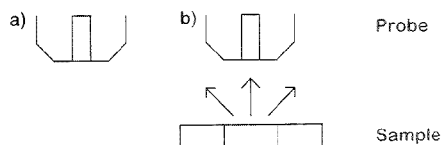


Figure 1. Principle of the SECM collection mode. (a) In the bulk solution, no Faradaic current is detected. (b) The tip electrode detects the product of the reaction at the substrate.

of biosensor surfaces is delayed because a low or missing output signal can have two possible causes: failure to properly immobilize the antibodies or inhibition of the detection mechanism. Lengthy procedures are needed to pin down the limiting factors. This is normally done by preparing assay series with variation of one preparation step.

After Engstrom et al.¹² had probed diffusion layers near electrodes using microelectrodes, Bard et al.¹³ introduced scanning electrochemical microscopy (SECM). The latter group^{14,15} and Wang et al.¹⁶ were successful in detecting immobilized enzymes using SECM measurements. Two modes of operation are possible. In the simplest case, a microelectrode is moved over the immobilized enzymes and detects the product of the enzymatic reaction (collection mode, Figure 1). The probe electrode may be a very small amperometric electrode,¹⁷ an amperometric enzyme electrode¹⁸ or a pH-sensitive microelectrode.¹⁹ We will follow the terminology of Bard et al. and refer to the scanning probe as the tip electrode. Compared to collector experiments, a much higher lateral resolution has been demonstrated with the enzyme-generated feedback mode.^{14,15} A quasi-reversible redox mediator enables communication between an amperometric tip electrode and the enzyme-modified surface. The mediator is converted at the tip electrode, and the product of this reaction represents a cofactor for the enzymatic reaction, by which in

Present address: Department of Chemistry, University Leipzig, Linnéstrasse 2, D-04103 Leipzig, Germany.

[†] Present address: Sun Chemical Corp., 631 Central Ave., Carlstadt, NJ 07072.

- (1) Ngo, T. T., Ed. *Electrochemical Sensors in Immunological Analysis*; Plenum Press: New York, 1987.
- (2) Norde, W. In *Polymer Science and Technology, Vol. 12, Adhesion and Adsorption of Polymers*; Lee, L. H., Ed.; Plenum Press: New York, 1980; pp 801–825.
- (3) Grant, W. H.; Dehl, R. E. In *Polymer Science and Technology, Vol. 12, Adhesion and Adsorption of Polymers*; Lee, L. H., Ed.; Plenum Press: New York, 1980; pp 827–835.
- (4) Larentev, V. V.; Chasovnikova, L.; Sorokin, J. In *Polymer Science and Technology, Vol. 12, Adhesion and Adsorption of Polymers*; Lee, L. H., Ed.; Plenum Press: New York, 1980; p 847.
- (5) Morrissey, B. W.; Smith, L. E.; Stromberg, R. R.; Fenstermaker, C. A. *J. Colloid Interface Sci.* **1976**, *56*, 557–563.
- (6) Morrissey, B. W. *Ann. N. Y. Acad. Sci.* **1977**, *283*, 50–64.
- (7) Morrissey, B. W.; Han, C. C. *J. Colloid Interface Sci.* **1978**, *65*, 423–431.
- (8) Fair, B. D.; Jamieson, A. M. *J. Colloid Interface Sci.* **1980**, *77*, 525–534.
- (9) Jönsson, U.; Lundström, I.; Rönnerberg, I. *J. Colloid Interface Sci.* **1987**, *117*, 127–138.

(10) Emons, H.; Schmidt, T. In *Biosensors—Fundamentals, Technologies and Applications*; Scheller, F.; Schmid, R. D., Eds.; VCH: Weinheim, 1992; pp 287–290.

(11) Caprani, A.; Lacour, F. *Bioelectrochem. Bioenerg.* **1991**, *25*, 241–258.

(12) Engstrom, R. C.; Weber, M.; Wunder, D. J.; Burgess, R.; Winquist, S. *Anal. Chem.* **1986**, *58*, 844–848.

(13) Liu, H.-Y.; Fan, F.-R. F.; Lin, C. W.; Bard, A. J. *J. Am. Chem. Soc.* **1986**, *108*, 3838–3839.

(14) Pierce, D. T.; Unwin, P. R.; Bard, A. J. *Anal. Chem.* **1992**, *64*, 1795–1804.

(15) Pierce, D. T.; Bard, A. J. *Anal. Chem.* **1993**, *65*, 3598–3604.

(16) Wang, J.; Wu, L.-H.; Li, R. *J. Electroanal. Chem.* **1989**, *272*, 285–292.

(17) Lee, C.; Kwak, J.; Bard, A. J. *Proc. Natl. Acad. Sci. U.S.A.* **1990**, *87*, 1740–1743.

(18) Horrocks, B. R.; Schmidtke, D.; Heller, A.; Bard, A. J. *Anal. Chem.* **1993**, *65*, 3605–3614.

(19) Horrocks, B. R.; Mirkkin, M. V.; Pierce, D. T.; Bard, A. J.; Nagy, G.; Toth, K. *Anal. Chem.* **1993**, *65*, 1213–1224.

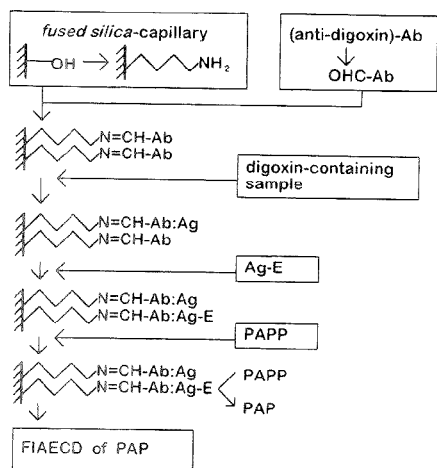


Figure 2. Schematic representation of an electrochemical immunoassay according to ref 20. Ab, antibody; Ag, antigen; Ag-E, enzyme-labeled antigen; PAPP, *p*-aminophenyl phosphate; PAP, *p*-aminophenol; FIAECD, flow injection analysis with electrochemical detection.

return the educt (substrate) is regenerated for the electrochemical reaction at the tip electrode. This leads to an increase of the tip current i_T over the tip current in the bulk solution $i_{T_{\text{ref}}}$. At an unmodified insulating surface, the tip current falls below the reference value $i_{T_{\text{ref}}}$, because the surface blocks the diffusion of the mediator toward the tip electrode surface.

After reaction with a suitable enzyme-labeled antigen or hapten, appropriate SECM modes for imaging enzyme activity may be applied to visualize the immobilized antibodies. To demonstrate this approach, the immobilization procedure of capillary enzyme immunoassay for the antigen (Ag) digoxin,²⁰ developed in this laboratory, has been investigated. The general principle of the assay is outlined in Figure 2. The assay capillary is prepared by coupling an oxidized monoclonal anti-digoxin antibody (Ab) to the aminated inner surface of a fused silica capillary. The digoxin-containing sample is introduced into a 10-cm piece of the capillary by ultrafiltration, and digoxin (Ag) is bound to the antibodies. After rinsing, remaining free binding sites are saturated with the alkaline phosphatase-labeled digoxin (Ag-E). The enzyme labels convert the added redox-inactive enzyme substrate 4-aminophenyl phosphate (PAPP) to the redox-active 4-aminophenol (PAP), which is detected amperometrically in a flow-through setup (FIAECD). The immobilization of the antibody was studied on pieces of microscope slides. The fused silica capillary material can be considered as an "ideal glass"²¹ because its chemical composition is similar to that of glass. The fused silica has a greater mechanical flexibility and contains fewer surface metal contaminants. Since flat fused silica specimens could not be obtained from commercial sources, carefully cleaned glass slides were used as the closest match to the capillary material in question.

The collection mode of the SECM was chosen for this investigation because the enzyme label does not require a redox-

active cosubstrate and, therefore, cannot be imaged with the SECM feedback mode.

EXPERIMENTAL SECTION

Instruments. Differential pulse voltammograms were recorded with a Bioanalytical Systems electrochemical analyzer, BAS 100A (Bioanalytical Systems, West Lafayette, IN), connected to a glassy carbon working electrode (BAS), a Ag/AgCl/3 M NaCl reference electrode (BAS), and a platinum wire auxiliary electrode. SECM measurements were performed with a home-built SECM consisting of a modified commercially available micropositioning system driven by three Inchworm motors (Burleigh Inc., Fishers, NJ), a home-built bipotentiostat,²² and an analog-digital (AD)/digital-analog (DA) converter.²³ Details of the hardware and software of the SECM were published elsewhere.²⁴ The electrochemical three-electrode cell consisted of a platinum tip electrode of 30 μm diameter,²⁵ a platinum wire as auxiliary electrode, and a silver wire as quasi-reference electrode. The solution for the SECM measurements contained 0.1 M potassium chloride to define the potential of the quasi-reference electrode. Its potential was +82 mV versus the Ag/AgCl/3 M NaCl reference electrode, to which all potentials are referred in this paper. The tip electrode was held at +280 mV in all experiments, and the horizontal scan rate was 7.9 $\mu\text{m s}^{-1}$.

Oxidation of Antibodies. Five milligrams of monoclonal goat (anti-digoxin) Ab (Centers for Disease Control, Atlanta, GA) in 300 μL of 0.1 M acetate buffer (pH 5.5) was mixed with 6 μL of 0.5 M NaIO₄ solution and allowed to react for 20 min in the dark. The functionalized antibodies were separated from the low molecular weight components of the reaction mixture by gel filtration on a Sephadex G25 column (Pharmacia LKB, Uppsala, Sweden) and eluted with acetate buffer (pH 4.5, 0.1 M acetate, 0.15 M NaCl, 0.02% NaN₃).

Preparation of Test Plates and SECM Investigation. Microscope slides were cut into pieces of 2.5 cm \times 2.0 cm and cleaned with boiling Piranha solution (1 volume part 30% H₂O₂, 4 volume parts 96% H₂SO₄). **Caution!** This mixture reacts violently with all organic materials. The solution has to be handled with extreme care to avoid personnel injury and property damage. After being rinsed with water, the plates were treated with 3 M NaOH solution. Afterward, the formed silanol groups were allowed to react with [3-(2,3-epoxypropoxy)propyl]trimethoxysilane (Aldrich, Milwaukee, WI) in 0.1 M acetate buffer (pH 5.5) at 90 $^{\circ}\text{C}$ for 5 h. Poly(ethylene glycol) (PEG, mean molecular mass 3350 g mol⁻¹, 16% in 1,4-dioxane; Sigma, St. Louis, MO) was coupled to the immobilized epoxy function. Terminal hydroxyl groups of the PEG were activated with *N,N'*-dicarbonyldiimidazole (28.5% in 1,4-dioxane; Aldrich; 15 min, room temperature). The activated group forms a carbazic acid ester with adipic acid dihydrazide (0.38 M solution in 1 M acetate buffer, pH 3.0, 12 h). The modified surface was covered by waterproof Scotch tape (3M, St. Paul, MN) with five application holes (1600 μm diameter) previously punched into the tape. The oxidized antibodies were incubated in these holes for 36 h (4 $^{\circ}\text{C}$), during which time they were covalently attached

(22) Blubaugh, E. A.; Russell, G.; Racke, M.; Blubaugh, D. A.; Ridgway, T. H.; Mark, H. B., Jr. In *Diagnostic Biosensor Polymers*; Usmani, A. M.; Akmal, N., Eds.; ACS Symposium Series 556; ACS: Washington, DC, 1994; Chapter 11.

(23) Paul, D. W. Ph.D. Thesis, University of Cincinnati, Cincinnati, OH, 1986.

(24) Wittstock, G.; Emons, H.; Ridgway, T. H.; Blubaugh, E. A.; Heineman, W. R. *Anal. Chim. Acta* 1994, 293, 285-302.

(25) Matysik, F.-M. Diploma thesis, Universität Leipzig, Leipzig, Germany, 1990.

(20) Kancig, N.; Xu, Y.; Kumari, A.; Halsall, H. B.; Heineman, W. R.; Kissinger, P. T. *Anal. Chim. Acta* 1994, 287, 253-258.

(21) Lee, M. L.; Wright, B. W. *J. Chromatogr.* 1980, 184, 235-312.

to the aminated surface. Subsequently, the plates were rinsed thoroughly with Krebs-Ringer solution (138 mM NaCl, 11 mM $MgCl_2$, 0.02% NaN_3 , adjusted to pH 7.5 with HCl). An excess of alkaline phosphatase-labeled digoxin (Immunotec, Boston, MA) was allowed to react with the immobilized antibodies. After rinsing, the cover was removed, and the plates were placed in the SECM cell. The enzyme substrate was added (4 mM PAPP, 1 mM $MgCl_2$, 0.1 M KCl, 0.02% NaN_3 , 0.1 M tris(hydroxymethyl)aminomethane (Tris), adjusted to pH 9.0 with HCl). Solutions of 4 mM PAP or 4 mM PAPP in 1 mM $MgCl_2$, 0.02% NaN_3 , 0.1 M Tris-HCl, pH 9.0, were used for the DPV investigation to determine the optimum detection potential. The redox-active PAP was formed under the condition of enzyme-substrate saturation²⁵ and was detected in the collection mode of the SECM.

The positioning of the tip very close to the substrate represents a problem in collection mode experiments because there is no general relation available between tip-sample distance and current magnitude. This situation differs from SECM feedback experiments, where a general relation between tip-sample distance and current magnitude has been established²⁷ and can be applied to determine tip-sample distances from the steady-state current at microdisk electrodes in close proximity to insulating or conducting substrates. Several approaches have been described to perform tip positioning in collection mode experiments. The most accurate approach is certainly the use of the feedback mode to position the tip at a defined distance from the sample for a subsequent collection mode experiment.¹⁹ In the cited example, dissolved oxygen was used as a redox-active agent for the observation of the negative feedback over an insulating sample. Preliminary studies had shown for the system under study here that reliable and reproducible results could be expected only if the PAPP was added to a solution that had already been purged thoroughly by nitrogen to remove dissolved oxygen. It had also been shown that the enzyme kinetics depends strongly on a well-balanced solution composition, pH, and the exclusion of inhibitors.²⁶ Therefore, we decided not to add a second redox mediator to the solution, since this would make the comparison of the SECM results with the actual immunoassay more difficult because interference with the enzyme reaction might occur. Two alternative tip positioning procedures are known from the literature. The determination of the tip-sample distance from the solution resistance¹⁸ is feasible only if the sample is an electronic conductor. For the glass plates used here, a method was applied which had been used previously for other collection mode experiments.^{18,28} The tip electrode was moved down over the unmodified regions of the sample at a scan rate of $1.4 \mu m s^{-1}$. The motion was halted when contact between tip and glass plate could be detected clearly from visual inspection. In such a situation, the electrode could still slide laterally on the unmodified glass surface without damage. The sliding could be detected very sensitively from spikes in the current versus location plots recorded during such lateral test scans above the unmodified glass surface. The spikes show a very abrupt rise and a slow decrease ("tailing"), which have not been observed in undisturbed SECM experiments. The tip was then retracted in $5\text{-}\mu m$ increments at a scan rate of $1.4 \mu m s^{-1}$ until no spikes were recorded in lateral test scans. This was taken as an indication of a contact-free

(26) Thompson, R. Q.; Barone, G. C.; Halsall, H. B.; Heineman, W. R. *Anal. Biochem.* **1991**, *192*, 90-95.

(27) Kwak, J.; Bard, A. J. *Anal. Chem.* **1989**, *61*, 1221-1227.

(28) Scott, E. R.; White, H. S.; Phipps, J. B. *Anal. Chem.* **1993**, *65*, 1537-1545.

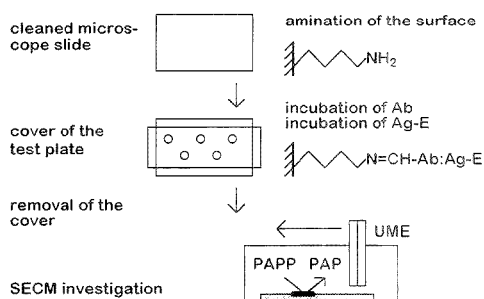


Figure 3. Schematic representation of the sample preparation for the investigation of antibody immobilization with the SECM. UME ultramicroelectrode, or tip electrode.

movement. However, the actual distance between sample and microdisk electrode may be larger than $5 \mu m$, because the contact between the tip and the sample was most likely due to the shielding of the electrode. The total diameter of the shielding was about 1 mm. Experiments with the same microdisk electrode in feedback experiments above gold surfaces suggest that the actual distance between the microdisk electrode and the glass surface may range between 10 and $20 \mu m$ and cannot be specified more accurately. Once the vertical position had been reached, it was held constant throughout the scans over the five spots on one test plate. The plate was placed in a cell with a flat bottom mounted on an optical table. The tilt of the optical table was controlled by two screws to ensure that its surface was parallel to the x - y plane of the micropositioning system. The success of the adjustment was routinely checked by a minilevel and by feedback scans over large gold electrodes. Since the tip-sample distance cannot be controlled more accurately, only measurements made over spots of the same plate can be compared semiquantitatively, while plate-to-plate comparisons are of qualitative nature only.

After the vertical adjustment, the tip approached horizontally the spots with immobilized Ab. To simplify the search for the modified parts of the glass surface, the areas had been marked on the unmodified side of the transparent plates with a waterproof pen. Figure 3 summarizes the chosen approach. It allowed the investigation of various antibody coatings under the same conditions with one filling of the SECM cell and one vertical positioning of the tip electrode only.

To study nonspecific adsorption, oxidized antibodies were incubated for 36 h on a cleaned but not aminated microscope slide. The subsequent preparation steps were the same as above.

RESULTS AND DISCUSSION

The optimum amperometric detection potential of PAP in the presence of PAPP was determined using differential pulse voltammetry (Figure 4). A potential of +280 mV was used at the tip electrode for the SECM investigations. At this potential, PAP is oxidized under diffusion-controlled conditions, while the oxidation of PAPP proceeds only at potentials more positive than +360 mV.

Figure 5 shows five horizontal SECM scans over areas with immobilized antibodies. Different dilutions of the antibody stock solution were applied to the five regions. Afterward, all spots were incubated with the same solution of phosphatase-labeled antigen.

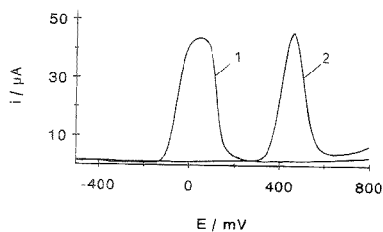


Figure 4. Differential pulse voltammograms of (1) 4 mM PAP in 1 mM MgCl_2 , 0.02% NaN_3 , 0.1 M Tris-HCl, pH 9.0, and (2) 4 mM PAP in 1 mM MgCl_2 , 0.02% NaN_3 , 0.1 M Tris-HCl, pH 9.0. Potential scan rate, 20 mV s^{-1} ; potential pulse height, 50 mV for both experiments.

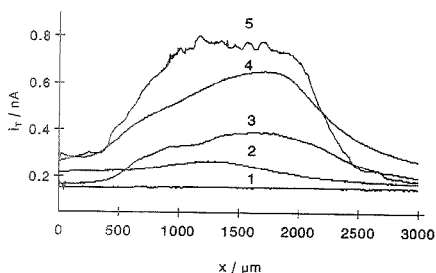


Figure 5. Horizontal line scans across spots with covalently attached monoclonal anti-digoxin Ab after reaction with enzyme-labeled digoxin. Dilutions of the incubated Ab solutions: (1) no Ab solution applied, (2) 1:8, (3) 1:4, (4) 1:2, and (5) undiluted antibody stock solution, 0.141 mg mL^{-1} protein. Measurement solution: 4 mM PAP, 1 mM MgCl_2 , 0.1 M KCl, 0.02% NaN_3 , 0.1 M Tris-HCl, pH 9.0. Tip scan rate, 7.9 $\mu\text{m s}^{-1}$; tip-substrate distance, 10–20 μm ; tip radius, 15 μm ; tip potential, +280 mV ($\text{Ag}/\text{AgCl}/3\text{M NaCl}$).

After the samples were fixed in the SECM cell and PAP solution was added, the enzymes, which had been retained by the immunological reaction between anti-digoxin Ab and enzyme-digoxin conjugates, converted the redox-inactive substrate PAP to the redox-active PAP. Because Ag–Ab complexes are attached at only five very small areas and the measurement takes only a short time, the bulk solution composition is not altered markedly. Thus, a concentration gradient of PAP is formed and can be visualized with the SECM in the collection mode. Curve 1 in Figure 5 shows the control experiment in which no Ab solution had been incubated on the glass. Consequently, the applied solution of phosphatase-labeled digoxin contacts the aminated surface. The signal intensity is not changed relative to the background at this spot, which demonstrates that the labeled antigen is not adsorbed or bound to the modified surface without a previously attached Ab.

Curves 2–5 in Figure 5 correspond to increasing concentrations of applied antibody solutions. The signals at half-height match fairly well the diameter of the holes in the cover during incubation of the Ab ($\sim 1600 \mu\text{m}$). In curves 2–5, the current rises only where phosphatase–digoxin conjugates are bound by immobilized Ab. If the PAP concentration is high enough to maintain zero-order enzyme kinetics, the magnitude of the current represents a measure for the density of active binding sites in the layer of immobilized antibodies. Two consecutive line scans were recorded over each modified glass area, of which one is shown in Figure 5. There were no systematic differences between

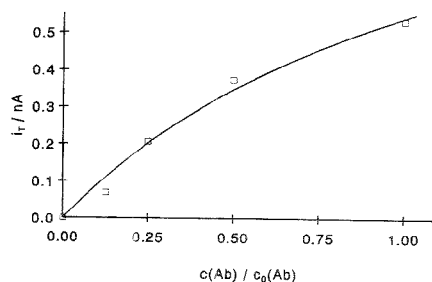


Figure 6. Plot of the signal height of Figure 5 (\square) versus the dilution of applied Ab solution. Solid line is the numeric fit $i_r/nA = 1.2[0.803x/(1 + 0.803x)]$, where $x = c(\text{Ab})/c_0(\text{Ab})$.

the two scans across the same spot. The lack of an apparent time dependency of the recorded signals over a spot can be understood best by considering the high PAP concentration supplied in a comparatively large cell volume (5 mL) and the small ratio of Ab-modified to unmodified parts of the glass surface, leading to a constant product formation rate at the modified spots (controlled by the amount of immobilized enzyme) and dispersion of the products into a quasi-infinite reservoir (diffusion controlled). The same conclusion can also be drawn from the only slight increase in the background currents due to the slow increase in the bulk PAP concentration during the measurement (2 h for all curves, ~ 20 min for one spot).

A plot of the signal height versus the dilution of the applied serum shows a saturation curve (Figure 6). The solid line was calculated using the mathematical structure of a Langmuir isotherm. Because of the good fit to the experimental data, it is tempting to speculate that the form of the product accumulation curve is the result of Langmuir-type adsorption (Ab monolayer, limited number of equivalent binding places for antibody immobilization on the aminated surface) rather than being caused by a dendritic growth pattern in which a covalently attached antibody provides terminal NH_2 groups for the covalent attachment of further antibodies. However, it should be noted that, under the conditions when the tip electrode moves slowly in close proximity across an Ab-modified spot, substrate depletion cannot be excluded by worst-case estimations, and the limited number of concentration steps, as well as the nonequilibrium character of the studied immobilization procedure, prohibits a detailed investigation in this form. Further experiments are needed to clarify this point.

Only in the case of the highest concentration of the incubated Ab solution (Figure 5, curve 5) could inhomogeneities of the modified surface be resolved with the SECM. A two-dimensional horizontal scan of the same area is shown in Figure 7. The decreasing currents in the left foreground mark the transition to the unmodified glass surface. The transition is not sharp because the immobilization procedure in holes of Scotch tape does not result in absolutely abrupt changes from modified to unmodified surfaces and because the resolution of the images taken with the collection mode of the SECM suffers from diffusional blurring more than corresponding images recorded employing the SECM feedback mode.

Nonspecific adsorption of the antibodies is regarded as a major source of systematic errors in this type of immunoassay. Adsorptively immobilized antibodies may be washed out during one

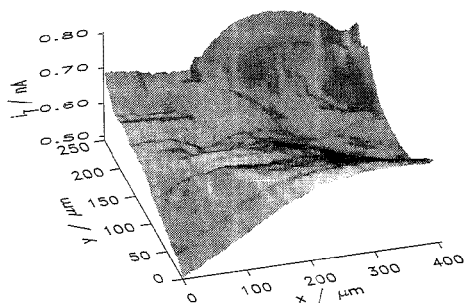


Figure 7. Two-dimensional scan over the area of curve 5 in Figure 5. Experimental parameters were the same as in Figure 5.

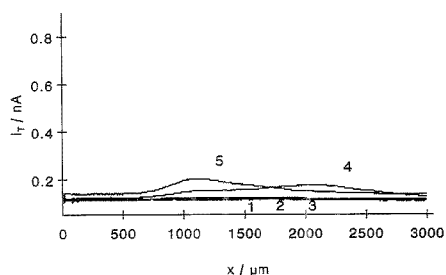


Figure 8. Horizontal scans over adsorptively immobilized antidigoxin Ab on glass after reaction with enzyme-labeled Ag. Dilution of the applied Ab solution: (1) no Ab solution applied, (2) 1:8, (3) 1:4, (4) 1:2, and (5) undiluted antibody stock solution, 0.326 mg mL^{-1} protein. Other experimental parameters were the same as in Figure 5.

of the rinsing steps in the course of the assay. This would lead to a change in the number of binding sites during the assay, which can cause errors that are difficult to quantify. To estimate the influence of nonspecific adsorption in this immunoassay, different antibody dilutions were incubated on the cleaned but not aminated surface of the microscope slide. The corresponding horizontal scans are shown in Figure 8. Curve 1 in Figure 8 was obtained from the spot where no Ab solution had been incubated, similar to Figure 5, curve 1. The enzyme-labeled Ag is not retained by the non-aminated surface. Curves 2–5 correspond to increasing concentrations of the applied Ab solution. No significant difference from the control experiment (curve 1) is found for the Ab dilutions 1:8 (curve 2) and 1:4 (curve 3). This concentration range was used to prepare the capillaries for the assay. Detectable amounts of antibodies adsorb to the glass surface if more concentrated Ab solutions are incubated (curves 4 and 5). The adsorbed antibodies are able to bind enzyme-labeled antigen. The signal obtained for the nonspecific adsorption of antibody (curve 5) is approximately equal to 10% of the current resulting from covalent attachment of the most concentrated Ab solution to the aminated surface (Figure 5, curve 5).

The SECM investigation indicated that in the concentration range used to prepare the capillaries for the assay, neither inhomogeneities in the order of hundreds of micrometers are to be expected, nor should nonspecific adsorption of antibody or the labeled antigen to the glass surface influence the assay result.

CONCLUSION

Although the SECM experiments exploiting the enzymatically generated feedback effect^{14,15} result in images with better lateral resolution than those in this paper, the application of the collection mode was mandatory for imaging phosphatase activity because no redox-active cosubstrates are converted in this enzymatic reaction. The achieved resolution is comparable to those obtained with other collection mode experiments, e.g., the imaging of a urease gel target recorded with a potentiometric microelectrode.¹⁹ Compared to previous reports,^{14,15} the situation is more complicated in this work because the primary immobilized agent is the antibody, which is made detectable by the reaction with a suitable antigen–enzyme conjugate. For that reason, the total enzyme activity per area is smaller than that in enzyme gels. A prospective application of the enzymatically generated feedback mode to achieve a higher lateral resolution in conjunction with smaller tip electrodes would require an oxidase-labeled antigen and a tremendous increase in the sensitivity of the bipotentiostat. The latter follows from the quantitative detection limit given by Bard et al.¹⁴

The possibility to image the density of *active* binding sites on modified surfaces regardless of optical properties (transparent or reflecting) or their electrical nature (conductor or insulator) represents a special advantage for biosensor research. If antibodies are immobilized directly on a transducer (for example, an amperometric electrode), they may inhibit the signal generating process (for example, electron transfer). In such situations, the optimization of modified surfaces is frequently delayed because one cannot assign the reduced signals to either an inhibition of the detection reaction or a failure in forming antigen–antibody complexes. The latter case might occur if the antibody is immobilized but the binding sites were altered during the chemical modification or are not accessible to the analyte. SECM investigations as presented in this paper allow a straightforward distinction between these two possibilities.

ACKNOWLEDGMENT

The authors thank F.-M. Matysik for the preparation of the microelectrode. Financial support of the U.S. Department of Energy (Grant No. 86ER-60487 to W.R.H.) is gratefully acknowledged. G.W. was a fellow of the German National Scholarship Foundation and visiting scholar at the University of Cincinnati.

Received for review January 3, 1995. Accepted June 29, 1995.⁹

AC9500141

⁹ Abstract published in *Advance ACS Abstracts*, August 15, 1995.

Electrocatalytic Surface for the Oxidation of NADH and Other Anionic Molecules of Biological Significance

Wilbur B. Nowall and Werner G. Kuhr*

Department of Chemistry, University of California, Riverside, California 92521

A simple electrochemical treatment of a carbon fiber electrode surface has been found to dramatically improve the voltammetry of NADH and several other anionic molecules under steady-state and fast scan (100 V/s) conditions. The electrocatalytic surface is generated through the electrochemical oxidation of NADH on a carbon fiber electrode that exhibits product adsorption. The oxidative product is reacted with ascorbic acid at elevated temperatures to create a surface which has very little overpotential for the oxidation of dopamine and many metabolites such as NADH, DOPAC, uric acid, and ascorbate. The electrochemical properties of the modified surface were examined voltammetrically at both slow and fast scan rates. The surface shown in this paper shifts the oxidation overpotentials different magnitudes for each analyte tested, thus allowing discrimination between analytes of interest and their major interferences. Another benefit of this new electrocatalytic wave is that it decreases the limit of detection for NADH by ~1 order of magnitude. Therefore, this new carbon surface not only gives better discrimination between two analytes but also gives better detection limits for certain analytes of interest.

The analytical performance of carbon electrodes (i.e., sensitivity and response time) is highly dependent on the manner by which the carbon surface is prepared. Additionally, there is significant variability in the structure and chemistry of the different forms of carbon. A number of different forms of carbon have substantial differences in morphology, e.g., glassy carbon (GC) and highly ordered pyrolytic graphite (HOPG).¹⁻⁴ Common to both GC and HOPG are "edge" and "basal" regions where physical and electrochemical properties are considerably different. Facilitated charge transfer is promoted in the edge plane as dictated by the stacking arrangement of sp² carbon orbitals in the lattice, and carbon-oxygen complexes are predominantly found at edge sites of carbon fibers prior to any pretreatment.⁵ Consequently, the edge orientation has the most facile electron transfer kinetics in aqueous solutions but shows an undesirably high background charging current and can be subject to detrimental memory

effects.⁵ Mechanical polishing,^{7,8} electrochemical anodization,⁹⁻¹⁵ radio frequency oxygen plasma,^{6,16,17} microwave plasma,¹⁸ dispersion of metal oxide particles (i.e., alumina)^{19,20} in situ laser,^{5,21-24} and vacuum heat treatments^{2,25,26} have all been shown to improve heterogeneous electron transfer rates (*k_h*) for selected redox couples at carbon electrodes.

Electrochemical anodization and radio frequency generated oxygen plasmas are especially noted for their ability to increase the density of carboxyl, quinone, phenolic, and other surface oxygen groups on the edge plane of carbon electrodes.^{6,27} In conjunction with cleaning the surface (removing chemi- and physisorbed impurities) and roughening the surface (increasing the geometric area of the electrode), the incorporation of surface functionalities is thought to enhance the rate of heterogeneous electron transfer for various redox couples by acting as an interfacial redox mediator.⁷ The growth and removal of an oxide film on the surface of GC electrodes following anodization, associated with Kepley and Bard, has been shown to be a function of the electrode's activation and deactivation toward several quinone/hydroquinone redox couples.¹⁵ Several interpretations have been proposed, most notably those involving π -bonding orbital interactions¹⁰ and the resonance stabilization provided by surface phenolic and carboxyl groups to assist in proton-coupled

- (1) Panzer, R. E.; Elving, P. J. *Electrochim. Acta* **1975**, *20*, 635-647.
- (2) Bellby, A. L.; Carlsson, A. J. *Electroanal. Chem.* **1988**, *248*, 283-304.
- (3) Van der Linden, W. E.; Dieker, J. W. *Anal. Chim. Acta* **1980**, *119*, 1-24.
- (4) Kinoshita, K. *Carbon: Electrochemical and Physicochemical Properties*; John Wiley and Sons: New York, 1988; p 533.
- (5) Kozłowski, C.; Sherwood, P. M. A. *J. Chem. Soc., Faraday Trans. 1* **1985**, *81*, 2745-2756.

- (6) Evans, J. F.; Clark, R. A.; Bowden, E. F. *Anal. Chem.* **1994**, *66*, 2565-2598.
- (7) Hu, L. F.; Karwsek, D. H.; Kuwana, T. *J. Electroanal. Chem.* **1985**, *188*, 59-72.
- (8) Kamau, G. N.; Willis, W. S.; Rusling, J. F. *Anal. Chem.* **1985**, *57*, 545-551.
- (9) Noel, M.; Anantharaman, P. N. *Analyst* **1985**, *110*, 1095-1103.
- (10) Nagaoka, T.; Yoshino, T. *Anal. Chem.* **1986**, *58*, 1037-1042.
- (11) Engstrom, R. C. *Anal. Chem.* **1982**, *54*, 2310-2314.
- (12) Kovach, P. M.; Deakin, M. R.; Wightman, R. M. *J. Phys. Chem.* **1986**, *90*, 4612-4617.
- (13) Proctor, A.; Sherwood, P. M. A. *Carbon* **1983**, *21*, 53-59.
- (14) Wang, J.; Hutchins, L. D. *Anal. Chim. Acta* **1985**, *167*, 325-334.
- (15) Kepley, L. J.; Bard, A. J. *Anal. Chem.* **1988**, *60*, 1459-1467.
- (16) Miller, C. W.; Karwsek, D. H.; Kuwana, T. *Anal. Chem.* **1981**, *53*, 2319-2323.
- (17) Evans, J. F.; Kuwana, T. *J. Electroanal. Chem.* **1977**, *80*, 409-416.
- (18) Xie, Y. M.; Sherwood, P. *Appl. Spectrosc.* **1990**, *44*, 797-803.
- (19) Zak, J.; Kuwana, T. *J. Am. Chem. Soc.* **1982**, *104*, 5514-5515.
- (20) Dong, S.; Kuwana, T. *J. Electrochem. Soc.* **1984**, *131*, 813-818.
- (21) Foon, M.; McCreery, R. L. *Anal. Chem.* **1986**, *58*, 2745-2750.
- (22) Foon, M.; McCreery, R. L.; Engstrom, R. *Anal. Chem.* **1988**, *60*, 1725-1730.
- (23) Rice, R. J.; McCreery, R. L. *Anal. Chem.* **1989**, *61*, 1637-1641.
- (24) Strein, T. G.; Ewing, A. G. *Anal. Chem.* **1994**, *66*, 3864-3872.
- (25) Fagan, D. T.; Hu, L. F.; Kuwana, T. *Anal. Chem.* **1985**, *57*, 2759-2763.
- (26) Proctor, A.; Sherwood, P. M. A. *J. Electroanal. Chem. Relat. Phenom.* **1982**, *27*, 39-56.
- (27) Wightman, R. M.; Deakin, M. R.; Kovach, P. M.; Kuhr, W. G.; Statts, K. J. *J. Electrochem. Soc.* **1984**, *131*, 1578-1867.

electron transfer reactions.^{8,28,29} Many experimental strategies to utilize these chemistries have been reviewed recently.²

Conversely, the oxygen-depleted surface created by laser and vacuum heat treatments has also been observed to increase k_0 by several orders of magnitude for model redox systems, such as the one-electron outer-sphere reduction of ferri/ferrocyanide and the two-electron oxidation of ascorbic acid and dopamine.^{17,21,22,25} Fagan, Hu, and Kuwana have shown that the freshly exposed and unroughened carbon surface obtained after vacuum heat treatment provides a cleaned surface that exhibits enhanced electrochemical activity.²⁵ Additionally, the reduced density of surface functional groups resulted in a diminished background charging current. Even though it was suggested that more redox couples need to be evaluated (especially at more positive potentials, where surface redox species could participate in mediating electron transfers), these observations question the role of surface functional groups in electron transfer mechanisms.²⁵

The laser-activated carbon surface is similar to carbon surfaces that have been treated electrochemically, in that they have been cleaned as well as roughened with visible cracks and defects.¹² McCreery and co-workers used Raman spectroscopy prior to and following activation of GC and HOPG electrodes to correlate the increase in density of edge sites with the growth in size of the 1360 cm^{-1} Raman vibrational band of the carbon spectra.³⁰ Coupled with capacitance and adsorption studies, this spectroscopic marker allowed them to quantitatively correlate increased rates of electron transfer with the increase in density of edge defects created by laser activation of basal plane regions.^{23,31,32} Strien and Ewing found that in situ laser activation of the carbon fiber surface dramatically improved the reversibility of the electrochemical oxidation of dopamine and several other molecules.²⁴ The modification of carbon electrodes with molecules acting as redox mediators has resulted in the dramatic improvement of nicotinamide adenine dinucleotide (NADH) electron transfer. For example, covalent modification of carbon electrodes with quinone decreases the overpotential for the oxidation of NADH, with subsequent control of the NADH oxidation potential dictated by the surface-bound quinone/hydroquinone couple.³³

The goal of the present experiment is to form a new electrocatalytic surface on a carbon fiber electrode. This new carbon surface decreases the overpotential for the oxidation of some neurotransmitters and their major interferences, such as NADH and ascorbate. Redox mediators have also been used to reduce the overpotential of NADH^{34,35} but suffer from the inability to discriminate between electroactive species. The surface shown in this paper shifts the oxidation overpotentials different magnitudes for each analyte tested, thus allowing discrimination between analytes of interest and their major interferences. Another benefit to this new electrocatalytic wave is that it decreases the limit of detection for NADH by ~ 1 order of magnitude. Therefore, this new carbon surface not only gives better discrimination between

two analytes but also gives better detection limits for certain analytes of interest.

EXPERIMENTAL SECTION

Chemicals. β -Nicotinamide adenine dinucleotide, reduced form (NADH, Sigma); L-ascorbic acid (Sigma); 3,4-dihydroxyphenylacetic acid (DOPAC, Sigma); 3-hydroxytyramine (dopamine, Sigma); Epon 828 Resin (Shell Oil); and triethylenetetraamine (TETA, Miller Stephenson) were used as received. The phosphate buffer consisted of 100 mM sodium phosphate heptahydrate and 150 mM sodium chloride adjusted to pH 7.4 unless otherwise indicated. All solutions were prepared in water purified by a Milli-Q water purification system (Millipore).

Carbon Fiber Microelectrodes. Fabrication of the 32 μm diameter carbon fiber microelectrodes (Textron Specialty Materials) will be discussed briefly. One carbon fiber is inserted, by hand, into a glass capillary tube (1.2 mm o.d., 0.69 mm i.d., Sutter Instrument Co. Catalog No. BF120-69-10), and a tapered end is generated after the electrode is pulled by a Narishige Model PE-2 microelectrode puller. A seal between the fiber and capillary is obtained by using Epon epoxy with 12% (w/w) TETA as hardener. A fresh electroactive surface was achieved by cleaving the surface with a scalpel.

Instrumentation. Cyclic staircase voltammetry was performed with an EI-400 potentiostat (Ensmann Instruments, Bloomington, IN), where all waveforms were generated and currents acquired via an 80386 personal computer using an A/D-D/A interface (Labmaster DMA, Scientific Solutions, Solon, OH). A 100 MHz digital oscilloscope (Hewlett-Packard 54501A) was used to observe all transients, and a Hewlett-Packard LaserJet II P was used to print out the data. A sinusoidal waveform was produced by a 30 MHz waveform generator (Stanford Research Systems Model DS345) and modulated at 50 Hz at an amplitude of $1V_{(p-p)}$ with a 600 mV bias. The flow injection analysis system consisted of a pneumatic actuator (Rheodyne, Model 5701) controlled via a solenoid valve (Rheodyne kit, Model 7163). A locally built solenoid driver circuit allowed computer control of the compressed air-driven valves which switched flow from the buffer loop to the sample loop of the FIA. The electrochemical cell was constructed from Plexiglas in such a way as to allow the microelectrode to be positioned ~ 6 mm from the outlet of the FIA sample loop. The cell was designed to match the internal diameter of the FIA tubing (0.75 mm) in order to minimize diffusional broadening of the analyte as it was transported to the microelectrode. The electrochemical cell was immersed in a Plexiglas water bath and was heated via Teflon tubing that was coiled around the inside of the cell. Water flowed through the tubing from a Haake FJ external heater and pump combination (Haake Model 70504). Finally, the flow of buffer (1.2 mL/min) was controlled by a peristaltic pump (Scientific Industries Model 203, Bohemia, NY).

Microelectrode Surface Modification. Freshly cleaved carbon surfaces were examined for the presence of an adsorptive prewave (~ 530 mV) for the oxidation of NADH. The presence of this wave was determined by cyclic voltammetry from 0 to 1100 mV (100 V/s) and by FIA of 100 μM NADH. Next, the electrode was subjected to a sine wave excitation ($1V_{(p-p)}$, 50 Hz, 600 mV bias) for 7–10, 5 s injections of 100 μM NADH at 38 $^\circ\text{C}$, with a 1 min pause between each injection. Finally, the electrode was exposed to 1 mM ascorbic acid, readjusted to pH 7.4, for 7–10 injections under the same conditions. The electrode was then

(28) Cananiss, G. E.; Diamanis, A. A.; Murphy, W. R., Jr.; Liton, R. W.; Meyer, T. J. *J. Am. Chem. Soc.* **1985**, *107*, 1845–1853.

(29) Gunasingham, L.; Fleet, B. *Analyst* **1982**, *107*, 895–902.

(30) Bowling, R.; Packard, R.; McCreery, R. L. *J. Electrochem. Soc.* **1988**, *135*, 1605–1606.

(31) Bowling, R.; Packard, R.; McCreery, R. L. *J. Am. Chem. Soc.* **1989**, *111*, 1217–1223.

(32) Rice, R. J.; Pontikos, N. M.; McCreery, R. L. *J. Am. Chem. Soc.* **1990**, *112*, 4617–4622.

(33) Tse, D. C.-S.; Kuwana, T. *Anal. Chem.* **1978**, *50*, 1315–1318.

(34) Gorton, L. *J. Chem. Soc., Faraday Trans. 1* **1986**, *82*, 1245–1258.

(35) Ni, F.; Feng, H.; Gorton, L.; Colton, T. M. *Langmuir* **1990**, *6*, 66–73.

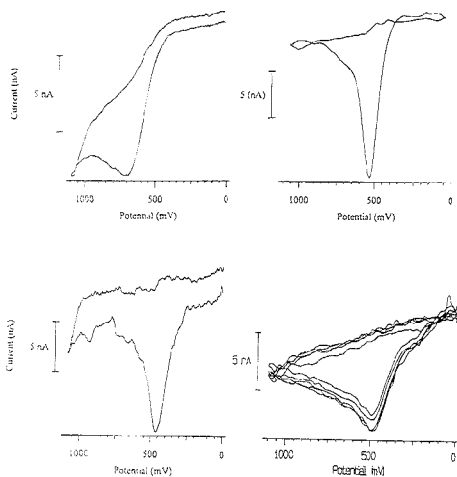


Figure 1. Effect of pretreatment on NADH voltammetry. Voltammetry of 100 μM NADH (100 V/s) in pH 7.4 phosphate buffer shown for three cleaved 32 μM carbon fiber microelectrodes at the following conditions: upper left, untreated carbon fiber with a diffusion-limited oxidation wave at 750 mV; upper right, unstable surface with oxidation wave at 529 mV; lower left, electrocatalytic modified carbon surface with an oxidation wave at 474 mV; lower right, stability of NADH on an electrocatalytic surface of 32 μM carbon fiber microelectrodes. Voltammetry (100 V/s) of 100 μM NADH on an electrocatalytic surface in pH 7.4 phosphate buffer as a function of the total number of scans on the electrode. The numbers of scans from bottom to top are 100, 1100, 2600, 4600, and 10 600 scans, respectively.

retested with 100 μM NADH under CV conditions to ensure the production of the electrocatalytic wave at ~ 474 mV.

RESULTS AND DISCUSSION

Voltammetry of NADH at Carbon Fiber Microelectrodes.

There is considerable variability in the reversibility of NADH oxidation at different carbon fiber microelectrodes. The voltammetry of NADH at carbon fibers has been studied extensively in this laboratory. As observed previously, oxidation of NADH at slow scan rates (< 10 V/s) fouled the electrode.³⁶ We found that consistent and reproducible voltammetry of NADH was observed at faster scan rates (100 V/s) at these electrode surfaces following mild electrochemical pretreatments.³⁶ An untreated carbon fiber surface can produce an oxidation wave with a diffusion-controlled peak potential at any value between 600 and 1100 mV vs Ag/AgCl at 100 V/s, as shown in Figure 1 (upper left). Although the oxidation wave can change dramatically from electrode to electrode, the voltammetry of NADH at any particular electrode is very consistent at these fast scan rates. Oxidation in a buffer of pH 7 or above decreases the overpotential for the diffusion-controlled wave but also introduces a sharp, symmetrical prepeak at 529 mV, which is presumably due to the adsorption of the oxidation product (Figure 1, upper right).³⁶

Adsorption of an analyte onto the electrode surface is often used to increase the sensitivity of an electrochemical measure-

ment.^{33,37} This has been especially true for the measurement of the catecholamine neurotransmitters, where fast adsorption kinetics allow preconcentration of dopamine onto the electrode surface, resulting in greatly enhanced detection limits without the loss of temporal response.^{37,38} Adsorption could serve the same purpose for NADH (i.e., improve detection limits). Previously, the magnitude of NADH adsorption was found to diminish as a function of the voltammetric scans applied to an electrode.³⁶ Diffusional behavior could be obtained at any of these surfaces simply by cycling the electrode for a few thousand scans in buffer at 100 V/s. When this was done, the adsorption wave disappeared and a reproducible diffusion-controlled oxidation wave was produced at the electrode.

Production of an Electrocatalytic Surface for the Oxidation of NADH. Our purpose was to stabilize the surface wave observed at 529 mV (Figure 1, upper right) and then to produce an electrocatalytic surface for the oxidation of NADH. This was accomplished by cycling the electrode between 0.1 and 1.0 V at 50 Hz while introducing 100 μM NADH 10 times by flow injection and then exposing the electrode to 1 mM ascorbate (see Experimental Section for details). This produced an electrocatalytic surface that produces a peak-shaped oxidation wave for NADH at 474 mV (Figure 1, lower left). This electrocatalytic surface is produced only when NADH is introduced before ascorbate and the temperature is kept above 38 $^{\circ}\text{C}$. If any of these parameters are altered, no electrocatalytic surface is generated. If ascorbate is omitted in the procedure, a prewave is formed but disappears with subsequent CV scans, as observed previously at the untreated surface.³⁶

In order to fully appreciate the utility of this method, it is necessary to consider the events occurring at the surface of the electrode. The surface wave for the oxidation of NADH that appears at ~ 529 mV at the freshly cleaved carbon fiber surface disappears upon repeated cycling of the electrode from 0 to 1100 mV. Therefore, any quantitation of NADH using this wave would be difficult due to the continuously changing surface properties of this electrode surface. After the formation of the electrocatalytic surface, the surface wave is transformed into an electrocatalytic surface with a peak at ~ 474 mV. The response of the electrocatalytic surface is linear between 1 μM and 1 mM, and the limit of detection for NADH is ~ 1 μM ($S/N = 5$); this is an order of magnitude lower than observed at unmodified electrodes using identical electrochemical protocols (i.e., cyclic voltammetry at 100 V/s).³⁶ This electrocatalytic wave is stable over a wide potential range and repetitive cycling and even withstands continuous fast scan voltammetry to 1.3 V (50 Hz, -0.2 to 1.3 V, 20 s) without appreciable changes in the electrocatalytic or diffusional portions of the wave. The stability of the electrocatalytic surface was determined by performing repetitive CV scans at 100 V/s from 0 to 1100 mV on a single electrode. As shown in Figure 1 (lower right), the oxidation wave for NADH changed only marginally over 10 600 scans, indicating that the electrocatalytic surface is very stable. Electrodes prepared in this manner had stable electrocatalytic surfaces for at least 30 days when stored in air, but storage in aqueous solution eventually resulted in loss of the electrocatalytic surface after ~ 4 days.

(36) Kuhr, W. G.; Barrett, V. L.; Gegnon, M. R.; Hopper, P.; Pantano, P. *Anal. Chem.* 1993, 65, 617-622.

(37) May, L. J.; Kuhr, W. G.; Wightman, R. M. *J. Neurochem.* 1988, 51, 1060-1069.

(38) Kuhr, W. G.; Wightman, R. M. *Brain Res.* 1986, 381, 168-171.

Table 1. Properties of Electrodes Observed with Fast Scan (100 V/s) Voltammetry

electroactive species	surface condition	E_{peak} (oxidation) (mV) ^a	E_{peak} (reduction) (mV) ^b
NADH	bare carbon	750	
	electrocatalytic surface	474 ± 8	
ascorbate	bare carbon	>1100	
	electrocatalytic surface	283 ± 9	
dopamine	bare carbon	273 ± 13	-107 ± 0
	electrocatalytic surface	332 ± 7	-39 ± 4.7
DOPAC	bare carbon	345 ± 12	-163 ± 4.7
	electrocatalytic surface	341 ± 10	-137 ± 4.2
uric acid	bare carbon	330 ± 10	-32 ± 4.7
	electrocatalytic surface	322 ± 5	98 ± 0

^a Observed E_{peak} (oxidation) vs Ag/AgCl at 100 V/s in pH 7.4 phosphate buffer. Errors represent standard deviation ($n \geq 3$).
^b Observed E_{peak} (reduction) vs Ag/AgCl at 100 V/s in pH 7.4 phosphate buffer. Errors represent standard deviation ($n \geq 3$).

The temperature of the buffer was a critical factor in the preparation of the electrocatalytic surface. A reproducible electrocatalytic surface was produced at temperatures at or above 38 °C in the first step of the procedure, but no electrocatalytic surface was produced at temperatures below 38 °C. Even the adsorptive wave observed at the bare carbon fiber disappeared after treatment at lower temperatures. Additionally, the stabilization of the electrocatalytic wave involved the exposure of the NADH-modified surface to ascorbate at elevated temperatures. Initially, a sine wave (1V_(0→p), 50 Hz, 600 mV bias) was applied to the electrode, and the ascorbate solution was maintained at either 23 or 38 °C. No electrocatalytic surface was generated at 23 °C, but an electrocatalytic surface was observed at 38 °C. This indicates that the ascorbate treatment also requires elevated temperatures to produce a stable electrocatalytic surface. The necessity for an electrochemical oxidation of ascorbate was examined by placing a NADH-treated surface in a static cell of 1 mM ascorbate, but no potential was applied. Again, this resulted in the production of a stable electrocatalytic surface at 38 °C, but not at 23 °C. This indicates that this procedure does not require the electrochemical oxidation of ascorbate to take place in order for an electrocatalytic surface to be produced. This would seem to indicate that ascorbate acts as a reductant in a homogeneous reaction, with the product of the NADH oxidation deposited on the surface of the electrode, and that thermodynamic factors are involved in the production of the electrocatalytic surface.

Electrochemical Properties of the Electrocatalytic Surface.

The electrochemical properties of this surface were examined by looking at a number of electroactive species at both fast (100 V/s, Table 1) and slow (10 mV/s, Table 2) scan rate cyclic voltammetry. At slow scan rates, all the electroactive species tested showed an appreciable reduction in the $E_{1/2}$ for oxidation at the electrocatalytic surface when compared to the untreated control.

Slow Scan Voltammetry of NADH. The formal potential of NADH oxidation has been calculated to be -560 mV vs SCE in homogeneous solution.³⁹⁻⁴¹ In this work, we have found that the bare carbon surface shows an $E_{1/2}$ for NADH oxidation at 453

Table 2. Properties of Electrodes Observed with Slow Scan (10 V/s) Voltammetry

electroactive species	surface condition	$E_{1/2}$ oxidation (mV) ^a
NADH	bare carbon	453 ± 16
	electrocatalytic surface	346 ± 9
ascorbate	bare carbon	>1100
	electrocatalytic surface	-27 ± 2
dopamine	bare carbon	164 ± 8
	electrocatalytic surface	60 ± 1
DOPAC	bare carbon	162 ± 8
	electrocatalytic surface	153 ± 2
uric acid	bare carbon	285 ± 8
	electrocatalytic surface	208 ± 2

^a Observed $E_{1/2}$ vs Ag/AgCl at 10 mV/s in pH 7.4 phosphate buffer. Errors represent standard deviation ($n \geq 3$).

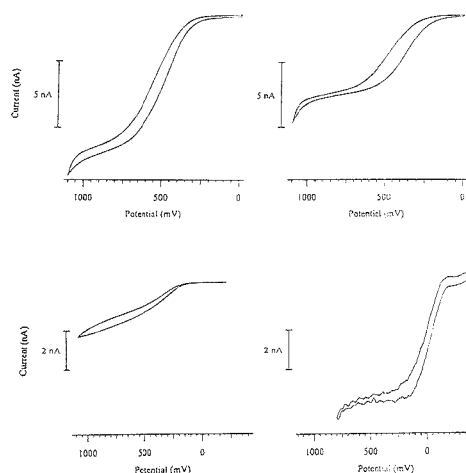


Figure 2. Voltammetry of 100 μM NADH and 1mM ascorbic acid (10 V/s) in pH 7.4 phosphate buffer shown for two cleaved 32 μM carbon fiber microelectrodes at the following conditions: upper left, untreated carbon with a diffusion-limited wave that has an $E_{1/2}$ at 453 mV; upper right, electrocatalytic modified carbon surface with an $E_{1/2}$ at 346 mV; lower left, voltammogram for ascorbate on untreated carbon with an oxidation wave at >1100 mV; lower right, voltammogram for ascorbate on the electrocatalytic surface of a pretreated electrode with an oxidation wave at -27 mV.

mV vs Ag/AgCl (Figure 2, upper left; see Table 2), while the electrocatalytic surface has an $E_{1/2}$ at 346 mV at 10 mV/s at pH 7.4 (Figure 2, upper right; see Table 2). Several investigators have reported that the presence of oxygen functionalities on the carbon surface facilitates the electron transfer kinetics of NADH.⁴² Kuwana and Tse have shown that by adsorbing different catechols on the surface of the electrode, NADH oxidation could occur at ~295, ~396, and 625 mV vs Ag/AgCl at pH ~7 and 50 mV/s, depending on the catechol adsorbed.³³ Blaedel and Jenkins⁴³ as well as Moiroux and Elving³⁹ showed NADH oxidation at 495 mV

(39) Moiroux, J.; Elving, P. J. *Anal. Chem.* **1979**, *51*, 346-350.

(40) Moiroux, J.; Elving, P. J. *J. Am. Chem. Soc.* **1980**, *102*, 6533-6538.

(41) Samec, Z.; Bresnahan, W. T.; Elving, P. J. *J. Electroanal. Chem.* **1982**, *133*, 1-23.

(42) Moiroux, J.; Elving, P. J. *Anal. Chem.* **1978**, *50*, 1056-1062.

(43) Cenas, N. K.; Kanapieniene, J. J.; Kulyš, J. J. *J. Electroanal. Chem.* **1985**, *189*, 163-169.

(44) Gorton, L.; Torstensson, A.; Jaegfeldt, H.; Johansson, G. J. *Electroanal. Chem.* **1984**, *161*, 103-120.

(45) McCreery, R. L. In *Electroanalytical Chemistry*; Bard, A. J., Ed.; Dekker: New York, 1991; Vol. 17, pp 221-374.

(46) Blaedel, W. J.; Jenkins, R. A. *Anal. Chem.* **1975**, *47*, 1337-1343.

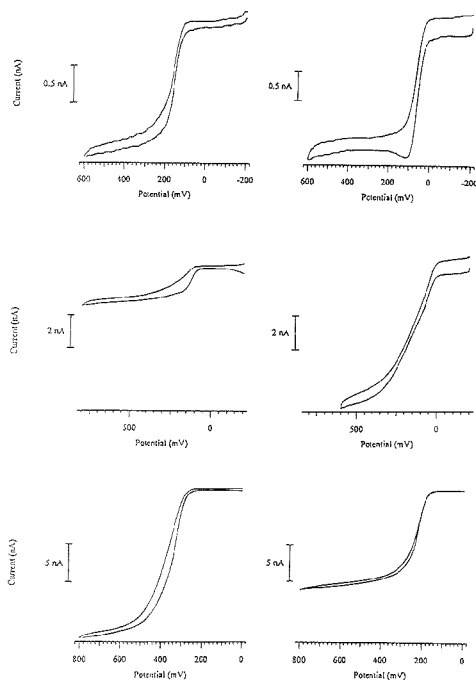


Figure 3. Effect of the electrocatalytic surface on $E_{1/2}$. Voltammetry (10 mV/s) on cleaved carbon fiber microelectrodes. top left, 100 μ M dopamine on an untreated carbon surface with an $E_{1/2}$ at 164 mV; top right, 100 μ M dopamine on electrocatalytic modified surface with an $E_{1/2}$ at 60 mV; middle left, 100 μ M DOPAC on an untreated carbon surface with an $E_{1/2}$ at 162 mV; middle right, 100 μ M DOPAC an electrocatalytic surface with an $E_{1/2}$ at 153 mV; bottom left, 100 μ M uric acid on an untreated carbon with an $E_{1/2}$ at 285 mV; bottom right, 100 μ M uric acid on an electrocatalytic surface with an $E_{1/2}$ at 208 mV.

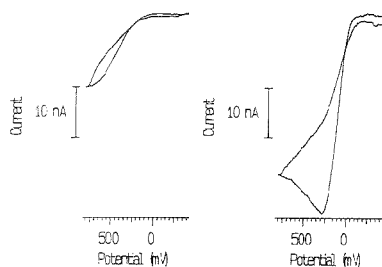


Figure 4. Voltammetry (100 V/s) of 1 mM ascorbate in pH 7.4 phosphate buffer at a cleaved 32 μ M carbon fiber microelectrode. Right: voltammogram for ascorbate on untreated carbon with an oxidation wave at >1100 mV. Left: voltammogram for ascorbate on the electrocatalytic surface of a pretreated electrode with an oxidation wave at 283 mV.

vs Ag/AgCl at pH ~ 7 . Engstrom and Strasser used an electrochemical anodization to yield an $E_{1/2}$ for the oxidation of NADH at 265 mV vs Ag/AgCl through the use of a rotating disk electrode.¹⁷ Others have used redox mediators such as Meldela Blue and Nile Blue to reduce the overpotential of NADH on carbon

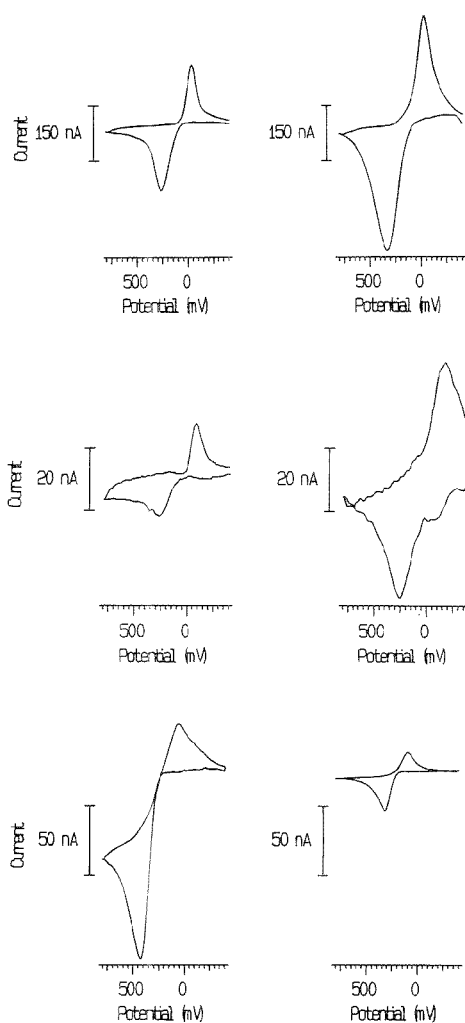


Figure 5. Effect of the electrocatalytic surface on oxidation waves. Voltammetry (100 V/s) on cleaved carbon fiber microelectrodes. Top left, 100 μ M dopamine on an untreated carbon surface with an oxidation wave at 273 mV; top right, 100 μ M dopamine on electrocatalytic modified surface with an oxidation wave at 332 mV; middle left, 100 μ M DOPAC on an untreated carbon surface with an oxidation wave at 345 mV; middle right, 100 μ M DOPAC an electrocatalytic surface with an oxidation wave at 341 mV; bottom left, 100 μ M uric acid on an untreated carbon surface with an oxidation wave at 380 mV; bottom right, 100 μ M uric acid on an electrocatalytic surface with an oxidation wave at 322 mV.

surfaces to -130 and -175 mV vs Ag/AgCl, respectively.²⁴ Although the redox mediators do greatly diminish the overpotential of NADH, they also suffer from the problem of not being able to discriminate between redox species. This is because all redox species have the same potential when redox mediators are

(47) Engstrom, R. C.; Strasser, V. *A. Anal. Chem.* **1985**, *56*, 136.

used; therefore, ascorbic acid, a common interference for NADH, cannot be discriminated from the actual NADH signal. The discrimination between analytes of interest and such interferences is crucial to in vivo experimentation.

Slow Scan Voltammetry of Other Redox Species. The role of ascorbic acid as an antioxidant and its tendency to be the major interference of NADH has recently brought to the forefront the importance of the detection and discrimination of ascorbic acid in vivo. Thus, sensors that have the ability to detect ascorbic acid and discriminate it from other signals are of considerable interest. Ascorbic acid has a very high overpotential at a bare carbon surface; the $E_{1/2}$ is greater than 1100 mV vs Ag/AgCl at 10 mV/s (Figure 2, lower left). The overpotential is almost completely removed at the electrocatalytic surface: the $E_{1/2}$ for ascorbic acid drops to -27 mV under the same conditions (Figure 2, lower right). This is comparable to the effects of many other electrocatalytic pretreatments, including a variety of methods including laser activation, electrochemical pretreatment, and heat pretreatments.^{21,22,27,47-50} The $E_{1/2}$ values for the oxidation of ascorbic acid ranged from ~ -20 to ~225 mV vs Ag/AgCl, with scan rates ranging from 10 to 100 mV/s.

Dopamine and DOPAC are two other chemicals which are of great importance in in vivo experimentation. Dopamine has an $E_{1/2}$ of 164 mV vs Ag/AgCl at a bare carbon surface, 10 mV/s at pH 7.4 (Figure 3, top left). The $E_{1/2}$ drops to 60 mV vs Ag/AgCl on the electrocatalytic surface (Figure 3, top right). McCreery and Allred⁴⁹ and Wightman et al.⁵⁰ showed electrocatalytic surfaces that reduced the overpotential of dopamine to 90 and ~195 mV vs Ag/AgCl, respectively. McCreery et al. used laser activation of the carbon surface to reduce the dopamine overpotential to 32 mV vs Ag/AgCl.²¹ DOPAC has an $E_{1/2}$ of 162 mV vs Ag/AgCl at pH 7.4 and 10 mV/s for bare carbon (Figure 3, middle left). The $E_{1/2}$ drops to 153 mV vs Ag/AgCl at the electrocatalytic surface (Figure 3, middle right). Various electrochemical pretreatments of the electrode have been shown to decrease the DOPAC oxidation potential to ~395 and ~120 mV vs Ag/AgCl at pH 7.4 and 100 mV/s.^{48,50} McCreery et al. reduced the overpotential to 109 and 27 mV vs Ag/AgCl at pH 7 and at 10 and 100 mV/s, respectively, with different pretreatments.^{21,49} The oxidation potentials observed for dopamine and DOPAC at the electrocatalytic surface prepared in this paper are comparable to these values. Uric acid was also tested at both the bare carbon surface and the electrocatalytic surface under the same conditions as dopamine

and DOPAC. The $E_{1/2}$ was 285 mV for the bare surface (Figure 3, bottom left) and 208 mV for the electrocatalytic surface (Figure 3, bottom right).

Fast Scan Voltammetry of Redox Species. Ascorbate, which classically has shown an oxidation wave at high overpotentials at 100 V/s (Figure 4, left), exhibits variable voltammetry at bare carbon surfaces. This is dramatically more reversible at an electrocatalytic surface (Figure 4, right). Not only is the overpotential for the oxidation of ascorbate decreased (as evidenced by the large change in the $E_{1/2}$ observed under steady-state voltammetric conditions, Table 2), but the apparent kinetics are much faster as well (as shown by the shift in the observed peak potential for the oxidation of ascorbate at fast scan rates, Table 1). This is clearly indicated by a well-defined peak at 283 mV, even at scan rates of 100 V/s (Figure 4, right), rather than the long and drawn out peak of the untreated electrode (Figure 4, left).

Several other redox species were examined at 100 V/s as well (Figure 5). Dopamine (Figure 5, top) was marginally less reversible at the electrocatalytic surface than on the untreated carbon surface. However, DOPAC (Figure 5, middle) and uric acid (Figure 5, bottom) are more reversible on the electrocatalytic surface than on an untreated carbon surface. These results are summarized in Table 1.

General observations of these data would indicate that the electrocatalytic properties are most dramatic for negatively charged species (i.e., ascorbate, uric acid, and NADH), by increasing their electron transfer characteristics, and for cationic species, by slowing down their electron transfer at fast scan rates. At slow scan rates, all analytes demonstrated an increase in their electron transfer characteristics, but it is much more dramatic for the anionic species over the cationic species. This allows one to discriminate between anionic interferences, i.e., ascorbate and NADH, because the overpotentials of the two redox species are shifted by different magnitudes, while giving more sensitive detection for NADH.

ACKNOWLEDGMENT

This work was supported, in part, by the National Institutes of Health (GM44112-01A1) and a Presidential Young Investigator Award (W.G.K.) from the National Science Foundation (CHE-8957394).

Received for review March 7, 1995. Accepted June 29, 1995.*

AC950229A

* Abstract published in *Advance ACS Abstracts*, August 15, 1995.

(48) Stutts, K. J.; Kovach, P. M.; Kuhn, W. G.; Wightman, R. M. *Anal. Chem.* **1983**, *55*, 1632-1634.

(49) Allred, C. D.; McCreery, R. L. *Anal. Chem.* **1992**, *64*, 444-448.

(50) Kovach, P.; Wilson, R. L.; Ewing, A. G.; Wightman, R. M. *J. Neurosci. Methods* **1984**, *10*, 215-227.

Photocurable Polymer Matrices for Potassium-Sensitive Ion-Selective Electrode Membranes

Andrey Bratov,[†] Nataliya Abramova,[†] Javier Muñoz,[‡] Carlos Domínguez,^{*,‡} Salvador Alegret,[†] and Jordi Bartroli[†]

Sensors and Biosensors Group, Department of Chemistry, Universitat Autònoma de Barcelona, and Centre Nacional de Microelectrònica, Campus U.A.B., 08193 Bellaterra, Barcelona, Spain

Photocurable oligomers based on urethane and Bisphenol A (epoxy) diacrylates have been studied as an alternative polymer matrix for ion-selective membranes of ion sensors. The compatibility of the polymers with various plasticizers commonly used in PVC-based ion-selective membrane formulations has been tested, and it has been shown that the urethane-based membranes may hold more than 50% of a plasticizer, while epoxy-based compositions are not fully compatible with them. Potassium-sensitive electrodes with an inner reference solution and a membrane formed by photocured urethane containing valinomycin as the ionophore have been investigated. The influence of the amount and the type of photoinitiator, cross-linking agent, and plasticizer on ion response of the ion-selective electrode has been studied. Ion-selective electrodes with an optimized membrane composition show a sensitivity of 57 mV/decade, a range of linear response from 1 to 10⁻⁵ mol/L of KCl, and a limit of detection around 10⁻⁶ mol/L. The developed polymer matrix was used to make an ISFET-based potassium sensor.

Though coated wire electrodes (CWE) in which a polymer incorporating a suitable ionophore is deposited directly onto a metallic conductor have been known for more than a decade,¹ interest in the development of ion sensors based on polymer membranes with solid-state contacts has renewed considerably in recent years,²⁻⁴ mainly due to advantages offered by modern microelectronic technology. These advantages include, among others, sensor miniaturization and its integration with microfabricated analytical systems, multisensor array fabrication, on-chip integration with signal processing circuits, and low-cost mass production.

Attempts to use poly(vinyl chloride) (PVC) as a polymer matrix for ion sensors with a solid contact faced certain difficulties due to the poor adhesion of this material to a solid substrate surface. Several approaches were made to solve this problem including chemical anchoring of PVC membranes containing OH groups

to an oxide surface^{5,6} via cross-linking with SiCl₄. Utilization of photo-cross-linkable⁷ and high molecular weight plasticizers⁸ to improve the adhesion of the PVC layers must also be noted. Several other polymer materials including silicon rubber,^{9,10} poly(methyl methacrylate),¹¹ and polyurethane¹² were tested as possible ion-sensitive membrane matrices for solid-state ion sensors. Among these, polyurethane seems to be more feasible for the development of sensors for biomedical applications due to its biocompatibility.¹²

Two main methods compatible with microelectronic technology that can be used for ion-selective membrane deposition and patterning are screen printing and photolithography, the latter being the most promising approach from a technological point of view. In this case, an ion-sensitive membrane (or several membranes of different types) may be formed on an integrated chip by a standard photolithography process. Among possible photocurable polymers that can be applied as ion-selective membrane matrices, acrylate- and methacrylate-based compositions,^{11,12} methacrylated siloxane resins,^{13,14} epoxyacrylates,^{15,16} and polystyrene¹⁷ were studied.

It must be noted that most of the investigation done on new polymer matrices for ion sensors was carried out using ISFETs^{10,11} or ion-selective electrodes with a solid inner contact.^{12,18} In both cases, poorly defined from a thermodynamic point of view, the

(5) Harrison, D. J.; Cunningham, L. L.; Li, X.; Teclerian, A.; Permann, D. J. *Electrochem. Soc.* **1988**, *135*, 2473–2478.

(6) Moody, G. J.; Thomas, J. D. R.; Slater, M. J. M. *Analyst* **1988**, *113*, 1703–1707.

(7) Harrison, D. J.; Teclerian, A.; Cunningham, L. L. *Anal. Chem.* **1989**, *61*, 246–251.

(8) Igarashi, I.; Ito, T.; Taguchi, T.; Tabata, O.; Inagaki, H. *Sens. Actuators B* **1990**, *1*, 8–11.

(9) Van der Wal, P. D.; Siowronska-Pusinska, M.; Van den Berg, A.; Sudholter, E. J. R.; Reinhoudt, D. N. *Anal. Chim. Acta* **1990**, *231*, 41–52.

(10) Van der Wal, P. D.; Van den Berg, A.; de Rooij, N. F. *Sens. Actuators B* **1994**, *18–19*, 200–207.

(11) Moody, G. J.; Slater, M. J. M.; Thomas, J. D. R. *Analyst* **1988**, *113*, 103–108.

(12) Cha, G. S.; Liu, D.; Meyerhoff, M. E. *Anal. Chem.* **1991**, *63*, 1686–1672.

(13) Levechev, S. S.; Bratov, A. V.; Vlasov, Yu. G. *Sens. Actuators B* **1994**, *18–19*, 325–328.

(14) Reinhoudt, D. N.; Engbersen, J.; Brzozka, Z.; Van der Vlekkert, H. H.; Honig, G.; Holterman, H.; Verkerk, U. *Anal. Chem.* **1994**, *66*, 3618–3623.

(15) Cardwell, T. J.; Cattrall, R. W.; Iles, P. J.; Hamilton, I. C. *Anal. Chim. Acta* **1985**, *177*, 229–242.

(16) Cardwell, T. J.; Cattrall, R. W.; Iles, P. J.; Hamilton, I. C. *Anal. Chim. Acta* **1989**, *219*, 135–140.

(17) Tietje-Girault, J.; MacInnes, I.; Schroder, M.; Tennat, G.; Girault, H. H. *Electrochim. Acta* **1990**, *35*, 777–783.

(18) Cardwell, T. J.; Cattrall, R. W.; Iles, P. J.; Hamilton, I. C. *Anal. Chim. Acta* **1988**, *204*, 329–332.

[†] Universitat Autònoma de Barcelona.

[‡] Centre Nacional de Microelectrònica.

(1) Cattrall, R. W.; Hamilton, I. C. *Ion-Sel. Electrode Rev.* **1984**, *6*, 125–172.

(2) Cosofret, V. V.; Erdosy, M.; Lindner, E.; Johnson, T. A.; Buck, R. P. *Anal. Lett.* **1994**, *27*, 3039–3063.

(3) Cadogan, A.; Gao, Z.; Lewenstam, A.; Ivaska, A. *Anal. Chem.* **1992**, *64*, 2496–2501.

(4) Van den Berg, A.; Van der Wal, P. D.; Van der Schoot, B. H.; de Rooij, N. F. *Sens. Mater.* **1994**, *6*, 23–43.

interface between the polymer membrane and the electronic conductor or insulator (ISFET) does not permit the separation of processes associated solely with the ion-selective membrane. Earlier we reported¹⁹ on an ammonium-sensitive ISFET with a photocurable polymer ion-selective membrane. To obtain more detailed information on electrochemical properties of the membranes with different compositions, a conventional ion-selective electrode configuration with liquid inner contact was used in this work.

EXPERIMENTAL SECTION

Reagents. Valinomycin, bis(2-ethylhexyl) sebacate (DOS), bis(2-ethylhexyl) phthalate (DOP), dibutyl phthalate (DBP), di-5-nonyl adipate (DNA), dioctyl phenylphosphonate (DOPP), 2-nitrophenyl octyl ether (NPOE), 4-nitrophenyl phenyl ether (NPPE), tetraundecylbenzhydrol-3,3',4,4'-tetracarboxylate (ETH 2112), potassium tetrakis(*p*-chlorophenyl)borate (K-TpCIPB), and tetradodecylammonium bromide were purchased from Fluka. Aliphatic urethane diacrylates (oligomers Ebecryl 230 and 270 of molecular weights 5000 and 1500, respectively), epoxy acrylates (oligomers Ebecryl 150 and 600, molecular weight 500), amine functional acrylate (Ebecryl 7100), unsaturated copolymerizable benzophenone derivative (Ebecryl P-36), tripropylene glycol diacrylate (TPGDA), and hexanediol diacrylate (HDDA) were donated by UCB Chemicals. Photoinitiators 2,2'-dimethoxyphenylacetophenone (Irgacure 651) and 2-hydroxy-2-methyl-1-phenylpropan-1-one (Darocure 1173) were from Ciba-Geigy. All other chemicals were analytical-reagent grade. Standard solutions were prepared with deionized water.

Preparation of Ion-Selective Membranes. The exact compositions of photocurable polymer membranes of potassium-sensitive electrodes studied in this work are presented later in the text. The typical procedure for membrane formation consisted of preparing the main polymer composition by mixing together the acrylated oligomer, reactive diluent (HDDA or TPGDA), and photoinitiator (Irgacure 651 or Darocure 1173). A 0.3 g sample of the main polymer composition was then dissolved in 0.2 mL of tetrahydrofuran, and to this solution plasticizer were added valinomycin and potassium tetrakis(*p*-chlorophenyl)borate. The mixture was thoroughly stirred in an ultrasonic bath until homogeneous and then left for several hours to evaporate the solvent. Ion-selective membranes 8 mm in diameter and 0.3–0.4 mm thick were formed by pipeting several drops of the membrane cocktail into a special cylindrical holder. This layer was exposed to UV using standard mask aligner equipment with an irradiance of 22 mW·cm⁻² at wavelength 365 nm. Typical exposure time was 2 min. After being rinsed with ethanol, the membranes were glued to the end of an acrylate plastic tube (8 mm o.d., 6 mm i.d.) using the main polymer composition without a plasticizer and with exposure to UV for 10 s.

Methods of Membrane Electrochemical Characterization. The membranes were characterized in the conventional ion-selective electrode (ISE) configuration with an inner liquid contact based on a 0.1 mol/L KCl solution. At least three electrodes were prepared to characterize each membrane composition. Chlorinated silver wire served as an inner reference electrode. Double-junction Ag/AgCl reference electrode (Orion 90-02) was used as an external electrode. To prevent interference due to leaching

of the solution from the salt bridge of the reference electrode, the salt bridge was filled with a 0.1 mol/L solution of lithium acetate. Calibration curves were obtained in the concentration range 10⁻⁷–10⁻¹ mol/L in pure solutions of KCl by adding a known amount of prepared stock solutions under stirring. The activities of the ions were calculated using the Debye–Hückel approximation.²⁰ The emf values were measured on a Crison micropH 2002 digital potentiometer with ±0.1 mV accuracy. All the measurements were carried out at 25 ± 1 °C in a thermostated laboratory room. Between measurements, the electrodes were stored in a 10⁻² mol/L solution of KCl.

To obtain selectivity coefficients, the separate solution method as well as the mixed solution method were used. In the second method, the concentration of interfering ion remained constant (0.1 mol/L) while the concentration of the primary ion was changed.

Electric resistivity of the membranes was evaluated by impedance measurements carried out in 0.1 mol/L KCl solution with a platinum plate as an auxiliary electrode in a 50 kHz–0.01 Hz frequency range using an AutoLab electrochemical system (Eco Chemie B.V., Utrecht, The Netherlands).

RESULTS AND DISCUSSION

Photopolymerization of Acrylic Oligomers and Their Compatibility with Plasticizers. Acrylic monomers and oligomers are among the most widely used UV-curable systems²¹ because of their high reactivity and low volatility. A variety of structures with different properties can be obtained, depending upon the prepolymer backbone and the reactive diluent used. There is a large choice of commercially available multifunctional acrylates based on urethanes, Bisphenol A (epoxy) derivatives, polyethers, etc., with high cross-link density which, after exposure to UV, give coatings that are insoluble in organic solvents. This property can be used in lithographic applications of these systems.

For acrylic compounds, light-induced polymerization that transforms a monomer into a macromolecule by a chain reaction is initiated by radicals formed by dissociation of a photoinitiator under UV irradiation. Because of the high viscosity of the oligomers, reactive diluents must be introduced in the formulation. For these purposes, mono- or multifunctional acrylates are used that provide good application of the resin film to a substrate and at the same time increase the cure speed.

The exact structure of the commercial oligomers used in this work is not available, but typical structural formulas of compounds of these classes are presented in Figure 1. For the Bisphenol A derivative, a typical value of *n* lays between 1 and 2. Urethane diacrylates used in photocurable composition usually have *n* between 5 and 10, depending on the chain length of the aliphatic substituents R and R'. Two types of reactive diluents used were hexanediol diacrylate and tripropylene glycol diacrylate (Figure 1). As recommended by the manufacturer, Darocure 1173 and Irgacure 651 have been used as photoinitiators for epoxy acrylates and for urethane acrylates, respectively.

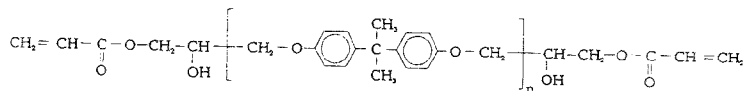
One of the roles of a polymer matrix of an ion-selective membrane is to hold a large amount (up to 60%) of plasticizer in which the ionophore is dissolved. To test the compatibility of different oligomers with plasticizers most commonly used for ISE fabrication, a 0.3–0.5 mm thick layer of a mixture composed of

(19) Braiov, A. V.; Abramova, N.; Muñoz, J.; Domínguez, C.; Alegret, S.; Bartoló, J. *J. Electrochem. Soc.* **1994**, *141*, 1111–1112.

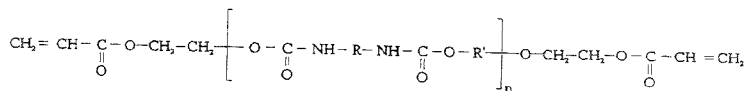
(20) Meier, P. C. *Anal. Chim. Acta* **1982**, *136*, 363–368.

(21) Chandra, R.; Soni, R. K. *Prog. Polym. Sci.* **1994**, *19*, 137–169.

Bisphenol A (epoxy) diacrylate



Aliphatic urethane diacrylate



Tripropyleneglycol diacrylate (TPGDA) Hexanediol diacrylate (HDDA)

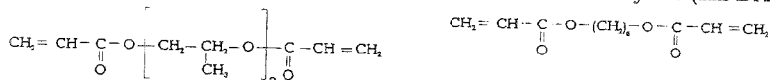


Figure 1. Chemical structures of the oligomers and monomers used for the preparation of photocured polymers.

Table 1. Compatibility and Photopolymerization Ability of Different Polymer Compositions with Plasticizers

no.	polymer ^a	dioctyl phenylphosphonate	dibutyl phthalate	diisooctyl sebacate dinonyl adipate	NPhPh ether NPhO ether	diisooctyl phthalate
A	Eb-600 (59%)	1 min	1 min	2 min	no polymer	1 min
	HDDA (39%)	opaque	transp	white		1 min
	DAR (2%)	brittle	soft	solid		opaque
B	Eb-150 (59%)	1 min	1 min	10 min		solid
	HDDA (39%)	white	transp	white solid		1 min
	DAR (2%)	porous	no adhes			white
C	Eb-600 (50%)	1 min	1 min	2 min		solid
	Eb-7100 (10%)	transp	opaque	white		1 min
	Eb-P36 (15%)	soft	solid	porous		opaque
	HDDA (25%)					solid
D	Eb-150 (50%)	1 min	1 min	2 min	white	1 min
	Eb-7100 (15%)	opaque	white			
	Eb-P36 (5%)	soft	solid	porous		porous
E	Eb-250 (81%)	1 min	1 min	1 min		1 min
	HDDA (17%)	transp	transp	transp		transp
	IRG (2%)	soft	soft	soft		soft
F	Eb-270 (81%)	2 min	1 min	1 min		low adh.
	HDDA (17%)	transp	transp	transp		1 min
	IRG (2%)	soft	soft	soft		transp
						soft

^a DAR and IRG are photoinitiators Darocure 1173 and Irgacure 651, respectively.

the main polymer composition and the plasticizer in a 1:1 ratio was applied to a glass substrate. After UV exposure to remove the upper tacky layer, the polymers were rinsed with ethanol. Properties of the resulting polymers are presented in Table 1. Formulations A–D are based on epoxy acrylates and E and F on aliphatic urethane diacrylates. Instead of low molecular weight photoinitiators, a copolymerizable photoinitiator (Ebecryl P35) was used in compositions C and D. In order to raise the efficiency of the photoinitiator, amine functional acrylate (Ebecryl 7100) was also introduced into these compositions. Several seconds of exposure to UV was enough to achieve complete polymerization of the main polymer compositions without plasticizer. The introduction of a plasticizer led to longer exposure times necessary to complete polymerization due to dilution of the oligomers and also to additional absorption of UV by the plasticizer. No polymerization occurred when NPOE or NPPE were used as plasticizers. This fact can be attributed to the inhibition of radical polymerization due to the presence of nitro groups.¹⁵

From the results in Table 1 it follows that epoxy acrylate-based compositions with most plasticizers except dibutyl phthalate give white or opaque solid films after rinsing with ethanol. We ascribe this fact to the inhomogeneity of the polymer–plasticizer composition. During the polymerization, small globules of a plasticizer are formed in the polymer network. Rinsing with ethanol leads to the extraction of the plasticizer from the polymer, thus giving a pore structure.

Urethane acrylate-based compositions (E, F) gave soft transparent films with all the plasticizers used except those with a nitro group.

Polymer Matrix Permselectivity Measurements. The role of a polymer matrix in ion-selective electrodes is not only a mechanical one, to hold a suitable plasticizer; its chemical properties play an important role in the proper functioning of a sensor. Though a polymer matrix is thought to be inert from the chemical point of view,²² it contains different impurities²³ that can drastically affect the properties of a sensor such as sensitivity.

Table 2. Composition^a and Properties of Studied Ion-Selective Membranes

no.	polymer, amt (%)	cross-linker, amt (%)	photoinitiator	plasticizer, mat (%)	slope (mV/pa _K)	-log K _{K/Na}
1	Eb-270, 52.4	HDDA, 10.9	1.3	DOS, 35.3	47	
2	Eb-230, 50.6	HDDA, 10.6	1.3	DOP, 37.5	42	
3	Eb-270, 77.8	HDDA, 11.3	1.9		40	
4	Eb-230, 77.8	HDDA, 11.3	1.9		40	
5	Eb-270, 48.1	HDDA, 10.1	1.1	DOS, 38.5	57.4	3.2
6	Eb-270, 50.9	HDDA, 10.6	0.5	DOS, 35.5	54.8	2.8
7	Eb-270, 46.2	HDDA, 9.6	0.2	DOS, 41.7	54.9	2.2
8	Eb-270, 53.4		1.6	DOS, 42.8	54.4	3.1
9	Eb-270, 45.7	TPGDA, 9.6	1.1	DOS, 40.8	57.5	2.1
10	Eb-270, 48.2	HDDA, 10.1	1.1	TPGDA, 38.5		
11	Eb-270, 42.9	HDDA, 9.0	1.0	DOS, 44.8	57.3	3.2
12	Eb-270, 30.9	HDDA, 6.5	0.8	DOS, 59.2	57.8	3.1
13	Eb-270, 47.8	HDDA, 10.0	1.2	DNA, 38.4	56.8	3.3
14	Eb-270, 46.8	HDDA, 9.8	1.2	DOP, 39.4	56.1	2.7
15	Eb-270, 49.5	HDDA, 10.40	1.2	ETH 2112, 36.0	54.8	2.0
16	Eb-270, 46.9	HDDA, 9.8	1.2	DOS, 43.0	45.0	2.0

^a All the compositions contained additionally 2% valinomycin and 0.5% K-TpCIPB except for 16, which was prepared without K-TpCIPB.

limit of detection, and selectivity. The latter parameter is the most sensitive one. Impurities in a polymer (or its own functional groups) may form anionic or cationic sites that take part in an ion-exchange process between membrane and solution phases, thus altering the parameters of a sensor. To achieve better selectivity, the polymer matrix of a cation-sensitive membrane must have some anionic sites. The intrinsic selectivity of a polymer is called permselectivity²⁴ and can be determined using ISEs with blank membranes containing only plasticizer without ionophore.

The membranes studied were composed of the main polymer composition based on urethane diacrylate and a plasticizer DOS or DOP (compositions 1 and 2 in Table 2). Ion response was measured in KCl solutions after 2–3 h of electrode preconditioning in a 10⁻² mol/L solution of KCl. As seen from the calibration curve presented in Figure 2, cation permselectivity is characteristic for this type of polymer matrices. One way to estimate the concentration of ionic impurities is to add to the membrane small amounts of lipophilic anion exchangers, such as tetradodecylammonium bromide, that act as lipophilic counterions of the anionic impurities. Various amounts of TDAB were added to composition 1 before the photopolymerization was carried out, and the response of the electrodes toward the increase of KCl concentration was measured. From the results presented in Figure 2, the concentration of intrinsic anionic impurities in the studied membrane matrix is low enough and the addition of 0.05% of TDAB changes the response from cationic to anionic at high salt concentrations in the solution.

Characterization of Polyurethane Matrices without Plasticizer. It is known that some polymers, such as silicone resin¹⁰ may function well as an ion-selective membrane without any additional plasticizer. According to Ruzicka,²⁵ polyurethane-based membranes with valinomycin also may be used without plasticizer. To test this point, four electrodes based on urethane acrylate

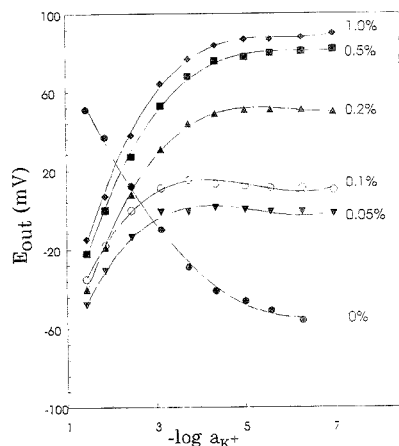


Figure 2. Response curves of ion-selective electrodes with photocured polyurethane membranes plasticized with DOS that contain different amounts of anion exchanger (tetradodecylammonium bromide). The response is measured in KCl solutions.

compositions containing 4% of the ionophore and no plasticizer (compositions 3 and 4 in Table 2) were prepared. It was found that ion response of these membranes is not linear and the sensitivity in a 10⁻²–10⁻⁴ mol/L concentration range of KCl is low (40–45 mV per concentration decade).

Influence of the Polymer Matrix Composition on ISE Properties. Results reported above reveal that the photocured polyurethane may be regarded as a feasible material for ion-selective membrane formation. To narrow the possible set of polymer membrane formulations, Eb 270 was chosen for further investigation as having better adhesion to a solid support.¹⁹

ISE properties depend strongly on a polymer membrane composition. Taking into consideration that the polymer under investigation is composed of different components, it is necessary to optimize the composition of the membranes. To study the influence of photoinitiator, cross-linker, plasticizer, and lipophilic additives on the properties of the electrodes, different membrane formulations presented in Table 2 were tested.

(22) Mori, W. *The principles of ion-selective electrodes and of membrane transport*; Akademiai Kiado: Budapest, 1981.

(23) Van den Berg, A.; Van der Wal, P. D.; Skowronska-Plasinska, M.; Sudholter, E. J. R.; Reinhoudt, D. N. *Anal. Chem.* **1987**, *59*, 2827–2829.

(24) Buck, R. F. *Ion-selective electrodes in analytical chemistry*; Freiser, H., Ed.; Plenum Press: New York, 1978; pp 1–142.

(25) Fiedler, U.; Ruzicka, J. *Anal. Chim. Acta* **1973**, *67*, 179–193.

Photoinitiator. Introduction of a photoinitiator into the mixture of acrylated oligomers and monomers is necessary to start the reaction of radical polymerization. It is well-known²⁶ that the photoinitiator is not totally consumed in the reaction, so the concentration of this component needs to be optimized in order to attain the best compromise with regard to cure speed and low unreacted residues. Though the photoinitiator concentration in the membranes is not very high, it is comparable with the concentration of ionophore and so may affect the ion-selective properties of the resulting membrane. Characterization of ISE based on compositions 5–7 (Table 2) with the concentration of photoinitiator varying in the range from 0.2 to 1.1% showed that the response slope and the selectivity of potassium-selective membranes with a low amount of photoinitiator are inferior to those with high amounts. Taking also into consideration the properties of the electrodes based on composition 12 with 0.8% photoinitiator, it may be assumed that the optimum concentration range is 0.8–1.2%. The influence of the concentration of photoinitiator on the polymer structure is not straightforward, but it is generally admitted²⁷ that in the processes of radical polymerization the average chain length of the resulting polymer increases as both the initiator efficiency and concentration decrease.

Cross-Linker. Low molecular weight monomers are usually introduced into photocurable polymer compositions to reduce the viscosity of the mixture, but being incorporated into the polymer network they also alter the mechanical and chemical properties of the polymer. Difunctional acrylates give additional cross-linkage to a polymer network, resulting in more rigid films. To test the influence of the cross-link density on the electrode characteristics, the polymer matrix of electrode 8 was prepared without HDDA and so must have a less dense structure. The selectivity of the electrode did not change but the sensitivity was affected and became lower in comparison to electrode 5.

Another cross-linking agent that is commonly used in acrylic compositions is TPGDA (Figure 1), which is more hydrophilic than HDDA. Introduction of TPGDA instead of HDDA into the membrane composition (electrode 9) reduced the selectivity of the sensor.

Plasticizer. For PVC-based electrodes, a typical polymer/plasticizer ratio in membrane formulations is 1:2. Usually, lower plasticizer loading leads to the distortion of electrode characteristics of PVC-based sensors.²⁸ For a potassium sensor with polyurethane photocured membranes the influence of the amount of plasticizer (DOS) in the membrane was studied and it was found that in the range of 34–60% of the plasticizer content (electrodes 5, 11, and 12) the parameters of the sensor are not affected. This is in agreement with the most recent data reported on the potassium sensor based on a carboxylated PVC polymer membrane.²⁹

Figure 3 shows the chemical response of the sensors with different plasticizers. Substitution of DOS by DNA in potassium-selective membranes resulted in nearly identical electrode behavior including slope, limit of detection, and selectivity. Introduction of DOP and especially ETH 2112 gives a reduction in the

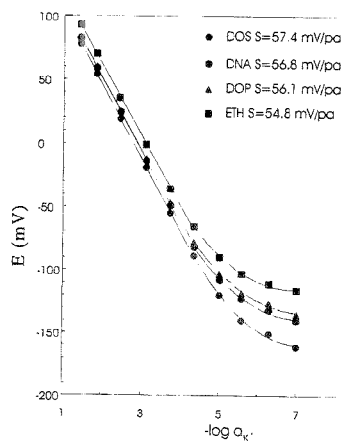


Figure 3. Response curves of ion-selective electrodes with photo-cured polyurethane membranes containing different plasticizers.

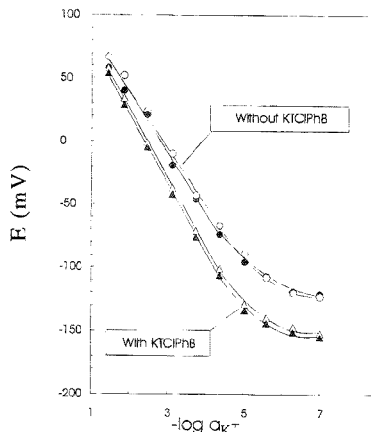


Figure 4. Influence of the addition of 0.5% of KTCIPhB into the membrane formulation on the response of the potassium ion-selective electrode.

sensitivity and the selectivity of the sensors. ETH 2112 was designed as a highly lipophilic plasticizer to prevent the leaching of organic phase into the analyte, but unfortunately, its application seriously affects the parameters of ion-selective electrodes.³⁰

K-TpCIPB. Addition of mobile cation-exchange sites based on K-TpCIPB into the polymer membranes of ISE was shown to be favorable in many respects,²² producing reduction of interferences by lipophilic sample anions, reduction of response time and electric membrane resistance, and reduction of the activation barrier for the cation-exchange reaction at the membrane/solution interface. All the compositions in Table 2 except 16 contained 0.5% K-TpCIPB. Data presented in Figure 4 reveal that without lipophilic salt the sensitivity of the sensor is far from ideal. The selectivity is also affected, $-\log K_{K/Na} = 2.0$, comparing to the value of 3.2–3.3 for the electrodes with K-TpCIPB.

(26) Pappas, S. P. *Radiation Curing: Science and Technology*; Plenum Press: New York, 1982.

(27) Stevens, M. P. *Polymer Chemistry, An Introduction*, 2nd ed.; Oxford University Press: New York, 1990.

(28) Horvai, G.; Graf, E.; Toth, K.; Pungor, E. *Anal. Chem.* 1986, 58, 2735–2740.

(29) Cosofret, V. V.; Erdosy, M.; Buck, R. P.; Kao, W. J.; Anderson, J. M. *Analyst* 1994, 119, 2283–2292.

(30) Huser, M.; Gehrig, P.; Morf, W.; Simon, W.; Lindner, E. *Anal. Chem.* 1991, 63, 1389–1386.

The results obtained permit us to formulate the optimized membrane composition for the potassium ion sensor with a polymer membrane based on photocurable polyurethane: urethane diacrylate (Eb-270) 30–45%; hexandiyl diacrylate 10%; photoinitiator 0.8–1.2%; plasticizer (DOS or DNA) 35–55%; valinomycin 2%; K-TpCIPB 0.5%. The properties of the resulting ion-selective electrodes may be characterized by the following parameters: sensitivity 57.4 mV/decade; range of linear response from 1 to 10^5 mol/L; detection limit 2.5×10^{-5} mol/L. The selectivity coefficients obtained by the separate solution method and the mixed solution method were nearly identical: $\log K_{K/Na} = -3.2$, $\log K_{K/Li} = -3.4$, $\log K_{K/H} = -1.8$, $\log K_{K/Cl} = -4.2$, and $\log K_{K/Mg} = -3.3$. The impedance spectrum of the membrane measured in a symmetrical cell with a 0.1 mol/L KCl solution forms a semicircle. Intersection of the low-frequency part of the semicircle with the axis of the real part of the impedance gives the value of the membrane resistance, which is equal to 2.6 M Ω .

The parameters of the sensors stored between measurements in a 10^{-2} mol/L KCl solution at room temperature were studied in time. After the first month, the changes in the sensitivity and the detection limit were negligible, and after three months, they amounted to 54.3 mV/decade and 1×10^{-5} mol/L, respectively. These changes are usually associated with the leaching of plasticizer, ionophore, or both from the membrane.

It is necessary to recognize that the selectivity coefficients $K_{K/Na}$ for the obtained membrane are inferior to the best reported for PVC-based membrane ion-selective electrodes with valinomycin as ionophore,³¹ though they have the same order of magnitude as reported for ISE with modified PVC matrices.²⁹

It must be noted that not only cations interfere; the presence of lipophilic anions in solution may also strongly affect ISE response.^{24,31} This type of interference manifests itself as deviations from Nernstian response and even transition into an anionic response at high salt concentrations. For neutral carrier-based ion-selective membranes, the sequence of anions according to their interfering ability correlates with their energy of hydration and follows the well-known Hofmeister series (organic anions $> ClO_4^- > SCN^- > I^- > NO_3^- > Br^- > Cl^- > SO_4^{2-}$). The effect of the anions present in the solution on the response of the electrodes is presented in Figure 5. For K^+ sensors, anion interference reveals itself as a decline of the response from linearity that starts at concentrations higher than 4.3×10^{-2} mol/L. In the presence of thiocyanate and iodide anions, saturation on the response curve is evident at high salt concentrations but the slope does not become anionic. Results published in the literature^{24,31,32} reveal that anion interference in the case of PVC-based potassium-selective electrodes is much higher than for the studied polyurethane membranes.

One of the problems that may arise in photocurable polymer membranes is photobleaching of the membrane components upon extended UV illumination. It is known that the stability of tetraphenylborate ion is limited, especially in the presence of acids and oxidizing agents and under illumination.³³ Decomposition of tetraphenylborate derivatives goes with the consumption of protons, giving as a result neutral products. This means that the concentration of tetrakis(*p*-chlorophenyl)borate ion in a membrane

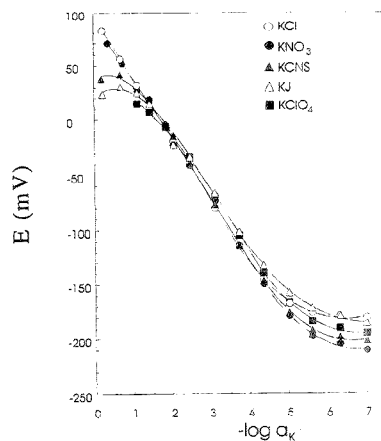


Figure 5. Influence of different anions on the response of the potassium ion-selective electrode with optimized membrane composition.

may depend upon the time of exposure to UV. The extent of anion interference may be used as an indicator for the K-TpCIPB content in the membrane. To test the influence of illumination, electrodes with membrane composition 5 were exposed to UV 10 and 20 min. The measurements carried out in KSCN solutions showed that the deviation from linear response expressed as the difference between the experimental value of emf obtained in a 1 mol/L KSCN solution and the value determined by linear extrapolation at the same concentration depends upon the exposure time. For the electrode with membrane 5 polymerized for 2 min, this value is equal to -48 mV. Electrodes illuminated for 10 and 20 min showed deviations of -90 and -101 mV, respectively. For comparison, the same parameter was measured for electrode 16 without K-TpCIPB. For this electrode, the slope in the 1–0.1 mol/L concentration range was anionic and the deviation in a 1 mol/L KSCN solution amounted to -145 mV. For thick (300–400 μ m) polymer layers used for the fabrication of ISE, exposure time lower than 2 min leads to the formation of very soft layers with a large amount of exuded plasticizer.

Characterization of K^+ -Sensitive ISFET. The final goal of the development of a photocurable polymer matrix is its application as an ion-sensitive membrane in miniature chemical sensors produced with the help of microelectronic technology. Among the requirements imposed on the properties of the material are good adhesion to a solid substrate and sufficient resolution of the image obtained after exposure through a mask and subsequent development in a suitable solvent. A preliminary study¹⁸ showed that the composition tested in this work satisfies these requirements, thus being suitable for the fabrication of potassium-sensitive ISFETs. Sensors were made using ISFETs with a SiO_2/Ta_2O_5 gate insulator. To enhance the adhesion of the polymer, the wafers were preliminarily silylated in a toluene solution of (methacryloxy)propyltrimethoxysilane. The mixture with the optimized composition for membrane formation was applied to a wafer by spin-coating and exposed to UV through the mask for 15 s. After development during several seconds in ethanol, 10–30 μ m thick membranes were formed over the gate region of

(31) Mori, W. E.; Simon, W. *Ion-selective electrodes in analytical chemistry*; Freiser, H., Ed.; Plenum Press: New York, 1978; Vol. 1, pp 211–286.

(32) Mikhelson, K. N. *Sens. Actuators B* 1994, 18–19, 31–37.

(33) Rosatiz, T.; Bakker, E.; Suzuki, K.; Simon, W. *Anal. Chim. Acta* 1993, 280, 197–208.

ISFETs on a wafer. After scribing, ISFETs were wire bonded and encapsulated using photocurable resins by a method reported elsewhere.³¹

The membranes showed excellent adhesion, and no peeling occurred after 5 months of contact with the solution. The sensitivity and the detection limit were found to be the same as for ISE with the corresponding membrane, but the selectivity coefficients were inferior ($\log K_{K/Na} = -1.8$, $\log K_{K/Li} = -2.1$, $\log K_{K/Cl} = -3.5$, and $\log K_{K/Mg} = -3.2$). During 2 months of constant contact with the solution, the sensitivity of ISFETs remained unchanged and decreased up to 53 mV/decade after 4 months.

Large differences in the selectivity coefficients between the thick membranes of ISE and the thin membranes of ISFET may be attributed to a loss of membrane components during the development process in ethanol. Further investigation is necessary to clarify whether it is possible to solve this problem simply by applying a thicker membrane or whether additional changes in the membrane composition must be introduced.

CONCLUSIONS

The results reveal that a polyurethane-based photocurable polymer may be regarded as an appropriate alternative matrix for ion-selective membranes. It contains a small amount of the anionic impurities that cause intrinsic cationic permselectivity. Being compatible with various plasticizers traditionally used in ion-selective membrane formulations, it may be used to make other sensors selective to cations as well as anions. For proper functioning, the membrane with neutral carrier as an ionophore should contain at least 35% of a suitable plasticizer and small amounts of a salt with a highly lipophilic anion. Addition of photoinitiator in a concentration close to that of the ionophore

does not affect the properties of the potassium ion sensor. As in the case of PVC-based ion-selective membranes,³⁵ the parameters of the sensor depend upon the structure of the membrane polymer network. Photocured polymer matrices with low cross-link density based on compositions without low molecular weight cross-linker HDDA or with a low amount of initiator give electrodes with lower selectivity and/or sensitivity. Analytical parameters, such as sensitivity, concentration range of linear response, and limit of detection of the potassium sensor with the optimized membrane composition, are comparable to those of PVC. Though the selectivity coefficients of the polyurethane membrane are higher than those of PVC-based ISE, they satisfy the requirements for measurements in blood.³⁶ Low interference from lipophilic anions and a long lifetime during constant contact with solution are characteristic for the membranes studied.

This polymer has excellent adhesion to a silylated oxide surface and being photosensitive can be directly patterned using conventional photolithographic techniques. These features permit the use of highly productive technology for sensor fabrication in which an ion-sensitive layer is deposited directly on a wafer with several devices on it. Moreover, application of photocurable polymers of the same class for encapsulation of miniature sensors³⁴ resolves the problem of compatibility between the encapsulating and the membrane materials.

ACKNOWLEDGMENT

The authors are grateful to UCB Chemicals for the supply of acrylated oligomers. Financial support from CIRIT, Barcelona, CICYT, Madrid (Program BIO93-0635), and INTAS, Brussels (Project 93-1418) is also acknowledged.

Received for review March 13, 1995. Accepted June 21, 1995.*

AC950249C

(34) Bratov, A.; Muñoz, J.; Domínguez, C.; Bartoli, J. *Sens. Actuators B*, in press.

(35) Moody, G. J.; Saad, B.; Thomas, J. R. D. *Analyst* **1987**, *112*, 1142-1147.

(36) *Ionophores for ion-selective electrodes and optodes*; Fluka Chemie AG: Buchs, 1991.

* Abstract published in *Advance ACS Abstracts*, August 1, 1995.

Detection of Bioactive Oligopeptides after Microbore HPLC with Electrochemical Detection of Their Cu(II) Complexes: Effect of Operating Parameters on Sensitivity and Selectivity

Jian-Ge Chen and Stephen G. Weber*

Department of Chemistry, University of Pittsburgh, Pittsburgh, Pennsylvania 15260

We used a microbore reversed phase column for acetonitrile/0.1% aqueous TFA gradient elution separation of peptides with the detection of their copper complexes by electrochemical detection. The copper complexes are formed in a short (1 or 1.5 min) postcolumn reactor following mixing of the eluent with the postcolumn reaction phase. Detection can be at an upstream anode or a downstream cathode of a dual-electrode electrochemical detector. The following parameters have been investigated for their effect on the sensitivity and the selectivity of the procedure: postcolumn pH, buffer type, temperature, reaction time, and anode potential. Of the 23 bioactive peptides used, there are several that fall into classes according to their chemical and electrochemical behavior with copper(II): those with a blocked terminal amine, those with aspartate in the third position, those that have an electroactive amino acid, and those that have a cyclic structure formed by the amide backbone through a Cys-Cys disulfide bridge. Depending on these attributes, the operating parameters have an influence on the sensitivity of the determination. Among the more well-defined results are the following. Uncomplicated peptides with a free amine terminus react rapidly in the postcolumn reactor and give signals in the range predicted by theory. There is evidence that longer peptides, and those with a blocked amine terminus, have a sensitivity limited by kinetic factors. The oxidations of tyrosine and tryptophan in peptides are dramatically influenced by buffer type at pH 9.8. At pH 8.0, there is no signal from several peptides in phosphate buffer, while in borate there is a signal.

Peptides play a very important role in biological processes, e.g., neurochemistry.¹ As a result, their determination is an important objective. Many peptide determinations are carried out by immunoassay. However, immunoassays have drawbacks that are not suffered by well-conceived chromatographic procedures: they can be slow, the selectivity among closely related species can be questionable, and they can miss the unexpected because the reagents are designed for molecular selectivity. On the other hand, they have the low detection limits required for much peptide work. The problem of selectivity among closely related species

can be solved by using HPLC with immunoassay detection.² This technique is extremely powerful, but by no means routine. For more routine work with good detection limits, amine-specific chemical derivatization can be used to form fluorescent adducts from amino acids and peptides. This has been demonstrated most convincingly with fluorescence detection in HPLC and CZE.³⁻⁹ These techniques have considerable merit. However, there are drawbacks to them. Numerous peptides in any given biological sample do not possess any primary amine, thus they will not be seen by the technique. Numerous amines in any given sample are not peptides. The challenge, then for the separation/detection approach is to have a broadly applicable system for peptides with the low detection limits required for biological and pharmaceutical studies. Further, it would be beneficial to have some gross selectivity control in the detection step to minimize the burden on the separation step.

We have been pursuing the latter goal using a postcolumn reaction followed by electrochemical detection.¹⁰⁻¹³ The derivatization reaction is simply reaction with Cu(II) in basic solution.^{13,16} The complexation for small peptides is fast and reversible. The product is easily oxidized, and the electrochemistry is also fast and reversible. The detector is a dual-electrode amperometric detector in which the upstream anode oxidizes Cu(II) to Cu(III) and the downstream cathode reduces Cu(III) back to Cu(II). As the chemical selectivity is for the peptide backbone, it is more purely a reagent for peptides than amine-reactive reagents.

(1) Hockfield, T. *Neuron* 1991, 7, 867.

- (2) Liu, D.; Dass, C.; Wood, G.; Desiderio, D. M. *J. Chromatogr.* 1990, 500, 395.
- (3) Dovichi, N. J. *Rev. Sci. Instrum.* 1990, 61, 3657.
- (4) Orwar, O.; Sandberg, M.; Jacobson, I.; Sundahl, M.; Folstad, S. *Anal. Chem.* 1994, 66, 4471.
- (5) Sweedler, J. V.; Fuller, R.; Tracht, S.; Timperman, A.; Tomo, V.; Khaib, K. *J. Microcolumn Sep.* 1993, 5, 403.
- (6) Dave, K. J.; Stobaugh, J. F.; Rossi, T. M.; Riley, C. M. *J. Pharm. Biomed. Anal.* 1992, 10, 965.
- (7) Toulas, C.; Hernandez, L. *Analysis* 1992, 20, 583.
- (8) Bosick, J. M.; Strojek, J. W.; Metcal, T.; Kuvana, T. *Appl. Spectrosc.* 1992, 46, 1332.
- (9) Anumula, K. R.; Schulz, R. P.; Back, N. *Peptides* 1992, 13, 663.
- (10) Warner, A. M.; Weber, S. G. *Anal. Chem.* 1989, 61, 2664.
- (11) Tsai, H.; Weber, S. G. *J. Chromatogr.* 1990, 513, 451.
- (12) Tsai, H.; Weber, S. G. *J. Chromatogr.* 1991, 542, 345.
- (13) Tsai, H.; Weber, S. G. *Anal. Chem.* 1992, 64, 2897.
- (14) Chen, J.-G.; Vinski, E.; Colizza, K.; Weber, S. G. *J. Chromatogr. A* 1995, 105, 171.
- (15) Martell, A. E.; Smith, R. M. *Critical Stability Constants*, Vol. 1. *Amino Acids*; Plenum Press: New York, 1989.
- (16) Youngblood, M. P.; Chellappa, K. L.; Bannister, C. E.; Margerum, D. W. *Inorg. Chem.* 1981, 20, 1742.

Recently we demonstrated that the procedure is entirely compatible with the most common peptide separation mobile phase, 0.1% aqueous TFA with acetonitrile gradient.¹⁷ Detection limits with our microbore system range from 20–100 fmol (100 μ L of 0.2–1.0 nM) for the nonelectroactive peptides (using the cathode signal) and 6–40 fmol (100 μ L of 60–400 pM) for electroactive peptides (using the anode signal).¹⁷ Data were obtained with a pH 9.8 carbonate buffer postcolumn phase and a 1.5 min postcolumn reactor at 50 °C. The only control over selectivity is the separation; the detection does not typically distinguish among various peptides.

The major objective of the current work is to probe the major parameters that control the detection selectivity in chromatograms of peptide mixtures. Twenty-three bioactive peptides, from 4 to 18 amino acids long, have been studied. Among these compounds are peptides that have a particular property that influences the chemistry or electrochemistry of the Cu(II)–peptide complex. From the data presented, it is possible to choose conditions that detect peptides without much selectivity among peptide classes. On the other hand, one can also find conditions that yield considerable selectivity for, or against, a particular class of peptides.

EXPERIMENTAL SECTION

Reagents. All peptides, trifluoroacetic acid (TFA; spectroscopic grade), and 1-propanol (spectroscopic grade) were purchased from Sigma (St. Louis, MO). Acetonitrile (HPLC grade) was purchased from Fisher (Pittsburgh, PA). Analytical grade boric acid (Fisher), sodium bicarbonate (Mallinckrodt, Paris, KY), sodium carbonate (Fisher), glycerol (Fisher), sodium hydroxide (Fisher), and sodium phosphate monobasic and dibasic (both from Fisher) were used without further purification. Both the ACS certified copper sulfate pentahydrate (Fisher) and sodium potassium tartrate dihydrate were recrystallized from water before use. All solutions were made with Milli-Q house-deionized water. Peptide stock solutions were prepared according to the product sheet or solubility information provided by Sigma.

Mobile Phases. The binary gradient was made from solvent A: 0.1% TFA/3% 1-propanol in water, or B, 0.1% TFA/3% 1-propanol/60% acetonitrile in water. The 3% 1-propanol used in the mobile phase is to shorten the reequilibration time after the gradient.¹⁸ Gradient elution timing is provided in the figures.

Postcolumn Buffers. For pH 9.8, we used three buffer systems: (1) 1.2 M carbonate buffer, prepared from bicarbonate and carbonate, (2) 0.6 M boric acid/NaOH buffer, and (3) 0.6 M boric acid/0.6 M glycerol/NaOH buffer (also pH 9.5 and 10.0). For pH 8.0 buffers, we used two buffer systems: (1) 0.4 M phosphate buffer and (2). 0.6 M boric acid/NaOH buffer. Postcolumn copper concentrations are always in excess (>500 times the analyte). The copper to tartrate molar ratio is always 1:6.

One letter standard abbreviations are used for all peptides: A = Ala, C = Cys, D = Asp, E = Glu, F = Phe, G = Gly, H = His, I = Ile, K = Lys, L = Leu, M = Met, N = Asn, P = Pro, Q = Gln, R = Arg, S = Ser, T = Thr, V = Val, W = Trp, Y = Tyr.

Instrumentation. Figure 1 shows the setup of the microbore HPLC system. Mobile phases were pumped with a Waters 600 MS quaternary pump (Waters, Medford, MA). The separation is

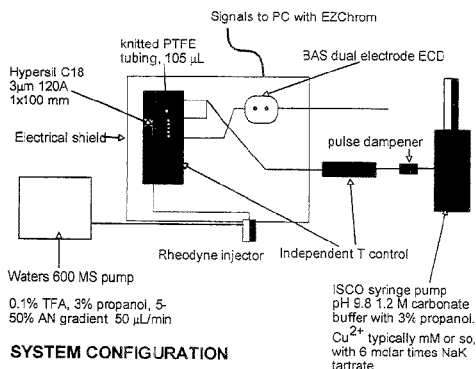


Figure 1. Microbore HPLC instrumentation.

done with a Hypersil C18 1 \times 100 mm column with guard (1 \times 20 mm, Keystone Scientific, Bellefonte, PA). The postcolumn phase is pumped with an Isco Model 100DM syringe pump (Isco, Lincoln, NE). The eluents from the pumps are mixed in a mixing Y. The postcolumn reactors are knitted Teflon tubing (0.01 in. i.d.). The postcolumn reactor temperature and the postcolumn phase before it reaches the reactor are independently controlled by BAS temperature controllers. The Cu(II)–peptide complex is detected with a BAS LC-4C dual-electrode electrochemical detector with standard glassy carbon electrodes and 0.0005 in. microbore spacer (BAS, W. Lafayette, IN). All injection volumes are 100 μ L. All potentials given are referenced to Ag/AgCl (3 M KCl). Signals from the detector are collected at 1 Hz by EZChrom (Scientific Software, San Ramon, CA). Areas were determined after manually specifying the limits of integration for each peak.

RESULTS AND DISCUSSION

We begin by discussing sensitivity. Following this, we discuss selectivity of detection. The selectivity discussion is in two parts, potential dependence and matrix dependence.

Sensitivity and Linearity. Sensitivity in electrochemical detection can be calculated.¹⁹ Logical units to use are current/concentration or charge/mole. We advocate the use of nanocoulombs per picomol as units for sensitivity scaling because that unit roughly reflects the percent conversion of Cu(II)–peptide to Cu(II)–peptide; i.e., for a one-electron reaction, 1 mol of analyte gives 96 500 C. Thus, for 100% conversion of a one-electron analyte, the sensitivity would be 96.5 nC/pmol. Furthermore, as a measure of area, it is independent of band broadening so it is a figure of merit of the detector. We estimate that the reproducibility of sensitivities over long times (weeks) is at worst 20%.

Sensitivity of the Detection System. In prior work¹⁷ we established that the theoretical and experimental values for sensitivity were in good agreement for a small peptide GGFL, a hydrolysis product of Leu-enkephalin. For this peptide, which can only bind one Cu(II) in a bidentate complex, the sensitivity is \sim 20 nC/pmol when the potential is in the diffusion-limited range. Longer peptides could in principle bind more than one Cu(II), and this would increase the sensitivity. However, an increase in size for a peptide that binds a single Cu(II) lowers the sensitivity

(17) Chen, J.-G.; Woltman, S. J.; Weber, S. G. *J. Chromatogr. A* 1995, 691, 301
(18) Cole, L. A.; Dorsey, J. G. *Anal. Chem.* 1990, 62, 16

(19) Weber, S. G.; Long, J. T. *Anal. Chem.* 1988, 60, 903A

Table 1. Linear Regression (nC vs pmol) Results of Cathodic Signal (0.09 V) of Nonelectroactive Peptides at Two Different Anodic Potentials and Postcolumn Buffer Systems with Gradient Elution^a

peak no.	compound ^c	sequence	I, nC/pmole	σ	R^2	n	II, nC/pmole	σ	R^2	n
6	des-Y-Leu-enkephalin	GGFL	9.9	0.15	0.999	6	5.2	0.08	0.999	6
17	SPF 6-11 ^b	QPFGLM-NH ₂	4.7	0.02	1.000	5	0.22	0.02	0.952	6
20	ALILTLVS	ALILTLVS	5.6	0.10	0.999	5	2.9	0.03	1.000	6
21	HPFGRHF 14-26	DAENLDSFQEV	1.7	0.11	0.987	5	1.4	0.04	0.996	6
8	fibrinopeptide A	ADSGEFDLAEGGGVR	2.9	0.13	0.996	4	0.98	0.07	0.977	6
16	octadecaneuropeptide	QATVGDVNTDRPGLLDLK					0.95	0.04	0.993	3
1	RFDS	RFDS					5.5	0.06	1.000	3
5	speract	GFDLNGGGVG					0.61	0.01	0.999	5
14	N-formyl-MLF	N-formyl-MLF	2.4	0.11	0.994	5	3.6	0.06	0.999	5
	N-formyl-MLFF	N-formyl-MLFF	0.66	0.02	0.998	5	1.9	0.10	0.988	5
18	pE ⁸ -SPF 6-11	pEFFGLM-NH ₂	4.4	0.06	0.999	5	1.6	0.09	0.987	6

^a All y-intercepts within a 95% confidence intervals are zero. σ , standard deviation, R^2 , coefficient of correlation, and n , number of data points on the line; (I) Postcolumn reagents, 0.6 M pH 10.0 borax/glycerol/NaOH buffer with 3% 1-propanol and 0.5 mM CuSO₄; 1.5 min postcolumn reaction time; anodic potential of 0.50 V; and range from 0.5 to 100 pmol. (II) Postcolumn reagents, 0.4 M pH 9.8 carbonate buffer with 40% acetonitrile and 1.0 mM CuSO₄; 1.0 min postcolumn reaction time, anodic potential of 0.80V, and range from 2 to 50 pmol. Peak numbers correspond to numbers in the chromatograms. ^b SPF, substance P fragment.

through the diffusion coefficient. We can estimate, albeit roughly, the extent of the latter effect. Values for the diffusion coefficient of the biuret complexes of G₃, G₄, and G₅ have been determined previously.²⁰ A linear regression of log (D) vs log (MW) yields a fit with $r^2 = 0.994$ and a slope of $-0.33 (\pm 0.025)$. This is a reasonable value of the exponent for this dependence. Sensitivity depends on the $2/3$ power of D , and D depends on the $-1/3$ power of MW, so sensitivity depends to the $-2/9$ power of MW. If the sensitivity of GGFL is 20 nC/pmole, we would predict a sensitivity for fibrinopeptide A (primary sequences are in Table 2) of $(MW_{GGFL}/MW_{FP-A})^{2/9} \times 20$ or ~ 15 nC/pmole. This represents the range of anode sensitivities to be expected from a single Cu(II) biuret complex for the size range of peptides considered here. Larger sensitivities imply a second electroactive center in the molecule. Lower sensitivities imply that the complex is not fully formed in the reaction time given, or the potential is not at the diffusion-limited value for that complex. Cathode sensitivities are proportional to anode sensitivities. The ratio for uncomplicated, reversible electron transfer is 0.37.²⁰

Ideally, each value of sensitivity would be determined as the slope of the relevant calibration curve. Practically, this is so time consuming as to be excessively burdensome. Thus, we have chosen to establish linearity for the Cu(II) complexes of the nonelectroactive peptides under two very different sets of conditions. All sensitivities have been determined based on gradient elution peak areas integrated by EZChrom with manually determined baselines.

Linearity of the Detection System. Table 1 gives linear regression results from data obtained with two totally different potentials and matrices for a series of peptides that do not contain any electroactive amino acid residue. Linear regression results for peptides with native electrochemistry are given elsewhere.¹⁷ As shown by Table 1, the calibrations are linear from 0.5 to 100 pmol or 5 nM to 1 μ M (100 μ L). With the 1 μ M injection, however, we begin to see overloading of the column. We conclude then that our detection system is linear in the nanomolar range and we will use repeated concentration injections at a single concentration to determine sensitivity under a variety of conditions.

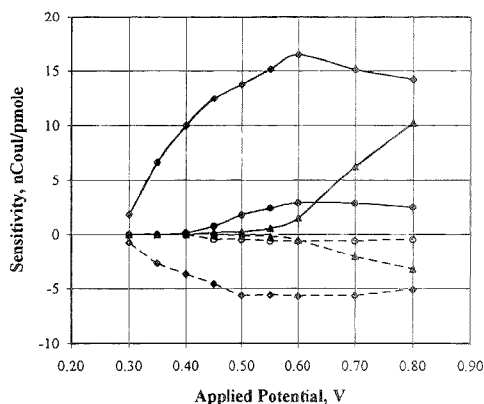


Figure 2. Hydrodynamic voltammograms of 0.5 μ M fibrinopeptide A (upper, diamond), 0.5 μ M speract (middle, triangle), and 1.0 μ M N-formyl-MLFF (lower, circle) obtained by gradient elution with a pH 9.8 carbonate postcolumn phase: anode, potentials shown, solid symbols; cathode, 0.1 V, open symbols.

Potential Dependence of Signal. Figures 2 and 3 give the hydrodynamic voltammograms (HDVs) of fibrinopeptide A (FP-A), speract, N-formyl-MLFF, and oxytocin (Table 2 has amino acid compositions). Individual points are sensitivities from chromatograms with a pH 9.8 carbonate postcolumn phase. These are representatives of four classes of compounds being studied, namely, the ordinary oligopeptides (peptides in which there is nothing particularly noteworthy about their electrochemistry or Cu(II) coordination chemistry), peptides with Asp in the third position, N-acylated peptides, and peptides containing electroactive amino acid residues, respectively. Where comparisons have been made, these and other HDVs obtained by HPLC are well in agreement with HDVs by a rotating ring-disk electrode system, where the disk electrode resembles the upstream anode and the ring corresponds to the downstream cathode.¹⁷

FP-A, an ordinary peptide, forms the Cu(II)-peptide complex with its amine and three amido nitrogens as ligands in a square-planar geometry as evidenced by its low half-wave potential

(20) Woltman, S. J.; Alward, M. A.; Weber, S. G. *Anal. Chem.* **1995**, *67*, 541.

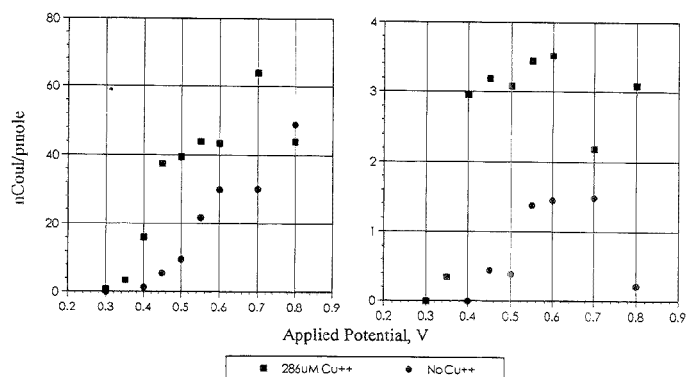


Figure 3. Hydrodynamic voltammograms of 0.1 μM oxytocin obtained by gradient elution with a pH 9.8 carbonate postcolumn phase: left, anode; right, cathode.

Table 2. pH Selectivity of the Biuret Detection System^a

peak no.	compound	sequence ^{a,b}	pH 9.8		pH 8.0	
			0.50 V	0.80 V	0.50 V	0.80 V
6	dcx-Y-Leu-enkephalin	GGFL	15 (46)	16 (51)	6.5 (17)	13 (23)
17	SPF 6-11	QFFGLM-NH ₂	4.7 (32)	4.6 (39)	4.0 (55)	4.4 (41)
20	ALILTLVS	ALILTLVS	3.4 (35)	2.1 (57)	2.0 (55)	1.8 (47)
21	HPPGRHF 14-26	DAENLIDSFQEIV	0.95 (26)	6.0 (52)	0.0 (-)	0.0 (-)
8	fibrinopeptide A	ADSGEGDPLAEGGGVR	8.7 (38)	18 (37)	0.0 (-)	0.0 (-)
16	octadecaneuropeptide	QATVGDVNTDRPGLLDLK	4.5 (36)	13 (31)	5.4 (52)	6.9 (38)
1	R ^h FS	R ^h FS	0.0 (-)	28 (34)	0.0 (-)	18 (41)
5	speract	GFDLNGGGVG	0.0 (-)	9.9 (35)	0.0 (-)	5.4 (46)
14	N-formyl-MLF	N-formyl-MLF	5.5 (45)	6.0 (52)	0.0 (-)	0.0 (-)
	N-formyl-MLFF	N-formyl-MLFF	1.6 (32)	2.8 (23)	0.0 (-)	0.0 (-)
18	pE ⁸ -SPF 6-11	β EFFGLM-NH ₂	6.0 (45)	5.8 (57)	0.0 (-)	0.0 (-)
1	DSIP	WAGGDASGE	8.3 (13)	24 (4.2)	1.7 (37)	9.1 (5.6)
11	WMDF-NH ₂	WMDF-NH ₂	15 (5.1)	130 (1.7)	0.0 (-)	38 (3.2)
4	leucokinin II	DPGFSSWG-NH ₂	26 (20)	110 (3.3)	2.3 (0.0)	21 (2.2)
10	Leu-enkephalin	YGGFL	43 (5.1)	90 (5.4)	8.8 (36)	33 (9.7)
18	α -endorphin	YGGFMTSEKSQTFLVT	24 (5.4)	49 (4.1)	22 (25)	31 (5.5)
7	oxytocin	<i>C(YIQN)</i> CPLG-NH ₂	34 (8.3)	69 (2.6)	14 (31)	18 (7.2)
3	Lys ⁸ -vasopressin	<i>C(YFQN)</i> CPLG-NH ₂	30 (7.3)	89 (1.0)	16 (23)	21 (19)
15	neurotensin	β ELEYENKRRRPYIL	22 (10)	110 (2.9)	2.8 (42)	22 (14)
12	angiotensin II	DRVVIHFP	18 (5.5)	63 (3.2)	1.7 (0.0)	27 (8.9)
2	RKD ¹ VY	RKD ¹ VY	6.5 (6.6)	110 (1.3)	0.78 (0.0)	44 (1.8)
13	ACTH 1-10	YSMEHFRWG	22 (4.2)	94 (2.7)	9.3 (24)	24 (9.2)
21	Tyr-somatostatin	YAGC(KNFFWKIFT)S	1.7 (4.1)	10.0 (2.8)	6.7 (18)	10 (7.6)

^a Anodic sensitivities (nC/pmol) are given. Percent collection efficiency is given in parentheses. Peak numbers correspond to numbers in the chromatograms. ^b Italic type, important functional groups mentioned in text; boldface type, electroactive amino acid residue.

(Figure 2, ~ 0.45 V vs Ag/AgCl).²¹ Experimentally, FP-A yields a mass transport-limited sensitivity (16 nC/pmol, Table 2) equivalent to one electron, showing that, with our postcolumn reactor (50 °C for 1.5 min), only one Cu(II) binds to FP-A. The collection efficiency (cathode signal/anode signal) is approaching the theoretical maximum (0.37). This behavior is consistent with our smaller model compounds representing "ordinary" peptides.¹⁷

Speract represents an interesting class of peptides. When Asp is in the third position, the fourth ligand in the square-planar copper complex is not the amido nitrogen; rather it is the carboxylate of the Asp residue.²² As a consequence of this altered environment around the Cu(II), the half-wave potential of the

complex is rather high (Figure 2). It is the same as that of a tripeptide, (~ 0.7 V vs Ag/AgCl) because oxygen is not as good a donor ligand as nitrogen in stabilizing the Cu(II)-peptide complex. On the other hand, this copper complex is easier to form than a tripeptide copper complex because it forms a six-membered ring in the square-planar geometry rather than a five-membered ring as in a tripeptide. The collection efficiency for this peptide is also near-theoretical, but the sensitivity is slightly low. As can be seen from Figure 2, the diffusion-limited current is not attained at 0.8 V, and this is confirmed by the numerical value of the sensitivity.

Fluorescence detection based on derivatization of primary amines cannot detect N-acylated peptides, cyclic peptides, and peptides with pyroglutamate (in which the γ -carboxylate forms a lactam with the primary amine) at the amine terminus. The

(21) Bossu, F. P.; Chellappa, K. L.; Margerum, D. W. *J. Am. Chem. Soc.* 1976, 99, 2195.

(22) Decock-Lé Reverend, E.; Lebikiri, A.; Livera, C.; Petit, L. D. *Inorg. Chim. Acta* 1986, 129, 1-9.

present system, though not used to investigate cyclic peptides yet, shows promising results for the other two classes of peptides. The HDV of *N*-formyl-MLFF (Figure 2) clearly shows the formation of the Cu(II)-peptide complex with a half-wave potential of ~ 0.5 V vs Ag/AgCl, typical of a Cu(II)(peptide H_{-2}) complex. The H_{-2} indicates that the peptide has lost $3H^+$ to form the complex. However, in comparison to the sensitivity of FP-A under the same postcolumn reaction conditions (pH 9.8, 50 °C for 1.5 min), the sensitivity is rather low. This is likely due to incomplete formation of the complex. This hypothesis and other examples of this class of peptide, including neurotensin (with pE in the N-terminus), *N*-formyl-MLF, and pE³-substance-P fragments 6–11, will be discussed below when we consider the effect of postcolumn temperature and pH.

The electrochemistry of the Cu(II) complexes in small peptides containing electroactive amino acid residues is complicated and has been discussed.^{14,23} In short, the half-wave potentials without the biuret reaction at pH 9.8 of Tyr- and Trp-containing peptides are about 0.50 and 0.57 V vs Ag/AgCl, respectively, corresponding to a one- to two-electron transfer.^{11,14,22,24} In the presence of the biuret reagent, however, the half-wave potentials are lower (as low as 0.35 V), corresponding to two- to three-electron transfers for both cases. The example given here is oxytocin. Its primary sequence is C(YIQN)CPLG-NH₂. The parentheses indicate that the Cys residues are involved in a cycle formed from an S–S bond and the peptide backbone. The HDV (Figure 3) clearly shows the formation of the Cu(II)-peptide complex with a half-wave potential of only 0.4 V vs Ag/AgCl. This example shows two things: First, even though it is possible to detect electroactive peptides without the biuret reaction, the potential required is lower with the Cu(II)-peptide complex and the sensitivity is higher both at the anode and the cathode. Second, this example indicates that the S–S bridge does not hinder the complexation, as will also be seen with data for Lys⁸-vasopressin and Tyr-somatostatin presented below. We also note that the negative influence of the electroactive amino acids on the cathodic signal is less in these bioactive peptides than in the model peptides that have been studied.^{14,23} This is good, for it means that the cathode can be used for determinations of bioactive peptides, irrespective of their composition.

Matrix Dependence of Signal. pH Dependence of Signal at Two Potentials. Table 2 gives sensitivities for pH 9.8 (carbonate) and pH 8.0 (borate), at 0.50 and 0.8 V anodic potentials and the corresponding downstream cathode sensitivities at 0.10 V. Cu(II)-peptide complexes containing at least four amino acids exist in two forms in weakly basic solutions.^{15,16} If we denote a peptide that has lost n peptide bond hydrogens as pepH_{- n} , then copper complex with four N atoms in the coordination environment, one amine and three amido, is denoted as Cu-pepH_{- n} . This is a base, the conjugate acid of which has a pK_a in the range of 8–9. The half-wave potential for the Cu(pepH₋₂) form of the complex is ~ 0.7 V, while for Cu(pepH₋₃) it is ~ 0.45 V.²⁰ Thus, for an ordinary peptide we would expect about half the anode signal at pH 8.0, 0.50 V in comparison to pH 8.0, 0.8 V because at the lower potential only the Cu(H₋₂) form is oxidized while both are oxidized at higher potentials. There is some augmentation of the low potential wave with respect to the high potential wave because of the deprotonation of Cu(pepH₋₂) that occurs. The importance of

this process depends on flow velocity and the rate constant for the process.^{17,20} Also, we expect that all of the peptide is in the easily oxidized form at pH 9.8. Of the ordinary peptides in Table 2 (peaks 6, 17, 20, 21, 8, and 16), three correspond somewhat to this picture (peaks 6, 8, and 16).

It appears that longer nonelectroactive ordinary peptides (FP-A, HPPGRHF 14-26), as well as *N*-acylated peptides, and peptides with pyroglutamate in the amine terminus (14, *N*-FMLFF, 18), require higher pH for the complexation. Sensitivities at the higher pH are somewhat lower than expected.

Data for electroactive peptides at 0.8 V anodic potential are difficult to interpret because the current comes from both Cu(II) and the electroactive residue. The anodic sensitivity can correspond to as many as five electrons (WMDF-NH₂). Furthermore, and fortunately, the cathode signal when the anode is at 0.8 V is analytically significant for all of the electroactive peptides. When the applied anodic potential is 0.50 V at pH 8.0, only copper electrochemistry is seen, because the half-wave potentials of Tyr and Trp are above 0.5 V at pH 8.0.²⁴

The fact that not all peptides show what would be expected from equilibrium considerations at pH 8.0 leads to the conclusion that the rate of mixing or chemical reaction is a limiting factor in the formation of the signal-generating species for some peptides. As there should be very little change in mixing upon changing the pH, yet a significant effect of pH is seen on the signal; we infer that, for some peptides, the kinetics of the reaction are limiting the amount of signal formed. Kinetics notwithstanding, it is clear from Table 2 that all peptides yield useful signals under some condition. Because of the clear implication of kinetic control of signal, we have turned to the postcolumn temperature and time to see if the sensitivity can be improved through increases in either or both.

Postcolumn Temperature Dependence of Signal. Table 3 gives anodic and cathodic sensitivities for postcolumn temperatures 30 (column I) and 50 °C (column II) obtained with a pH 9.8 carbonate buffer postcolumn phase along with other data which we will discuss later. The observation of the anodic signal is consistent; for all but a few peptides, which are discussed below, the higher the temperature, the higher the sensitivity. This reflects the kinetic barrier to the formation of the signal-producing species. The sensitivity is higher at higher temperature because higher temperature leads to more copper complex formation within the postcolumn reaction time window. At the cathode, the nonelectroactive and the electroactive peptides behave differently. For nonelectroactive peptides, the cathode signal increases with temperature, reflecting the increase in anode signal. For the electroactive peptides, however, the higher temperature generally leads to a decrease in cathode sensitivity. Our investigations of smaller, model peptides containing Trp and Tyr have led to the conclusion that at 0.8 V the likely reaction product of the oxidation is a Cu(III) complex of a peptide with an oxidized Tyr or Trp residue. The peptide may have been oxidatively cleaved as well.^{14,23} The two-electron oxidation products can be further oxidized,¹⁰ but we have not seen evidence of that on the subsecond time scale of voltammetry. Here however, the longer time scale allows for further reactions, probably the reduction of Cu(III) by the modified Tyr or Trp. The increase in temperature speeds up the chemical process of degrading the Cu(III)-peptide complexes. This observation, in conjunction with the knowledge that the collection efficiency is better at 0.50 V for electroactive peptides.

(23) Tsai, H.; Chen, C.; Chen, J.-G.; Wolman, S. J.; Weber, S. G., in preparation.
(24) Harriman, A. J. *Phys. Chem.* 1987, 91, 6102.

Table 3. Sensitivities (nC/pmol) at Different Temperatures and with Various Buffer Types at pH 9.8 and pH 8.0^a

peak no.	compound ^a	I (pH 9.8, carbonate, 30 °C)	II (pH 9.8, carbonate, 50 °C)	III (pH 9.8, borax/glycerol, 50 °C)	IV (pH 9.8, borax, 50 °C)	V (pH 8.0, phosphate, 50 °C)	VI (pH 8.0, borax, 50 °C)
6	des-Y-Leu-enkephalin	13 (5.7)	16 (8.1)	15 (8.0)	14 (8.2)	0.0 (0.0)	13 (3.0)
17	SPF 6-11	4.3 (2.0)	4.6 (1.8)	5.6 (2.4)	3.7 (1.9)	0.0 (0.0)	4.5 (1.8)
20	ALILTLVS	1.1 (0.65)	2.1 (1.2)	1.2 (1.1)	1.8 (0.90)	0.0 (0.0)	1.8 (0.85)
21	HPPGRHF 14-26	1.7 (0.88)	6.0 (3.1)	2.5 (0.51)	1.0 (0.48)	0.0 (0.0)	0.0 (0.0)
8	fibrinopeptide A	12 (2.9)	18 (6.7)	5.5 (1.6)	6.5 (2.8)	0.0 (0.0)	0.0 (0.0)
16	octadecaneuropeptide	9.3 (2.8)	13 (4.0)	7.9 (3.4)	7.0 (3.1)	0.0 (0.0)	6.9 (2.6)
1	RFDS	24 (6.0)	28 (9.4)	14 (7.0)	13 (5.8)	22 (8.7)	18 (7.4)
5	speract	6.8 (1.9)	9.9 (3.5)	4.8 (2.7)	5.0 (2.6)	7.0 (2.5)	5.5 (2.5)
14	N-formyl-MLF	5.9 (2.7)	6.0 (3.1)	0.85 (0.52)	0.72 (0.62)	0.0 (0.0)	0.0 (0.0)
	N-formyl-MLFF	1.3 (0.2)	2.8 (0.65)	0.82 (0.44)	2.4 (0.42)	0.0 (0.0)	0.0 (0.0)
18	pE ⁸ -SPF 6-11	5.0 (2.5)	5.8 (3.3)	2.6 (2.3)	2.7 (1.4)	0.0 (0.0)	0.0 (0.0)
1	DSIP	52 (2.8)	24 (1.0)	15 (0.60)	6.6 (0.53)	25 (0.81)	9.1 (0.51)
11	WMDF-NH2	65 (4.9)	126 (2.2)	50 (4.5)	25 (5.8)	83 (0.78)	38 (1.2)
4	leucokinin II	83 (3.6)	109 (3.6)	36 (2.5)	19 (3.9)	6.2 (0.0)	21 (0.46)
10	Leu-enkephalin	92 (7.1)	90 (4.9)	55 (5.3)	31 (6.9)	63 (2.1)	33 (3.2)
18	α -endorphin	88 (5.0)	49 (2.0)	47 (4.1)	24 (3.2)	68 (3.1)	31 (1.7)
7	oxytocin	57 (2.8)	69 (1.8)	32 (2.5)	15 (2.2)	45 (1.7)	18 (1.3)
3	Iys ⁸ -vasopressin	82 (1.8)	89 (0.93)	34 (2.7)	15 (2.2)	4.8 (0.0)	21 (4.0)
15	neurotensin	55 (2.9)	112 (3.3)	37 (3.8)	17 (3.4)	66 (2.7)	22 (3.0)
12	angiotensin II	92 (3.8)	63 (2.0)	26 (2.7)	13 (2.8)	4.3 (0.80)	27 (2.4)
2	RKQVY	63 (1.3)	111 (1.4)	48 (0.98)	23 (0.93)	65 (1.7)	44 (0.78)
13	ACTH 1-10	84 (3.9)	94 (2.5)	38 (3.4)	19 (4.2)	73 (0.0)	24 (2.2)
21	Tyr-somatostatin	51 (3.9)	10.0 (0.28)	15 (1.5)	7.5 (1.4)	36 (0.0)	10.0 (0.76)

^a All applied potentials are anode 0.80 V and cathode 0.10 V. Cathodic sensitivities are given in parentheses. ^b Italic type, compounds contain important function groups mentioned in text.

suggests that it is more selective to detect small electroactive oligopeptides with both the cathode and anode when the anode is at 0.50 V and at 30 °C rather than 50 °C. On the other hand, it is much more sensitive to detect all peptides at the anode (0.80 V) with higher postcolumn temperature.

The sensitivities of a few of the electroactive peptides, but of none of the nonelectroactive peptides, decrease with temperature at the anode. Although all of the solvents are degassed before use, there is certainly enough oxygen in solution to oxidize these species. It is very likely that oxidation of the analyte occurs during the postcolumn reaction time, more rapidly at higher temperatures. The remainder of Table 3 will be considered following a discussion of the postcolumn reaction time dependence of the signal.

Postcolumn Reaction Time Dependence of Signal. Table 4 provides both the peak area (nC) and peak height (nA) obtained with a 1.0 and a 1.5 min knitted Teflon postcolumn reactor at 50 °C for the nonelectroactive series of peptides. The observation is the expected one: the longer the reaction time, the higher the percent conversion or the larger the peak area. On the other hand, the peak height stays relatively constant for small ordinary oligopeptides (up to eight amino acid residues) because narrower peaks were observed with the shorter postcolumn reactor due to the presence of less band broadening. With larger peptides, N-acylated peptides, and peptides with pyroglutamate in the first position, the difference in peak height is significant when the postcolumn reactor changes from 1.0 to 1.5 min. We conclude that we can detect selectively smaller oligopeptides with a shorter, less obtrusive, postcolumn reactor. For the detection of other peptides we mentioned, however, a longer reaction time is desirable.

Postcolumn Buffer Dependence of Signal. In Table 3, columns II-VI show the effect of different postcolumn buffer systems used in this study for pH 9.8 and pH 8.0. For pH 9.8, we have used three buffer systems, namely, bicarbonate/carbonate, boric acid/

Table 4. Effects of Postcolumn Reaction Time (PCRT) on Cathodic Peak Area and height with a pH 9.8 Postcolumn Reagent^a

peak no.	compound	1.0 min PCRT		1.5 min PCRT	
		area (nC)	ht (nA)	area (nC)	ht (nA)
6	des-Y-Leu-enkephalin	29	1.1	32	1.0
17	SPF 6-11	10.0	0.32	11.0	0.36
20	ALILTLVS	6.5	0.27	9.5	0.31
21	HPPGRHF 14-26	6.0	0.25	9.5	0.34
8	fibrinopeptide A	3.8	0.19	8.5	0.25
16	octadecaneuropeptide	9.0	0.33	9.5	0.31
1	RFDS	25	0.99	27	1.0
5	speract	5.5	0.24	6.5	0.25
14	N-formyl-MLF	4.0	0.17	7.0	0.28
	N-formyl-MLFF	0.0	0.0	3.1	0.07
18	pE ⁸ -SPF 6-11	11.0	0.47	15.0	0.56

^a Upstream anode at 0.80 V. Injection, 50 nM and 100 μ L. Peak numbers correspond to numbers in the chromatograms.

sodium hydroxide, and boric acid/glycerol/sodium hydroxide. The latter buffer was an attempt to increase the organic solvent compatibility of the postcolumn phase. The pK_a (~9.3) of borax stays about the same in the presence and absence of 1 equiv of glycerol. Columns II-IV of Table 3 give the anodic and cathodic (in parentheses) sensitivities (anode at 0.80 V) for the three buffer systems. For the nonelectroactive peptides, the carbonate buffer is preferable to the other two. The largest differential effect tends to be for those peptides that have displayed kinetically limited sensitivity, e.g., FP-A, N⁶-MLF, pE⁸-SPF 6-11, and HPPGRHF 14-26. The enhancement by carbonate is not limited to these, however, e.g., RFDS, speract, and octadecaneuropeptide. From our earlier work,²⁵ we can say that in the carbonate buffer a significant fraction of the peptide exists as the α -aminocarbamate. It is possible that the anionic carbamate may react more rapidly

(25) Chen, J.-G.; Sandberg, M.; Weber, S. G. *J. Am. Chem. Soc.* **1993**, *115*, 7343.

with Cu(II) than the neutral amine terminus (the pK_a of the primary ammonium group in peptides is considerably lower than in amino acids).¹⁵ This is purely speculation at this stage.

It is known^{16,20} that, in carbonate-containing solution, copper–oligoglycine complexes are in equilibrium with a mixed-ligand complex consisting of Cu(II), peptide, and carbonate or bicarbonate. It is also possible that carbonate promotes exchange of Cu(II) between the reagent (tartrate complex) and the peptide (which exists as the carbamate). Thus the rate of the formation of the peptide complexes would be higher in carbonate buffer than in borate buffer.

Finally, we should mention for completeness that the mixed-ligand complex of Cu(II)–peptide–carbonate/bicarbonate is not electroactive at pH 9.8 and 0.8 V.²⁰ Carbonate inhibits the electrooxidation of the complex. This seems to contradict the data, but attention to time scales resolves the conflict. Because the exchange rate is significant, the inhibition is only seen on the millisecond time scale. The time scale of our detection is in the range of seconds. Thus, even though the electroinactive carbonate complex is present, it is oxidized because it proceeds through a chemical step, loss of carbonate/bicarbonate, before being oxidized. As a result, for the electroinactive peptides, the only effect of carbonate should be on the formation of the complex, not on its electrochemistry (but for a negligible effect of the difference in diffusion coefficients of the carbonate-containing complex and the carbonate-free complex).

Column II of Table 3 shows that the cathode signal reflects the anode signal; thus the carbonate has little influence on the reactions of the Cu(III) complex. This reinforces the earlier conclusion that the carbonate is not involved in the oxidation chemistry.

For the electroactive peptides, the dependence of the signal on buffer is remarkable and unexpected both for its magnitude and for its consistency among the peptides. We have discussed^{14,23} the oxidation mechanisms of Tyr- and Trp-containing peptides on model compounds and have related that to some bioactive peptides. A general result is that reactive intermediates are formed upon oxidation of Tyr and Trp residues. The reactions probably follow the commonly seen sequence²⁶ of electron transfer followed by proton transfer, and another electron transfer and so on, or the ECE mechanism. One reactive species is the neutral radical formed by the one-electron, one-proton oxidation of Tyr or Trp residues. We know it is reactive because of the ECE behavior of the residues^{14,23} that results often in the two-electron oxidation of these species. Two-electron oxidations result when the product of the first one-electron oxidation is a powerful reductant (easily oxidized) compared to the starting material. In the current context, such a reactive intermediate has two possibilities: reduce the electrode or reduce Cu(II). Which occurs depends on kinetics, mass transport, and concentrations.^{27,28}

To return to the current data, we see that, in the presence of carbonate, there is more signal at the anode, and less at the cathode, in comparison to the borate buffers. In turn, the same can be said for borate/glycerol in comparison to borate. Lower anodic current corresponds to higher cathodic current. This pattern is completely consistent with a buffer-sensitive chemical

reaction (C step) occurring in an ECE, or more complex, scheme. A faster C step provides more reactive species near the electrode where further oxidation occurs, increasing anodic sensitivity. A faster C step increases the rate of reduction of Cu(III), lowering the cathode signal. The effect is to a degree correlated with pK_a : the bicarbonate/carbonate pK_a is 9.8, while the pK_a measured in our laboratory for the borate is 9.30, and for the borate glycerol complex, 9.25. General-base catalysis of the proton loss is a plausible hypothesis for this effect.

Columns V and VI of Table 3 show the effect of the two buffer systems used for pH 8.0 buffering, namely, phosphate buffer and the borax buffer, for the same anodic and cathodic potentials as described above. Once again, it is clear that N-acetylated peptides and peptides with pyroglutamate in the amine terminus do not form the copper complex at such a low pH with either the phosphate or the borax buffer. It is clear that phosphate should be avoided, unless one can take advantage of the selectivity offered for a particular peptide. In conclusion, the borax buffer is a better choice of buffer for pH 8.0.

Example Chromatograms. Figure 4 shows the gradient elution of 100 nM (10 pmol) each of the 23 bioactive peptides used in this study obtained with a pH 9.5 boric acid/glycerol/NaOH postcolumn buffer and a 1.0 min postcolumn reactor at 50 °C. The top chromatogram is the anode and the bottom is the cathode at 0.8 and 0.085 V, respectively. All peaks are separated except two: peaks 1 (DSIP and RFDS) and 21 (Tyr-somatostatin and HPPGRHF 14–26). Inspection of the anode reveals the higher sensitivity for the electroactive peptides over the nonelectroactive peptides; all the tallest peaks correspond to electroactive peptides. There is no such selectivity with the cathode signals, though. On the other hand, inspection of the collection efficiency, given in parentheses in the figure legend, tells which peptides are electroactive (low efficiency) and which are not electroactive (high efficiency). The chromatogram shown in Figure 5 is the cathode with an upstream anode at 0.50 V. Peptides with Asp in the third position, such as speract, RKDVY, and WMDF-NH₂, and kinetically slowly reacting peptides, such as N-formyl-MLF and N-formyl-MLFF, are selectively filtered out of the chromatogram as compared with the cathode given in Figure 4. The collection efficiency is also given in parentheses. These numbers could be used as fingerprints for peptide identification and purification control. In general, nonelectroactive peptides have collection efficiencies around the theoretical maximum of 0.37, and tyrosine-containing peptides have the lowest. Besides identification, these collection efficiencies provide chemical insights into the amino acid composition of a peptide.

CONCLUSIONS

The analytical significance of this work is to demonstrate the capabilities of the biuret reaction in selective detection of peptides following their HPLC separation. All of the peptides investigated are detectable under the most forcing conditions: high pH and high potential. With appropriate control over these and the other conditions, it is possible to select for or against certain groups of peptides. In conclusion, we recommend the following conditions for interested readers who might consider using this detection system. First, phosphate buffer should be avoided under any circumstances. Second, anodic potential of 0.5 V and a cathodic potential of 0.1 V along with using a pH 9.8 carbonate buffer postcolumn phase is a good starting point for ordinary peptides. Third, a pH 8–9.5 postcolumn buffer and a ≤ 1.0 min postcolumn

(26) Albery, W. J.; Hitchman, M. L. *Ring-Disc Electrodes*; Clarendon Press: Oxford, U.K., 1971; pp 122–133.

(27) Amatore, C.; Saveant, J. M. *J. Electroanal. Chem.* **1977**, *85*, 27.

(28) Compton, R. G.; Mason, D.; Unwin, P. R. *J. Chem. Soc., Faraday Trans 1* **1988**, *84*, 183.

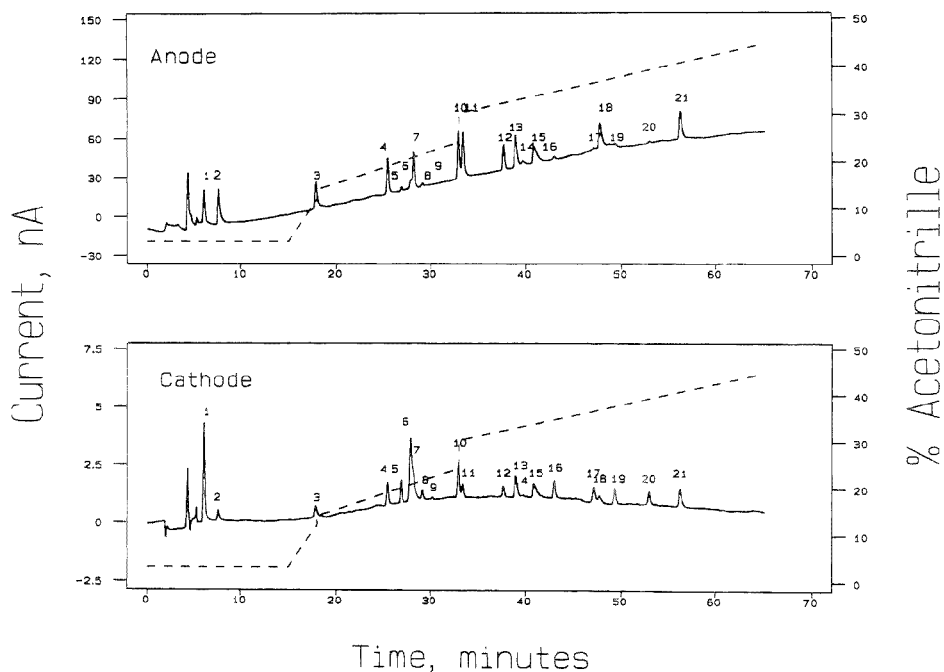


Figure 4. Separation of 23 bioactive peptides using stepwise linear gradient as shown (dotted line). Top is the anode at 0.8 V, and bottom is the cathode at 0.085 V. Parenthetical numbers are the percent collection efficiency. Peaks are 10 pmol each of the following: (1) DSIP and RFDS, (2) RKDVY (1.5), (3) Lys⁸-vasopressin (3.5), (4) leucokinin II (3.4), (5) speract (36), (6) des-Y-Leu-enkephalin (47), (7) oxytocin (4.6), (8) fibrinopeptide A (14), (9) impurity, (10) Leu-enkephalin (4.0), (11) WMDF-NH₂ (1.3), (12) angiotensin II (2.5), (13) ACTH 1-10 (4.4), (14) *N*-f-MLF, (15) neurotensin (4.7), (16) octadecaneuropeptide (30), (17) SPF 6-11, (18) α -Endorphin (1.8), (19) pE⁶-SPF 6-11(44), (20) ALILTLVS (47), and (21) Tyr-somatostatin and HPPGRHF 14-26.

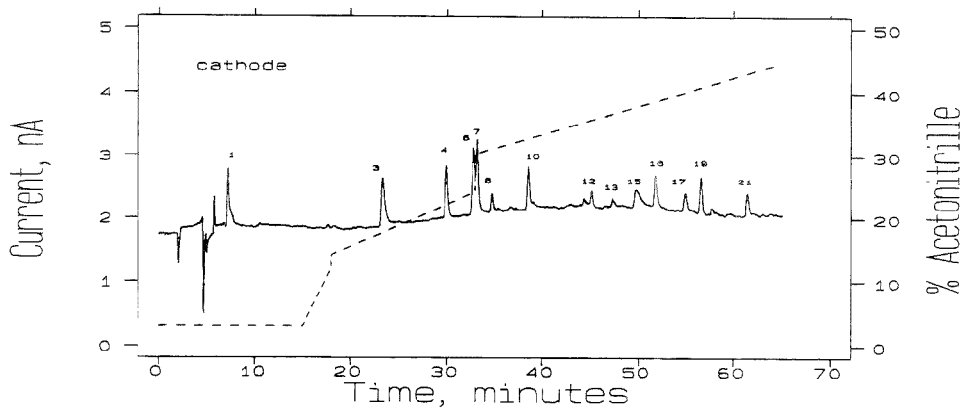


Figure 5. Same as in Figure 4 except it is 5 pmol instead of 10 pmol at 0.5 V anode and 0.1 V cathode. The chromatogram shown is the cathode. Parenthetical numbers are the percent collection efficiency. Peaks: (1) DSIP (23), (3) Lys⁸-vasopressin (15), (4) Leucokinin II (28), (6) des-Y-Leu-enkephalin (41), (7) oxytocin (14), (8) fibrinopeptide A (39), (10) Leu-enkephalin (11), (12) angiotensin II (4.6), (13) ACTH 1-10 (2.4), (15) neurotensin (17), (16) octadecaneuropeptide (35), (17) SPF 6-11 (28), (19) pE⁶-SPF 6-11 (44), and (21) Tyr-somatostatin and HPPGRHF 14-26.

reactor thermostated at 50 °C is recommended for the selective detection of smaller ordinary peptides (up to eight amino acid residues) over larger and N-blocked peptides. Fourth, for larger

ordinary peptides (up to 18 amino acid residues), it is recommended to use a pH 9.5-10 carbonate buffer and a ≥ 1.5 min postcolumn reactor thermostated at ≥ 50 °C. Fifth, use of a pH

> 10 postcolumn phase and a ≥ 1.5 min postcolumn reactor thermostated at ≥ 50 °C is recommended for N-blocked peptides. Sixth, for peptides containing Asp in the third position, it is recommended to use an anodic potential of 0.8 V rather than 0.5 V in addition to the conditions given above for different classes of peptides. Finally, for peptides containing electroactive amino acids, other than the above recommendations for different classes of peptides, it is recommended to use higher postcolumn reactor temperature and to use the anodic signal for better signal-to-noise ratio, but the use of a lower postcolumn temperature and the

cathodic signal is recommended for better selectivity. In addition, we have also noted that the separation works best at 50 °C.

ACKNOWLEDGMENT

We thank the NIH for their financial support through Grant GM-44842.

Received for review May 8, 1995. Accepted June 29, 1995.*

AC9504373

* Abstract published in *Advance ACS Abstracts*, August 15, 1995.

Patterning and Regeneration of Surfaces with Antibodies

David J. Pritchard, Hywel Morgan, and Jonathan M. Cooper*

Bioelectronics Research Centre, Department of Electronics & Electrical Engineering, University of Glasgow, Glasgow, G12 8QQ UK

We describe the application of a new technique for the site-specific immobilization of six different proteins within an area of $200\ \mu\text{m} \times 50\ \mu\text{m}$. The procedure involves coating the surface with deglycosylated avidin, which binds a photoactive biotin analogue, so providing a light-addressable surface onto which proteins can be immobilized. This is the first time that consecutive patterning of a number of different proteins has been described, and we demonstrate this with the fabrication of an immunospot for the qualitative visualization of the binding of multiple antigens. We also show that such a structured surface can be readily regenerated and subsequently repatterned.

Over the last decade, there has been great interest in site-specific deposition of biological molecules and in constructing complex patterns of immobilized biological molecules on surfaces.^{1–5} A central requirement for incorporating different molecules into such structures has been the development of an immobilization method for their selective deposition at designated sites, while preventing their nonspecific binding (NSB) at areas where they are not required. In addition, where patterning of biomolecules exploits their functionality (e.g., molecular recognition through ligand binding), then there has been considerable interest in being able to regenerate the surface.³

Previous methods for patterning proteins have been adapted either from conventional technologies in the printing^{1,2} or in the electronics industries.³ For example, screen printing¹ and ink-jet deposition² have both been used to place proteins at distinct sites. Alternatively, site-specific immobilization of some proteins has been achieved by using photoresists and lift-off techniques.³ Photoactivation and photodeactivation of functionalized surfaces have also been used to select regions where proteins are to be bound.^{4,5} To date, these techniques^{1–5} have suffered from

problems associated with the resolution obtainable, the number of proteins that can be deposited, and/or large amounts of NSB and have not, therefore, proved applicable for use in the formation of complex patterns or in multianalyte sensing for immunodiagnosics.

Recently, we described a process that is capable of immobilizing proteins at micrometer-scale resolution with minimal NSB.⁷ We now demonstrate this technique as a method for the site-specific attachment of six different proteins (including five functional antibodies) within an area of $200 \times 50\ \mu\text{m}$. We also show, for the first time, that such surfaces can be regenerated and subsequently repatterned.

The procedure we use exploits the fact that coating a surface with streptavidin or with deglycosylated forms of avidin will reduce the NSB of proteins.^{7,8} Such a functionalized surface may be used to specifically bind a photoactive ligand of biotin, called photobiotin, providing a light-addressable surface onto which proteins can be immobilized. This can be achieved since the photobiotin we used contains an aryl azide, which is activated with UV light. As a result, a reactive nitrene is formed⁹ which is capable of binding any protein present in the solution above it. Photoactivation of the surface, through a photolithographic mask, can be repeated sequentially using a number of different proteins, forming high-resolution patterns of proteins.

EXPERIMENTAL SECTION

A SiO₂ wafer was silanized with 2% 1,3-(trimethylsilyl)propyl-ethylenediamine in 95% ethanol/5% water for 2 min at room temperature. The wafer was rinsed in 95% ethanol/5% water and heated to 120 °C for 30 min prior to being incubated in 2% glutaraldehyde in phosphate-buffered saline [10 mM phosphate buffer, 2.7 mM KCl, and 137 mM NaCl, pH 7.4 (PBS)] for 15 min at room temperature and then in 0.2 mg mL⁻¹ Neutravidin (Pierce and Warriner, Cheshire, U.K.) in PBS containing 40 mM sodium cyanoborohydride at 4 °C for 16 h. The wafer was then incubated in 0.2 mg mL⁻¹ casein in PBS at room temperature for 1 h and subsequently in 10 μg mL⁻¹ long-arm photobiotin (Vector, Peter-

(1) Hart, J. P.; Wring, S. A. *Electroanalysis* 1994, 6, 617.

(2) Newman, J. D.; Turner, A. P. F.; Marrazza, G. *Anal. Chim. Acta.* 1992, 262, 13.

(3) Nakamoto, S.; Ito, N.; Kuriyama, T.; Kimura, J. *Sens. Actuators* 1988, 13, 165.

(4) Lowe, C. R.; Earley, F. G. P. U.S. Patent 4562157, 1985.

(5) Bhatia, S. K.; Teixeira, J. L.; Anderson, M.; Shriver-Lake, L. C.; Calvert, J. M.; Georger, J. H.; Hickman, J. J.; Dulcey, C. S.; Schoen, P. E.; Ligler, F. S. *Anal. Biochem.* 1993, 209, 197.

(6) Boiteux, J. L.; Biron, M. P.; Desmet, G.; Thomas, D. *Clin. Chem.* 1989, 35, 1026.

(7) Pritchard, D. J.; Morgan, H.; Cooper, J. M. *Angew. Chem., Int. Ed. Engl.* 1995, 34, 91.

(8) Hiller, Y.; Gershoni, J. M.; Bayer, E. A.; Wilchek, M. *Biochem. J.* 1987, 248, 167.

(9) Smith, P. A. S. In *Azides and Nitrenes. Reactivity and Utility*; Scriven, E. F. V., Ed.; Academic Press: London, 1984; pp 95–204.

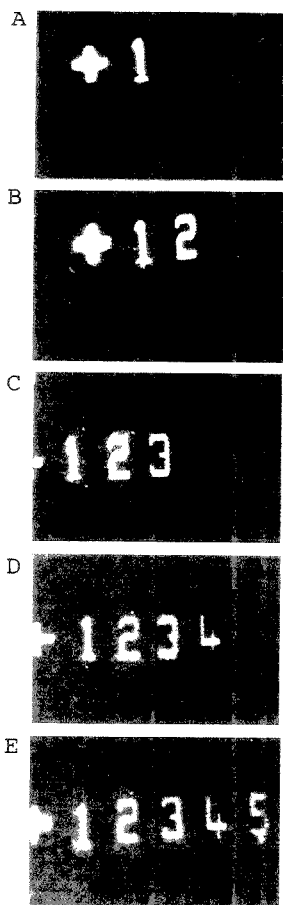


Figure 1. A series of fluorescence micrographs showing the sequential patterning of different antibodies on a SiO_2 surface (see text for details).

borough, UK) in PBS for 20 min in the dark. All reagents, unless otherwise stated were from BDH, (Poole, Dorset, UK) and all proteins were from Sigma (Poole, Dorset, UK).

Five different antibodies were sequentially bound to the surface by selective light activation of distinct areas using a 100 W high-pressure Hg lamp (irradiance, 9 mW cm^{-2}) and a series of five photolithographic masks, each with a common registration mark (+) and a different number between 1 and 5 ($50 \mu\text{m} \times 25 \mu\text{m}$ in size). Light, $\lambda < 300 \text{ nm}$, was removed with a Hoya SL filter. Polyclonal rabbit antibodies ($10 \mu\text{g mL}^{-1}$), raised against chicken, guinea pig, goat, mouse, and rat were patterned, in each case realigning the patterned substrate and the photolithographic mask by means of the registration mark and a CCD camera. Finally, the surface was flood-exposed with light in the presence of 10 mg mL^{-1} casein in PBS, so immobilizing the "blocking" protein at any previously unreacted photobiotin sites. The immunological pattern was developed by performing a heterogeneous sandwich

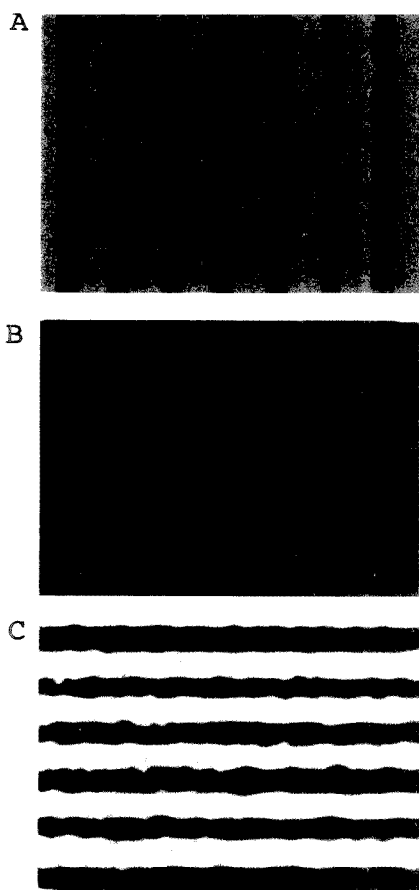


Figure 2. (A) A fluorescence micrograph of a pattern of goat anti-rabbit antibody developed by incubation in the presence of TRITC-labeled rabbit anti-rat. (B) The same functionalized surface as shown in (A), after treatment with guanidine; see text for details. (C) A fluorescence micrograph of the surface in (B) following repatterning using photobiotin immobilization of goat anti-rat antibody and FITC-labeled rat anti rabbit IgG. The mask has been rotated through 90° .

immunospot for visualization¹⁰ using tetramethylrhodamine isothiocyanate- (TRITC-) labeled antibody conjugates. The patterned surface was incubated with a mixture of complementary antigens (IgGs, $10 \mu\text{g mL}^{-1}$ each) of the immobilized antibodies for 1 h and was washed in PBS. Visualization of the protein pattern was achieved by the sequential addition of $10 \mu\text{g/mL}$ TRITC-labeled antispecies IgG antibodies in PBS and examination of the surface using fluorescence microscopy (Nikon Microphot, Nikon UK Ltd., Kingston, Surrey, UK) after the addition of each labeled antibody.

Repatterning (as shown in Figure 2) was achieved by functionalizing the SiO_2 surface with photobiotin, as described above, using a $4 \mu\text{m}$ equal mark-space ratio mask. The surface was

(10) Wood, P. In *Principles and Practice of Immunoassay*; Price, C. P., Newman, D. J., Eds.; Stockton Press: New York, 1991; pp 365-392.

patterned with goat anti-rabbit antibody and subsequently "developed" by incubation in the presence of TRITC-labeled rabbit anti-rat. Following inspection using fluorescence microscopy, the immunological construct was exposed to an aqueous solution of 6.0 M guanidine, pH 1.5, for 16 h at room temperature and reexamined, again using fluorescent microscopy. The treated SiO₂ was then reexposed to photobiotin, and the patterning process was repeated using goat anti-rat and fluorescein isothiocyanate-(FITC-) labeled rat anti-rabbit, with the photolithographic mask rotated through 90°.

RESULTS AND DISCUSSION

Figure 1 shows a sequence of the five individually patterned antibodies and their complementary antigens, as well as casein (a sixth protein). To our knowledge, this is the first example of micropatterning of multiple (>2) proteins. The method involves integrating surface chemistries with biological self-assembly in a fashion that is appropriate for the development of a multianalyte sensing device.

Figure 2A shows an equal mark-space pattern of goat anti-rabbit antibody on an avidin-photobiotin-modified SiO₂ substrate, which has subsequently been "developed" by incubation in the presence of TRITC-labeled rabbit anti-rat. Following treatment with guanidine, no pattern was visible, as shown in Figure 2B. Figure 2C, however, shows that, following a subsequent incubation in a solution of photobiotin, a protein pattern (in this case, immobilized goat anti-rat IgG "developed" with FITC-labeled rat anti-rabbit IgG) can be regenerated on the surface. In this latter case, the mask had been rotated through 90°. From this result,

it is possible to conclude that treatment of the original (TRITC) pattern with guanidine broke the avidin-biotin bond, otherwise repatterning would not have been possible. At low pH in the presence of guanidine hydrochloride (e.g., pH 1.5), there is a full dissociation of the binding complex. At higher pH, the avidin separates into four monomeric subunits and may subsequently unfold depending upon guanidine concentration. The process is, however, further complicated by the number of occupied biotin binding sites.¹¹

We have also demonstrated that patterning and repatterning can be achieved on gold surfaces, so providing potential application of the general technique to electrochemical bioassay.¹² In this latter work (data not shown), the avidin-modified surface was constructed on a thiol monolayer, formed with *N*-acetylcysteine and carbodiimide activation.¹³ The repatterning procedure was carried out, as described above. The fluorophore was situated on the construct sufficiently distant from the gold surface that quenching of the signal was not a problem.¹⁴

In conclusion, this is the first paper describing the micrometer-scale patterning and repatterning of a number of different antibodies. The technique is applicable to device miniaturization, with potential uses in bioassay development and immunodiagnosics. To this end, we have demonstrated the application of these methods to the fabrication of a sensor element for the visualization of an immunospot for different antigens.

ACKNOWLEDGMENT

This work was supported by ESPRIT as Project 7282 (TOPFIT) and Biotechnology and Biosciences Research Council GR/H 31967.

Received for review April 3, 1995. Accepted June 14, 1995.*

AC950324J

* Abstract published in *Advance ACS Abstracts*, August 1, 1995.

(1) Green, N. M. *Adv. Protein Chem.* **1975**, *29*, 85.

(12) Heinemann, W. R.; Halsall, H. B. *Anal. Chem.* **1985**, *57*, 1321A.

(13) Cooper, J. M.; Greenough, K.; McNeil, C. J. *J. Electroanal. Chem.* **1993**, *357*, 267.

(14) Volkenshtcin, M. S. *Biophysics*; Mir Publishers: Moscow, 1983; pp 158-160.

Cisplatin, Transplatin, and Their Hydrated Complexes: Separation and Identification Using Porous Graphitic Carbon and Electrospray Ionization Mass Spectrometry

Hans C. Ehrsson,* Inger B. Wallin, and Anita S. Andersson

Karolinska Pharmacy, P.O. Box 160, S-171 76 Stockholm, Sweden

Per Olof Edlund

Pharmacia AB, Biopharmaceuticals, S-112 87 Stockholm, Sweden

A new liquid chromatographic technique for the separation of the anticancer drug cisplatin, its trans isomer, and their corresponding cytotoxic hydrated complexes is presented. The separation is performed on porous graphitic carbon using an alkaline aqueous phase, where the hydrated complexes are present in their less reactive, uncharged form. The electrospray mass spectrum of cisplatin differed from that of transplatin, giving a sodiated adduct ion. The monohydrated complex of cisplatin showed $[M - H_2O]^-$, M^- , and $[M - H_2O + MeCN]^-$ clusters starting at m/z 263, 281, and 304, respectively, using a solvent mixture containing acetonitrile. The identity of m/z 304 was established by MS/MS.

Cisplatin (Scheme 1) is one of the most important drugs for the treatment of solid tumors, e.g., testicular and ovarian carcinomas. It is generally assumed that cisplatin is present as intact drug in extracellular fluids because of the high chloride concentration.¹ However, the chloride concentration is considerably lower inside the cell, which favors the formation of the hydrated complexes. The monohydrated complex is supposed to be the important cytotoxic species, its effect being mediated by reaction with DNA.²⁻⁴ The hydrated complexes have also been suggested to cause renal toxicity.⁵ Liquid chromatographic analysis of cisplatin has frequently been performed on strong anion-exchange columns or reversed phase columns with a mobile phase containing a lipophilic quaternary ammonium compound (for a review, see ref 6). Isolation of the mono- and dihydrated complexes by liquid chromatography has so far been carried out at low pH, where the complexes are present as cations. Strong cation exchangers⁷⁻⁹ or solvent-generated cation exchangers¹⁰⁻¹² have

in most cases been utilized. The hydrated complexes are highly reactive when protonated, while the corresponding uncharged forms are considerably less reactive.¹³ The aqua complexes react with frequently used mobile phase constituents like acetonitrile and phosphate buffers.^{10,14} The diaqua complex has also been found to interact with sodium perchlorate,¹⁵ usually regarded as a nonreactive salt in this respect.³

In the present study, we have for the first time separated cisplatin and its uncharged hydrated complexes on porous graphitic carbon (PGC) using aqueous sodium hydroxide as a mobile phase. We have also included transplatin and its hydrated complexes, putative impurities in commercial preparations of cisplatin.¹⁶ Furthermore, the identity of the compounds was established by electrospray ionization mass spectrometry.

EXPERIMENTAL SECTION

Chemicals. Cisplatin and transplatin were purchased from Sigma Chemical Co. (St. Louis, MO). Solutions containing *cis*- and *trans*-diammineaquachloroplatinum(II) ion were prepared from a hydrolysis equilibrium obtained by dissolving *cis*- and *trans*platin in distilled water (1 mM). The solution was left at room temperature and protected from light for 24 h. *cis*- and *trans*-diamminedihydroxoplatinum(II) were prepared by hydrolysis of *cis*- and *trans*platin (0.2-1 mM) in 0.003 M NaOH for 24 h at room temperature (protected from light).

Apparatus. The LC system consisted of a Valco Model C6W injector (Houston, TX) with a fixed loop volume of 100 μ L, a Kontron Model 420 pump (Rotkreuz, Switzerland), and an LDC Spectromonitor III photometric detector. The wavelength monitored was 283 nm. The platinum complexes were separated on a Hypercarb S (particle size, 7 μ m) column 100 \times 4.6 mm i.d. (Shandon, Runcorn, U.K.). The mobile phase was 0.001 M NaOH, with a flow rate of 0.5 mL/min. The analysis was carried out at 20 $^{\circ}$ C (room temperature) and at 0 $^{\circ}$ C (mobile phase and column

(1) Rosenberg, B. *Cancer Treat. Rep.* 1979, 63, 1433-1438.

(2) Johnson, N. P.; Hoeschele, J. D.; Rahn, R. O. *Chem. Biol. Interact.* 1980, 30, 151-169.

(3) Knox, R. J.; Friedlos, F.; Lydall, D. A.; Roberts, J. J. *Cancer Res.* 1986, 46, 1972-1979.

(4) Bancroft, D. P.; Lepre, C. A.; Lippard, S. J. *J. Am. Chem. Soc.* 1990, 112, 6860-6871.

(5) Daley-Yates, P. T.; McBrien, D. C. H. *Biochem. Pharmacol.* 1984, 33, 3063-3070.

(6) De Waal, W. A. J.; Maessen, F. J. M. J.; Kraak, J. C. J. *J. Pharm. Biomed. Anal.* 1990, 8, 1-30.

(7) Salfenstein, R.; Daye, M.; Guttenplan, J. B. *Cancer Lett.* 1983, 18, 329-338.

(8) Gonnet, F.; Lemaire, D.; Kozelka, J.; Choutard, J. C. *J. Chromatogr.* 1993, 648, 279-282.

(9) Andersson, A.; Ehrsson, H. *J. Chromatogr. B* 1994, 652, 203-210.

(10) De Waal, W. A. J.; Maessen, F. J. M. J.; Kraak, J. C. J. *J. Chromatogr.* 1987, 407, 253-272.

(11) Mistry, P.; Lee, C.; McBrien, D. C. H. *Cancer Chemother. Pharmacol.* 1989, 24, 73-79.

(12) Macka, M.; Borak, J.; Kiss, F. *J. Chromatogr.* 1991, 556, 291-295.

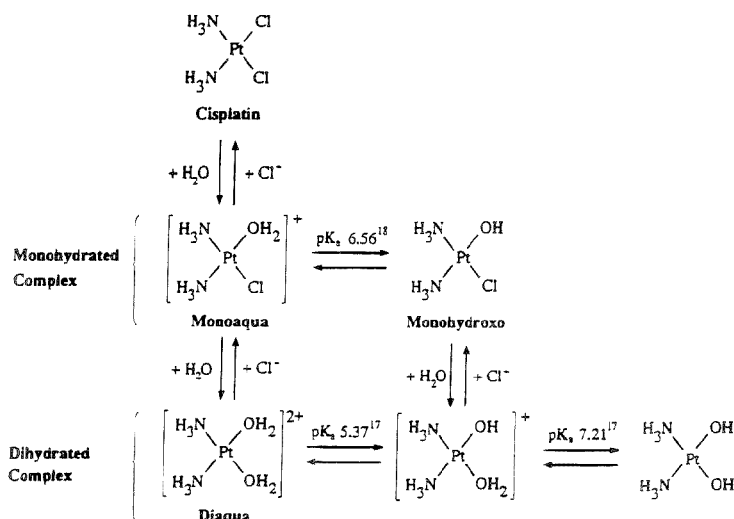
(13) Lim, M. C.; Martin, R. B. *J. Inorg. Nucl. Chem.* 1976, 35, 1911-1914.

(14) Segal, E.; Le Pecq, J. B. *Cancer Res.* 1985, 45, 492-498.

(15) Vrana, O.; Kleinwächter, V.; Brabec, V. *Experientia* 1984, 40, 446-451.

(16) Arpalahii, J.; Lippert, B. *Inorg. Chim. Acta* 1987, 138, 171-173.

Scheme 1^a



^a pK_a values from refs 17 and 18.

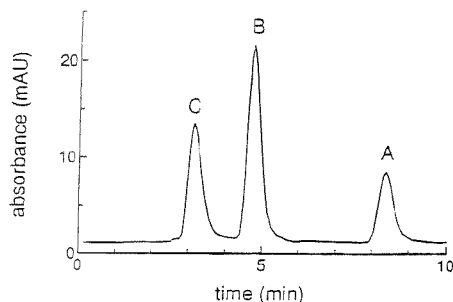


Figure 1. Chromatogram of cisplatin (A) and its mono- (B) and dihydrated (C) complexes. The mixture was prepared by adding cis-diamminedihydroxoplatinum(II) in 0.001 M NaOH to a hydrolysis equilibrium solution of cisplatin in distilled water. The concentrations were (A) 0.2, (B) 0.5, and (C) 0.3 mM. Column temperature, 0 °C.

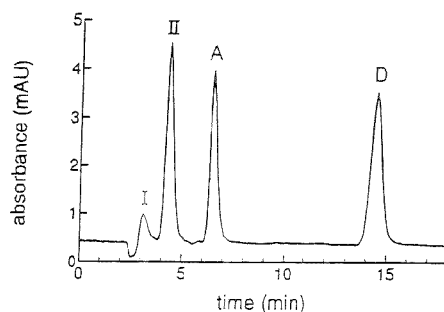


Figure 2. Chromatogram of cis- (A) and transplatin (D). I and II represent di- and monohydrated complexes, respectively. Initial concentrations: cisplatin, 0.1 mM; transplatin, 0.25 mM. Column temperature, 20 °C.

placed in an ice bath). The void volume of the system was determined by the front disturbance in the chromatograms on injection of water.

Electrospray mass spectra were obtained using a Quattro triple quadrupole instrument from Fison Instruments (Altrincham, U.K.). Cisplatin, transplatin, and the hydrated complexes were isolated using the liquid chromatographic conditions described above and collecting narrow fractions of the apex of the peaks (final concentration, 50–500 μM). The solutions were mixed with an equal volume of acetonitrile containing 0.5% acetic acid and injected by a 20 μL loop injector into a carrier stream of 1:1 acetonitrile–acetic acid (0.02% in water), with a flow of 10 $\mu\text{L}/\text{min}$. The spectrum of cis-diamminedihydroxoplatinum(II) was also obtained after dilution of the chromatographic effluent with methanol and using a carrier stream of methanol. The spectra were recorded by accumulation of 6–8 scans at unit mass resolution in the mass range of 10–500 m/z . The ion source was

Table 1. Influence of Temperature (T , °C) on the Capacity Factors

T	k'_{cisPt}	k'_{transPt}	$k'_{\text{mono-cis}}$	$k'_{\text{mono-trans}}$	$k'_{\text{di-cis}}$	$k'_{\text{di-trans}}$
20	1.88	5.48	0.89	0.95	0.39	0.40
0	2.48	8.24	0.97	1.09	0.31	0.33

tuned using the sodiated ion of cisplatin, giving the best response at conditions typical for low in-source fragmentation with a sampling cone voltage between 19 and 40 V. Daughter ion spectra were recorded after collision-induced fragmentation with argon at a cell pressure of 0.2 μbar and a collision energy of 80 eV.

RESULTS AND DISCUSSION

This study shows that cisplatin, transplatin, and their corresponding hydrated complexes can be separated on PGC with a strongly alkaline (0.001 M NaOH) mobile aqueous phase, where

Table 2. Influence of Temperature (T , °C) on the Resolution between the Mono- and Dihydrated Complexes of Cis- and Transplatin

T	R_s mono/di(cis)	R_s mono/di(trans)
20	1.50	1.72
0	2.07	2.48

Table 3. Theoretical Isotopic Distribution in Molecules Containing $PtCl_n$, Given as Relative Abundance, Where $n = 0, 1, \text{ or } 2$

	A^n	$A+1$	$A+2$	$A+3$	$A+4$	$A+5$	$A+6$	$A+7$	$A+8$
Pt	97	100	75	30	21	0	0	0	0
PtCl	92	94	100	30	43	0	6	0	0
PtCl ₂	71	73	100	47	58	7	16	0	2

^a Corresponds to the isotope ¹⁹⁴Pt.

the hydrated complexes are present in a less reactive, uncharged form (Scheme 1).^{17,18} A chromatogram illustrating the separation of cisplatin and its corresponding mono- and dihydrated complexes is given in Figure 1. It can be calculated that <1% of the monohydrated complex is converted to the dihydrated complex during the chromatographic run (25 °C) using the rate constants given in ref 19. Hence, it is possible to isolate the pure monohydrated complex, supposed to be the ultimate cytotoxic agent of cisplatin, from an equilibrium mixture of cisplatin in distilled water for subsequent use in *in vitro* and *in vivo* studies. Cisplatin has a planar structure and is highly polar.²⁰ PGC has previously been found to strongly interact with planar structures by dispersion and charge transfer interactions.^{21,22} The excellent separation of cis- and transplatin is illustrated in Figure 2. The shorter retention of cisplatin as compared to transplatin is most probably attributed to its dipolar character. The capacity factors increased for cis- and transplatin when the analysis was carried out at 0 °C as compared to room temperature (Table 1), while the capacity factors for the hydrated complexes were virtually unaffected. However, the resolution between the mono- and dihydrated complexes was improved at the lower temperature (Table 2). A similar effect on resolution has previously been observed on pyrocarbon containing supports²³ and on PGC.²⁴

Previous mass spectrometric studies of platinum-containing compounds involve ionization by electron impact,^{25,26} fast atom bombardment,^{27,28} field desorption,²⁹ laser desorption,³⁰ and ²⁵²Cf

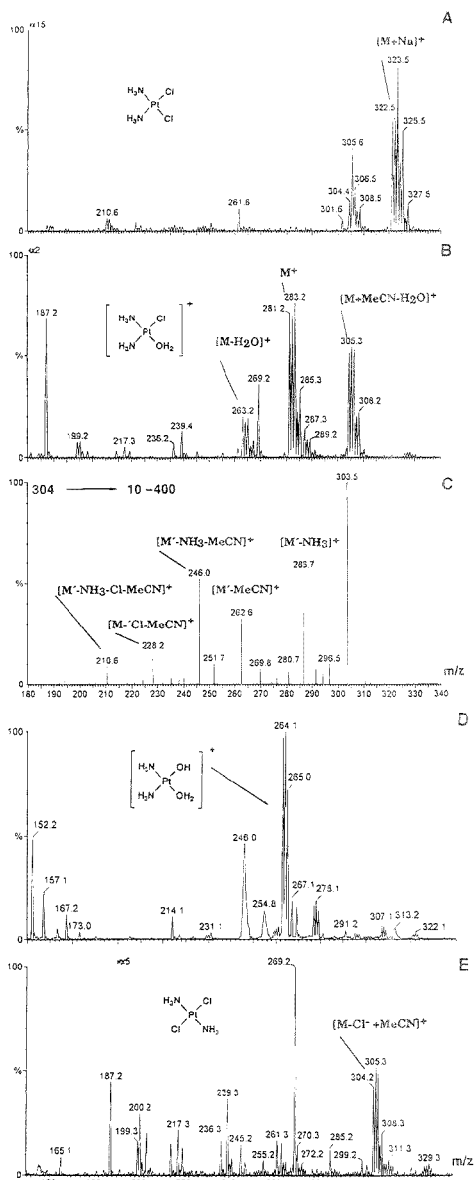


Figure 3. Electro spray mass spectra of cisplatin (A) and the monohydrated complex of cisplatin (B), together with daughter ion mass spectra of m/z 304 produced from the monohydrated complex of cisplatin (C), the dihydrated complex of cisplatin (D), and transplatin (E). Spectra A, B, and E were obtained using water–acetonitrile–acetic acid; spectrum D was obtained using water–methanol–sodium hydroxide.

plasma desorption.¹⁸ Electro spray is one of the softest ionization techniques available for nonvolatile and thermally unstable compounds, e.g., cisplatin, iproplatin, and tetraplatin.³¹ Electro spray

- (17) Berners-Price, S. J.; Frenkiel, T. A.; Frey, U.; Ranford, J. D.; Sadler, P. J. *J. Chem. Soc., Chem. Commun.* **1992**, 789–791.
- (18) Andersson, A.; Hedennalm, H.; Elfsson, B.; Ehrsson, H. *J. Pharm. Sci.* **1994**, *83*, 859–862.
- (19) Miller, S. E.; House, D. A. *Inorg. Chim. Acta* **1989**, *166*, 189–197.
- (20) Soucard, J. P.; Ha, T. T. B.; Cros, S.; Johnson, N. P. *J. Med. Chem.* **1991**, *34*, 863–864.
- (21) Bassler, B. J.; Kaliszan, R.; Hartwick, R. A. *J. Chromatogr.* **1989**, *461*, 139–147.
- (22) Tanaka, N.; Kimata, K.; Hosoya, K.; Miyayoshi, H.; Araki, T. *J. Chromatogr. A* **1993**, *656*, 265–287.
- (23) Colin, H.; Diez-Masa, J. C.; Guiochon, G.; Czajkowska, T.; Miedziank, I. *J. Chromatogr.* **1978**, *167*, 41–65.
- (24) Stefansson, M.; Hoffman, K. J. *Chirality* **1992**, *4*, 509–514.
- (25) Haake, P.; Mastin, S. H. *J. Am. Chem. Soc.* **1971**, *93*, 6823–6828.
- (26) Weller, R. R.; Eyer, J. R.; Riley, C. M. *J. Pharm. Biomed. Anal.* **1985**, *3*, 87–94.
- (27) Siegel, M. M.; Biha, P.; Child, R. G.; Hlavka, J. J.; Lin, Y.; Chang, T. T. *Biomed. Environ. Mass Spectrom.* **1986**, *13*, 25–32.

mass spectrometry was used in the present work to confirm the identity of the hydrated forms of cisplatin and to compare the mass spectra of cis- and transplatin. Electrospray ionization usually gives ions that reflect the analyte ions present in the solution infused to the interface, while analytes without protolytic properties can be detected as adducts with alkali metal salts or ammonia.³² Ion evaporation is thought to be the most important ionization mechanism during ESI, but gas phase reactions must also be considered. The analytes are declustered by low-energy collisions with gas molecules in the intermediate pressure region of the ES source and adduct ions in the solvent, or fragment ions can be formed, depending on the experimental conditions.

Cisplatin gave a sodiated adduct ion $[M + Na]^+$ (Figure 3A) showing an isotope cluster starting at m/z 321, with the distribution 67:68:100:41:60:7:12:1:3. This isotope pattern is in excellent agreement with the theoretical values given in Table 3 for an ion containing one Pt and two Cl substituents. In contrast to cisplatin, the spectrum of transplatin (Figure 3E) does not show the $[M + Na]^+$ ion. The monohydrated complex of cisplatin shows $[M - H_2O]^+$, M^+ and $[M - H_2O + MeCN]^+$ clusters (Figure 3B), starting at m/z 263, 281, and 304, respectively. Collision-induced dissociation of the ion at m/z 304 by MS/MS was performed to

confirm the adduct with acetonitrile (Figure 3C). Daughter ions were found at m/z 287, 263, 246, 228, and 211, and the proposed structures of the fragment ions are given. The dihydrated complex showed no M^{2+} ion (m/z 132) but did show another doubly charged ion at m/z 155, corresponding to the substitution of both aqua groups with acetonitrile. The charge state at m/z 155 was assigned to 2 since the isotope peaks were 0.5 Da apart (data not shown). The $[M + H]^+$ ion at m/z 263 was detected when the same sample was diluted with methanol instead of acidified acetonitrile (Figure 3D), showing the isotope cluster expected for an ion consisting of one Pt atom. Good sensitivity was obtained when the samples were infused in a water-acetonitrile mixture acidified with acetic acid, but fewer gas-phase reactions occurred at slightly alkaline conditions (0.5 mM NaOH) with methanol as the organic modifier. A careful tuning of the kinetic energy of the analyte ions within the ion source (cone voltage) was important in order to be able to produce a spectrum of the hydrated Pt complexes.

In conclusion, it has been shown that cisplatin, transplatin, and their hydrated complexes can be separated on porous graphitic carbon using an alkaline mobile phase. Furthermore, the importance of electrospray mass spectrometry in the structure elucidation of these platinum-containing compounds has been demonstrated.

Received for review January 25, 1995. Accepted July 12, 1995.*

AC9500904

* Abstract published in *Advance ACS Abstracts*, September 1, 1995.

- (28) Claereboudt, J.; De Spiegeleer, B.; Lippert, B.; De Bruijn, E. A.; Claeys, M. *Spectrosc. Int. J.* **1989**, *7*, 91-112.
(29) Dalietos, D.; Furst, A.; Theodoropoulos, D.; Lee, T. D. *Int. J. Mass Spectrom. Ion Processes* **1984**, *61*, 141-148.
(30) Claereboudt, J.; De Spiegeleer, B.; De Bruijn, E. A.; Gijbels, R.; Claeys, M. *J. Pharm. Biomed. Anal.* **1989**, *7*, 1599-1610.
(31) Poon, G. K.; Mistry, P.; Lewis, S. *Biol. Mass Spectrom.* **1991**, *20*, 687-692.
(32) Kebaric, P.; Tang, L. *Anal. Chem.* **1993**, *65*, 972A-986A.

Author Index

- Abramova, N., 3589
Alegret, S., 3589
Amatore, C., 3382
Andersson, A. S., 3608
Arbault, S., 3382
- Bai, J., 3482
Bai, S., 3433
Bartrófi, J., 3589
Biesuz, R., 3558
Bratov, A., 3589
Brumley, R. L., Jr., 3405
Buxton, E. C., 3405
- Carless, H. A. J., 3401
Chen, D., 3405
Chen, J.-G., 3596
Chung, M.-J., 3571
Cooper, J. M., 3605
Cravens, E., 3541
- Davison, W., 3391
Deinzer, M. L., 3476
Dominguez, C., 3589
Dowrey, A. E., 3377
- Edlund, P. O., 3608
Ehrsson, H. C., 3608
Eichinger, P. C. H., 3476
- Farrant, R. D., 3401
Feng, Z. Q., 3564
Fingas, M., 3491
- Gavaghan, C., 3401
Gerhart, B. B., 3536
Giddings, M. C., 3405
Glunz, L., 3550
Gomez, F. A., 3526
Gorshkov, M. V., 3412
Grant, D. M., 3433
- Halsall, H. B., 3578
Hansen, B. N., 3541
Hansen, K. J., 3541
Harrata, A. K., 3515
- Harris, J. M., 3441
Heineman, W. R., 3578
Hindsgaul, O., 3509
- Jankowski, J. A., 3382
Jorgenson, J. W., 3448, 3456, 3464
- Köhler, M., 3501
Kouzes, R. T., 3412
Kuhr, W. G., 3583
- Landriault, M., 3491
Laramée, J. A., 3476
Leary, J. A., 3501
Lee, C. S., 3515
Levin, I. W., 3377
Lewis, E. N., 3377
Li, L., 3509
Liang, X., 3482
Lindon, J. C., 3401
Liu, H., 3550
Liu, Y.-H., 3482
Lubman, D. M., 3482
- Mammen, M., 3526
Marcott, C., 3377
Mayne, C. L., 3433
Mazurkiewicz, P., 3476
Moore, A. W., Jr., 3448, 3456, 3464
Morgan, H., 3605
Muñoz, J., 3589
- Nakagawa, T., 3520
Nicholson, J. K., 3401
Niki, K., 3564
Nowall, W. B., 3583
- Ohara, T., 3520
Oldenburg, K. E., 3421
Ong, S., 3550
- Palcic, M. M., 3509
Pantano, P., 3382
Pesavento, M., 3558
- Peterson, M. D., 3405
Pidgeon, C., 3550
Pritchard, D. J., 3605
Pugmire, R. J., 3433
- Reeder, R. C., 3377
Ren, F. Y., 3441
Ridgway, T. H., 3578
- Sagara, T., 3564
Shibukawa, A., 3520
Sidelmann, U. G., 3401
Sievers, R. E., 3541
Sigouin, L., 3491
Smith, L., 3405
Smith, L. M., 3405
Smith, P. B., 3536
Soper, S. A., 3427
Story, G. M., 3377
Sweedler, J. V., 3421
- Tang, Q., 3515
Timperman, A. T., 3421
Treado, P. J., 3377
- Venta, P. J., 3482
Vuillaume, M., 3382
- Waite, S. W., 3441
Wallin, I. B., 3608
Wang, F. C.-Y., 3536
Wang, Z., 3491
Weber, S. G., 3596
Westphall, M., 3405
Whitesides, G. M., 3526
Whittal, R. M., 3509
Williams, D. C., 3427
Wilson, I. D., 3401
Wittstock, G., 3578
- Xu, N., 3491
- Yu, K., 3578
- Zen, J.-M., 3571
Zhang, H., 3391

BOTTOM LINE:

The more you read the higher you go.

Success for your company and your career means having the right information at the right time. And that's where *C&EN* comes in.

Week after week, *C&EN* delivers up-to-the minute news on every aspect of the chemical enterprise, from business to government, and research to education. Plus, you get an in-depth reporting of trends that puts it all in perspective.

You'll find practical information that enhances day-to-day business dealings, as well as long-range planning — information you can use to hold a competitive edge.

There's only one sure way to get the comprehensive chemistry news you need. Reading *C&EN* puts you on top. For subscription information, call toll-free:

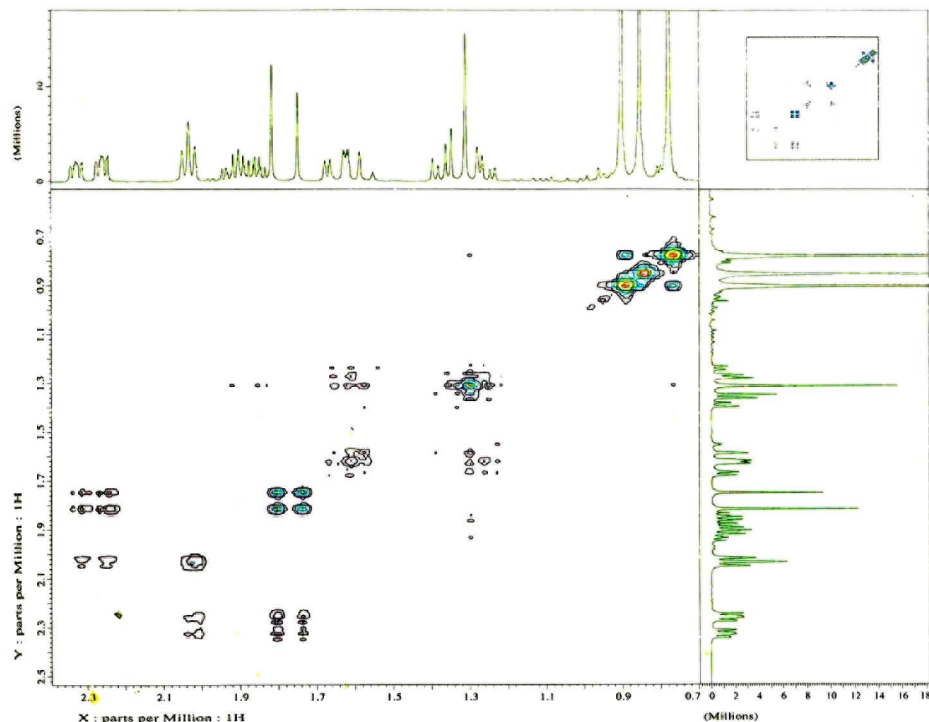
1-800-333-9511.

Success for your company and your career.



CHEMICAL & ENGINEERING NEWS
C&EN

ECLIPSE NMR Advantage: Gradient Enhanced 2D NMR Spectroscopy



The Better Way!

The ECLIPSE NMR Spectrometer from JEOL USA just increased your productivity. In less than one half of the 40 minutes usually required to complete the COSY, you can be back in your laboratory with proton, carbon and the COSY data. With JEOL's new low cost Matrix Gradients, this Double Quantum Filtered COSY

data was completed in less than 3 minutes. The ECLIPSE now expands the usual routine beyond the normal one dimensional proton survey spectrum to include the power of two dimensional NMR.

Now you can use the ECLIPSE NMR Advantage to your advantage.

JEOL USA, Inc.
11 Dearborn Road
Peabody, MA 01960
Tel: 508/535-5900
FAX: 508/536-2205
EMAIL: NMR@JEOL.COM



CIRCLE 7 ON READER SERVICE CARD